RAPIDITY DENSITY FLUCTUATIONS IN HADRON-NUCLEUS INTERACTIONS: SPIKES, INTERMITTENCY, AND FRACTAL PROPERTIES OF MULTIPLE PRODUCTION IN Ag, Au, AND Mg TARGETS WITH p, $\bar{p}$, π^+, AND π^- PROJECTILES AT 100 AND 320 GeV/c

A Dissertation

Submitted to the Graduate School of the
University of Notre Dame
in Partial Fulfillment of the Requirements for the Degree

Doctor of Philosophy

by

Margarita Claudia Krieghoff Mattingly, B.A., M.A.

William D. Shephard, Director

Department of Physics
Notre Dame, Indiana 46556

April, 1991

RAPIDITY DENSITY FLUCTUATIONS IN HADRON-NUCLEUS INTERACTIONS: SPIKES, INTERMITTENCY, AND FRACTAL PROPERTIES OF MULTIPLE PRODUCTION IN Ag, Au, AND Mg TARGETS WITH p, $\bar{p}$, π^+, AND π^- PROJECTILES AT 100 AND 320 GeV/c

Abstract

by

Margarita Claudia Krieghoff Mattingly

The space-time development of hadron-nucleus interactions is examined using bubble chamber and downstream particle identifier data from the hybrid spectrometer of Fermilab experiment E597. 5583 events representing 12 interactions are studied with conventional and fractal techniques. Comparisons are made to simulated events from the Lund Monte Carlo FRITIOF 1.6. Multiplicities are studied conventionally. Negative binomial descriptions of produced particle multiplicities are interpreted in terms of clusters and cascading and in terms of partial stimulated emission; forward-backward correlations, in terms of short- and long-range correlations and multiple scattering. Multiplicities are consistent with a multiple collision view of multiparticle production mechanisms and are investigated in terms of the number of collisions ν. Rapidity density fluctuations are studied fractally. The possibility of new dynamics is considered on the basis of event-by-event studies of spike phenomena, intermittency, and fractal dimensions. Results from these exploratory studies are consistent with predictions made for quark-gluon plasma transitions. 131 spike events are analyzed; intermittency is investigated with normalized factorial moments and cumulants; and fractal dimensions and correlations dimensions are calculated. Seagull effects and production region sizes from Bose-Einstein pion interferometry are also considered.

To my husband,

KEITH EDWARD KRIEGHOFF MATTINGLY,

for resonant companionship and joy;

my father,

CLAUDIO KRIEGHOFF,

for unyielding confidence and courage.

and my mother,

GERTRUD MARTHA SCHMIDT KRIEGHOFF,

for unfailing vision and dedication;

my daughter,

CLAUDINE YVETTE KRIEGHOFF MATTINGLY,

for bold creativity and resourceful caring;

and my son,

SEAN ELLIOTT KRIEGHOFF MATTINGLY,

for making high energy a family tradition.

TABLE OF CONTENTS

LIST OF TABLES

NDBC AND NDBASIC COORDINATES

FNAL E597 SPECTROMETER

MULTIPLICITY CORRECTIONS

LIST OF FIGURES

MULTIPLE COLLISIONS

SPIKES

INTERMITTENCY

NDBC AND NDBASIC COORDINATES

FNAL E597 SPECTROMETER

MULTIPLICITY CORRECTIONS

ACKNOWLEDGEMENTS

High energy physics being the community effort that it is, there are a number of individuals whose direct contributions to this dissertation should be recognized.

At the University of Notre Dame:

James Bishop for efficiently and creatively managing the computer system of the Notre Dame high energy group, and for facilitating its use to me personally by always being a willing and able problem solver.

Kathleen DeLanghe for coordinating the Notre Dame measurement of bubble chamber film images, for doing the ionization scan that identified particles, and for sharing cheer, encouragement, and her office.

William Shephard for incorporating me into the E597 Collaboration and serving as my advisor.

At the Pennsylvania State University:

James Whitmore for his leadership as spokesperson of the E597 Collaboration and unofficial mentor to its graduate students.

Bill Toothacker for his tenacious perseverence in hooking up the bubble chamber data with the downstream particle identifier.

Ray Lewis for his role in supervising the setup and running of the experiment and for teaching many of us the ropes about hardware.

At Cambridge University:

Patrick Elcombe for his tireless software development and aggressive involvement in successfully running the experiment.

John Hill for supervising the Cambridge measurement of bubble chamber film images, folding in the downstream particle identifier data, and producing data summary tapes.

At Fermilab:

Lou Voyvodic for his broad-based knowledge and continued interest in multiparticle production and for the optimistic enthusiasm that surrounds him.

At Lebedev Institute:

Igor Dremin for introducing me to the possibilities of fractal analysis.

At Andrews University:

Robert Kingman for willingly assuming extra responsibilities to release me time for study and research.

CHAPTER 1

INTRODUCTION

The analysis of rapidity density fluctuations in terms of the notions of density spikes, intermittency, and fractal measures is expected to discriminate between leading models of multiple production such as dual parton and cluster cascade models [Peschanski 87]. This study pursues a number of traditional avenues in order to better describe and understand multiple production. These include multiplicity moments, negative binomial descriptions, the proton multiplicity dependence of particle production, forward-backward correlations, and two-particle correlations. However, these as yet have individually and collectively failed to rule out any of the leading models. With the anticipation of SSC and nuclear collider high statistics data in the near future, this serious shortcoming becomes increasingly detrimental and makes the success of a fresh approach all the more important. Thus this study also includes an investigation of fluctuation non-linearities.

The apparent involvement of more than one process in multiple production complicates an already difficult many-body problem. With most studies necessarily limited to average behavior, the signatures of individual processes are smeared out. Intermittency and fractal structure studies, however, rely on the mathematics of deterministic chaos to preserve the signature of interwoven mechanisms. The self-similar, repeating patterns characteristic to intermittency and fractal structure suggest cascade processes over various scales whose superposed iterations can be studied without sacrificing features unique to each. These patterns, found among the fluctuations of produced particle rapidity distributions, may not only rule out one of the leading multiple production models but derive fundamental, mathematically-driven insight

from the chaos of concurrent multiple production mechanisms.

The most extreme rapidity density fluctuations, known as *spikes*, are a first step into non-linear descriptions of multiparticle production. They are also a unique testing ground for subsequent studies in intermittency and fractal structure. The possibilities for quark-gluon plasma (QGP) formation at high rapidity densities add interest to the *new physics* potential of these *spike* events [Van Hove 84; Gyulassy 84]. Enhanced intermittency in these anomalous events opens a new dimension, a fractal one, to the study of multiple production in general. In concert with the universal multiplicity dependence of spikes and the *ring* distributions of their constituent particles, unique fractal features in spike events may be signaling QGP in the context of Cerenkov gluon radiation [Dremin 87] in addition to mechanisms producing Bose-Einstein correlations [Ajinenko 89], matter density structure [Dias de Deus 87], cascades [Bialas 86a], and mini-jet production with its semi-hard parton-parton collisions and gluon bremsstrahlung [Navelet 85]. It could be heralding the advent of new physics.

But rapidity density fluctuations in normal events could also be displaying non-linear features. One of these, *intermittency*, clearly contrasts with homogeneous, statistically fluctuating features. The difference has been attributed to the power-law scaling which characterizes the factorial moments of rapidity distributions as they are calculated as functions of rapidity resolution [Bialas 86b]. Dual parton models (DPM) with their multi-chain mechanisms do not generally reproduce intermittency [Peschanski 87] while models like FRITIOF which use cluster cascading mechanisms do. Experimental evidence for intermittency thus favors cascade models over simple DPM models.

The study of *fractal* structure builds on this evidence with an event-by-event analysis technique. Based on the recently revived mathematics of fractals [Mandelbrot 77], interactions are categorized according to various dimensions [Paladin 87]. Non-integer values for these dimensions distinguish fractal geometries and thus point out self-similar properties.

Since rapidity density spikes, intermittency, and fractal dimensions are all

notions of fluctuation, scale, and power-laws [Bialas 86b, 88], they are expected to be interrelated. Intermittency is expected to become larger at smaller dimensions [Dremin 89b] and spike events are expected to display a smaller dimension than the average. Neither of these expectations have been previously confirmed.

1.1 MULTIPLE PRODUCTION

The term *multiparticle production* in this study refers to the production of hadrons in reactions of the form

$$a + b \rightarrow h_1 + h_2 + \cdots + h_N$$

with the number of hadrons N greater than the number of hadron reactants. Interactions which produce hadrons may be as simple as electron-positron annihilation (e^+e^-), a basic point-point collision; or as complex as a heavy ion collision (AA), a nucleus-nucleus interaction which involves two extended bodies, structures of extended particles which in turn are composites of point-like particles. Between these two extremes, lepton-hadron (ℓh), hadron-hadron (hh), and hadron-nucleus (hA) interactions present intermediate scales and levels of complexity. Adequate theories of multiple production should consistently cover all five interaction types: e^+e^-, ℓh, hh, hA, and AA. The hA interactions

$$h_{beam} + A \rightarrow h_1 + h_2 + \cdots + h_N$$

play a pivotal role in understanding and linking the others. The extrapolation from hh to hA is particularly critical. But where this extrapolation might be expected to introduce a hopeless level of complexity, hA interactions are not unmanageable and the additional level of structure serves as an intra-nuclear detection device.

1.1.1 Hard vs. soft collisions

The *hardness* of a collision depends on its associated momentum transfer. Large momentum transfers can often be selected on the basis of transverse momentum transfer. Hardness here is defined relative to 1 GeV/c transverse momentum exchanges. In

phase space *hard* interaction products populate regions where $p_\perp$ is greater than 1 GeV/c while *soft* ones exclusively populate regions where $p_\perp$ is less than 1 GeV/c. Thus soft interactions can be considered to occur at larger interaction distances than hard ones.

Multiparticle production is presumed to involve at least two(2) steps—1) a color field excitation, and 2) the hadronization of quarks and gluons. These may involve both hard and soft processes. While *hard* processes are the production mechanisms in identifiably hard or high-$p_\perp$ interactions seen in e^+e^- and ℓh interactions, *soft* processes are the hadronization mechanisms which are most obvious in soft hh, hA, and AA interactions. Hard processes are presumed to form a significant component in all soft interactions. In seagull plots of mean transverse energy as a function of Feynman x, hardness is gauged by the extent to which the *wings* are lifted. The wings of such plots lift higher for harder events like e^+e^-, but softer interactions like hh and hA still show the lifted trend. Bose-Einstein correlations can be used to determine whether these hard and/or soft processes represent coherent and/or incoherent sources. It is reasonable to expect that coherent and incoherent sources are mixed.

Highly collimated along the collision axis in a kind of low-$p_\perp$ jet, soft interactions may be subdivided into five(5) categories of longitudinal momentum in the center of mass system: target diffraction dissociation, target fragmentation, central, beam fragmentation, and beam diffraction dissociation regions. Soft, central processes dominate multiparticle hadron physics even at large energies. One of the most fundamental properties of multiparticle production is the minimal increase of mean $p_\perp$ which accompanies significant increases in mean $p_{||}$. With data from FNAL E597, on which the present study is based, **Figure 1.1.1** illustrates how hA interaction products populate phase space almost exclusively in the soft collision regions: proton secondaries in the target regions, and produced particles (protons and electrons excluded) predominantly in the central region. Comparing E597 results to existing hh data, **Figure 1.1.2** shows how the average transverse momentum $\langle p_\perp \rangle$ is somewhat higher for hA yet remains under .4 GeV/c for beam momenta of 100 and 320 GeV/c. In the full range of E597 targets, $p_\perp$ averages do not vary more than .02 GeV/c for

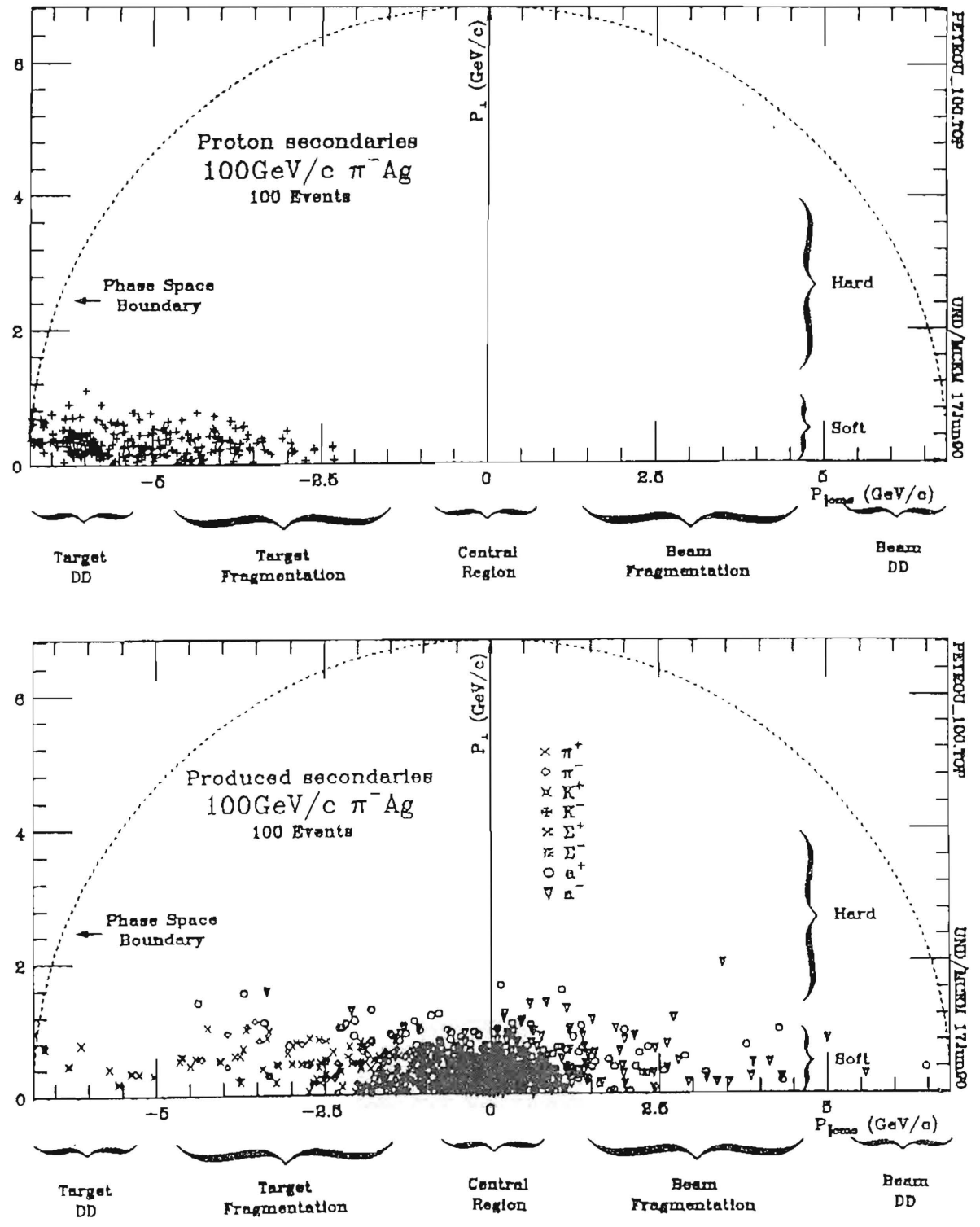

Figure 1.1.1 Peyrou plot for a) produced particle, and b) proton secondaries in a random sample of 100 $\pi^- Ag$ events at 100 GeV/c. The transverse momentum $p_\perp$ is noticably small in comparison with the longitudinal momentum $p_\parallel$ as is characteristic of all hA events.

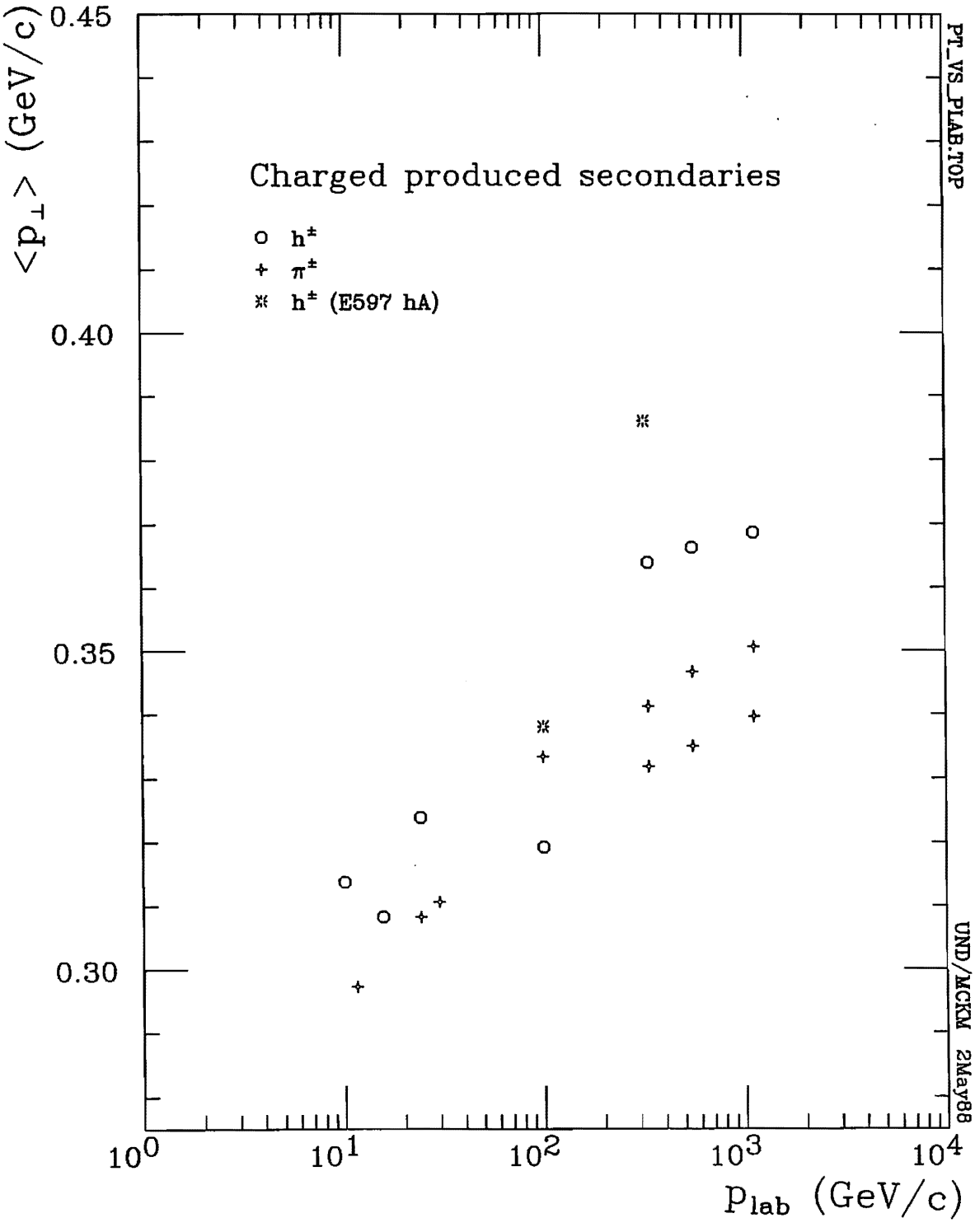

Figure 1.1.2 Average transverse momentum $< p_\perp >$ of charged produced particles as a function of the beam momentum p_{bm}^{lab} for hh and hA interactions. Though larger for hA in comparison with hh interactions, and for higher energy interactions, the average transverse momentum stays below .4 GeV/c in all cases.

any given beam charge as shown in **Figure 1.1.3.**

Learning what the *soft* dynamics really are is crucial to understanding multiple production. But neither the interaction mechanism nor the structure of its associated color field is understood. No real theory for soft hadron production exists. Hard processes are handled quite well in QCD since distances are small and perturbative techniques are valid. QCD reliably describes the evolution of high-$p_\perp$ jets in conjunction with some tuned hadronization models. But at larger distances, perturbative techniques are no longer valid and low-$p_\perp$ spectator jets are not described very well. Non-perturbative QCD is expected to hold for the soft component, but all efforts have been unable to unfold the soft and hard into a complete theory of multiparticle production. Instead, soft and hard interactions have been studied separately. The interplay between hard perturbative (production) and soft hadronization (fragmentation) mechanisms which associates the parton and hadron worlds has not been unveiled. Production mechanisms functioning at the parton level have not been successfully coupled to the fragmentation mechanisms which bring partons into the hadronic domain. An analysis of the fractal geometry in soft interactions, however, capitalizes on meshed patterns. By their unique ability to treat layered processes, fractal descriptions open new and necessary avenues to devise and test complete theories.

1.1.2 Multiple collisions

Typically in hA interactions, positive charge multiplicities exceed negative charge multiplicities even for negative h. This **positive charge excess** suggests that several nucleons somehow participate in the interaction. This participation may involve repeated collisions of the incoming hadron or its quark constituents (multiple collisions) or may involve subsequent collisions of produced particles (cascading) on the quark or the hadron level. QCD cascades are a viable interpretation at the quark level.

If all charged particles emanating from an hA interaction could be observed, the excess charge would be a reliable measure of the number of nucleons participating

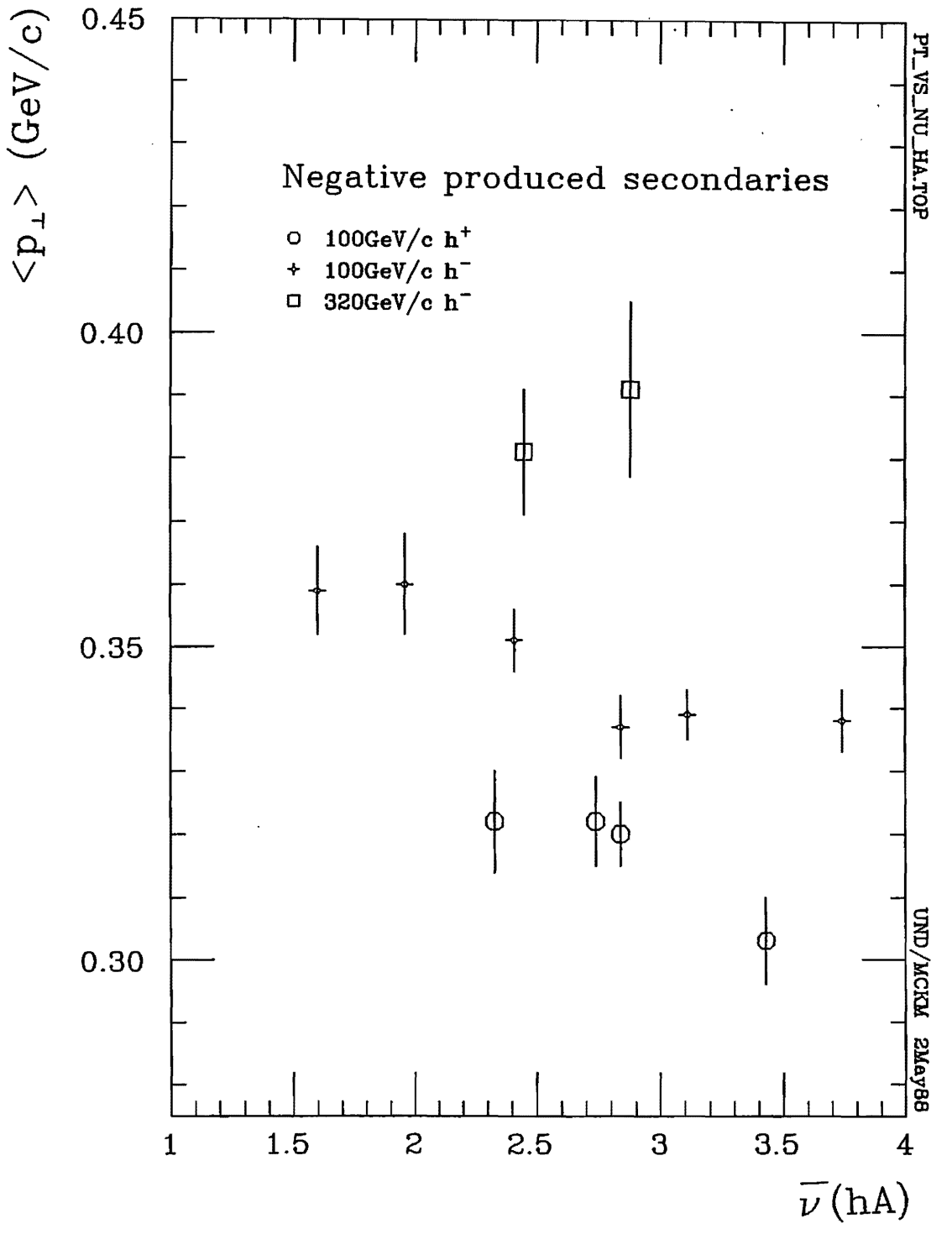

Figure 1.1.3 The average transverse momentum $< p_\perp >$ of negative produced particles as a function of $\bar{\nu}$ in 100 and 320 GeV/c hA interactions. The sample was restricted to particles for which $p_\perp < 2.6$ GeV/c, $d\theta < 3^o$, $d\phi < 6^o$, and $dp/p < .8$ and does not include CRISIS identification of fast particles.

in an interaction. In E597, however, many slow particles were not observable in the opaque thickness of the nuclear foils. Observed charge excess is a trend indicator rather than an absolute measure. Thus, the average amount of nuclear material involved in an inelastic interaction can be inferred more accurately from the ratio between the hadron-nucleus cross section σ_{hA} and the hadron-nucleon cross section σ_{hN}:

$$\bar{\nu} = A\sigma_{hN}/\sigma_{hA}$$

Assuming all collisions are governed by the dynamics of the hh interaction, this ratio represents the average number of inelastic collisions an incident hadron undergoes in traversing the nucleus. This interpretation can be tested for consistency with the mean number of collisions as a function of a) mean path length through nucleus/mean free path of pp; b) nuclear radius; and c) produced particle multiplicity.

1.1.3 Cascading

While the concept of multiple collisions involves the incoming hadron sustaining succeeding collisions itself, the idea of cascading involves collisions between production product(s) and other constituents of a nucleus subsequent to the initial collision between an incoming hadron and some constituent of the nucleus. Thus the sizes of the nuclei and the location and extent of spatial, momentum, and time production regions are needed to sort out the role cascading plays. Whether or not cascading is expected depends on *where* hadrons are formed. In fact, 'Where are hadrons formed?' is one of the most basic questions of particle production. If formation times are long compared to the time it takes to traverse the nucleus, they are produced *outside* and cascading cannot occur. If formation times are short so that production is completed *inside* the nucleus, wholesale intranuclear cascading is expected with very large accompanying multiplicities of produced particles. With relativistic cms speeds, E597 interactions involve formation times dilated by factors up to order 10, thereby significantly increasing the likelihood of multiple production *outside* the nucleus proper. But cascading cannot be excluded if the multiplicities of *slow* produced secondaries are large. Cas-

cading at least plays a partial role. This partial role can be probed by comparing the distribution of multiplicity with those derived for individual, independent collisions, *i.e.* Poisson distributions. If produced particle multiplicity distributions are *broader*, then cascading is strongly implied.

1.2 FRAMES OF REFERENCE

hA interactions cannot be studied in their center-of-mass. Nuclei are composite. While the collision axis is taken along the direction of the incoming hadron, the center-of-mass is ambiguous event by event. So multiparticle production in hA is usually described in the laboratory rather than the center-of-mass system. And parameters of study are usually limited to those which are either Lorentz invariant or whose distributions are Lorentz invariant. When comparing hp and hA phenomena or postulating multiple collisions, however, it is helpful to assume hA collisions to be composites of single hp collisions where p is at rest in the lab laboratory frame. Fermi motion must be considered for an accurate description and thus confuses the issue even more. Thus, the hp center-of-mass frame is adopted neglecting Fermi motion, thus satisfying the condition

$$p_{incoming\ h} + p_{target\ p} = 0$$

with a total center-or-mass energy of

$$\sqrt{s} = E^{cms}_{incoming\ h} + E^{cms}_{target\ p}$$

β and γ for hp center-of-mass systems are given in **Table 1.2.1** along with other values of interest for E597 kinematics.

For a laboratory system, one(1) of three(3) coordinate systems has been employed: the Notre Dame Bubble Chamber Reference System (NDBC), the Notre Dame Basic Reference System (NDBasic), and the analysis system (ASYS). Bubble chamber data are expressed in NDBC, which is the primary reference frame keyed to the bubble chamber fiducials. But all other device data are expressed in NDBasic.

Table 1.2.1 A summary of kinematic variable values specific to E597 data. Center-of-mass calculations assume hp interactions with the proton at rest in the laboratory system.

Beam Measurable			Values in various beam modes			
			π^-	π^+/π^-	K^+	p
m_{bm}		(MeV/c^2)	139.567	139.567	493.646	938.272
p_{bm}^{lab}		(GeV/c)	320	100	100	100
$1-\beta_{bm}^{lab}$	$1-p_{bm}^{lab}/E_{bm}^{lab}$	(10^{-7})	.951	9.740	121.853	440.174
p_{bm}^{cms}	$\gamma(p_{bm}^{lab}-\beta E_{bm}^{lab})$	(GeV/c)	12.24	6.83	6.83	6.82
$1-\beta_{bm}^{cms}$	$1-p_{bm}^{cms}/E_{bm}^{cms}$	(10^{-4})	.650	2.085	26.028	93.390

Target Measurable			Values in various beam modes			
			π^-	π^+/π^-	K^+	p
m_{tgt}		(MeV/c^2)	938.272	938.272	938.272	938.272
p_{tgt}^{lab}		(GeV/c)	0	0	0	0
$1-\beta_{tgt}^{lab}$	$1-p_{tgt}^{lab}/E_{tgt}^{lab}$		1	1	1	1
p_{tgt}^{cms}	$\gamma(p_{tgt}^{lab}-\beta E_{tgt}^{lab})$	(GeV/c)	-12.244	-6.833	-6.829	-6.817
$1+\beta_{tgt}^{cms}$	$1+p_{tgt}^{cms}/E_{tgt}^{cms}$	(10^{-4})	29.237	92.967	93.077	93.390

Center-of-mass Measurable			Values in various beam modes			
			π^-	π^+/π^-	K^+	p
$\sqrt{s}$	$E_{bm}^{cms}+E_{tgt}^{cms}$	(GeV)	24.524	13.732	13.740	13.763
$1-\beta$	$p_{bm}/(E_{bm}+m_{tgt})$	(10^{-4})	29.237	92.967	93.077	93.390
γ	$1/\sqrt{1-\beta^2}$		13.087	7.351	7.346	7.334
Δ	$cosh(\gamma)$		3.263	2.683	2.683	2.681
	$y^{lab}=y^{cms}+\Delta$					

Secondary Track Measurable		Values in various beam modes			
		π^-	π^+/π^-	K^+	p
$y_p^{cms\ min}$		-3.263	-2.683	-2.684	-2.686
$y_p^{cms\ max}$		3.263	2.683	2.684	2.686
	$y^{cms}=.5\ln(\frac{E^{cms}+p^{cms}_{\parallel}}{E^{cms}-p^{cms}_{\parallel}})$				
$y_\pi^{cms\ min}$		-5.169	-4.589	-4.589	-4.591
$y_\pi^{cms\ max}$		5.169	4.589	4.589	4.591
$y_p^{lab\ min}$		-0.000	-0.000	-0.001	-0.005
$y_p^{lab\ max}$		6.527	5.367	5.367	5.367
	$y^{lab}=.5\ln(\frac{E^{lab}+p^{lab}_{\parallel}}{E^{lab}-p^{lab}_{\parallel}})$				
$y_\pi^{lab\ min}$		-1.906	-1.906	-1.907	-1.910
$y_\pi^{lab\ max}$		8.432	7.272	7.272	7.272

KINETIC.TAB UND/MCKM 18May88

These are transformed to NDBC for the final data summary tapes (DSTs). Subsequently, analysis routines rotate DST data such that the beam momenta run along the x axis. **Appendix 1A** describes the NDBasic→NDBC transformation with details of how both coordinate systems are defined in terms of E597 components shown in the **Figure 1.2.1** schematic. The transformation to the ASYS is determined by reconstructed beam track angles.

1.3 DESCRIPTIVE PARAMETERS

As noted previously, the center-of-mass for hA systems is not generally known and could be changing event by event. With this limitation, many analysis tools like four-momentum and the Lorentz-invariant cross section $Ed^3\sigma/d^3p$ are of limited value. The parameters by which phenomena are to be described must be carefully chosen for their resistance to confusing center-of-mass shifts . Multiplicity, rapidity, transverse momentum, and related parameters retain their viability under these constraints and place important tests on soft hadron production models.

In **single-particle** *inclusive* **distributions**, parameters of final state characteristics are analyzed with no regard for concurrent products. Interactions are treated in an open-ended fashion as $h_{beam} + A \rightarrow h_1 + anything$. *Exclusive* distributions, by contrast, are restricted to single interaction channels.

In **two-variable correlations**, production of one particle type is related to that of another. The number of produced particles as a function of the number of protons observed is of particular interest since the number of protons suggests the degree to which multiple collisions are occurring. These correlations to $\bar{\nu}$ can integrate results involving different targets at comparable energies.

Two-particle correlations study the characteristics of pairs of produced particles in $h_{beam} + A \rightarrow h_1 + h_2 + anything$. The correlations between final state hadrons arise from production mechanisms (at the parton level) coupling to hadronization mechanisms (at the hadron level) and thus are of primary interest. Categorized with respect to phase space considerations, long-range correlations include forward-

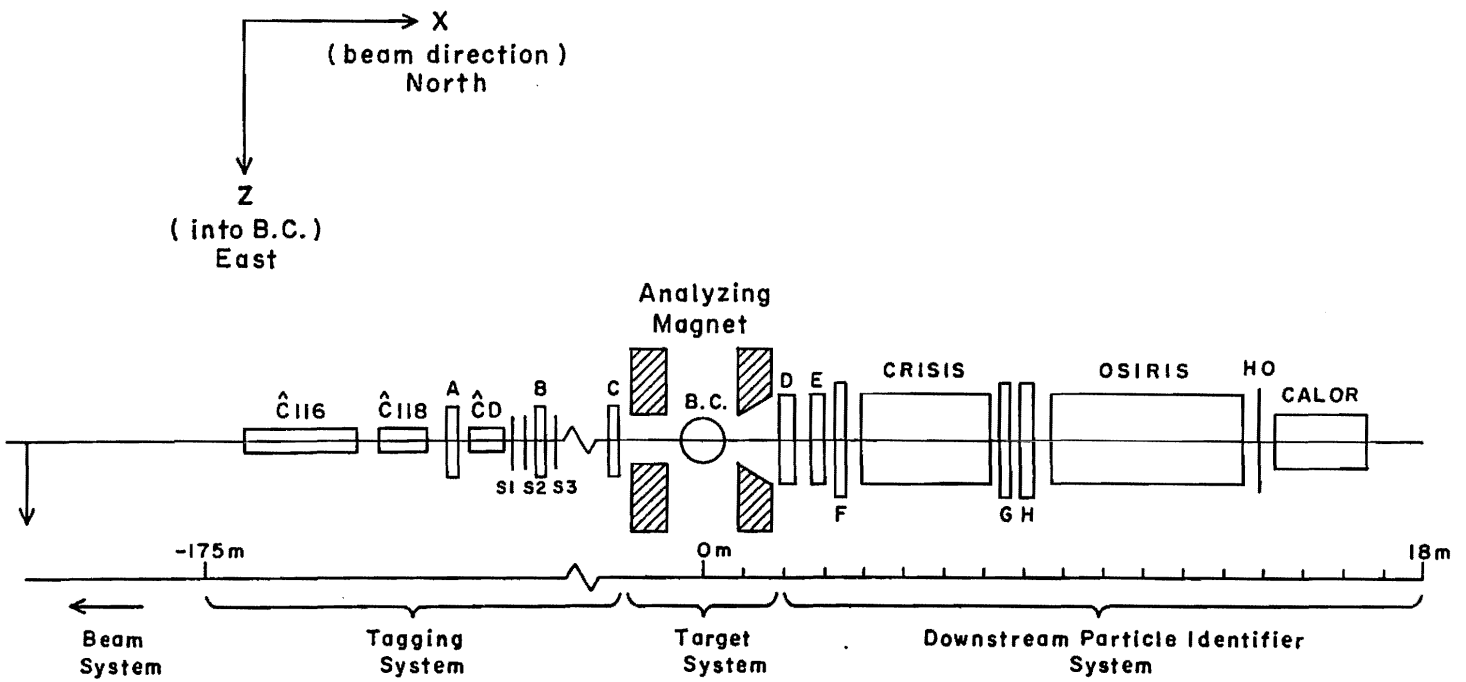

S = Scintillator
Ĉ = Ĉerenkov
A-E = Proportion Wire Chamber A: PWC1, ····
F-H = Drift Chamber
B.C. = Bubble Chamber
CRISIS = Considerably Reduced Identification System by Ionization Sampling
OSIRIS = He / N_2 Cerenkov
HO = OSIRIS Hodoscope
CALOR = Neutral Particle Calorimeter (Cal 1 - Cal 29)

Figure 1.2.1 Schematic of the FNAL E597 hybrid spectrometer.

backward correlations (FBC), while short-range correlations include intermittency and Bose-Einstein (BE) enhancements.

1.3.1 Multiplicity

Multiplicity N_i refers to the number of final state particles of type i produced in an interaction. The subscript i can be defined broadly (*e.g. charged*) or more specifically (*e.g. proton*) in particular regions of phase space. Distributions P_{N_i} for visible charged secondaries are global measures of final state characteristics in terms of simple comparisons. Because of its independence from the center-of-mass and other momentum-related ambiguities, multiplicity is an indispensable tool for studying particle production. Despite its simplicity and its global nature. multiplicity analyses can address questions concerning multiple collisions (thickness and cascading), collective effects, and long vs. short range correlations. Proton multiplicities are useful in estimating the number of collisions ν. The reliable particle identification and nearly 4π acceptance in E597 data make it particularly suited to studies of multiplicity.

A multiplicity distribution is most simply studied in terms of its first two moments: the *average* or *mean*, and the *dispersion*. Higher moments are also studied, but their definitions vary. Higher moments in this study are normalized according to the definition

$$C_j = \langle N^j \rangle / \langle N \rangle^j$$

But very little can be inferred from these moments. A more productive description of multiplicity fits data to a negative binomial distribution (NBD). Even in limited regions of phase space, NBD successfully describes e^+e^-, ℓh, hh, and hA multiplicity data. Because independent emission of single particles generates Poissonian distributions with a characteristic NBD fit (k=1), any deviation broadening the distribution signals other kinds of processes, *e.g.* cascading. And since competing processes are thought to contribute to different regions in phase space, NBD studies in limited phase space determine to what extent cascading contributes in each.

1.3.2 Number of collisions ν

A simple hypothesis of projectile multiple collisions in a target nucleus regards these collisions independent of one another. The additive quark model (AQM) considers each interaction to be a succession of individual, independent quark interactions between projectile and nucleon quarks in a sequence of a definite number of collisions. *i.e.* each quark in a projectile passes through a nucleus with ν independent collisions. Independence refers to the fact that the probability governing each quark-quark interaction is independent of which collision this is for this quark and independent of what happens to all the other quarks. Thus ν is a basic, natural parameter of all multiple collision models. An estimate $\bar{\nu}$ averaged over presumably broad probability distributions $\pi_{hA}(\nu)$ can be made:

$$\bar{\nu}_A = A\sigma_{hN}/\sigma_{hA}$$

However, considering the production of *grey* protons ($.3 < \beta < .7$) can more tightly determine the number of collisions. Bubble chamber experiments detect slow protons particularly well and thus make this approach particularly accessible.

1.3.3 Feynman x

Defined as $x_F = p_L/p_{max}$ where p_{max} is the maximum momentum a particle is allowed in the center-of-mass system, Feynman x varies from -1 to +1 and measures the fractional longitudinal momentum a produced particle carries. At high energies, p_{max} for hh can be approximated by $.5\sqrt{s}$. Except at small x_F values, its distribution is approximately energy-independent.

Phase space regions are often designated in terms of x_F. The so called *central* region is populated by particles carrying small fractions of available momentum, *i.e.* $|x_F|$ less than about .1 while the fragmentation regions are populated by particles carrying significant fractions of available momentum, *i.e.* x_F greater than about .1 and x_F less than about $-.1$, respectively, for the beam and target fragmentation regions. While the subdivision of phase space in the central and fragmentation regions

has been used extensively in e^+e^-, ℓh, and hh analyses, the center-of-mass definition of x_F seriously limits its use for hA interactions.

1.3.4 Rapidity

Rapidity is a preferred variable for hA studies. Under Lorentz boosts along the collision axis, the rapidity distribution shape does not change but rather the entire distribution shifts by $\cosh\gamma$ where γ is $\frac{1}{\sqrt{1-\beta^2}}$ and β is the velocity. Like x_F, rapidity is defined in terms of longitudinal momentum

$$y = .5\ln(E + p_L)/(E - p_L)$$

In hp interactions, the maximum rapidity y_{max} is $\ln(\sqrt{s}/m)$. Assuming hp interactions and hp center-of-mass systems, **Table 1.2.1** gives maximum center-of-mass and laboratory rapidities applicable to the hA interactions of this study.

In hp interactions, the y distribution shows plateau-like features in the Feynman x central region. True plateaus are expected to occur for interactions idealized for Feynman scaling. The length of this plateau increases with s but its height should remain constant if Feynman scaling is valid. In practice the height also tends to increase with s. Particle density in this plateau region increases approximately logarithmically with energy. But the forward and backward tails are energy independent in height and shape and are comparable to the Feynman x fragmentation regions.

A plateau is certainly not obvious for hp or hA interactions up to 320 GeV/c. The central region is dominated by produced particles and it is expected that soft mechanisms govern this region. There is some speculation that plateau features may develop at higher energies. Other speculations suggest that the overlap of multiple plateaus are responsible for the lack of observable plateau features. In the rest frame of this region, both the beam particle and target are Lorentz contracted as illustrated in **Figure 1.3.1(c)**.

In contrast, the target fragmentation region characterized by the smallest laboratory rapidities is dominated by proton secondaries and nuclear breakup fragments in whose rest frame the interaction looks quite different, **Figure 1.3.1(b)**,

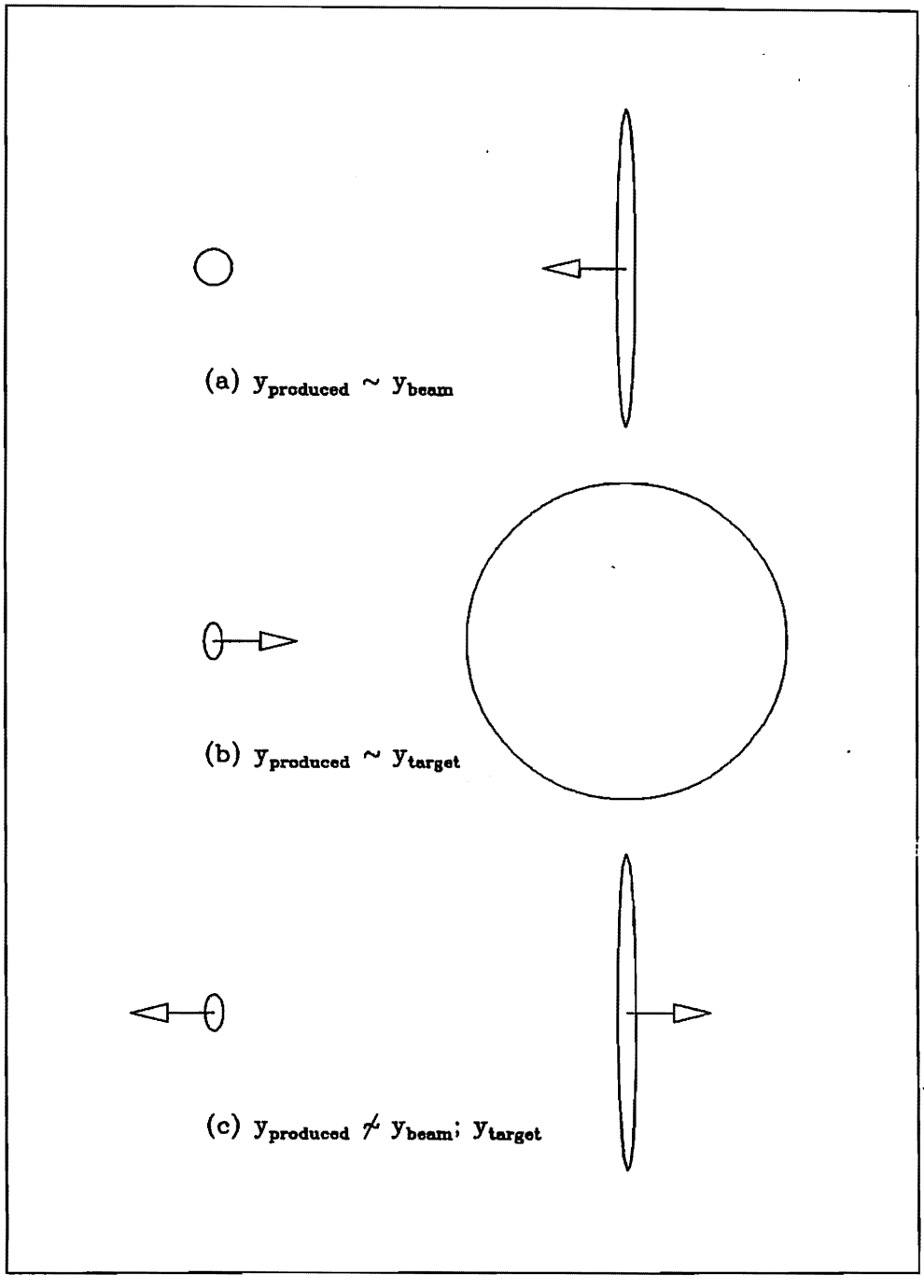

Figure 1.3.1 The hadron-nucleus interaction in the rest frames of produced particles in various regions of rapidity: a) beam fragmentation, b) target fragmentation, and c) central rapidity regions.

with only a contracted projectile.

The projectile fragmentation region characterized by the largest rapidities is dominated by leading particles and hard processes. Interactions in the rest frames of leading particles, *i.e.* particles whose rapidities are near those of the beam, are distinguished by a severely contracted nucleus, as seen in **Figure 1.3.1(a)**

E597 data are particularly well suited to rapidity-based analyses since momenta, charge, and particle identities are well measured. Rapidity distances between produced particle pairs establish the long- and short-range correlations which characterize production mechanisms. These correlations are responsible for non-Poissonian distributions in multiplicity and thus are entirely expected. Long-range correlations differ from short-range correlations according to the longitudinal range in rapidity over which they occur.

Short- vs. long-range correlations The two-particle rapidity correlation function between particles 1 and 2 is defined to be

$$C(y_1, y_2) = \rho^I(y_1)\rho^I(y_2)(\frac{\rho^{II}(y_1, y_2)}{\rho^I(y_1)\rho^I(y_2)} - 1)$$

where I and II refer to one- and two-particle densities, respectively. By introducing C_S and C_L defined as

$$C_S(y_1, y_2) = \sum_N P_N C_N(y_1, y_2)$$

$$C_L = \sum_N P_N(\rho^I(y_1) - \rho^I_N(y_1))(\rho^I(y_2) - \rho^I_N(y_2))$$

where N denotes fixed multiplicities, the overall correlation is expanded into two components:

$$C = C_S + C_L$$

C_S is simply an average over all multiplicities and behaves in a short-range fashion while C_L derives from differences in single particle distributions for different multiplicities and behaves in a long-range fashion. It is $C_S(y_2, y_2)$'s narrow peak about $y_1 = y_2$ that associates it with short range correlations at fixed multiplicity. On the other hand, $C_L(y_2, y_2)$'s broad distribution in $y_1 - y_2$ associates it with event mixing

at different multiplicities, each with different particle densities. Although it would be more appropriate to designate this term as a *mixing term*, it is in fact usually referred to as a long-range term in contrast to the short-range one. **Figure 1.3.2** shows how *short* is equivalent to about 2 units of rapidity while *long* spans the entire available rapidity range.

Forward-backward correlations An analysis of the simplest correlations, forward-backward correlations (FBC), divides rapidity into two regions about the hp center-of-mass, with gaps of varying width separating the two. FBC is sensitive to the transition from short- to long-range correlation features. The average number of produced particles in the backward hemisphere as a function of the number of charged particles in the forward hemisphere, as well as the forward as a function of the backward, largely depends on long range correlations. When gaps are introduced between the forward and backward regions eliminating any short range contributions, an even better measure of long range correlations is made. These long range correlations directly determine the multiple collision terms in dual parton models, while the short range correlations correspond to single scatters.

Limited rapidity regions Studying limited regions in rapidity, *e.g.* precisely the gaps introduced to enhance long range correlations, can access short range correlations, in effect probing production and/or hadronization in clusters. It is supposed that particles produced together, say in clusters, will be close in rapidity and exhibit a short range correlation. UA5 [Ward 88] claims that the cluster model folded in with the observed multiplicity behavior reasonably describes the correlations found in analyzing their data. [Bialas 86a], on the other hand, claims that clusters cannot describe the data as long as they are identically sized and distribute the energy evenly. However, some short-range correlations may be simply an outgrowth of two-particle symmetrization. Produced mesons, with their integer spins, possess symmetric wavefunctions. Thus they tend to cluster in phase space and show an enhancement at small two-particle momentum differences. The extent of this enhancement can de-

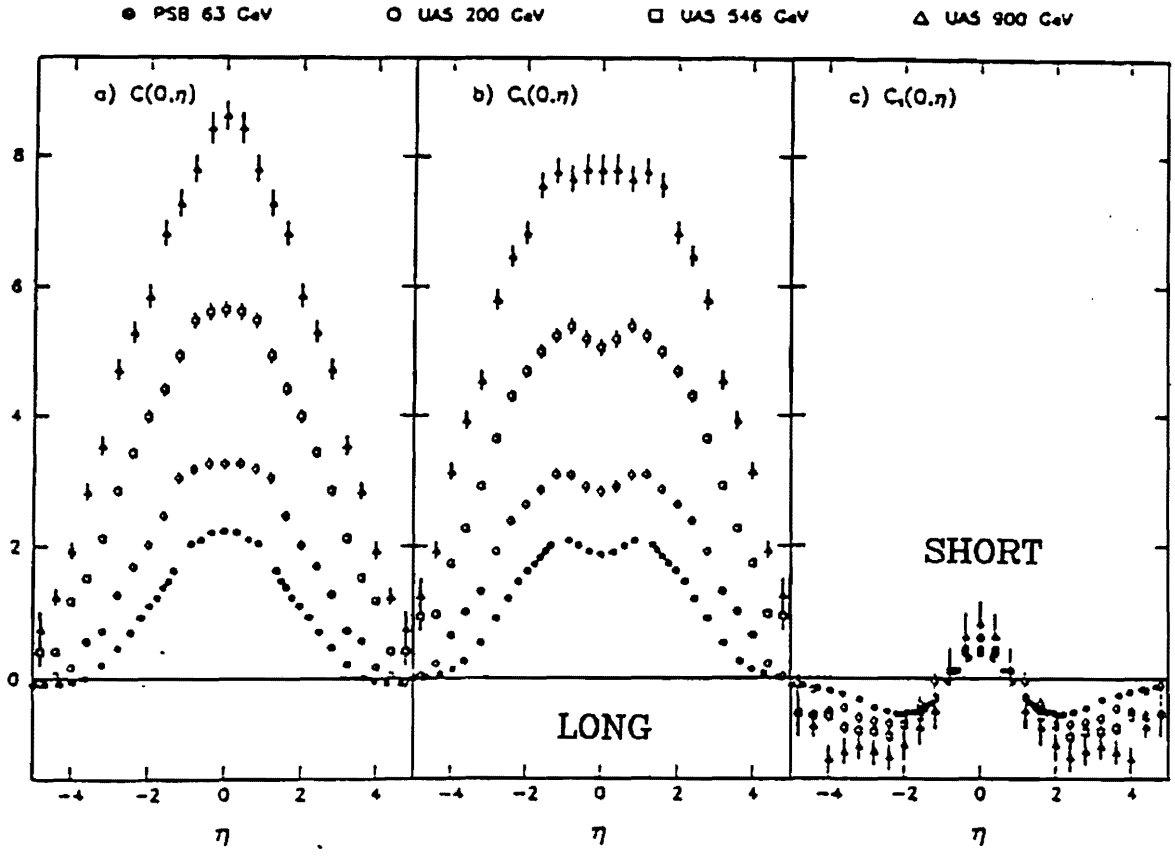

Figure 1.3.2 A comparison of *short*-range b) and *long*-range c) rapidity correlations from the decomposition of the charge correlation function $C(\eta_1, \eta_2)$ plotted for fixed $\eta_1 = 0$ *vs.* η_2 at 63, 200, 546 and 900 GeV [Ansorge 87].

termine the size of the space-time region from which the two particles originated. Protons, on the other hand, have half-integer spin and possess antisymmetric two-particle wavefunctions. Thus a depletion at small two-particle momentum differences commensurate with the production region size is expected. Correlations in limited rapidity regions centered at varying locations rather than at the hp center-of-mass investigate cluster centers-of-mass.

1.3.5 Pseudorapidity

Although rapidity is a variable well-suited to the analysis of E597 data, other experimental situations have provided angular but not momentum data, and thus make it impossible to calculate rapidity. However, when $p_L \gg p_\perp$, rapidity is closely approximated by the angular variable $\eta = -\ln(\tan\frac{\theta}{2})$ where θ is the production angle between the produced particle direction and the collision axis. As with rapidity distributions for hh interactions, a plateau region emerges in a central region along with two tail regions. Because of its close resemblance to rapidity, η is called *pseudorapidity*. Results from rapidity analysis can often be compared directly with those from pseudorapidity analysis.

1.3.6 Transverse momentum

Since E597 beam particles are not transversely polarized, only the total transverse momentum is relevant in our studies. That is helpful since it reduces the number of variables and is invariant under Lorentz transformations along the collision axis. For transverse momenta not exceeding a few GeV/c, the distribution of $p_\perp$ or $p_\perp^2$ is fit by very steep exponential or Gaussian functions and depends only weakly on the center of mass energy. The average transverse momenta for 100 and 320 GeV/c hA interactions, .338 and .386 GeV/c, respectively, do not differ greatly from hh averages. In calculating the E597 averages, cuts on $d\theta$, $d\phi$, and dp/p were made to prevent large measurement errors from producing spurious results in transverse momentum analyses. However, misidentified fast protons skew charged produced

particle $p_\perp$ averages so that realistic averages are best given for negative produced particles.

Seagull effects The *seagull* effect is an important transverse momentum feature of hA interactions and is indicative of hard effects. It is revealed when plotting the energy weighted average transverse momentum as a function of longitudinal momentum. More highly lifted *wings* accompany *harder* interactions. Thus this effect is an important signal of the interplay between hard and soft processes.

1.4 FNAL E597 SPECTROMETER

Run during a ten(10)-week period in the spring of 1982, Fermilab experiment E597 provides data with minimal limitations in acceptance and particle identification and maximal advantages in momentum determination and interaction coverage over a broad range of beams, targets, and energies. E597 was designed to excel in

- 4π track reconstruction
- minimum bias comparisons to determine A- and/or beam-dependence
- complete mass and momentum determination of secondary tracks

Approximately 582K bubble chamber exposures with ancillary electronic data support this study of multiple production.

The use of the FNAL 30 inch hydrogen-filled bubble chamber has made it possible to reconstruct tracks near the interaction point with a solid angle of nearly 4π. Only the vertex itself and tracks nearly perpendicular to the beam were obscured in the fiducial volume by six(6) metal targets: three(3) atomic numbers and two(2) thicknesses for which radiation lengths ranged between 6 and $26 g/cm^2$ and for which interaction lengths ranged between 100 and $230 g/cm^2$. With A ranging from 24 to 197, they have made direct studies of ν-dependence in hA interactions possible.

Direct studies of beam-dependence, on the other hand, have been facilitated by a mix of hadron beams tagged by an upstream tracking and mass identifying system. Three(3) upstream Cerenkov counters have provided data by which particle velocities can be be separated on the basis of Cerenkov light detected in the inner

and/or outer rings of the counters. Further details of the upstream tagging system appear in **Appendix 1B** with identification criteria in **Table 1B.4.2.** These form the basis for the tagging procedures described in Section 2.3. Data for five(5) beam modes over two(2) energies have made meson/baryon, particle/antiparticle, and energy comparisons possible.

Table 1.4.1 tabulates specific reference properties of the targets while **Table 1.4.2** summarizes the the relative compositions of the beam during various running modes and the available corresponding BC data.

Surrounded by a 20 kG analyzing magnet, the BC has also filled the functions of track and vertex reconstruction, momentum determination, and mass identification for slow particles that the DPI is designed to do for faster particles. Momenta have been determined on the basis of track curvature in the bubble chamber. When possible, these have been improved on the basis of data from the downstream tracking devices for higher momentum tracks. Proton secondaries at momenta less than 1.3 GeV/c can be distinguished from π's on the basis of their ionization in the bubble chamber, but π's cannot be distinguished from K's at momenta greater than .6 GeV/c. Tracks outside the BC identification range can only be identified in the DPI.

Laid out according to the schematic in **Figure 1.2.1**, the E597 spectrometer is divided into upstream beam, tagging, and target systems, and a downstream particle identifier (DPI) system. The DPI consisted of two(2) groupings of proportional wire chambers (PWCs 10-11 and 12-16), three(3) drift chamber triplets (DCs 1-3, 4-9, and 7-9), an identification-system-by-ionization-sampling device (CRISIS), a helium-nitrogen, atmospheric pressure, 8-cell Cerenkov counter (OSIRIS) with a matching 8-channel hodoscope (OSHOD), and a neutral particle calorimeter with muon counters. Data furnished by DPI devices supplement BC data for fast forward tracks. Since these tracks are not only prone to large momentum errors when reconstructed on the basis of BC data but also have ambiguous identity on the basis of ionization in the BC, the DPI is critical in analyzing fast tracks fully. Identification of forward secondary p's and $\bar{p}$'s is possible for tracks with momenta greater than about 1 GeV/c up to the full beam momentum of 100 or 320 GeV/c. Reconstruction on

Table 1.4.1 Nuclear target properties.

$^{A}_{Z}Target$			$^{108}_{47}Ag$		$^{197}_{79}Au$		$^{24}_{12}Mg$	
$A^{\frac{1}{3}}$			4.762		5.819		2.884	
$(r^2)^{\frac{1}{2}}$	(fm)		5.150		6.320		2.980	
Density	(g/cm^3)		10.50		19.30		1.74	
Target number			1	2	3	4	5	6
Width	(cm)		.9	1.4	1.7	.9	.9	.9
Thickness	(cm)		.18034	.06098	.02997	.08890	.37084	1.10998
	(g/cm^2)		1.894	.6401	.5784	1.716	.6453	1.931
Interaction Length	(g/cm^2)	π^+A	195.42		225.39		137.26	
		π^-A	195.89		226.29		137.18	
		pA	162.24		192.14		106.72	
		$\bar{p}A$	157.25		188.26		100.70	
# of Int Lengths		π^+	.97%	.33%	.26%	.76%	.47%	1.41%
		π^-	.97%	.33%	.26%	.76%	.47%	1.41%
		p	1.17%	.39%	.30%	.89%	.60%	1.81%
		$\bar{p}$	1.20%	.41%	.31%	.91%	.64%	1.92%
Radiation Length	(g/cm^2)		8.720		5.945		25.473	
# of Rad Lengths			21.72%	7.34%	9.73%	28.86%	2.53%	7.58%

TARGETPROP.TAB UND/MCKM 13Mar89

Table 1.4.2 Beam composition and gross sample size.

Mode No.	Beam Particle	Relative Composition	Momentum	Film Exposures
1	π^-	100%	320 GeV/c	110K
2	π^+	80%	100 GeV/c	80K
	K^+	20%		
3	p	95%	100 GeV/c	70K
	π^+	5%		
4 and 5	π^-	70%	100 GeV/c	322K
	$\bar{p}$	30%		
Total				472K
Grand Total				582K

BEAMCOMP.TAB UND/MCKM 14Mar87

fast tracks can be significantly improved on the basis of information from the downstream PWCs, DCs, and CRISIS. CRISIS can also assign mass when identification by ionization in the BC is not feasible. Further details for each device in the DPI appear in **Appendix 2B.**

1.5 SUMMARY OF OBJECTIVES

Various lines of analysis have been applied to E597 data. Precisely because soft interaction mechanisms are still not understood fundamentally, an array of analyses is needed to trigger new ideas and modify existing ones. A number of inferred properties indicate the possibility of *new* dynamics in hA interactions. The objectives of this study include **showing that the occurrence of anomalously high rapidity density events (*spikes*), the scaling of factorial moments down to very small rapidity resolutions (*intermittency*), and the fractional dimension of hA interactions (*fractals*) present evidence for *new* physics. They also include pursuing more conventional lines of analysis like Bose-Einstein correlations, forward-backward correlations, multiplicities for limited regions of rapidity, negative binomial descriptions of multiplicities, seagull effects, multiplicity moments, and two-particle correlations in order to probe the general characteristics of multiparticle production.**

After Chapter 2 introduces the data and Chapter 3 discusses the plausibility and extent of multiple collisions and cascades, the subsequent chapters examine candidate signals for *new* physics. Chapters 4 addresses the issue of spike events as a signal for QGP; Chapter 5 addresses the issue of intermittency as a signal for nonlinear production; and Chapter 6 addresses the issue of fractal properties as a signal for self-similar cascades.

CHAPTER 2

DATA SAMPLE

The hybrid nature of the experimental configuration necessitated pursuing each of various aspects of data acquisition in two parallel streams, one for data derived from the bubble chamber, the other for data derived from counter components of the experiment.

With the mechanical limitations on bubble chamber cycle times, the chamber itself could not be triggered in any way to discriminate between data associated with events of interest and all other data. *Junk* BC data were simply discarded after the fact when unsupported by counter information. However, the acquisition of meaningful data could be maximized by synchronizing BC expansions and camera action to incoming beams and to the special dead-time characteristics of spectrometer electronics. Thus in the context of this experiment, the term *trigger* refers only to the discrimination process when gathering and recording data from counter devices, not from the bubble chamber. Since data accumulation from these devices was synchronized to bubble chamber cycles producing manifestly minimum bias gates between BOP (beginning-of-ping) and EOP (end-of-ping) signals, the trigger can be said to have been minimum bias.

Bubble chamber information was gathered simultaneously on film by four(4) cameras. One of the cameras (View 3) was a high-resolution camera which gave a close-up, edge-on view of the metal targets. While film development was the only additional step in collecting and storing BC information, the collection and storage of counter information was more complex. ADCs accumulated and digitized signals from all detector devices other than the bubble chamber shown in **Figure 1.2.1:**

upstream PWCs 1-9, downstream PWCs 10-16, DCs 1-9, upstream Cerenkovs C116I, C116O, C118I, C118O, and CDoghouse, downstream Cerenkov OSIRIS cells 1-8, hodoscopes OSHOD channels 1-8, X1-X15, Y1-Y15, U1-21, CRISIS, calorimeter paddles Cal1-Cal29, and scintillation paddles S114, Muon1, Muon2, These were interfaced to a PDP-11 on-line computer and logged onto 6250bpi magnetic tape with the FNAL data acquisition program MULTI-11 during end-of-ping (EOP) interrupts. General running condition information, eg. temperatures, pressures, voltages, were logged during between-spill interrupts. Information from CRISIS dominated the physical records. Three physical records accompanied each interrupt: two(2) for CRISIS information, one(1) for everything else.

The quality of bubble chamber data was monitored by inspecting test strips of film taken from the end of each newly developed roll. Bubble chamber conditions were optimized with reference to these test strips to achieve acceptable bubble densities, bubble-to-gap ratios, lighting, and beam alignment onto the nuclear target with minimum boiling at the target brackets. Unacceptable camera function producing scratches and shifted frames was also checked routinely on test strips.

The function of counter devices was generally monitored via MULTI whose sophistication included the accumulation of useful plots for the data stream from each device. These were helpful in spotting malfunctioning devices, determining efficiencies, and generally administering the experiment. MULTI also permitted off-line reviews of data from tape during down time.

Upon the completion of a run, counter data did not in principle require further processing before becoming accessible. In practice, counter data needed to go through a process of its own before it was reduced to a convenient form. However, the bubble chamber data involved more processing before it took on a usable form. Neither had stand-alone capability. So, preparation of integrated data could take one of two routes. The counter data could be unfolded and used to select frames of interest to be measured and thus reduce the bulk of film handling. This presupposes a thorough understanding of alignment, efficiencies, and acceptance in the DPI. Or the bubble chamber photographs could be digitized first and unfolded to map out

tentative *roads* in the DPI by which to search out tracks in counter data. Although considerably slower in principle, bubble chamber data processing overtook counter data processing and the second option became the *modus operandi*. The following summarizes the integration process:

- **film measurement** digitizing film images
- **track reconstruction** transforming tracks into 3-dimensional space curves
- **upstream beam tracking** assigning master gates to observed beam tracks
- **beam tagging** assigning beam mass using upstream Cerenkovs
- **momentum determination** assigning momenta and calculating ionization
- **BC mass assignment** assigning particle identities by ionization
- **BC summary tape production** producing a Bubble Chamber Data Summary
- **DPI summary production** unfolding and summarizing counter information
- **hookup** hooking up BC to DPI and improving fast forward momenta
- **hookup summary tape production** integrating BC with DPI improvements
- **downstream particle identification** assigning particle identities using CRISIS
- **final data summary production** producing a data summary tape

The responsibility for preparing data for hA analysis was shared largely among three(3) of six(6) collaborating institutions: Cambridge University (CU), Pennsylvania State University (PSU), and the University of Notre Dame (ND). (A full listing of personnel and institutions appears in the Acknowledgements.) ND and CU high energy groups digitized most of the hadron-nucleus interactions and processed the data to produce data summaries for BC and DPI data. The PSU group was instrumental in hooking up the two streams of data, improving the quality of fast forward tracks significantly. Some additional assistance was rendered by Duke University and Fermilab groups in completing some digitization and particle identification by ionization. Although the procedures differed at the various institutions, results indicate that the consequent physics is comparable. In many cases, analyses have been run separately for data prepared by each institution to verify their consistency.

2.1 FILM DIGITIZATION

The digitization of bubble chamber film images involving hadron-nucleus interactions was one of the major responsibilities of the Notre Dame group. While the Cambridge

group used semi-automatic measuring machines to digitize its film, the Notre Dame group employed a team of experienced measuring technicians operating two film plane measuring machines whose mechanical stages provided least counts of .5 μm (Machine 5) and 1 μm (Machine 4) on film. Each measurer digitized points at selected fiducial marks and along tracks. The measurer singled out points (usually 10 along a track, at evenly and widely spaced intervals) with the aid of a fixed, lighted reticle while rotary hand controls moved the stage to bring desired portions of the tracks or fiducials in position before the reticle. These points were recorded by a Zenith H89 computer and uploaded into a VAX file. The measurer also visually inspected each track and entered its topological and ionization features.

Subsequently, each measured track was fed into a track-by-track version of the Three-view Geometry Program (TVGP) [Solmitz 66] for a preliminary geometric check. If TVGP successfully transformed its points into a space curve, it was automatically formatted into a standard record file. If TVGP could not transform a track's points into a space curve, the measurer remeasured the track. After repeated attempts, failing tracks were declared unmeasurable and so designated in the portion of each frame's record known as the *event character*. The measurer also entered a target identifying code (*foil number*), a hidden vertex code, and general comments into the event character. A standard set of 5 fiducials, was measured in each view for each measured frame to relate the three views and each frame record automatically included logistical data: time, date, and measurer.

Measurement was conducted on film from three of the four camera views available. View 4 was chosen as the primary view since it gave an upstream, edge-on view of the nuclear targets by which to discriminate between nuclear and hydrogen events. View 3 was a high resolution view which would have been more difficult to fold into the reconstruction, so Views 1 and 2 were chosen as secondary views. Tracks were measured in the order View 4, View 1, View 2. Only 18 of the 22 fiducial markings on the bubble chamber windows show in any one view. The film perspective on the nuclear targets and the fiducial markings is illustrated in **Figure 2.1.1**.

Whereas the main thrust of the digitization effort involved tracks emanating

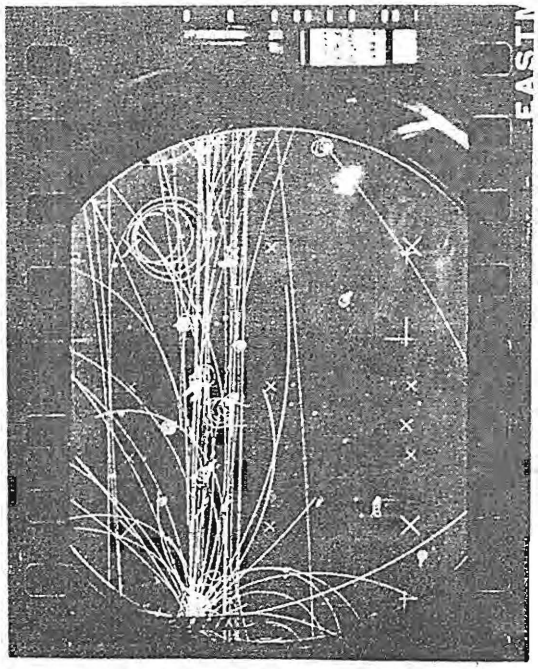

VIEW 1

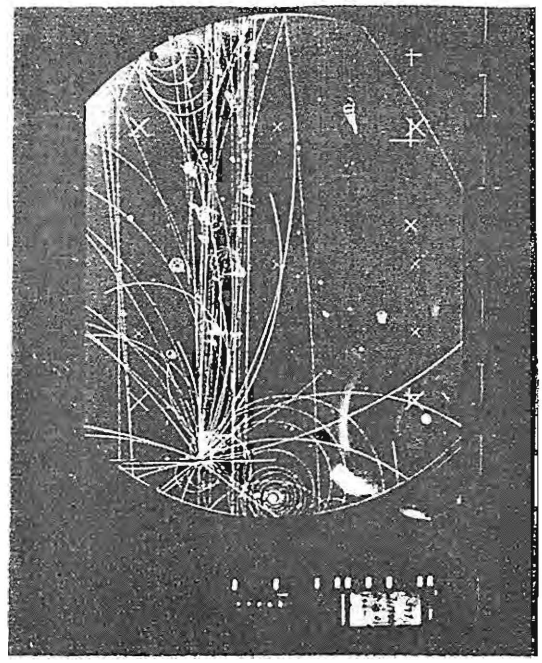

VIEW 4

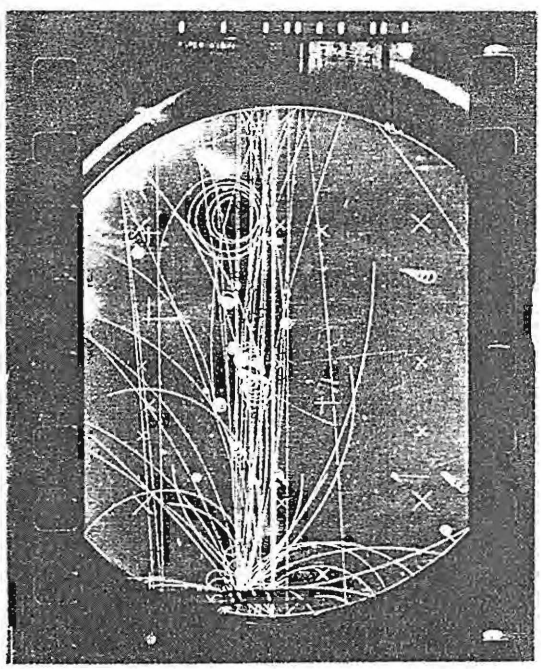

VIEW 2

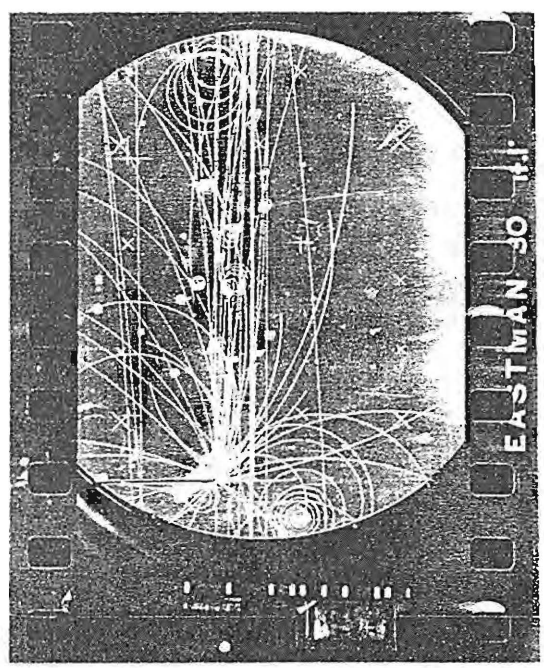

VIEW 3

Figure 2.1.1 Fiducials on film in four views for the 1981 test run. The 1982 run was comparable except for the fact that a high resolution camera was used for View 3.

from strong interaction hadron-nucleus vertices, two preliminary digitization projects were completed first: fiducial and beam measurements. Fiducial measurements produced a fixed reference by which to fix camera and track positions while beam measurements subsequently made it possible to associate specific beam particles with counter information.

2.1.1 Fiducial measurement

Digitizing the fiducial markings on the front and back windows of the bubble chamber, made it possible to determine camera locations and attitudes. With the program CAMAJUST, these determined the optical constants necessary to convert stereo plane images into true space curves in the reconstruction program TVGP.

At Notre Dame, measurers first digitized the 5 fiducials required by the measuring program (Fiducials 1, 5, 3, 2, 6 for Views 4 and 1; Fiducials 1, 6, 8, 9, 11 for View 2) and then each of the 18 fiducials in a given view as if they were 18 points on a beam or secondary track. These 18 fiducials were repeatedly measured up to 10 times, producing a measurement record similar to that of a beam track and up to 9 secondaries.

In ascertaining appropriate optical constants, FNAL fiducial measurements were also used. These measurements were conducted over a number of frames, rather than repeatedly on one frame only. Measurements from both Notre Dame and FNAL were used to calculate the optical constants used by Notre Dame track reconstruction.

To maintain sensitivity for fluctuations in optical constants for the entire extent of the run, the frames from which the fiducials were measured were spread over all five(5) beam modes. Specific optical constants were chosen on the basis of direct comparisons between reconstruction errors (track rms) in TVGP using each set of optical constants associated with a particular film roll's fiducial measurements. Choices were made on the basis of low track rms values, applicability over a significant range of the film, and the need to limit the number of different versions of the optical constants to a manageable number. Each roll for which event measurements were made at Notre Dame appears in Table 2.1.1 associated with the optical constants

Table 2.1.1 Constants used in final track reconstructions. TVGP version number depends on the constants calculated by CAMAJUST on the basis of fiducial measurements on specific rolls.

Version	201	202	203	204	205	206	207	208
Fiducial Roll	2058	2060	2079	2080	2081	2111A	2111B	2166

Mode 1 - 320GeV/c π^-

Roll	Events	Version							
2203	55		4.886						
2204	43				5.742				
2209	52					5.038			
2210	46				5.707				
2214	43								7.138
2217	24				5.498				
2218	58				5.592				
2223	52				6.431				
2229	60				5.260				
2230	37				4.481				

Mode 4 - 100GeV/c π^- and p

Roll	Events	RMS for Chosen Version							
2043	58					5.169			
2044	14					6.071			
2045	90					5.307			
2054	135		4.689						
2055	68		4.048						
2056	119		4.452						
2057	145		3.799						
2058		5.526							
2059		5.022							
2060			5.076						
2062	132								5.002
2063	114		5.050						
2064	41		4.661						
2066	77		4.007						
2075	135				4.764				
2076	108				4.991				
2077	141	4.213							
2078	138	5.045							
2079			5.636						
2080			5.851						
2083	43		4.175						
2084	69								5.462
2085	68								5.568
2086	55					4.875			
2095	139	3.744							
2098	49					3.960			

Version	201	202	203	204	205	206	207	208
Fiducial Roll	2058	2060	2079	2080	2081	2111A	2111B	2166

Mode 2 - 100GeV/c π^+ and K^+

Roll	Events	Version							
2125	58					5.319			
2126	101					4.643			
2127	116								5.382
2136	133				4.262				
2137	59	5.119							
2138	54	3.645							
2144	70		4.652						
2145	44	4.326							

Mode 3 - 100GeV/c p

Roll	Events	RMS for Chosen Version							
2099	58								5.073
2100	53					5.748			
2105	127								5.136
2106	117					4.279			
2111									5.957
2113	61								5.564
2117	51				4.145				
2118	64					4.973			

Mode 5 - 100GeV/c π^- and p

Roll	Events	RMS for Chosen Version							
2148	61					5.152			
2149	85					5.182			
2150	73					4.431			
2151	87					4.394			
2160	94								4.405
2161	88								5.095
2162	113	4.407							
2163	93					4.870			
2169	100								3.781
2170	90								4.954
2171	82					4.722			
2172	84								5.048
2177	88								5.304
2178	78								5.269
2179	85								5.580
2180	84								5.904
2185	80		5.109						
2186	83		6.071						
2187	86								
2188	80								4.818
2193	100		5.462						
2194	87					6.602			
2199	61				5.791				
2200	60		6.158						

CONSTANTS_1.TEX UND/MCKM 12Dec88
RMS.SUM (23Jan85) and DSBC.COM (25Jan86)

versions adopted for that particular roll and the its rms track error in microns. Also included in the tabulation are the numbers of the rolls from which fiducials were taken to calculate the various optical constant versions.

The possiblity that the optical constants might fluctuate with ping number was also investigated. Fiducials in a series of consecutive frames, ie. with successive ping numbers, were measured and optical constants were determined individually for each frame. No significant variation was found as a function of ping number. Thus optical constants were chosen irrespective of ping number.

2.1.2 Beam measurement

In order to determine the mass identity of a particular beam recorded on a bubble chamber photograph, and to associate DPI data properly with that beam's interaction products, that beam's trajectory must be linked to position data from upstream PWCs. Correspondence between a beam's BC position and PWC positions recorded for one of a ping's 5-8 mastergates established a correspondence between that beam and all upstream Cerenkov and downstream counter information. With the upstream Cerenkov information for a beam's mastergate, the beam could be tagged with a mass. With DPI data for a beam's mastergate, fast forward secondaries could be tagged with masses. Thus, measuring beam tracks was requisite in obtaining full event information for the beam and its secondaries. Measuring beam tracks was also requisite to saving a great deal of time in event measurement by excluding events for which the beam could not be identified.

At Notre Dame, beam track measurement was carried on in a one-pass scan/measure mode. The process was referred to as a *scan*, but it involved digitizing beam tracks visually associated with interactions. All frames were scanned for events with vertices within nuclear targets. About 25% of the Notre Dame data (18 rolls) were scanned with broad event criteria which included *delta rays* on beam tracks emanating from the foil targets and *tridents* or e^+e^- pairs on single beam-like tracks. 43% of events scanned under this criteria involved delta rays on beam tracks and tridents. Beam tracks were also measured every 10th or 20th frame. Such non-event

beams were differentiated from event beams by an event number.

Since upstream tracking devices could not be expected to be and were not 100% efficient, determining whether sufficient tagging information had been recorded made it possible to exclude events for which no beam tag could be made. However, when tagging lagged behind the event measurement, measurers measured all events, including those for which tagging information might be lacking. Thus, portions of the measurement records show larger percentages of tagged measured events than others. In 82 rolls with 15136 events scanned, 57.3% were successfully tagged. When 76 of those rolls were measured, 56.9% of those had been or were subsequently successfully tagged. So, overall, more than half of all interactions recorded on film were supported by sufficient counter information to unfold the mixed beam.

2.1.3 Event measurement

Event measurement proceeded from lists of event frames scanned. Whenever possible, these lists were amended to exclude frames for which the event beam could not be tagged. 69% of all measured events was measured in a tagged-events-only mode while 14% were measured in an all-events mode. The rest of the events were measured in a mixed mode. Only 82% of all tagged events were measured, but most of the balance included delta rays on beam tracks. During the early stages of tagged-events-only measurement, delta rays on beam tracks were included along with standard events, but this phase in measurement lasted only 14% into the event measurement effort.

A number of conditions precluded the measurement of individual tracks or entire events. These unmeasurable events and tracks distort all subsequent analyses; eg. cross sections, average multiplicities, multiplicity and rapidity distributions. In some cases, unmeasurability is biased to a particular particle or momentum. So, recording the occurence of unmeasured information maximizes one's ability to sidestep problem distortions. The occurence of unmeasurable events was carefully logged independent of the measurement process. In consultation with this information, corrections can be estimated for these missing records. For individual unmeasured tracks, measurers manually entered the number of unmeasured particles in five

categories after visually determining any obvious charge and mass identification. The number of unmeasured protons, negative and positive ambiguous particles (mostly pions), electrons, and positrons were entered into the event character with the flag character strings UMP, UMPIM, UMPIP, UMEM, and UMEP, respectively, followed immediately by a number indicating how many tracks of that category could not be measured.

Now in the few events where a track failed post-measurement, full-event, reconstruction (as opposed to the on-line, single-track reconstruction during event digitization), the failed track automatically was transferred into the ranks of the unmeasured tracks and deleted from the record. The number of such non-reconstructible tracks was well under 1%.

Referring to $\langle N_{p_{black}} \rangle um$ in **Table 2.1.2** it can be seen that about .5 proton tracks could not be measured per event. Since these unmeasured tracks were visually identified on the basis of their *black* appearance, they have been classified to be slow protons with $\beta < .3$. The unmeasured proton multiplicity makes up 25 to 50% of the final corrected black proton multiplicity. This large percentage of unmeasured protons stems from the fact that many of the slow protons stop so soon that only a short stub is visible, too short to measure and/or to reconstruct.

Unmeasurability was much less of a problem with electrons and ambiguous particles. Fewer than .1 electron tracks remained unmeasured per event. Of the particles whose identity remained in question and which were treated as pions by default, fewer than .1 tracks remained unmeasured per event. On the average 2% of the final corrected pion multiplicities were ambiguous unmeasured tracks.

2.1.4 Event record modifications

Once digitization of event tracks was completed (March 1984), a number of repairs, improvements and/or additions were made to the raw measurement records as bubble chamber data processing continued. Using SELECTVT the original records were permanently modified and the faulty or incomplete original discarded.

Table 2.1.2 Average number of unmeasured tracks per event.

THICK FOILS

Projectile	320GeV/c		100GeV/c									
	π^-		π^+		p		π^-			p		
$^{A}_{Z}Target$	$^{108}_{47}Ag$	$^{197}_{79}Au$	$^{108}_{47}Ag$	$^{197}_{79}Au$	$^{108}_{47}Ag$	$^{197}_{79}Au$	$^{24}_{12}Mg$	$^{108}_{47}Ag$	$^{197}_{79}Au$	$^{24}_{12}Mg$	$^{108}_{47}Ag$	$^{197}_{79}Au$
BTC	61	64	131	134	141	144	176	171	174	186	181	184
N_{events}	184	127	178	128	308	110	120	604	457	75	439	277
$\langle N_{p_{black}}\rangle$um	.223	.425	.247	.438	.299	.509	.092	.330	.602	.173	.355	.740
Δ	.038	.084	.048	.078	.042	.087	.029	.031	.057	.066	.036	.077
$\langle N_{a^+}\rangle$um	.125	.268	.062	.125	.104	.127	.058	.103	.142	.027	.144	.155
Δ	.030	.096	.024	.041	.021	.034	.024	.016	.020	.019	.023	.028
$\langle N_{a^-}\rangle$um	.092	.181	.096	.094	.078	.118	.083	.093	.153	.053	.103	.101
Δ	.025	.070	.027	.028	.015	.044	.035	.015	.029	.032	.018	.036
$\langle N_{e^+}\rangle$um	.049	.087	.045	.055	.062	.073	.008	.060	.092	.040	.112	.162
Δ	.018	.025	.016	.025	.016	.028	.008	.010	.015	.023	.020	.027
$\langle N_{e^-}\rangle$um	.076	.118	.079	.070	.101	.118	.008	.123	.133	-	.150	.162
Δ	.021	.048	.020	.023	.020	.036	.008	.015	.019	-	.021	.026

UM_THICK.TEX UND/MCKM 28Nov88

THIN FOILS

Projectile	320GeV/c		100GeV/c									
	π^-		π^+		p		π^-			p		
$^{A}_{Z}Target$	$^{108}_{47}Ag$	$^{197}_{79}Au$	$^{108}_{47}Ag$	$^{197}_{79}Au$	$^{108}_{47}Ag$	$^{197}_{79}Au$	$^{24}_{12}Mg$	$^{108}_{47}Ag$	$^{197}_{79}Au$	$^{24}_{12}Mg$	$^{108}_{47}Ag$	$^{197}_{79}Au$
BTC	62	63	132	133	142	143	175	172	173	185	182	183
N_{events}	137	135	124	112	169	129	224	406	403	181	276	280
$\langle N_{p_{black}}\rangle$um	.467	.726	.282	.571	.497	.705	.183	.542	.824	.171	.598	.882
Δ	.081	.101	.058	.093	.068	.141	.039	.049	.068	.036	.063	.083
$\langle N_{a^+}\rangle$um	.088	.141	.073	.089	.047	.132	.049	.074	.127	.066	.098	.154
Δ	.028	.055	.026	.030	.018	.042	.016	.017	.023	.023	.024	.029
$\langle N_{a^-}\rangle$um	.058	.119	.032	.089	.089	.124	.076	.113	.139	.061	.116	.121
Δ	.020	.033	.016	.032	.031	.035	.021	.030	.026	.019	.024	.121
$\langle N_{e^+}\rangle$um	.036	.037	.040	.036	.024	.023	.004	.057	.065	.006	.058	.061
Δ	.019	.016	.021	.022	.012	.013	.004	.012	.013	.005	.014	.017
$\langle N_{e^-}\rangle$um	.022	.059	.073	.027	.059	.031	.013	.071	.079	.035	.051	.082
Δ	.012	.023	.028	.015	.018	.010	.008	.016	.016	.013	.014	.016

UM_THIN.TEX UND/MCKM 28Nov88

$\langle N_{p_{black}}\rangle$um average black proton unmeasured multiplicity
$\langle N_{a^+}\rangle$um average positive ambiguous(default pion) unmeasured multiplicity
$\langle N_{a^-}\rangle$um average negative ambiguous(default pion) unmeasured multiplicity
$\langle N_{e^+}\rangle$um average positron unmeasured multiplicity
$\langle N_{e^-}\rangle$um average electron unmeasured multiplicity

Frame number The most obvious repair to the data involved correcting the frame number on the BC measurement record. The beam tagging program required that frame numbers increase monotonically. It referenced a control list of frame numbers for measured events as it hooked the measured events to the DPI data records. If a frame number was smaller than the previous, or larger than the following, the tagging program broke down. When this occurred as post-digitization tagging was carried on, the written measurement records were consulted to verify the manual input error, and the measurement records were corrected accordingly. Only a few records needed correction of this type.

Foil number In the process of digitizing event tracks, measurers determined by inspection the identity of the target in which the measured event occurred and entered a foil number code. When comparing these foil numbers entered by the measurers with the vertex coordinates as determined by TVGP in a plot of the y component of the vertex coordinate vs. the foil number, it is clear that a number of foil numbers were either misassigned or entered incorrectly. These were simply changed in the record. Better spatial reconstruction in later analyses, however, brought out even more foil number inconsistencies which could be verified on film. Thus, for subsequent analysis, the use of recorded foil numbers was abandoned entirely in favor of determining target identity by vertex position alone.

Histograms of the vertices calculated in the spatial reconstruction of the events also made it possible to pick out a few errors made by the measurers in determining whether or not an event had occurred in a particular target. A plot of vertex positions y vs. z showed a small number of vertices which lay clearly outside the known and recognizable boundaries of the six targets. These few were deleted from the records as non-nuclear events.

Events with beam angles differing a great deal from the average were also stricken from the record as being spurious.

2.1.5 Track record modifications

Once track identities were established by ionization in the bubble chamber, a high order code was added to an existing low order measurer code for each track record. This addition to the records completed the bubble chamber data.

Forced charge However, mass hypotheses associated with ionization predictions included both charge states of a particle. In order to force the reconstruction of an identified particle to a particular charge state, a code was added to the ionization code which designated the need to force the charge. This was necessary when the tracks were very straight.

Ping number At one point, it was thought that the optical constants might be varying with ping number. Thus, the ping numbers for measured events from a few rolls were sought from the original downstream data tapes. These were incorporated into the original measurement records for those rolls. However, there appeared to be no clear correlation between variations in optical constants and the ping numbers associated with the frames from which the fiducial measurements for the optical constant generation were made. With no clear anticipated need for the ping number, the downstream records were not reprocessed to pick up the ping numbers for the rest of the rolls. Thus, only a few rolls' measurement records include the addition of the ping number in what is known as the *trigger* slot of the measurement record.

Track deletions Spurious, duplicated, or otherwise incorrect tracks were deleted by placing a *kill* code into the track record rather than erasing the track completely. Repairs of this sort included the tracks which were obviously unassociated with interactions. These were deleted on the basis of an additional visual scan for track ionizations described later. Under 1% of the tracks were affected.

2.2 SPATIAL RECONSTRUCTION

Spatial reconstruction was carried out on three fronts: 1) camera positions to determine the relation between real and image trajectories; 2) beam tracks to hook an individual interaction with its beam's tagging information; 3) secondary tracks to determine vertices and momenta, and indirectly particle identity.

2.2.1 Camera positions and optical constants

In order to convert digitized 2-dimensional photo images into 3-dimensional space curves of actual particle paths in NDBC coordinate space, appropriate rotations, translations, and magnifications relating the bubble chamber window markings (the fiducials) to the camera film planes were ascertained. This involved a number of steps, beginning with a fiducial survey of physical positions (**Table 1.4.2**), and digitization of fiducial images on three(3) of the film views shown in **Figure 2.1.1**. Program FIDCALC took individual fiducial xy points (dummied into standard track measurement records), reordered them when necessary (usually the first track, which is stored in reverse order on the measurement record), averaged them, and found standard deviations. Noting that these averages varied from roll to roll, only intra-roll fiducial measurements were averaged for input into the camera program CAMAJUST. In the process of gathering many such averages, raw measurement points were carefully checked for suspicious discrepancies. Relative positions between fiducials were compared directly with surveyed positions, invoking the proper least count for the machine measuring the fiducials (.5 and 1 μm). Large standard deviations were investigated for potential irregularities in the data. In most cases, discrepancies stemmed from measured-out-of-order points or poorly-measured points. Once the discrepancies were understood, modifications were made by throwing out a measurement pass or switching fiducials.

The program CAMAJUST took FIDCALC's averaged points and, with the addition of general camera and chamber window parameters (survey fiducial positions, indices of refraction, media between bubble chamber interior and camera film

plane, etc.), produced a set of optical constants in a format ready to input into the reconstruction program TVGP. The optical constants summarize the CAMAJUST's basic output, namely calculated camera and fiducial positions as well as a summary of translations, rotations, and magnifications that relate the physical fiducials to their film plane images. Errors on the fiducial positions provided a further check on the integrity of a particular optical constants set. But once discrepancies were accounted for, optical constants still varied. No obvious pattern emerged from studying camera and fiducial positions and their errors, so additional studies were carried out to discover correlations between the optical constants and ping number, roll number, date, and/or measurer. No clear pattern emerged on the basis of these studies.

Finally all BC digitized tracks in the event sample were reconstructed, roll by roll, with TVGP using all available optical constants sets. For each event roll/constants roll combination, the TVGP root-mean-square(rms) track error was tabulated. The optimum constants set for each measured roll was chosen on the basis of least rms track error and relative distance (by roll) between event measurements and fiducial measurements. The finalized, optimized constants-to-roll tally for Notre Dame track reconstruction was previously shown in **Table 2.1.1**.

2.2.2 Vertex reconstruction

As already mentioned, track and vertex images were reconstructed into 3-space with the standard Three View Geometry Program (TVGP). This FORTRAN classic calculates the inverse of a track's curvature, its dip, and its azimuthal angles at the primary vertex from digitized track information and a set of optical constants. The dip angle λ describes the angle between a track's momentum vector and its projection onto the z-axis (ie. in the xy plane). The azimuthal angle ϕ describes the angle between the momentum vectors's projection onto the z-axis and the projection onto the y-axis. **Figure 2.2.1** illustrates how these two angles relate to the NDBC coordinate system.

Since the primary vertex was obscured, TVGP swims all outgoing tracks back to a common vertex. Inspection of the vertex distribution perpendicular to the beam, shown in **Figure 2.2.2**, reveals that the geometry of the TVGP reconstructed

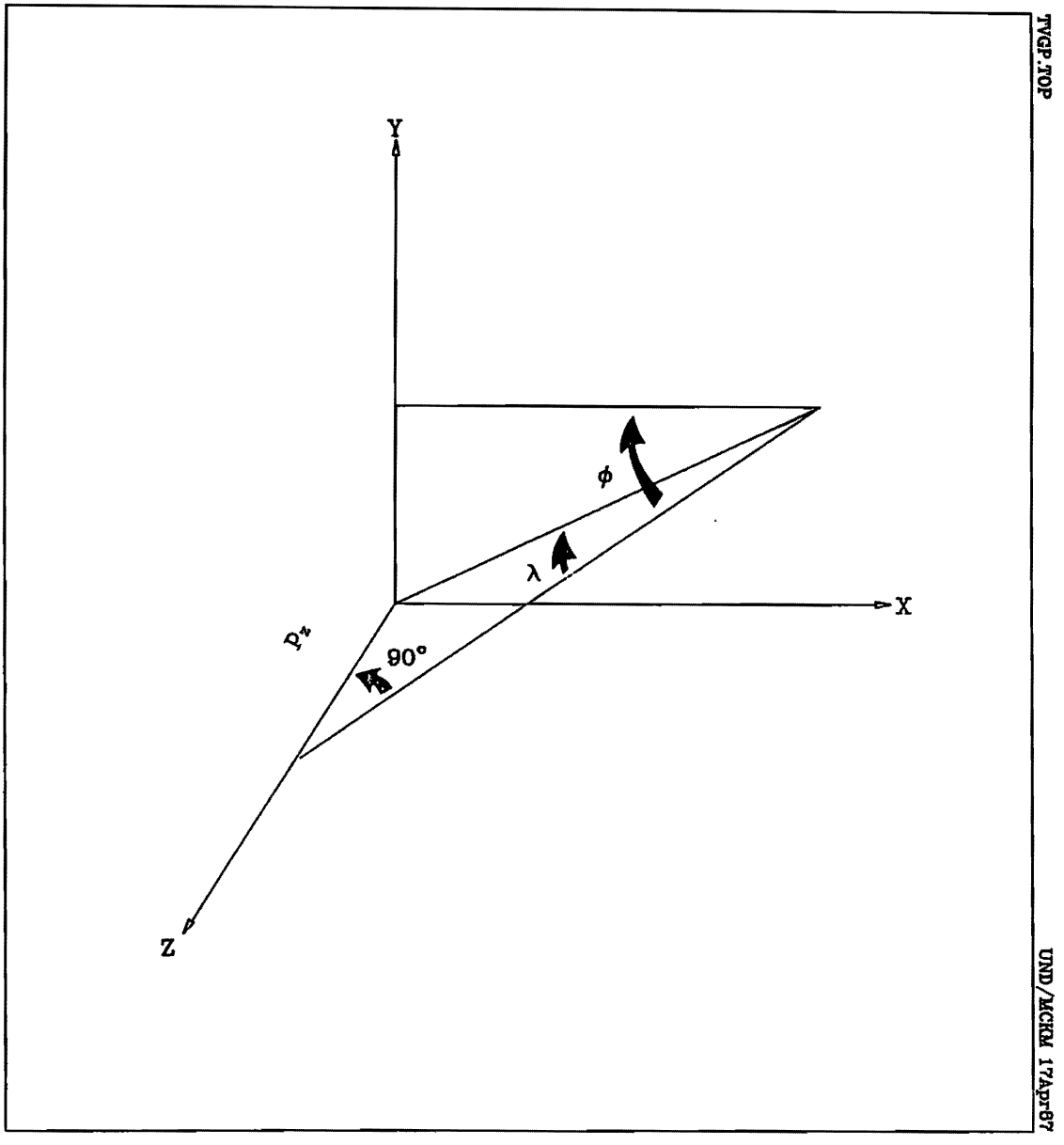

Figure 2.2.1 TVGP angle conventions for tracks reconstructed in the bubble chamber.

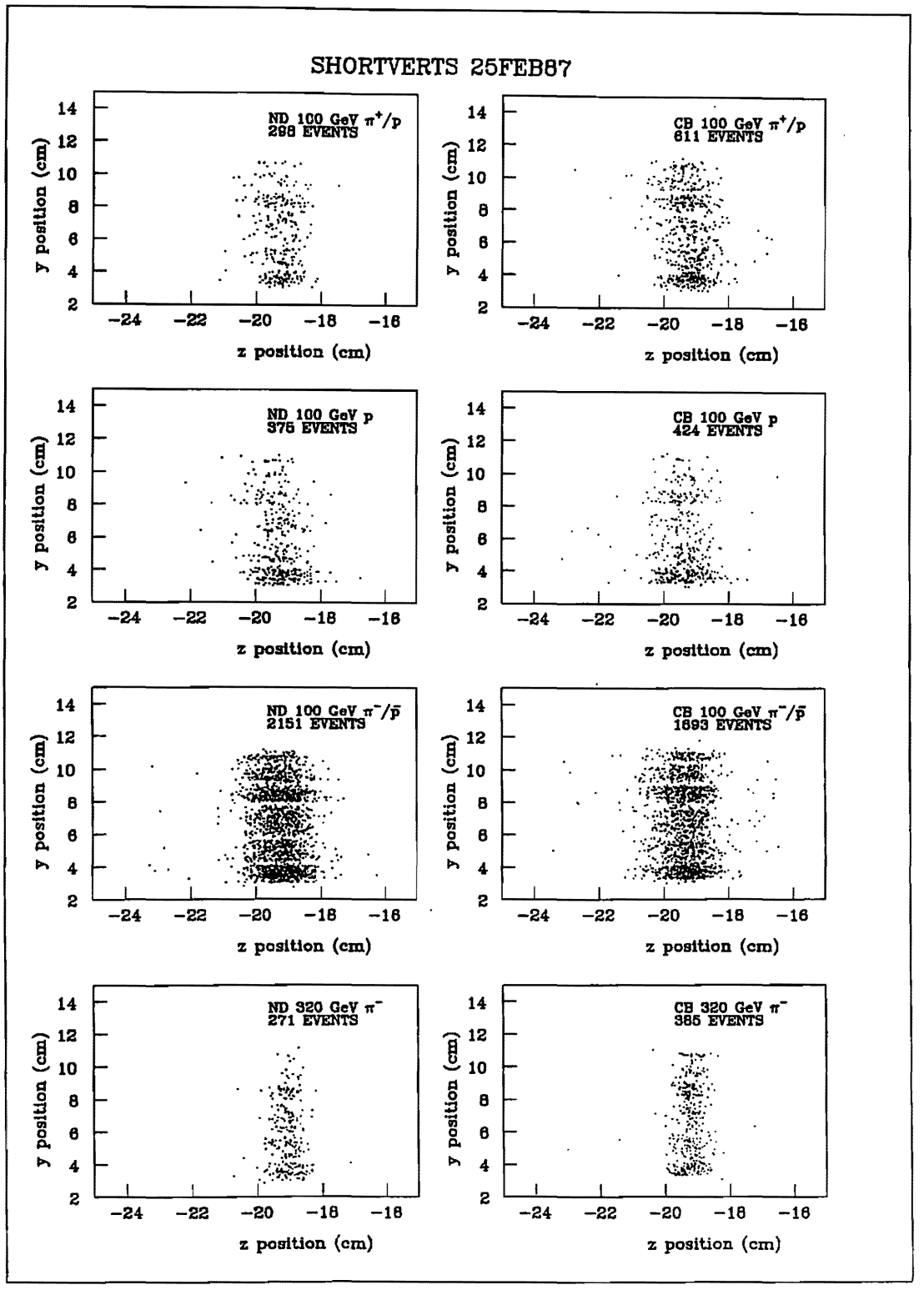

Figure 2.2.2 Distribution of reconstructed vertex positions in the yz plane.

vertices is indeed faithful to the geometry of the physical targets. The planes parallel to the beam do not give the same kind of correspondence as seen in **Figure 2.2.3**. However, good reconstruction along that axis is not expected. With few exceptions, attributable to non-nuclear events, all reconstructed vertices in the yz plane fall within the same physical region as the target, see **Figure 2.2.4**. On this basis, events were tagged with a target identification on the basis of vertex position. **Table 2.2.1** indicates the criteria by which these assignments were made.

2.2.3 Track reconstruction

Figures 2.2.5 and 2.2.6 show how smoothly track angles ϕ and λ are distributed between between -180° and 180° and between -90° and 90°, respectively. In the azimuthal angle ϕ, errors averaged under .4° as shown in **Figure 2.2.7**. This compares with average azimuthal errors under .3° for track reconstruction at Cambridge. In the dip angle λ, errors averaged .5° as compared to under .4° at Cambridge. These are shown in **Figure 2.2.8**. For analyses sensitive to errors in ϕ and in λ, cuts at 3° and 6°, respectively, were applied. These cuts represented less than 2% of the tracks.

The latter represent track reconstructions in the bubble chamber only. When fast forward secondaries were tracked in the DPI and hooked up to their bubble chamber trajectories, angular resolution generally improved. The MSU/PSU group made this improvement by minimizing the distance, in local coordinates, between each downstream PWC- and DC-determined position and the hypothesized trajectory point, transformed into the local coordinate system, where the trajectory intersects the device plane. Starting values were taken from the bubble chamber track reconstruction to create an initial *road* into the DPI devices. **Figures 2.2.9 and 2.2.10** show how the larger azimuthal errors were brought under control and how drastically the dip errors were reduced for charged tracks with momentum greater than 3 GeV/c when DPI was *hooked up*. **Table 2.2.2** shows how the average dip errors improved by roughly 90%. Since, however the azimuthal errors became larger, this was a trade-off justified by the fact that the dip angle errors were in much worse shape to start with and the fact that the large errors for both were brought under control.

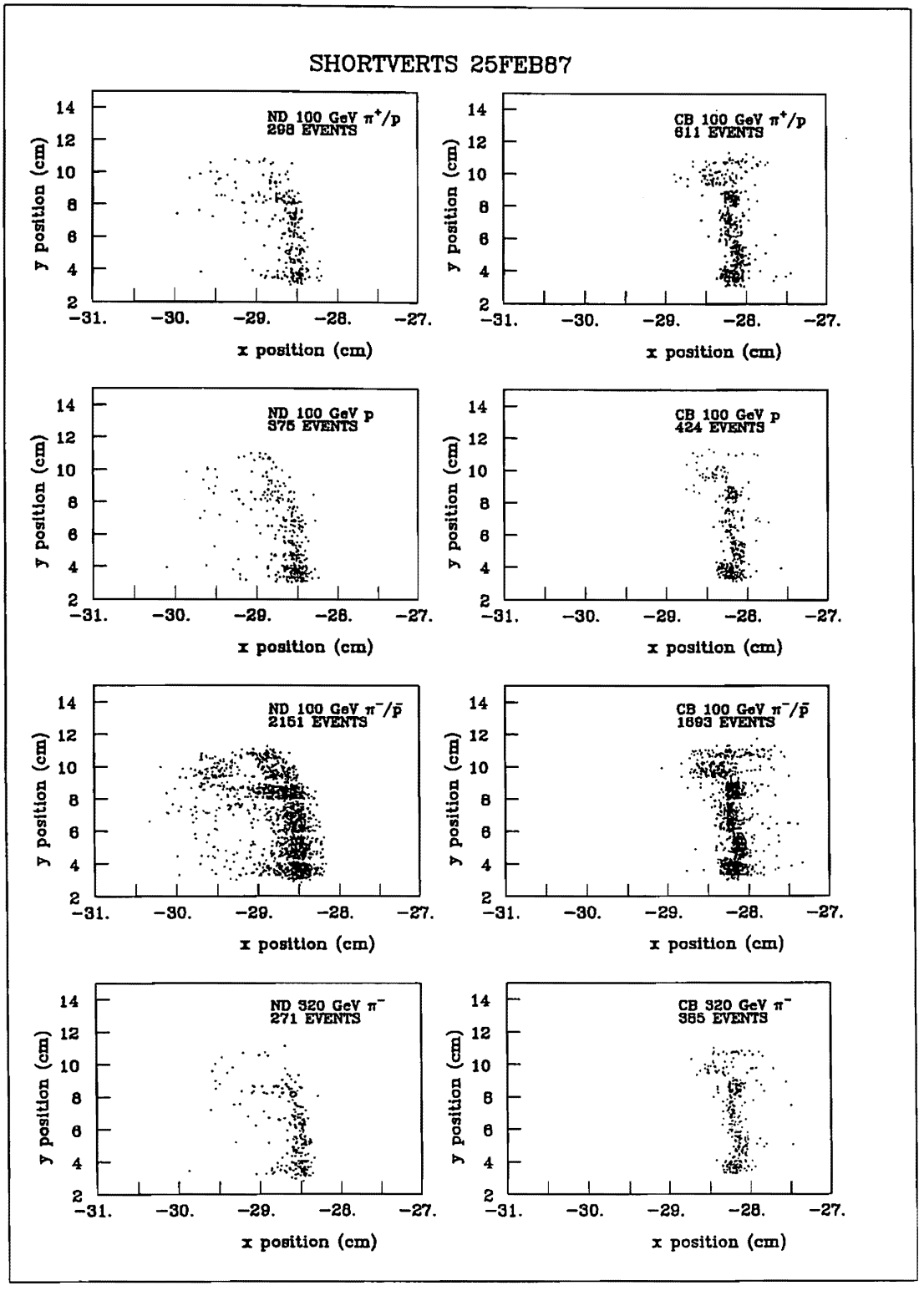

Figure 2.2.3 Distribution of reconstructed vertex positions in the yx plane.

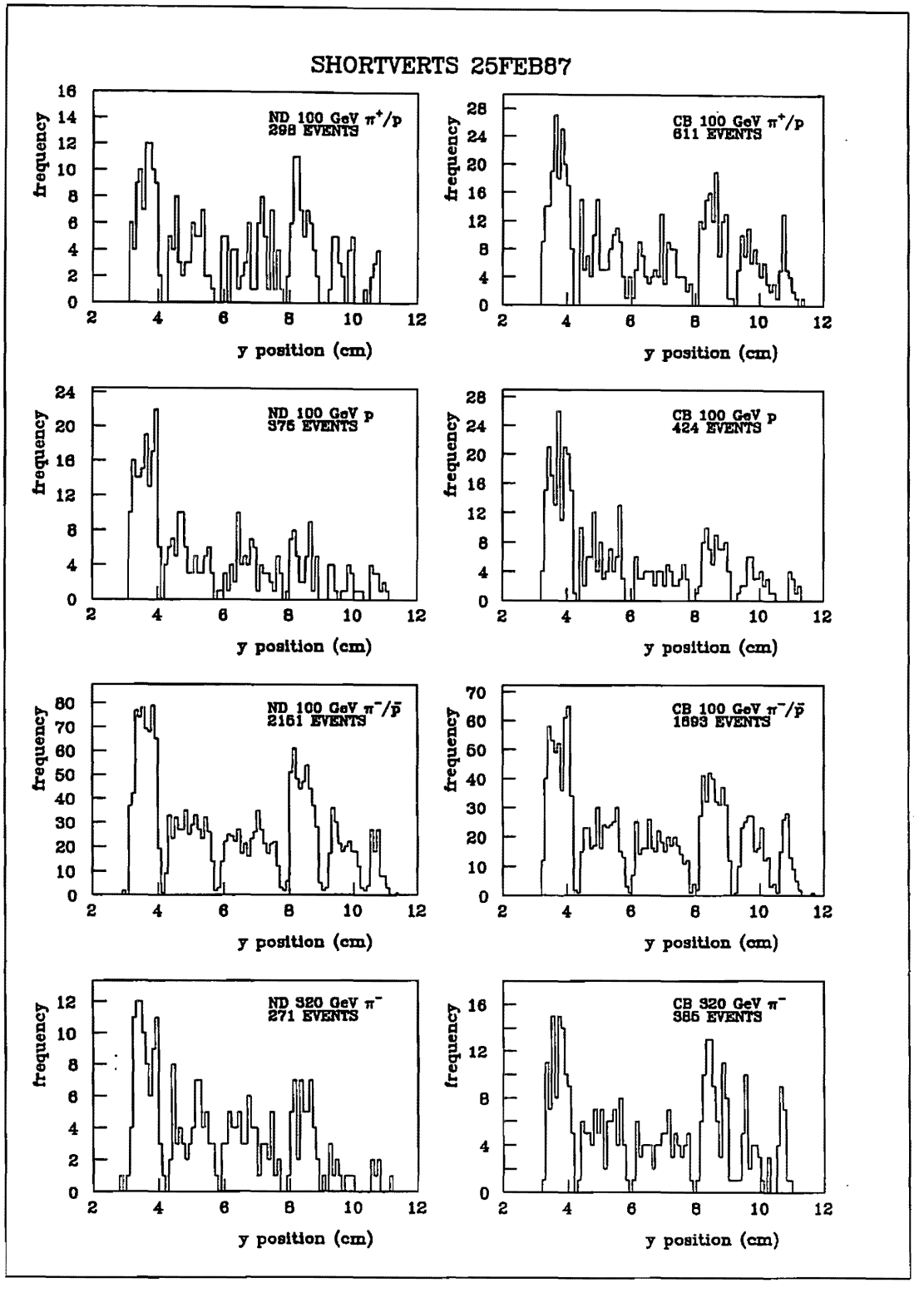

Figure 2.2.4 Distribution of reconstructed vertex positions along the y axis.

Table 2.2.1 Bubble chamber target position criteria for target identification as determined by reconstructed event vertices.

Target		Y Position Range	
Composition	Code No.	Minimum *(cm)*	Maximum *(cm)*
Ag	1	-	4.2
	2	4.2	5.9
Au	3	5.9	7.9
	4	7.9	9.1
Mg	5	9.1	10.4
	6	10.4	-

Ref: MM/May86(97)

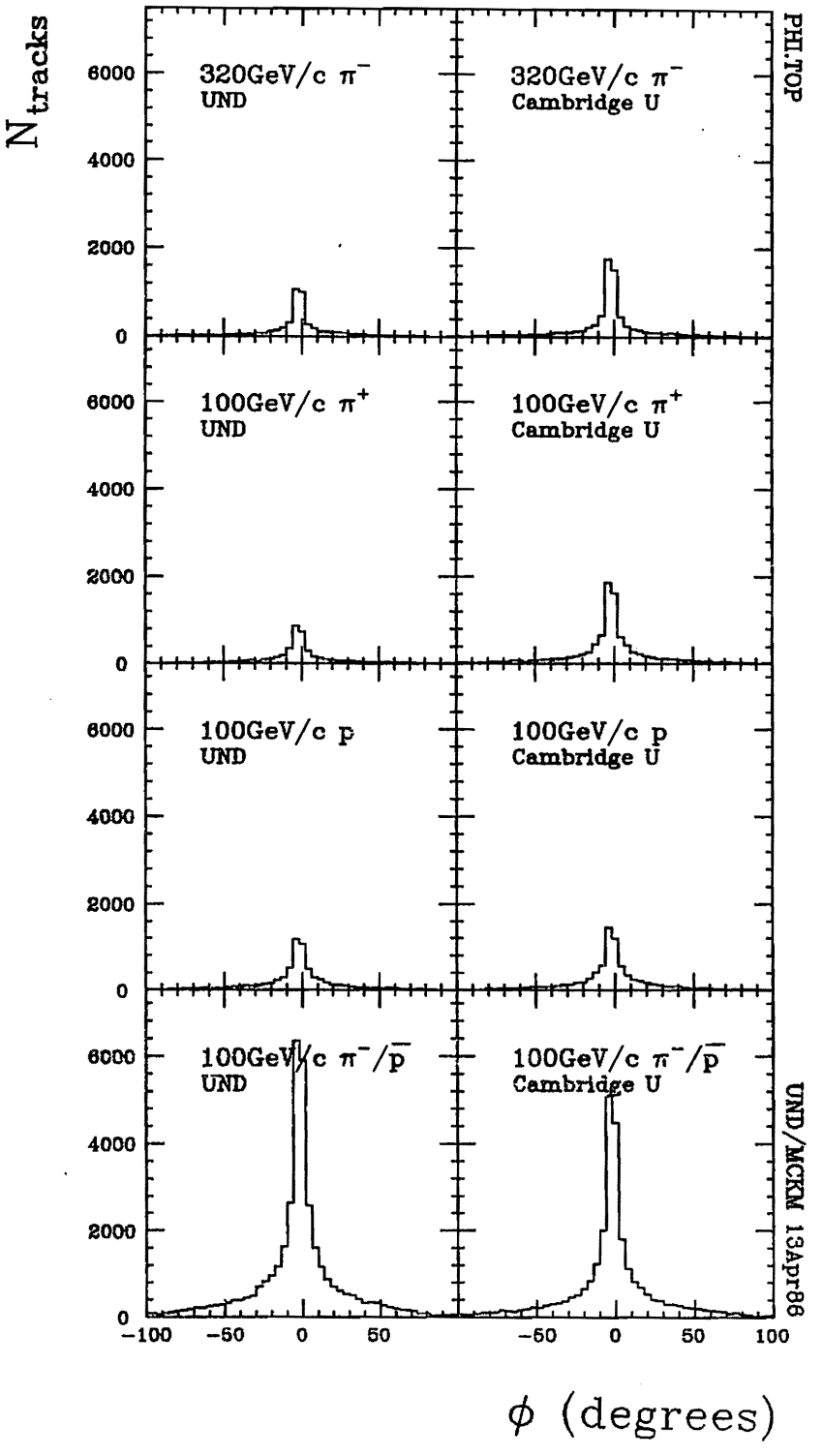

Figure 2.2.5 Distribution of measured track azimuthal angle ϕ.

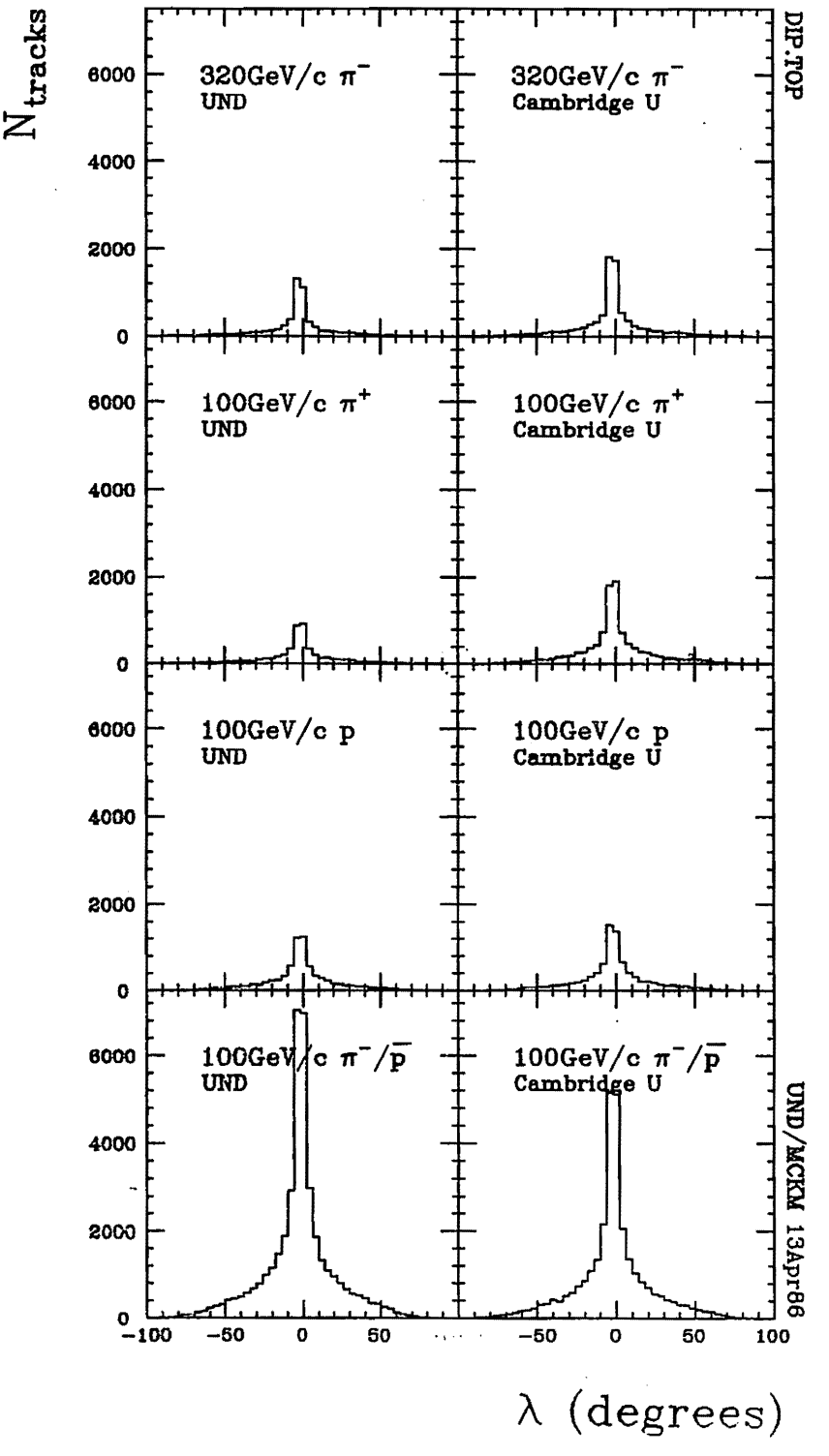

Figure 2.2.6 Distribution of measured track dip angle λ.

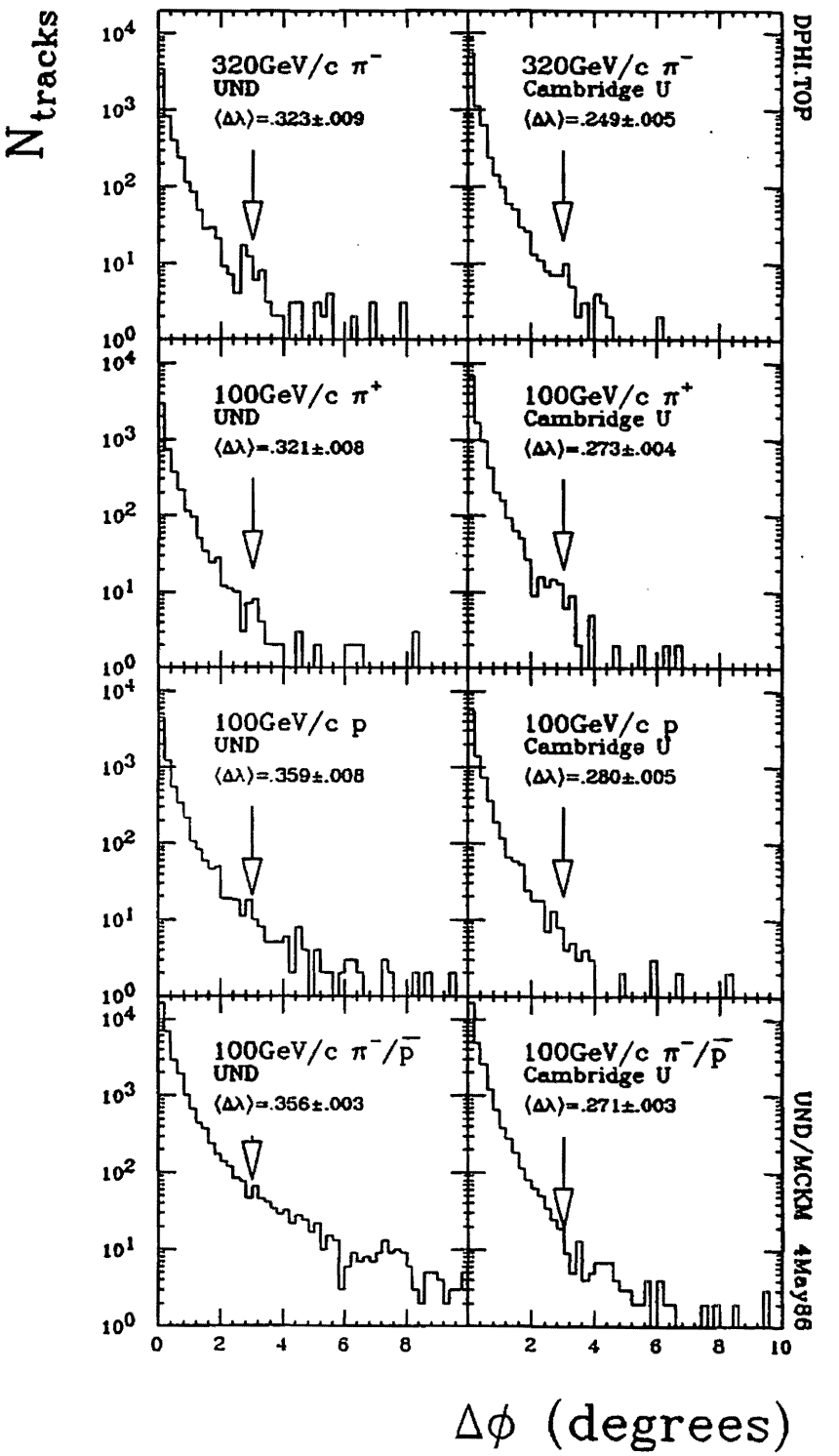

Figure 2.2.7 Distribution of errors for measured track azimuthal angle ϕ.

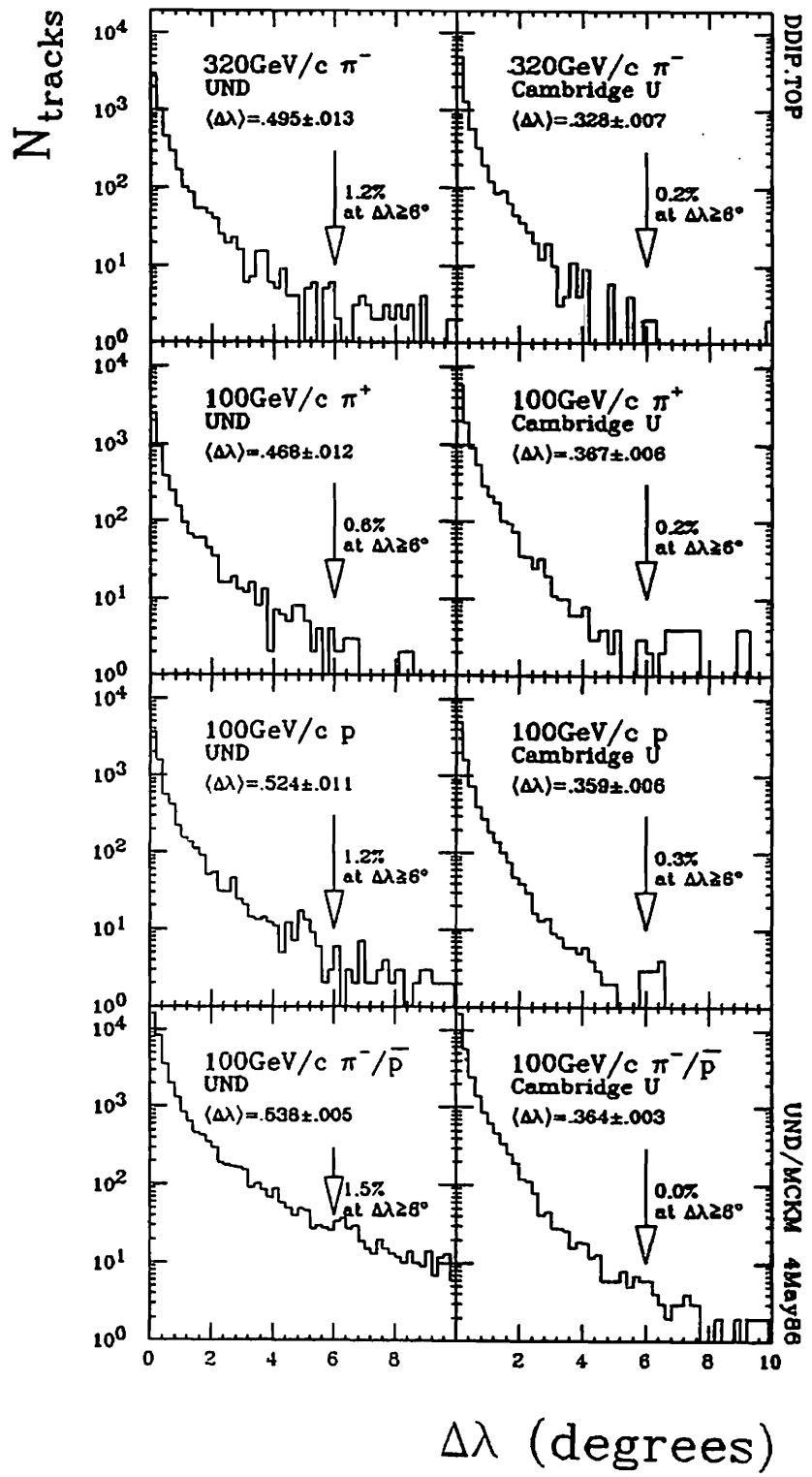

Figure 2.2.8 Distribution of errors for measured track dip angle λ.

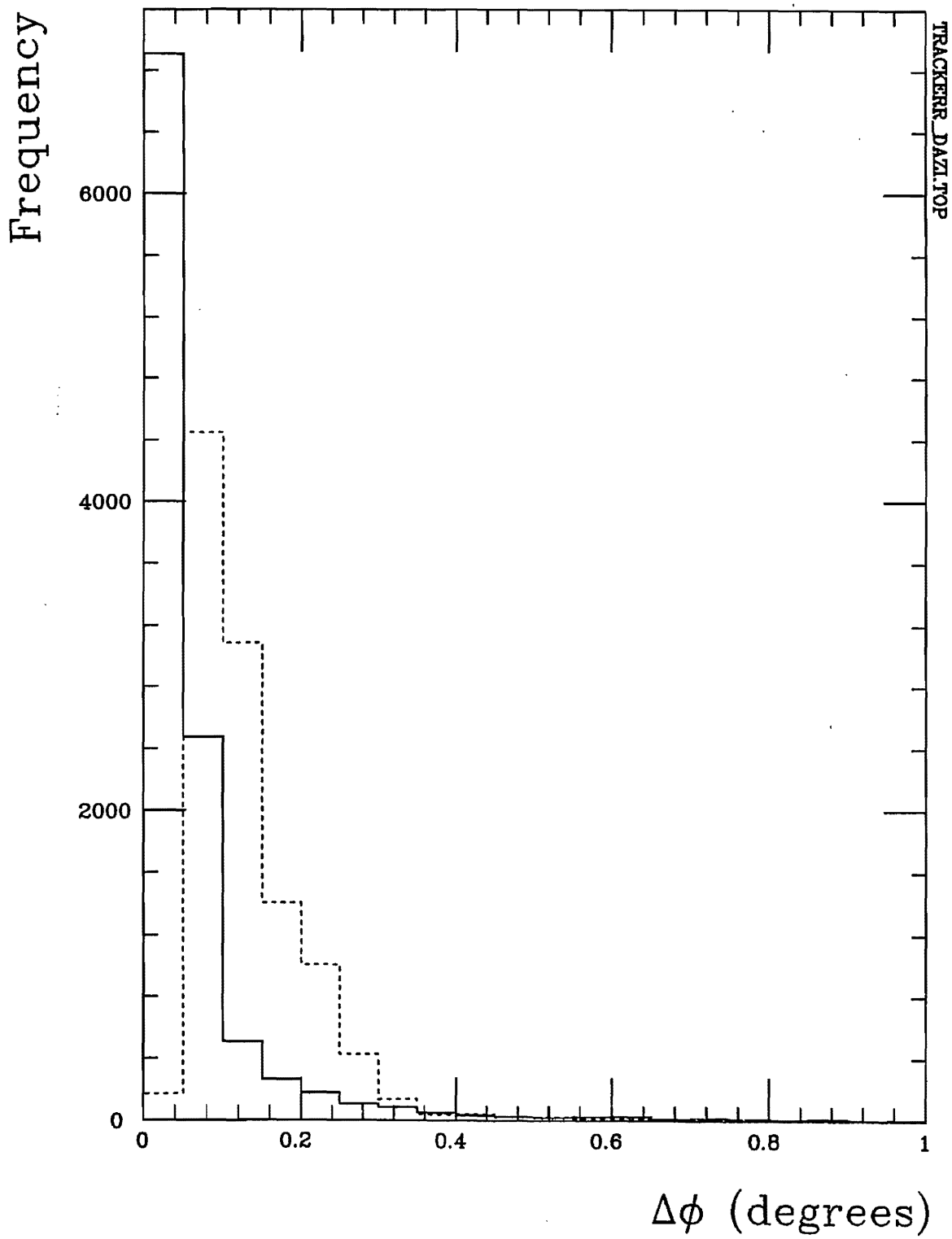

Figure 2.2.9 Comparing azimuthal errors for charged tracks (excluding electrons) with $p > .3$ GeV/c which could be hooked up to the DPI with those which could not. The solid outline shows the *unhooked* from the SHORTDST study sample, the dashed shows the *hooked* from the DSBC study sample normalized to the SHORTDST distribution.

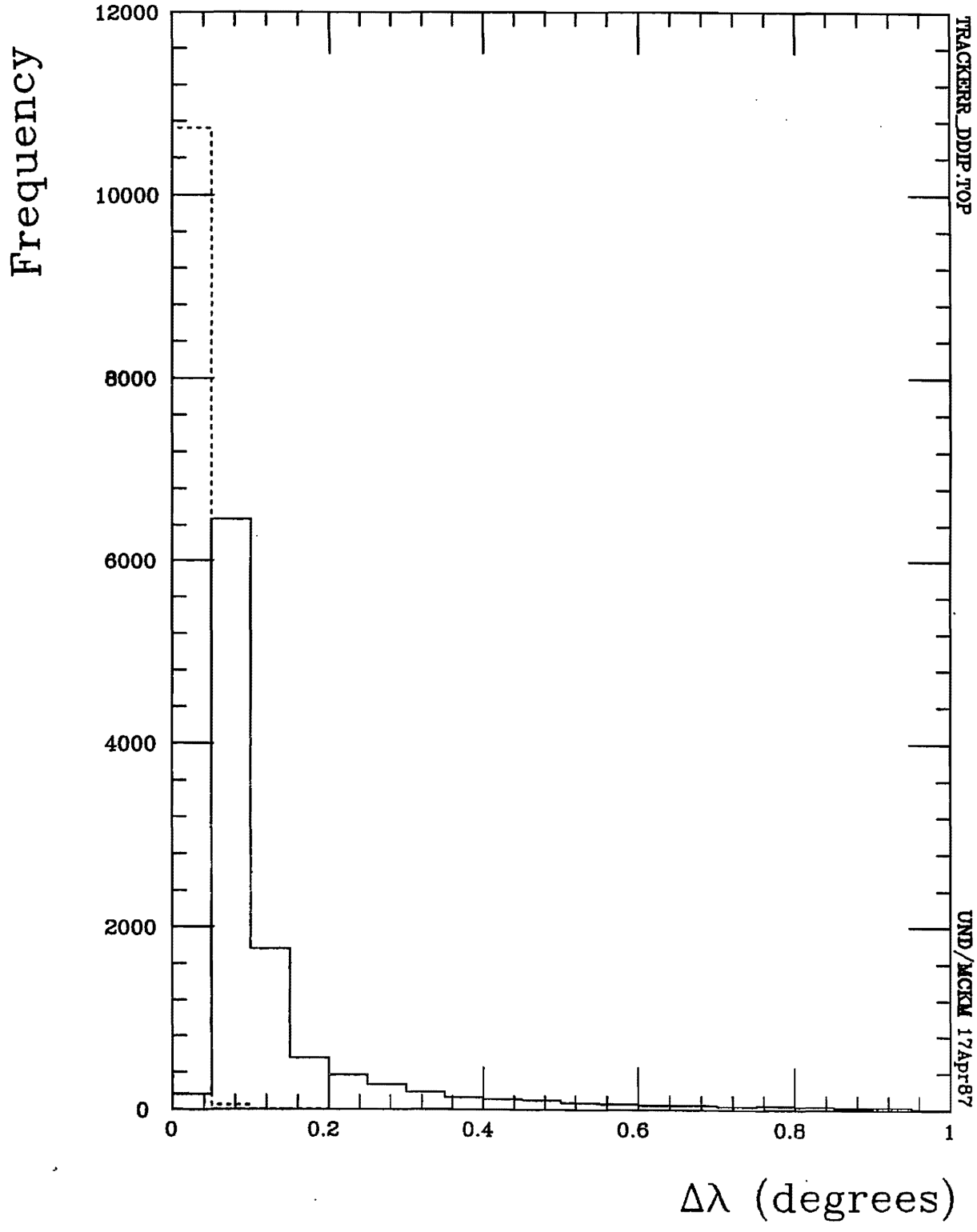

Figure 2.2.10 Comparing dip angle errors for charged tracks (excluding electrons) with $p > .3$ GeV/c which could be hooked up to the DPI with those which could not. The solid outline shows the SHORTDST study sample tracks which included hooked tracks, the dashed shows the DSBC study sample with no hooking attempted. The DSBC distribution is normalized to the SHORTDST distribution.

Table 2.2.2 Comparing SHORTDST597 hooked and unhooked track errors with DSBC track errors. *Hooked*(*unhooked*) tracks were(were not) tracked successfully through the DPI to improve the quality of track momenta and dip angles. Only tracks with $p > 3$ GeV/c successfully hooked into the DPI, thus, for comparative purposes, DSBC and unhooked SHORTDST597 data are limited to this range.

THICK FOILS

Projectile	320GeV/c		100GeV/c									
	π^-	π^-	π^+	π^+	p	p	π^-	π^-	π^-	$\bar{p}$	$\bar{p}$	$\bar{p}$
$^{A}_{Z}Target$	$^{108}_{47}Ag$	$^{197}_{79}Au$	$^{108}_{47}Ag$	$^{197}_{79}Au$	$^{108}_{47}Ag$	$^{197}_{79}Au$	$^{24}_{12}Mg$	$^{108}_{47}Ag$	$^{197}_{79}Au$	$^{24}_{12}Mg$	$^{108}_{47}Ag$	$^{197}_{79}Au$
BTC	61	64	131	134	141	144	176	171	174	186	181	184
$\langle dp/p \rangle$												
SHORT hooked	.083	.078	.058	.052	.054	.059	.061	.064	.061	.056	.088	.056
Δ	.003	.004	.002	.002	.002	.004	.003	.002	.002	.003	.002	.002
SHORT unhooked	.102	.081	.062	.060	.069	.063	.068	.076	.077	.090	.077	.080
Δ	.006	.006	.005	.007	.004	.007	.006	.003	.004	.012	.004	.005
DSBC	.128	.125	.062	.062	.071	.063	.081	.097	.089	.077	.077	.081
Δ	.005	.007	.003	.004	.003	.005	.005	.002	.003	.007	.003	.003
$\langle d\phi \rangle$ in degrees												
SHORT hooked	.114	.112	.128	.127	.122	.130	.127	.142	.138	.134	.146	.145
Δ	.003	.003	.004	.004	.003	.006	.005	.003	.003	.005	.003	.004
SHORT unhooked	.086	.088	.071	.066	.098	.080	.059	.075	.084	.090	.078	.077
Δ	.007	.010	.007	.005	.011	.008	.003	.005	.006	.011	.005	.005
DSBC	.069	.059	.046	.050	.071	.057	.051	.050	.056	.059	.055	.058
Δ	.003	.003	.002	.002	.006	.005	.003	.002	.003	.005	.002	.003
$\langle d\lambda \rangle$ in degrees												
SHORT hooked	.013	.011	.012	.012	.013	.013	.012	.013	.013	.012	.013	.013
Δ	.001	.000	.000	.000	.000	.000	.000	.000	.000	.000	.000	.000
SHORT unhooked	.190	.190	.154	.142	.176	.184	.132	.160	.175	.211	.167	.170
Δ	.013	.018	.016	.011	.012	.021	.009	.007	.010	.033	.008	.009
DSBC	.166	.135	.102	.107	.131	.130	.111	.108	.115	.143	.126	.130
Δ	.009	.008	.006	.006	.007	.013	.010	.003	.004	.017	.005	.005

Table 2.2.2 Continued.

THIN FOILS

Projectile	320GeV/c		100GeV/c									
	π^-	π^-	π^+	π^+	p	p	π^-	π^-	π^-	$\bar{p}$	$\bar{p}$	$\bar{p}$
$^{A}_{Z}Target$	$^{108}_{47}Ag$	$^{197}_{79}Au$	$^{108}_{47}Ag$	$^{197}_{79}Au$	$^{108}_{47}Ag$	$^{197}_{79}Au$	$^{24}_{12}Mg$	$^{108}_{47}Ag$	$^{197}_{79}Au$	$^{24}_{12}Mg$	$^{108}_{47}Ag$	$^{197}_{79}Au$
BTC	62	63	132	133	142	143	175	172	173	185	182	183
$\langle dp/p \rangle$												
SHORT hooked	.079	.073	.056	.057	.062	.064	.064	.067	.063	.062	.060	.066
Δ	.003	.003	.003	.003	.003	.005	.003	.002	.002	.002	.002	.003
SHORT unhooked	.104	.105	.066	.066	.071	.055	.081	.077	.084	.078	.087	.078
Δ	.008	.007	.007	.008	.006	.005	.006	.004	.004	.006	.005	.005
DSBC	.135	.138	.063	.072	.075	.064	.084	.097	.100	.074	.085	.085
Δ	.006	.007	.004	.005	.005	.004	.004	.003	.003	.004	.004	.004
$\langle d\phi \rangle$ in degrees												
SHORT hooked	.115	.111	.116	.131	.127	.122	.133	.135	.137	.140	.140	.132
Δ	.003	.003	.004	.005	.005	.005	.004	.003	.003	.004	.004	.003
SHORT unhooked	.093	.092	.074	.079	.072	.064	.072	.085	.090	.066	.088	.090
Δ	.011	.009	.009	.009	.007	.007	.005	.007	.006	.004	.007	.009
DSBC	.069	.074	.065	.057	.053	.048	.054	.055	.060	.050	.067	.058
Δ	.004	.006	.007	.004	.003	.003	.003	.003	.003	.002	.004	.003
$\langle d\lambda \rangle$ in degrees												
SHORT hooked	.012	.013	.012	.012	.012	.013	.012	.013	.013	.012	.012	.013
Δ	.000	.001	.000	.000	.000	.001	.000	.000	.000	.000	.000	.000
SHORT unhooked	.199	.197	.173	.166	.157	.127	.166	.187	.181	.146	.200	.183
Δ	.015	.017	.024	.021	.013	.010	.015	.012	.011	.012	.012	.012
DSBC	.163	.158	.136	.132	.119	.099	.121	.117	.124	.110	.156	.127
Δ	.010	.011	.013	.012	.007	.005	.007	.005	.005	.006	.008	.006

2.2.4 Beam reconstruction

Track reconstruction followed essentially the same procedures for beam tracks as for full events. In the measurement records used for beam track reconstruction, all the record slots normally reserved for secondaries in an event are simply used for the various beams in a single frame and the output is interpreted accordingly. However, beam tracks are very short in hA events. Therefore, the angles and momenta are generally very poorly determined. Measured *through beams* (ie. non-interacting beams) are much more reliably measured.

The average azimuthal and dip angles for the Cambridge-measured beam particles in the various modes were adopted for the entire sample on the basis of a number of studies with Notre Dame-measured events. A study was made of 1) directly measured beam angle distributions, 2) summed secondary track momenta, and 3) rotation angles by which summed momenta, projected onto y and z, would be symmetrically distributed about zero. It was concluded that the Cambridge-determined beam angles expressed the concensus. In the interests of uniformity, Notre Dame adopted their values. In all analyses, other than the cut on electromagnetic interactions for which the beam angle was determined event by event, all tracks were rotated by the average CB beam angles given in **Table 2.2.3.**

2.3 MOMENTUM DETERMINATION

Based on TVGP's reconstruction, namely the curvature and dip, another classic program ARROW associated each track with various masses and corresponding calculated momenta. When particle identification was made by ionization (discussed in the next section), the mass then in fact determined the selection of momentum assigned each track.

2.3.1 Secondary track momenta

Track momenta for produced secondaries are regularly distributed as seen in a representative plot of proton, π^+, and π^- secondaries in **Figure 2.3.1.** The magnitude

Table 2.2.3 Average beam angles for Notre Dame (ND) and Cambridge University (CB) measured events. When rotating an event's x-axis to the beam direction, the average beam angles for CB events was used. These are compared to the rotations θ and λ required for the medians of the sum of secondary momentum components p_y and p_z respectively to vanish.

Sub-Sample	Avg Azimuth (°)	Avg dip (°)	θ *Rotation* (°)	λ Rotation (°)
CB 320	-.1497	-.0489	-.10	.00
CB Plus	-.2496	-.0277	-.22	.02
CB Proton	-.2498	+.0639	-.28	-.03
CB Negative	-.2498	+.0060	-.22	-.04
ND 320	-.2804	-.0281	-.17	-.27
ND Plus	-.4848	+.0033	-.28	.04
ND Proton	-.2882	+.0326	-.21	-.01
ND Negative	-.2653	+.6358	-.24	-.04

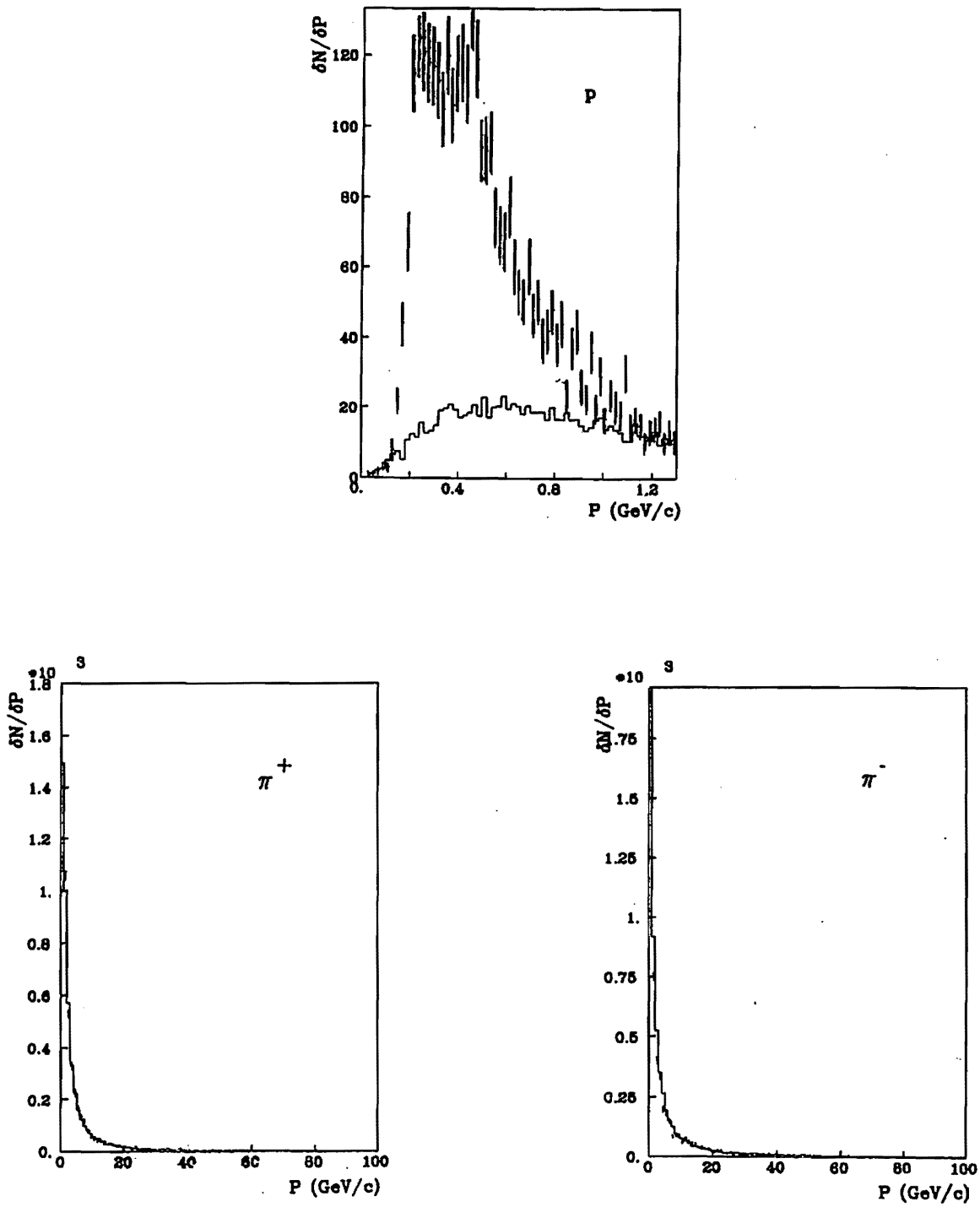

Figure 2.3.1 Representative distributions of proton, π^+, and π^- momenta in 100 GeV/c $\pi^- Au$ compared with 5000 comparable FRITIOF events normalized to the experimental sample of 860 hA.

remains largely below the beam momentum except where large errors plague the faster tracks in the bubble chamber. A Peyrou plot of transverse vs. longitudinal momentum in **Figure 1.1.1** has already shown the general low $p_\perp$ nature of hadron-nucleus interactions.

Momentum errors were considerably improved by hooking tracks into the DPI. With BC track reconstruction only, the minimum relative momentum error dp/p normally increases with momentum as shown in **Figure 2.3.2** with a slope of about $dp/p^2 = .3$. This minimum is seen to be considerably improved for hooked fast forward particles. The relative momentum errors for hooked tracks increase with a slope of $dp/p^2 = .2/(\mathrm{GeV/c})$ and are likewise limited to populate only the dp/p region below .2.

The relative momentum error distribution dp/p in **Figure 2.3.3** for the unimproved momentum in sample DSBC exhibits a rather extended tail, mostly attributable to tracks with momentum greater than 4 GeV/c, the range for which the DPI becomes useful. Whereas the relative momentum error distributions for the DSBC unimproved tracks typically extended out to and beyond 1.0, the DPI hookup contracted their extent in most cases to below .4.

However, the tracks with momentum less than 4 GeV/c (and thus ineligible for improvement by the DPI) already have a low dp/p. Thus in **Figure 2.3.4** it can be seen that the relative momentum errors for the hooked tracks in SHORTDST597 are still larger than those that remain unhooked. The tracks which made up the extended tail in the error distribution are incorporated into the main body of the distribution, shifting the distribution modes to slightly higher values. **Table 2.2.2** in the previous section shows how the average relative errors were reduced as much as 47% for the 320 GeV/c data and 37

For portions of the analysis particularly sensitive to momentum errors, eg. $p_\perp$ averages and seagull effects, a general cut on $dp/p \geq .8$ was made to clean up the worst tracks.

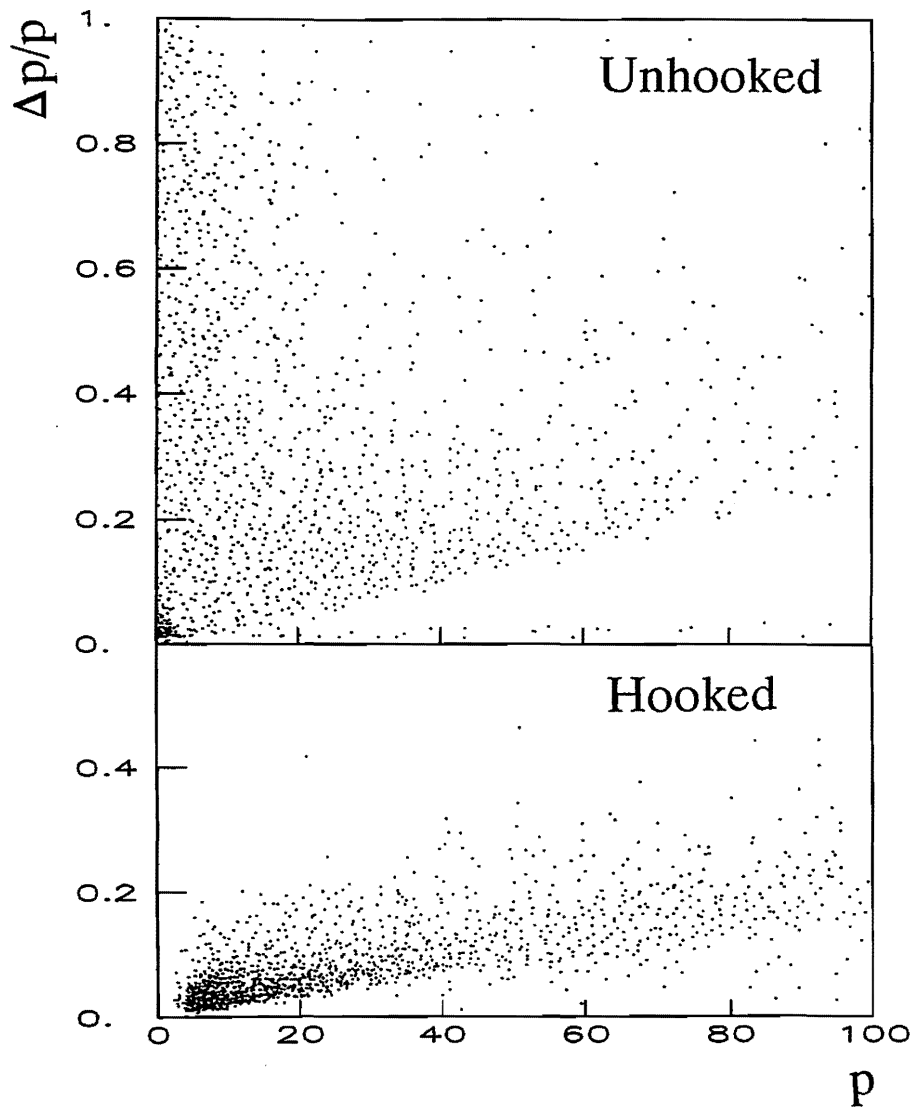

Figure 2.3.2 The relative momentum error $\Delta p/p$ *vs.* momentum p for measured tracks in the SHORTDST597 sample with $p > 4$ GeV/c which were NOT successfully hooked to DPI data and those which were.

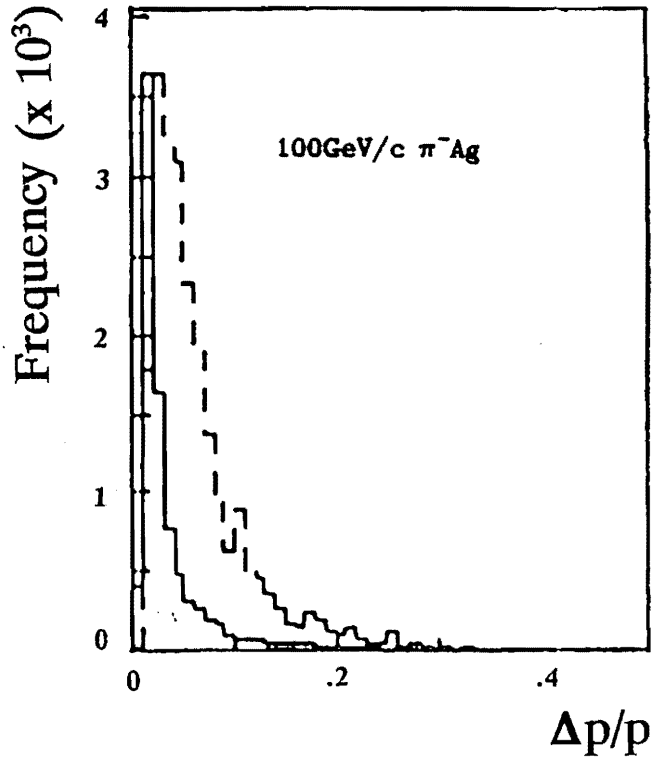

Figure 2.3.3 Comparing the distribution of relative momentum error $\Delta p/p$ for tracks with $p > 4$ GeV/c in the DSBC (dashed) and SHORTDST597 (solid) samples. The DSBC tracks have pre-momentum-improvement momenta and errors; SHORTDST597 tracks have post-momentum-improvement momenta and errors from successful hooks to DPI data.

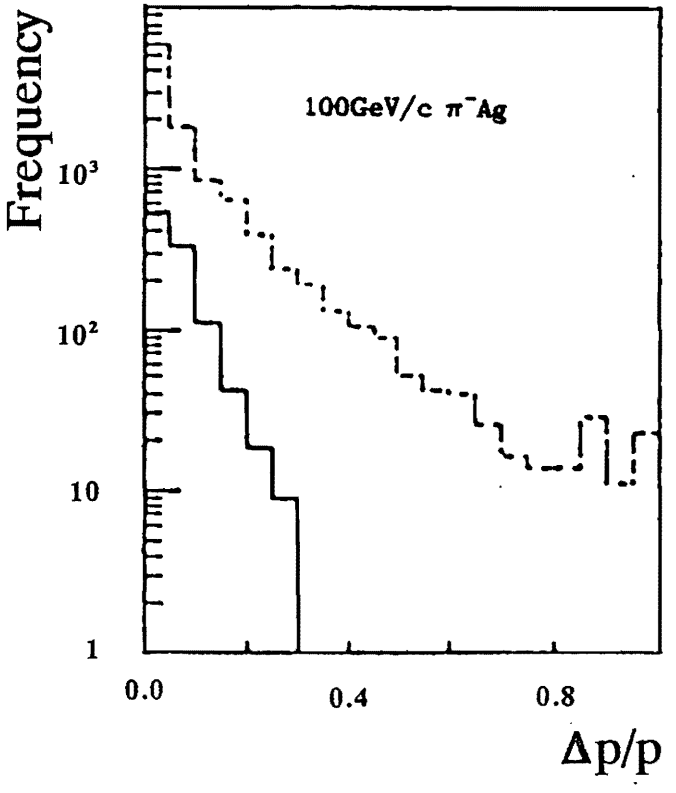

Figure 2.3.4 Comparing the distribution of relative momentum error $\Delta p/p$ for hooked (dashed) and unhooked (solid) tracks with $p > 4$ GeV/c in SHORTDST597 samples.

2.3.2 Beam momenta

Using zero field beam data, the Cambridge University group determined the various beam momenta. Bubble chamber reconstruction for beam tracks in the magnetic field is not good enough. The straightness of the tracks preclude decent reconstruction via TVGP. So their determination was made by comparing beam track positions in upstream and downstream PWCs in field-on and field-off beam data (recall that every 10 or 20 frames were measured for straight-through beam tracks). The beam momentum was determined by the momentum which would have been required to bend the zero-field tracks (given by their PWC positions) to coincide with the field-on tracks (defined by their PWC positions) with the fringe field. In this fashion, the so-called 100 GeV/c negative beam was determined to be 99.6±1.0 GeV/c. The so-called 100 GeV/c positive beam was determined to be 99.2±1.0 GeV/c. The higher energy beam, the so-called 320 GeV/c negative beam, was determined to be 308.0±5.0 GeV/c. These values were used in all calculations throughout for beam and maximum secondary momenta. However, beams will be referred to in terms of their nominal 100 GeV/c and 320 GeV/c values.

2.4 PARTICLE IDENTIFICATION

Since projectiles were mixed in E597, mass identification was as important for the beam as for the produced secondaries. Mass identification on the beam was carried out with upstream Cerenkov information. Secondary particles were identified either by bubble chamber ionization or by means of DPI information.

2.4.1 Beam tagging

A number of steps preceded the identification process for projectiles. First, a list of event frame numbers was compiled with the program FRAMELIST. This list governed the program CONCISE's reformatting of the DPI records into a more concise form, excluding irrelevant non-event data. Then the program MMTRAK reconstructed beam tracks of interest using upstream data alone. Finally, the program MMTAGG

compared these tracks with bubble chamber tracks parameters. When a DPI track coincided with a bubble chamber track to within PWC resolution, the BC track was assigned the DPI track's mastergate number and its Cerenkov data.

The Cerenkov data were expressed in terms of the code IOIOD. The code digits I, O, and D take on the values 1 and 0, depending on whether light was or was not detected, respectively, in the particular Cerenkov associated with the digits' place values. The ten-thousands place was associated with the Cerenkov Inner 116; the thousands, with Outer 116; the hundreds, with Inner 118; the tens, with Outer 118, and the ones, with the *Doghouse* Cerenkov. The tagging scheme was summarized previously in **Table 1.4.2** on the basis of the Cerenkov running conditions.

Later, in post-measurement analysis while graphically comparing CRISIS and BC track reconstructions, it became apparent that a significant number of events had been tagged incorrectly, ie. had been associated with the wrong mastergate. Therefore, all beams were retagged in the overall PSU momentum improvement project, using the downstream counters to determine the mastergate, and the upstream counters for the beam tag. An undetermined number of the previously untagged and unmeasured events would have increased our sample size had they been tagged with the downstream as well as the upstream information initially.

2.4.2 Track identification by ionization

The particle identity of tracks can be ascertained by considering the following track characteristics in the bubble chamber:

- curvature in a magnetic field
- signature decays
- stopping distance (range)
- energy deposition rate (bubble density)

Track curvature alone can often identify very light particles, ie. electrons. Electron tracks under 120 MeV/c will spiral noticeably in the BC fiducial volume with rapidly decreasing radius. For faster electrons, however, the spiral may not be

obvious in the bubble chamber and they are usually misidentified as pions on the basis of their minimum ionization.

Some particles can be identified according to specific decay signatures which can be readily recognized, eg. $\pi \rightarrow \mu + e$. Others can be identified by their range in hydrogen. Along with momentum determinations, the program ARROW estimates the range of each track for each mass hypothesis. Thus whether a track stops in the bubble chamber fiducial volume can often determine its mass.

The assignment of particle identity can also be made by track bubble density. The momentum determination program ARROW calculated the level of ionization expected for various mass hypotheses. These were quantified in terms of minimum ionizing tracks. ARROW assigned each track an *ionization value* which gave the bubble density ratio between the reconstructed track and minimum ionizing tracks, projected onto the xy plane.

Visual estimates of this ratio can be made directly on a track by contrasting its appearance (*darkness*) with minimum ionizing tracks. Then comparing the ARROW assignment with the visual estimate, protons can be separated from pions, kaons, and electrons.

The density of bubbles on a given track varies as the inverse square of the velocity of the ionizing particle. Slower particle tracks (the more massive particles) appear darker in comparison with the faster ones at comparable momenta. The designations *black*, *grey*, and *shower* correspond to relative velocities $\beta < .3$, $.3 \leq \beta < .7$, and $\beta \geq .7$, respectively. Slow protons leave smoothly black tracks; slow pions leave less smoothly black or grey tracks, ie. with gaps. In particular, below minimum ionizing velocities, the bubble density m in hydrogen can be expressed in the form $m = \frac{A}{\beta^b}$ where b typically takes on values around 2 and A around 10, depending on the chamber running conditions. Assuming then that the bubble density is essentially inversely proportional to the square of the relativistic velocity, $m = \frac{A}{\beta^2}$, then the ratio R_{bd} of proton to pion track bubble density will be

$$R_{bd} = \frac{\beta_\pi^2}{\beta_p^2} = \frac{p^2 + m_p^2}{p^2 + m_\pi^2}$$

This ratio along with K:π, p:K, and π:e is plotted in **Figure 2.4.1** for momenta 0 to 2.5 GeV/c. At low momentum, the separation between particles is significant.

Time constraints precluded measuring track density (bubbles per cm) on each track with the measuring equipment available. Hence, densities were estimated visually after digitization and reconstruction. Due to the fluctuations in lighting and film development, it was inadvisable to set an absolute scale by which to ascertain track density on the basis of *darkness*. So these visual density estimates were made relative to minimum densities seen on the fast tracks which exhibit *minimum ionization*. In other words, the technician calibrated her estimates on beam tracks and straight, high-momentum secondaries. She assigned a number to each track reflecting its relative density. An assignment of 1 was equivalent to 'as dark as' minimum ionizing tracks; 2, 'twice as dark as' minimum ionizing tracks; 4, 'four times darker than' minimum ionizing tracks; and so forth. In addition, some consideration had to be given to track dip angles. Tracks with large dip angles appeared darker than their bubble densities warranted. Thus, the technician kept alert for large dip angles as she made her assignments. To minimize the subjectivity inherently involved in these determinations, one person carried out the bulk of this particle identity project.

Although all tracks should in principle be identifiable by this ionization method, the fact that ionization was determined visually limits realistic comparisons to a specific region in momentum. Outside this limited region, the bubble density ratios are ambiguous. Two tracks with ionization levels below 1.5 could not be reliably distinguished from one another in terms of their bubble density. By the same token, density ratios less than 1.5 between two secondaries are not reliably perceptible. Thus protons can only only be distinguished below about 1.3 GeV/c and K's below about .65 GeV/c. At higher momenta, the ratios distinguishing these particles are small enough that no attempt at identification was made.

Similarly, two dark tracks with relative levels greater than about 4 could not be distinguished from one another. If ARROW calculated ionization levels greater than 4 for two mass hypotheses on a track, a default pion identification was made since positive identification was untenable. For example, a relative ionization prediction

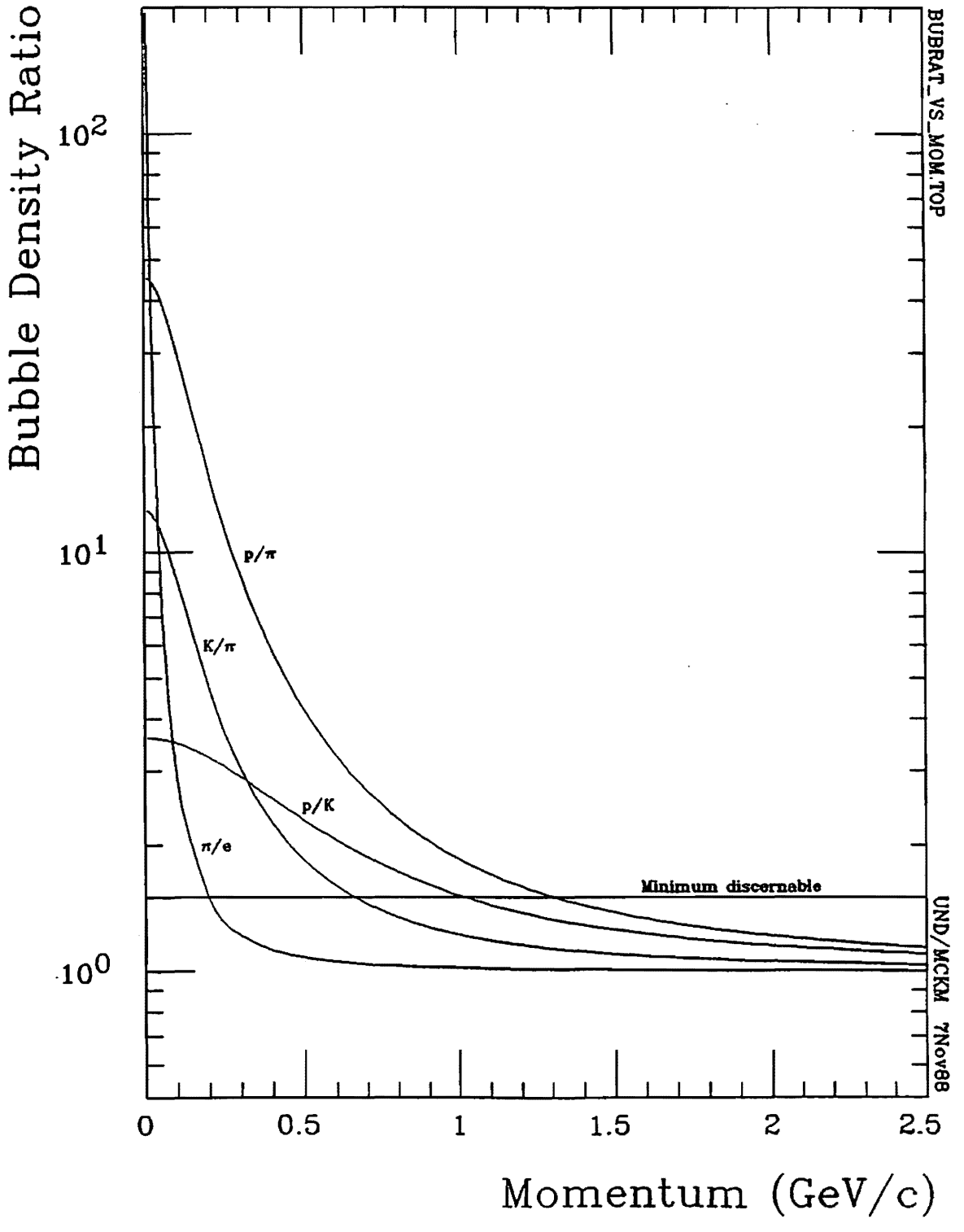

Figure 2.4.1 Bubble density ratios as a function of momentum.

of 7 for the proton hypothesis compared with 5 for the pion hypothesis leaves its identification ambiguous since a 5 and a 7 will appear essentially the same on film to the naked eye. Measured default pions are counted into the *ambiguous* multiplicities N_{a+}^{m} and N_{a-}.

After visually estimated ionizations were compared with ARROW calculations, appropriate particle identities were selected from ARROW's choices and encoded on ARROW printout. These identities were subsequently merged into the measurement record by adding a high order code (a millions digit code as per **Table 2.4.1**) to the original 'special track characteristics' word. Examples of these merged track identity and characteristic codes are tabulated for reference in **Table 2.4.2.**

2.4.3 Identification in CRISIS

Tracking particles into the DPI, mass was determined by ionization sampling in CRISIS and the characteristic relativistic rise for various mass hypotheses. Analysis at Notre Dame was made using particle identifications determined at PSU with their CRISIS analysis calibrated roll-to-roll to CRISIS cell fluctuations. PSU provided six(6) files, corresponding to six interaction types from a restricted sample. These files listed particle masses along with track distinguishing momenta for tracks successfully identified in CRISIS.

2.5 EVENT SELECTION

A number of undesirable event-types should be excluded from the data sample due to their association with beam contaminants. Hadron-hadron studies often exclude diffractive events with cuts on multiplicity less than or equal to 3, but no such cut is reasonable in hA events due to their probable multiple-collision nature. Thus no attempt has been made to exclude events of specific multiplicity. However, specific beams, event topologies and summed transverse momenta have been excluded from the analysis sample.

All events tagged with proton beams in the film rolls exposed during the

Table 2.4.1 Code scheme for track identity by ionization and special characteristic code scheme used by University of Notre Dame in E597 measurement records.

Code	Track Identity	Special Characteristic
1xxxxxx	electron/positron	
2xxxxxx	pion	
3xxxxxx	charged kaon	
4xxxxxx	neutral kaon	
5xxxxxx	proton	
6xxxxxx	lambda	
7xxxxxx	sigma	
8xxxxxx	muon	
9xxxxxx	undetermined	
xxxxxx1		non-stopping dense track with gaps
xxxxxx2		non-stopping dense track without gaps
xxxxxx3		forced positive charge
xxxxxx4		forced negative charge
xxxxxx5		pion
xxxxxx6		decay track but did not measure as decay
xxxxxx8		track has secondary scatter
xxxxxx9		electron (either positive or negative)
xxxxx10		stopping track
xxxxx11		stopping proton with gaps (rare)
xxxxx12		stopping proton without gaps

Table 2.4.2 Examples of merged track-identity-by-ionization and special-track-characteristic codes used by Notre Dame for E597 measurement records.

Code	Interpretation
1000009	electron/positron
1000903	positron forced positive
1000904	electron forced negative electron
2000000	pion
2000001	pion non-stopping dense track with gaps
2000002	pion non-stopping dense track without gaps
2000003	pion forced positive
2000004	pion forced negative
2000006	pion with unmeasured decay
2000008	pion that scatters
2000501	pion dense track with gaps
2000502	pion dense track without gaps
2000506	pi-mu-e decay
2000803	pion forced positive that scatters
2005203	pion forced positive, dense without gaps
5000000	proton
5000001	proton non-stopping dense track with gaps
5000002	proton non-stopping dense track without gaps
5000012	proton stopping dense track without gaps
5000103	proton non-stopping dense track with gaps, forced positive
5000203	proton non-stopping dense track without gaps, forced positive
5000213	proton stopping dense track without gaps, forced positive
5000802	proton non-stopping dense track without gaps that scatters
5008203	proton non-stopping dense track without gaps, forced positive, that scatters
9000000	undetermined track
9000002	undetermined non-stopping dense track without gaps
9000003	undetermined track forced positive
9000004	undetermined track forced negative
9000008	undetermined track that scatters
9000203	undetermined non-stopping dense track without gaps, forced positive
9000803	undetermined track that scatters, forced positive

IONIZEXAMPLE.TEX

π^+/K^+ beam mode were discarded. The positive meson beam mode was to provide only π's and K's. However, a handful of protons crept into the sample, presumably by misidentification. Since so few events were involved, they were simply excluded from the sample. In the interests of prioritizing proton-induced collisions at one point, the π^+-induced events were also excluded for rolls exposed during the positive baryon beam mode notwithstanding the planned 5% π^+ contribution to the beam.

2.5.1 Hadronic events

Since E597 was conceived to study strong interactions, all electromagnetic events must be excluded. No electromagnetic events were expected, but muons contaminating the mixed beam potentially generated electromagnetic interactions.

As noted earlier, Notre Dame measured a number of δ-ray on beam track events as well as so-called tridents. These definitely fall into the electromagnetic event category and were culled simply on the basis of event topology. All events with multiplicities 1 and 2, all with electron masses, were excluded. Other electromagnetic events, whose reaction products have been ambiguously or mistakenly determined to be hadronic, must be excluded another way. Tracks in purely electromagnetic events are expected to individually exhibit small transverse momenta relative to the beam direction. Therefore the sum of the squared momenta is expected to be very small in comparison to hadronic events whose sums of momenta might be small but whose squared momentum sums are not. Analysis of clearly identifiable electromagnetic events suggests that these expectations are borne out in our data.

A beam direction was established event by event by summing all track momenta. Momentum components transverse to this direction were determined for each track and averaged in quadrature. The log of this average square transverse momentum measures how closely the tracks parallel the beam. These events were found to preferentially populate the lower multiplicities.

The feasibility of this approach with E597 data was checked by selecting out clearly electromagnetic events from DSBC. This selection was made on the basis of one of the two sets of criteria below:

δrays

- sum of identified electrons(meas and um) = 1
- sum of ambiguous particles(meas and um) = 1
- no other particles

tridents

- sum of identified electrons(meas and um) = 2
- sum of ambiguous particles(meas and um) = 1
- no other particles

Figure 2.5.1, a plot of log(average squared transverse momentum) vs. multiplicity for these selected events, illustrates how electromagnetic events populate almost exclusively the lower regions below -4.0 and in most samples below -5.0. A comparison with a similar plot for *all* events, **Figure 2.5.2**, indicates a sharp separation between electromagnetic events and hadronic events on the basis of the average squared transverse momentum $\langle p_\perp^2 \rangle$ relative to $\sum \langle p_i \rangle$. The identifiably electromagnetic events account for most of the lower region points at multiplicities 2 and 3. Thus a cut on events with $\ln\langle p_\perp^2 \rangle$ less than or equal to -5.0 was invoked on interaction types. In some cases this event cut reduced the number of events by half.

2.5.2 Duplicate records

During the process of improving the momenta of fast tracks, at which time the mastergate was redetermined by matching the downstream tracks with the downstream device records (final beam tagging), ambiguities in mastergate number were not resolved. Instead, the momentum was improved assuming each of the mastergates involved. The results from each mastergate assumed were written in separate records along with all downstream device data . Thus, record duplications persisted for single events.

Rather than applying a broad criterion to resolve these ambiguities, they were examined individually and categorized in a fashion that would make it easy to sort them out. A printout of the full BC records in DST597 which were in duplication

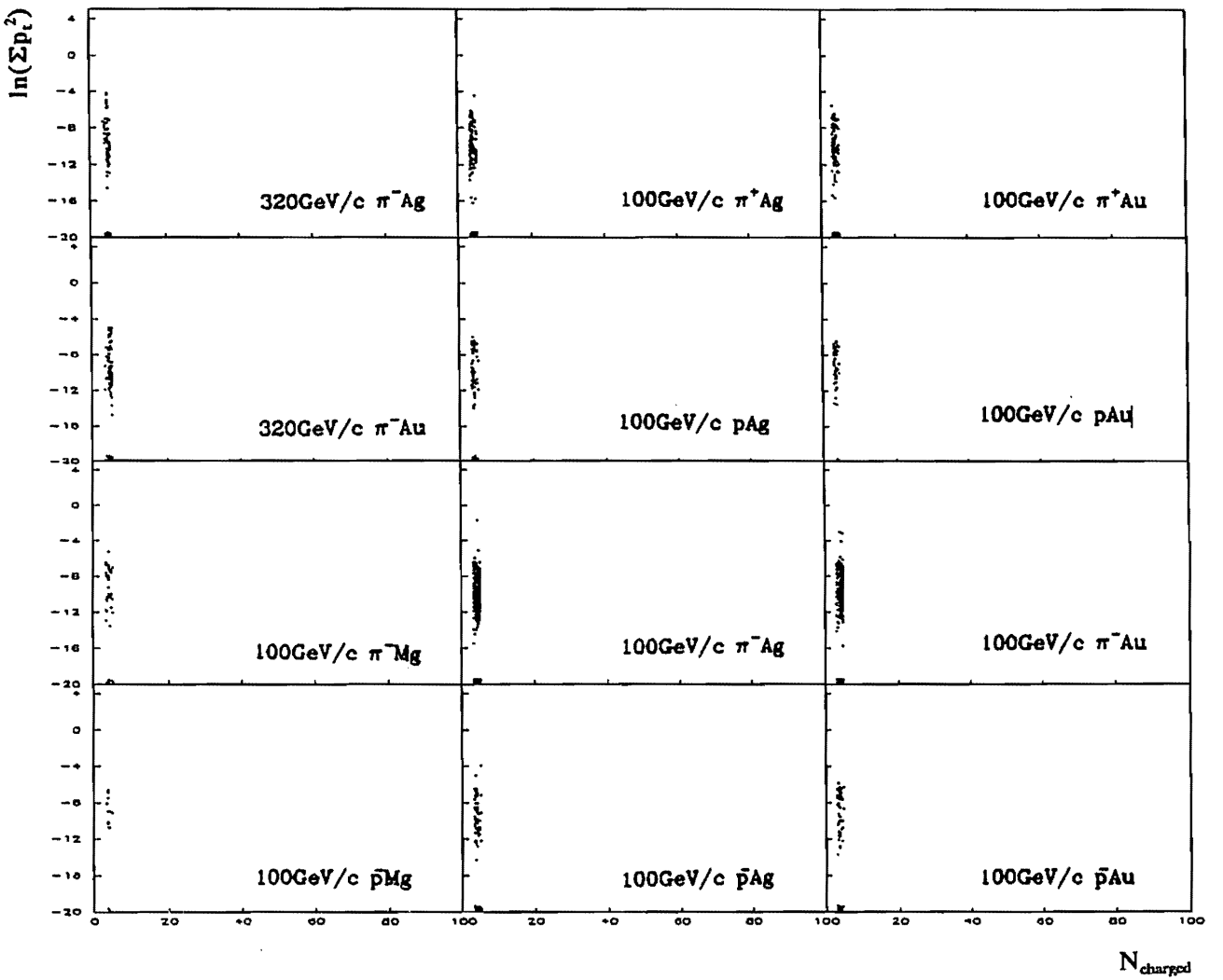

Figure 2.5.1 Log of the sum of the transverse momentum squared vs. multiplicity for clearly electromagnetic events.

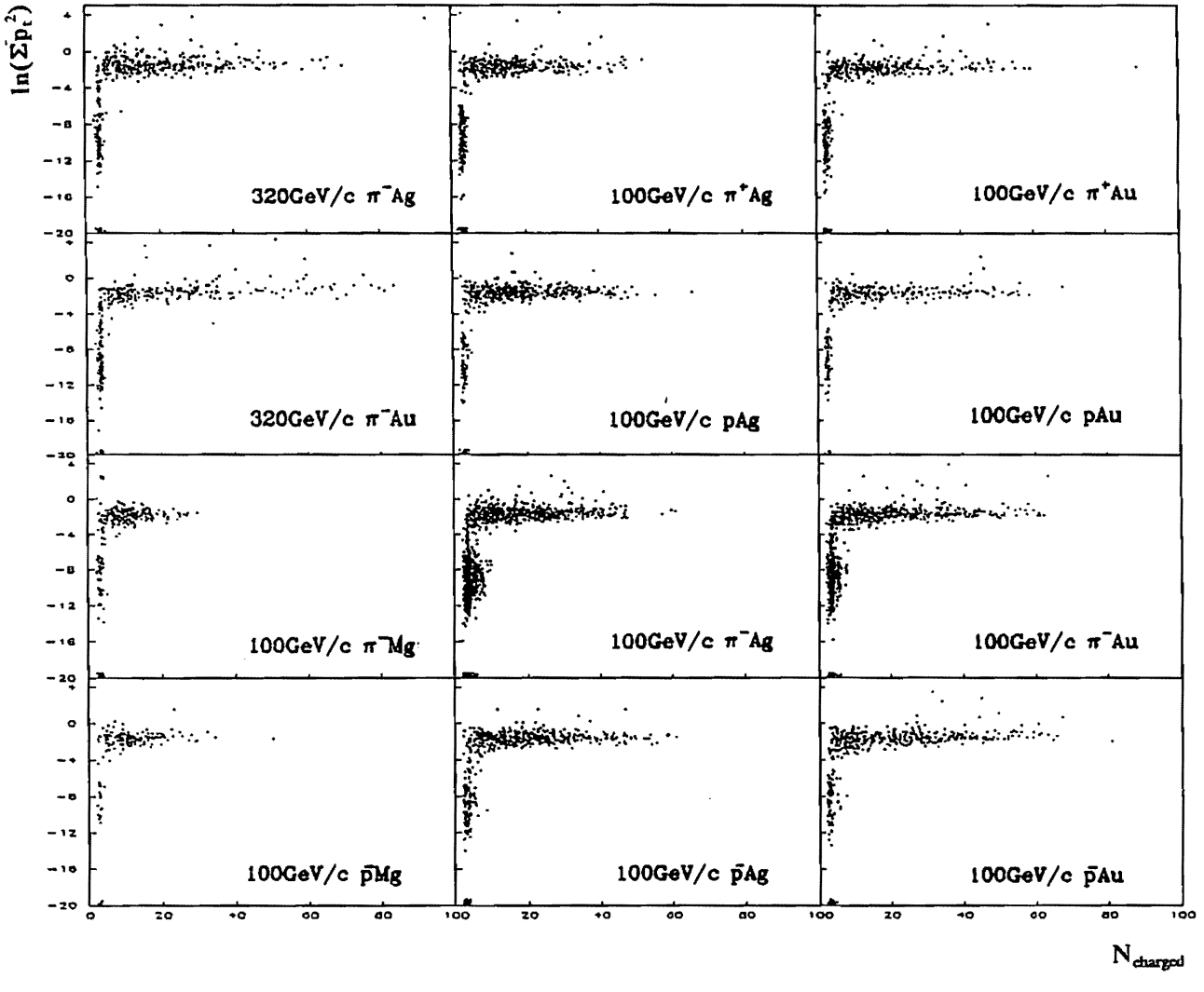

Figure 2.5.2 Log of the sum of the transverse momentum squared vs. multiplicity for all measured events.

– about 500 records – was the beginning point. To determine which of the duplicated BC event gates to select for the analysis sample, the following were noted for each record: 1) the number of secondaries hooked up, 2) whether the duplicate records involved different beam tags or not, and 3) whether the duplicate records involved different target assignments (foil number) or not. If the duplicate records differed in target assignment, the one which did not concur with the bubble chamber assignment was excluded. (look at duplicate subroutine for criteria list as to whether use or not) A master list of duplicate event exclusions was made and was referenced when producing the final DST.

2.6 ANALYSIS SAMPLES

This study incorporated twelve(12) of the eighteen(18) interaction types represented by the full raw-data sample. These interactions take place between three(3) nuclear targets in two(2) thicknesses and five(5) of the six(6) available projectiles. Due to the smaller statistics of the K^+ beam and the Mg target portions, all K^+ beam data and most of the Mg target data are excluded. **Tables 2.6.1** summarize the number of events and measured tracks included at the various stages of the data summary designated by the different DST names. Particular data samples will be referenced according to these names. Data summary tapes (DSTs) were made followed either an iteration of bubble chamber track reconstruction, momentum determination, and particle identification or the hookup up to the DPI tracking devices and their improvements on the momenta.

Initially, a summary named DS2 was made was made for tracks whose parameters were determined in the bubble chamber with preliminary optical constants. With new optical constants, DS2V was made. The next summary, DSBC, included reconstruction on the basis of the best optical constants found in the exhaustive comparative study illucidated earlier. It also excluded electromagnetic events outright. When downstream information was incorporated and momentum refinements made for fast forward tracks, DST597 was made, using DSBC as a foundation. DST597

Table 2.6.1 Data summary tape event contents. DS2V is the preliminary study sample used for initial studies. DSBC is the final complete bubble chamber data summary used for input into the hookup with DPI data. DST597 merges DPI information with bubble chamber data, includes momentum improvements on the basis of DPI reconstructions, but does not include events deemed to be electromagnetic. SHORT-DST597 is a convenient, short format sample based on DST597 which excludes vee's, duplicate events, all events involving K^+ projectiles, and most events involving Mg targets due to their scarcity.

DS2V DATA SUMMARY TAPE

Projectile	Events
320 GeV/c π^-	816
100 GeV/c $\pi^-/\bar{p}$	3953
100 GeV/c π^+/K^+	1079
100 GeV/c p	890
Total	6738

DSBC DATA SUMMARY TAPE

Projectile	Events
320 GeV/c π^-	1023
100 GeV/c $\pi^-/\bar{p}$	7589
100 GeV/c π^+/K^+	1564
100 GeV/c p	1199
Total	11375

DST597 DATA SUMMARY TAPE

Projectile	Events
320 GeV/c π^-	675
100 GeV/c $\pi^-/\bar{p}$	4204
100 GeV/c π^+/K^+	950
100 GeV/c p	945
Total	6774

SHORTDST597 DATA SUMMARY TAPE

Projectile	Events
320 GeV/c π^-	583
100 GeV/c $\pi^-/\bar{p}$	3742
100 GeV/c π^+	542
100 GeV/c p	716
Total	5583

SAMPLESIZES.TAB UND/MCKM 15Dec88

integrated DSBC with appropriate substitutions for newly improved track reconstructions in the DPI as well as unpacked, formatted records of all DPI data. When studies were made which did not require all the downstream information, but simply the downstream improvements on the momentum, DST597 was reformatted into a briefer version called SHORTDST597 which also sorted out the duplicate events. SHORTDST597 has been the most widely used data summary in our studies. When CRISIS information was folded in to make limited identifications of fast forward protons and antiprotons, this information was not integrated into any data summary but kept in parallel reference files named CRISIS. These files were not available at the time of most analyses and thus may not be assumed to have been used unless specifically noted.

2.7 FRITIOF SIMULATIONS

FRITIOF 1.6 [Nilsson-Almqvist 86a; Nilsson-Almqvist 86bAndersson 87b] is a Monte Carlo specifically designed to simulate hA as well as hh and AA interactions. It is a model for low $p_\perp$ processes and is based on the Lund fragmentation model [Sjostrand 82; Sjostrand 85]. FRITIOF treats hadrons as string-vortex lines in a superconducting QCD vacuum. It is a multiple scattering model and considers hadronization to take place outside nuclei. It assumes no intranuclear cascading and provides the option to consider Fermi motion. 2000 simulated events have been generated and compared with E597 results for each of the E597 interactions. A number of comparisons have been made, including proton and produced particle multipliticies.

Table 2.7.1 displays the proton multiplicities in three(3) momentum regions as produced FRITIOF. As expected since cascading is assumed to play a role in slow proton production, FRITIOF does not reproduce proton multiplicities very well. **Figure 2.7.1** makes the comparison of multiplicity distributions between FRITIOF and E597 data. Throughout, corrections on E597 data have not been applied except to estimate their impact on average multiplicities.

Table 2.7.1 Average baryon multiplicities in Monte Carlo (FRITIOF) events corresponding to experimental (E597) data.

Fritiof

Projectile	320GeV/c		100GeV/c									
	π^-		π^+		p		π^-			$\bar{p}$		
$^{A}_{Z}Target$	$^{108}_{47}Ag$	$^{197}_{79}Au$	$^{108}_{47}Ag$	$^{197}_{79}Au$	$^{108}_{47}Ag$	$^{197}_{79}Au$	$^{24}_{12}Mg$	$^{108}_{47}Ag$	$^{197}_{79}Au$	$^{24}_{12}Mg$	$^{108}_{47}Ag$	$^{197}_{79}Au$
BTC	61/2	63/4	131/2	133/4	141/2	143/4	175/6	171/2	173/4	185/6	181/2	183/4
N_{events}	2000	2000	2000	2000	2000	2000	2000	2000	2000	2000	2000	2000
$0. < p < 1.3$												
$\langle N_p \rangle$Fritiof	.792	.946	.840	.965	1.006	1.210	.599	.864	.994	.726	1.126	1.329
Δ	.020	.022	.020	.022	.022	.025	.017	.021	.022	.019	.024	.026
$1.3 < p < 4.0$												
$\langle N_p \rangle$Fritiof	.381	.451	.313	.369	.382	.444	.229	.319	.336	.255	.367	.436
Δ	.014	.015	.013	.014	.014	.015	.011	.013	.013	.011	.014	.015
$p\rangle 4.0$												
$\langle N_p \rangle$Fritiof	.266	.279	.159	.166	.719	.739	.106	.135	.141	.112	.122	.133
Δ	.012	.012	.009	.009	.019	.019	.007	.008	.008	.007	.008	.008
Total												
$\langle N_p \rangle$Fritiof	1.438	1.676	1.311	1.499	2.106	2.393	.934	1.317	1.470	1.092	1.615	1.898
Δ	.027	.029	.026	.027	.032	.035	.022	.026	.027	.023	.028	.031
$0. < p < 1.3$												
$\langle N_{\bar{p}} \rangle$Fritiof	.006	.009	.003	.008	.002	.003	.005	011	.007	.008	.013	.019
Δ	.002	.002	.001	.002	.001	.001	.002	.002	.002	.002	.003	.003
$1.3 < p < 4.0$												
$\langle N_{\bar{p}} \rangle$Fritiof	.058	.060	.035	.040	.043	.047	.037	.043	.052	.047	.068	.072
Δ	.005	.005	.004	.004	.005	.005	.004	.005	.005	.005	.006	.006
$p\rangle 4.0$												
$\langle N_{\bar{p}} \rangle$Fritiof	.230	.252	.096	.100	.066	.084	.083	.124	.123	.680	.710	.680
Δ	.011	.011	.007	.007	.006	.006	.006	.008	.008	.018	.019	.018
Total												
$\langle N_{\bar{p}} \rangle$Fritiof	.294	.320	.133	.147	.110	.133	.124	.178	.181	.734	.790	.771
Δ	.012	.013	.008	.009	.007	.008	.008	.009	.010	.019	.020	.020

FRITIOF_P_MULT.TEX UND/MCKM 4Sep88

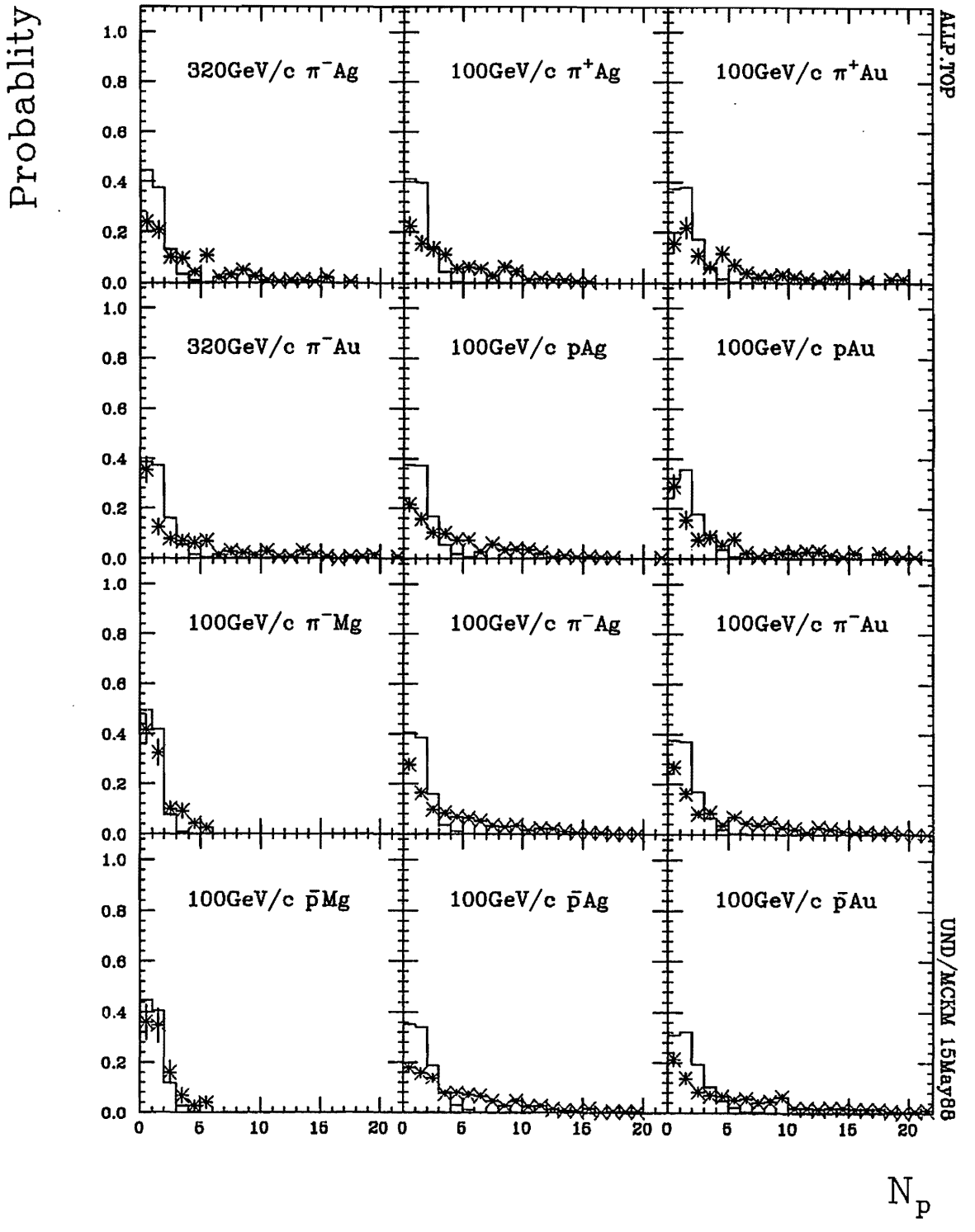

Figure 2.7.1 A comparison of E597 (×) total proton multiplicities including unmeasured protons with FRITIOF (–) results.

Black proton distributions, **Figure 2.7.2**, have the largest discrepancies, with *grey* proton distributions, **Figure 2.7.3**, still not very closely reproduced. *Shower* production, **Figure 2.7.4**, is more closely reproduced.

Nuclear disintegration (evaporation) and intranuclear cascading are expected to produce slow protons and thus *black* tracks. FRITIOF does not include evaporation or cascading processes in its simulation. Thus to make an equitable comparison with FRITIOF, experimentally determined multiplicities of evaporated protons must be extrapolated to zero thickness, **Figure 2.7.5** and added to the FRITIOF proton multiplicity. **Figure 2.7.6** plots the multiplicities for hA events at two(2) thicknesses and for FRITIOF events at zero thickness with an evaporation multiplicity correction. **Appendix 2B** outlines this and other multiplicity corrections. A definite thickness dependence is evident. Thus that thickness dependence has been averaged over all beams for each target and identification level (with or without CRISIS identification) and determined a zero-thickness value which is displayed with a * in the same figure. $\bar{p}$ multiplicities have been treated similarly.

Table 2.7.2 displays produced particle multiplicities as produced by FRITIOF. Here FRITIOF is doing very well in predicting produced particle production. Certainly our results agree with FRITIOF averages to within experimental errors. But FRITIOF also produced multiplicity distributions in good agreement with the experimental data. In **Figures 2.7.7** and **2.7.8** for positive and negative produced particles, FRITIOF gives a slight excess right of the peak and does not reproduce the experimental tail. **Figures 2.7.9** and **2.7.10** plots produced particle multiplicities as a function of thickness, and again a residual thickness dependence lingers.

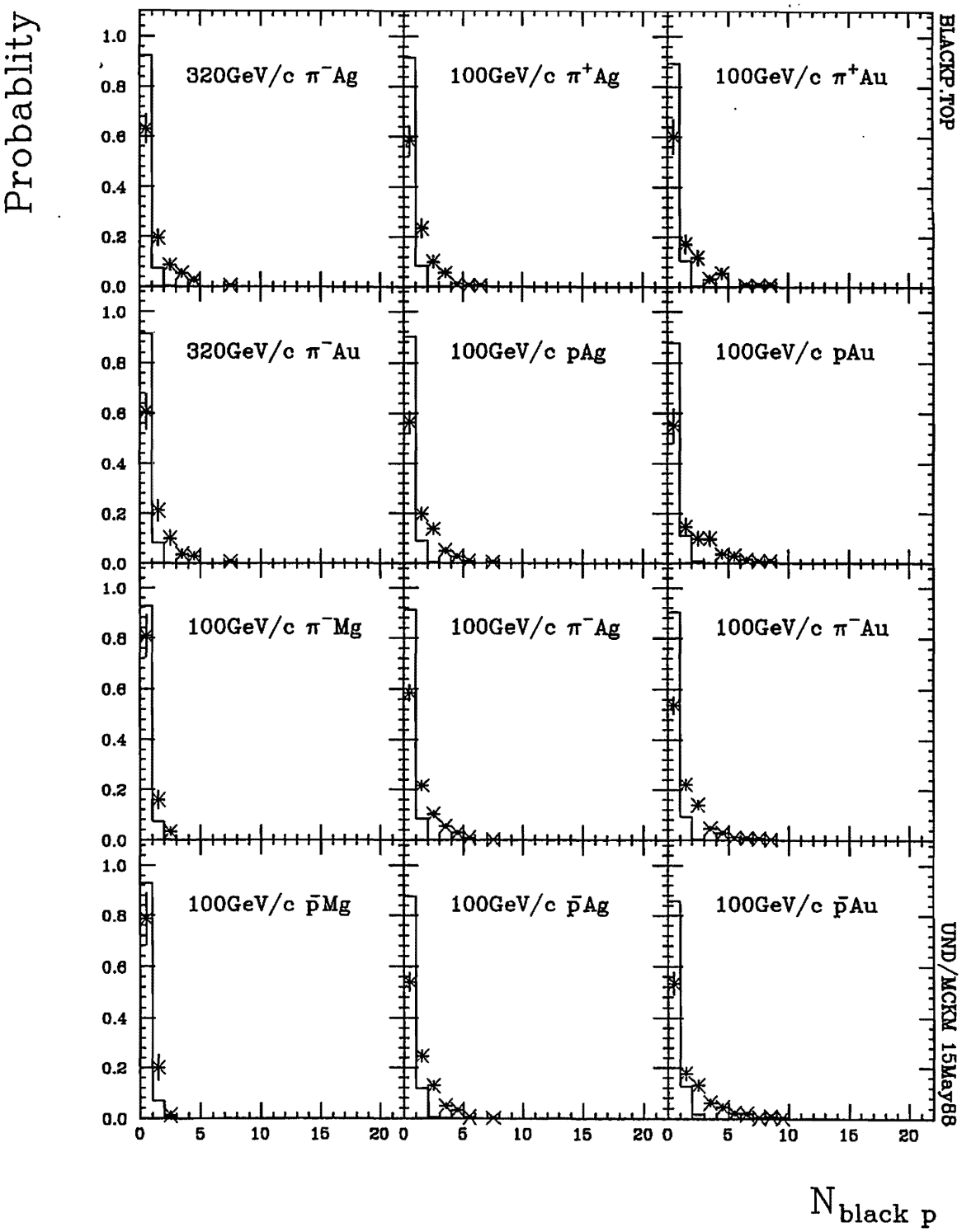

Figure 2.7.2 A comparison of E597 (×) *black* proton multiplicities including unmeasured protons with FRITIOF (–) results.

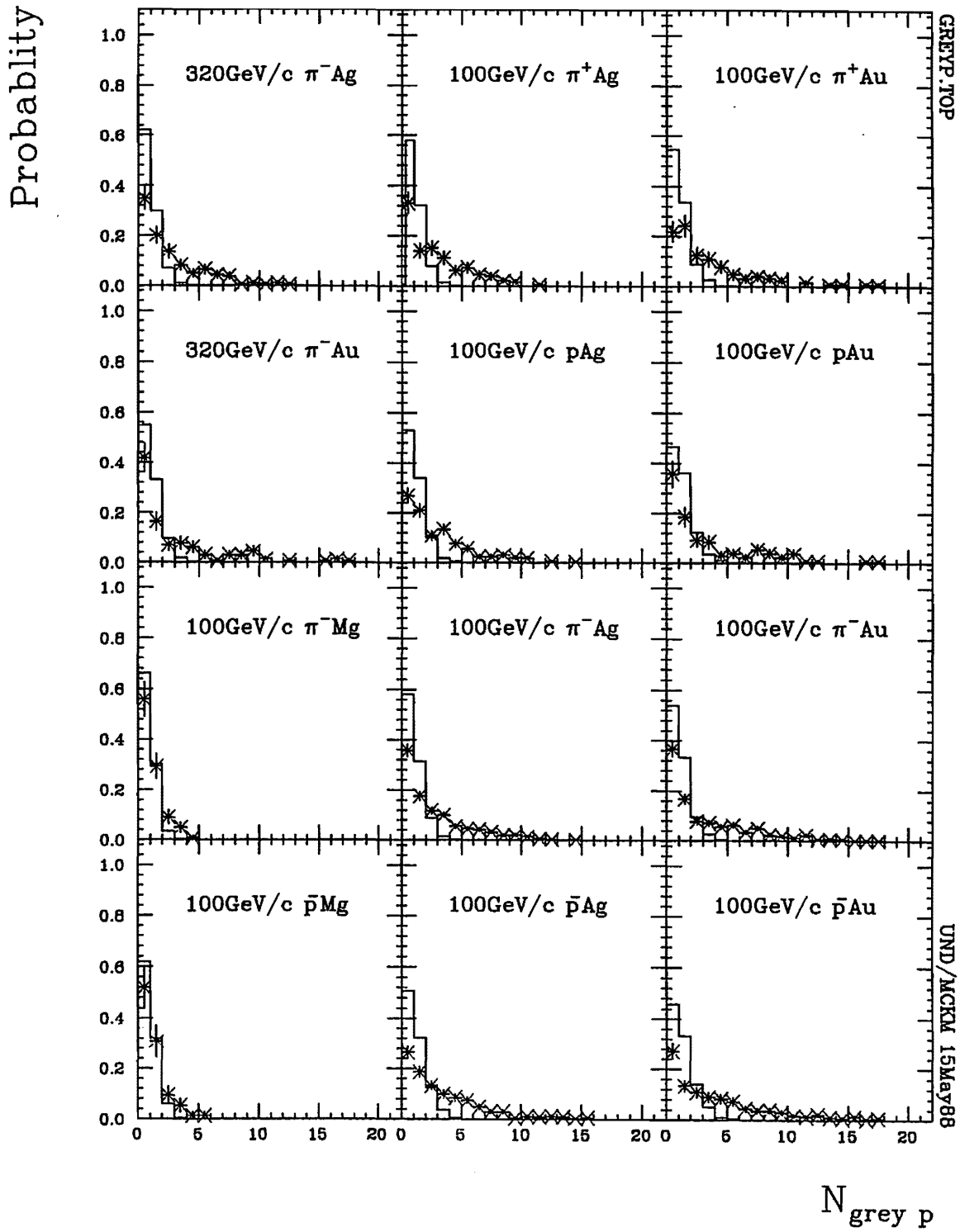

Figure 2.7.3 A comparison of E597 (×) *grey* proton multiplicities with FRITIOF (–) results.

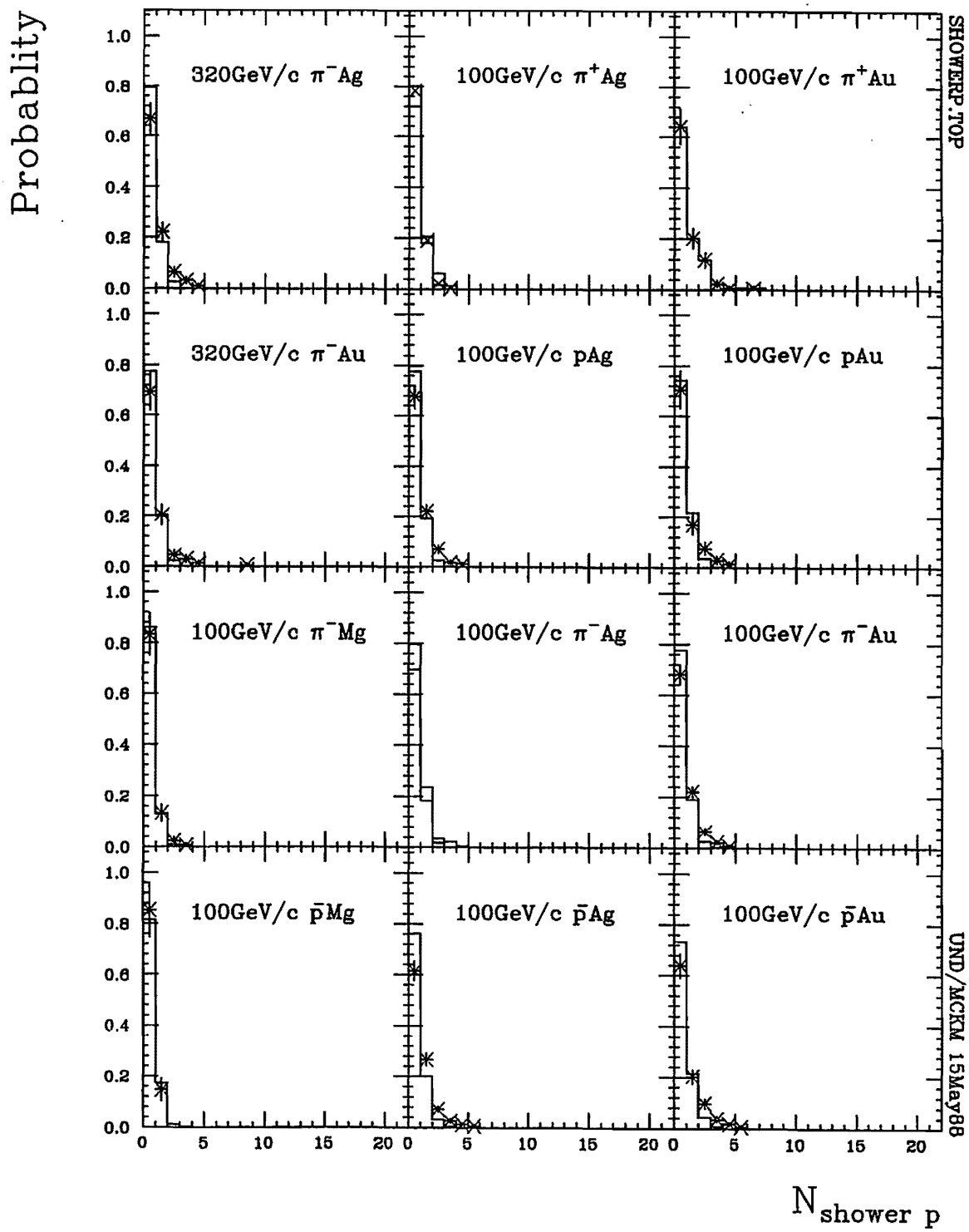

Figure 2.7.4 A comparison of E597 (×) *shower* proton multiplicities with FRITIOF (–) results.

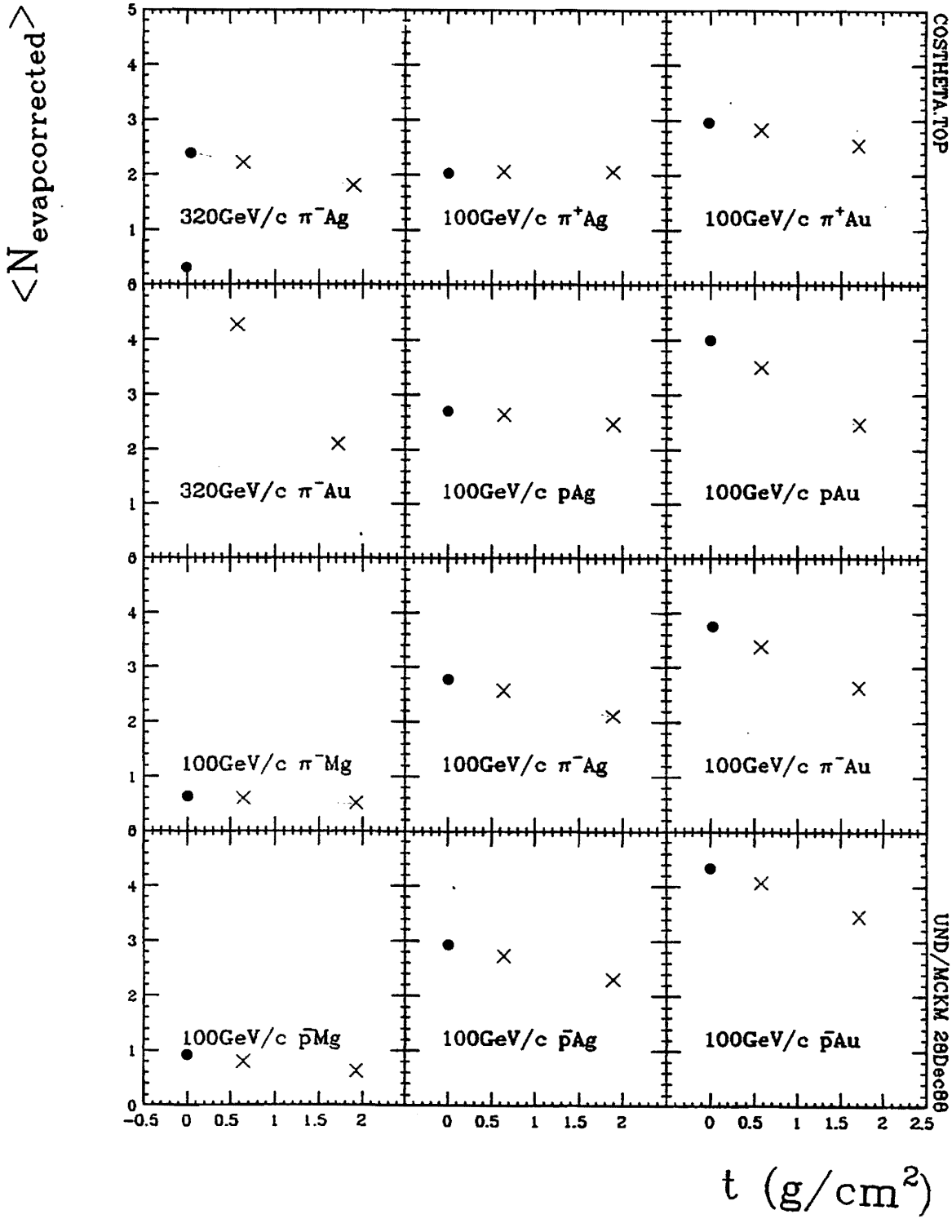

Figure 2.7.5 Estimated average number of protons from nuclear evaporation as a function of target thickness.

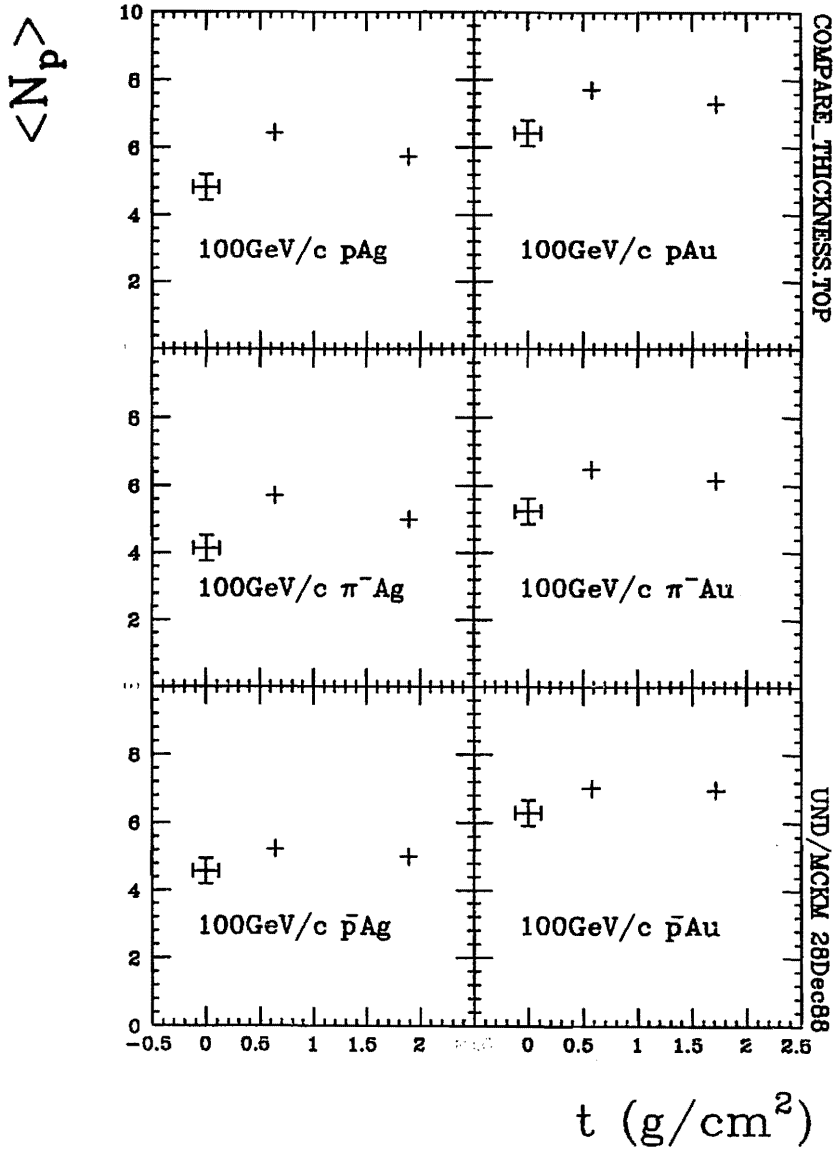

Figure 2.7.6 Average proton multiplicity as a function of target thickness.

Table 2.7.2 Average produced particle multiplicities in Monte Carlo (FRITIOF) events corresponding to experimental (E597) data.

Projectile	320GeV/c		100GeV/c									
	π^-		π^+		p		π^-			p		
$\frac{A}{Z}$ Target	$^{108}_{47}Ag$	$^{197}_{79}Au$	$^{108}_{47}Ag$	$^{197}_{79}Au$	$^{108}_{47}Ag$	$^{197}_{79}Au$	$^{24}_{12}Mg$	$^{108}_{47}Ag$	$^{197}_{79}Au$	$^{24}_{12}Mg$	$^{108}_{47}Ag$	$^{197}_{79}Au$
BTG	61/2	63/4	131/2	133/4	141/2	143/4	175/6	171/2	173/4	185/6	181/2	183/4
N_{events}	2000	2000	2000	2000	2000	2000	2000	2000	2000	2000	2000	2000
$0. < p < 1.3$												
$< N_{\pi^+} >$Fritiof	1.760	2.004	1.888	2.122	2.170	2.505,	1.150	1.703	1.953	1.487	2.227	2.598
Δ	.030	.032	.031	.033	.033	.035	.024	.020	.031	.027	.033	.036
$1.3 < p < 4.0$												
$< N_{\pi^+} >$Fritiof	1.584	1.720	1.398	1.516	1.418	1.611	.004	1.249	1.430	1.067	1.427	1.624
Δ	.028	.020	.020	.028	.027	.028	.021	.025	.027	.023	.027	.028
$p > 4.0$												
$< N_{\pi^+} >$Fritiof	2.488	2.647	1.733	1.758	1.200	1.238	1.090	1.226	1.262	.020	1.091	1.131
Δ	.035	.036	.020	.030	.025	.025	.023	.025	.025	.022	.023	.024
Total												
$< N_{\pi^+} >$Fritiof	5.700	6.460	5.019	5.396	4.796	5.353	3.152	4.177	4.654	3.483	4.746	5.352
Δ	.054	.057	.050	.052	.049	.052	.040	.046	.048	.042	.049	.052
$< N_{K^+} >$Fritiof	.571	.604	.398	.461	.405	.476	.286	.394	.422	.285	.398	.456
Δ	.017	.017	.014	.015	.014	.015	.012	.014	.015	.012	.014	.015
$< N_{prod+} >$Fritiof	6.361	7.063	5.417	5.856	5.200	5.829	3.440	4.571	5.076	3.768	5.142	5.808
Δ	.056	.060	.052	.054	.051	.054	.041	.048	.050	.043	.051	.054
$0. < p < 1.3$												
$< N_{\pi^-} >$Fritiof	2.187	2.567	1.809	2.096	2.268	2.726	1.402	2.124	2.536	1.685	2.511	3.068
Δ	.033	.036	.030	.032	.034	.037	.026	.033	.036	.020	.035	.039
$1.3 < p < 4.0$												
$< N_{\pi^-} >$Fritiof	1.641	1.830	1.210	1.366	1.371	1.585	1.087	1.417	1.560	1.101	1.536	1.710
Δ	.020	.030	.025	.026	.026	.028	.023	.027	.028	.023	.028	.029
$p > 4.0$												
$< N_{\pi^-} >$Fritiof	3.095	3.305	1.230	1.282	1.081	1.133	1.701	1.790	1.772	1.101	1.235	1.250
Δ	.030	.041	.025	.025	.023	.024	.020	.030	.030	.023	.025	.025
Total												
$< N_{\pi^-} >$Fritiof	6.022	7.710	4.267	4.743	4.710	5.444	4.190	5.330	5.870	3.886	5.281	6.038
Δ	.059	.062	.046	.049	.049	.052	.046	.052	.054	.044	.051	.055
$< N_{K^-} >$Fritiof	.506	.526	.208	.337	.254	.281	.240	.334	.360	.272	.317	.363
Δ	.016	.016	.012	.013	.011	.012	.011	.013	.013	.012	.013	.013
$< N_{prod-} >$Fritiof	7.428	8.235	4.564	5.070	4.073	5.724	4.430	5.678	6.230	4.158	5.508	6.400
Δ	.061	.064	.048	.050	.050	.053	.047	.053	.056	.046	.053	.057

FRITIOF_PROD_MULT.TEX UND/MCKM 4Sep88

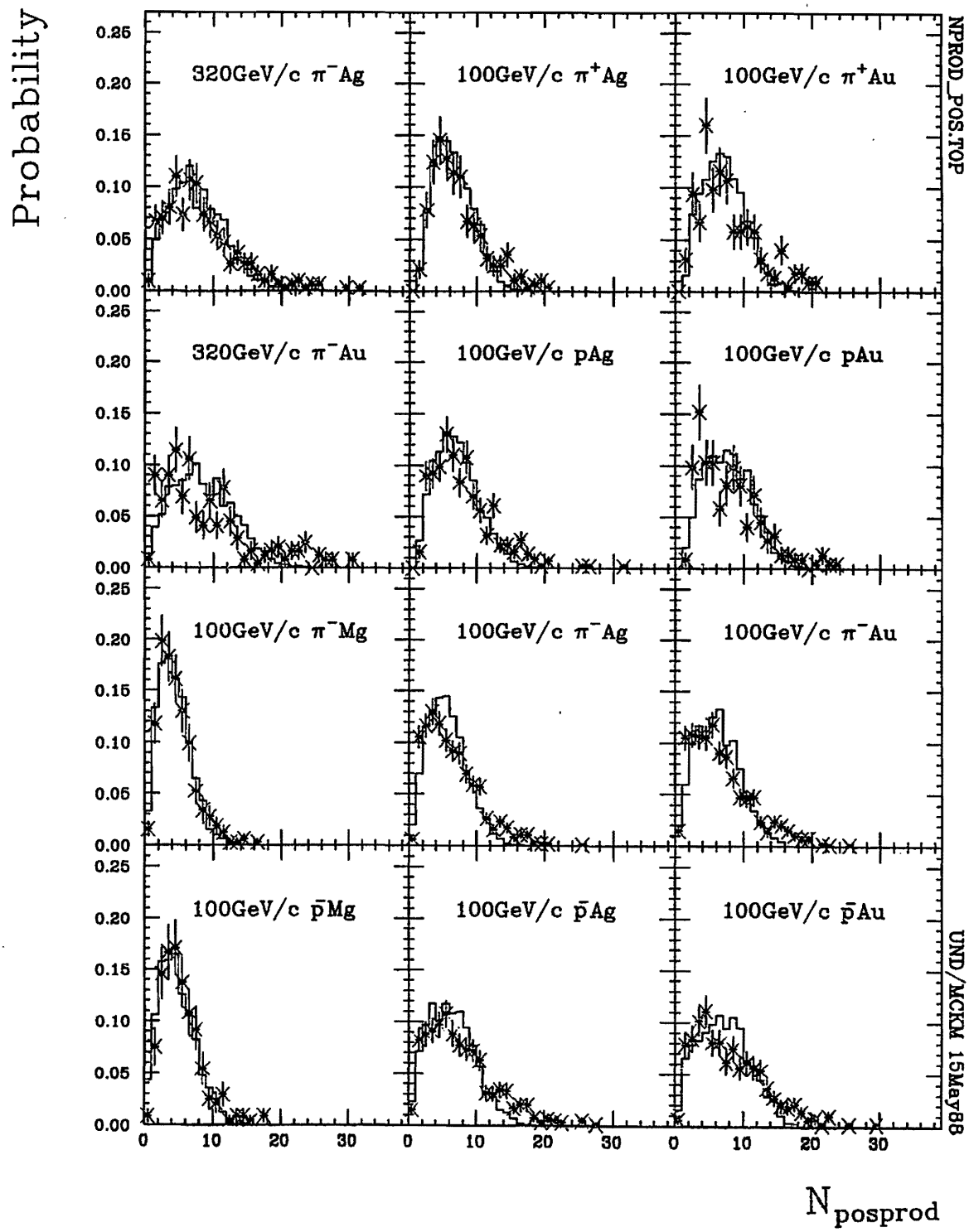

Figure 2.7.7 A comparison of E597 (×) positive produced particle multiplicities with FRITIOF (–) results.

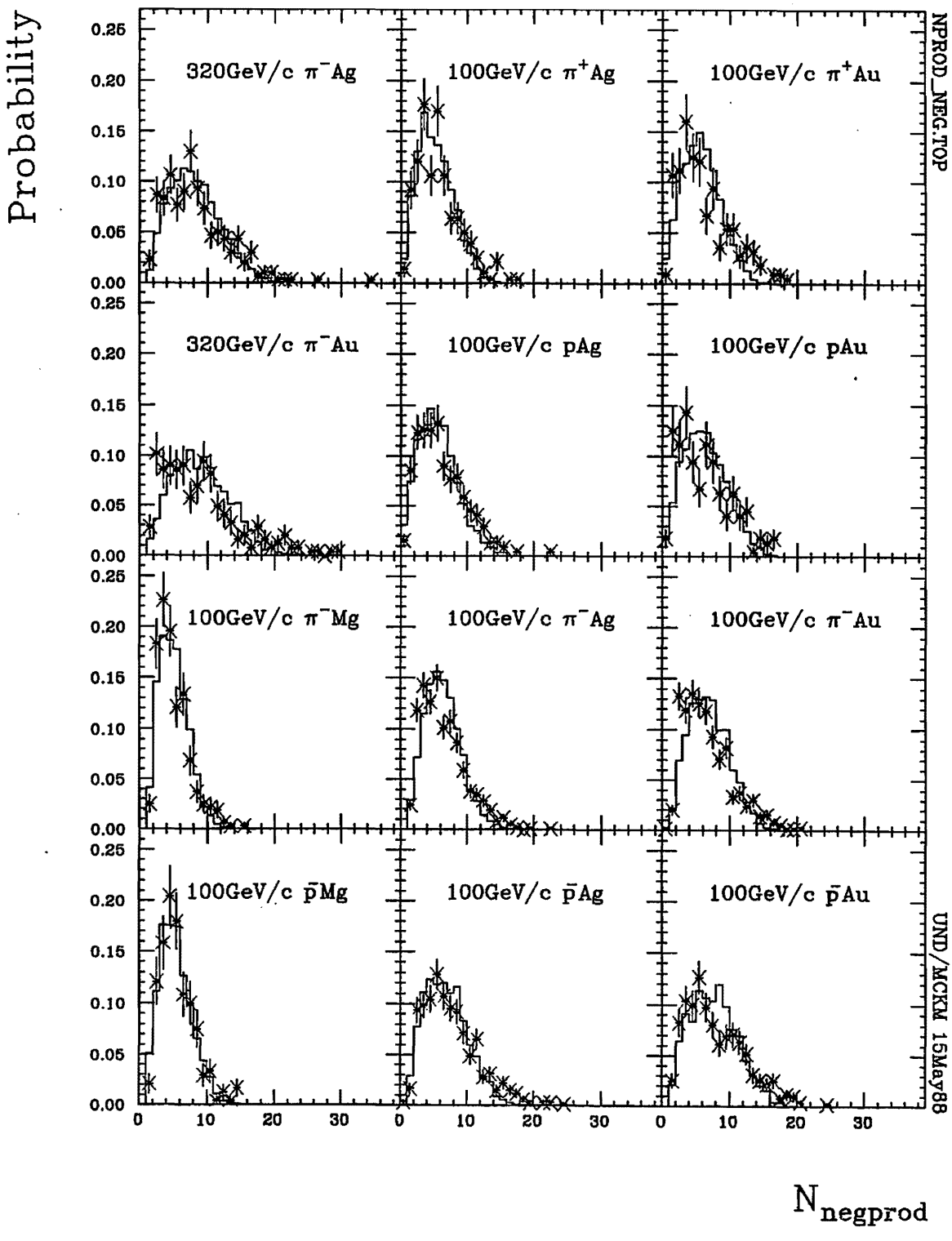

Figure 2.7.8 A comparison of E597 (×) negative produced particle multiplicities with FRITIOF (–) results.

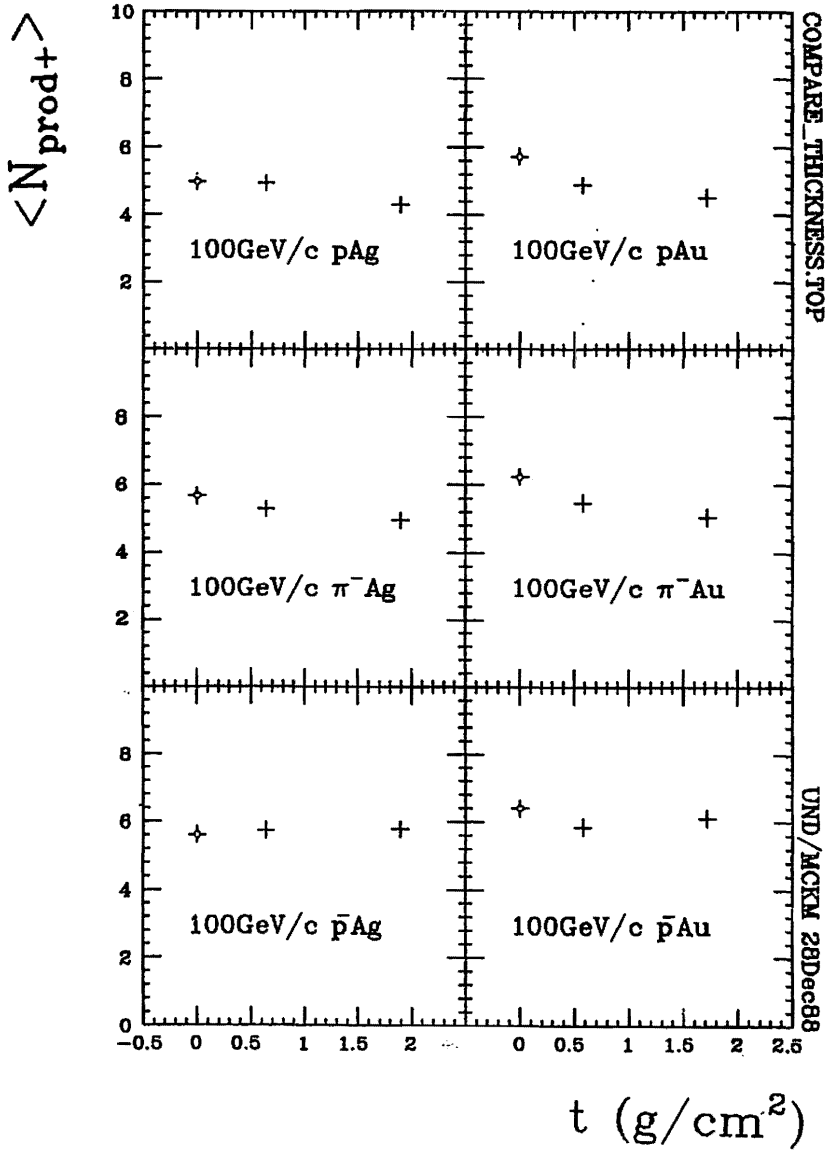

Figure 2.7.9 Average positive produced particle multiplicities as a function of thickness, including zero-thickness FRITIOF results.

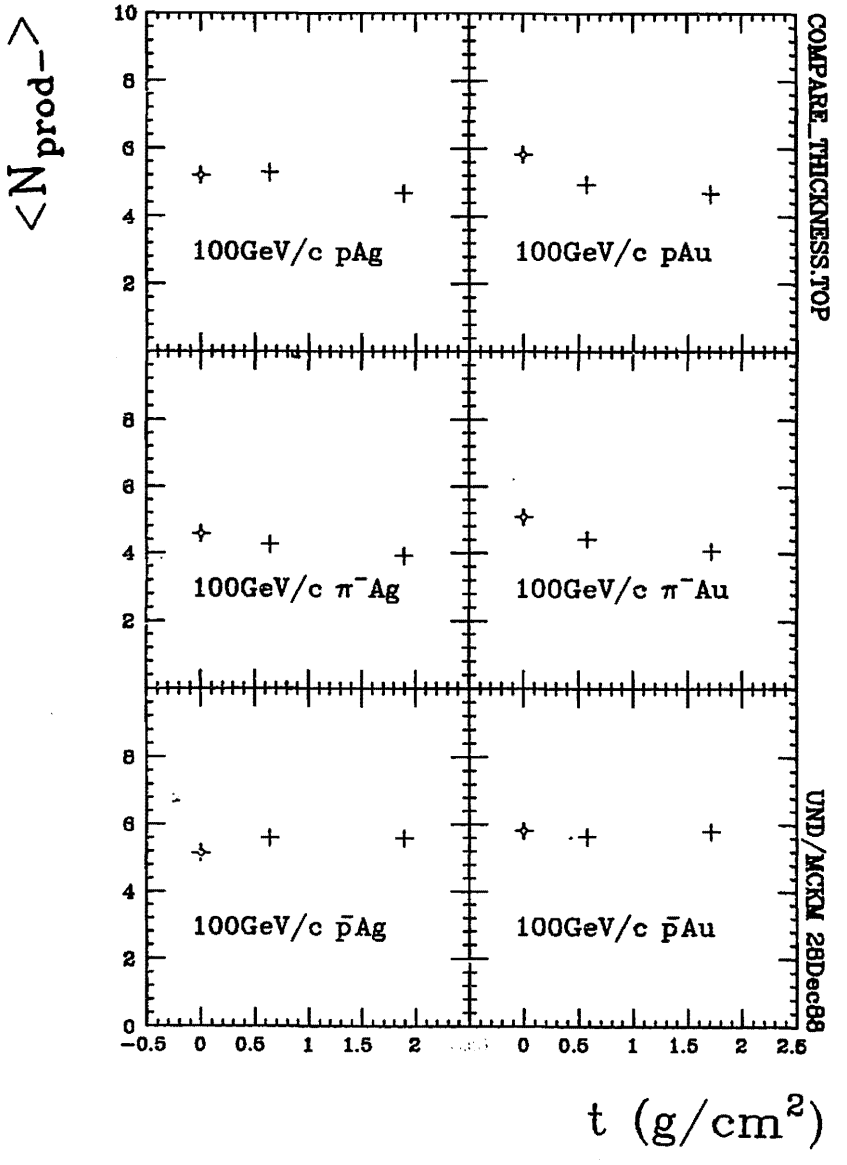

Figure 2.7.10 Average negative produced particle multiplicities as a function of thickness, including zero-thickness FRITIOF results.

CHAPTER 3

MULTIPLE COLLISIONS

Potentially new phenomena and physics associated with spike events, intermittency, and fractal dimensions may include exotic elements but they probably involve phenomena and physics which can be understood in the context of multiple collisions. Multiple interaction schemes can involve 1) projectile rescattering, and/or 2) secondary cascading. But since hA interactions involve composite structures of quarks and/or hadrons, it is reasonable to expect that single interactions between hadrons and nuclei are in fact convolutions of multiple collisions.

Many models assume that multiple production in hA interactions follows exclusively from a sequence of independent primary collisions between beam particles and nucleons and not from secondary cascades. Each of the ν collisions is assumed to be independent from previous, subsequent, and concurrent collisions and secondaries are presumed not to interact with the nucleus. Lorentz time dilation and length contraction make secondary interactions improbable since secondaries are generally produced outside the nucleus and thus have no further opportunity to interact with it. In this scenario the projectile energy decreases with successive interactions and the inelastic hadron-nucleon (hN) cross section is approximately constant, to the extent that it is energy independent, throughout the projectile trajectory through the nucleus.

Other models exclusively assume cascading scenarios, either in the sense of QCD cascades or in the sense of multiple collisions involving secondary particles. The latter are particularly important for slow secondaries in the laboratory since their first appearance cannot be presumed to take place outside the nucleus. Reality no doubt

combines aspects of both scenarios as they are contrasted in **Figure 3.0.1**. Thus an attempt will be made to estimate the degree to which interdependent secondary interaction schemes supplement independent primary ones.

Because so many models adopt the picture of primary multiple scattering at some level, it is of particular interest to determine ν, the number of projectile collisions. As a basic natural parameter, ν can check, refine, and unify predictions which would otherwise proliferate unmanageably as a consequence of beam/target combinatorics. In principle, ν can be varied by varying the intranuclear pathlength. This pathlength which is dependent on 1) nuclear size and 2) impact parameter as illustrated in **Figure 3.0.2**. Varying the nuclear size is limited to varying A between 1 and 238. This effectively varies the radius by a factor of 6. But experimentally varying the impact parameter is ludicrous. However, the suggestion that the number of emitted protons is correlated to impact parameter opens a way for estimating ν. This approach has distinct advantages beyond its obvious ease of application. When making A-varying comparisons, effects associated with the largest ν (smallest impact parameters) for any one nucleus are damped out by those associated with the smaller ν's (larger impact parameters) whose effects are superposed. In the tangle of impact parameters, the full range of ν cannot be observed. However, by varying impact parameters on a fixed A nucleus, the formerly limited range of ν can be extended to its full extent. Once the relation between ν and proton emission is understood, results from different nuclei can be combined on the basis of proton multiplicity.

Throughout this study, FRITIOF Monte Carlo simulations have been employed to probe impact parameter dependencies directly. Though FRITIOF fails to reproduce observed proton multiplicities quantitatively (a clear indiction that cascading must be included to describe the data adequately), it does show variations in proton multiplicity as a function of ν. So, rather than relating proton emission directly to impact parameters, comparison are made between FRITIOF results as functions of impact parameter, experimental results as functions of proton multiplicities, and subsequent results from analytical models.

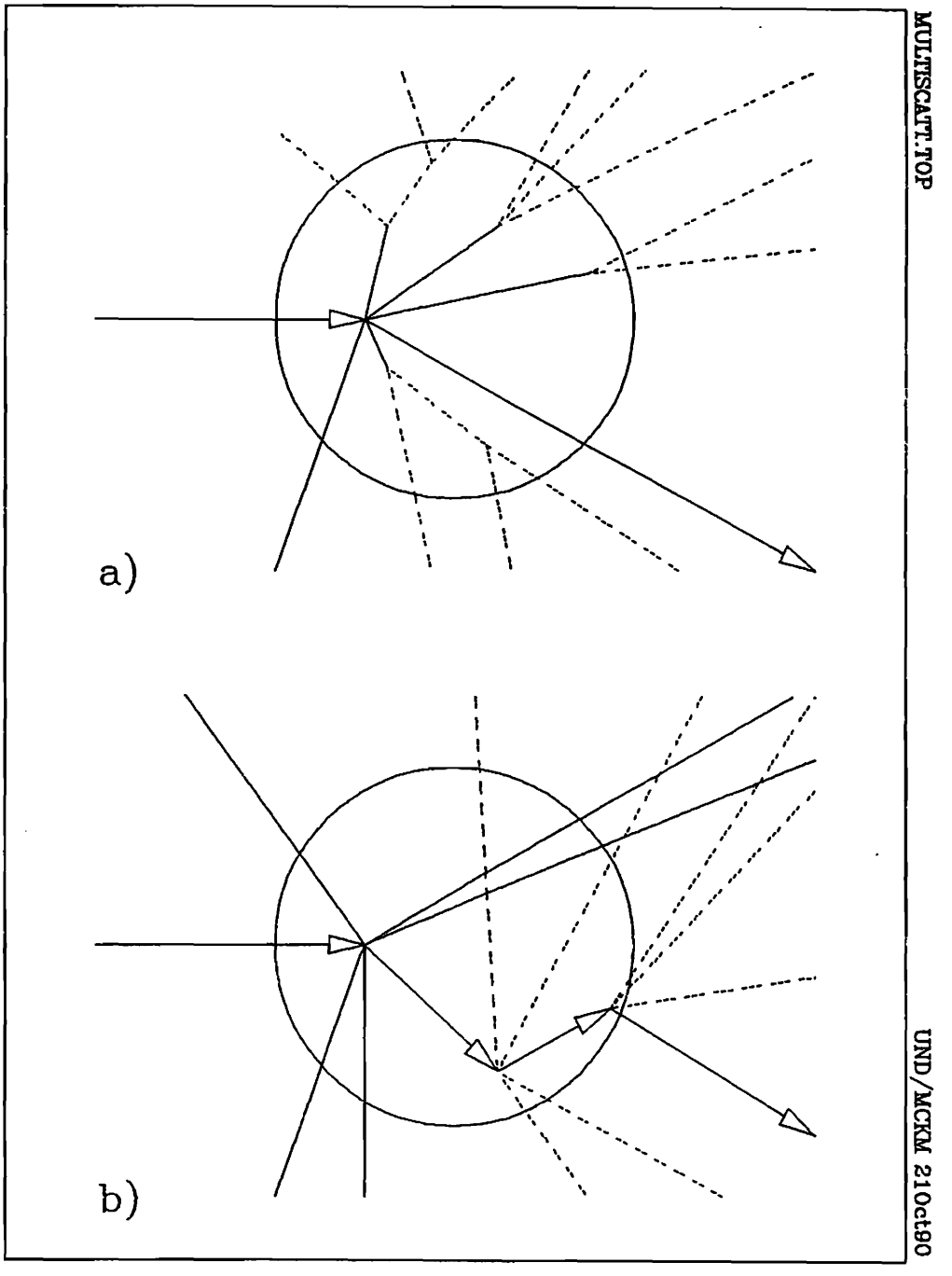

Figure 3.0.1 Multiple collisions visualized in the laboratory rest frame for two basic types of multiple production models: a) cascading with no projectile rescattering, b) projectile rescattering with no cascading.

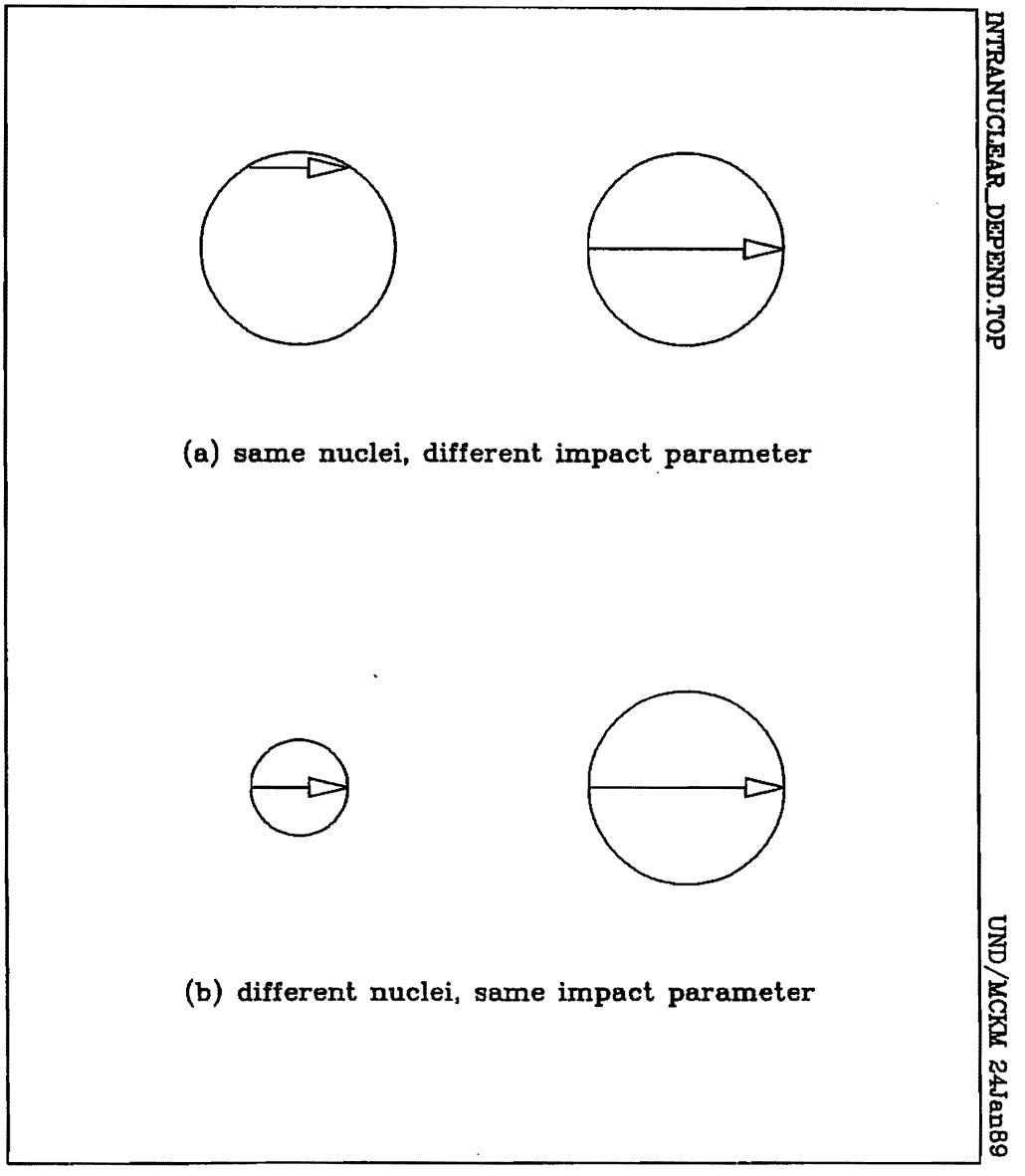

Figure 3.0.2 Experimental means of varying intranuclear pathlength and the number of intranuclear collisions.

3.1 AVERAGE NUMBER COLLISIONS $\bar{\nu}(hA)$

A first-order estimate of the number of projectile collisions is calculated employing hh and hA cross sections. With ζ defined to be the number of collisions per unit probability, ζ is simply the ratio between the number of collisions ν and the interaction cross section σ. The number of collisions ν is distributed broadly according to some undetermined A-dependent probability distribution $\Pi_{hA}(\nu)$. So if $\nu = A$ in hA interactions, $\zeta_{hA} = A/\sigma(hA)$. For hN interactions, $A = 1$, so $\zeta_{hN} = 1/\sigma(hN)$. Thus, a reasonable estimate of the average number of collisions is defined by ζ_{hA}/ζ_{hN} so that

$$\bar{\nu}(hA) = \frac{A/\sigma(hA)}{1/\sigma(hN)} = \frac{A\sigma(hN)}{\sigma(hA)}$$

For hA interactions with only one collision each, i.e. $\nu = 1$, one thus expects

$$1 = \bar{\nu}_{\nu=1}(hA) = \frac{A\sigma(hN)}{\sigma_{\nu=1}(hA)}$$

so the cross section $\sigma_{\nu=1}(hA)$ is simply the hN cross section multiplied by A

$$\sigma_{\nu=1}(hA) = A\sigma(hN)$$

However, if ν collisions were to occur in hA interactions then ζ_{hA} would be ν times that for a single collision, *i.e.* ζ_{hN}:

$$\zeta_{hA} = \frac{1}{\sigma_\nu(hA)} = \nu\frac{1}{\sigma_{\nu=1}(hA)} = \nu\frac{1}{A}\frac{1}{\sigma(hN)} = \frac{\nu}{A\sigma(hN)}$$

and

$$\bar{\nu}_\nu(A) = A\frac{\sigma(hN)}{\sigma_\nu(hA)} = A\frac{\sigma(hN)}{A\sigma(hN)/\nu} = \nu$$

The values of $\bar{\nu}(hA) = A\frac{\sigma(hN)}{\sigma(hA)}$ are calculated for E597 interactions in **Table 3.1.1** using parameters from [Elias 80] to calculate cross sections. These values, interpreted in terms of independent, consecutive collisions along a projectile's intranuclear pathlength, are expected to scale linearly with the cube root of A or the nuclear radius. In **Figure 3.1.1** $\bar{\nu}(hA)$ indeed increases linearly with $A^{1/3}$. Since baryons have a greater number of constituent quarks available for multiple scattering, the increase in nuclear radius makes a greater difference in the number of collisions sustained, thus the larger slopes for pA and $\bar{p}$A interactions.

Table 3.1.1 The number of projectile collisions $\bar{\nu}_{hA} = A\sigma(hN)/\sigma(hA)$ calculated for E597 interactions using parameters from [Elias 80] to calculate hA cross sections.

Projectile	320GeV/c		100GeV/c									
	π^-	π^-	π^+	π^+	p	p	π^-	π^-	π^-	$\bar{p}$	$\bar{p}$	$\bar{p}$
Target	Ag	Au	Ag	Au	Ag	Au	Mg	Ag	Au	Mg	Ag	Au
$\bar{\nu}(hA)$	2.45	2.88	2.33	2.74	2.84	3.43	1.60	2.41	2.84	1.96	3.11	3.74
$\Delta\bar{\nu}(hA)$	.04	.04	.07	.09	.04	.05	.02	.04	.04	.05	.08	.10

NUHA.TEX UND/MCKM 12May88

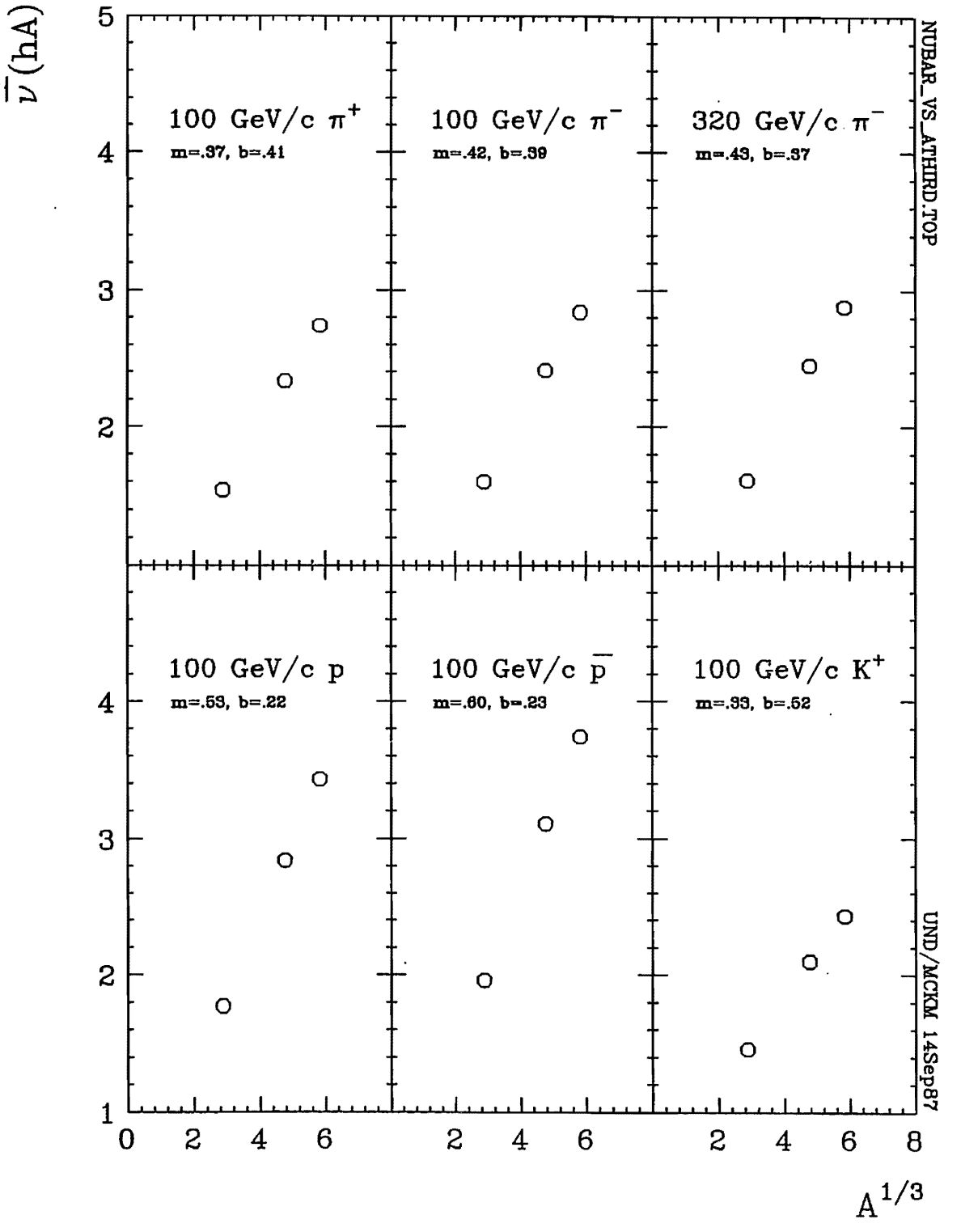

Figure 3.1.1 The average number of independent collisions $\bar{\nu}_{hA} = A\sigma(hN)/\sigma hA$ as a function of $A^{1/3}$ for E597 targets based on **Table 3.1.1** values. The parameters m and b of the linear fit $\bar{\nu}(hA) = mA^{1/3} + b$ are given for each beam category.

Values of $\bar{\nu}(hA)$ should also be compared to estimates of ν based on net secondary charge, including all but the *black* protons. Since each collision, be it primary or secondary, produces additional positive charge when it involves a proton, and no extra charge when it involves a neutron, an average total number of collisions $(\bar{\nu}_{primary} + \bar{\nu}_{secondary})$ can be estimated on the basis of the total summed secondary charge Q in excess of the beam's charge. This estimate $\bar{\nu}_{excess}$, because it includes both primary and secondary collisions, is greater than $\bar{\nu}(hA)$ and any other estimates of the number of primary collisions, made later in this study. In **Section 3.3**, the number of secondary collisions will be studied by taking the difference between $\bar{\nu}_{excess}$ and $\bar{\nu}_A$, and between $\bar{\nu}_{excess}$ and $\bar{\nu}_L$.

Assuming comparable contributions from target protons and neutrons, the number of nucleon collisions per target nucleon can be estimated from the number of proton collisions per target proton:

$$\frac{\bar{\nu}_{excess}}{A} = \frac{\nu_{proton}}{Z} = \frac{Q}{Z}$$

where

Q = average net charge of all observed secondaries - beam charge

A = target nucleus' mass number

Z = target nucleus' atomic number or charge

Figure 3.1.2 shows how $\bar{\nu}_{excess}$ relates to $\bar{\nu}(hA)$. Though at first glance the relation seems to be linear, $\bar{\nu}_{excess}$ cannot be truly linear since its linear extrapolation to $\bar{\nu}(hA) = 0$ is not zero. When the number of primary collisions $\bar{\nu}(hA)$ is zero, the number of secondary collisions should also be zero. Consequently, the sum of primary and secondary collisions $\bar{\nu}_{excess}$ should be zero. However, though not a linear function of $\bar{\nu}(hA)$, $\bar{\nu}_{excess}$ displays a strong correlation to $\bar{\nu}(hA)$ which differs for meson and baryon beam interactions. A given number of primary interactions produces a greater number of secondary interactions when the beam is a meson than when it is a baryon.

Assuming independence in the nature of collisions, the number of particles produced in multiple collisions could be expected to scale linearly with $\bar{\nu}(hA)$. Produced particle multiplicities plotted in **Figure 3.1.3** confirm a somewhat linear

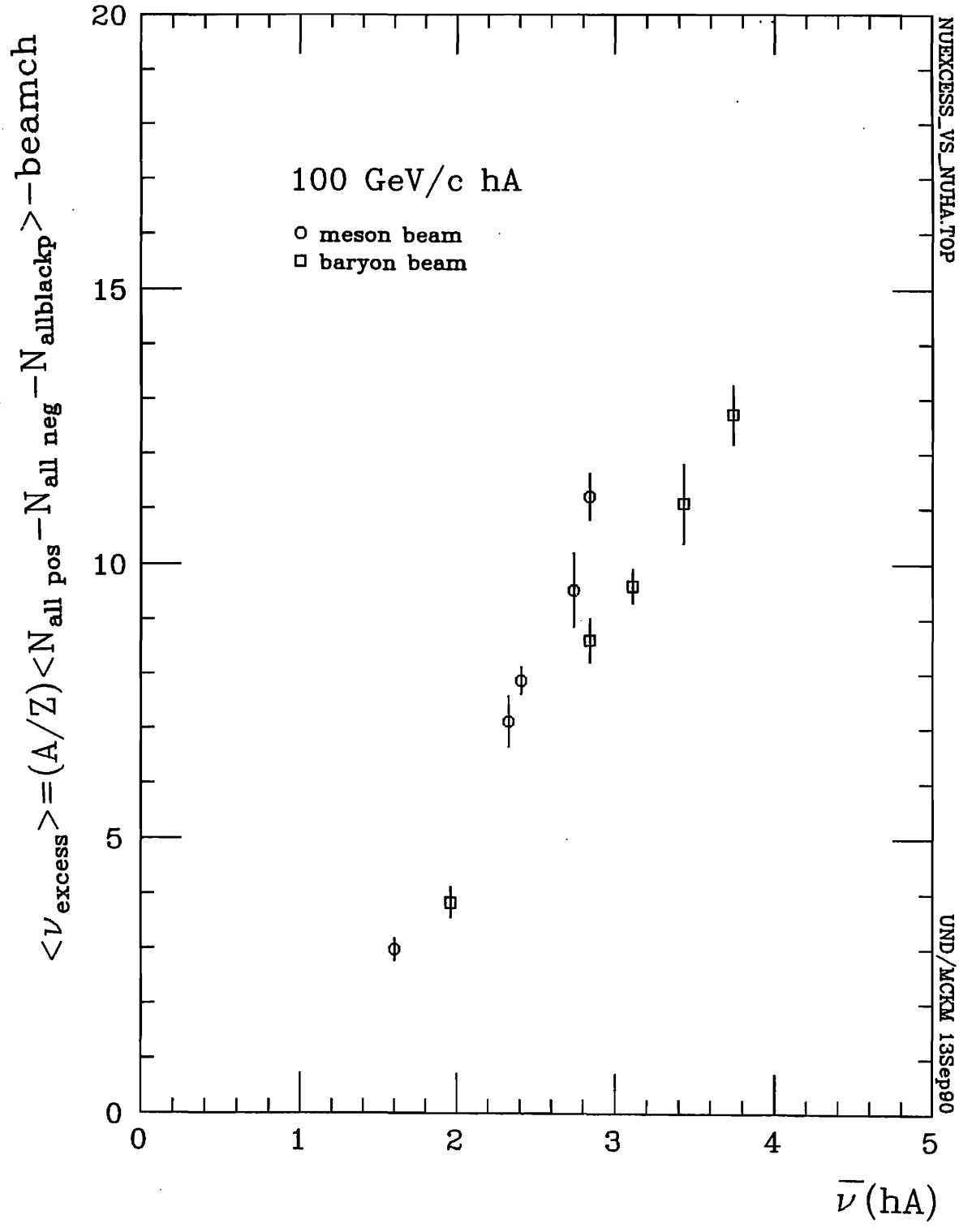

Figure 3.1.2 $\bar{\nu}_{excess}$ as a function of $\bar{\nu}(hA)$. $\langle\bar{\nu}_{excess}\rangle$ is expected to extrapolate to the origin.

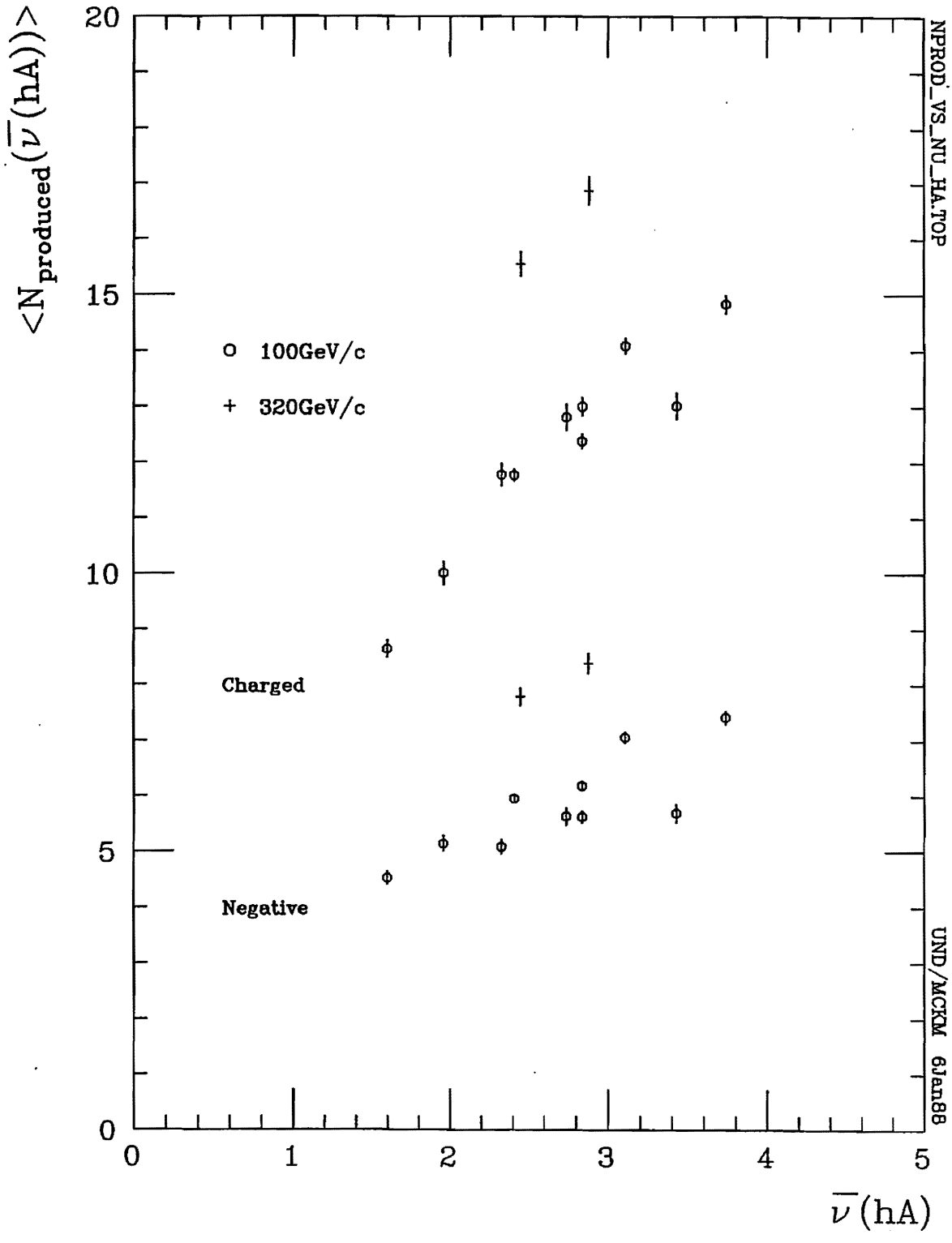

Figure 3.1.3 Average charged and negative multiplicity of produced particles as a function of the average number of collisions $\bar{\nu}_{hA}$.

correlation between produced particle multiplicity and $\bar{\nu}$. But it is reasonable to expect that $\langle N_{prod} \rangle \rightarrow 0$ as $\bar{\nu} \rightarrow 0$. This is not confirmed by **Figure 3.1.3** if linearity is inferred. It could be that the outcome of each collision is not absolutely independent of every other collision. Some component of N_{prod} may be associated with an interdependency of collisions in which secondary collisions could be instrumental. In any case, $\bar{\nu}(hA)$ is of limited value since ν is so broadly distributed. More narrow estimates are needed to characterize multiple collisions on an event-by-event basis.

3.2 MONTE CARLO $\Pi_{hA}(\nu)$

A classical calculation of probability $\Pi_{hA}(\nu)$ that a projectile collides ν times inside a nucleus of mass A can be made employing a Monte Carlo technique described by [Nilsson 80]. It calculates the probabilities in a geometric approach associated with the Glauber model [Andersson 75; Gurtu 74]. The LUND Monte Carlo FRITIOF uses this approach in its SUBROUTINE ANGANTYR, calculating ν event by event as well as tracing the spacetime history of each projectile as it passes through a nucleus. So the probability distributions for ν are inferred directly from the Monte Carlo event data which include not only the number of collisions sustained but also the impact parameter.

When FRITIOF calculates the number of collisions, it begins with a simulation of a nucleus' configuration. That means randomly generating, for each nucleon in the nucleus, r_o-values consistent with the nucleus' A and Z, the experimentally determined $\bar{\nu}(hA)$ for the hA interaction of interest, and the Woods-Saxon distribution of nuclear density

$$P(r)dr = \frac{K}{1 + e^{\frac{r - r_o A^{1/3}}{c_o}}} dr$$

where K normalizes P(r) so that

$$A = \int_0^\infty P(r)dr$$

$$= K c_o \ln 2$$

Here, c_o, with a value of .54614 fm, is the constant of skin thickness t of the nucleus

$$t = 2c_o \ln 9 = 2.4 \text{ fm}$$

so K takes on values 63.399, 285.295, and 520.399 for Mg, Ag, and Au, respectively. The Woods-Saxon distributions appropriate to E597 target nuclei are shown in **Figure 3.2.1.** Values for r_o, input values which result in Monte Carlo cross sections comparable to experimental ones, appear in **Table 3.2.1.** Actually, r_o was adjusted such that FRITIOF averages of $\Pi_{hA}(\nu)$ distributions shown in **Figure 3.2.2** agreed with the accepted values of $\bar{\nu}(hA)$.

The Monte Carlo generation of the nuclear configuration can be summarized by the following steps:

1) an r-value consistent with a Woods-Saxon charge distribution is randomly generated
2) two angles are randomly generated
3) position is determined by r and two angles
4) if position is closer to previously accepted nucleon positions in this nucleus than $r_{min} = \sqrt{\frac{40 \text{ mb}}{\pi}} = 1.12838$ fm
   then two new angles are generated (*i.e.* go back to step 2)
5) if the position is such that the radius is too small to allow enough space between nucleon and previous nucleons, a new radius is generated (*i.e.*go back to step 1)
6) repeat step 1) unless all nucleons have been generated

Nucleon motion inside the nucleus is ignored since the projectile velocities are so much larger than those possible for nucleons inside the nucleus. Once the configuration is determined, the simulated nucleus is bombarded with a hadron beam traveling parallel to FRITIOF'S z-axis at a randomly generated impact parameter in limits comparable to the nuclear radius. The beam is considered to have 'interacted' with a nucleon if its path brings it within a distance r_{sc} from that nucleon's position. This minimum distance is calculated from the hN inelastic cross sections (18, 21, and 32 mb for K^+, π and p beams, respectively, and $\bar{p}$ is treated like p) in the relation

$$r_{sc} = \sqrt{\frac{\sigma_{hN,inelastic}}{\pi}}$$

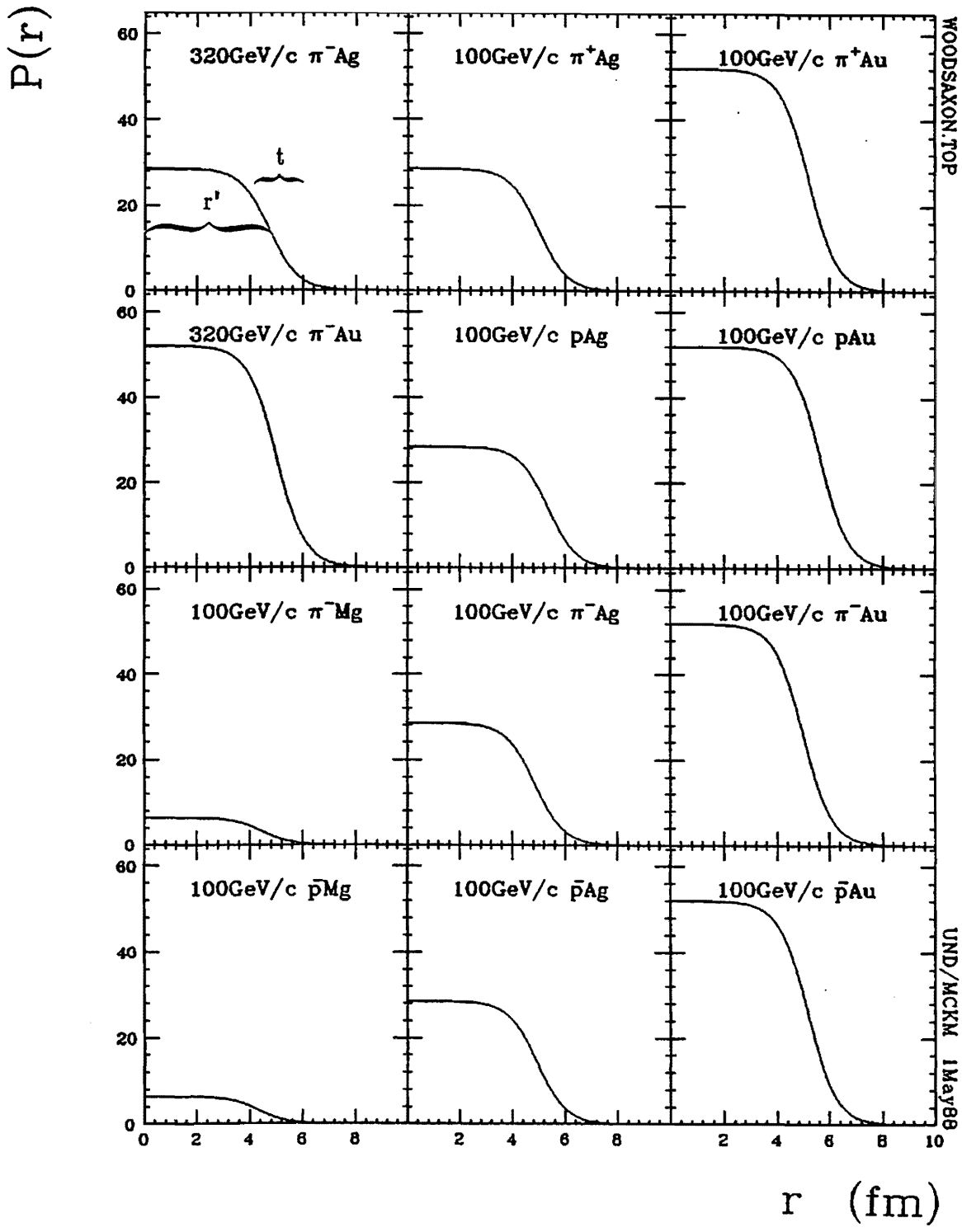

Figure 3.2.1 Woods-Saxon distributions appropriate to E597 target nuclei where r'is the rms radius and t is the skin thickness extending from .1 to .9 times $P_{max}(r)$.

Table 3.2.1 Probability $\Pi_{hA}(\nu)$ of ν projectile collisions in a target nucleus A as calculated geometrically by FRITIOF's SUBROUTINE ANGANTYR for interactions corresponding to the E597 data. In the Monte Carlo, the cross section is adjusted to the average number collisions $\bar{\nu}_(hA)$ through the values of r_o.

Projectile	320GeV/c		100GeV/c									
	π^-	π^-	π^+	π^+	p	p	π^-	π^-	π^-	$\bar{p}$	$\bar{p}$	$\bar{p}$
Target	Ag	Au	Ag	Au	Ag	Au	Mg	Ag	Au	Mg	Ag	Au
r_o	1.0050	1.0650	1.0635	1.1065	1.1400	1.2010	.9500	1.0360	1.0640	.9400	1.0520	1.1000
$\langle\nu_F\rangle$	2.466	2.892	2.327	2.746	2.818	3.426	1.597	2.402	2.857	1.961	3.102	3.747
$\Delta\langle\nu_F\rangle$	.032	.038	.031	.036	.039	.047	.019	.032	.038	.026	.044	.053
ν	$\Pi_{hA}(\nu)$											
1	.3410	.2680	.3670	.2850	.3040	.2275	.5865	.3480	.2820	.4775	.2845	.2345
2	.2310	.2115	.2530	.2240	.2085	.1825	.2670	.2565	.2140	.2505	.1875	.1445
3	.1985	.1885	.1860	.1955	.1735	.1540	.1130	.1745	.1700	.1545	.1520	.1325
4	.1235	.1430	.1090	.1375	.1335	.1350	.0305	.1305	.1470	.0790	.1345	.1340
5	.0740	.1060	.0590	.0965	.0935	.1295	.0030	.0610	.1090	.0305	.1080	.1040
6	.0225	.0530	.0195	.0430	.0510	.0815	-	.0200	.0515	.0065	.0650	.1055
7	.0080	.0240	.0055	.0135	.0235	.0490	-	.0060	.0190	.0010	.0425	.0730
8	.0010	.0060	-	.0040	.0095	.0250	-	.0030	.0060	.0005	.0165	.0370
9	.0005	-	.0005	.0005	.0020	.0095	-	.0005	.0010	-	.0065	.0230
10	-	-	.0005	.0005	.0005	.0050	-	-	.0005	-	.0025	.0095
11	-	-	-	-	.0005	.0015	-	-	-	-	.0005	.0015
12	-	-	-	-	-	-	-	-	-	-	-	.0010

PIHA.TEX UND/MCKM 12May88

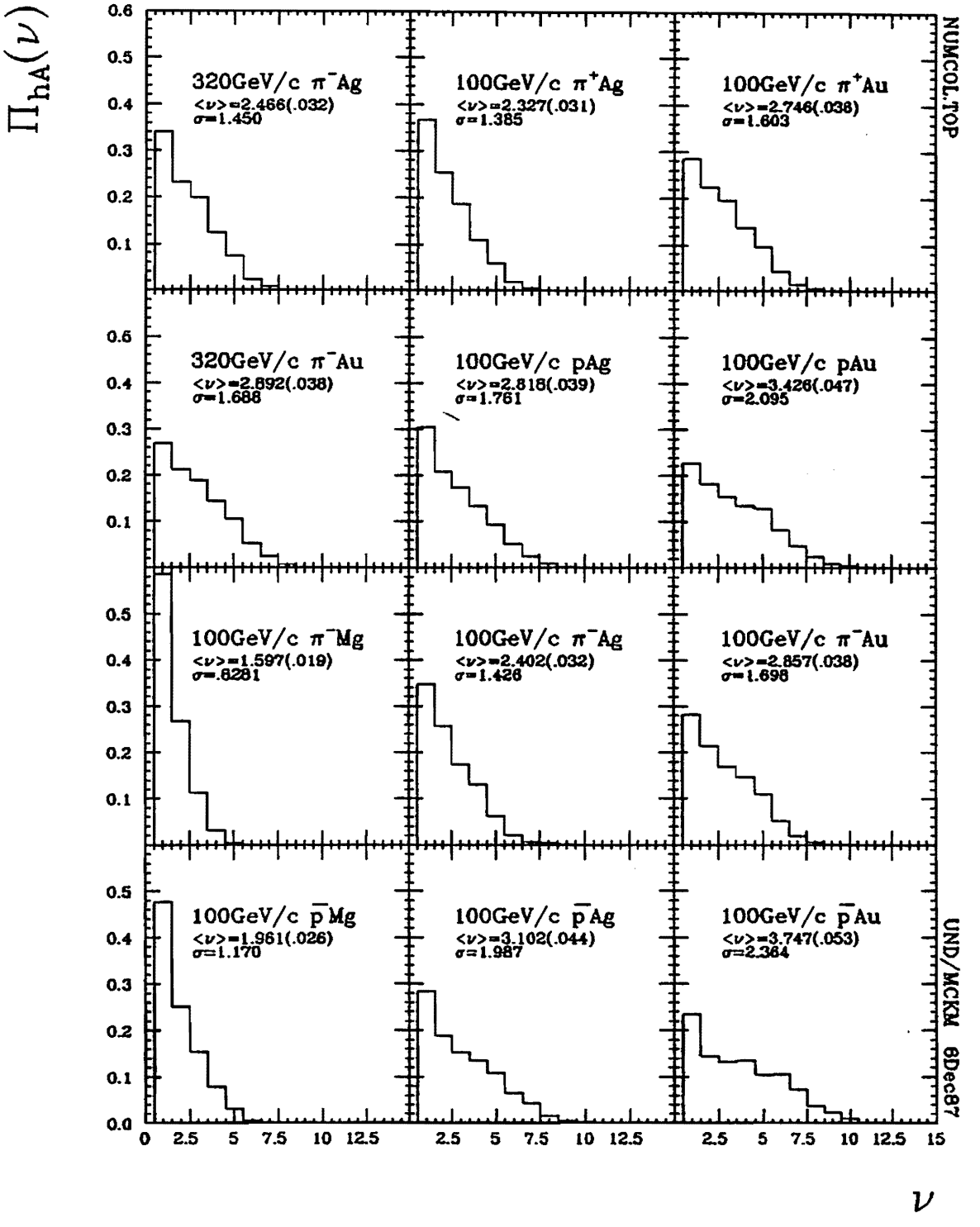

Figure 3.2.2 The probability distribution of the number of projectile collisions from a Glauber calculation in FRITIOF for 2000 events each of 12 interactions with beam-target-energy combinations corresponding to E597 data. The number of collisions is directly accessible from Monte Carlo event output.

To find the number of collisions sustained by the beam particle, the nucleons within distance r_{sc} of the beam path are simply counted.

Since the the hN interaction probability is σ_{hN}, the hA interaction probability is A times larger, *i.e.* $A\sigma_{hN}$. But it has already been shown that $A\sigma_{hN} = \bar{\nu}\sigma_{hA}$ when $\bar{\nu}(hA)$ was first estimated. So finding the hA interaction probability is equivalent to finding the probability of ν interactions between a hadron and an A-nucleon nucleus as a whole. Since the same cross section determines $\bar{\nu}(hA)$ and r_{sc}, $\bar{\nu}(hA)$ is automatically preserved in the Monte Carlo calculation.

Results for πAg interactions agree reasonably well with previous calculations [Nilsson 80], with minor discrepancies attributable to Nilsson's use of slightly different, older $\bar{\nu}$ values (and thus r_o) and to this study's differentiating between oppositely charged beams.

3.3 $\bar{\nu}_A(N_{lightp})$ AND $\bar{\nu}_V(N_{lightp})$

Once the probability of a given number of primary collisions is known, the correlation between knocked-out protons and the number of primary collisions can be calculated. Since collisions often knock out nuclear protons, the total positive charge of the secondaries increases and readily identifiable, characteristically dark, secondary tracks are observable. In fact, most of the grey-track-producing particles are indeed fast target protons which can be expected to correlate with the number of projectile collisions during the beam's passage through the nucleus. **Figure 3.3.1** justifies this expectation by showing the correlation between the grey proton multiplicity N_{greyp} and the number of collisions $\bar{\nu}(hA)$. *Grey* protons are defined in terms of their measured velocity $.3 < \beta < .7$.

But *grey* is not always defined exactly this way. Results in [Andersson 78], [Adamus 88a], and [De Marzo 82] have been presented for *grey* protons defined by different velocity ranges: $.283 < \beta < .713$, $.2 < \beta < .7$, and $.106 < \beta < .539$, respectively. In this study, *light* protons spanning a momentum range corresponding to $.300 < \beta < .831$ will be used instead of *grey* ones to indicate the level of multiple

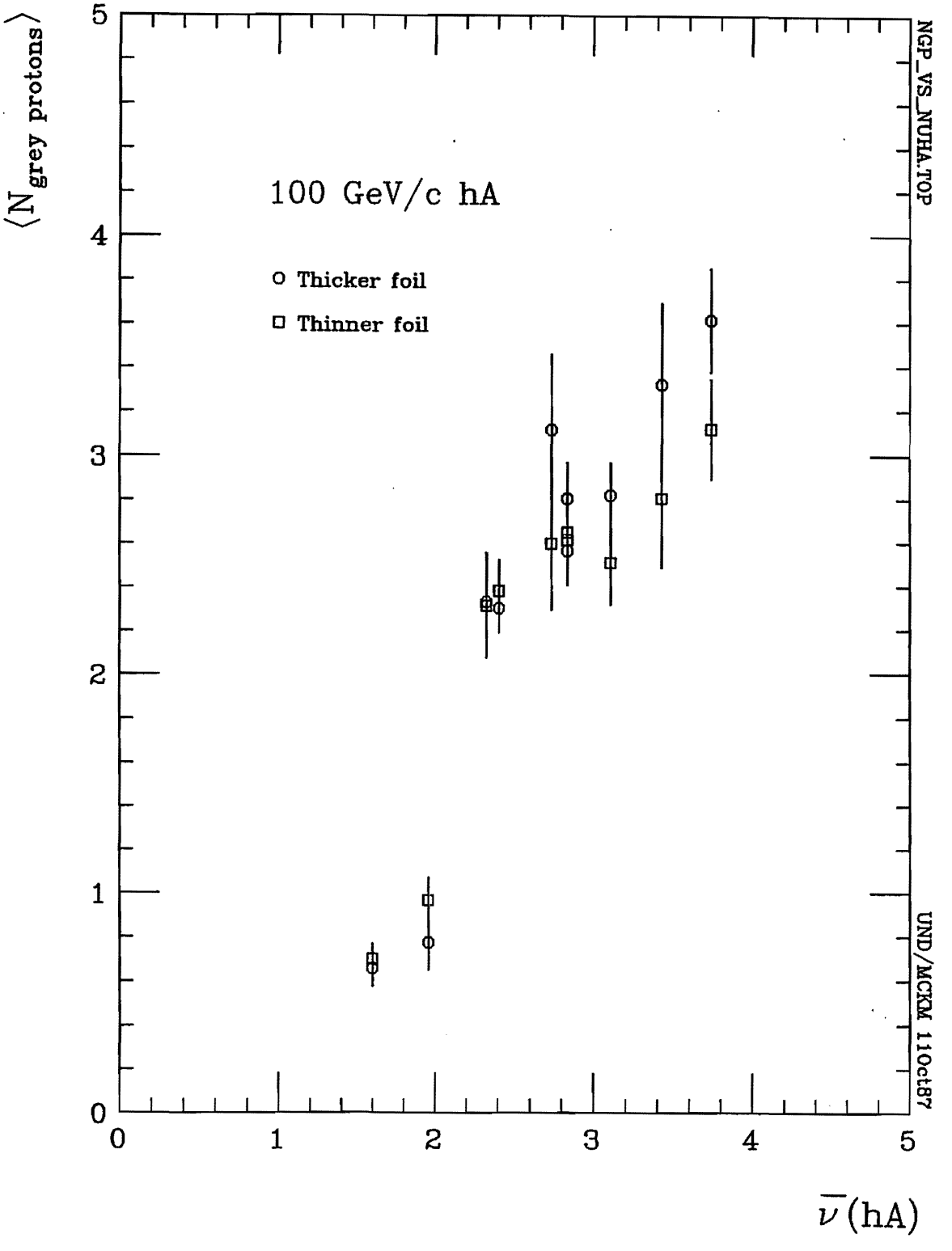

Figure 3.3.1 Average *grey* proton multiplicity as a function of $\bar{\nu}(hA)$.

interactions. The lower limit excludes most *evaporation* protons, those associated with the disintegration of the nucleus, and the extended upper limit slightly improves track statistics. All analysis sequences have also been conducted employing *grey* proton multiplicities rather than *light* proton multiplicities, but results are not significantly different.

In an attempt to relate the number of observed knocked-out or *light* protons to the number of projectile collisions, knocked-out protons are viewed from a useful but oversimplified perspective. They are presumed to to be produced exclusively from primary interactions, and each primary interaction is presumed to produce identical probability distributions of knocked-out protons

$$P^A_{\nu=1}(N_{lightp}) = (1-x)x^{N_{lightp}}$$

where $x = \frac{\frac{<N_{lightp}>^A}{\bar{\nu}}}{1+\frac{<N_{lightp}>^A}{\bar{\nu}}}$ [Andersson 78]. then $\frac{<N_{lightp}>^A}{\bar{\nu}}$ is just the average number protons knocked out per collision. Obviously this distribution depends on A since it depends on the number of protons knocked out. To determine the light proton multiplicity distribution for ν greater than 1, ν independent distributions $P^A_{\nu=1}(N_{lightp})$ are convoluted to produce

$$P^A_{\nu}(N_{lightp}) = \begin{pmatrix} N_{lightp}+\nu-1 \\ N_{lightp} \end{pmatrix} (1-x)^{\nu} x^{N_{lightp}}$$

Of course, this means that primary-produced protons are not being distinguished from secondary-produced protons. A complete description would account for knocked-out protons originating from both cascades (collisions between target nucleons and secondary particles as they traverse the nucleus) and primary interactions. However, for simplicity's sake consistent with the no-produced-particle-cascades assumption made earlier, the possibility of cascading protons is being ignored. But to check the extent to which this approach is valid, an attempt is made to isolate, or at least exaggerate, the single-collision-event component of the experimental data in order to compare the probability distribution of *light* protons for this subsample with the calculated probability distribution of *light* protons specifically for $\nu = 1$. Events undergoing single collisions are expected to be characterized by 1) leading beam-

like particles with greater-than-average rapidity, and 2) less-than-average produced particle multiplicity. With collisions subsequent to the first, a greater and greater degradation of energy in the beam particle is anticipated due to multiple momentum transfers. Thus the rapidity of the leading beam-like particle is expected to decrease as the number of collisions increases. An increase in the number of produced particles as the number of collisions increases is also expected since each independent collision is assumed to produce its own distribution of produced particles superposed on those associated with the other collisions.

To enrich the data sample for single-collision events, cuts are made on produced particle multiplicity and the rapidity of the leading particle, pion mass assumed. [De Marzo 82] successfully applied a similar cut on the rapidity of the leading charged particle ($y > 5 units$) and on total charged secondary multiplicity ($N_{ch} < \langle N_{ch} \rangle$) with good agreement between calculated [Andersson 78] and NA5 experimental values for *grey* charged multiplicity. Since E597 distinguishes between particles, produced particle multiplicities play the role of the total charged multiplicities. Single collisions probably produce fewer than the average number of particles, so the cut should be made at about $\langle N_{produced} \rangle$. A single collision should also look the same for all nuclei, so the same multiplicity cut should be applied for each of the three nuclei in the E597 sample. Some distinction, however, will be made between meson and baryon beams and between 100 and 320 GeV/c beam momenta.

To establish the optimum limits by which to enrich the sample for single collision events, the scatters of leading charged, negative, and positive particle rapidities were studied as a function of produced particle multiplicities in FRITIOF events of known ν. This revealed a trend and suggested how well $\nu = 1$ events might be enhanced. Confidence in this approach is bolstered by the fact that the scatter plots of positive and negative produced particle rapidities as functions of the total charged produced multiplicity, **Figure 3.3.2**, compare favorably with FRITIOF simulations in **Figure 3.3.3**. When the distributions of points for single, double, and triple collision Monte Carlo events are compared, **Figures 3.3.4, 3.3.5**, and **3.3.6**, respectively, the distribution patterns for leading beam-like (*i.e.* same charge as the beam)

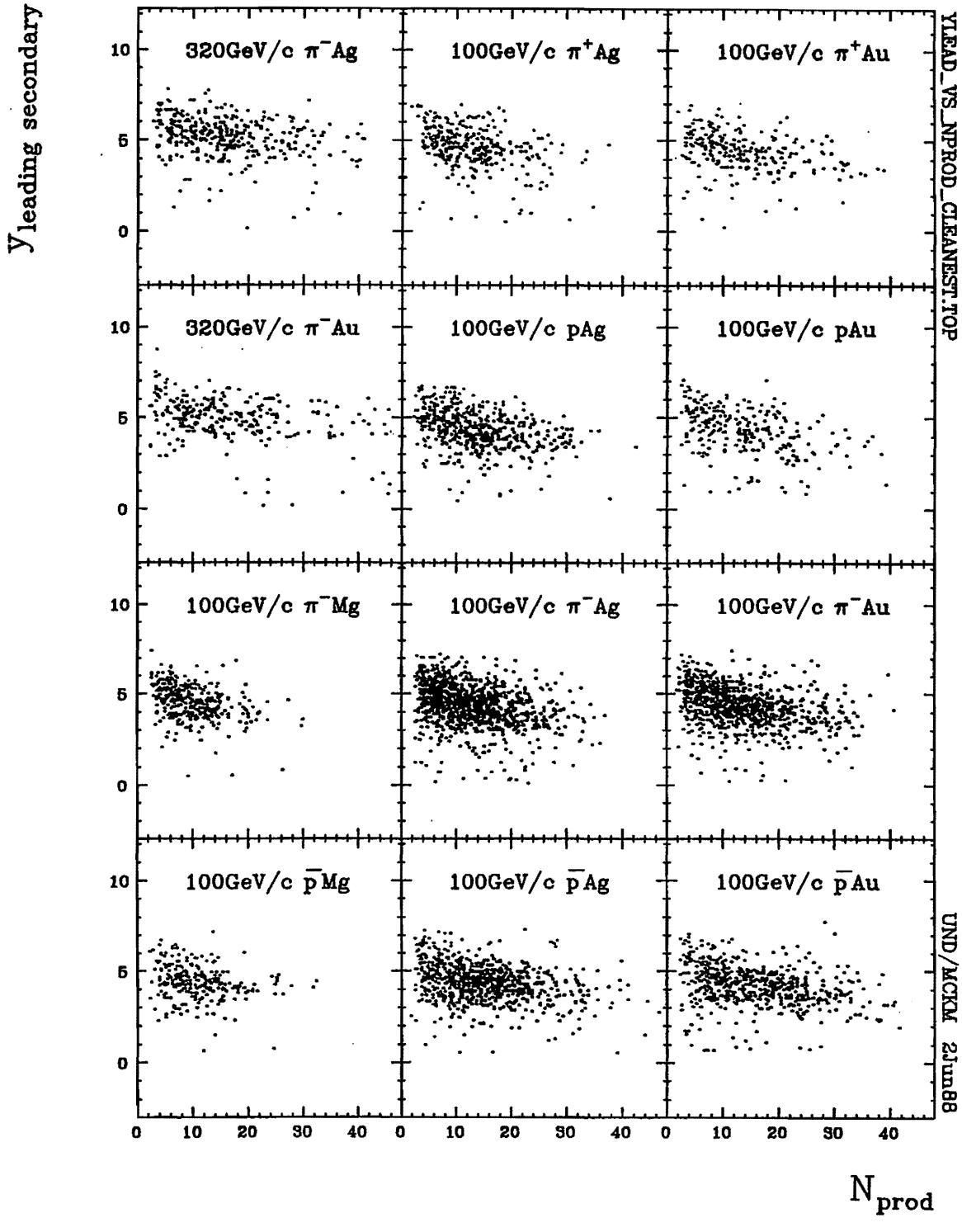

Figure 3.3.2 Scatter plots of leading charged produced particle rapidities as functions of total charged produced multiplicity for E597 data.

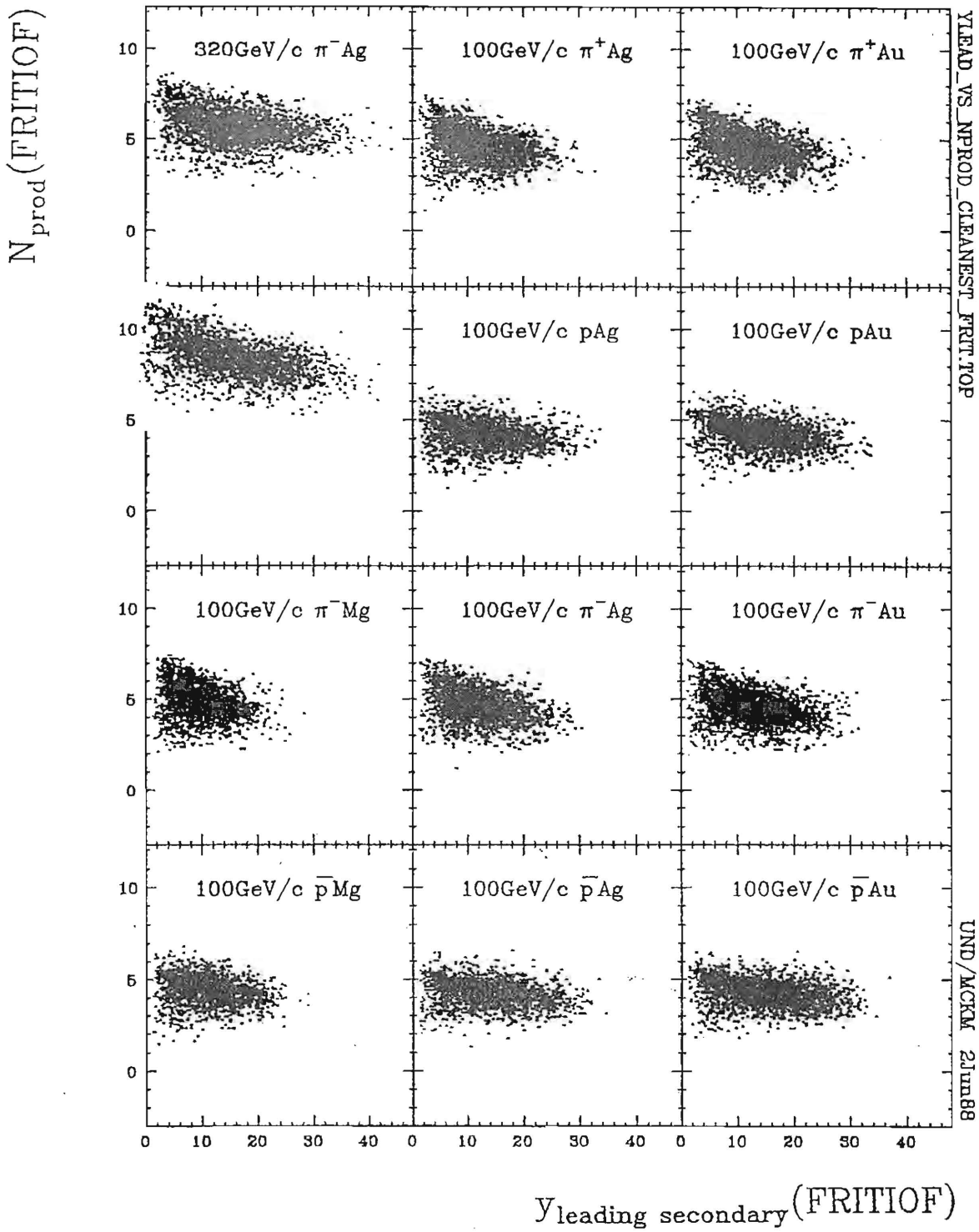

Figure 3.3.3 Scatter plots of leading charged produced particle rapidities as functions of total charged produced multiplicity for FRITIOF simulations of E597 data.

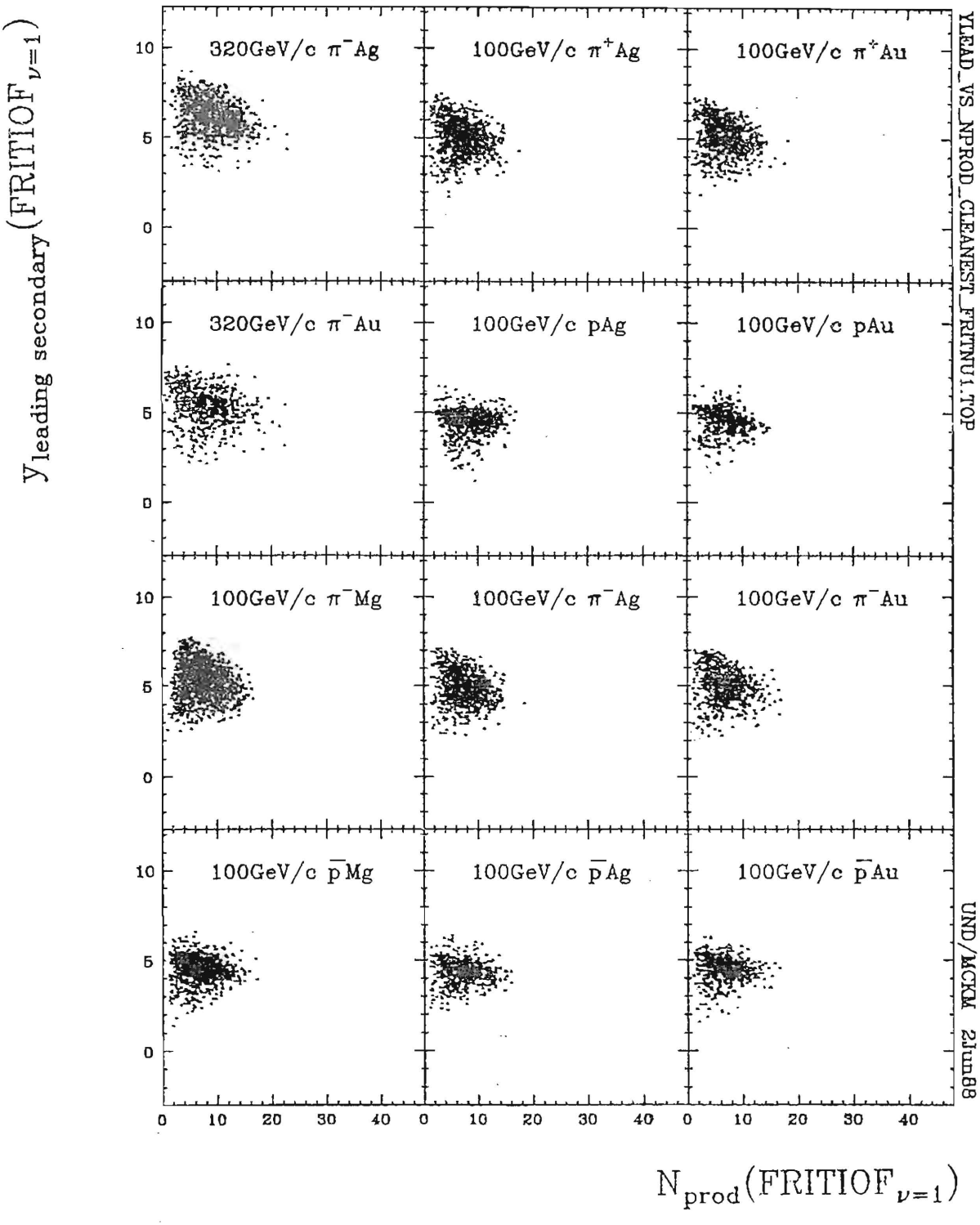

Figure 3.3.4 The rapidity of leading charge produced tracks as functions of charged produced particle multiplicity in FRITIOF Monte Carlo events sustaining 1 collision only.

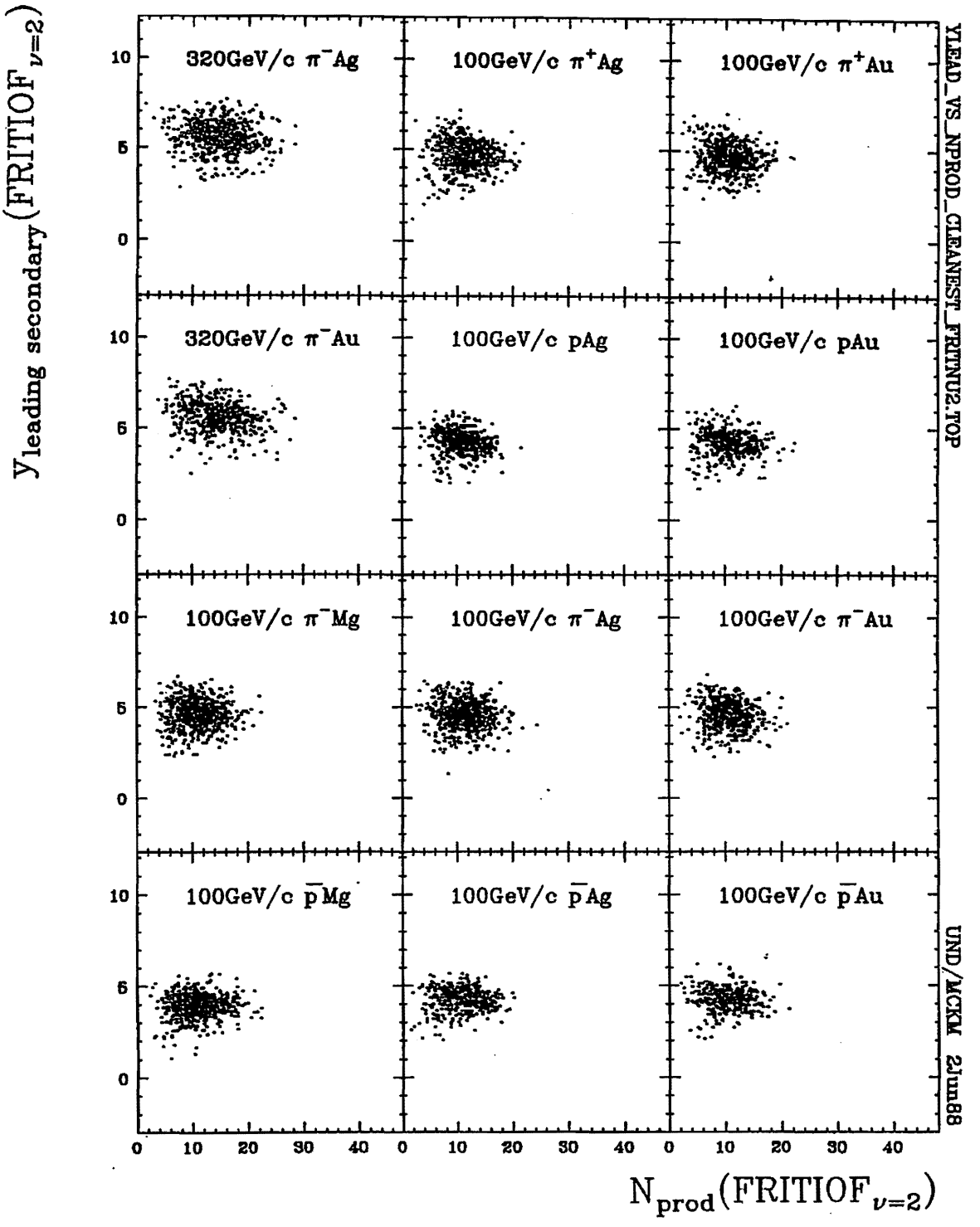

Figure 3.3.5 The rapidity of leading charged produced tracks as functions of charged produced particle multiplicity in FRITIOF Monte Carlo events sustaining 2 collisions only.

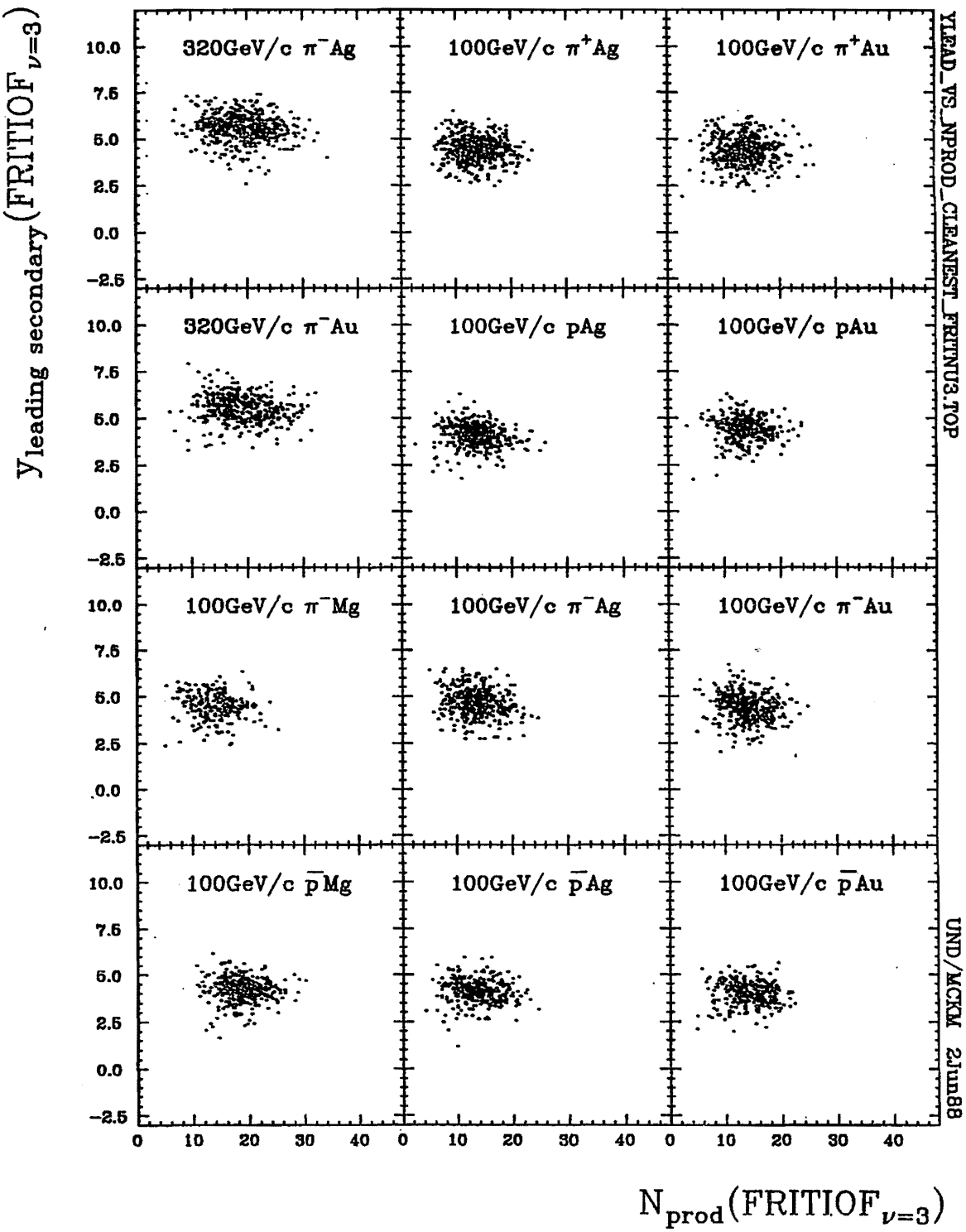

Figure 3.3.6 The rapidity of leading charged produced particle tracks as functions of charged produced particle multiplicity in FRITIOF Monte Carlo events sustaining 3 collisions only.

particles is clearly different from the non-beam-like. For the leading beam-like particles, the probability density is much greater at small produced particle multiplicity and large leading beam-like particle rapidity whereas for the leading non-beam-like particles, a tail at low rapidity appears. As the number of collisions increases, the distribution of points for leading beam-like particles moves decidedly towards higher produced multiplicities, and less dramatically towards lower rapidity. These results confirm the expectation that data can be significantly enriched for single collision events on the basis of multiplicity and rapidity cuts. These cuts are summarized in **Table 3.3.1** and illustrated for $\pi^- Ag$ FRITIOF events in **Figure 3.3.7**. Using the number of collisions associated with each FRITIOF event, the probability of finding ν=1 events nearly doubles when the multiplicity and rapidity limits are applied. **Table 3.3.2** shows the increase and the fact that $\bar{\nu}$ decreases appropriately, especially for the heavier nuclei. This is precisely what is intended since it is the interaction samples with heavier nuclei that have the most pronounced admixture of higher ν. The cut modifies the distributions of ν inside and outside the restricted regions as shown in **Figure 3.3.8**. The *inside* sample, which represents between 25 and 50% of the total, is clearly enriched in lower ν over the *outside* sample.

These same cuts render a similarly enriched sample when applied to E597 data. **Figure 3.3.9** shows that the fraction of events *inside* is comparable with FRITIOF's and that the distribution of *light* proton multiplicity shifts much like the ν distribution did with FRITIOF events. **Figure 3.3.10** also shows how closely the *light* proton probability for the supposed ν=1 enriched sample lies to the $\nu = 1$ Andersson model curves [Andersson 78]. As might be expected, the points at large N_{lightp}, which probably include more $\nu > 1$ events, lie further from the $\nu = 1$ curves.

Now, with the probability distribution of the number of collisions in a nucleus Π_{hA} (for projectile dependence) and the probability distribution of light proton multiplicity for given numbers of collisions, two(2) parameters can be calculated which are readily verifiable with experimental data: 1) the probability distribution of light proton multiplicity

$$P(N_{lightp}) = \sum \Pi_{hA}(\nu) P_{\nu}^{A}(N_{lightp})$$

Table 3.3.1 Cuts made to enrich samples for single collision events ($\nu = 1$). The produced particle multiplicity N_{prod} must be less than $N_{prod}^{newercut}$. The leading charged secondary particle (assumed pion mass) with the same charge as the beam must have rapidity greater than $y^{newercut}$.

Projectile	320GeV/c		100GeV/c									
	π^-	π^-	π^+	π^+	p	p	π^-	π^-	π^-	$\bar{p}$	$\bar{p}$	$\bar{p}$
Target	Ag	Au	Ag	Au	Ag	Au	Mg	Ag	Au	Mg	Ag	Au
$\langle N_{chg} \rangle$	19.6	22.2	15.9	17.7	17.7	18.4	16.1	17.4	9.8	19.0	20.9	11.5
$N_{prod}^{newercut}$	15	15	11	11	12	12	11	11	11	12	12	12
$y^{newercut}$	5.4	5.4	4.3	4.3	4.3	4.3	4.3	4.3	4.3	4.3	4.3	4.3

NEWERCUT_PARAM.TAB UND/MCKM 16Jun88

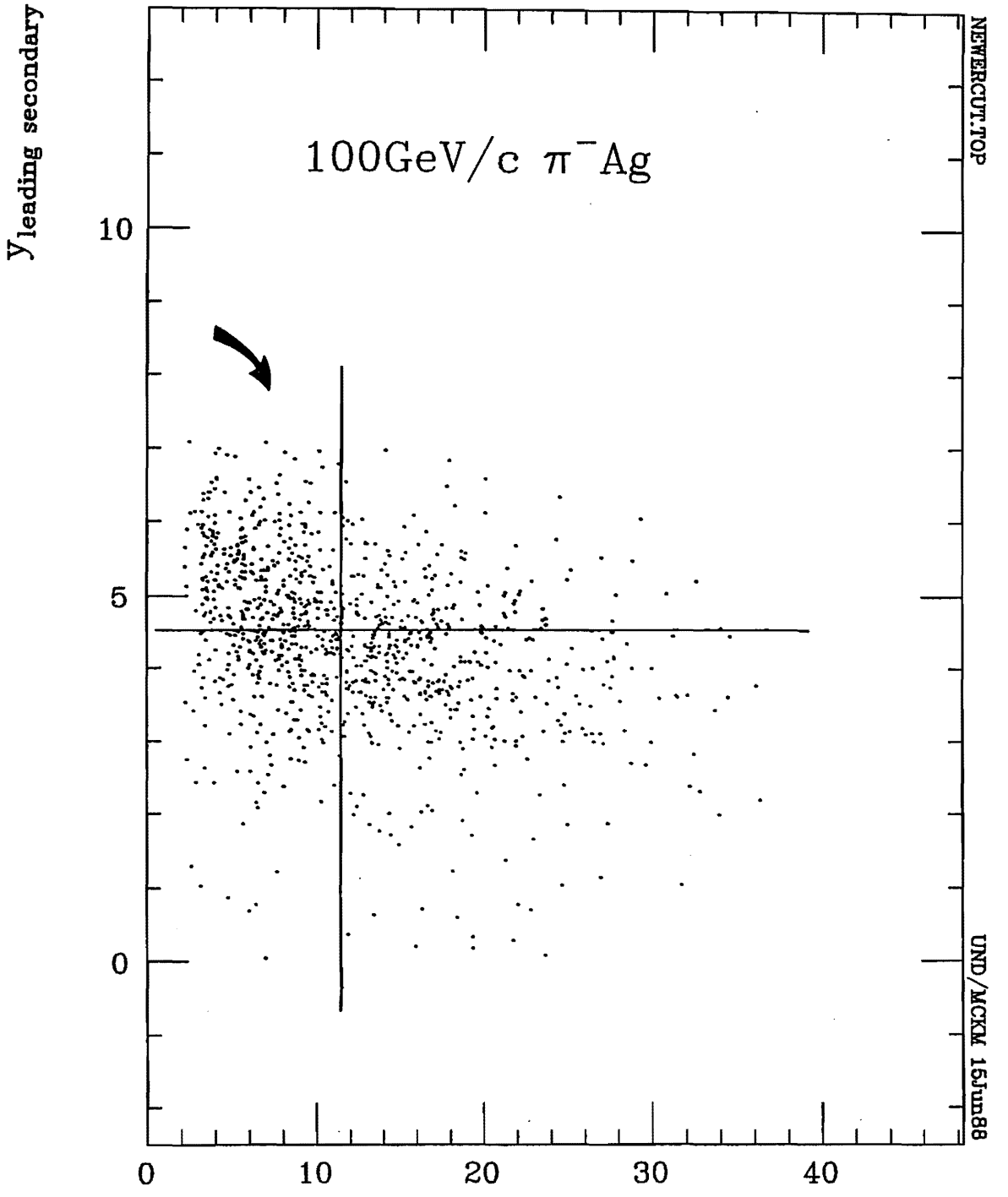

Figure 3.3.7 An example of the NEWERCUT region (the quadrant indicated by the arrow) taken from 100 GeV/c $\pi^- Ag$ data. Leading particle rapidity cuts and total charged produced particle multiplicity cuts enrich data for ν=1 events.

Table 3.3.2 Comparing the probability $P_{\nu=1}$ of only one collision occuring in general events with the probability of only one collision occuring in events limited by 'newercut' restrictions meant to enhance samples for single collisions. Also the average number of collisions directly calculated with FRITIOF simulations for general and 'newercut'-qualifying events.

Projectile	320GeV/c		100GeV/c									
Target	π^- Ag	π^- Au	π^+ Ag	π^+ Au	p Ag	p Au	π^- Mg	π^- Ag	π^- Au	p Mg	p Ag	p Au
	$P_{\nu=1}$ =probability of an event involving $\nu = 1$ primary collisions											
All events	.34	.27	.37	.29	.30	.23	.59	.35	.28	.48	.29	.24
Newercut events	.65	.63	.69	.66	.63	.61	.79	.67	.66	.72	.64	.66
Increase of $\nu = 1$ events	.91	1.34	.88	1.30	1.07	1.70	.35	.93	1.33	.51	1.23	1.83
Ratio $\frac{p^{allevents}_{\nu=1}}{p^{newercutevents}_{\nu=1}}$	1.92	2.34	1.88	2.30	2.07	2.70	1.35	1.93	2.33	1.51	2.23	2.83
	$\langle \nu^{FRITIOF} \rangle$ = average number collisions											
All events	2.47	2.89	2.33	2.75	2.82	3.43	1.607	2.40	2.86	1.96	3.10	3.75
Newercut events	1.96	2.02	1.89	1.96	2.06	2.08	1.75	1.92	1.95	1.87	2.05	2.04

NU1PROB_NEWERCUT.TAB UND/MCKM 16Jun88

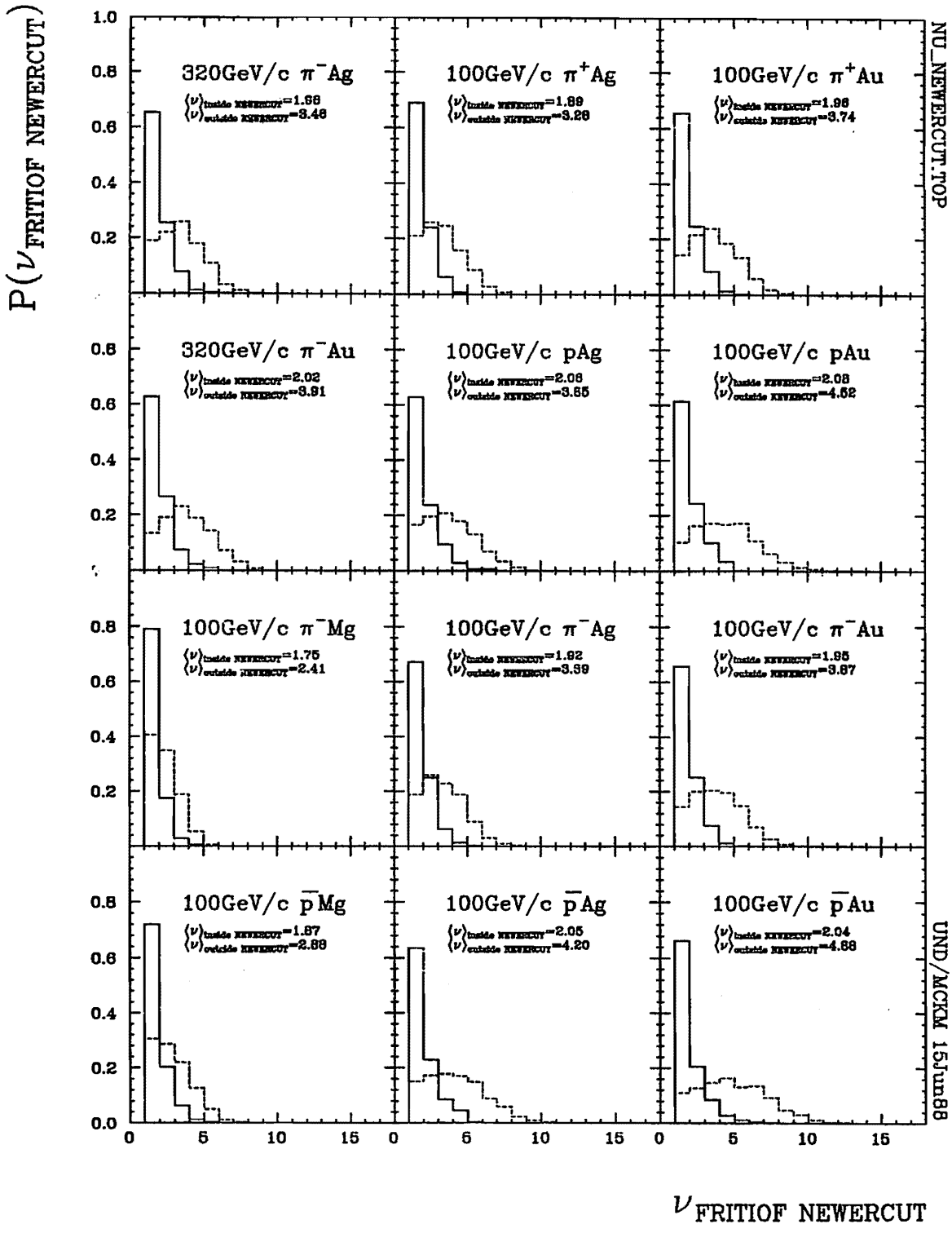

Figure 3.3.8 The frequency distributions of ν in FRITIOF Monte Carlo events comparing regions inside and outside the area NEWERCUT intended to represent an enriched data sample for ν=1 events.

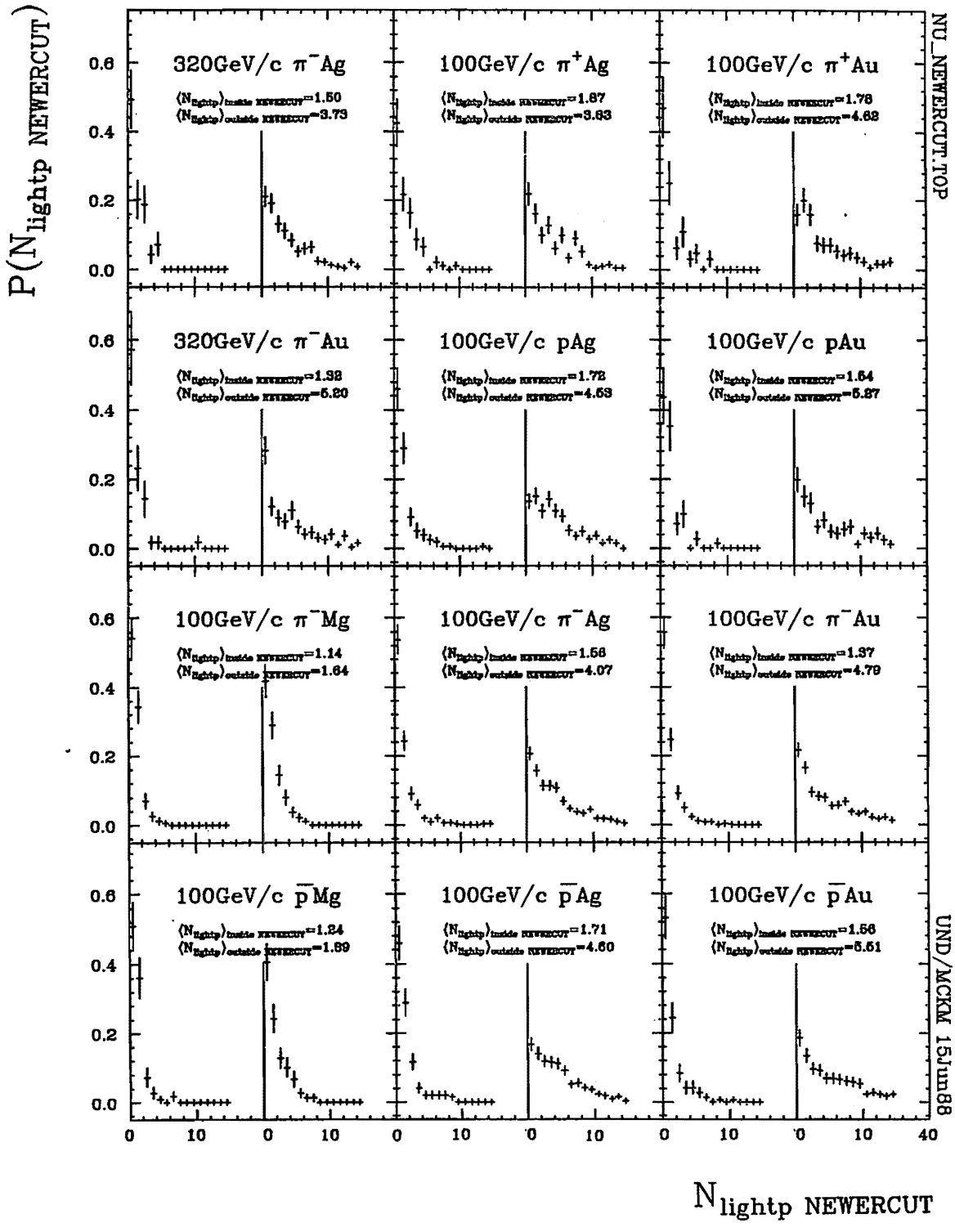

Figure 3.3.9 Distribution of N_{lightp}, the *light* proton multiplicity, in E597 hadron events inside and outside the area NEWERCUT intended to represent the data sample enriched for ν=1 events.

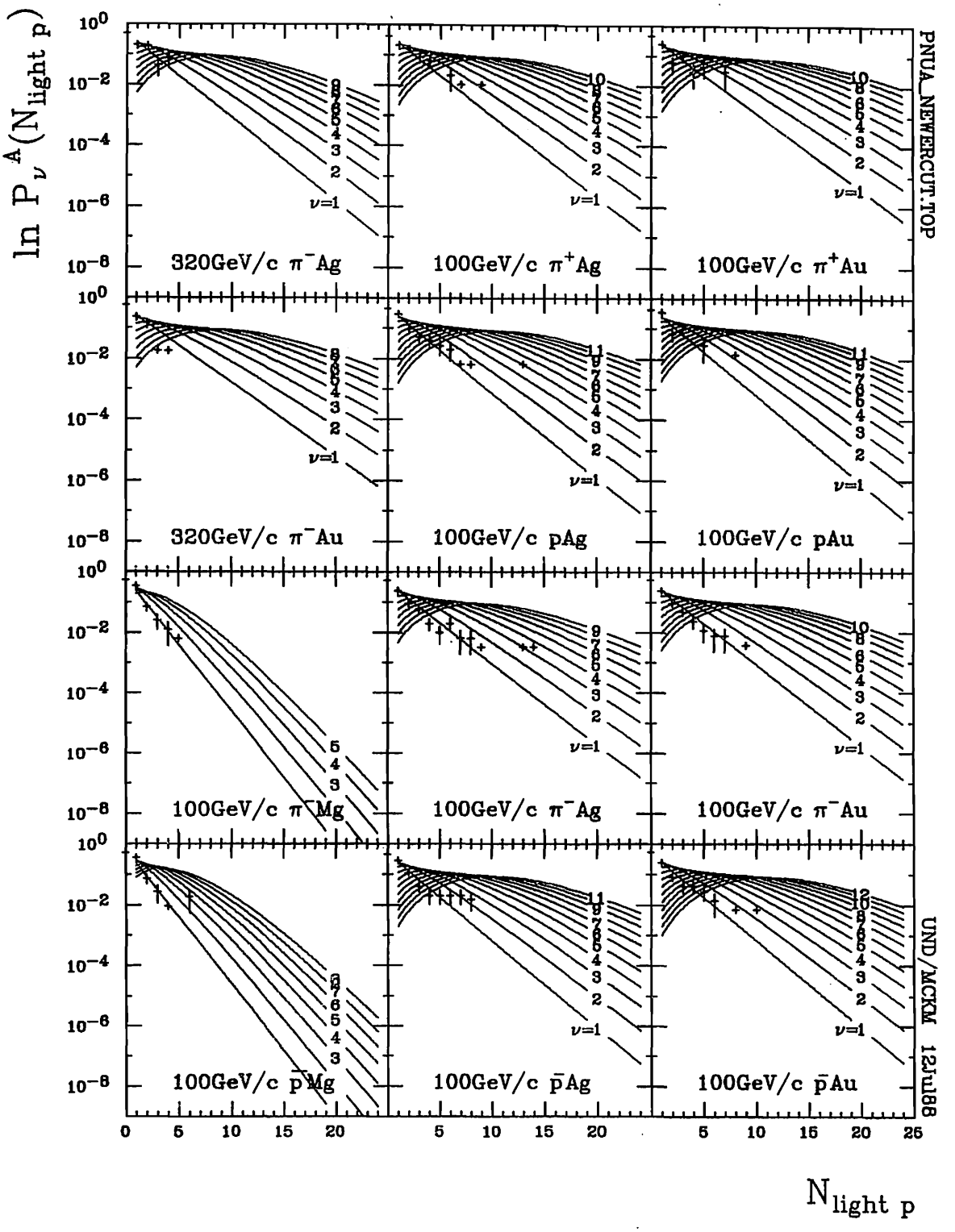

Figure 3.3.10 Probability distributions of *light* proton multiplicities for given numbers of collisions calculated according to [Andersson 78] in the context of *light* proton multiplicity and results from the data sample enriched for ν=1 events.

and 2) the average number of projectile collisions

$$\bar{\nu}(N_{lightp}) = \frac{\sum \nu \Pi_{hA}(\nu) P_\nu^A(N_{lightp})}{\sum \Pi_{hA}(\nu) P_\nu^A(N_{lightp})}$$

Similar calculations have been made for emulsion data [Andersson 78]. The results for E597 data in **Figure 3.3.11** are in fair agreement with calculated values of the probability as a function of the light proton multiplicity. The predicted values, however, consistently overshoot the experimental values at low multiplicities and undershoot at higher multiplicities with the magnitude of these discrepancies clearly growing with A. The curve must be characterized by more of an 'S' shape in order to reproduce the data. It may be that Π_{hA} is shifted too far towards smaller ν compounded by the fact that N_{lightp} is underrepresented due to the nuclear target thickness.

The calculated average number of collisions as a function of light proton multiplicity $\bar{\nu}(N_{lightp})$is given in **Figure 3.3.12** and is tabulated in the look-up **Table 3.3.3.** This estimate of $\bar{\nu}$ is better than $\bar{\nu}(hA)$. When the dispersion $\Delta\bar{\nu}(N_{lightp})$ for this estimate is calculated by

$$\Delta\nu(N_{lightp}) = \sqrt{\frac{\sum \nu^2 \Pi_{hA}(\nu) P_\nu^A(N_{lightp})}{\sum \Pi_{hA}(\nu) P_\nu^A(N_{lightp})} - \left(\frac{\sum \nu \Pi_{hA}(\nu) P_\nu^A(N_{lightp})}{\sum \Pi_{hA}(\nu) P_\nu^A(N_{lightp})}\right)^2}$$

it is often less than the dispersion $\Delta\bar{\nu}(hA)$ for $\bar{\nu}(hA)$. **Figure 3.3.13** shows that $\Delta\bar{\nu}(N_{lightp})$ is generally lower except for light nuclei. $\bar{\nu}(N_{lightp})$ is an improved estimate of ν for heavy nuclei. But it is better not only because of its smaller dispersion but more importantly because it ties all interactions to a common parameter. While N_{prod} is definitely seen to be correlated to N_{lightp} in **Figure 3.3.14**, the importance of that correlation is frustrated by the fact that N_{lightp} is not associated to equivalent production processes in the various interactions. But when N_{prod} is plotted as a function of $\bar{\nu}_A(N_{lightp})$ rather than N_{lightp}, not only is the stage set to compare and unify interactions directly, but the correlation, seen in **Figure 3.3.15**, becomes more linear. The slopes differ somewhat with FRITIOF simulations at large ν, but this can be partially accounted for by the same discrepancies that appeared in N_{lightp} probability distributions (**Figure 3.3.11**). These discrepancies distort $\bar{\nu}(N_{lightp})$ curves at high N_{lightp} (**Figure 3.3.12**) and decrease the slopes in **Figure 3.3.15**.

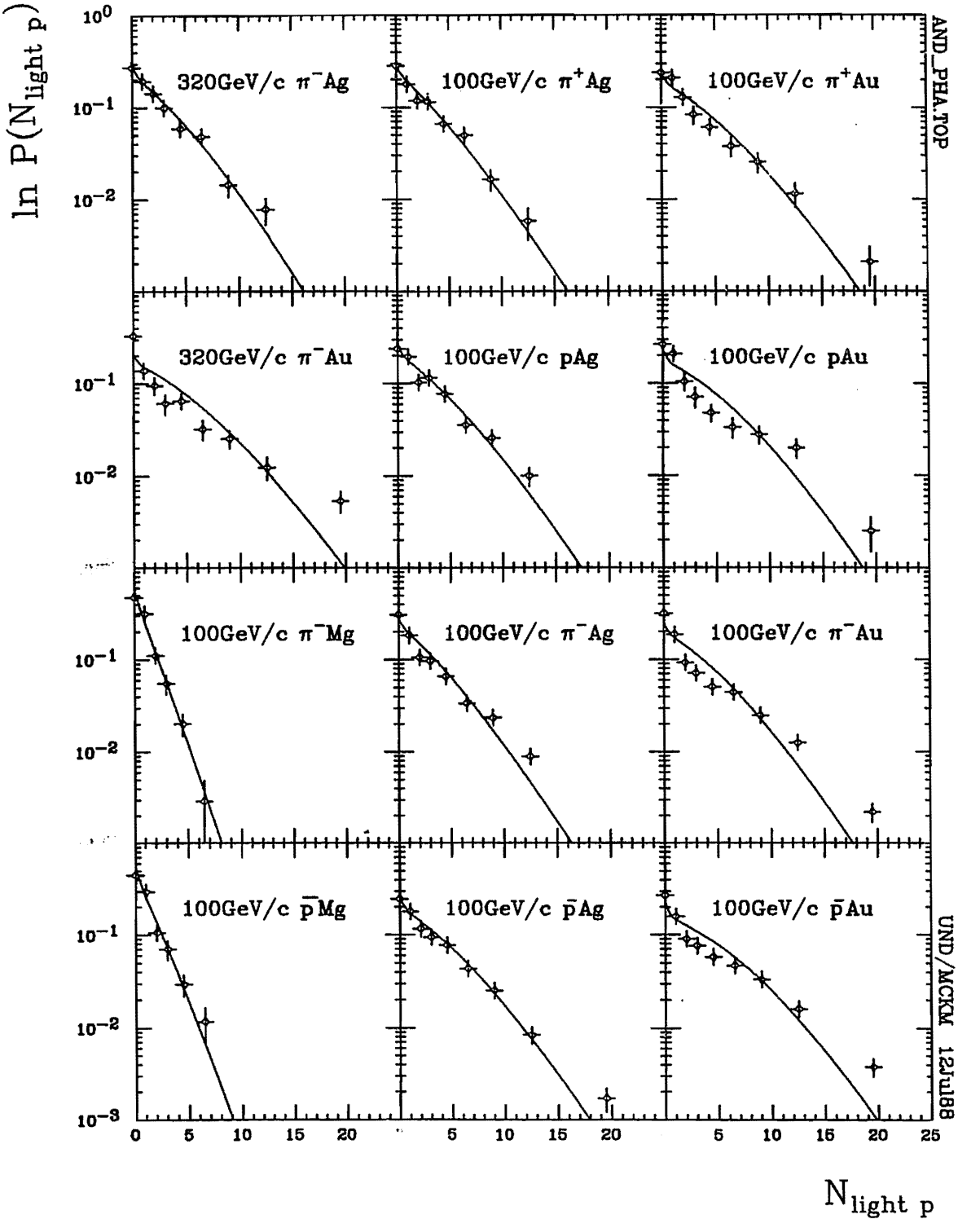

Figure 3.3.11 The probability distribution of *light* proton multiplicity in E597 data overlaid with calculated values according to [Andersson 78] for *light* protons.

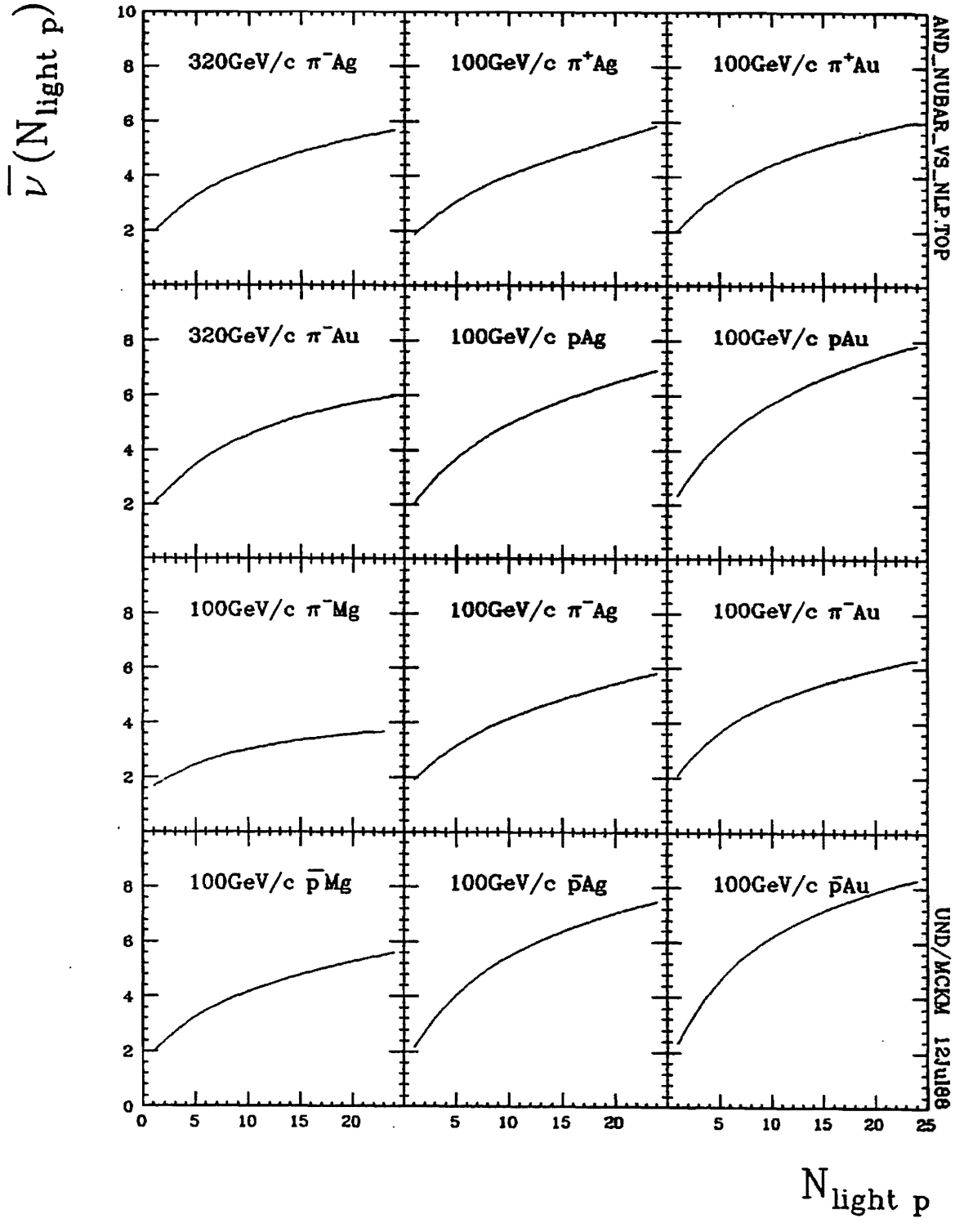

Figure 3.3.12 Average number of collisions for given *light* proton multiplicity calculated according to [Andersson 78] for *light* protons.

Table 3.3.3 Look-up table of $\bar{\nu}_A(N_{lightp})$, the average number of collisions calculated as per [Andersson 78] for *light* proton multiplicities.

Projectile	320GeV/c		100GeV/c									
	π^-	π^-	π^+	π^+	p	p	π^-	π^-	π^-	$\bar{p}$	$\bar{p}$	$\bar{p}$
Target	Ag	Au	Ag	Au	Ag	Au	Mg	Ag	Au	Mg	Ag	Au
BTCode	61	63	131	133	141	143	175	171	173	185	181	183
N_{lightp}	$\nu_A(N_{lightp})$											
1	1.95	2.00	1.86	2.00	2.06	2.31	1.66	1.90	2.09	1.97	2.15	2.31
2	2.36	2.44	2.22	2.42	2.54	2.90	1.91	2.28	2.57	2.37	2.71	2.99
3	2.71	2.82	2.54	2.79	2.97	3.42	2.13	2.61	2.98	2.72	3.22	3.60
4	3.01	3.17	2.83	3.11	3.36	3.87	2.31	2.91	3.34	3.01	3.66	4.14
5	3.27	3.47	3.08	3.40	3.69	4.27	2.47	3.17	3.66	3.26	4.05	4.60
6	3.51	3.73	3.31	3.65	4.00	4.62	2.61	3.40	3.93	3.48	4.40	5.01
7	3.71	3.97	3.52	3.88	4.27	4.93	2.73	3.61	4.17	3.68	4.71	5.36
8	3.90	4.19	3.71	4.08	4.51	5.21	2.84	3.81	4.38	3.86	4.99	5.67
9	4.07	4.38	3.89	4.27	4.74	5.47	2.94	3.99	4.58	4.02	5.24	5.95
10	4.23	4.55	4.05	4.44	4.95	5.70	3.03	4.15	4.75	4.17	5.47	6.20
11	4.37	4.71	4.20	4.59	5.14	5.92	3.10	4.31	4.91	4.31	5.68	6.43
12	4.51	4.86	4.34	4.74	5.32	6.12	3.18	4.46	5.06	4.44	5.87	6.63
13	4.63	4.99	4.48	4.87	5.49	6.31	3.24	4.60	5.20	4.56	6.05	6.83
14	4.75	5.11	4.61	5.00	5.64	6.49	3.30	4.73	5.33	4.67	6.22	7.00
15	4.86	5.23	4.74	5.12	5.80	6.66	3.36	4.86	5.45	4.78	6.38	7.17
16	4.97	5.33	4.87	5.24	5.94	6.82	3.41	4.98	5.57	4.89	6.53	7.33
17	5.07	5.43	4.99	5.35	6.08	6.98	3.46	5.10	5.68	4.99	6.67	7.47
18	5.17	5.52	5.11	5.46	6.21	7.12	3.50	5.22	5.78	5.08	6.80	7.61
19	5.26	5.61	5.23	5.56	6.34	7.26	3.54	5.33	5.88	5.18	6.93	7.74
20	5.35	5.69	5.35	5.66	6.46	7.39	3.58	5.43	5.98	5.27	7.05	7.86
21	5.43	5.76	5.48	5.75	6.58	7.51	3.62	5.53	6.07	5.35	7.17	7.98
22	5.52	5.83	5.60	5.84	6.70	7.63	3.65	5.63	6.16	5.44	7.27	8.09
23	5.60	5.90	5.72	5.93	6.81	7.74	3.69	5.73	6.25	5.52	7.38	8.20
24	5.67	5.96	5.84	6.02	6.92	7.85	3.72	5.82	6.33	5.59	7.48	8.30

NUANDER.TEX UND/MCKM 14Dec87

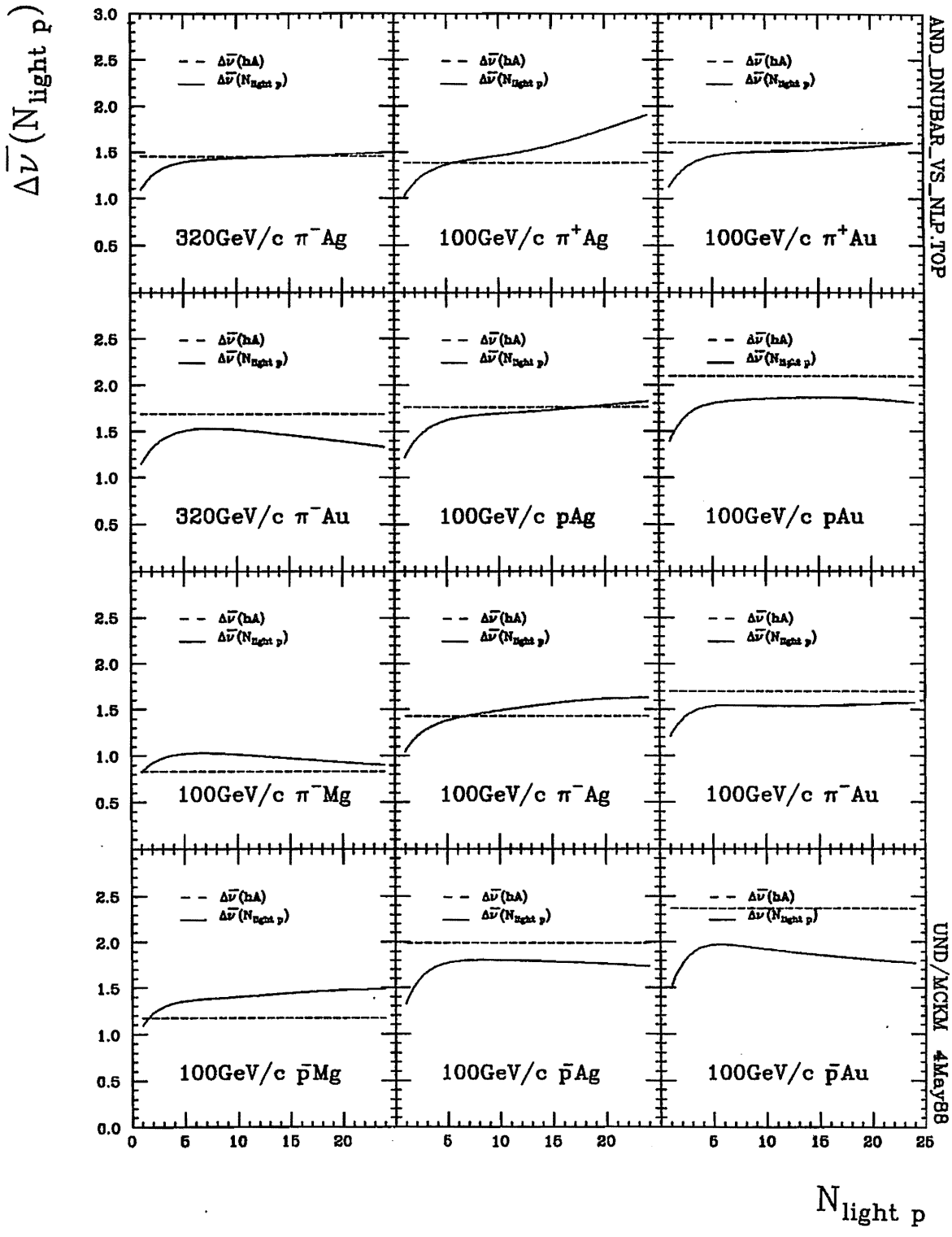

Figure 3.3.13 The dispersion of the average number of collisions $\bar{\nu}$ calculated according to [Andersson 86] *light* protons as a function of *light* proton multiplicity N_{lightp}.

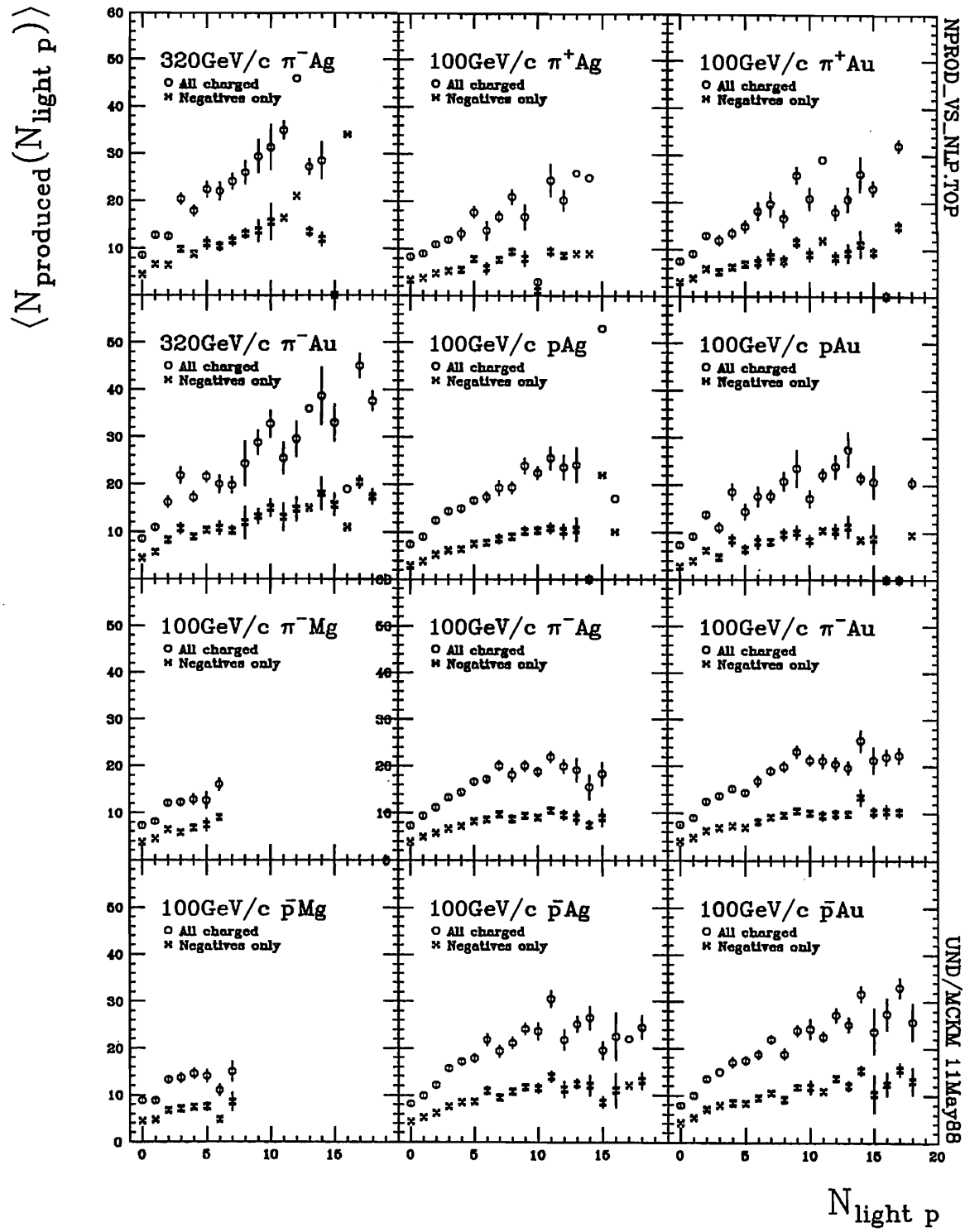

Figure 3.3.14 The average produced particle multiplicity $\langle N_{prod} \rangle$ as a function of *light* proton multiplcity N_{lightp}.

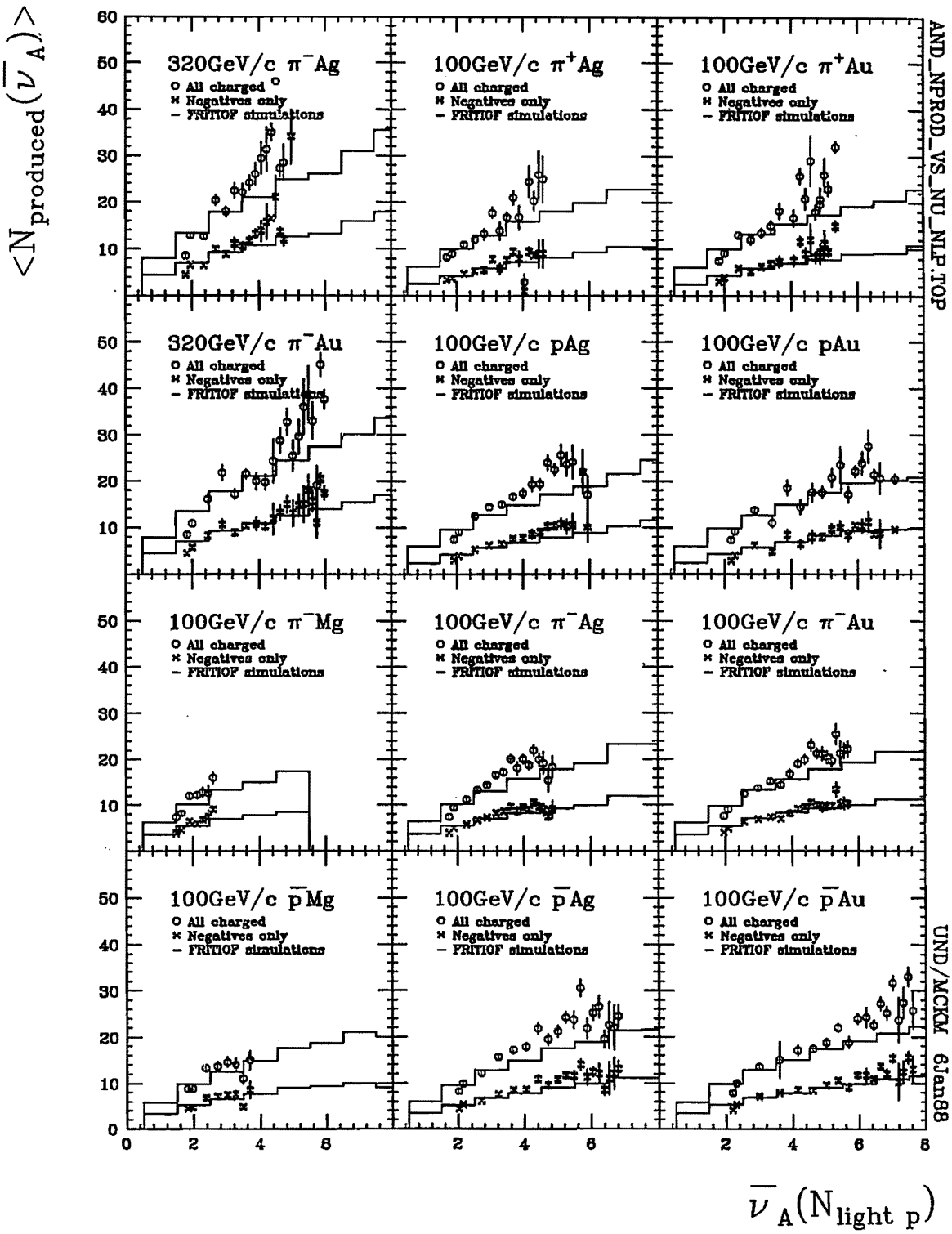

Figure 3.3.15 The average produced particle multiplicity as a function of the average number of collisions calculated according to [Andersson 78] for specific *light* proton multiplicity overlaid with FRITIOF simulated results.

In an effort to improve representations of proton emission, it has been has suggested that the geometrical distribution of grey protons in the Andersson model be replaced with negative binomial distributions (NBD) [Verbeure 83] which would accommodate dispersion characteristics as well as means. The modification is simple, noting that the geometrical distribution corresponds to k=1 in NBD where k is one of the fit parameters. (NBD is discussed in detail in **Section 3.5** and in **Appendix 3A.**) Following this suggestion, the basic probability calculation is modified to

$$P_{\nu}^{V}(N_{lightp}) = \begin{pmatrix} N_{lightp} + k \cdot \nu - 1 \\ N_{lightp} \end{pmatrix} (1-x)^{k \cdot \nu} x^{N_{lightp}}$$

with

$$x = \frac{\frac{<N_{lightp}>A}{\bar{\nu}}}{1 + \frac{<N_{lightp}>A}{\bar{\nu}}}$$

The proton multiplicity distributions are fitted to NBD as shown in **Figure 3.3.16** with the NBD parameters tabulated in **Table 3.3.4.** Essentially all of these fits are adequate. These contrast with NBD fits with fixed k=1 (implied in the Andersson approach) shown **Figure 3.3.17** with NBD parameters tabulated in **Table 3.3.5.** While some of the fits are adequate, others are rather poor. In most cases, the k=1 fits are associated with slightly depressed m values. Subsequently, an analysis sequence was conducted parallel to that used in conjunction with Andersson model. Similar distributions of N_{lightp} probabilities as functions of ν appear in **Figure 3.3.18**); overall N_{lightp} probability in **Figure 3.3.19**); $\bar{\nu}(N_{lightp})$ in **Figure 3.3.20**) with an associated look-up in **Table 3.3.6**; and a display of produced particle multiplicity as a function of $\bar{\nu}_V$ (**Figure 3.3.21**). A comparison of **Figures 3.3.19** with **3.3.11** shows that the NBD approach slightly improves the agreement between model and experimental values at high proton multiplicities although significant systematic differences between model and experimental values are still evident for larger A. But agreement with FRITIOF in **Figure 3.3.21** is worse. This lack of agreement could reflect problems in FRITIOF itself as well as a problem in the Andersson model.

It is supposed that products from secondary interactions (*e.g. cascading*) are mixed with products from primary ones. It is further supposed that when cascading

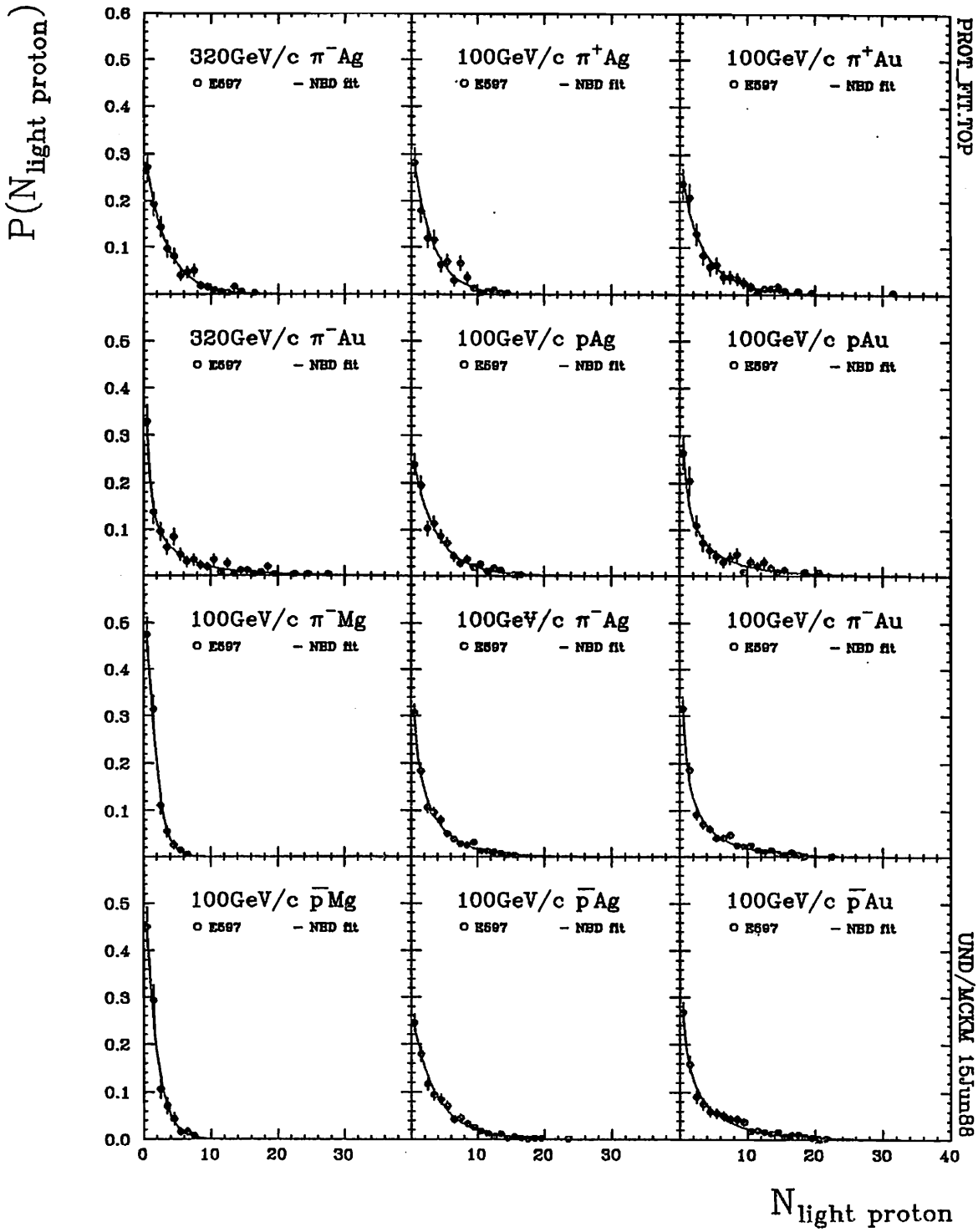

Figure 3.3.16 *Light* proton multiplicities fit to a NBD.

Table 3.3.4 NBD parameters m and k fit to *light* proton multiplicity distributions.

Projectile	320GeV/c		100GeV/c									
	π^-	π^-	π^+	π^+	p	p	π^-	π^-	π^-	p	p	p
Target	Ag	Au	Ag	Au	Ag	Au	Mg	Ag	Au	Mg	Ag	Au
N_{events}	321	262	302	240	177	239	344	1010	860	256	715	557
$\langle N_{grcyp} \rangle$	2.24	3.26	2.33	2.88	2.60	3.05	.69	2.34	2.72	.91	2.71	3.37
$\Delta\langle N_{grcyp} \rangle$	.09	.12	.10	.12	.08	.12	.05	.05	.06	.07	.07	.08
m	2.16	3.87	2.15	2.99	2.66	3.32	.68	2.15	2.66	.82	2.63	3.11
Δm	.14	.46	.16	.24	.13	.33	.05	.09	.12	.08	.10	.17
k	.87	.12	.92	.74	.96	.55	1.15	.72	.56	1.27	.89	.68
Δk	.15	.08	.15	.13	.12	.10	.49	.07	.05	.42	.09	.08
χ^2	10.82	9.08	6.85	4.56	12.81	10.80	2.94	19.56	32.73	9.34	21.17	16.30
NDF	12	19	11	16	12	16	1	12	17	6	16	18
$\langle N_{lightp} \rangle$	2.75	3.87	2.73	3.47	3.13	3.66	.91	2.89	3.25	1.11	3.30	3.99
$\Delta\langle N_{lightp} \rangle$	.17	.31	.17	.28	.15	.29	.06	.10	.14	.09	.11	.19
m	2.67	1.96	2.56	3.31	3.27	1.12	.92	3.07	3.18	1.16	3.29	1.28
Δm	.15	.03	.15	.25	.16	.50	.06	.13	.16	.10	.12	.23
k	.96	.18	.96	.84	.95	.58	1.57	.71	.58	1.01	.91	.66
Δk	.15	.09	.15	.14	.11	.10	.15	.06	.05	.27	.09	.07
χ^2	9.66	17.74	19.66	13.29	15.32	16.93	3.63	12.19	26.52	4.72	12.75	15.55
NDF	11	21	13	17	11	16	5	11	18	6	19	20

P_MULT_FITNEGBIN.TAB UND/MCKM 19Jul88

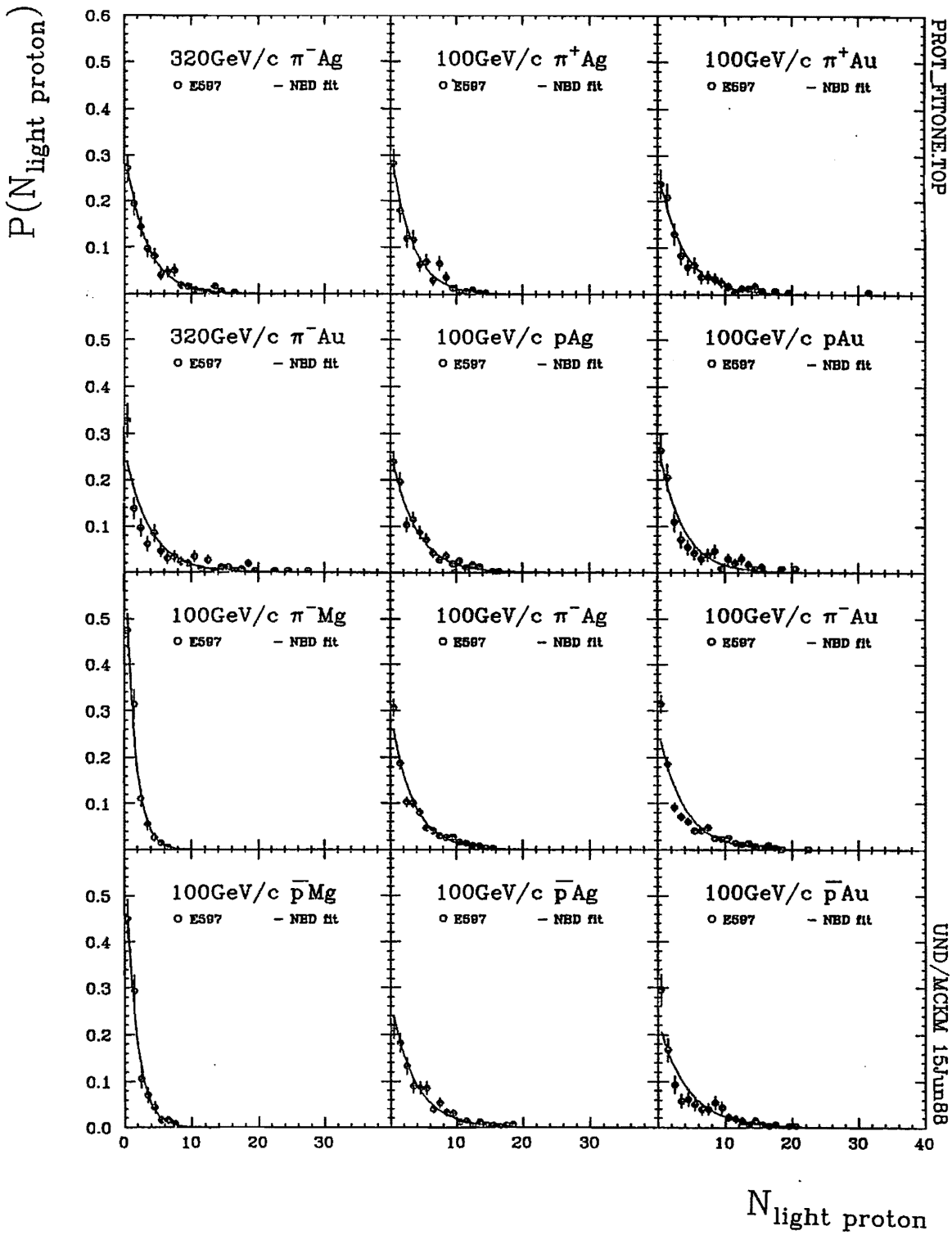

Figure 3.3.17 *Light* proton multiplicities fit to a NBD with k=1.

Table 3.3.5 NBD parameters m fit to *light* proton multiplicity distributions when k=1.

Projectile	320GeV/c		100GeV/c									
	π^-	π^-	π^+	π^+	p	p	π^-	π^-	π^-	p	p	p
Target	Ag	Au	Ag	Au	Ag	Au	Mg	Ag	Au	Mg	Ag	Au
N_{events}	321	202	302	240	477	239	344	1010	660	256	715	557
$\langle N_{lightp} \rangle$	2.75	3.87	2.73	3.47	3.13	3.66	.91	2.89	3.25	1.11	3.30	3.99
$\Delta\langle Nlightp \rangle$	.17	.31	.17	.28	.15	.29	.06	.10	.14	.09	.14	.19
m	2.66	3.24	2.67	3.19	3.27	3.04	.96	2.91	3.24	1.11	3.28	4.20
Δm	.15	.21	.05	.22	.16	.23	.07	.10	.12	.10	.11	.18
χ^2	9.73	44.54	20.18	14.55	15.58	32.10	6.26	33.32	83.85	4.71	13.32	38.37
NDF	15	22	14	18	15	19	6	15	19	7	20	21

P_MULT_FITNEGBINONE.TAB UND/MCKM 10Jul88

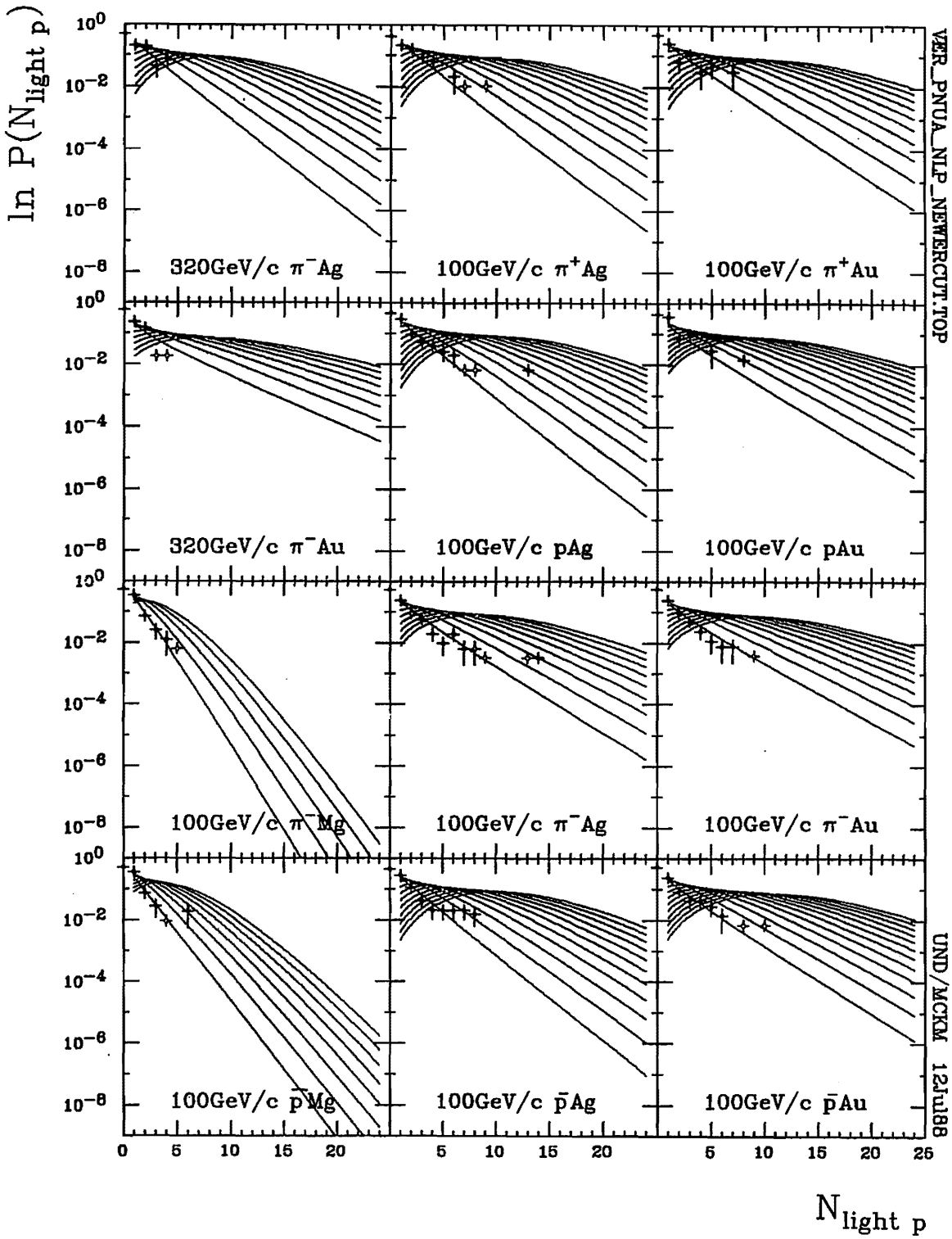

Figure 3.3.18 Probability distributions of *light* proton multiplicities for given numbers of collisions calculated according to [Verbeure 83] with modifications for *light* protons and results for data enriched for $\nu = 1$. Curves are ordered in ν as in **Figure 3.3.10** with the lowest curve associated with $\nu = 1$.

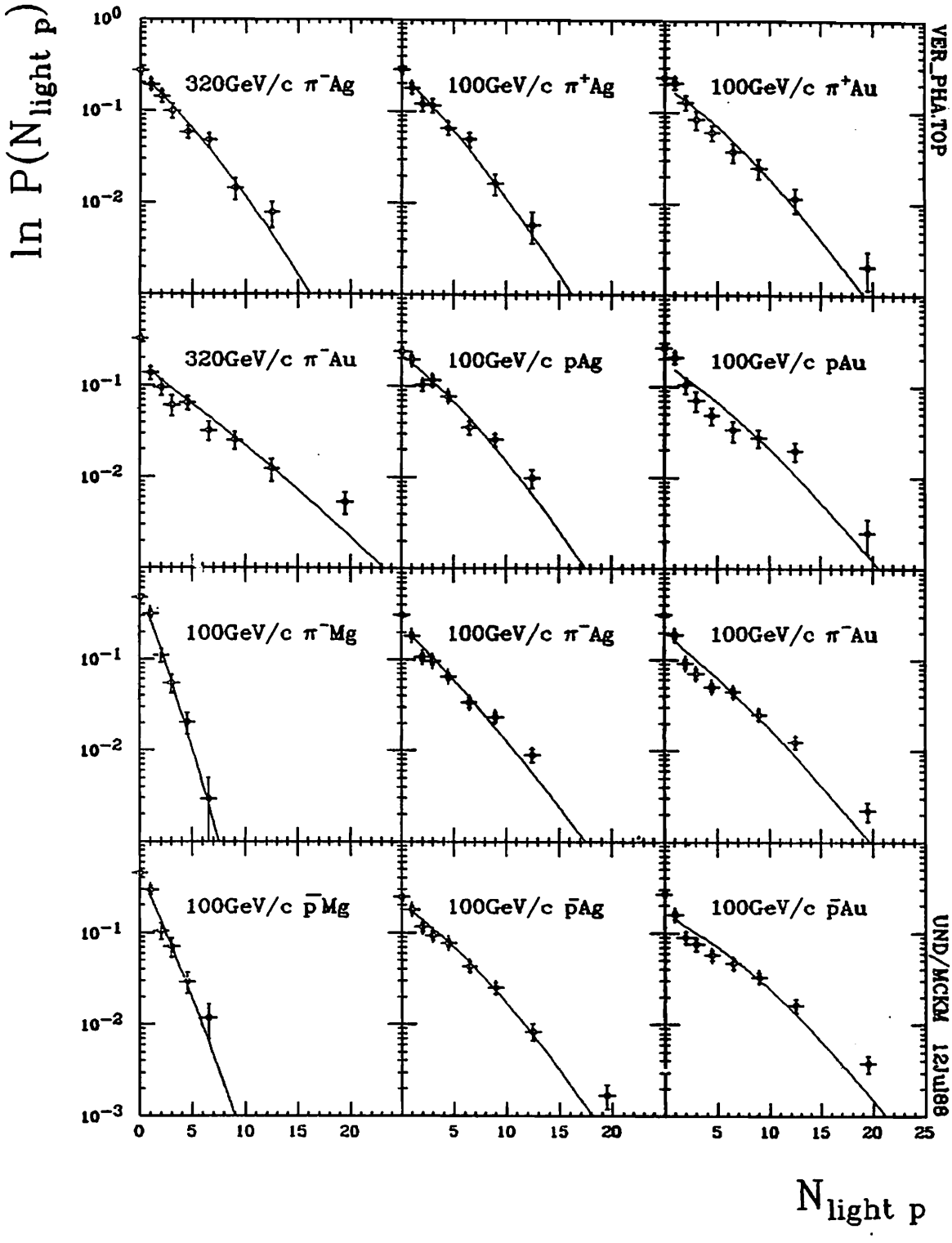

Figure 3.3.19 The probability distribution of *light* proton multiplicity in E597 data overlaid with calculated values according to [Verbeure 83] for *light* protons.

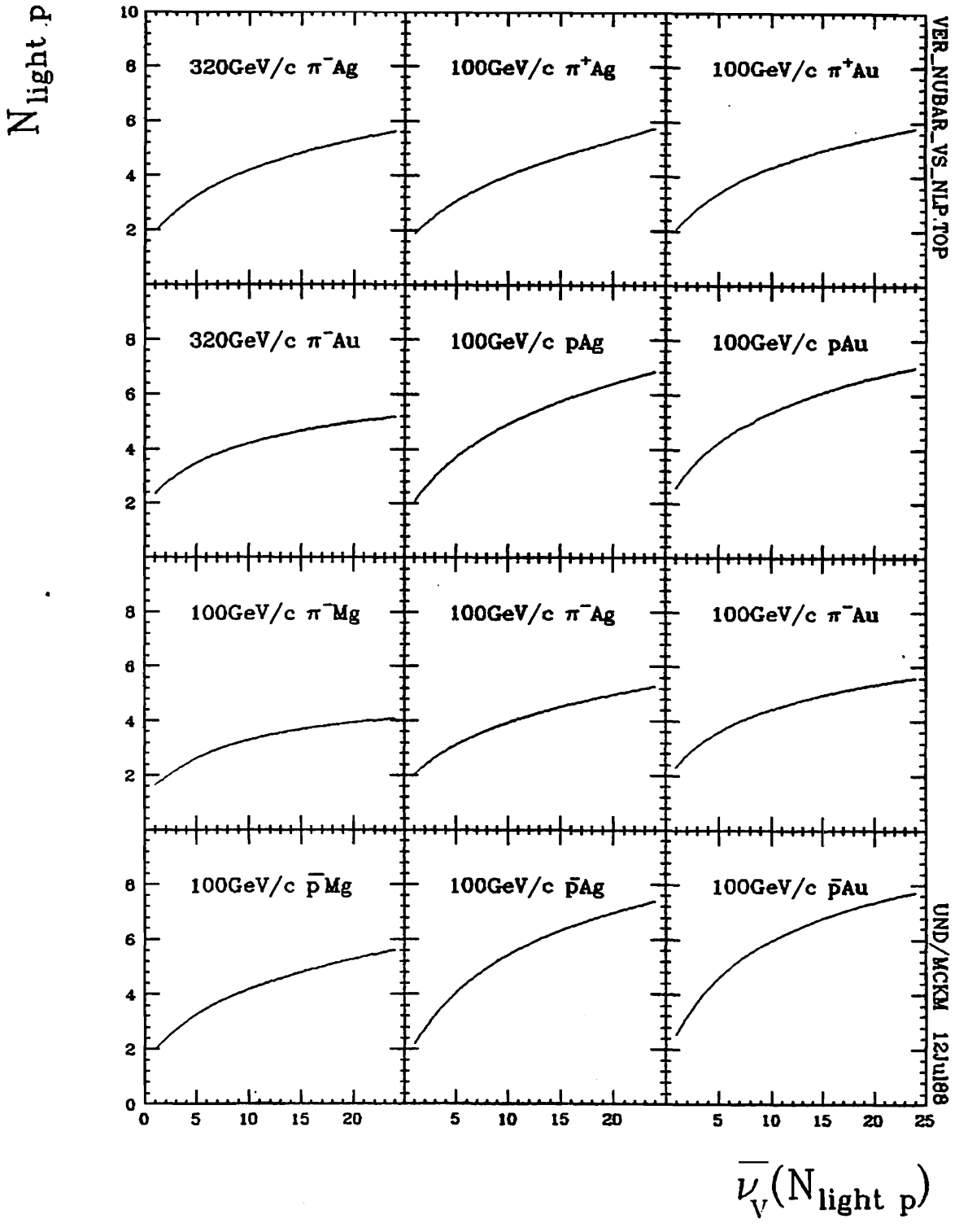

Figure 3.3.20 The average number of collisions calculated as per [Verbeure 83] as a function of *light* proton multiplicity N_{lightp}.

Table 3.3.6 Look-up table of $\bar{\nu}_V(N_{lightp})$ calculated as per [Verbeure 83] for *light* proton multiplicities..

Projectile	320GeV/c		100GeV/c									
	π^-	π^-	π^+	π^+	p	p	π^-	π^-	π^-	$\bar{p}$	$\bar{p}$	$\bar{p}$
Target	Ag	Au	Ag	Au	Ag	Au	Mg	Ag	Au	Mg	Ag	Au
BTCode	61	63	131	133	141	143	175	171	173	185	181	183
N_{lightp}	$\nu_V(N_{lightp})$											
1	1.97	2.32	1.87	2.06	2.08	2.57	1.63	1.99	2.30	1.97	2.18	2.54
2	2.37	2.71	2.23	2.47	2.56	3.12	1.92	2.35	2.74	2.37	2.73	3.19
3	2.71	3.01	2.55	2.82	2.98	3.56	2.18	2.65	3.08	2.72	3.23	3.74
4	3.01	3.26	2.83	3.12	3.36	3.93	2.42	2.90	3.36	3.01	3.66	4.20
5	3.27	3.47	3.08	3.39	3.69	4.24	2.62	3.12	3.61	3.27	4.05	4.60
6	3.49	3.65	3.30	3.62	3.98	4.52	2.79	3.32	3.81	3.49	4.39	4.94
7	3.70	3.81	3.51	3.83	4.25	4.76	2.94	3.49	4.00	3.69	4.69	5.24
8	3.88	3.95	3.69	4.02	4.49	4.93	3.08	3.65	4.16	3.86	4.96	5.51
9	4.05	4.08	3.86	4.19	4.71	5.18	3.19	3.80	4.31	4.03	5.20	5.74
10	4.20	4.20	4.02	4.34	4.91	5.37	3.30	3.94	4.44	4.18	5.43	5.96
11	4.34	4.30	4.17	4.49	5.10	5.54	3.39	4.07	4.56	4.31	5.63	6.15
12	4.48	4.40	4.31	4.62	5.28	5.69	3.48	4.19	4.67	4.44	5.82	6.33
13	4.60	4.49	4.45	4.74	5.44	5.84	3.55	4.30	4.78	4.57	6.00	6.49
14	4.72	4.57	4.58	4.86	5.59	5.97	3.62	4.41	4.87	4.68	6.16	6.64
15	4.82	4.65	4.70	4.97	5.74	6.10	3.69	4.51	4.97	4.79	6.32	6.78
16	4.93	4.72	4.82	5.08	5.88	6.22	3.74	4.61	5.05	4.90	6.46	6.91
17	5.03	4.79	4.94	5.18	6.02	6.34	3.80	4.71	5.13	5.00	6.60	7.04
18	5.12	4.85	5.06	5.27	6.15	6.45	3.85	4.80	5.21	5.10	6.73	7.15
19	5.21	4.92	5.18	5.37	6.27	6.55	3.89	4.88	5.28	5.19	6.85	7.26
20	5.30	4.97	5.29	5.45	6.39	6.65	3.94	4.97	5.35	5.28	6.97	7.36
21	5.38	5.03	5.41	5.54	6.50	6.74	3.98	5.05	5.42	5.37	7.08	7.46
22	5.46	5.08	5.53	5.62	6.62	6.83	4.02	5.13	5.48	5.45	7.19	7.56
23	5.54	5.13	5.64	5.70	6.73	6.92	4.05	5.20	5.55	5.53	7.29	7.65
24	5.62	5.17	5.76	5.78	6.83	7.00	4.09	5.28	5.61	5.61	7.39	7.73

NUVER.TEX UND/MCKM 13Jul88

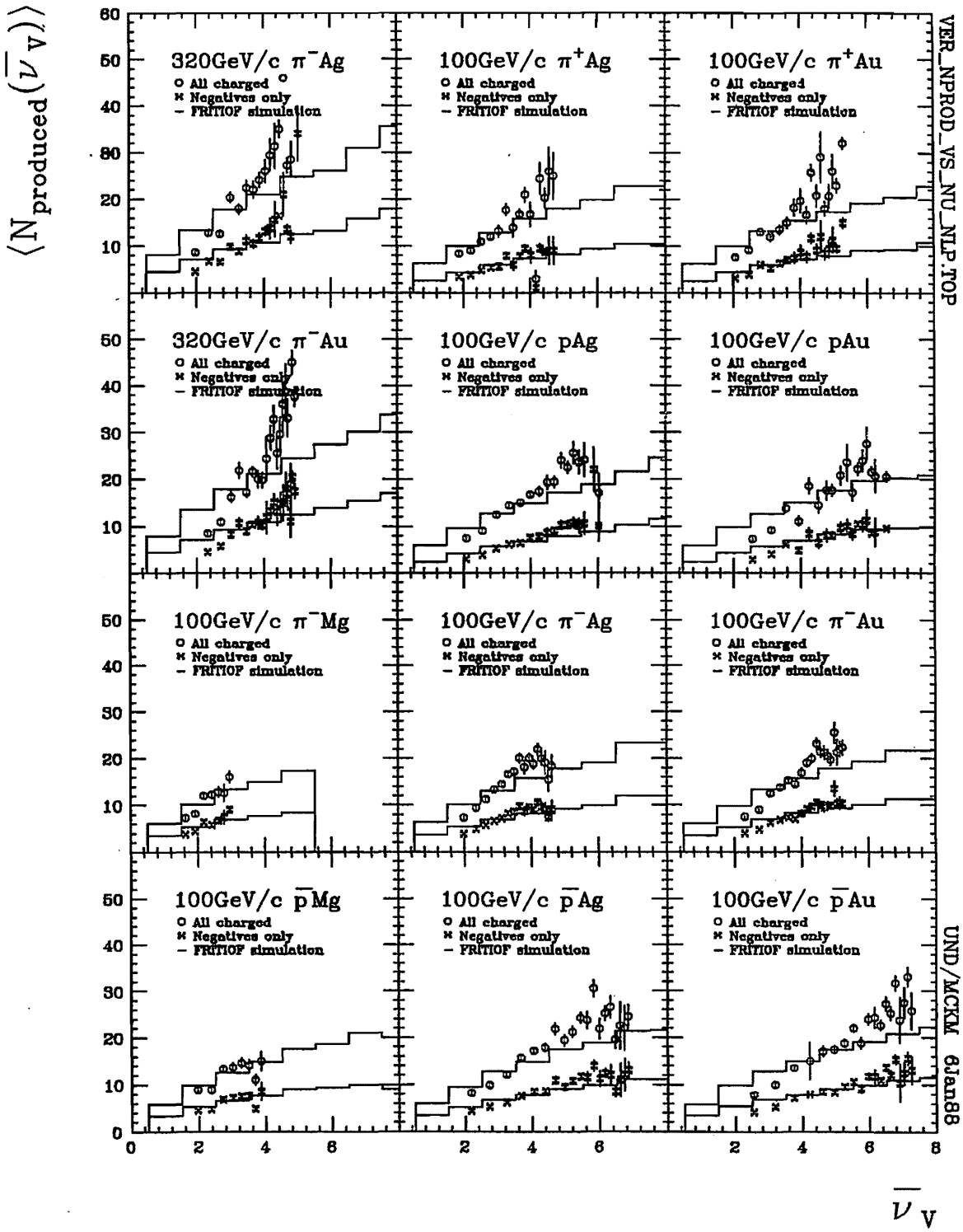

Figure 3.3.21 The average produced particle multiplicity as a function of the average number of collisions for specific *light* proton multiplicity calculated according to [Verbeure 83] for *light* protons overlaid with FRITIOF results.

occurs, the numbers of secondary collisions are related to the primary collisions by a power law. The feasibility of this picture was already shown in the discussion of **Figure 3.1.2.** The number of secondary collisions ν_k, representing the *small scale* cascading component of $\bar{\nu}_{excess}$, can thus be estimated by subtracting the number of primary collisions from the total number of collisions. The number of primary collisions can be given by $\bar{\nu}(hA)$ and the total number of collisions by $\bar{\nu}_{excess}$, but a larger range of primary collisions can be studied by restricting both $\bar{\nu}(hA)$ and $\bar{\nu}_{excess}$ to a specific rather than average light proton multiplicity. The number of primary collisions as a function of light proton multiplicity is estimated by $\bar{\nu}_A$. The number of secondary collisions ν_k expected as a result of specific numbers of primary collisions clearly points to a power law, as seen in the log-log plot of **Figure 3.3.22.** Since secondary collisions do not occur in the absence of primary ones, it is expected that $\nu_k = 1$ occur at $\bar{\nu}_A = 1$. If the lowest values of $\bar{\nu}_A$ are excluded, the other points do connect with each other and with $(\bar{\nu}_A, \nu_k)$ =(1,1) in a reasonably linear fashion. Excluding $\bar{\nu}_A \sim 2$ is justified since it corresponds to $N_{lightp} = 1$ and thus underrepresents $\nu = 1$.

The slopes in **Figure 3.3.22** are roughly 2 for all the interactions. The A-independence is expected for cascading, which should not be particularly interaction dependent if the cascades are formed in regions larger than the differences between nuclear radii. These slopes generally agree with similar estimates based on pXe, pAr, and pNe data at 200 GeV/c [De Marzo 82].

3.4 $\bar{\nu}_L(N_{lightp})$

A much simpler approach produces more linear relations between N_{prod} and ν and better alignment with FRITIOF results. This approach presumes a relation between $\bar{\nu}$ and the square root of the number of protons with $\beta < .848$ [Ledoux 86]:

$$\bar{\nu}(N_p) = C_A\sqrt{N_p}$$

with C_A such that

$$< \bar{\nu}(N_p) >= \bar{\nu}$$

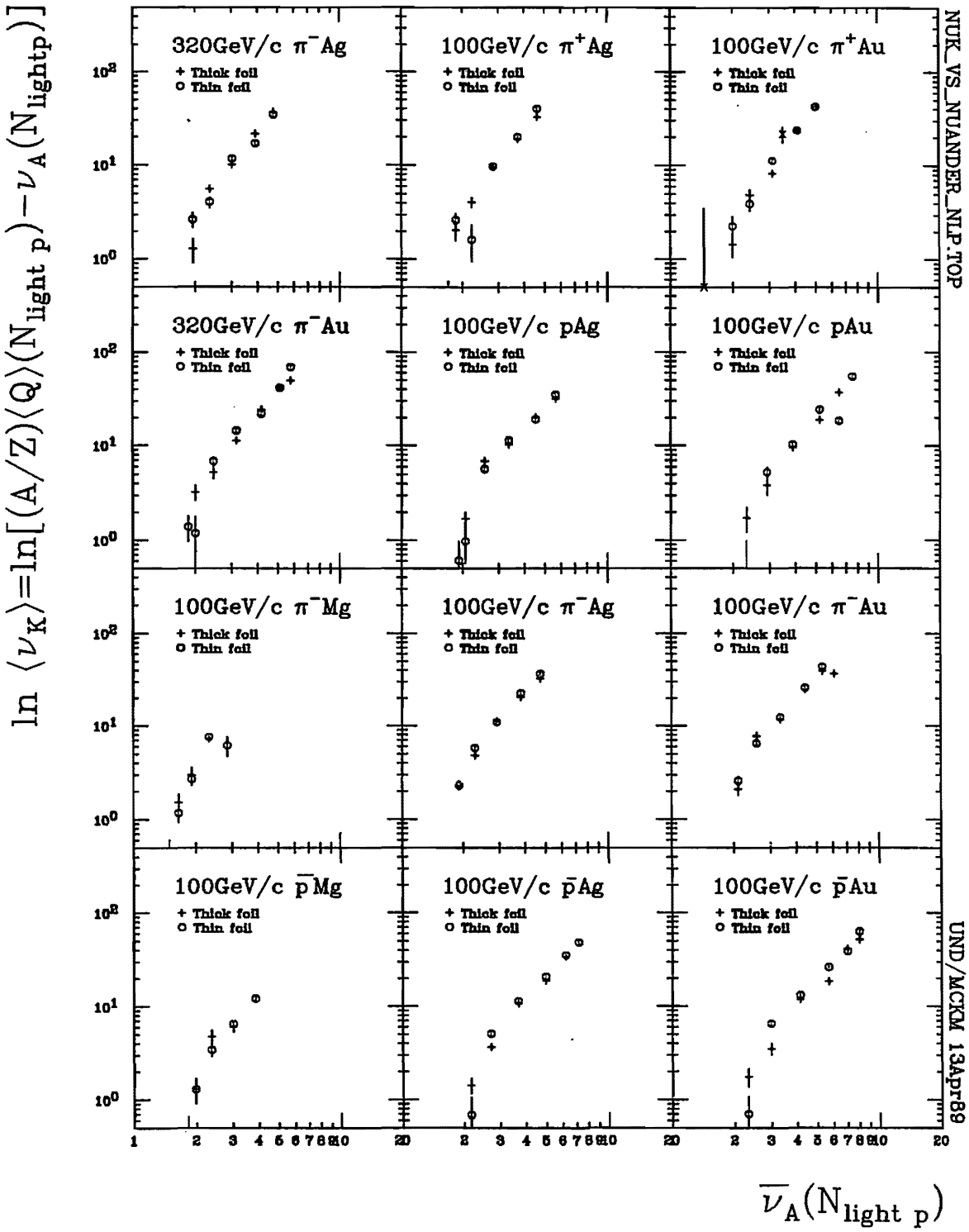

Figure 3.3.22 $\bar{\nu}_K(N_{lightp})$ as a function of Andersson model estimates $\nu_A(N_{lightp})$.

Since *light* protons were used as a measure of ν, *light* protons will be used exclusively so that

$$\bar{\nu}(N_{lightp}) = C_A\sqrt{N_{lightp}}$$

with C_A such that

$$< \bar{\nu}(N_{lightp}) >= \bar{\nu}$$

The trivial distribution of $\bar{\nu}(N_{lightp})$ is shown in **Figure 3.4.1** for reference and values of C_A for *light* protons are listed in the look-up table for $\bar{\nu}(N_{lightp})$ **Table 3.4.1.**

This approach brings about some improvements to the results achieved using the previous Andersson and Verbeure approaches. Average produced multiplicity as a function of $\bar{\nu}_L$ is plotted in **Figure 3.4.2.** It is clearly more linear than it was in the Andersson and Verbeure model results. FRITIOF is also more closely represented. Plotted as a function of $\bar{\nu}_L$ in **Figure 3.4.3**, ν_k calculated on the basis of $\bar{\nu}_L$ is also more linear than it was on the basis of $\bar{\nu}_A$. The points near $\bar{\nu}_L$ = 2 line up much better, suggesting that this simpler approach better describes the peripheral interactions. The slopes themselves, with values of approximately 1.5 for all interactions, are somewhat reduced from those from the $\bar{\nu}_A$-based analysis.

3.5 NEGATIVE BINOMIAL DESCRIPTIONS

While the number of primary and secondary collisions in multiple production interactions can be estimated on the basis of proton production, the dynamic(s) governing the single collision and the emission of single particles can be probed by the statistical analysis of produced particle multiplicities. If collisions are responsible for the independent emission of single particles, produced particle multiplicities will be distributed according to Poisson functions. Deviations from Poisson distributions thus signal correlations between emitted particles and reveal some aspects of the fundamental nature of collisions. If particles are emitted in clusters, the shape of the distribution will directly reflect their size and number.

A number of functions have been used to describe multiplicity distributions, but the negative binomial distribution (NBD) has been used most widely, successfully

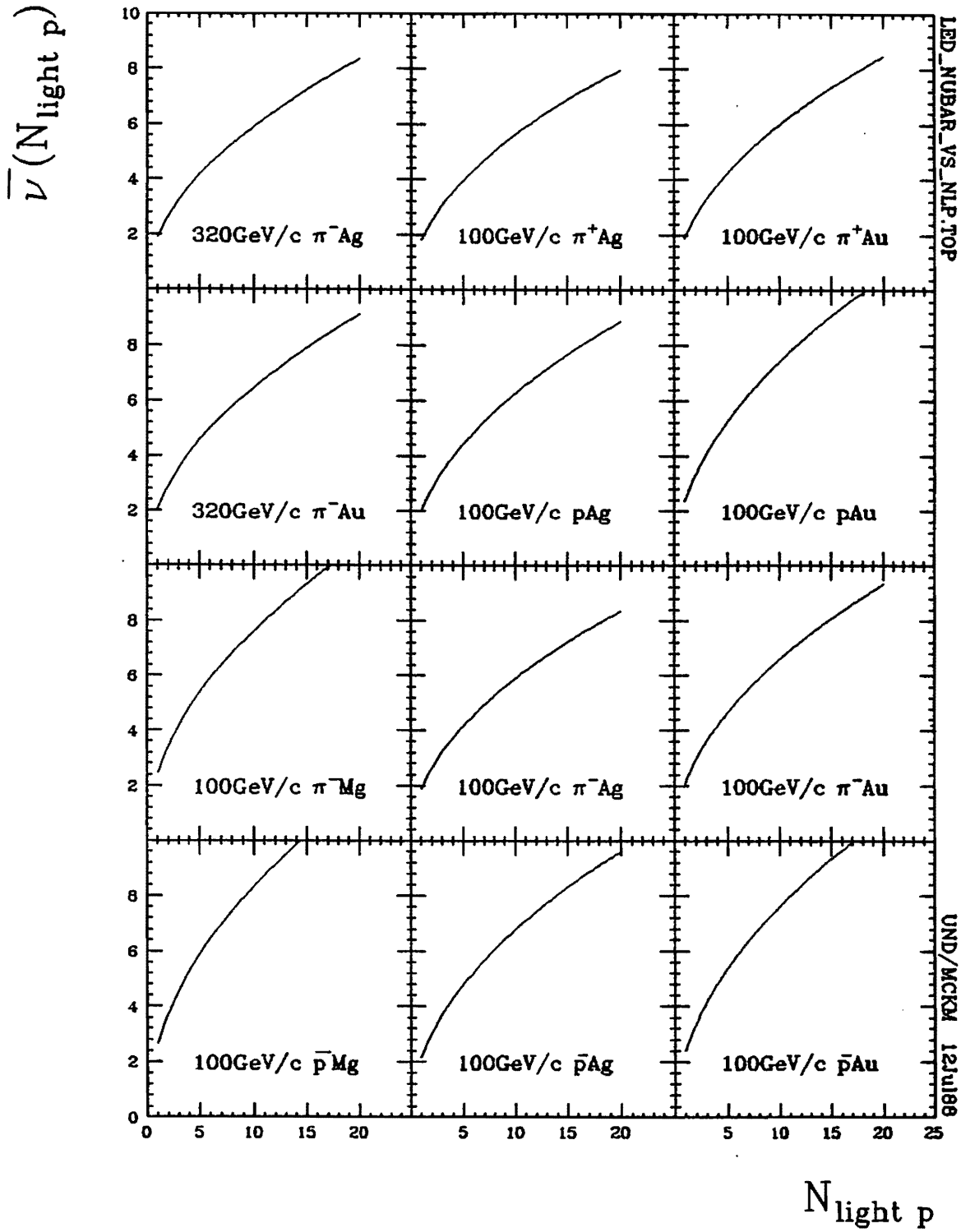

Figure 3.4.1 A reference plot of $\bar{\nu}_L$, the average number of collisions calculated as per [Ledoux 86], as a function of *light* proton multiplicity N_{lightp}.

Table 3.4.1 Look-up table of $\bar{\nu}_L(N_{lightp})$ calculated as per [Ledoux 86] for *light* proton multiplicities.

Projectile	320GeV/c		100GeV/c									
	π^-	π^-	π^+	π^+	p	p	π^-	π^-	π^-	$\bar{p}$	$\bar{p}$	p
Target	Ag	Au	Ag	Au	Ag	Au	Mg	Ag	Au	Mg	Ag	Au
ν (hA)	2.45	2.88	2.33	2.74	2.84	3.43	1.60	2.41	2.84	1.96	3.11	3.74
$C_{h,d}$	1.86	2.04	1.78	1.89	1.98	2.35	2.41	1.87	2.09	2.64	2.15	2.41
N_{lightp}	$\nu_L(N_{lightp})$											
1	1.86	2.04	1.78	1.89	1.98	2.35	2.41	1.87	2.09	2.64	2.15	2.41
2	2.64	2.88	2.51	2.68	2.80	3.32	3.40	2.64	2.95	3.73	3.04	3.41
3	3.23	3.53	3.08	3.28	3.43	4.06	4.17	3.23	3.62	4.56	3.72	4.18
4	3.73	4.08	3.55	3.78	3.96	4.69	4.81	3.73	4.17	5.27	4.30	4.83
5	4.17	4.56	3.97	4.23	4.43	5.24	5.38	4.17	4.67	5.89	4.80	5.40
6	4.57	4.99	4.35	4.63	4.85	5.74	5.89	4.57	5.11	6.46	5.26	5.91
7	4.93	5.39	4.70	5.01	5.24	6.20	6.37	4.94	5.52	6.97	5.68	6.38
8	5.27	5.77	5.02	5.35	5.60	6.63	6.81	5.28	5.90	7.45	6.08	6.83
9	5.59	6.11	5.33	5.68	5.94	7.04	7.22	5.60	6.26	7.91	6.44	7.24
10	5.89	6.45	5.62	5.98	6.26	7.42	7.61	5.90	6.60	8.33	6.79	7.63
11	6.18	6.76	5.89	6.28	6.57	7.78	7.98	6.19	6.92	8.74	7.12	8.00
12	6.46	7.06	6.15	6.55	6.86	8.12	8.34	6.47	7.23	9.13	7.44	8.36
13	6.72	7.35	6.41	6.82	7.14	8.46	8.68	6.73	7.53	9.50	7.75	8.70
14	6.97	7.63	6.65	7.08	7.41	8.77	9.00	6.99	7.81	9.86	8.04	9.03
15	7.22	7.89	6.88	7.33	7.67	9.08	9.32	7.23	8.08	10.21	8.32	9.35
16	7.46	8.15	7.11	7.57	7.92	9.38	9.63	7.47	8.35	10.54	8.59	9.65
17	7.68	8.40	7.32	7.80	8.16	9.67	9.92	7.70	8.61	10.87	8.86	9.95
18	7.91	8.65	7.54	8.03	8.40	9.95	10.21	7.92	8.86	11.18	9.11	10.24
19	8.12	8.88	7.74	8.25	8.63	10.22	10.49	8.14	9.10	11.49	9.36	10.52
20	8.34	9.12	7.94	8.46	8.86	10.49	10.76	8.35	9.34	11.79	9.61	10.79

NULEDOUX.TEX UND/MCKM 14Dec87

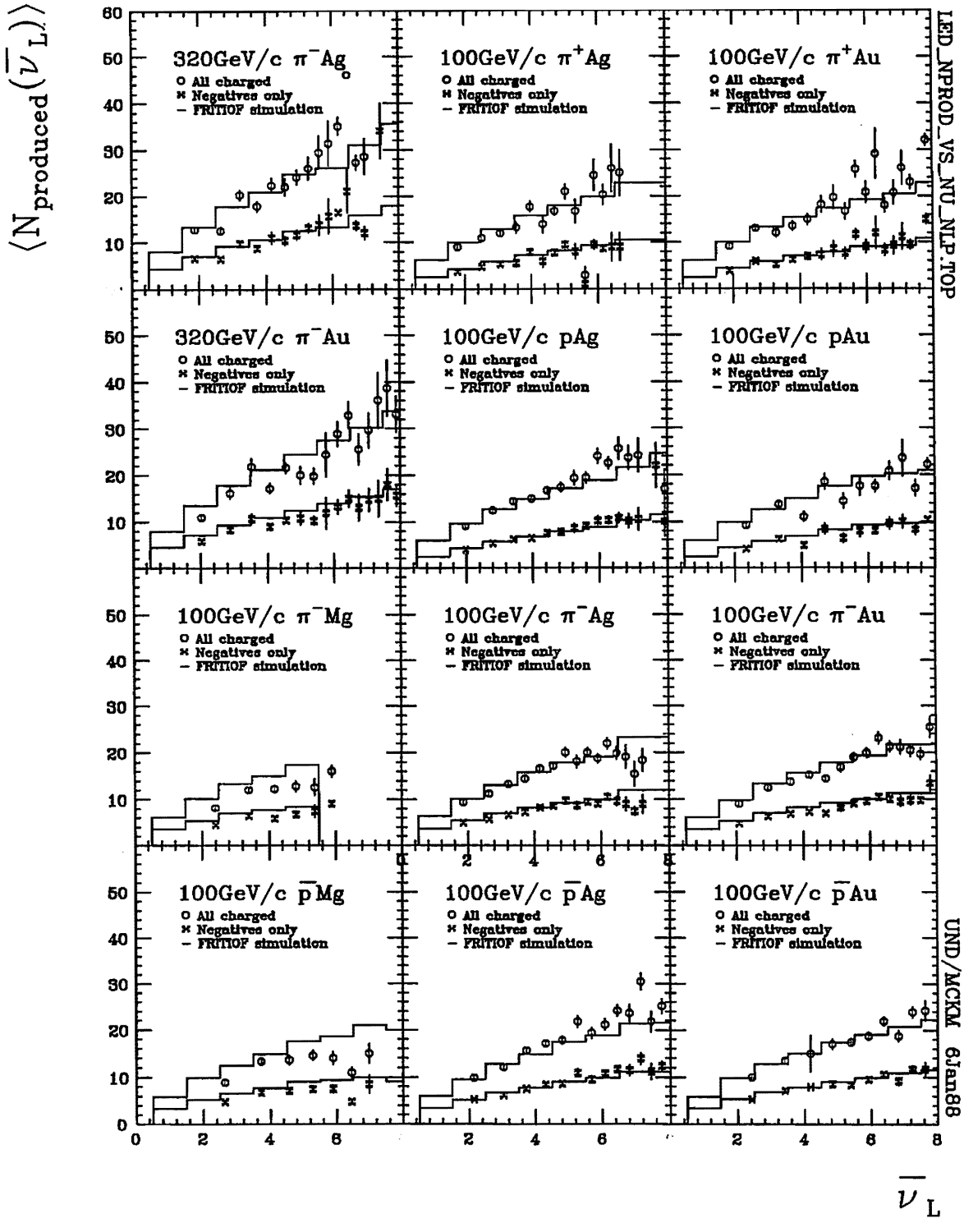

Figure 3.4.2 The average produced particle multiplicity as a function of the number of collisions calculated according to [Ledoux 86] for *light* protons for E597 data (points) and FRITIOF simulations (lines). The upper curves are for all produced particles, the lower for negative produced particles only.

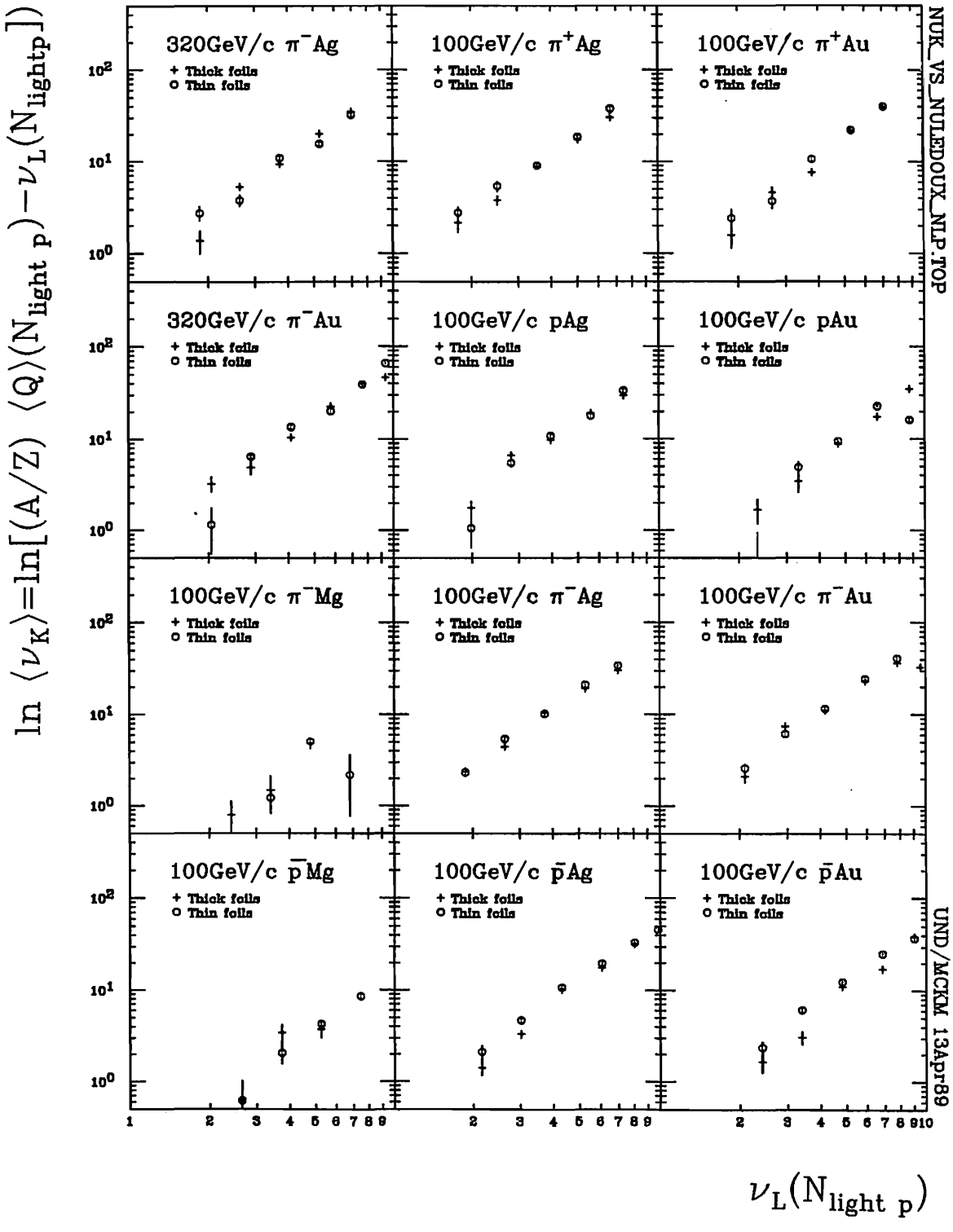

Figure 3.4.3 $\bar{\nu}_K(N_{lightp})$ as a function of Ledoux model estimates $\nu_L(N_{lightp})$.

describing 1) proton as well as produced particle multiplicities, 2) limited as well as full phase space, and 3) e^+e^- [Derrick 86] as well as hh [Alner 85, Adamus 86], and hA [Adamus 88a]. The fact that it is naturally related to the Poisson distribution makes it particularly attractive and a logical choice. To set the context for the conclusions drawn from NBD fits, some basics are reviewed in Appendix 3A.

NBD fits can be employed for parameterization purposes alone, but the notion that they are also associated with physical implications is attractive. **Figure 3.5.1** shows how well two-parameter NBD fits describe *produced* particle multiplicities, *i.e.* secondaries exclusive of protons and electrons, in full phase space and in limited regions of phase space. Fourteen(14) such regions are investigated, nested about the hp center-of-mass rapidities (2.68 and 3.26 units rapidity respectively for 100 and 320 GeV/c interactions) and ranging in half-width from .25 to 3.5 units rapidity. As expected, the rapidity distributions for charged produced particles, shown in **Figure 3.5.2** are peaked somewhat backward of the hp cms rapidity (further evidence for ν greater than 1) and contrast sharply with proton rapidity distributions, **Figure 3.5.3**, centered at roughly .5 units of rapidity. **Table 3.5.1** gives the NBD parameter m (associated with the mean) for charged produced particles; **Table 3.5.2** gives the NBD parameter k (associated with the distribution shape or width), while **Table 3.5.3** gives the χ^2 number of degrees of freedom for the fits. The NBD fit parameters m closely parallel average produced particle multiplicities $\langle N_{prod} \rangle$ in all regions represented in **Figure 3.5.4**. The fit parameters k describe the spread of the distribution. **Figure 3.5.5** shows how they increase as the distributions widen and how k increases faster with y_{cut} for the lighter nuclei than for the heavier nuclei. This is in general agreement with results comparing pAr and pXe interactions at 200 GeV/c [Dengler 86] except for the fact that the pXe slope actually becomes negative. While not in agreement with the pXe data, however, this study's pAg results are in general agreement with Fialkowski's simple multiple collision model predictions with its smaller but still positive slope [Fialkowski 86b]. The k intercept values are understandably smaller for the higher energies.

In the partial stimulated emission (PSE) interpretation of NBD, k inverse

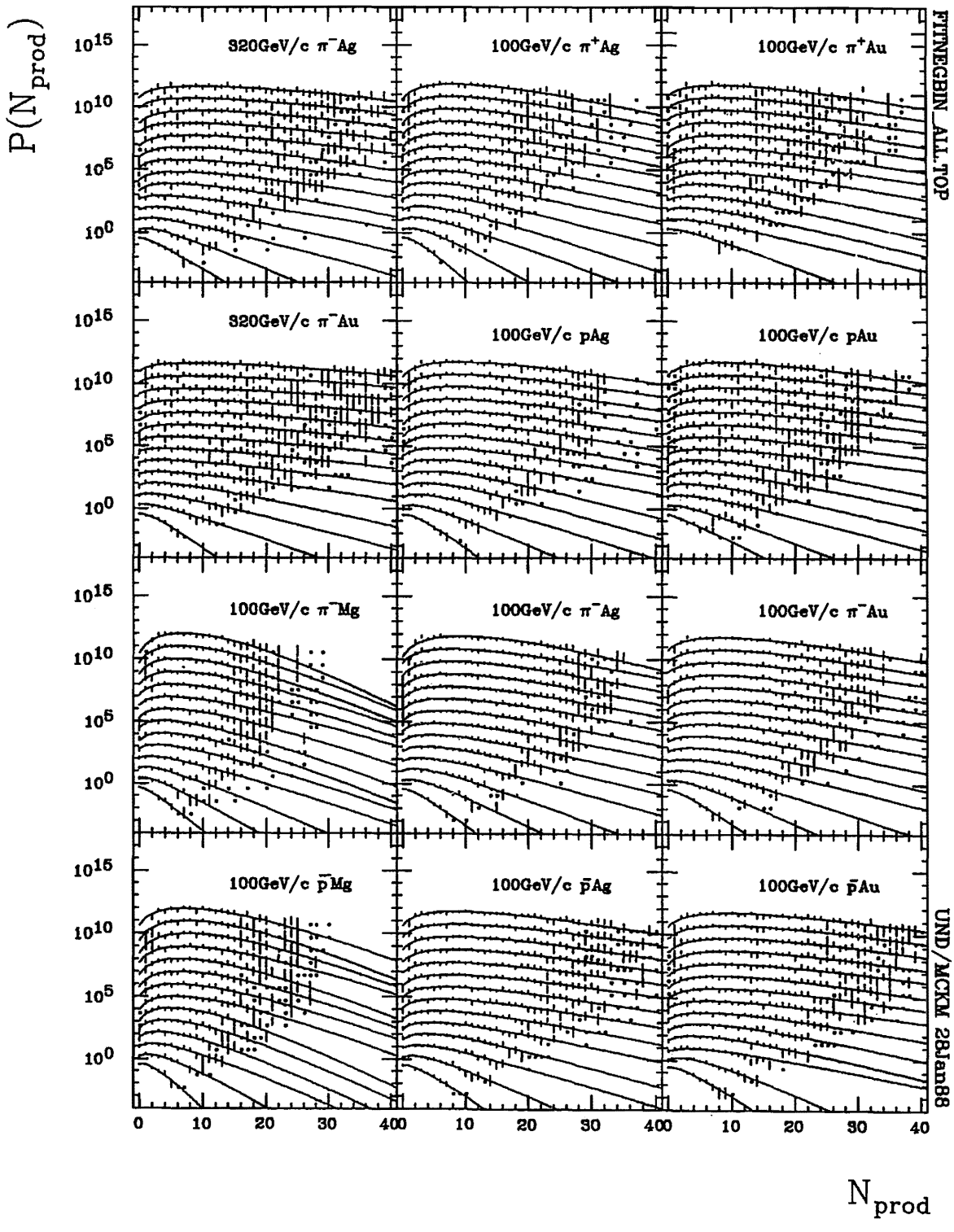

Figure 3.5.1 NBD fits of charged produced particle multiplicity distributions in limited regions of rapidity. Rapidity regions are centered about the hp cms rapidity with half-widths y_{cut} ranging from .25 to 3.5 units rapidity in increments of .25 units. The fits are displayed offset by orders of magnitude for increasing widths.

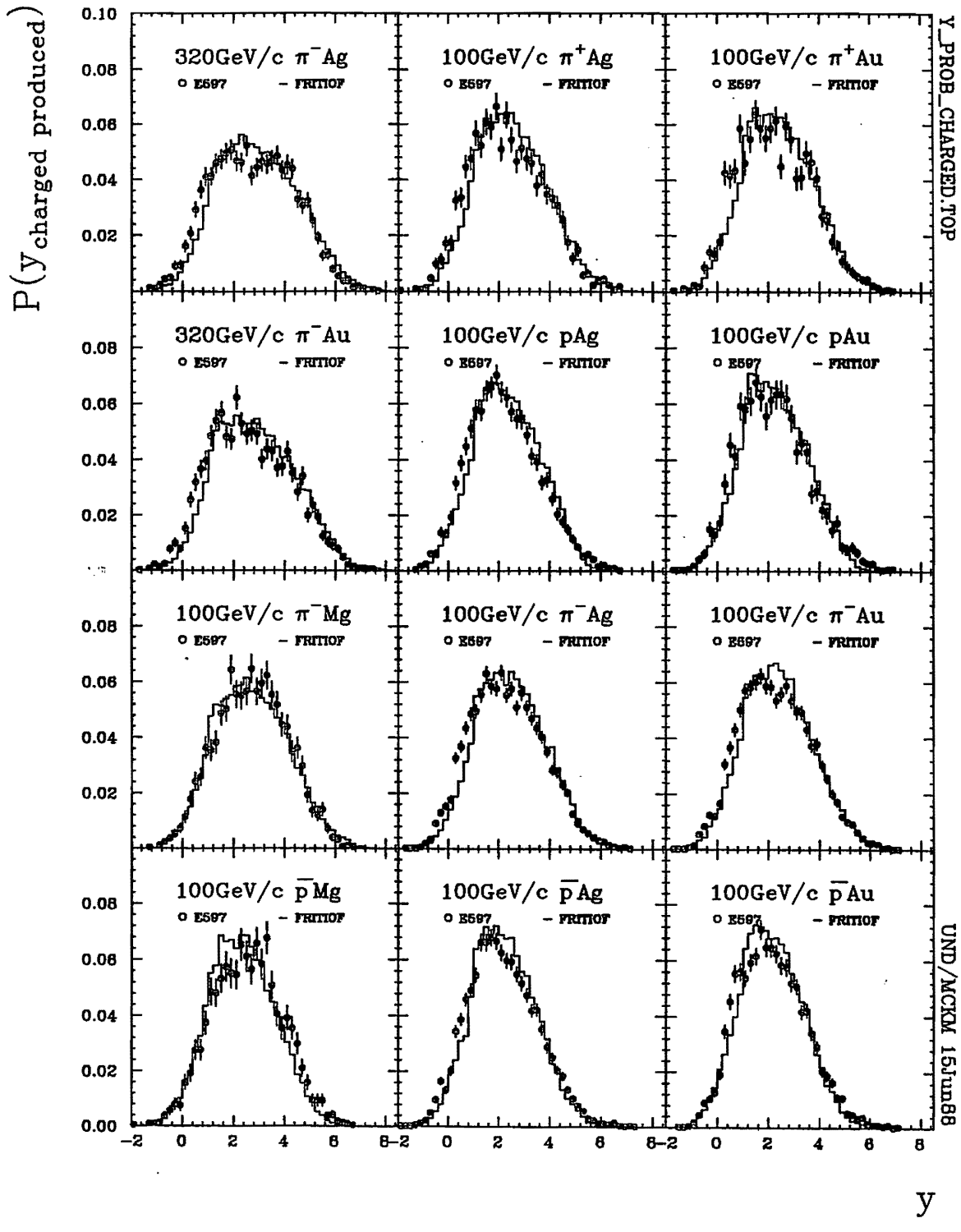

Figure 3.5.2 Rapidity distributions of charged produced particles for E597 data and FRITIOF simulations.

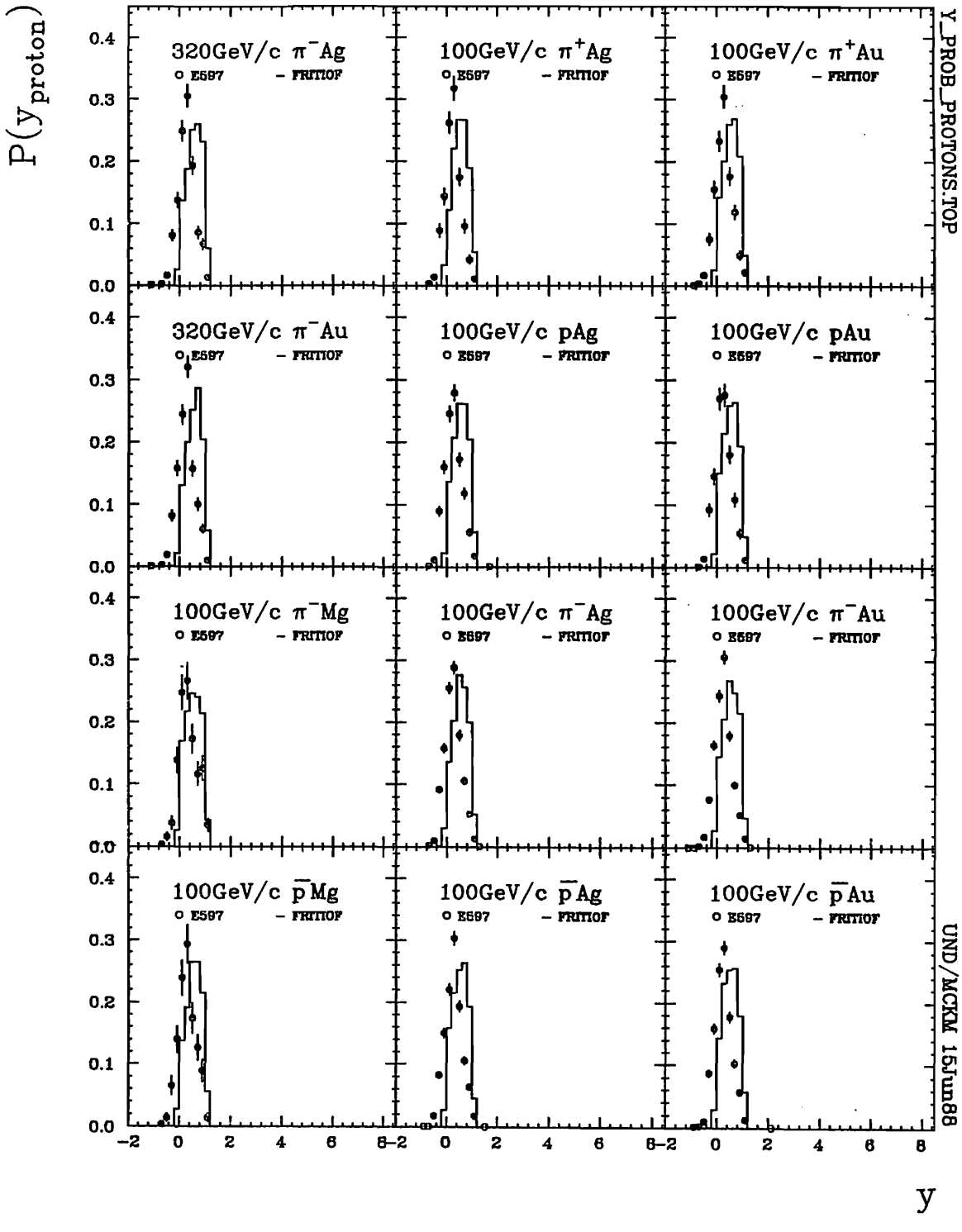

Figure 3.5.3 Rapidity distributions of identified protons in E597 data and comparable FRITIOF simulations.

Table 3.5.1 Parameters m for NBD fits of charged produced particle multiplicities in limited central regions of phase space of width y_{cut} centered about the hp cms rapidity.

Projectile	320GeV/c		100GeV/c									
	π^-		π^+		p		π^-			$\bar{p}$		
$^{A}_{Z}Target$	$^{108}_{47}Ag$	$^{197}_{79}Au$	$^{108}_{47}Ag$	$^{197}_{79}Au$	$^{108}_{47}Ag$	$^{197}_{79}Au$	$^{24}_{12}Mg$	$^{108}_{47}Ag$	$^{197}_{79}Au$	$^{24}_{12}Mg$	$^{108}_{47}Ag$	$^{197}_{79}Au$
y_{cut}	Fit parameter m $\sim \langle N_{prod} \rangle$ = average produced particle multiplicity. Errors below values.											
.25	1.53	1.49	1.26	.77	1.58	1.67	1.06	1.35	1.48	1.27	1.60	1.75
	.09	.15	.06	.04	.05	.01	.05	.03	.04	.06	.04	.05
.50	2.98	3.13	2.58	1.77	3.13	2.93	1.96	2.67	2.76	2.70	3.19	3.55
	.12	.15	.09	.10	.09	.02	.07	.05	.06	.08	.07	.09
.75	4.60	4.69	3.95	2.36	4.72	4.83	2.94	3.90	4.30	3.81	4.96	5.27
	.20	.22	.14	.10	.13	.06	.10	.07	.08	.14	.11	.09
1.00	6.18	6.20	5.12	3.26	6.02	6.13	4.18	5.35	5.72	4.70	6.42	7.00
	.23	.26	.16	.13	.14	.06	.10	.09	.12	.14	.12	.19
1.25	7.96	8.38	6.36	4.09	7.19	7.68	5.15	6.49	6.91	5.70	8.03	8.30
	.31	.40	.19	.17	.16	.10	.16	.11	.13	.16	.15	.18
1.50	9.06	9.73	7.75	4.95	8.73	8.22	6.02	7.58	8.03	6.62	9.23	9.81
	.28	.35	.26	.22	.21	.10	.14	.12	.14	.17	.14	.21
1.75	10.86	11.27	8.69	5.39	9.97	10.20	5.98	8.75	9.20	7.73	10.49	11.40
	.35	.56	.26	.20	.23	.00	.16	.14	.16	.23	.18	.27
2.00	11.67	12.53	9.50	6.02	10.22	11.49	6.99	9.42	10.20	7.90	11.47	12.30
	.36	.57	.34	.25	.20	.30	.19	.13	.18	.21	.21	.27
2.25	11.99	13.85	10.48	6.42	11.45	12.91	7.53	10.32	10.81	8.43	12.39	12.56
	.33	.56	.35	.26	.24	.35	.21	.15	.15	.20	.23	.25
2.50	13.68	14.53	10.56	6.46	12.02	12.83	7.77	10.78	11.11	8.35	12.70	14.07
	.45	.57	.31	.21	.27	.36	.19	.15	.26	.20	.23	.31
2.75	13.03	15.44	10.77	6.70	12.43	12.73	8.14	11.06	11.48	9.32	13.06	14.21
	.59	.60	.30	.23	.31	.21	.19	.15	.19	.25	.25	.20
3.00	14.69	17.33	10.95	6.88	12.37	13.55	8.08	11.38	11.95	9.57	12.96	14.19
	.37	.33	.30	.24	.26	.31	.18	.16	.17	.24	.22	.31
3.25	14.37	17.21	11.30	6.88	12.97	13.70	8.25	11.46	12.13	9.25	13.43	14.43
	.16	.82	.38	.23	.30	.34	.08	.15	.21	.20	.23	.30
3.50	15.39	16.34	11.32	7.02	13.22	13.35	8.42	11.96	12.23	9.16	13.09	14.76
	.46	.66	.38	.17	.31	.35	.17	.14	.21	.24	.24	.32

NEGBIN_M_CALL.TAB UND/MCKM 14Apr88

Table 3.5.2 Parameters k for NBD fits of charged produced particle multiplicities in limited central regions of phase space of width y_{cut} centered about the hp cms rapidity.

Projectile	320GeV/c		100GeV/c									
	π^-		π^+		p		π^-			p		
$^{A}_{Z}$ Target	$^{108}_{47}Ag$	$^{197}_{79}Au$	$^{108}_{47}Ag$	$^{197}_{79}Au$	$^{108}_{47}Ag$	$^{197}_{79}Au$	$^{24}_{12}Mg$	$^{108}_{47}Ag$	$^{197}_{79}Au$	$^{24}_{12}Mg$	$^{108}_{47}Ag$	$^{197}_{79}Au$
y_{cut}	Fit parameter k. Errors below values.											
.25	1.65	2.21	2.58	7.26	2.52	1.38	1.83	2.01	2.11	3.38	2.05	2.30
	.48	.68	.53	2.96	.36	.21	.33	.17	.21	.84	.19	.27
.50	1.49	1.64	2.67	1.86	2.29	1.75	1.95	2.18	2.03	2.97	2.39	2.67
	.31	.26	.37	.32	.25	.25	.25	.13	.15	.31	.24	.23
.75	1.78	1.72	2.38	2.42	2.34	1.84	1.99	2.31	2.15	2.74	2.30	2.62
	.20	.23	.29	.38	.20	.20	.22	.12	.14	.37	.16	.13
1.00	2.01	1.90	2.70	2.38	2.76	2.11	2.07	2.29	2.07	3.75	2.87	2.47
	.25	.24	.24	.28	.24	.21	.14	.12	.12	.64	.18	.14
1.25	2.01	1.67	2.60	2.78	2.96	2.28	2.65	2.48	2.39	4.68	2.70	2.70
	.24	.20	.23	.39	.24	.21	.26	.13	.11	.58	.15	.17
1.50	2.65	1.69	2.60	2.91	2.73	2.43	2.57	2.71	2.50	6.09	2.83	2.58
	.28	.24	.22	.34	.20	.21	.16	.13	.14	.63	.16	.16
1.75	2.69	1.68	2.98	3.18	2.78	2.26	3.64	2.86	2.56	5.01	2.89	2.50
	.29	.19	.26	.33	.19	.13	.35	.12	.19	.53	.15	.14
2.00	2.49	1.76	3.13	3.24	3.23	2.19	3.78	3.24	2.66	4.60	2.95	2.83
	.25	.19	.48	.37	.22	.17	.34	.13	.14	.52	.16	.14
2.25	3.01	2.10	3.02	3.23	3.50	2.36	3.42	3.37	2.78	5.54	2.95	3.16
	.22	.22	.26	.38	.19	.17	.37	.13	.15	.71	.15	.15
2.50	2.82	2.26	3.71	4.45	3.45	2.42	4.18	3.57	2.97	5.94	2.90	2.91
	.26	.23	.25	.49	.20	.17	.43	.13	.06	.91	.16	.14
2.75	2.55	2.22	3.81	5.26	3.06	3.11	4.86	3.84	3.42	5.15	3.14	3.09
	.25	.23	.29	.62	.22	.23	.49	.14	.15	.63	.07	.10
3.00	3.12	1.77	4.07	5.17	3.51	2.94	6.01	3.87	2.81	6.53	3.24	3.23
	.22	.21	.35	.63	.24	.21	.61	.14	.14	.84	.18	.10
3.25	2.69	1.92	3.92	5.47	3.48	2.89	6.60	3.81	3.30	7.24	3.17	3.16
	.24	.22	.38	.70	.23	.21	.84	.16	.16	.82	.17	.15
3.50	2.84	2.24	4.24	5.39	3.68	3.12	8.66	5.49	3.38	5.79	3.50	3.10
	.33	.24	.19	.56	.23	.25	.89	.19	.16	.87	.18	.15

NEGBIN_K_CALL.TAB

UND/MCKM 14Apr88

Table 3.5.3 χ^2/NDF for NBD fits of charged produced particle multiplicities in limited central regions of phase space of width y_{cut} centered about the hp cms rapidity.

Projectile	320GeV/c		100GeV/c									
	π^-		π^+		p		π^-			p		
$\frac{A}{Z}$ Target	$^{108}_{47}Ag$	$^{197}_{79}Au$	$^{108}_{47}Ag$	$^{197}_{79}Au$	$^{108}_{47}Ag$	$^{197}_{79}Au$	$^{24}_{12}Mg$	$^{108}_{47}Ag$	$^{197}_{79}Au$	$^{24}_{12}Mg$	$^{108}_{47}Ag$	$^{197}_{79}Au$
y_{cut}	χ^2/NDF											
.25	.31	.90	.78	1.23	.14	.7	.78	.55	.89	.96	1.87	.37
χ^2	2.50	5.42	3.92	7.36	1.01	6.29	5.43	4.39	7.12	5.77	16.83	3.31
NDF	8	6	5	6	7	9	7	8	8	6	9	9
.50	1.36	.53	.83	1.56	.74	1.57	1.53	1.51	2.85	1.43	1.47	6.57
χ^2	17.74	6.36	8.28	15.56	8.10	18.81	18.39	18.08	37.02	12.91	19.12	6.57
NDF	13	12	10	10	11	12	12	12	13	9	13	13
.75	.64	.97	.74	.71	1.07	.26	1.44	3.19	1.10	.88	1.00	.58
χ^2	11.60	15.57	9.68	8.52	16.08	3.95	10.15	51.07	17.56	10.51	15.95	9.21
NDF	18	16	13	12	15	15	14	16	16	12	16	16
1.00	.93	1.04	1.25	.54	1.36	.89	.59	1.34	1.05	1.16	1.20	1.03
χ^2	18.59	20.70	20.02	9.16	25.93	17.72	10.03	25.39	21.04	19.74	28.48	20.58
NDF	20	20	16	17	19	20	17	19	20	17	22	20
1.25	1.32	.59	.72	4.44	1.57	.92	.54	1.65	1.51	18.04	1.28	1.22
χ^2	29.01	14.64	14.46	88.74	36.02	20.29	10.29	37.98	34.73	18.04	30.74	30.39
NDF	22	25	20	20	23	22	19	23	23	19	24	25
1.50	1.72	.72	.54	.67	1.10	.99	.49	1.10	1.39	1.19	1.37	1.03
χ^2	44.68	20.94	11.37	15.44	27.59	25.74	9.78	28.61	36.14	24.89	42.53	27.69
NDF	26	29	21	23	25	26	20	26	26	21	31	27
1.75	.69	.75	.75	2.37	.81	1.61	1.70	1.13	1.17	.55	1.77	1.28
χ^2	20.05	23.88	18.86	56.99	22.67	43.37	33.99	30.53	33.89	12.15	56.70	38.38
NDF	29	32	25	24	28	27	20	27	29	22	32	30
2.00	1.01	.94	.56	.77	1.11	1.23	.93	1.12	.82	.97	1.35	1.44
χ^2	34.36	34.00	14.56	20.04	35.60	34.57	20.36	32.53	24.73	22.33	47.17	47.51
NDF	34	36	26	26	32	28	22	29	30	23	35	33
2.25	.73	.75	.81	1.29	1.02	1.07	.66	1.10	1.11	.91	1.22	1.91
χ^2	26.31	29.11	21.90	38.57	33.55	32.16	14.60	33.97	35.61	21.83	42.70	68.93
NDF	36	39	27	30	33	30	22	31	32	24	35	36
2.50	1.04	.83	.67	1.07	.98	1.19	.98	1.15	1.57	1.23	1.28	1.20
χ^2	37.34	33.36	19.50	33.24	33.38	35.64	23.47	38.09	53.49	30.78	46.16	45.64
NDF	36	40	29	31	34	30	24	33	34	25	36	38
2.75	.91	.88	.67	1.33	.73	1.55	.85	1.47	2.05	.65	1.08	1.39
χ^2	34.39	37.80	20.24	41.25	24.05	51.23	20.48	49.87	69.65	15.53	40.88	55.75
NDF	38	43	30	31	33	33	24	34	34	24	38	40
3.00	1.16	.79	.86	1.48	.94	1.46	1.08	1.19	1.29	1.02	1.58	1.64
χ^2	47.67	33.20	26.65	44.37	31.96	48.17	24.89	41.70	42.46	25.42	59.85	60.66
NDF	41	42	31	30	34	33	23	35	33	25	38	37
3.25	1.15	.91	.84	1.58	.97	1.55	1.05	1.73	1.84	1.50	.96	1.47
χ^2	44.88	37.21	24.41	47.47	32.94	49.50	24.07	57.06	60.56	37.38	39.20	57.19
NDF	39	41	29	30	34	32	23	33	33	25	41	39
3.50	.94	.87	.93	1.66	1.13	1.32	1.57	3.81	1.64	1.35	1.47	2.94
χ^2	36.65	37.40	28.84	51.59	38.57	43.57	36.07	129.70	54.12	32.36	60.21	114.53
NDF	39	43	31	31	34	33	23	34	33	24	41	39

NEGBIN_CHI2_CALL.TAB UND/MCKAI 14Apr88

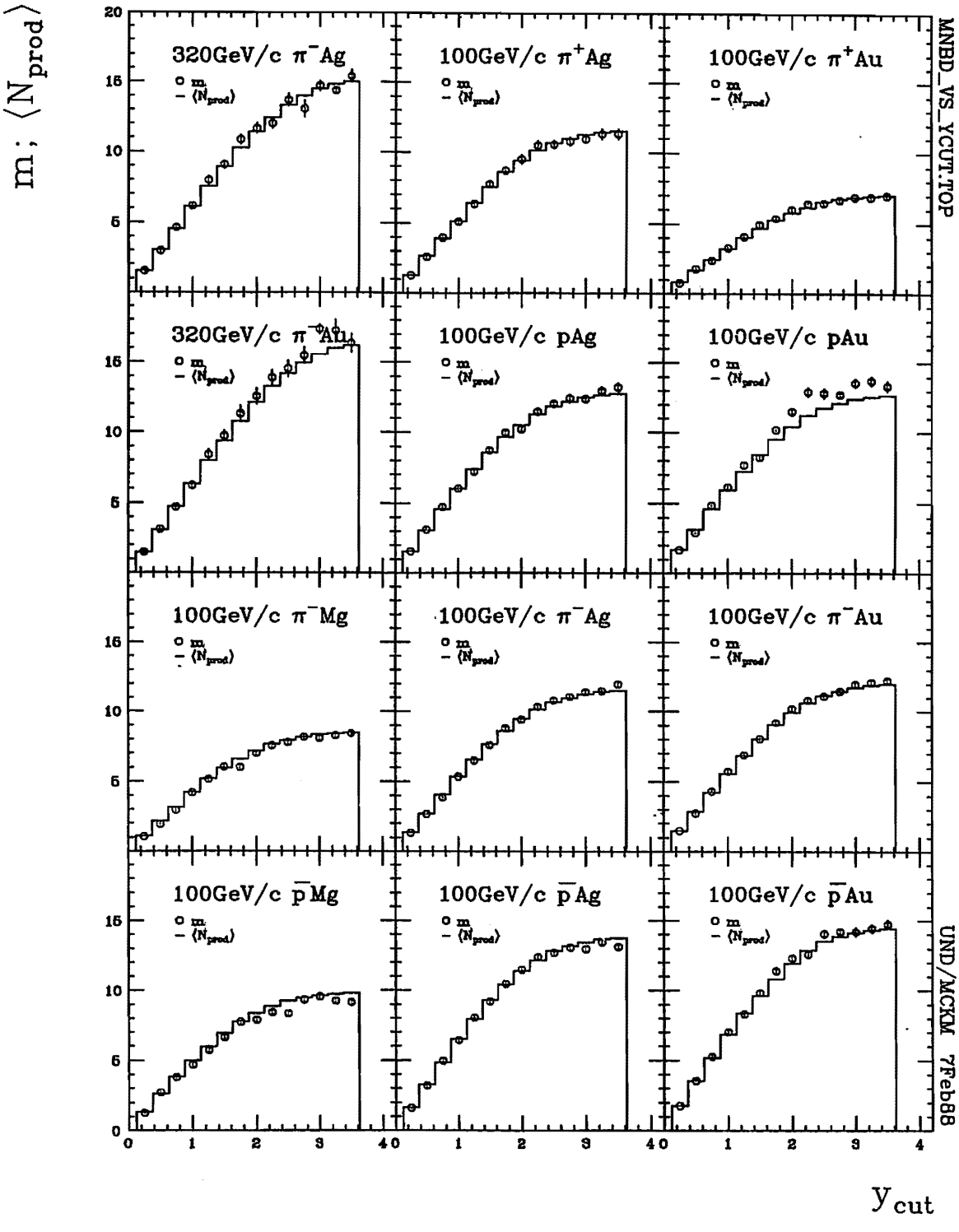

Figure 3.5.4 NBD fit parameters m for charged produced particle multiplicity distributions compared to average charged produced particle multiplicities as functions of the half-width y_{cut} of limited rapidity regions centered about the hp cms rapidity.

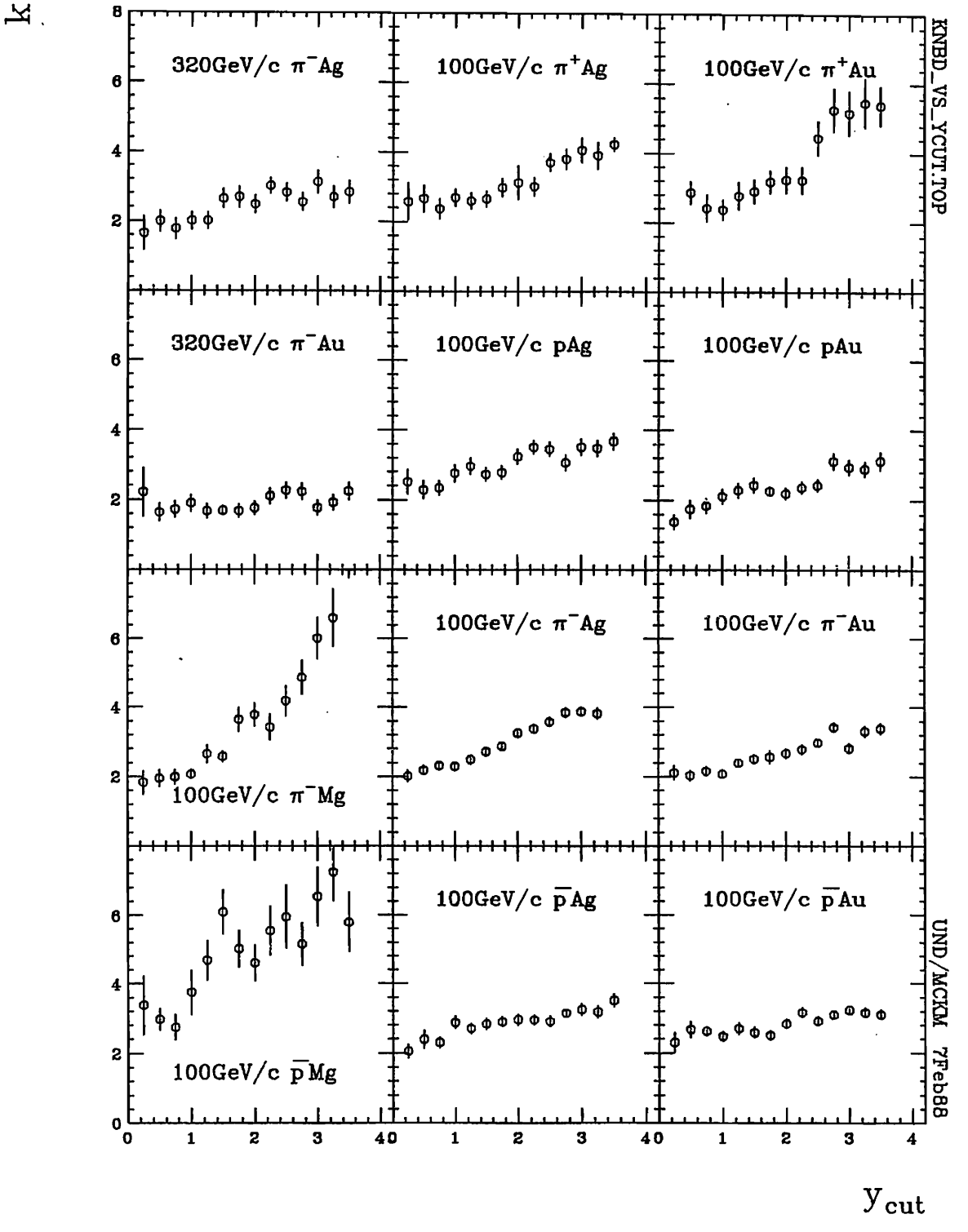

Figure 3.5.5 NBD fit parameters k for charged produced particle multiplicity distributions as functions of the half-width y_{cut} of limited rapidity regions centered about the hp cms rapidity.

is associated with the fraction of particles which stimulate the emission of additional particles. In that case, a larger number of collisions would increase that fraction. Using values of k for a rapidity region with a half-width of 3.5 units, k inverse indeed increases with $\bar{\nu}(hA)$ in much the same way for all interactions except for the higher energy interactions for which k inverse is higher. The trend of k inverse as a function of $\bar{\nu}(hA)$ is shown in **Figure 3.5.6**. It is observed that the fraction of stimulating particles in PSE is energy dependent. This dependence agrees with results from the e^+e^-, ℓh, and pp interactions cited in [Kittel 87b], but the fractions themselves are considerably higher for E597 and NA5 [Fialkowski 86b] hA interactions than for e^+e^-, ℓh, and pp interactions in the same approximate energy range. But of particular interest is the fact that a loose extrapolation of the trend of k inverse values as a function of $\bar{\nu}(hA)$, **Figure 3.5.6**, is consistent at $\bar{\nu}(hA) = 1$ with pp results. Thus, k inverse is strongly correlated to the number of collisions sustained. That could mean that the fraction of particles stimulating emission is correlated to the number of collisions sustained.

In the NBD cluster interpretation, the size and number of clusters can be estimated in terms of NBD parameters. Background and details for the calculation of this estimate in the cluster interpretation developed by Giovannini and Van Hove can be found in Appendix 3A. Plotting the calculated cluster size n_c as a function of rapidity region half-width y_{cut}, **Figure 3.5.7** shows that the cluster size for most interactions saturates at $y_{cut} = 1.5 - 2.0$ units rapidity. The turnover points where saturation takes place may be signaling the rapidity extent of clusters. Limited rapidity regions exclude some clusters and cut through others, thus limiting both their number and their content unless they are about the same size as the average cluster. As explained in [Giovannini 86a], with increasing rapidity region width, more clusters contribute particles into the interval (so N_{clus} grows) and more particles from a given cluster fall into the interval (so n_c grows). Saturation occurs close to the kinematic limit. Thus, clusters may be said to extend a full width of 3-4 units rapidity on the average. Clusters for pp interactions saturate at $y_{cut} \sim 1.5$ units [Kittel 87b], and thus are said to extend 3 units rapidity. That means hA clusters are about the same

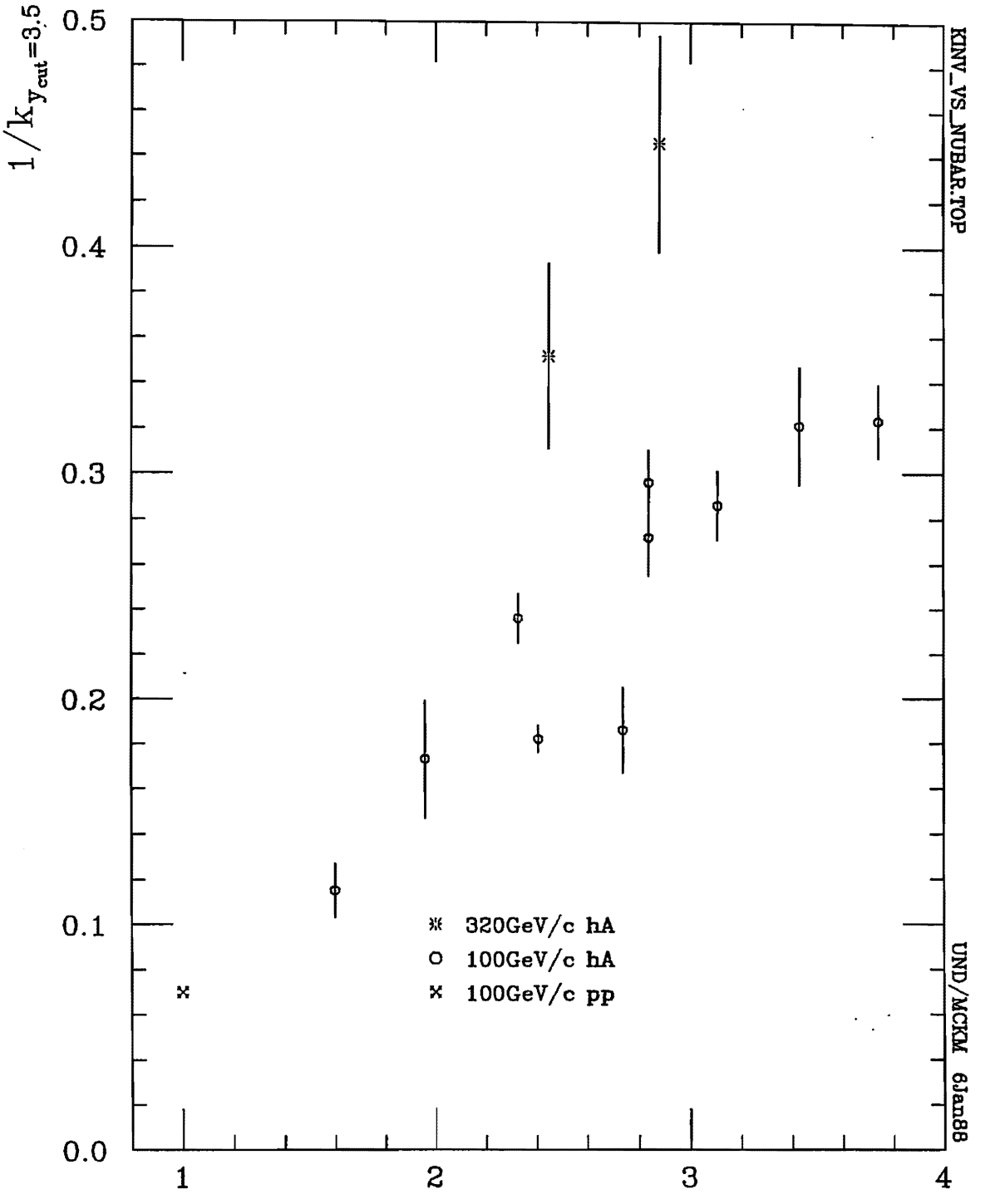

Figure 3.5.6 The inverses of NBD fit parameters k as functions of $\bar{\nu}(hA)$. The dependence extrapolates down to hp interaction values at $\bar{\nu} = 1$.

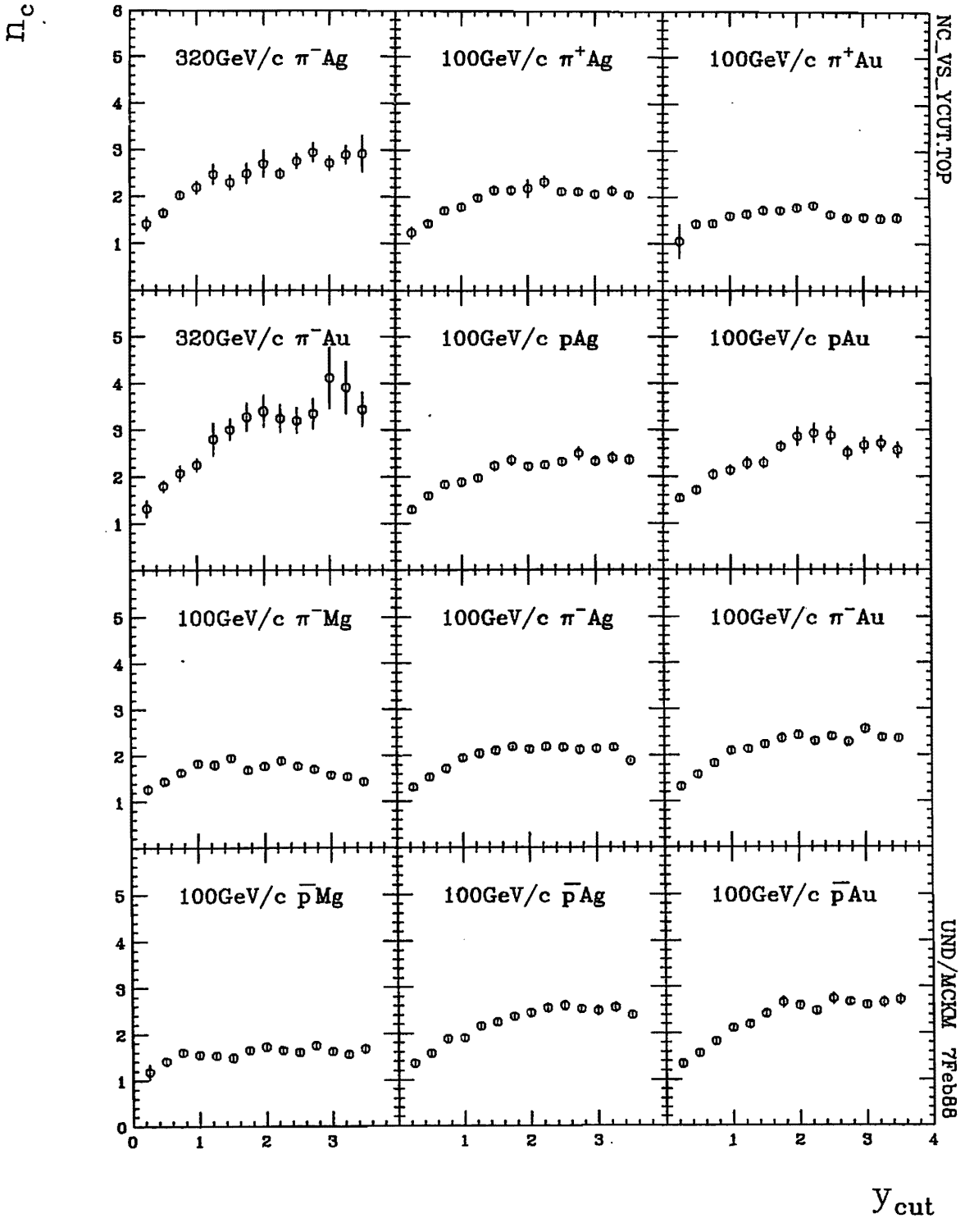

Figure 3.5.7 The number of particles in a cluster calculated in a cluster interpretation of NBD parameters ($n_c = -\frac{b}{(1-b)\ln(1-b)}$ where $b = m/(m+k)$) as a function of the half-width y_{cut} of limited rapidity regions centered about the hp cms rapidity.

size as hh clusters.

Plotting the calculated number of clusters $N_{clusters}$ as a function of rapidity region half-width y_{cut}, **Figure 3.5.8** also shows that the number of clusters begins to saturate at y_{cut} near 2 units rapidity. Since values of N_{clus} saturate at around 5, considerable overlap must occur between clusters in rapidity.

It is also noticed that the the number of particles comprising a cluster is energy sensitive. Comparable interactions have larger values of n_c at 320 GeV/c than at 100 GeV/c, as seen in **Figure 3.5.9**. At the higher energy, clusters are larger, on the average, by an additional particle, increasing the average cluster content from 2 to 3. This could be due to greater numbers of collisions at higher energies. Plotted as a function of the number of collisions in **Figure 3.5.10**, the maximum particle content of clusters does increase with additional numbers of collisions. TASSO studies of e^+e^- at $\sqrt{s} = 14$ and 22 result in $n_c = 1.08$ and 1.14, respectively. An extrapolation of the trend in **Figure 3.5.10** to $\bar{\nu} = 1$ shows that E597 hA data is consistent with e^+e^- results and the view that cluster content is dependent on the number of collisions sustained in an interaction.

The number of clusters, in contrast to the cluster content, does not show a very strong, if any, dependence on energy. This can be seen in **Figure 3.5.11**. The fact that there is also no clear dependence of N_{clus} on $\bar{\nu}(hA)$ is consistent with this lack of energy dependence since $\bar{\nu}(hA)$ is energy dependent. However, an energy independent number of clusters is not expected. Cluster models lend themselves to a picture of higher and higher energies producing more and more clusters of about the same particle content. The greater numbers of collisions at higher energies as well as interpretations of clusters as resonance effects are also very naturally associated with increasing numbers of clusters rather than increasing cluster content. But results from this study and hh studies [Breakstone 88] based on the cluster interpretation contradict this picture. Increasing energies in the cluster interpretation produce about the same number of clusters packed with increasing numbers of particles.

As for possible beam dependencies, it may be noted in **Figure 3.5.12** that N_{clus} is smaller for meson beam interactions than for baryon beam interactions. The

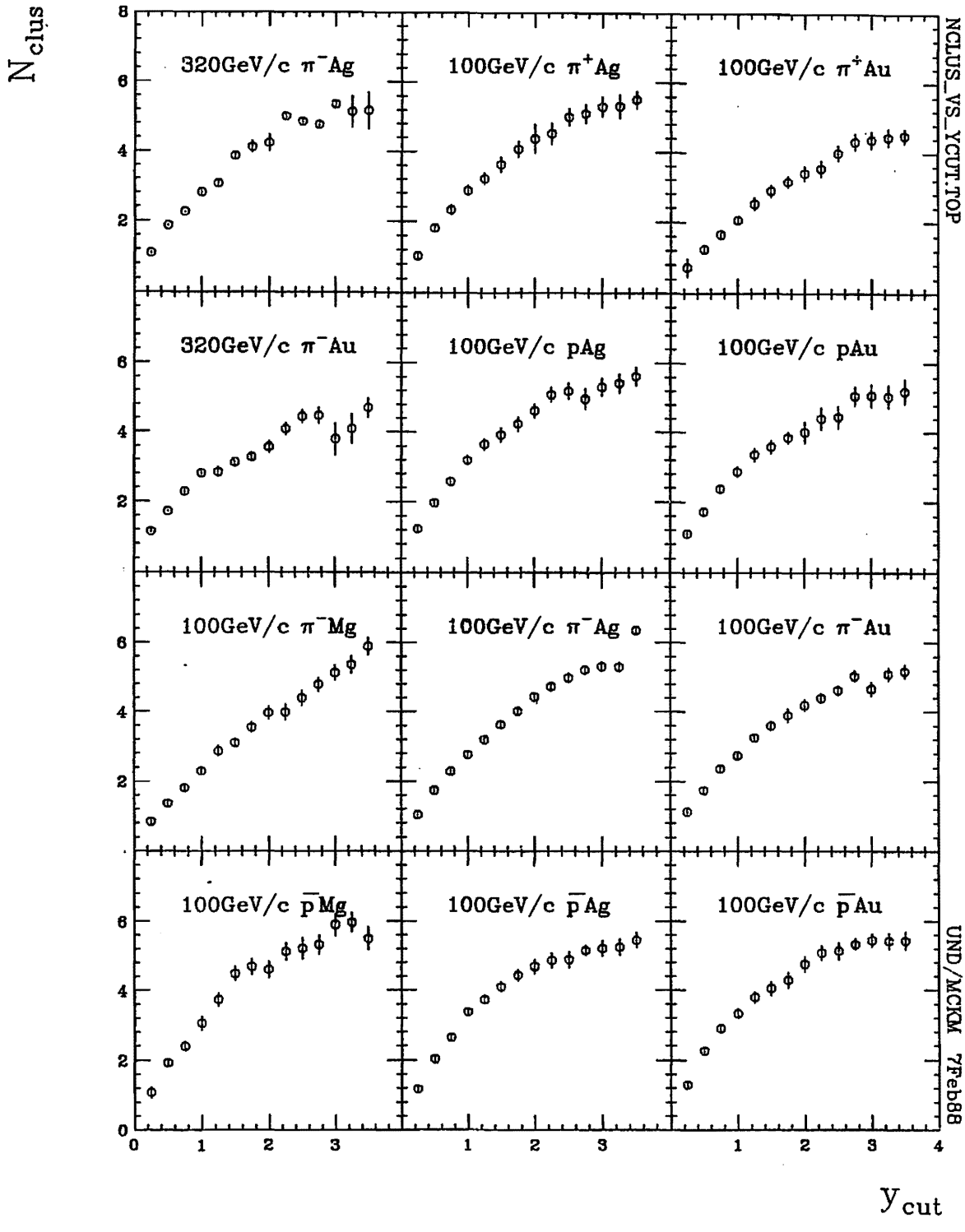

Figure 3.5.8 The number of clusters calculated in a cluster interpretation of NBD parameters ($N_{clus} = m/n_c$) as a function of the half-width y_{cut} of limited rapidity regions centered about the hp cms rapidity.

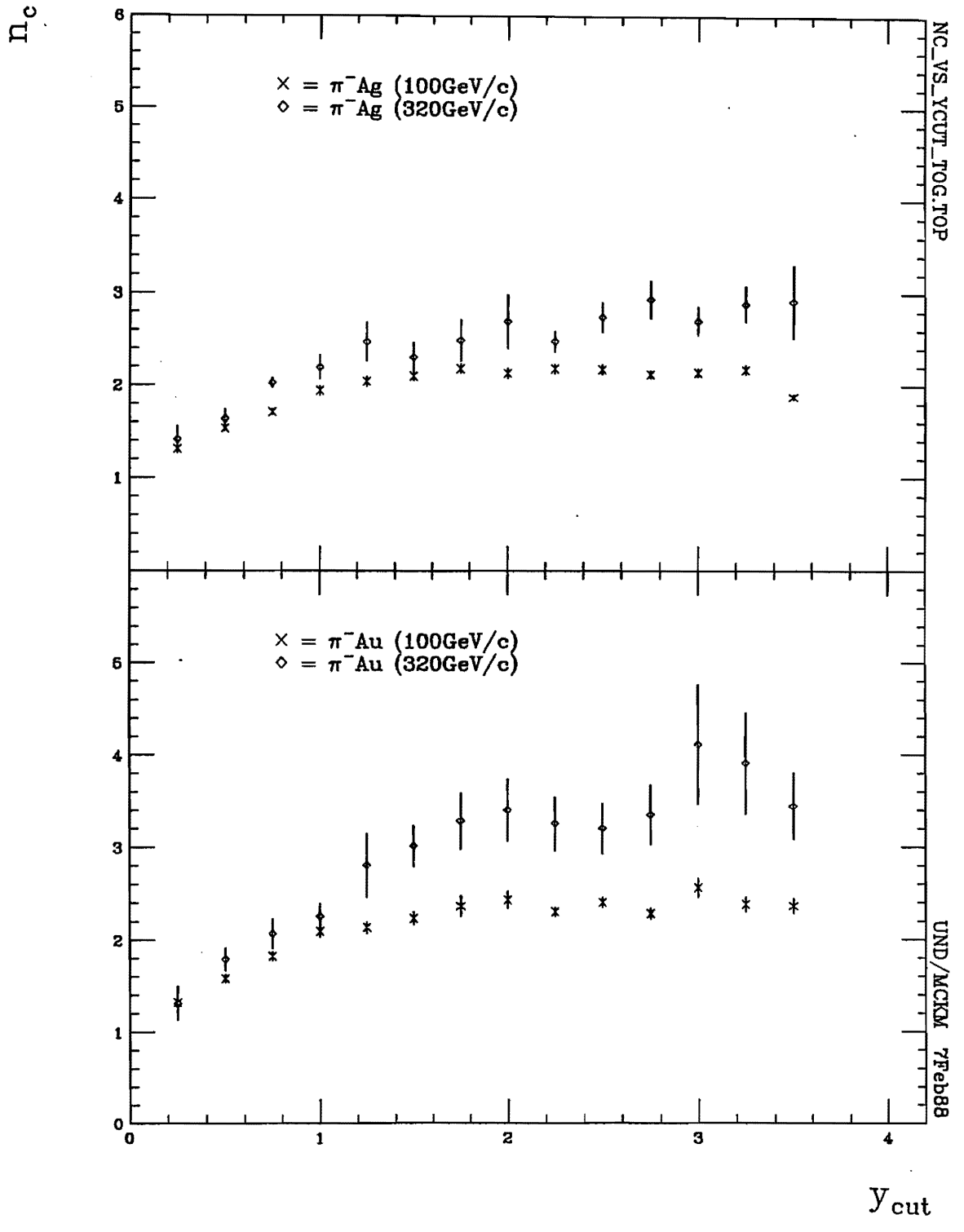

Figure 3.5.9 An energy comparison of results for $\pi^- Ag$ and $\pi^- Au$ interactions at 100 GeV/c and 320 GeV/c. The number of particles n_c in a cluster is calculated in a cluster interpretation of NBD fit parameters as a function of the half-width y_{cut} of limited rapidity regions centered about the hp cms rapidity.

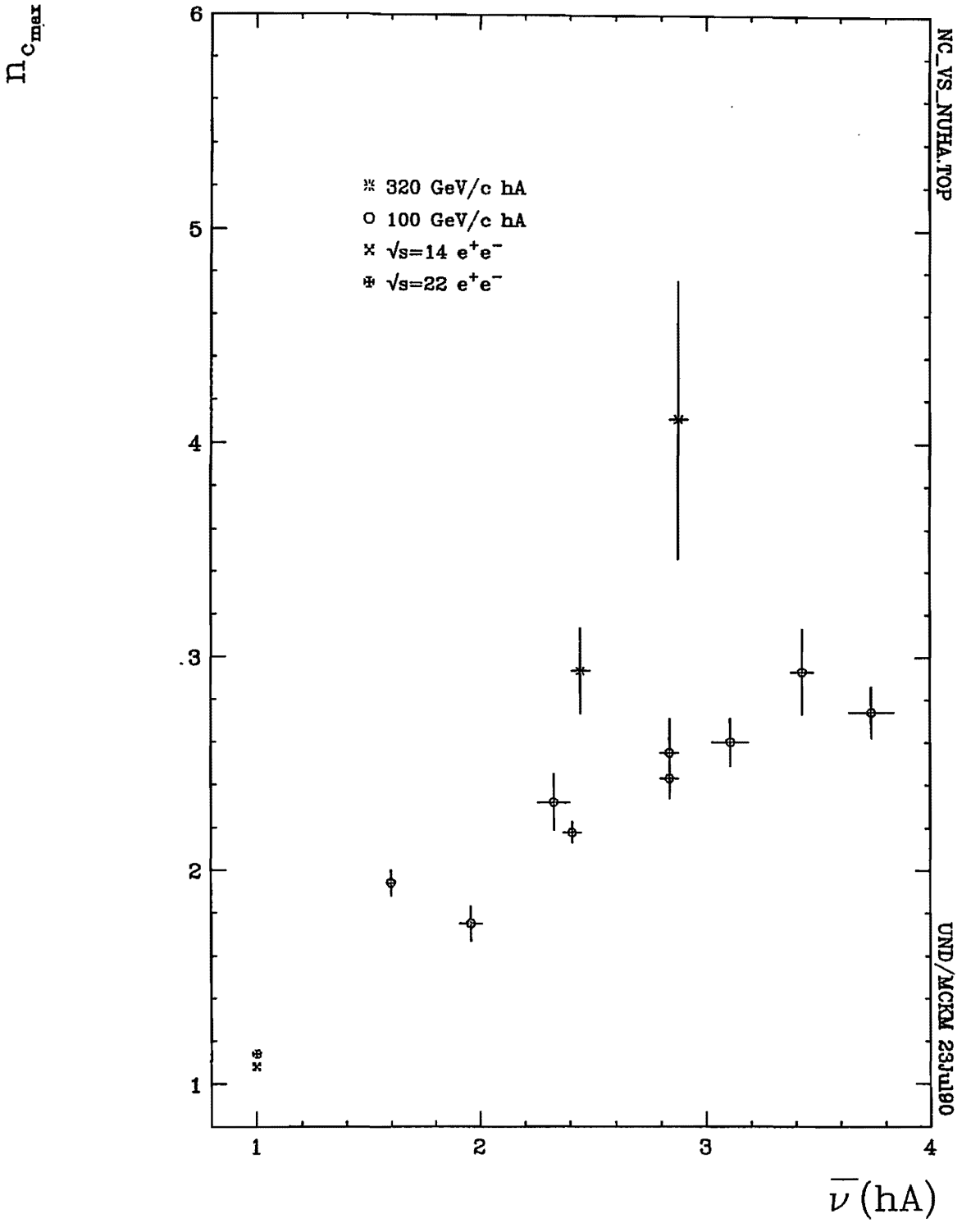

Figure 3.5.10 The maximum number of particles found in clusters, calculated in a cluster interpretation of NBD fit parameters, as a function of the number of collisions $\bar{\nu}(hA)$.

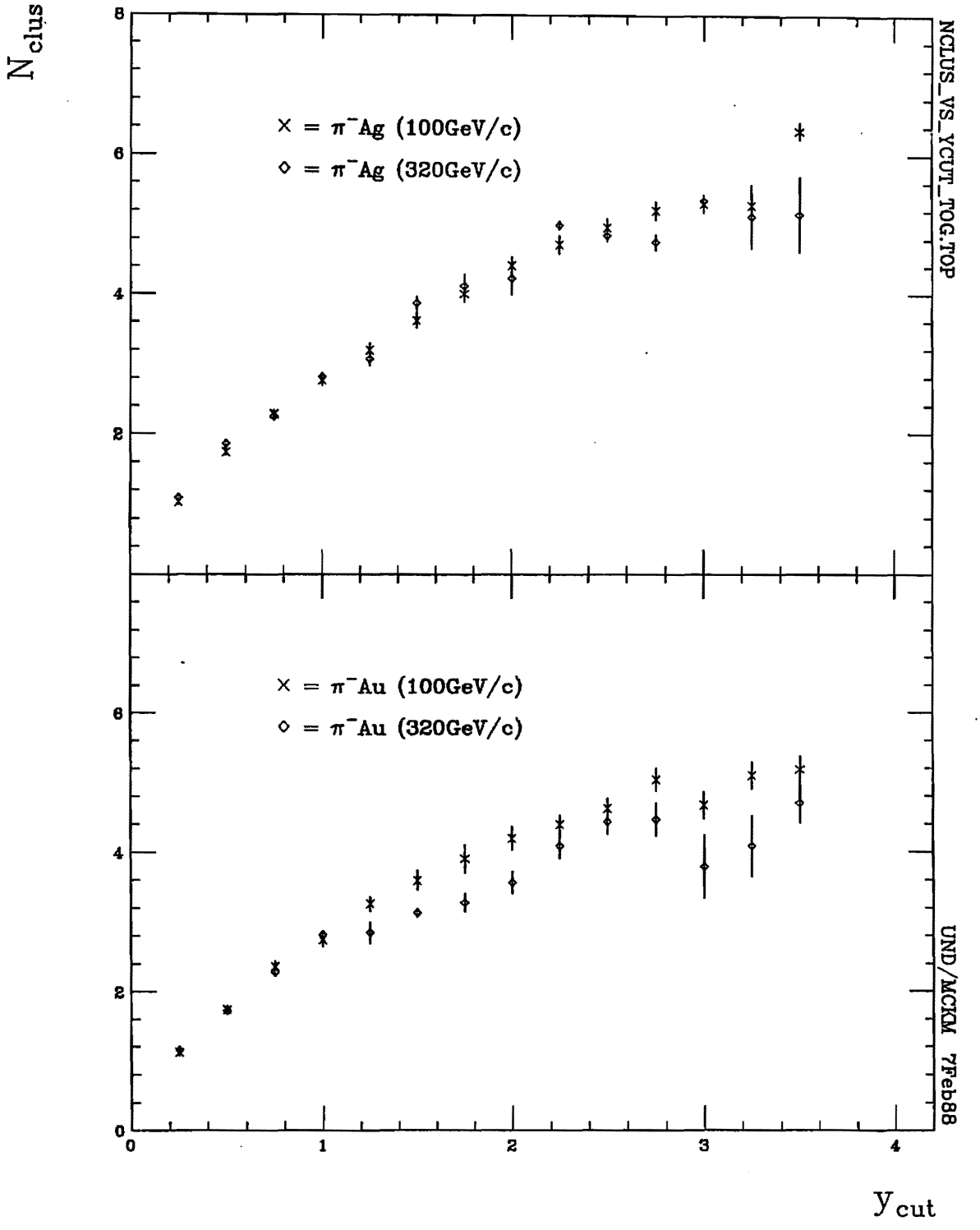

Figure 3.5.11 An energy comparison of results for $\pi^- Ag$ and $\pi^- Au$ interactions at 100 GeV/c and 320 GeV/c. The number of clusters is calculated in a cluster interpretation of NBD fit parameters as a function of the half-width y_{cut} of limited rapidity regions centered about the hp cms rapidity.

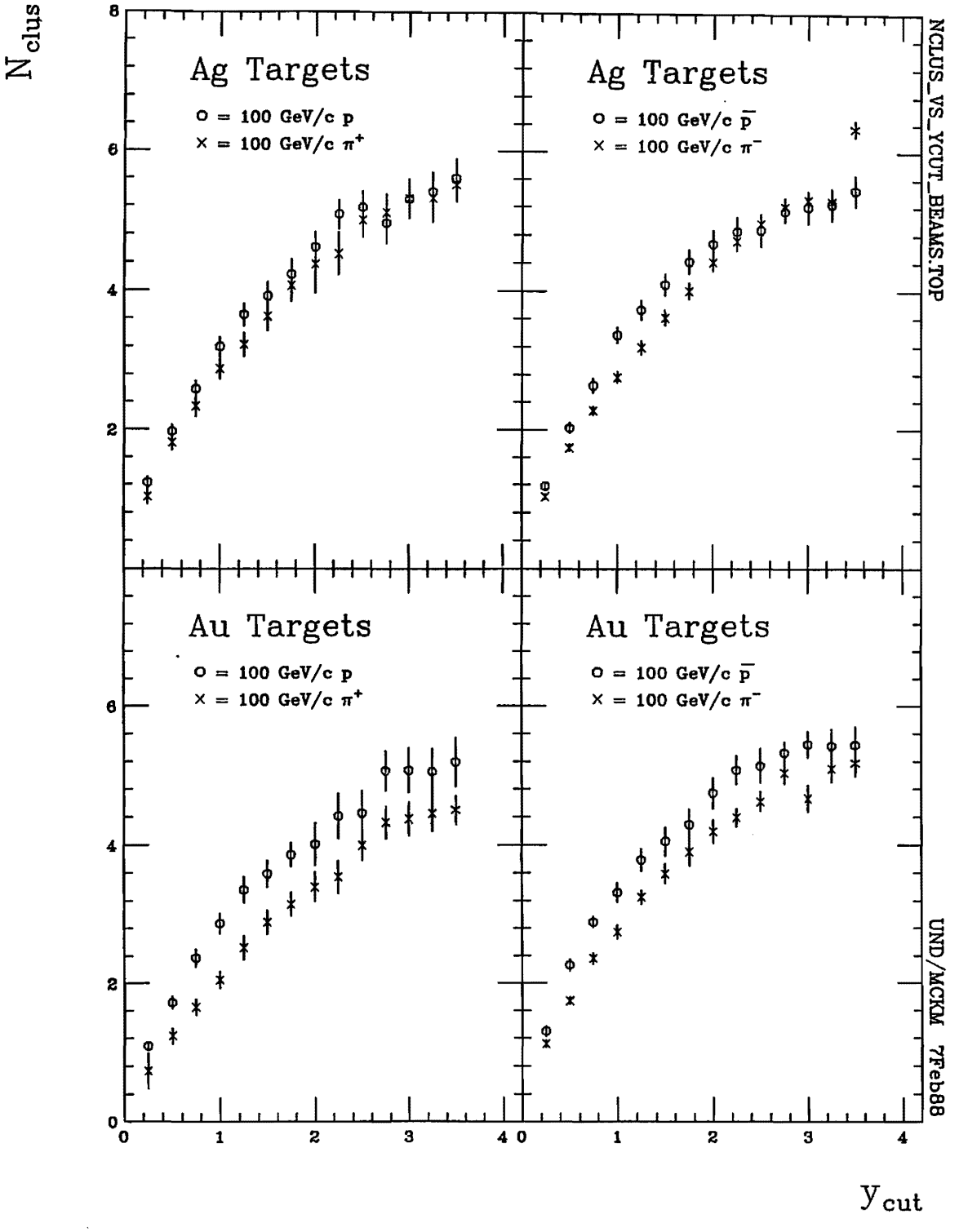

Figure 3.5.12 A comparison of the numbers of clusters calculated on the basis of NBD for meson and baryon beam interactions at 100 GeV/c.

cluster content n_c is also consistently smaller for meson beams than for baryon beams as shown in **Figure 3.5.13**. That means N_{clus} is at least weakly dependent on $\bar{\nu}$ since $\bar{\nu}$ is always smaller for mesons than for baryons interacting on a given target. The fact that n_c is smaller for meson interactions than for baryon interactions reconfirms n_c's strong $\bar{\nu}$-dependence. Evidently, the number of constituent quarks in the beam particles make a difference in both the number and content of hA clusters according to the cluster interpretation of the NBD description of multiplicities.

3.6 FORWARD-BACKWARD CORRELATIONS

Clustering can be studied further in the context of forward-backward correlations (FBCs) since they are sensitive to both cluster content, size, and location in rapidity. Giovannini-Van Hove model predictions do not reproduce UA5 FBC results [Alpgard 83] and the discrepancy is thought to persist regardless of adjustments made to the content and extent of clusters randomly emitted along the rapidity axis unless their characteristics vary with rapidity. Since identical clusters cannot account for observed FBCs, [Ansorge 88; Alner 87; Alpgard 83; Carruthers 85]. it has been suggested that larger clusters in the central region and smaller ones in the fragmentation regions might reconcile UA5 results with a cluster model [Bialas 86a].

Important models other than cluster models have used FBCs to set their models apart. FBC for hh has been found to be a sensitive test for the multistring nature of dual parton models (DPM). With the ideas of short range order, single inelastic scatters inducing short range correlations, and multiple scattering inducing long range ones, [Capella 82e] obtained the large FBC slopes reported for hh interactions at ISR and SPS energies. Subsequently, [Capella 83b] predicted significant FBC for *properly* chosen forward and backward regions in hA interactions. [De Marzo 82] measured a strong correlation which [Ranft 85] qualitatively reproduced. It was also verified that when a central region $2.25 > y > 3.75$ was excluded, the correlations all but disappeared. This was described in terms of sea-quark (valence-quark) projectile(target) chains at small rapidities in the lab frame not extending beyond y=3.75.

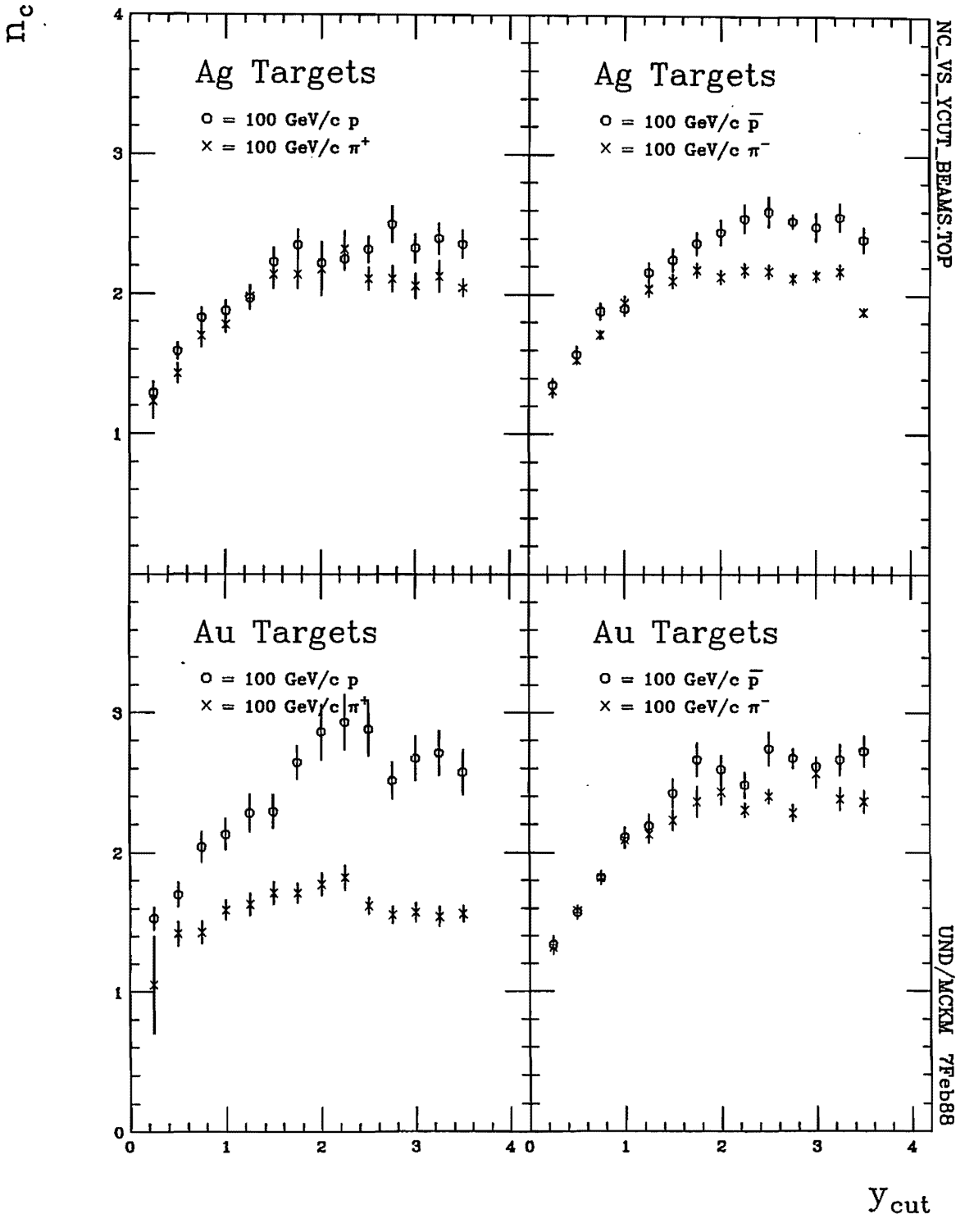

Figure 3.5.13 A comparison of the numbers of particles in clusters calculated on the basis of NBD for meson and baryon beam interactions at 100 GeV/c.

The only difference between multi-chain models for hh and hA interactions is a shift in the cms rapidity about which additional chains are centered. For hA interactions additional chains are centered about $y_{lab} \sim 2.68$ *or* 3.26. For hh they are centered about $y_{cms} \sim 0$. In both cases, chains have short rapidity lengths compared to the maximum rapidity.

Though very different models have predicted forward-backward correlations, FBCs are wonderfully simple tools which probe long-range correlations without getting tangled in the details of any particular model. Dependent only on multiplicities in two rapidity regions, they are easy to calculate and are inherently resistant to the plague of limited data statistics. They make the best use of sometimes marginal statistics in very narrow rapidity windows. But though at greatest advantage for low statistics, FBC techniques are relevant and important at moderate and large statistics.

In the past, surprisingly few experimental studies have included FBCs despite their simplicity. Emulsion experiments have provided much of the experimental data [Wosiek 77; Jain 81; Azimov 81] for FBCs, but these have serious disadvantages. Simple comparisons are complicated by the mix of nuclear targets whereby A-dependent effects are smeared out. The ambiguity of *shower* particle identities in emulsion is another serious disadvantage since evaporation protons contaminate the produced particle sample. However, E597 beams, targets, and secondaries are well determined and thus provide a better stage for FBC studies, supplementing other direct hA studies.

3.6.1 FBC basics

Forward-backward correlations are usually characterized by the slopes b_B and b_F, assuming linear relationships between the *forward* and *backward* regions. These slopes parameterize the average backward multiplicity as a function of forward multiplicity,

$$\langle N_B \rangle = a_B + b_B N_F$$

and the average forward multiplicity as a function of backward multiplicity,

$$\langle N_F \rangle = a_F + b_F N_B$$

But while the two hemispheres symmetrically straddle zero rapidity in the cms for pp interactions and other interactions between hadrons of the same mass, the 'zero'-point for non-symmetric hh interactions (*e.g.* πp) and all hA interactions is shifted. For the non-symmetric hh interactions, the shift is unambiguously determined, but for hA interactions, the shift is ambiguous in so far as the collision participants are not known. It is presumed, however, that the 'zero'-point is near the hp cms rapidity. Thus *forward* and *backward* will respectively refer to laboratory rapidity regions to the right and left of 2.68(3.26) units rapidity for hA interactions at 100(320) GeV/c in this study in order to approximate $y = 0$ in the cms. While symmetric interactions (e^+e^-, pp, $\bar{p}p$, etc.) imply b_F identical to b_B, b_F is in general not identical to b_B for hA interactions since the interactions are asymmetrical and the cms undetermined. The asymmetry of hA interactions requires separate calculations for b_F and b_B. Their behavior is expected to differ.

In a multiple collision scenario, even finding a 'zero' point for which the b_F and b_B are equal might only give an effective cms. Thus FBC slopes cannot be expressed generically as

$$b = \frac{cov(N_F,N_B)}{\sqrt{var(N_F)var(N_B)}}$$

$$= \frac{\langle (N_F - \langle N_F \rangle)(N_B - \langle N_B \rangle) \rangle}{\sqrt{\langle (N_F - \langle N_F \rangle)^2 (N_B - \langle N_B \rangle)^2 \rangle}}$$

The most straight forward way to determine b_B and b_F is to perform least squares, straight-line fits to average multiplicity data for one hemisphere as a function of the *other* hemisphere's multiplicity to determine slopes b_B in the relation

$$\langle N_B(N_F) \rangle = b_B N_F + a_B$$

and slopes b_F in the relation

$$\langle N_F(N_B) \rangle = b_F N_B + a_F$$

Though the backward multiplicity N_B is not exactly linear as a function of N_F, its role as a function of forward multiplicity N_F can be described approximately as a linear function. **Figure 3.6.1** shows how linear the function really is. Similarly, N_F can be described approximately as a linear function of N_B. This function is shown in **Figure 3.6.2.**

Slopes b_B and b_F can alternatively be calculated in terms of forward and backward variances and covariances:

$$b_B = \frac{\langle N_F N_B \rangle - \langle N_F \rangle \langle N_B \rangle}{\langle N_F^2 \rangle - \langle N_F \rangle^2} = \frac{cov(N_F, N_B)}{var(N_F)}$$

$$b_F = \frac{\langle N_F N_B \rangle - \langle N_F \rangle \langle N_B \rangle}{\langle N_B^2 \rangle - \langle N_B \rangle^2} = \frac{cov(N_F, N_B)}{var(N_B)}$$

Slopes b_B and b_F have been determined in this study using both methods and have proved to be interchangeable, differing by amounts well within their error bars. In this study the linear fit method is preferred, particularly when conducted in limited rapidity windows.

The sensitivity of FBCs to long range effects can be illustrated in terms of its intimate relation with NBD parameters. In the absence of dynamical effects, the NBD fit parameter k and FBC parameter b_B are related through the forward and backward average multiplicities [Carruthers 85]:

$$b_B = \langle N_B \rangle / (k + \langle N_F \rangle)$$

Long-range effects are indicated when the NBD estimate of FBC slopes above is different from observed slopes. Only when no long- range effects are present is the NBD calculation valid as an estimate of the the FBC slopes. Results from the E597 hA data show that the observed slopes are significantly lower than NBD estimates predict in the absence of long-range effects. In fact, the overall behavior of the NBD estimate and the actual fitted slope as a function of y_{cut} differs markedly as seen in **Figure 3.6.3.** This difference is expected when particles are produced in clusters [Carruthers 85].

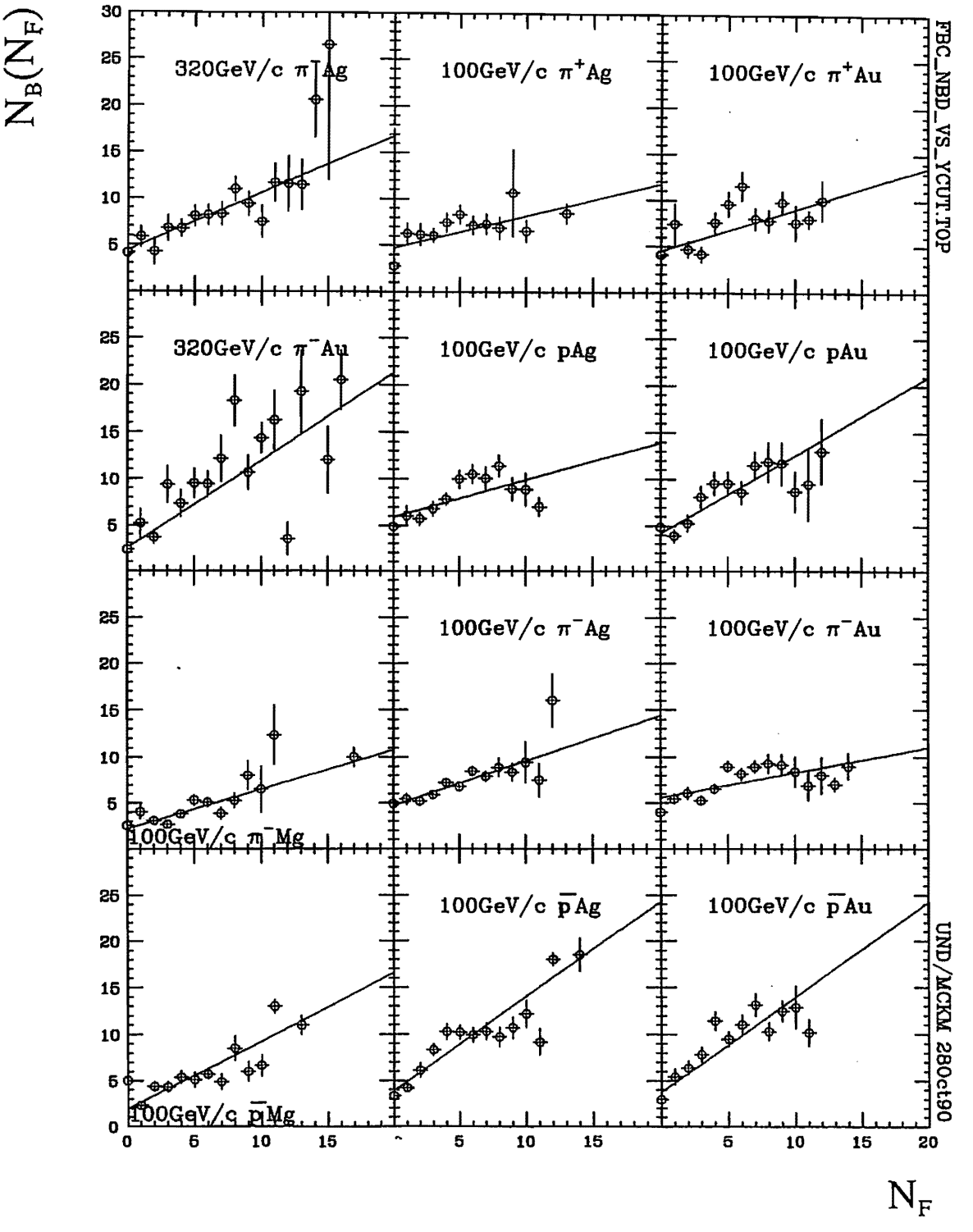

Figure 3.6.1 The backward charged produced multiplicity N_B as a function of the forward charged produced multiplicity N_F in a rapidity window 6 units wide (nearly full phase space). y_{cut} is the half-width of the limited rapidity region centered about the hp cms.

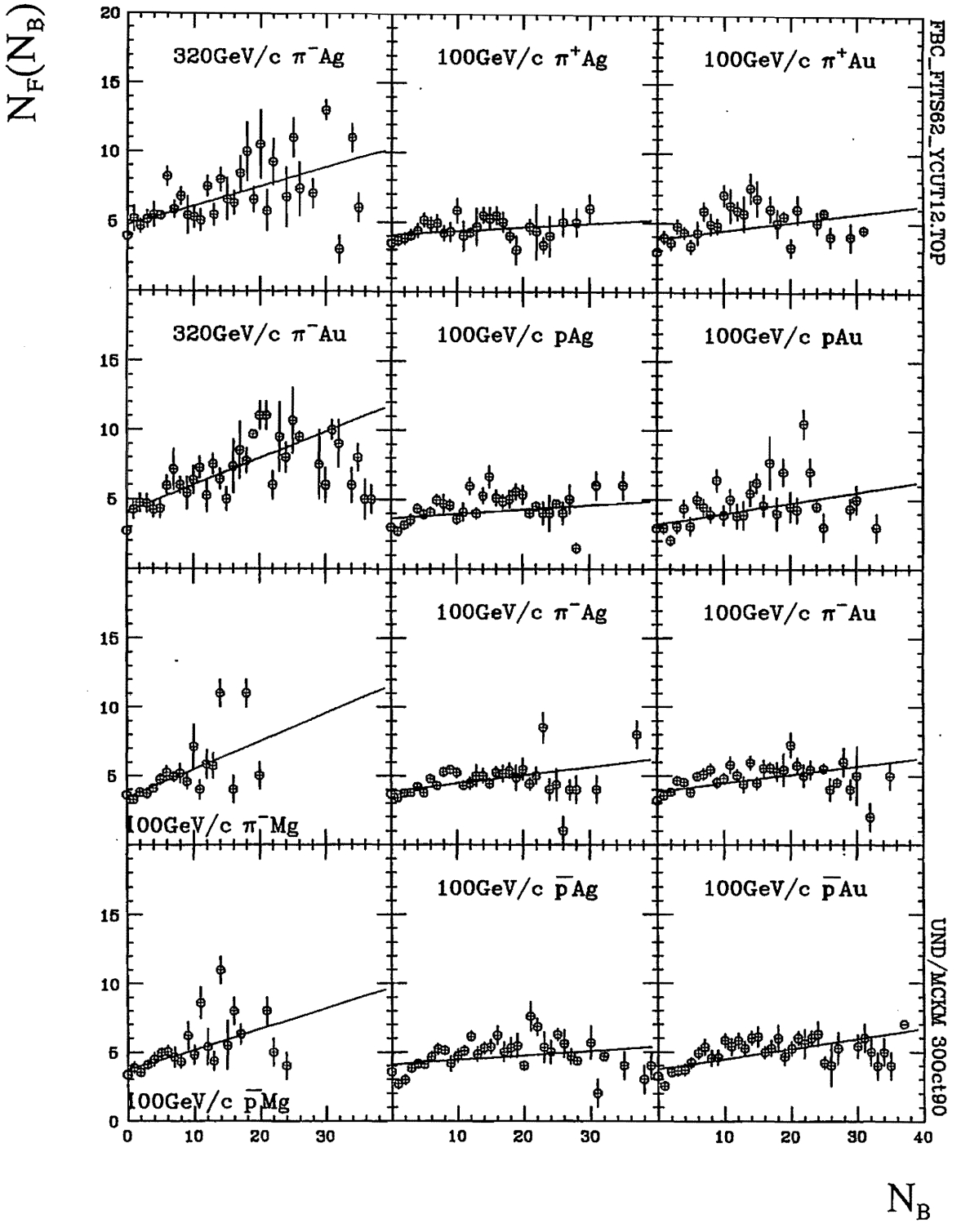

Figure 3.6.2 The forward charged produced multiplicity N_F as a function of the backward charged produced multiplicity N_B in a rapidity window 6 units wide (nearly full phase space). y_{cut} is the half-width of the limited rapidity region centered about the hp cms.

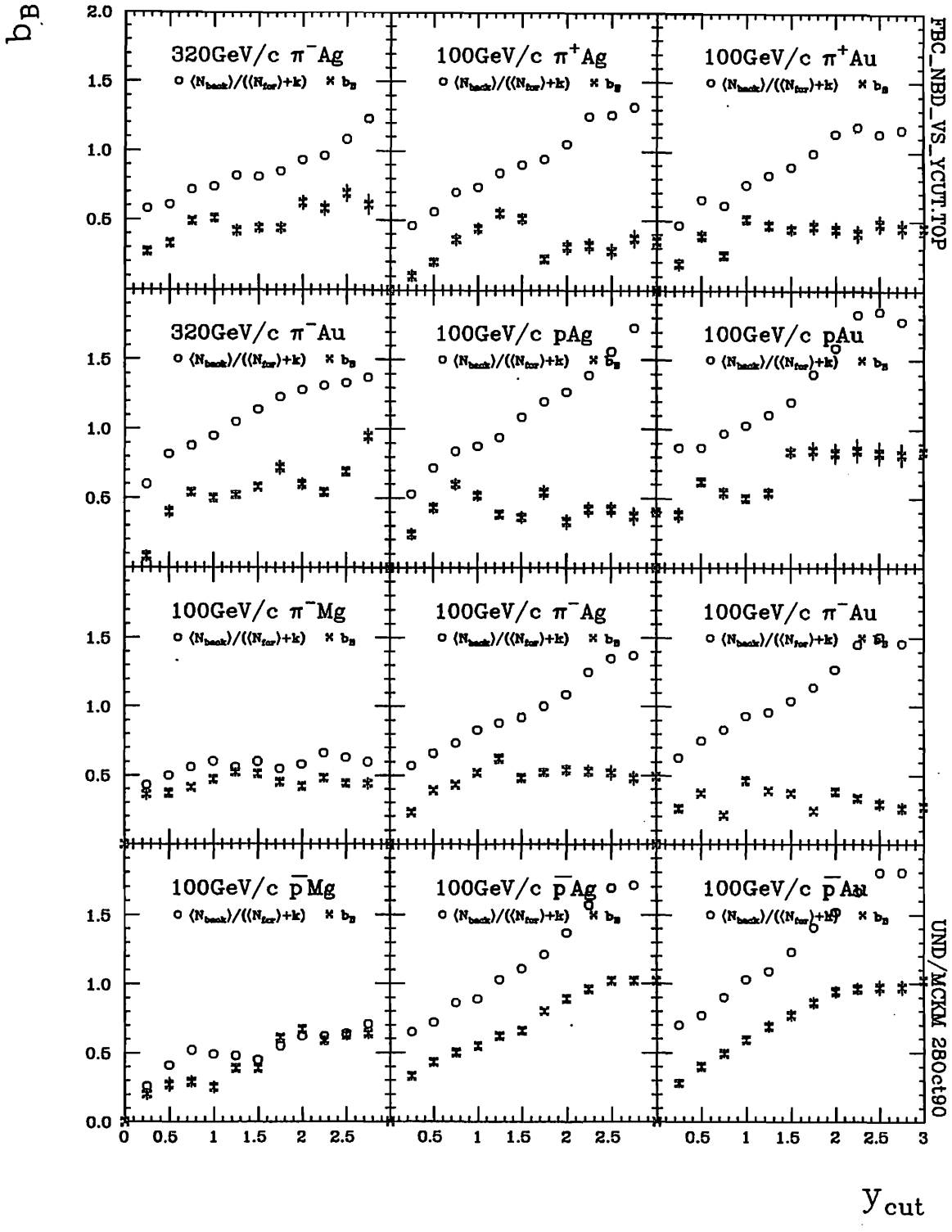

Figure 3.6.3 A comparison of FBC slopes b_B as a function of y_{cut} and the NBD predictions in the absence of long range effects.

3.6.2 Energy dependence

Tenable models should pass tests of energy dependence. Thus hh interaction models should account for a strong increase in the FBC slope b between ISR (63 GeV) [Uhlig 78] and SPS (640 GeV) [Alpgard 83] energies. The slope increases logarithmically with energy from $\sqrt{s}$=10 to 900 GeV for pp and $p\bar{p}$ [Grassler 87]. FBC slopes for hA interactions also increase with energy as seen in **Figure 3.6.4** where E597 π^- data are shown for two(2) energies and two(2) targets. But this increase is much larger than the increase of FBC slopes b_B in hh interactions summarized in [Aivazyan 88] and reproduced for convenience in **Figure 3.6.5**. Successful models should account for this marked difference in energy dependence between hh and hA interactions.

It has been pointed out that e^+e^- interactions exhibit weaker FBC correlations than ℓh interactions, which in turn have weaker correlations than hh interactions [Kittel 87a]. Thus it might be expected that hh interactions show weaker correlations than hA interactions and that hA interactions with smaller A show weaker correlations than those with larger A. Correlations are indeed stronger for hA than for hh interactions. **Figure 3.6.4** also suggests that the correlations involving heavier nuclei are smaller than those involving lighter nuclei. But it is not clear that correlations are generally smaller for heavier nuclei. A comparison of E597 data for identical beams and varying targets shows that only positive beam interactions consistently develop correlations which are clearly stronger in Au interactions than in Ag interactions:

$$b_B^{\pi^+ Ag} = .25(.05) \qquad b_B^{pAg} = .42(.06)$$
$$b_B^{\pi^+ Au} = .44(.07) \qquad b_B^{pAu} = .83(.09)$$

The negative beam interactions do not consistently show this same trend. In fact, for π^- interactions, the correlations are stronger for Ag than for Au interactions, a clearly opposite trend. Thus the A dependence of b_{back} is cannot be conclusively determined.

3.6.3 Central production

Figure 3.6.6(a) shows FBC slopes for charged produced particles in central regions

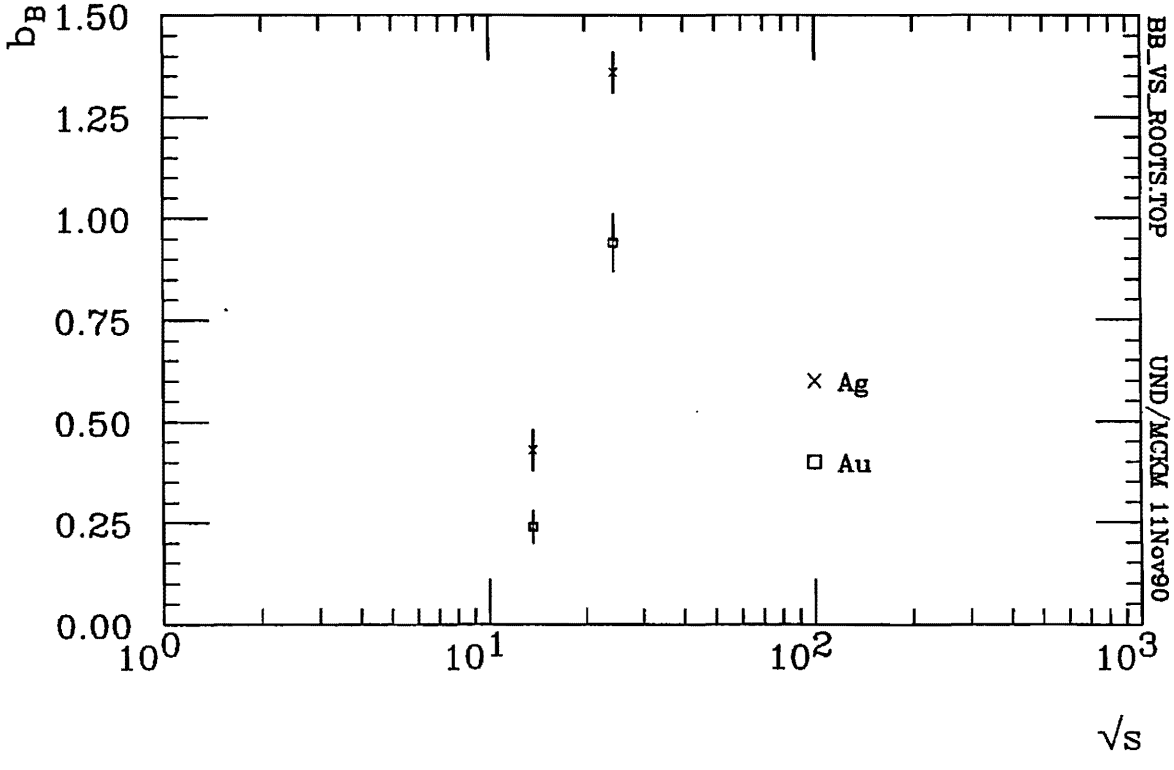

Figure 3.6.4 The energy dependence of FBC slopes for $\pi^- A$ interactions. $\sqrt{s}$ is calculated assuming one(1) hp collision.

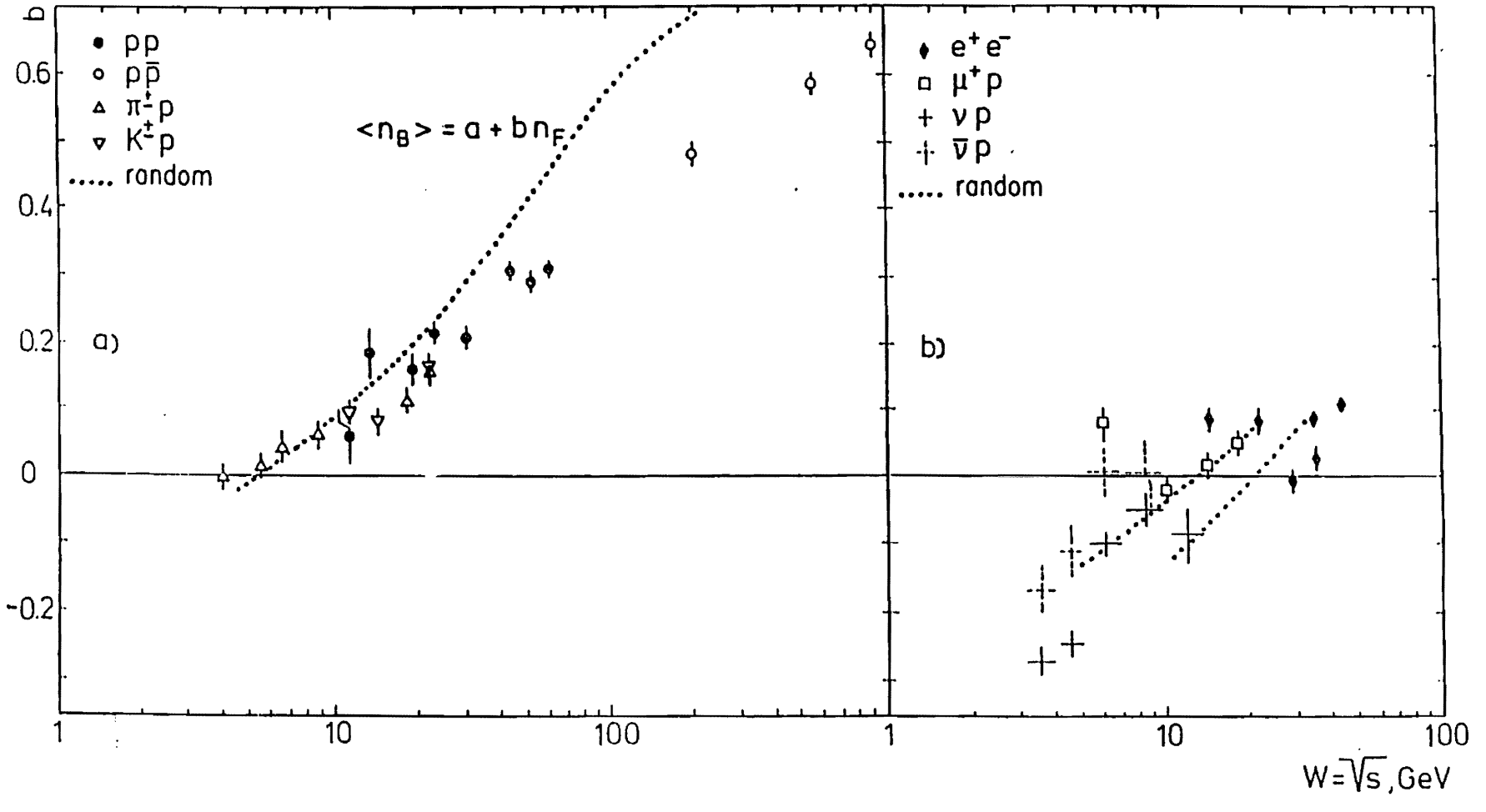

Figure 3.6.5 FBC slopes b as a function of cms energy for a) hh collisions, and b) for e^+e^- and ℓN collisions. The dotted lines correspond to the expectation from the energy dependence of NBD parameter 1/k under the assumption of random partitioning. Reproduced from [Aivazyan 88].

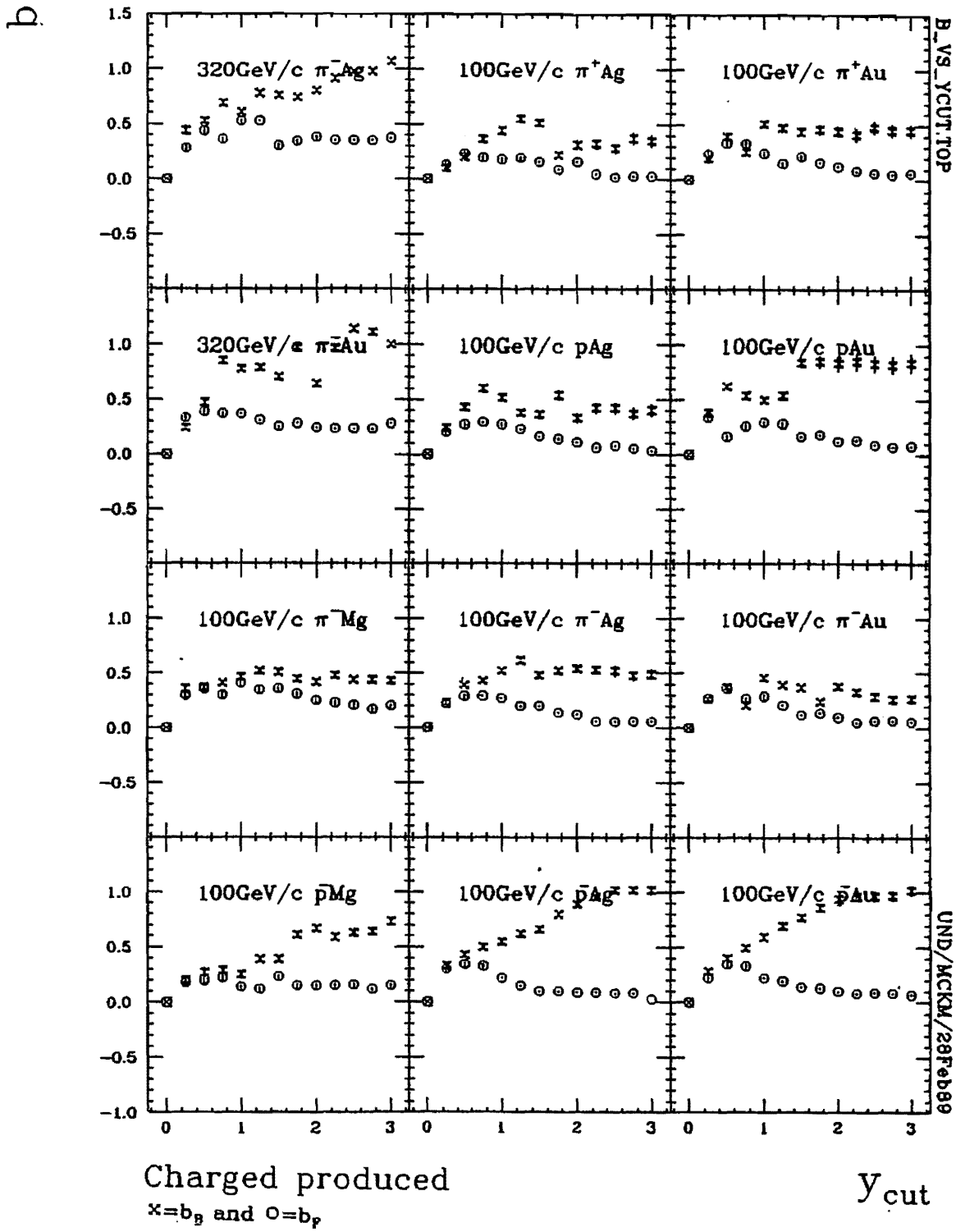

Figure 3.6.6 FBC slopes for limited central regions of rapidity half-width y_{cut} centered about the lab rapidity of the hp cms for a) charged produced, b) negative produced, c) positive produced, d) negative/forward with positive/backward produced, and e) positive/forward with negative/backward produced particles.

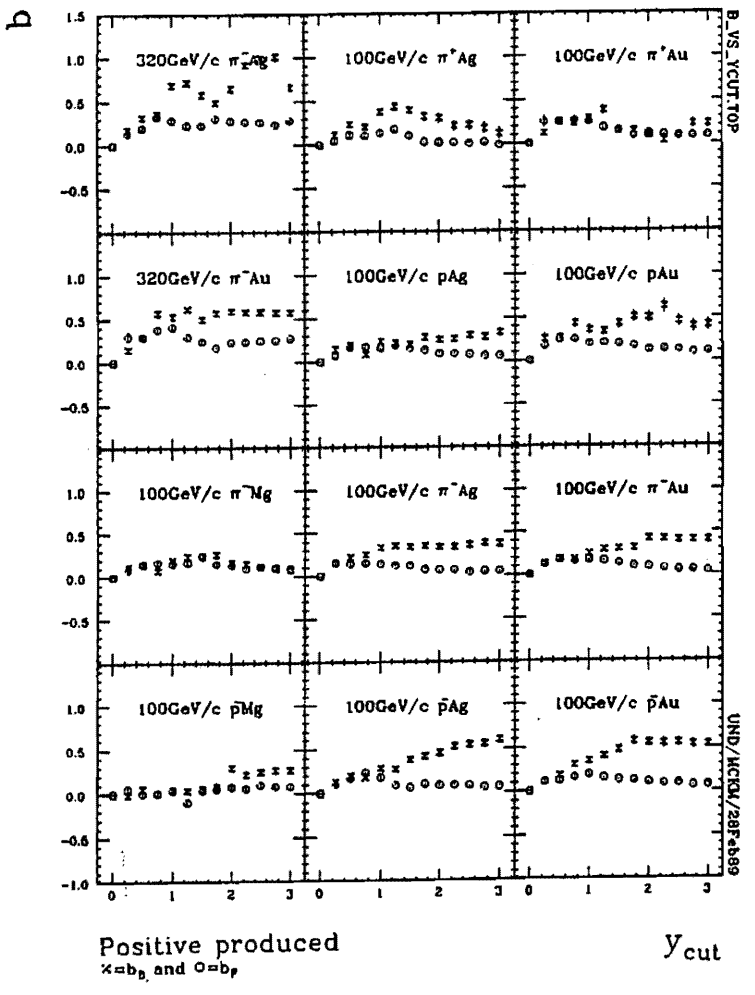

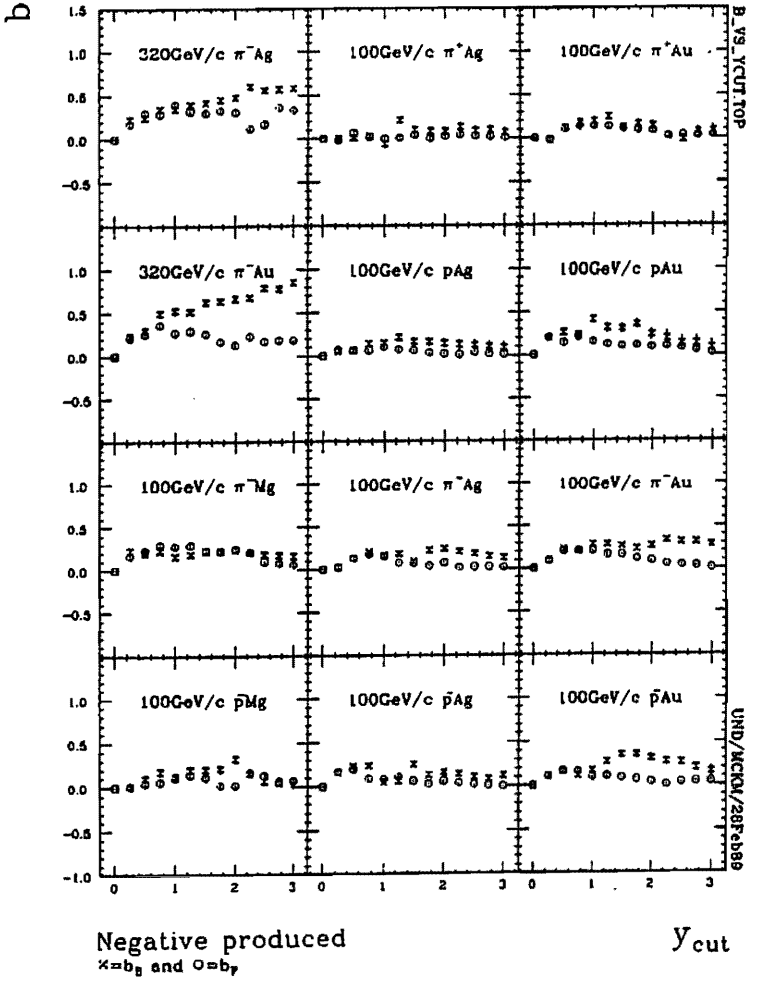

Figure 3.6.6 Continued.

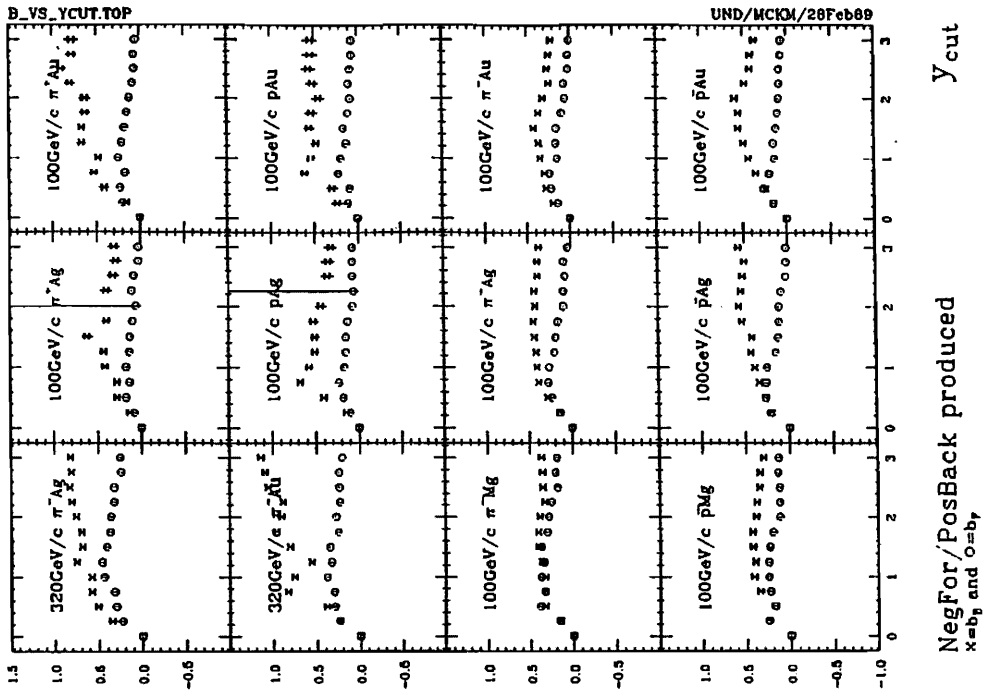

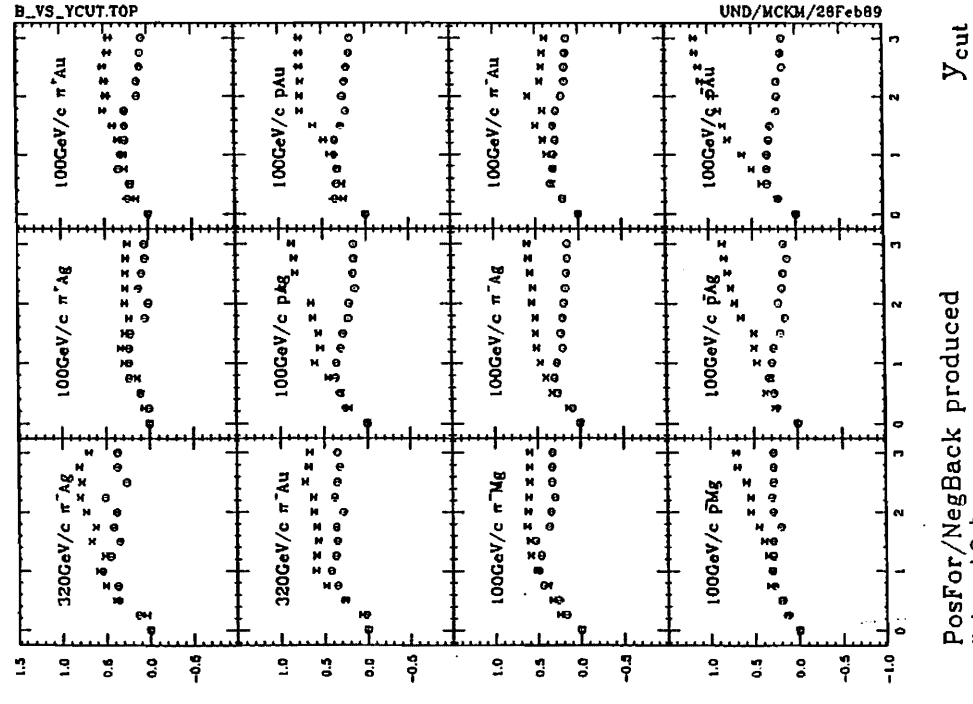

Figure 3.6.6 Continued.

of varying width as a function of half-widths y_{cut}. These regions are centered about the hp cms for each interaction. In most 100 GeV/c interactions (excluding the $\bar{p}A$ interactions), b_B increases up to $y_{cut} = 1$ and then levels off (for y_{cut} distances of up to 2 units rapidity) with a slight decrease as y_{cut} approaches the kinematic limit. Because of this plateau-like behavior, b_B for hA interactions is much higher than for hh interactions in comparable rapidity regions of half-width greater than 1. The steady retention of a correlation beyond $y_{cut} = 1$ contrasts with observed π^+p and pp results [Aivazyan 88] which do not feature any kind of plateau in the correlation slope. Having reached maximum at $y_{cut} \sim 1$, b_B for these hh interactions immediately decreases to its $y_{cut} = .25$ value by $y_{cut} = 3$.

Though hh and hA interactions differ on specific aspects of FBC behavior, results from π^+p, K^+p, and pp interactions [Aivazyan 88] corroborate E597's observation that negative-negative FBCs are in general much smaller than charged-charged FBCs. They also corroborate the observation that the largest correlations are attributable to centrally produced particles. Both hh and hA interaction results show FBC strongest for rapidity regions of half-width $y_{cut} = 1$ centered about the hp cms. With b_B increasing directly to a maximum near $y_{cut} = 1$, FBC must be be associated with central production.

Now the central production region in hh interactions is centered about $y_{cms} = 0$ with a full-width of 2 units. One supposes that the central production region in hA interactions is centered about the hp cms with a full-width of about 2 units also since maximum FBCs are achieved in regions of this width. Whether or not the hp cms is a valid center for the central region, however, can be investigated by sliding a rapidity window 2 units wide along the full rapidity span and plotting the FBC slope as a function of the rapidity window center y_{zero}. **Figure 3.6.7(a)** displays FBC slopes for negative/forward with positive/backward charged produced secondaries. The maxima of all b_B curves occur near the hp cms rapidity so FBCs can be reasonably associated with 2 unit rapidity windows centered at the hp cms. Closer inspection reveals, however, that though these maxima occur near the hp cms rapidity, they are all at rapidities less than the hp cms rapidity. This suggests that

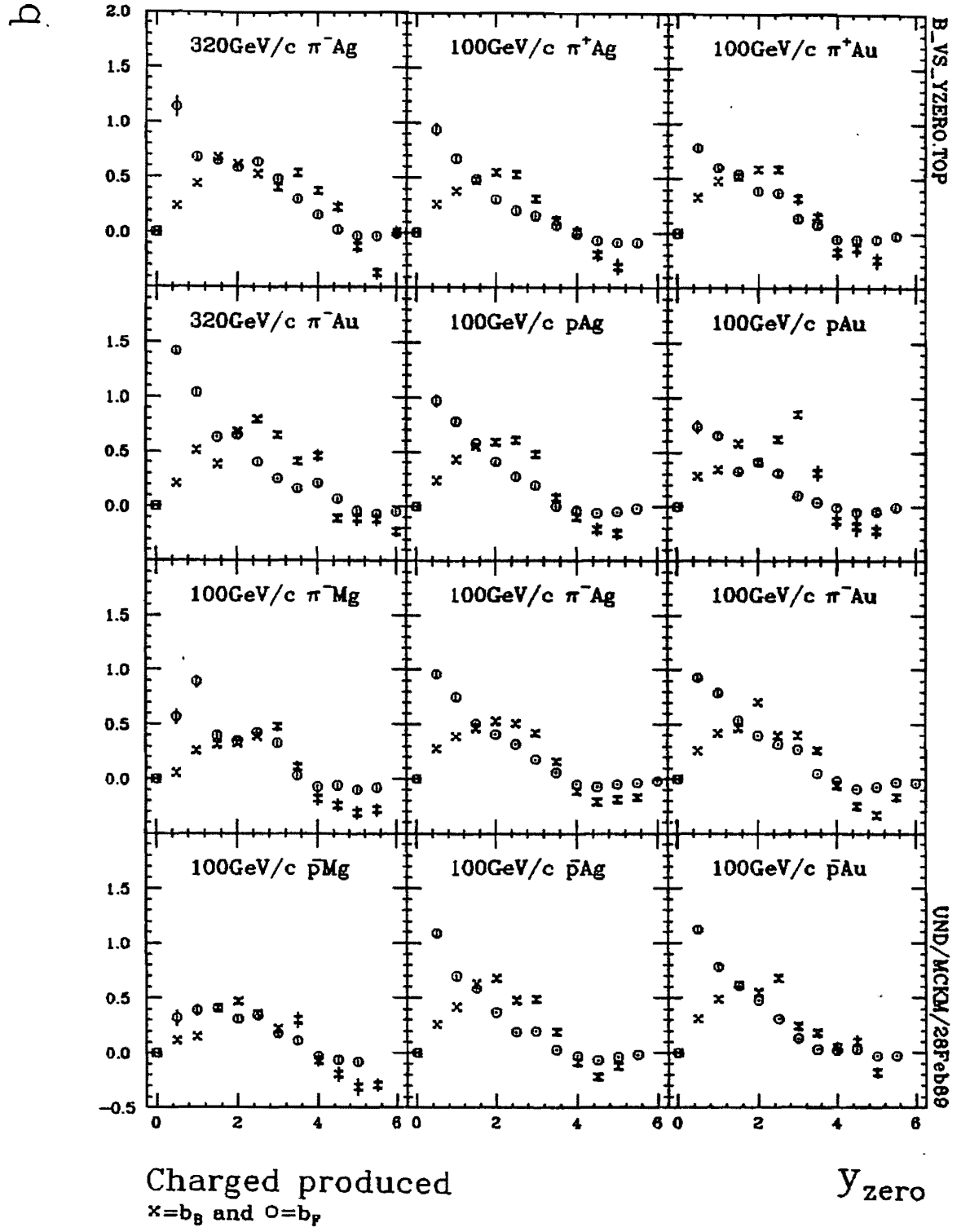

Figure 3.6.7 FBC slopes for limited central regions of rapidity half-width 1 unit centered about the rapidity y_{zero} for a) charged produced, b) negative produced, c) positive produced, d) negative/forward with positive/backward produced, and e) positive/forward with negative/backward produced particles.

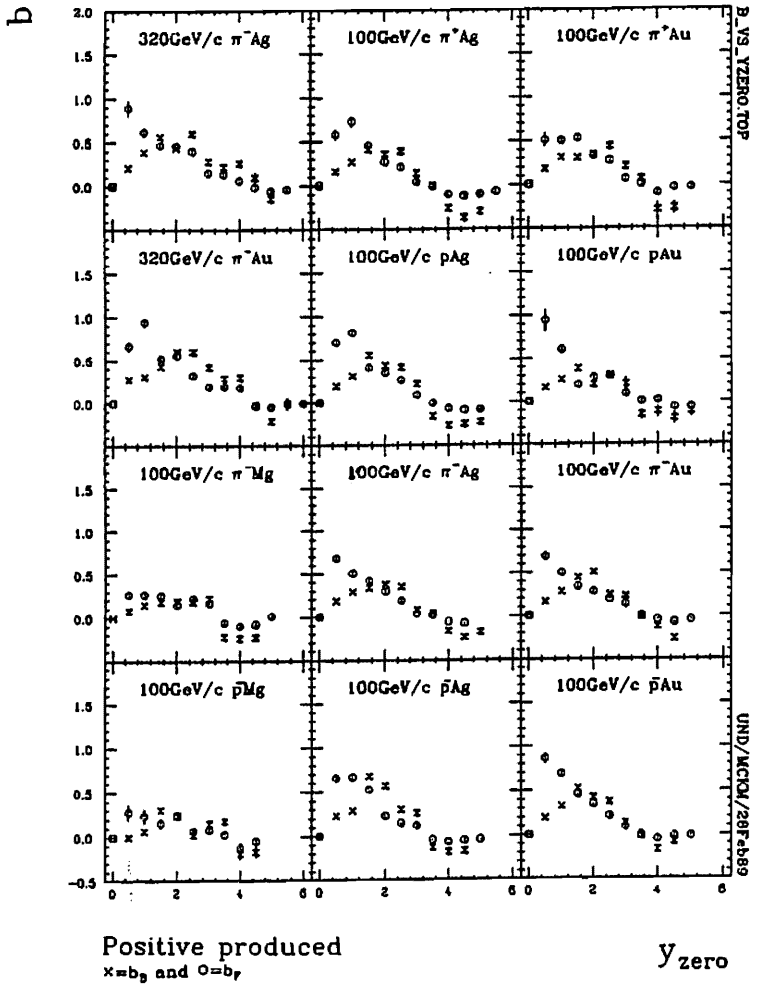

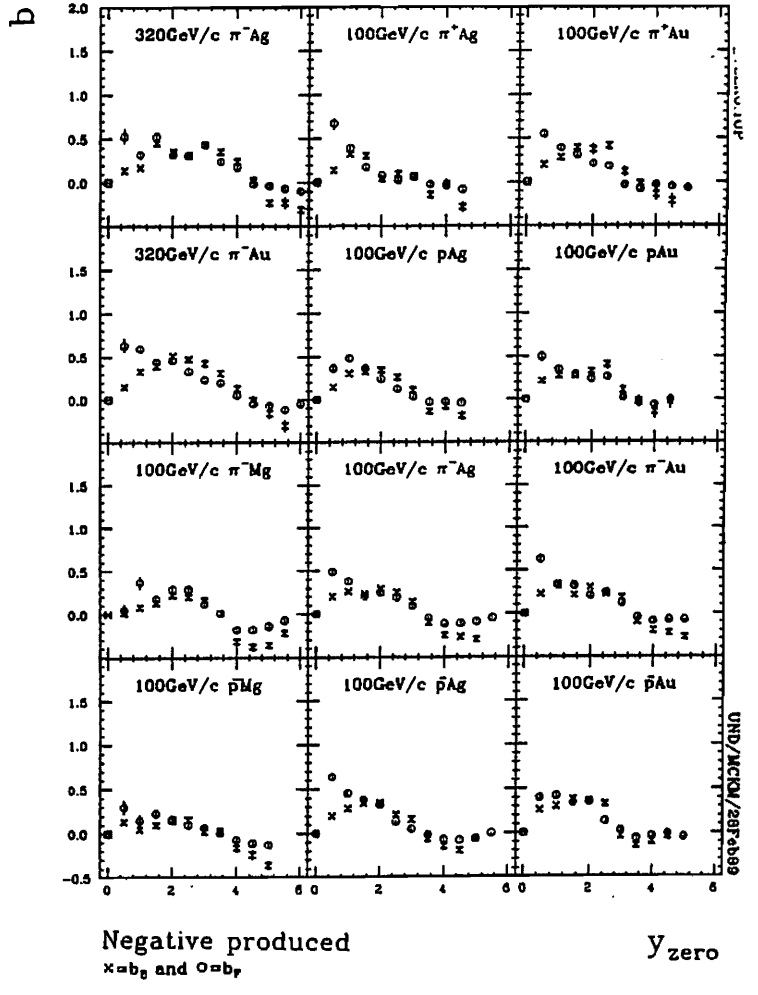

Figure 3.6.7 Continued.

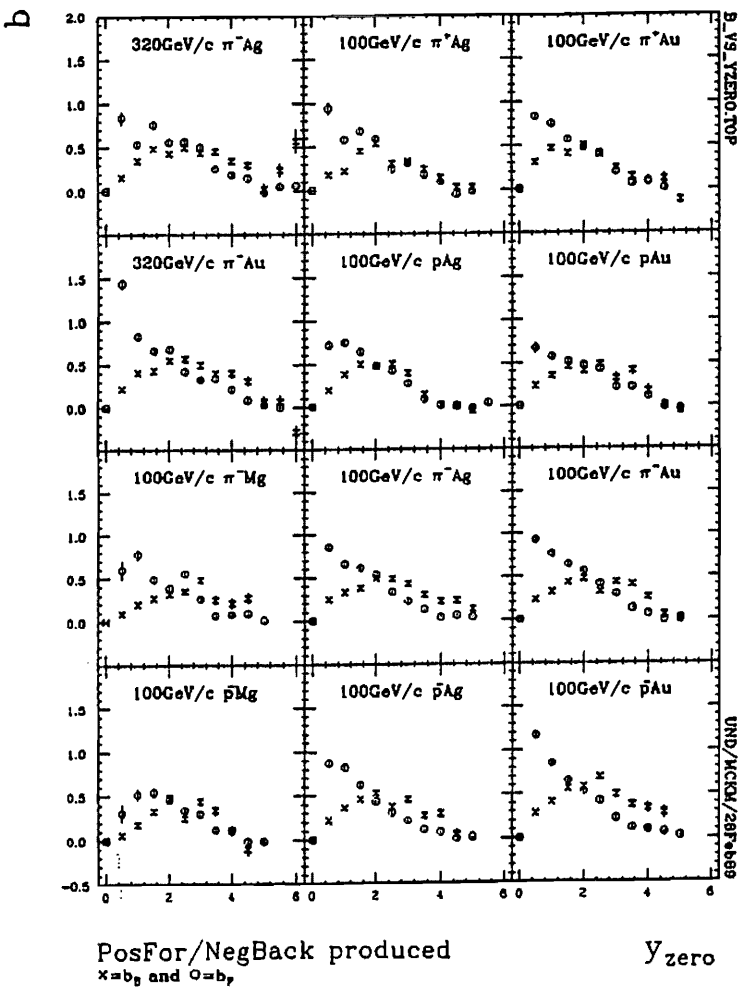

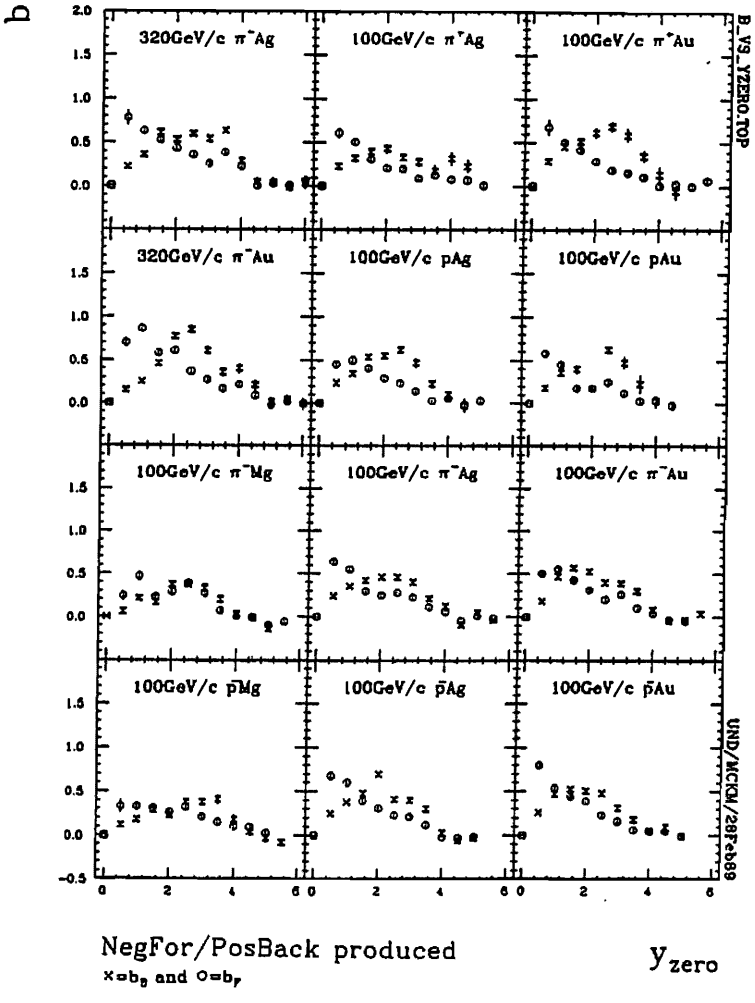

Figure 3.6.7 Continued.

the effective cms rapidity is less than the hp cms rapidity. This is consistent with a multiple collision viewpoint which necessarily proposes a smaller cms rapidity.

Now an effective cms rapidity approximates the cms rapidity for a comparable symmetric interaction (for which $b_B = b_F$). So the intersection point between the b_B and b_F curves approximates the effective cms rapidity. Indeed the intersection point coincides approximately with the b_B maxima for positive/forward with negative/backward produced particles and thus confirms the conclusion that the effective cms rapidity is slightly smaller than the hp cms rapidity. In the charge/hemisphere combinations for which FBC is not as strong, the intersection point is shifted to even lower values of rapidity, **Figure 3.6.7(b)-(e)**.

In agreement with ISR and SPS $p\bar{p}$ results, E597 $\bar{p}A$ results are consistent with the conclusion that FBC correlations emanate from the central region. However some unusual behavior occurs in that region. The correlation b_B increases smoothly and steadily right up to the phase space limit rather than leveling off as in other hA interactions. This unique trend is noted not only for charged-charged FBCs shown in **Figure 3.6.6(a)** but particularly for positive forward-negative backward FBCs in **Figure 3.6.6(e)**. It is absent or considerably diminished for negative-negative and positive-positive FBCs in **Figures 3.6.6(b)** and **(c)** and negative forward-positive backward FBCs in **Figures 3.6.6(d)**. Evidently an especially strong correlation exists between forward positives and backward negatives. This correlation cannot be a leading particle effect since it occurs for positive forward secondaries from a negative beam interaction. But it does show some A dependence, with the Au interactions achieving the largest FBCs ($b_B > 1$); Ag interactions, the second largest; and Mg interactions, the third largest.

3.6.4 Multiple scattering terms

Any model which ascribes short range correlations to single inelastic collisions attributes long range correlations to multiple-scattering terms. Thus when long range correlations are found, they discriminate between different types of multiple scattering models. Some hh [Fialkowski 82; Capella 83] and hA [Capella 84] results agree

with DTU descriptions. However, a dramatic decrease in b as a function of gap width, seen in hh interactions at ISR and SPS was not expected *a priori* and has far reaching physical consequences. Multiple scattering models which distribute available energy equally among an event's ν inelastic collisions, cannot account for this decrease since it implies multiple collision contributions at rapidities beyond where correlations cease. Models like FRITIOF and DPM approximate this decrease quite well.

Since both short and long range correlations occur in the same rapidity windows, a rapidity gap may be introduced between the forward and the backward regions to eliminate short range effects. Minimum rapidity gaps of 2 units are introduced since 2 units is the full width of the hp central region. By comparison, NBD clusters are approximately 4 units wide in rapidity, so these gaps will not eliminate NBD cluster contributions for $y_{cut} = 1 - 2$. But the gaps will eliminate contributions from resonance production since the relative momentum of resonance decay products (particularly of light resonances) is small compared to the relative momenta of uncorrelated pairs simultaneously emitted into either region.

In **Figure 3.6.8(a)-(e)**, the FBC slopes are shown for regions separated by gaps with half-widths y_{cut} centered at the hp cms. b_B not only shows a dramatic decrease within the first few gap increments but takes on negative values and a minimum. Before the total width of the gap reaches 1 unit rapidity, the long range correlation is gone and an anticorrelation begins to build. The maximum anticorrelation is as large as the maximum correlation in the central regions and generally occurs for the 100 GeV/c samples when the gap has a half-width of about 1.5 units. This behavior is seen in all charge modes.

The initial plunging trend of the FBC slope b_B with increasing gap width is in agreement with results from π^+p and pp interaction data [Aivazyan 88]. They both plunge into negative values as the gap widens. However, there are some major differences. Anticorrelations in hA interactions persist beyond $y_{cut} = 1.5$ whereas they disappear in hp interactions at $y_{cut} = 1.5$ beyond which a positive correlation peak centered around $y_{cut} \sim 2.5$ builds up. Also the marked differences between

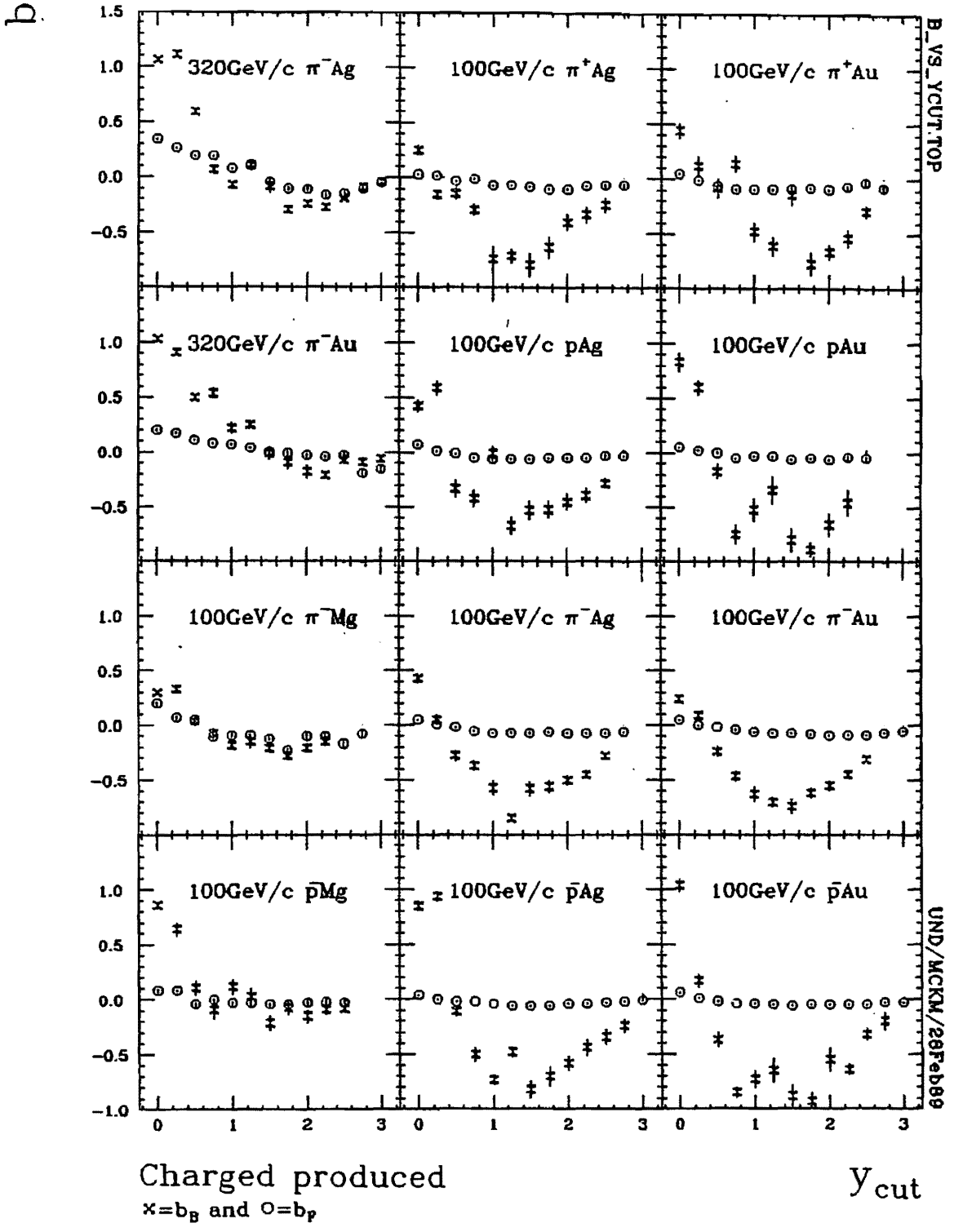

Figure 3.6.8 FBC slopes in limited rapidity regions separated by gaps of half-width y_{cut} centered about the lab rapidity of the hp cms for a) charged produced, b) negative produced, c) positive produced, d) negative/forward with positive/backward produced, and e) positive/forward with negative/backward produced particles.

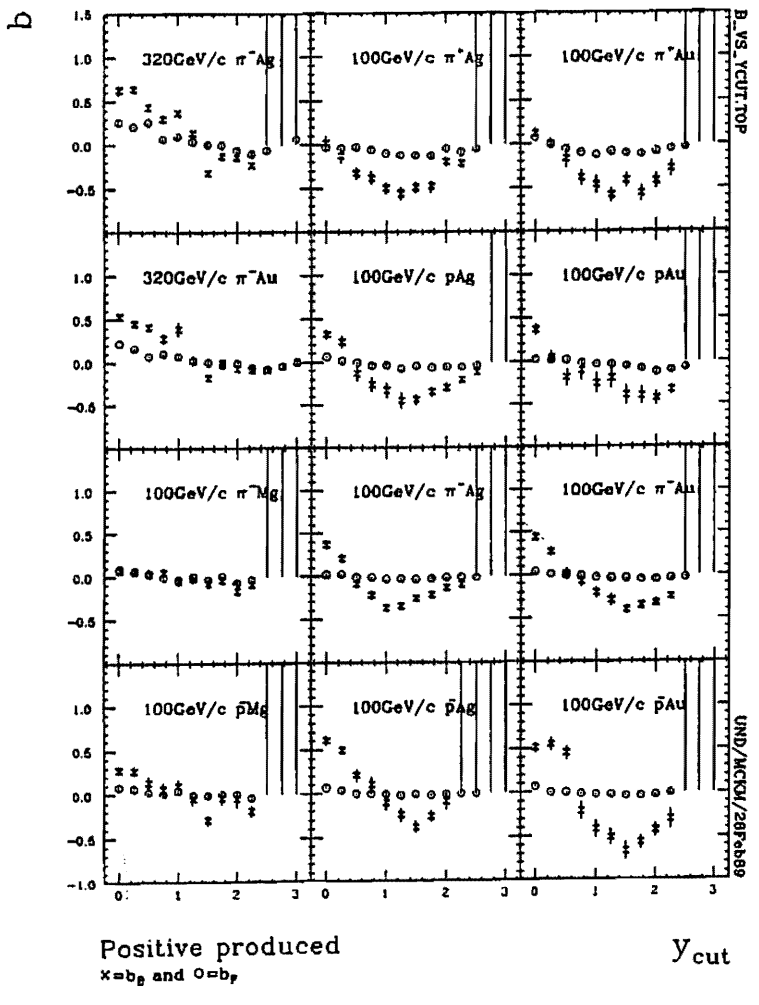

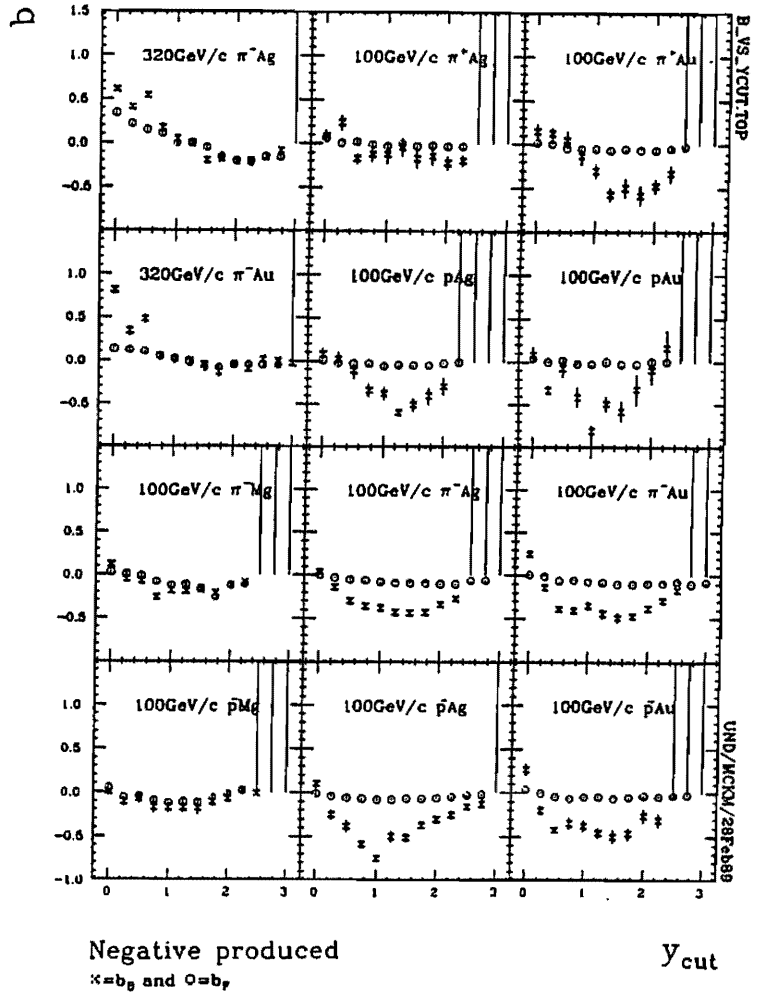

Figure 3.6.8 Continued.

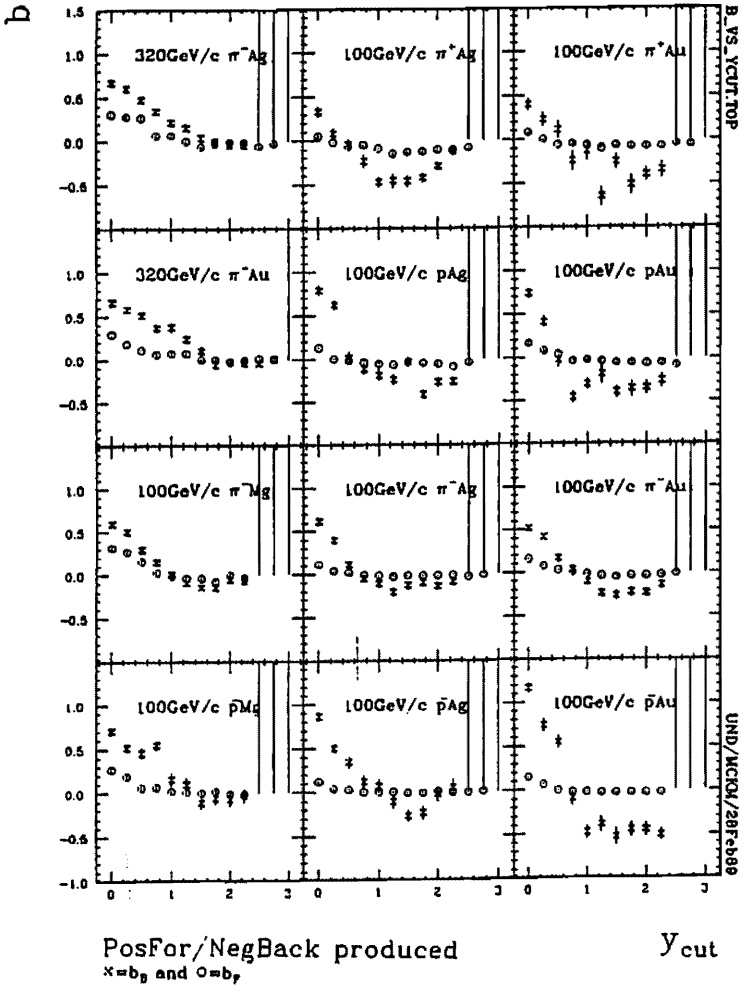

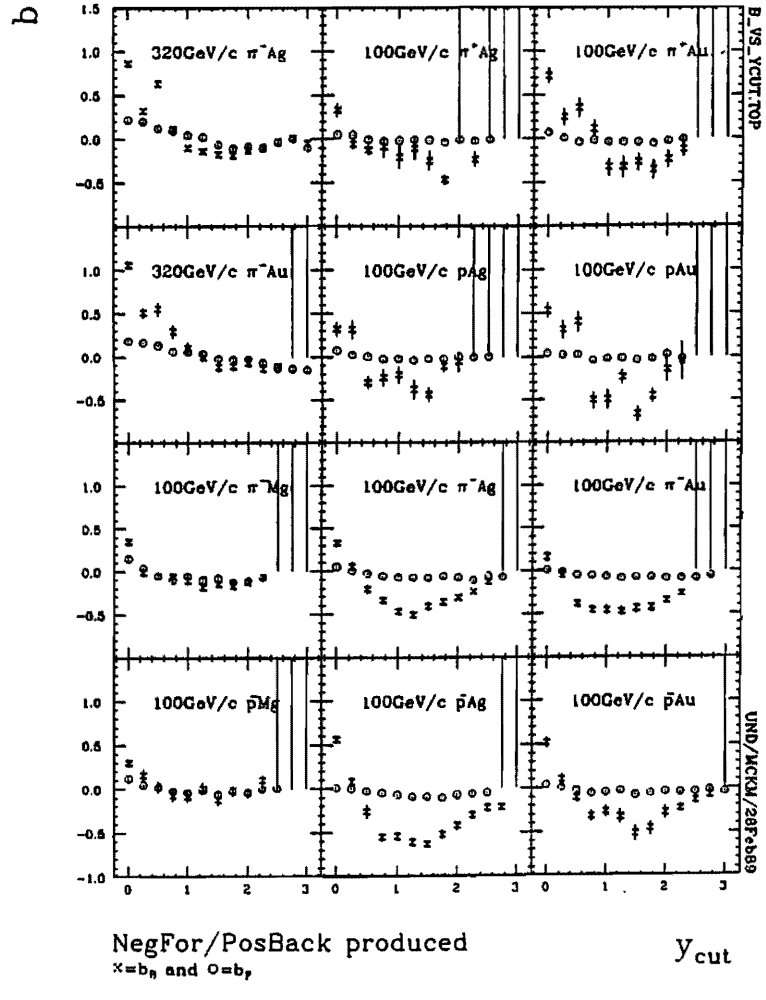

Figure 3.6.8 Continued.

charged-charged and negative-negative mode results in hp results are not found in hA results.

From a DPM viewpoint, $q\bar{q}$ chains are much shorter in rapidity than the available rapidity length, so FBC slopes decrease with increasing gap size. In this way multichain DPM models successfully account for dramatic decreases in b_B [Capella 82e]. The same basic interpretation of decreasing b_B with increasing gap size holds for any multiple scattering model as long as particles are produced in single collisions with short ranges of rapidity, and multiple scatters with long ranges of rapidity. However, the degree to which b_B actually decreases is unexpected in standard multiple-scattering models. The dramatic decrease cannot be accounted for by multiple scattering which distributes available energy equally among various inelastic collisions.

3.6.5 $\bar{\nu}$ dependency

The exact dynamical origins of FBC correlations are not understood. Thus the fact that e^+e^- [Althoff 85a; Derrick 86], ℓh (μp [Arneodo 85], νp and $\bar{\nu}$p [Grassler 83]) data show no FBC effects comparable to those found in hh and hA data may in itself be helpful. Since none of these $\nu = 1$ interactions show FBC effects, and since all $\nu > 1$ interactions do show FBC effects, it is likely that $\bar{\nu}$ dependencies will surface in hA interactions. Wounded nucleon models [Nikolaev 81] have contributions to FBC only from the first collisions. Therefore, if $\bar{\nu}$ dependencies can be found for FBC effects, these models can be ruled out. If only the first collision contributes to FBC, FBC characteristics would be similar for hh and hA interactions. Since it is already known that FBC characteristics differ between hh and hA interactions, it is expected that a one collision contribution to FBC is not adequate to explain FBCs as observed and that FBCs increase with increasing $\bar{\nu}$.

Now for hh interactions in general, the width of rapidity distributions decreases with increasing fixed multiplicity. This narrowing increases the central height with little effect at large y, so large multiplicities are associated either with large average numbers of $q\bar{q}$ sea chains (in DPM) or with large average numbers of collisions (in

standard multiple scattering models). Since multiplicities have already been shown to be $\bar{\nu}$ dependent, FBC effects in both model viewpoints can be studied in terms of $\bar{\nu}$, *i.e.* in the context of hA interactions. In the viewpoint of multiple collision models, FBC tests whether forward particle multiplication by consecutive collisions is a valid assumption. Multiple collision models generally account for differences between hh and hA spectra assuming that 1) the first collision is just like an hh, with its characteristic average multiplicity N and dispersion D symmetric in the cms, and that 2) subsequent collisions produce N/2 backward particles and ϵN/2 forward particles where ϵ is small and positive. In addition, a complete description would include cascading and energy degradation in consecutive collisions.

To study FBC as a function of the number of collisions ν, FBCs have been compared on the basis of $\bar{\nu}$ simply by comparing full phase space results from different interactions (different beams and/or targets). NA5 pAr and pXe data [De Marzo 82] have been analyzed in this way and have been compared favorably to predictions from a minimal model [Fialkowksi 86c]. A similar comparison of E597 results for all charged particles in **Figure 3.6.9** suggests that b_B indeed increases with $\bar{\nu}$. This trend is not perceived for negative particles, nor for negatives traveling forward and positives, backward (-+). It is more than marginally perceived for positives. However, the dependence of b_B on $\bar{\nu}$ is strongest and clearest for positives traveling forward and negatives, backward (+-), as seen in **Figure 3.6.10**. Results from πp and pp data have shown that the largest FBC effects are seen in the unlike charge mode [Aivazhan 88].

Closer inspection, however, reveals that the spread of points is not random and is in fact influenced by the target nucleus. Thus the spread can be seen as three(3) approximately parallel sequences of points, each sequence associated with a given target nucleus. Each sequence intercepts the $\bar{\nu}$ axis at larger values as the mass of the nucleus increases. To unify results from all nuclei, $\bar{\nu}$ values for each point may be shifted by some A-dependent amount. Linear regressions of Ag and Au target sequences suggest that an $A^{.2378}$ dependency exists. Visually recognizable alignment

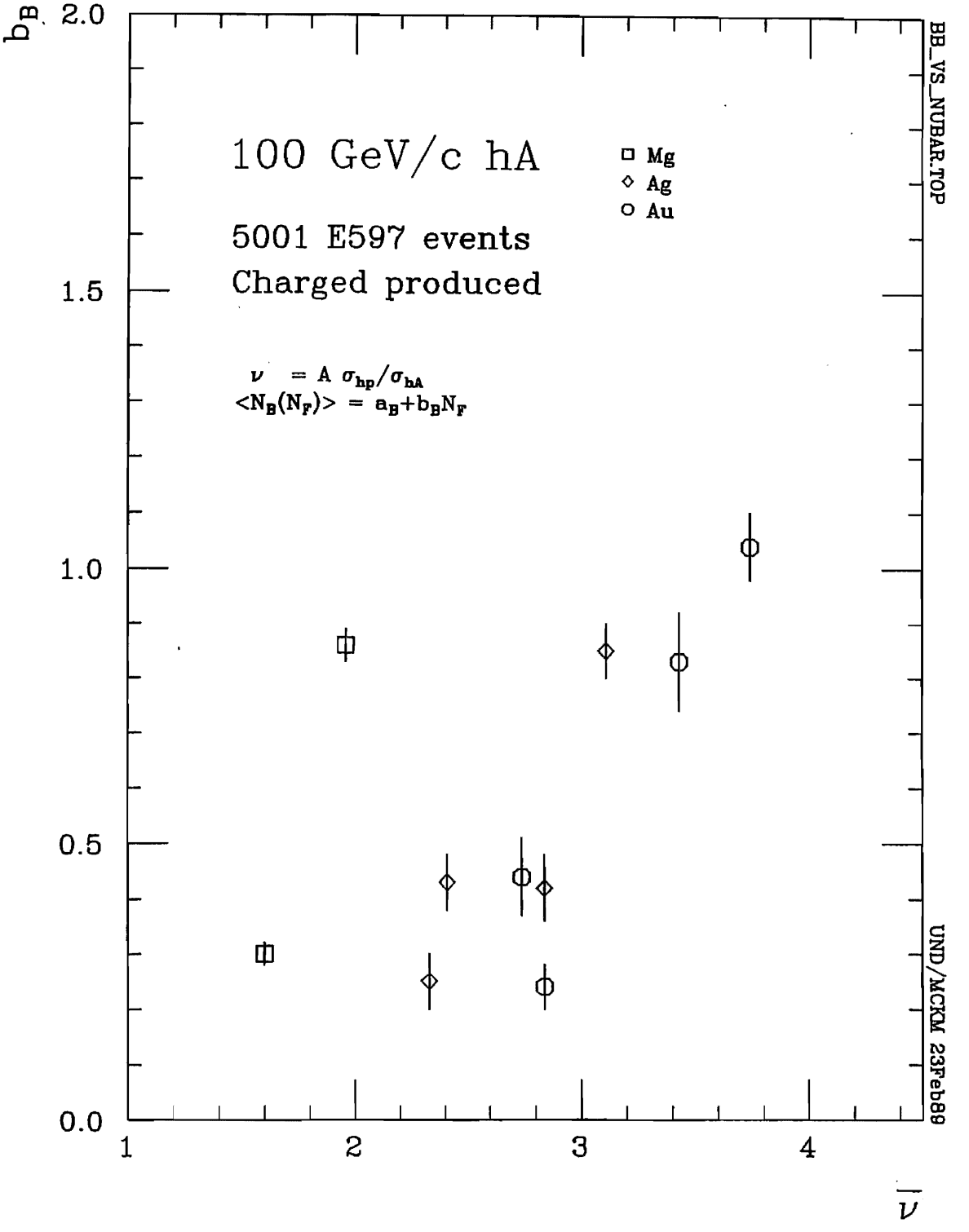

Figure 3.6.9 FBC slopes as a function of the average number of collisions for E597 100 GeV/c hA interactions.

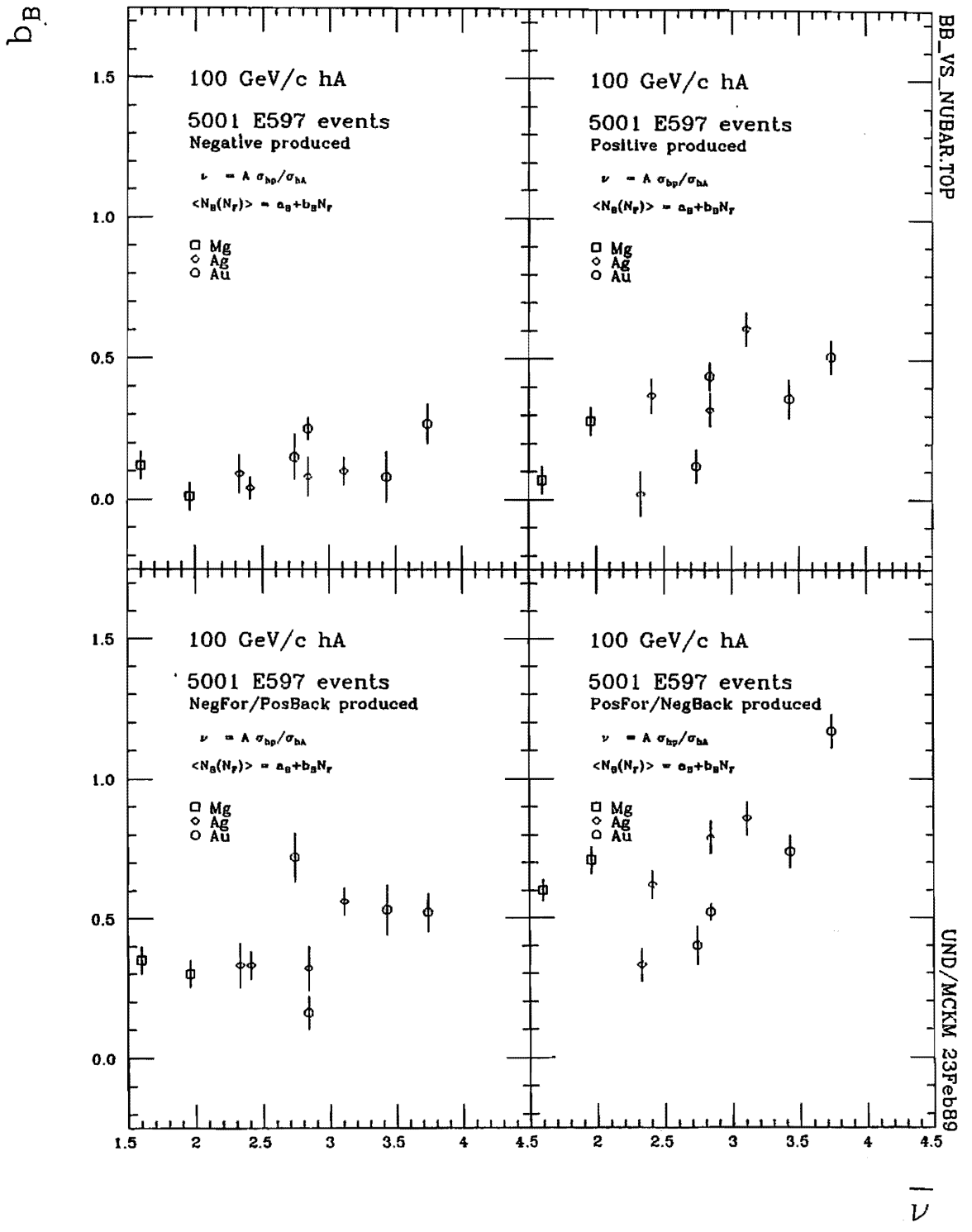

Figure 3.6.10 FBC slopes as a function of the average number of collisions $\bar{\nu}$ for various charge modes: a) negative/forward with negative/backward, b) positive/forward with positive/backward, c) negative/forward with positive/backward, and d) positive/forward with negative/backward.

is achieved between the three(3) target sequences when a shift of

$$\bar{\nu}_{shift} = -A^{.2378} + 2$$

is applied to all hA values of $\bar{\nu}$. This alignment, seen in **Figure 3.6.11**, extrapolates nicely to the pp point inferred from **Figure 3.6.5** and becomes even more marked for positive/forward-negative/ backward correlations.

One explanation for the effectiveness of the shift may be found in $\bar{\nu}Z/A$-dependence rather than $\bar{\nu}$-dependence, where $\bar{\nu}Z/A$ is the number of proton collisions. Plotting the same b_B values as a function of $\bar{\nu}Z/A$ produces a similar if not better degree of alignment, at least for Ag and Au data. Statistically, the significance of the deviation of the Mg data from the Ag and Au data is not only limited by the number of events, but also by lower multiplicities. In this light, the close agreement between the Ag and Au data somewhat justifies entertaining the possibility of proton collision dependencies seriously when interpreting FBC effects.

3.7 SUMMARY

- Produced particle multiplicities are linearly correlated to $\bar{\nu}(hA)$. *Multiple production involves multiple collisions.*

- $\Pi_{hA}(\nu)$ distributions can be calculated geometrically by Monte Carlo. Andersson and Verbeure model predictions of light proton multiplicity probability distributions, based on such $\Pi_{hA}(\nu)$ distributions, are generally consistent with E597 data. *Light proton multiplicity is an indicator of the number of multiple collisions undergone in an interaction.*

- Events with customized cuts on leading particle rapidity and total charged multiplicity are consistent with the Andersson model predictions for single collisions. *Data samples may be enriched for single collision events by applying leading particle rapidity and total charged multiplicity cuts.*

- Andersson model estimates of ν on the basis of N_{lightp} have a smaller dispersion

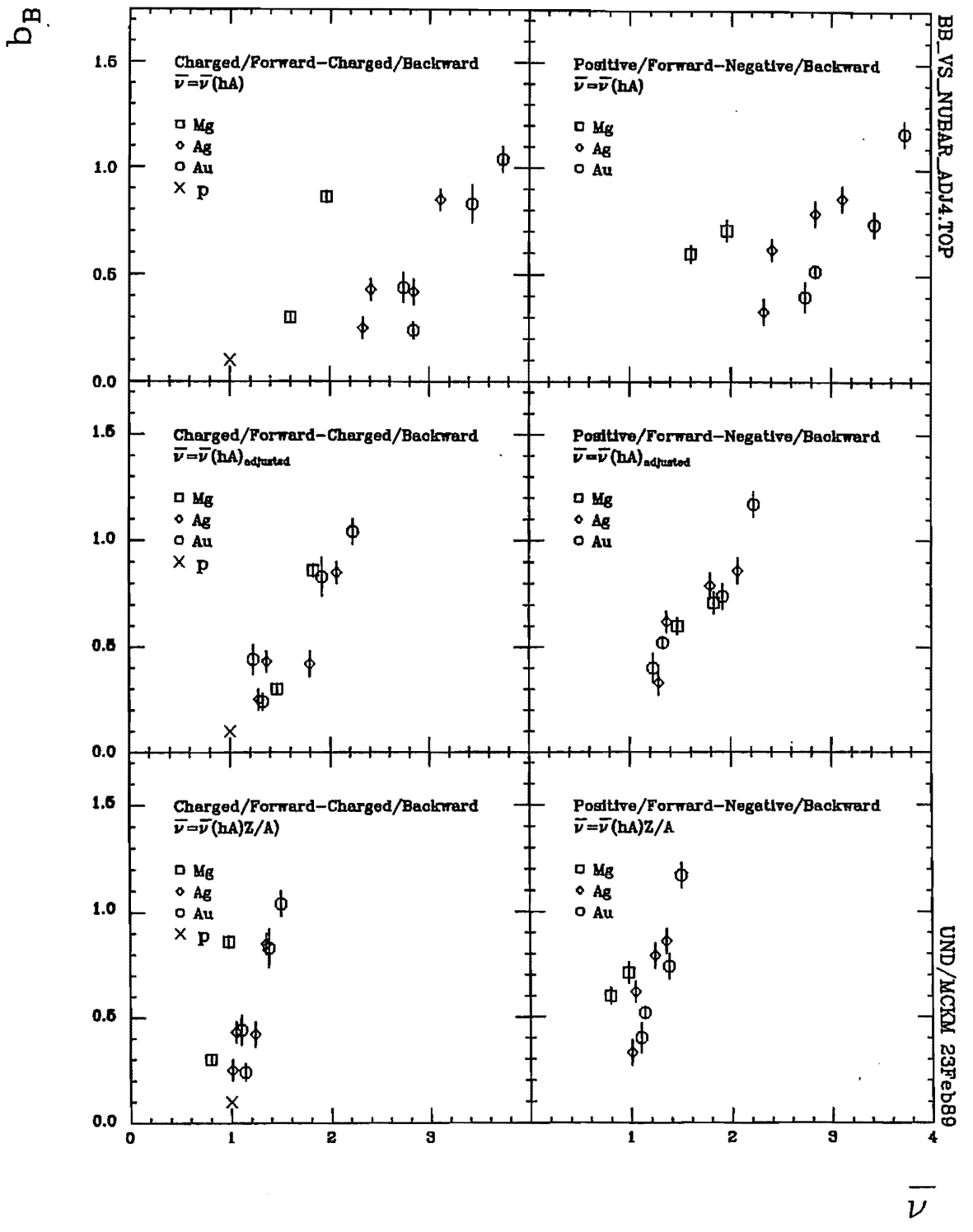

Figure 3.6.11 Adjusted FBC slopes of **Figure 3.6.9** and **Figure 3.6.10** for charge/forward with charge/backward and positive/forward with negative/negative modes as a function of the total number primary collisions $\bar{\nu}$ (top), of an adjusted average number of collisions $\bar{\nu} - A^{.2378} + 2$ (center), and of the number of proton collisions $\bar{\nu}Z/A$ (bottom).

than $\bar{\nu}(hA)$. *$\nu_{Andersson}(N_{lightp})$ is a better measure of the number of multiple collisions than $\bar{\nu}(hA)$.*

- Proton multiplicity distributions can be described adequately by NBD in phase space regions associated with *black*, *grey*, and *light* velocity designations. *Multiple collision models can use NBD parameters to prescribe the way multiple collisions affect slow proton emission.*

- Andersson model estimates of ν on the basis of N_{lightp} are not significantly improved by Verbeure modifications which include the shape of the N_{lightp} distribution (described by NBD parameter k) as well as its average value as parameters. However, a simple approach used by Ledoux et al. estimates ν on the basis of $\sqrt{N_{lightp}}$ and produces a more linear correlation than either Andersson and Verbeure models can between produced particle multiplicity and the number of collisions inferred from N_{lightp}. *$\nu_{Ledoux}(N_{lightp}) = \sqrt{N_{lightp}}$ may be a closer estimate of ν than Andersson and Verbeure estimates.*

- Produced particle multiplicities are not correlated to Andersson and Verbeure estimates of $\bar{\nu}(N_{lightp})$ in the same way that FRITIOF's produced particle multiplicities are correlated to its simulated numbers of collisions. Deviations mainly occur at large ν. Produced particle multiplicities are correlated, however, to Ledoux estimates of $\bar{\nu}(N_{lightp})$ very much like FRITIOF's produced particle multiplicities are correlated to its simulated numbers of collisions. *FRITIOF's simulated events are more consistent with Ledoux's simple model than the Andersson and Verbeure models.*

- The inverse of NBD parameter k is energy dependent and strongly correlated to the number of collisions sustained. *When extrapolated to one collision, 1/k for hA is the same as for hp. The energy dependence of 1/k is in agreement with partial stimulated emission interpretations of NBD.*

- In the cluster model interpretation of NBD parameters, clusters in E597 hA interactions extend about 4 units in rapidity. *In the cluster model interpretation,*

hA clusters extend about the same in rapidity as clusters in pp interactions.

- The number of particles in an NBD-based cluster increases with energy. *In the cluster model interpretation, cluster populations are energy dependent.*

- In the cluster model interpretation, the particle content of NBD clusters increases with additional numbers of collisions, while the number of clusters does not.

- NBD clusters in E597 hA interactions contain an average number of particles between 1 and 4 particles in 1 to 7 different clusters. *In the cluster model interpretation, considerable overlap exists between clusters.*

- The number of NBD clusters is not energy dependent in E597 interactions. However, the number of clusters tends to be is smaller for meson beam interactions than for baryon beam interactions. *In the cluster model interpretation, the number of clusters seems to be beam dependent.*

- The short and long range correlations observed for charged particles are due primarily to correlations between particles of different charge.

- For central rapidity intervals of varying width, slopes b_B reach maximum at about 1.25 units half-width except for $\bar{p}$ interactions ($\bar{p}Mg$ and $\bar{p}Ag$) for which they steadily increase into a kind of plateau. *Short range correlations have a rapidity range of about 2.5 units.*

- FBC slopes b_B sharply decrease and become negative when a gap is introduced between forward and backward sectors. *The sharpness of the decrease cannot be accounted for by multiple collision models that partition energy equally among collisions.*

- The differences between FBC results for total charged and negative charged produced particle multiplicities as a function of increasing gap size between forward and backward sectors which are seen in hp interactions are not seen in hA interactions. In hp interactions a positive correlation peak appears in the charged mode but not in the negative charged mode. In hA interactions, no positive

correlations appear beyond the gap size at which the minimum occurs. FBC slopes reach minimum values at about 1.25 units and come back up to zero, but never becomes positive again as they do for hp interactions. *Anticorrelations dominate long range hA interaction phenomena up to the kinematic limit.*

- FBC slopes b_B tend to increase with the number of collisions $\bar{\nu}$ in target-dependent sequences. With an A-dependent shift of $\bar{\nu}$, FBC slopes can be unified to show a single ν dependence for all targets in agreement with pp results. *Multiple collisions must be coupled with some other A-dependent mechanism to produce FBC effects.*

- The tendency for b_B to increase with the number of collisions $\bar{\nu}$ is strongest and the most pronounced for positive/forward with negative/backward charge modes, suggesting a proton collision mechanism. FBC slopes are dependent on the number of proton collisions in approximately the same way for all target nuclei. *FBC effects show more correlation with number of proton collisions than with total number of collisions.*

CHAPTER 4

DENSITY SPIKES

Indications of large produced particle densities within small rapidity and pseudorapidity windows (density spikes) first emerged from cosmic ray data [Aleksejeva 62; Arata 78; Apanasenko 79; Burnett 83; Marutyan 79]. Subsequently, hadron-hadron data revealed similar density spikes [Rushbrooke 83, 84; Carlson 84; Geich-Gimbel 85; Ward 86]. Recently, a report of an anomalous event with a ten(10)-particle cluster within a rapidity width of .386 units [Adamus 87] has stimulated considerable interest in high density exotic phenomena. The possible connections between density fluctuations and QGP have sparked further experimental searches for spike events and intermittency in the full range of hadron interactions — hh, hA, and AA as well as μp and e^+e^- interactions.

4.1 DYNAMICAL RELEVANCE

Before the results of a search for spike events in E597 data can be evaluated, it must first be ascertained whether the number of spike events is expected to be statistically rather than dynamically driven. Thus the maximum produced particle population per rapidity bin is determined for each event, and histograms accumulated for each interaction sample. Gaussian fluctuations in the rapidity spectra imply Gaussian probabilities for finding spikes of given height in an event [Dremin 87]. Fitted to a Gaussian in the range of spike heights less than 5 (*normal events*), the experimental frequency distribution for spike heights greater than 4 (*spike events*) overshoots the otherwise good fit for all reactions as shown in **Figure 4.1.1.** For the most part, the upper end of each distribution exhibits an exponential decreases, thereby ruling

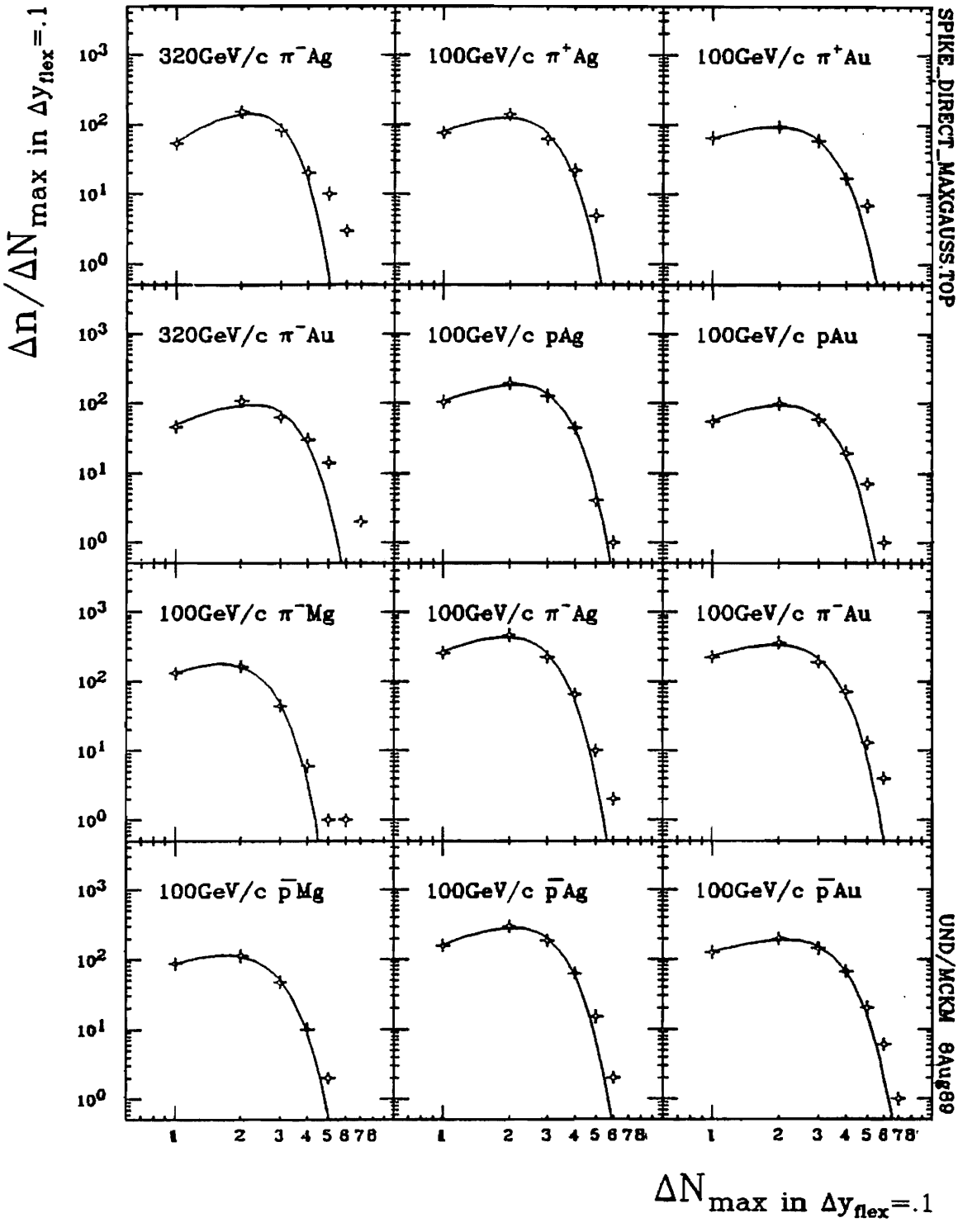

Figure 4.1.1 Frequency distributions of maximum produced particle populations within rapidity intervals of .1 unit.

out pair-wise coupling, random or otherwise [Dremin 87]. The unexpectedly high frequency with which spike events occur cannot be waved away by adjusting parameters but must be considered to be fundamental. It may be concluded that these spike events are physically significant and indicative of genuine multiparticle correlations.

This conclusion differs from UA5 collaborators, who insist that the fact that their Monte Carlo reproduces spikes implies that random superpositions of particles and clusters must dominate spike production [Ward 88]. The UA5 Monte Carlo program does generate spikes at comparable rates to those experimentally observed by UA5, but it does so without explaining their dynamical roots. As a 'no physics' simulator employing some experimental results, it generates particles in clusters which decay isotropically while conserving momentum and energy and introducing leading particle effects. It successfully reproduces charged multiplicity, transverse momentum, and rapidity distributions. It also reproduces rapidities at fixed multiplicity, multiplicities in fixed windows of rapidity, and mini-jet events. However, the various properties seem to be so interrelated that the success of this model, anchored on one property to reproduce the others correctly without involving additional physical considerations, is expected. So, rather than summarily interpreting spikes as a random phenomenon, UA5's success is a warning that a model's ability to reproduce event features does not necessarily vindicate its dynamical (or non-dynamical) basis. Bose-Einstein (BE) effects, based on quantum statistical clustering, have also been suspected of producing spikes in a non-dynamical way. BE effects increasing quadratically with cluster size have yet to be shown responsible for spike effects.

4.2 SEARCH FOR SPIKES

In a flexible bin scan for spike events, 131 events (29 at 320 GeV/c and 102 at 100 GeV/c) qualified under the criterion that produced particle populations in rapidity space be 5 or greater within .1 unit. Spike events were not required, as some comparable studies have, to have a specified rapidity distance separating large local rapidity cluster from all other tracks. The term *isolated spike* will designate spikes which

stand apart by a given rapidity distance, as opposed to simple spikes without such a criterion. The E597 data have been searched for spikes using fixed as well as flexible rapidity windows. With a criterion of 5 or more particles within *any* .1 unit interval δy_{flex}, almost four(4) times the number of spike events have been found as compared with the search using a comparable fixed-bin partition of event rapidities. Results are presented exclusively in the flexible bin mode of searching for spikes. The fixed placement of the bins cuts through a good number of high density spikes. The rapidity interval width of .1 unit has been selected in order to avoid short range correlation scales at greater widths and rapidity errors at lesser widths. Of the qualifying events, 73% had 100% of their produced secondaries well measured. In the remaining events, no more than 5% of the tracks were unmeasurable. On the average, 99% of all produced secondaries in spike events can be studied with reliable rapidity information. A scan for these events appears in **Table 4.1.1**, having employed flexible bins of width .1 units rapidity..

Nearly all spikes occurred between 0 and 2 units in laboratory rapidity. They exclusively occur in the backward beam-nucleon hemisphere. (The forward and backward hp rapidity regions are divided in the laboratory system at 2.68 and 3.26 units rapidity, respectively, for 100 and 320 GeV/c beam momenta.) **Figure 4.2.1** illustrates their distribution in this region. While proton rapidity distributions, as shown previously in **Figure 3.5.3**, cover an approximate range of 0 to 1 units, most spike centers reside above 1 unit rapidity. However, while they do not include evaporation protons since misidentification is minimal in this region of rapidity space, spikes may include groups of cascade products.

4.3 MULTIPLICITY DEPENDENCE

Local rapidity densities calculated over actual spike widths can be seen in **Figure 4.3.1** to be distributed over a range of 50 to 136, with 8 events showing densities greater than 100 particles/unit rapidity. Spike populations range between 5 and 7 produced particles. Spike widths range down to .035 and are distributed in the

Table 4.1.1 Flexible bin scan for events qualifying under the *spike* criterion of maximum rapidity density greater than or equal to 5 particles per .1 units rapidity.

Frame	Spike Rapidity Density	Number Particles in Spike	Spike Width	Low Edge Track Number	Spike Rapidity Center	N_{totm}	N_{prod}	N_{prod+}	N_{prod-}	N_{lp}
					π^-Ag 320GeV/c					
258589	54.95	5	0.09	22	1.79	31	26	12	14	4
279658	116.58	5	0.04	36	0.64	39	32	15	17	3
322579	50.89	5	0.10	17	1.14	43	31	14	17	7
338076	71.52	5	0.07	4	1.91	19	18	9	9	0
341202	120.09	6	0.05	54	0.73	64	46	19	27	6
342300	63.15	6	0.10	24	1.02	25	22	12	10	1
263093	51.65	5	0.10	17	0.88	38	23	11	12	10
264467	75.47	5	0.07	32	1.65	39	27	14	13	6
307662	57.08	5	0.09	12	1.29	39	30	13	17	6
309348	56.81	5	0.09	30	1.31	35	29	16	13	1
312159	51.83	5	0.10	55	0.61	57	37	17	20	11
346704	62.37	6	0.10	20	1.19	90	65	34	31	15
346999	54.52	5	0.09	22	0.73	46	38	16	22	3
					π^-Au 320GeV/c					
260831	52.39	5	0.10	59	0.97	67	40	21	19	19
275452	77.34	5	0.06	16	0.61	61	41	19	22	15
292673	68.61	5	0.07	16	0.81	63	44	20	24	9
293760	53.30	5	0.09	59	0.36	75	48	23	25	18
294171	72.97	7	0.10	47	0.59	75	55	25	30	14
300344	68.46	5	0.07	13	1.28	52	44	22	22	3
300867	58.02	5	0.09	13	0.51	59	44	21	23	12
300918	72.49	7	0.10	24	1.07	65	53	27	26	8
302037	56.63	5	0.09	17	0.49	81	46	21	25	24
303124	71.76	5	0.07	8	1.14	47	41	21	20	2
303273	57.15	5	0.09	9	1.11	52	34	13	21	9
321149	68.73	5	0.07	9	2.15	24	15	9	6	6
339191	67.30	5	0.07	14	0.60	66	42	20	22	16
343505	50.73	5	0.10	25	0.87	58	33	15	18	18
265268	56.51	5	0.09	8	1.11	45	31	17	14	8
346912	60.25	5	0.08	48	1.03	56	43	20	23	10

SPIKESCAN_1.TAB UND/MCKM 18Aug89

Table 4.1.1 Continued.

Frame	Spike Rapidity Density	Number Particles in Spike	Spike Width	Low Edge Track Number	Spike Rapidity Center	N_{totm}	N_{prod}	N_{prod+}	N_{prod-}	N_{lp}
					pMg 100GeV/c					
810100	51.93	5	0.10	18	1.29	31	29	13	16	1
880679	55.34	5	0.09	12	0.96	30	27	12	15	1
					pAg 100GeV/c					
856422	62.72	5	0.08	31	0.46	49	31	14	17	11
861808	50.86	5	0.10	16	1.16	22	19	9	10	1
911502	86.49	5	0.06	17	0.79	45	33	17	16	6
929941	58.50	5	0.09	13	0.82	41	33	13	20	4
932125	107.08	5	0.05	50	0.61	58	31	17	14	23
110206	65.30	5	0.08	14	1.29	55	32	16	16	16
120186	68.10	6	0.09	31	0.67	52	43	22	21	6
222493	50.72	5	0.10	13	0.67	56	37	16	21	11
223522	51.82	5	0.10	20	0.73	55	40	18	22	4
245658	50.78	5	0.10	37	1.03	50	32	13	19	9
822969	60.12	6	0.10	15	0.64	59	48	21	27	7
837126	51.09	5	0.10	11	0.81	43	28	12	16	10
131379	54.04	5	0.09	12	0.81	29	22	10	12	4
135852	63.93	5	0.08	24	0.96	26	20	9	11	4
137851	60.10	5	0.08	9	0.75	43	26	11	15	8
194366	59.92	5	0.08	4	0.46	53	38	18	20	6
236903	56.51	5	0.09	16	0.68	38	27	14	13	9
					pAu 100GeV/c					
789319	58.00	5	0.09	20	1.42	30	24	11	13	3
859464	121.03	5	0.04	6	0.65	37	26	11	15	7
870853	52.80	5	0.09	35	0.68	44	34	16	18	7
910845	51.83	5	0.10	40	1.00	59	39	19	20	15
917970	90.44	6	0.07	28	1.39	50	28	16	12	12
114202	54.50	5	0.09	42	0.93	68	44	20	24	16
117257	79.17	5	0.06	30	1.27	54	35	15	20	10
173214	63.91	6	0.09	22	1.30	39	32	15	17	2
226148	63.39	5	0.08	3	0.86	17	14	7	7	1
243625	72.12	7	0.10	23	0.94	65	40	18	22	17
244262	94.47	6	0.06	15	0.39	55	37	15	22	10
244463	66.86	5	0.07	22	0.96	25	22	13	9	2
783354	78.63	5	0.06	8	1.12	27	23	12	11	2
785572	70.35	5	0.07	14	1.55	45	30	16	14	9
812785	66.23	5	0.08	21	0.54	35	27	10	17	5
813256	67.71	6	0.09	14	0.76	40	22	9	13	14
817675	78.86	5	0.06	21	0.91	48	32	15	17	8
824703	62.96	5	0.08	6	0.82	38	29	16	13	7
842407	51.17	5	0.10	6	0.56	50	33	14	19	12
101243	65.42	6	0.09	36	0.72	40	27	12	15	5
102870	65.03	5	0.08	20	1.12	22	18	9	9	1
161036	66.45	5	0.08	4	0.52	28	21	12	9	3
162076	54.10	5	0.09	26	0.85	57	30	13	17	18
165726	83.53	6	0.07	22	0.97	44	31	14	17	5
168496	50.84	5	0.10	54	0.56	57	44	18	26	4
196563	92.13	5	0.05	38	0.42	15	23	12	11	13
238244	60.41	5	0.08	10	1.73	16	15	8	7	0

SPIKESCAN_1.TAB UND/MCKM 18.Aug89

Table 4.1.1 Continued.

Frame	Spike Rapidity Density	Number Particles in Spike	Spike Width	Low Edge Track Number	Spike Rapidity Center	N_{totm}	N_{prod}	N_{prod+}	N_{prod-}	N_{lp}
					π^-Mg 100GeV/c					
787758	56.40	5	0.09	15	0.95	30	25	11	14	2
188890	68.63	6	0.09	9	1.52	30	27	15	12	2
					π^-Ag 100GeV/c					
801444	60.15	5	0.08	25	0.82	33	21	10	11	6
804417	72.75	5	0.07	9	0.59	36	27	11	16	6
809975	52.93	5	0.09	35	0.62	37	26	11	15	5
864052	74.64	6	0.08	25	1.38	46	34	16	18	9
233971	57.41	5	0.09	14	0.77	48	36	17	19	9
244918	63.07	5	0.08	27	1.56	46	34	15	19	5
819271	68.67	5	0.07	6	0.89	55	34	17	17	8
842282	71.56	5	0.07	19	1.06	29	21	10	11	6
104735	112.21	6	0.05	29	0.94	38	23	11	12	13
164789	63.83	5	0.08	7	0.61	34	19	6	13	8
213175	75.52	5	0.07	14	1.31	30	23	10	13	5
213745	60.11	5	0.08	35	1.34	39	28	15	13	7
					π^-Au 100GeV/c					
793554	116.56	5	0.04	6	0.71	25	18	7	11	3
802955	51.27	5	0.10	43	0.61	57	31	12	19	15
857754	89.24	5	0.06	33	0.52	53	35	17	18	13
909045	55.65	5	0.09	44	0.38	53	33	15	18	10
921677	54.56	5	0.09	2	0.92	30	20	9	11	7
930686	72.69	6	0.08	15	0.52	44	28	14	14	12
182512	135.91	5	0.04	27	0.89	47	40	20	20	3
205555	63.80	6	0.09	22	1.13	53	34	16	18	7
206040	53.52	5	0.09	17	1.17	18	14	7	7	0
240969	91.08	6	0.07	3	0.64	36	29	13	16	1
812721	54.10	5	0.09	36	1.52	42	31	14	17	7
846319	73.66	6	0.08	34	0.31	51	35	20	15	13
886081	69.47	5	0.07	41	1.03	50	29	15	14	13
934448	51.56	5	0.10	2	0.60	19	16	9	7	1
140027	113.29	5	0.04	28	0.10	42	32	15	17	7
170056	64.43	5	0.08	47	0.60	62	41	16	25	9
193433	50.42	5	0.10	40	0.53	42	27	13	14	7

SPIKESCAN_3.TAB UND/MCKAI 18Aug89

Table 4.1.1 Continued.

Frame	Spike Rapidity Density	Number Particles in Spike	Spike Width	Low Edge Track Number	Spike Rapidity Center	N_{totm}	N_{prod}	N_{prod+}	N_{prod-}	N_{lp}
					π^+Ag 100GeV/c					
16645	66.73	5	0.07	31	0.63	46	23	9	14	14
70575	59.15	5	0.08	16	1.65	28	21	11	10	3
90173	55.15	5	0.09	29	1.10	35	26	10	16	4
60018	52.55	5	0.10	16	0.36	37	23	10	13	7
60982	58.24	5	0.09	27	1.02	34	27	14	13	6
					π^+Au 100GeV/c					
46505	51.82	5	0.10	12	0.71	53	36	17	19	13
74866	64.64	5	0.08	7	0.63	47	31	12	19	7
79646	57.27	5	0.09	12	1.12	42	25	11	14	7
82207	58.35	5	0.09	21	0.75	85	37	18	19	30
92852	95.62	5	0.05	26	0.95	48	35	16	19	7
61787	82.10	5	0.06	17	0.73	49	31	14	17	14
84147	57.85	5	0.09	22	0.61	28	21	11	10	5
					pAg 100GeV/c					
970689	89.98	5	0.06	27	0.31	38	27	10	17	4
977610	69.54	5	0.07	2	0.61	35	26	10	16	4
992632	85.87	5	0.09	22	0.95	30	22	11	11	5
964382	64.73	6	0.09	6	0.50	66	48	22	26	13
983660	57.33	5	0.09	43	0.61	46	32	15	17	9
					pAu 100GeV/c					
961254	58.24	5	0.09	35	0.44	47	30	12	18	9
976803	54.60	5	0.09	26	0.49	40	30	12	18	6
977164	53.04	5	0.09	30	1.34	57	38	16	22	13
14709	52.88	5	0.09	11	0.77	63	36	15	21	20
964466	66.65	6	0.09	19	1.38	22	14	7	7	4
964474	56.58	5	0.09	41	0.70	44	26	14	12	8
970092	55.62	5	0.09	21	0.40	37	21	12	9	12
990197	50.10	5	0.10	15	0.79	43	32	15	17	4

SPIKESCAN_2.TAB UND/MCKM 18Aug89

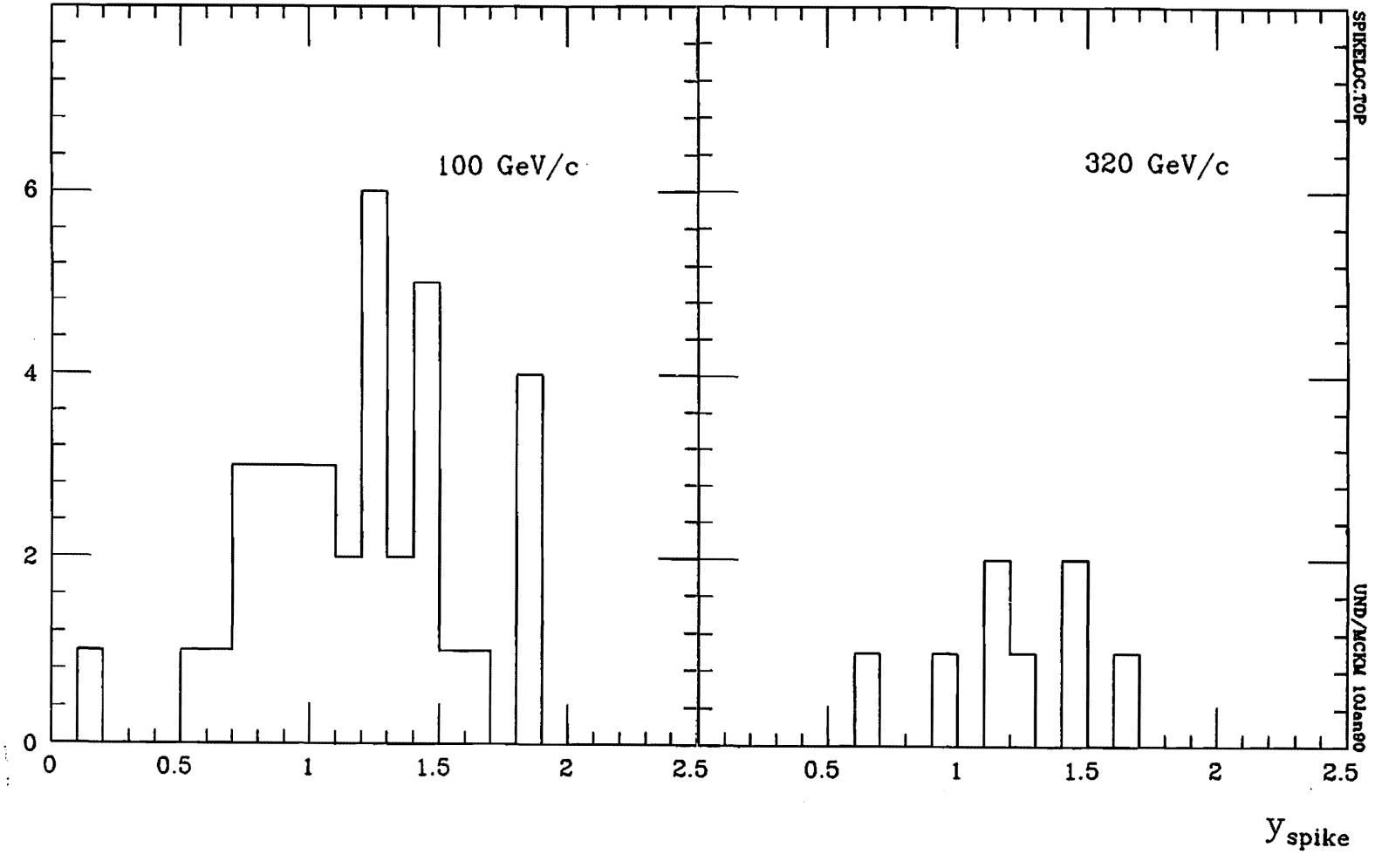

Figure 4.2.1 Frequency distributions of spike rapidity centers for events satisfying the criteria of 5 or more produced particles within fixed .1 unit rapidity bins.

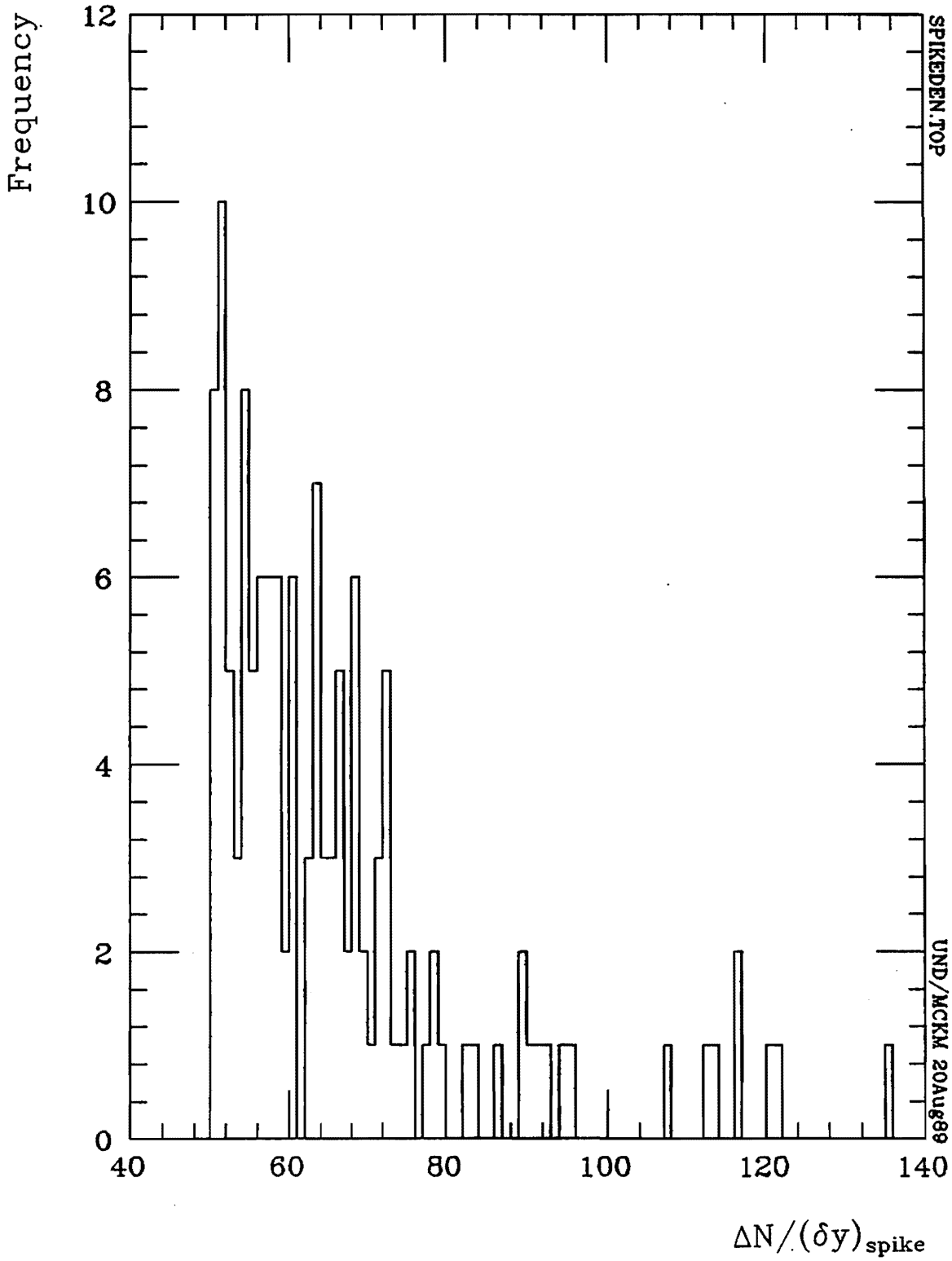

Figure 4.3.1 Local rapidity densities calculated over spike rather than bin widths for both 100 and 320 GeV/c data.

region $\Delta y_{spike} \leq .1$ unit rapidity as shown by **Figure 4.3.2.** Local rapidity densities themselves are strongly correlated with multiplicity. The average number of produced particles found in the most heavily populated rapidity width less than or equal to .1 units rapidity can be seen to be an approximately linear function of the multiplicity in **Figure 4.3.3.** No significant difference is seen between results using flexible and fixed rapidity widths.

On the basis of this dependence, it is clear that spike events occur preferentially among high multiplicity events. But it is also worth noting that spike heights show the same basic linear dependence in all reactions, regardless of the beam, target, or energy. Compared with pp interactions [Kittel 87b; Ward 88], the same basic slope of 1 particle per unit rapidity width for each particle produced seems to be universal once adjustments are made for the various analyses' rapidity widths. This conformity to a supposed standard suggests a basic mechanism whose characteristics are common to both hadron and nuclear scales – an idea conducive to intermittency and fractal measures since both are embedded in concepts of scale. Thus there have been attempts to explain density fluctuations in terms of an intermittency model [Dias de Deus 87; Dremin 87] in order to probe their origins. Most intermittency effects have been attributable to a small number of events.

4.4 ANGULAR INDEPENDENCE

A survey of E597 spike events shows that produced particles within spikes populate rapidity space in a random fashion exemplified by ring patterns as shown in **Figure 4.4.1.** Each point represents the tip of a vector whose length is equal to the rapidity and whose direction is the momentum direction in the transverse plane, ie. $ysin\phi$ is plotted as a function of $ycos\phi$ where $\phi = tan^{-1}\frac{p_x}{p_y}$. This is the same kind of angular independence found for NA22's anomalous spike event [Adamus 87].

Now if the processes involved in spike production are non-linear, then the question of angular independence is crucial in discriminating between regular dynamics (with preferential direction) and stochastic dynamics (with randomized direction).

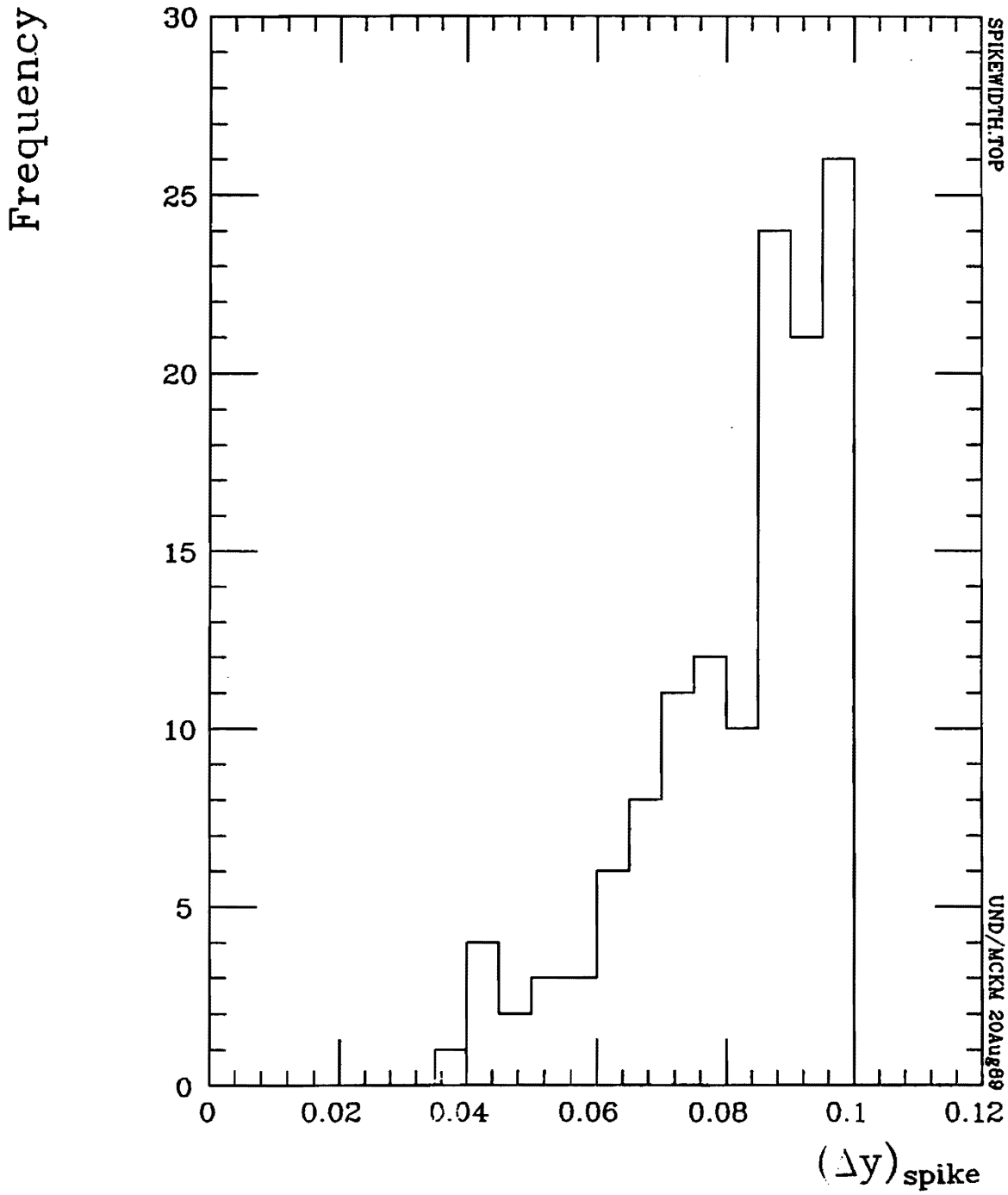

Figure 4.3.2 Spike rapidity widths for both 100 and 320 GeV/c data.

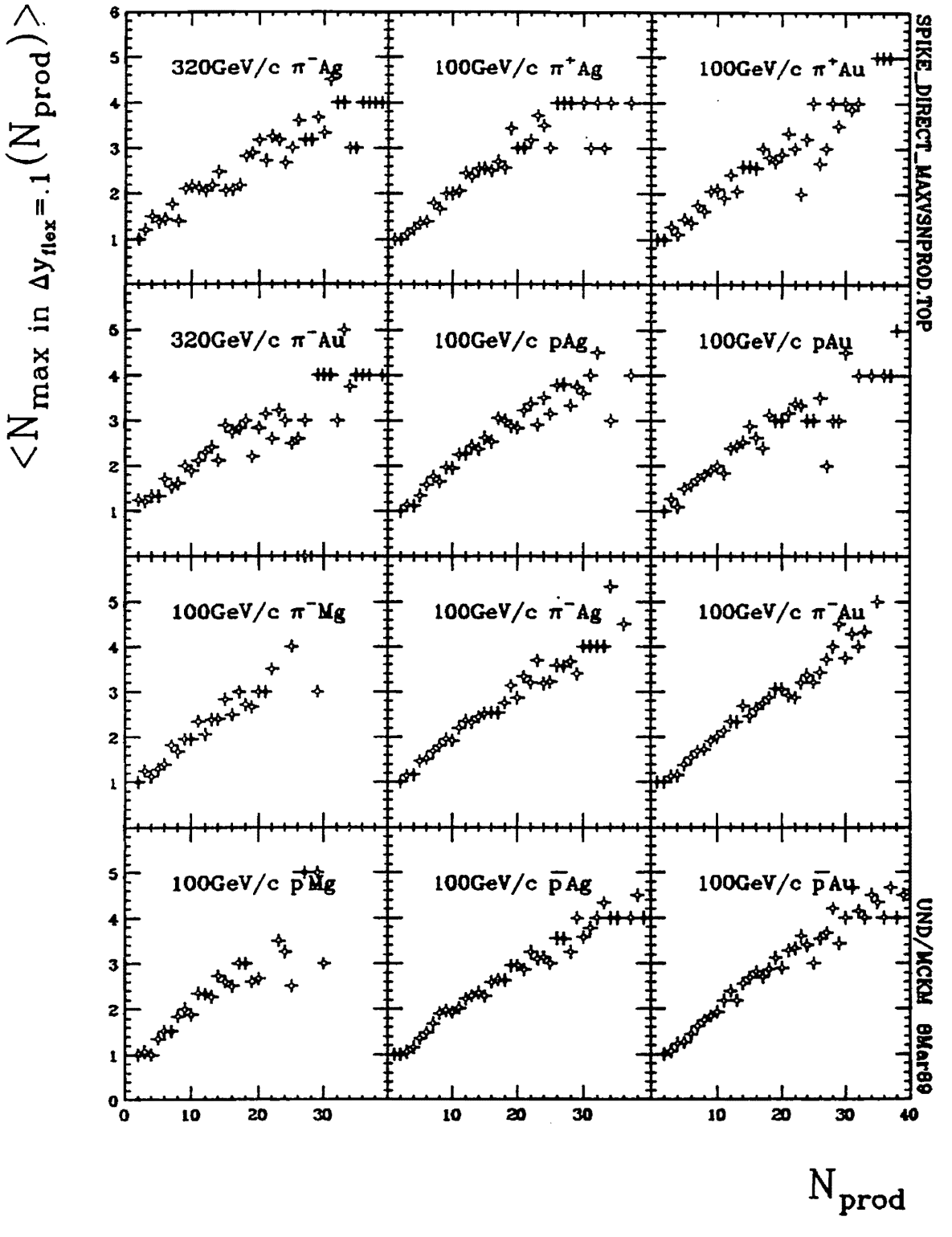

Figure 4.3.3 Maximum produced particle population within flexible rapidity windows of width .1 units as a function of produced particle multiplicity.

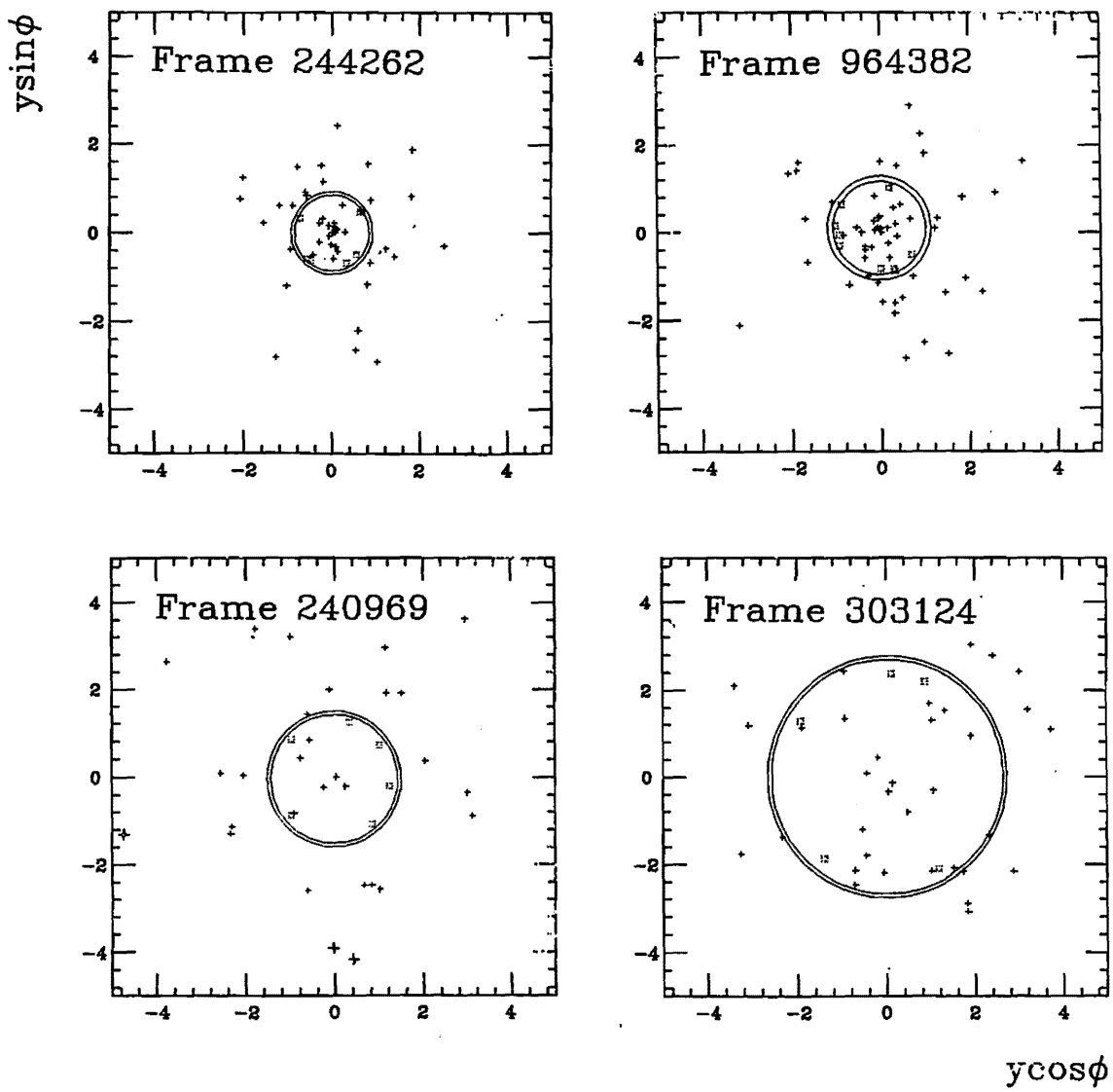

Figure 4.4.1 Demonstrative examples of ring-like particle distributions in spikes. Plotted is *ysinϕ vs. ycosϕ* for all produced particles. Spike particles are distinguished by open asterisks. Circles with radii approximating the average rapidity of the spike particles are provided to guide the eye.

It has been proposed that coherent hadrons analogous to Cerenkov radiation would be produced by valence quarks in preferred emission angles dependent on QGP plasma properties. Thus the produced particles found in spikes would populate rapidity space in rings. (In fact, an alternate appellation for spike events is *ring events*) [Dremin 89].) The fact that the data show this *ring* behavior is consistent with the speculation that spike particles be associated with Cerenkov gluons.

4.5 SEAGULL EFFECTS

Gluon radiation could account for distinctive seagull effects [Kittel 87a]. These effects are seen in the energy-weighted dependence of average transverse momentum on Feynman x, and have the characteristic appearance of a seagull with its head lowered at $x_F = 0$ and its wings raised significantly at $\mid x_F \mid > .4$ and has been seen in e^+e^-, ℓh, and hh interactions. First seen in hh interactions down to cms energies of 22 GeV [Pernegr 60; Bardadin 63], seagull effects have been noteworthy in e^+e^- and ℓh interactions. In string models of e^+e^- interactions [Andersson 80], the dramatic rise of one of the wings with increasing cms energy accompanies the hard gluon that one of the two leading quarks begins to emit beginning at about 10 GeV. By 22 GeV, approximately E597's upper energy limit, one wing lifts higher by a factor of two over its position at 14 GeV, approximately E597's lower energy limit. This behavior of the seagull has been a valuable signal for hard processes [Ajinenko 87].

At 100 and 320 GeV/c, the lifting of the seagull's wing is clearly seen in all E597 hA interactions, **Figure 4.5.1**. In the analysis, only cuts reducing errors in $p_\perp$ have been made. All have the head dipped down at $x_F \approx .35$ and the beam fragmentation wing rises steadily to higher average transverse momenta at 320 GeV/c. In all cases, FRITIOF is unable to reproduce the lift of wing because it has not included multi-gluon radiation with large momentum transfer components. Thus the seagull effects seen in hA are consistent with gluon radiation, though not necessarily of the Cerenkov persuasion. It may be noted, however, that average transverse momenta, like maximum event rapidity densities, have been shown to be strongly correlated to

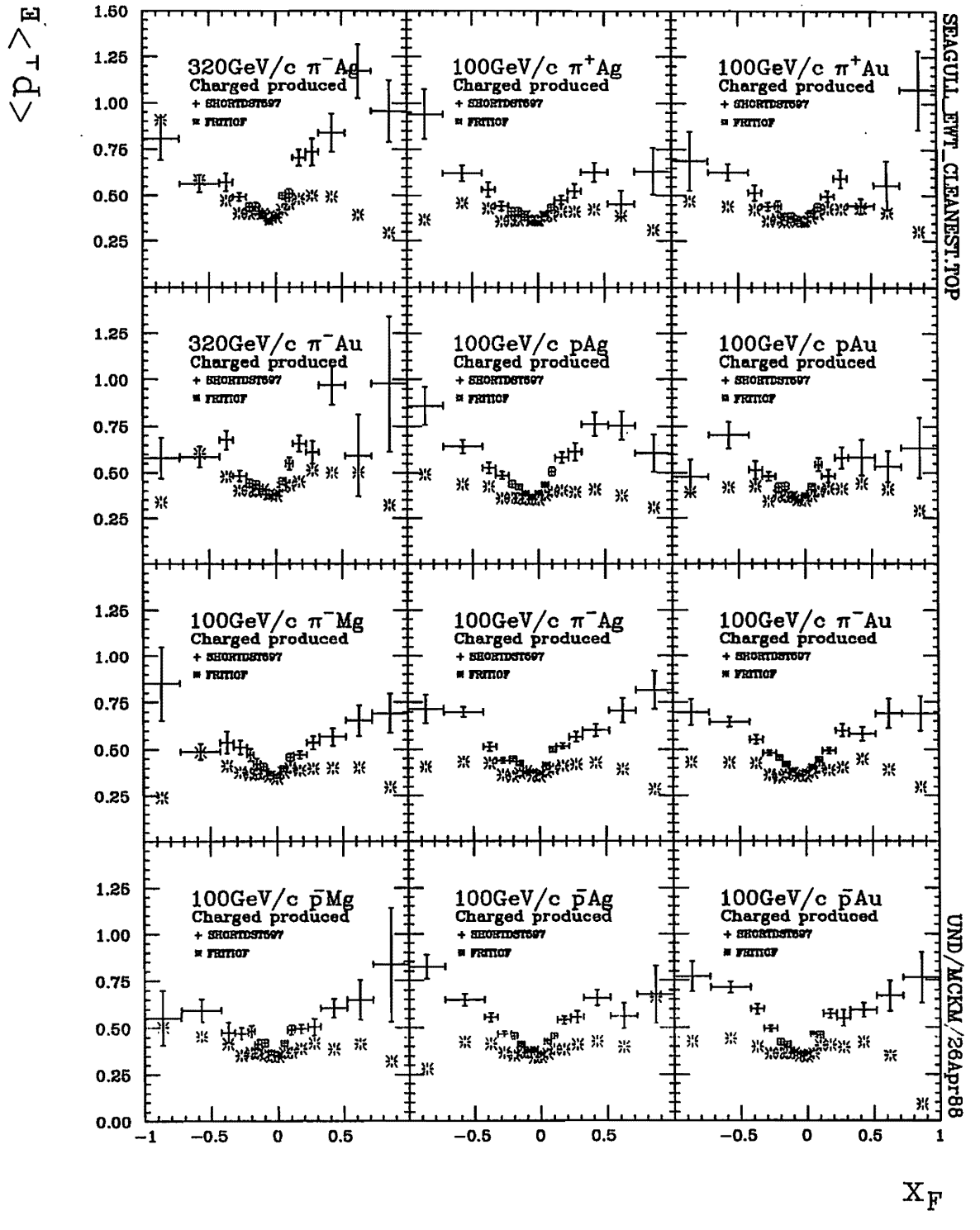

Figure 4.5.1 Energy-weighted average transverse momentum as a function of Feynman x to show the seagull effect in hA interactions for charged produced particles.

charged produced particle multiplicity, particularly when limited to high transverse momenta [Van Hal 87].

Seagull effects are even more pronounced in distributions restricted to produced particles charged oppositely from the beam, **Figures 4.5.2** and **4.5.3**. Wing elevations in excess of 1 GeV/c rise over their beam-charged counterparts in the beam fragmentation region. In the target fragmentation region, the other wing is clearly rising higher for positive produced particle distributions in contrast to those for negative produced particle distributions. Multiple collisions are no doubt responsible for the rise in the target fragmentation region, but other reasons must be found for the rise in the beam fragmentation region.

4.6 Production region size

It may be argued that QGP interpretations of spikes are consistent with production region sizes in hA interactions. A first approximation of emission regions can be made based on the uncertainty principle and average transverse momenta:

$$\langle \Delta r \rangle \approx \hbar / p_{\perp} \approx .5 \text{ fm}$$

However, along the collision axis, this region could be Lorentz contracted into a Fermi pancake in the center of mass reference system, or extended into a multiple collision hot dog bun in the laboratory system. QGP is theoretically expected at temperatures of $1-2$ GeV/fm^3 so whether or not QGP can be expected in hA collisions depends on the extent of the production region along the collision axis and subsequent volume.

The radius of an *emission* region can be inferred from Bose-Einstein (BE) correlations – enhancements of like-boson pairs at small momentum differences known as the GGLP effect [Goldhaber 60] with the radial direction perpendicular to the momentum difference. Based on Hanbury Brown-Twiss interferometry methods of radio astronomy [Hanbury Brown 56], and predicted for excited nuclei and resonance decays [Grishin 71], correlations between identical particles can reveal something of the space-time structure of hadronic interactions [Cocconi 74], in principle the lifetime and precise shape of the interaction *fireball*. In principle, studies of any particles

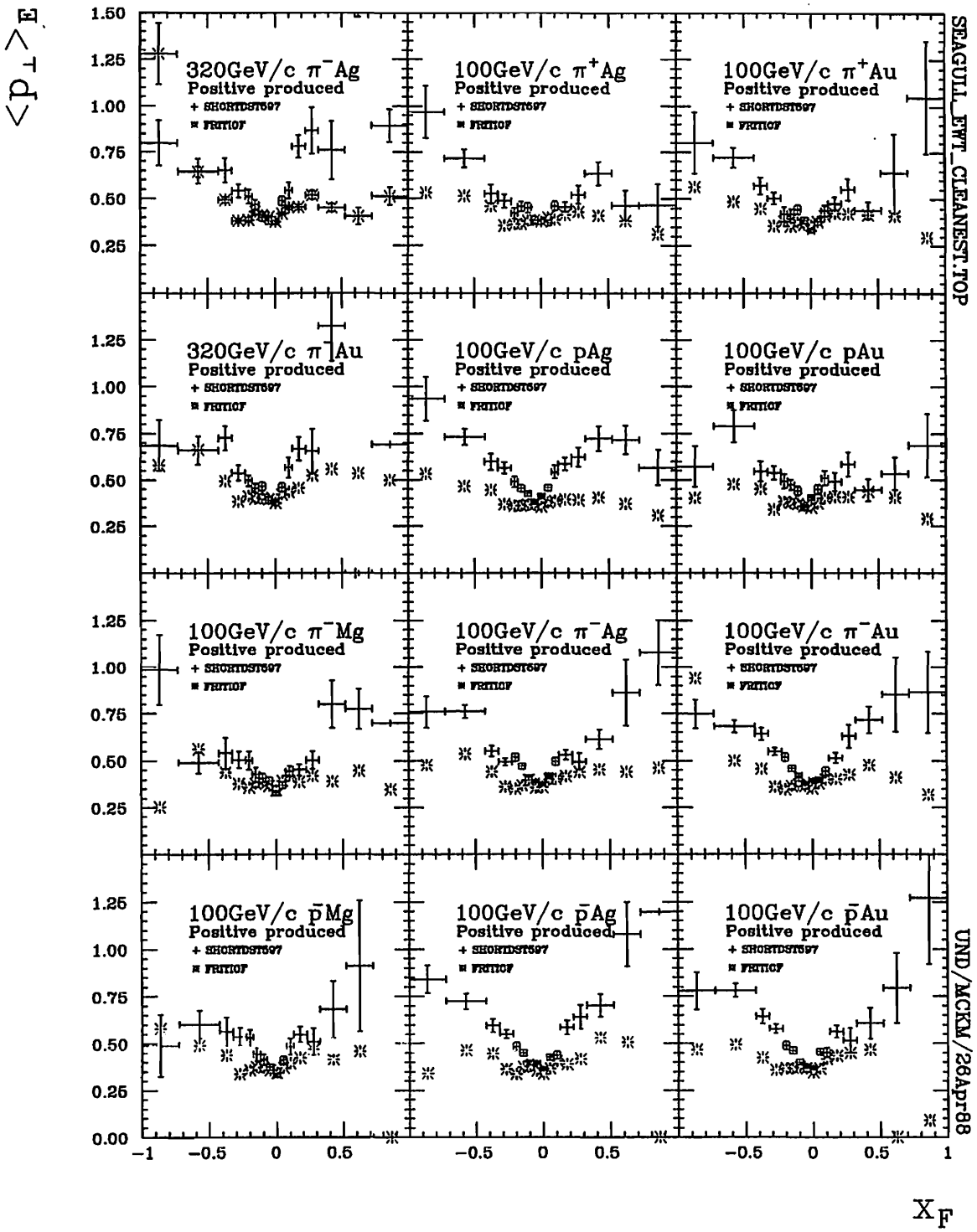

Figure 4.5.2 Energy-weighted average transverse momentum as a function of Feynman x to show the seagull effect in hA interactions for positive produced particles.

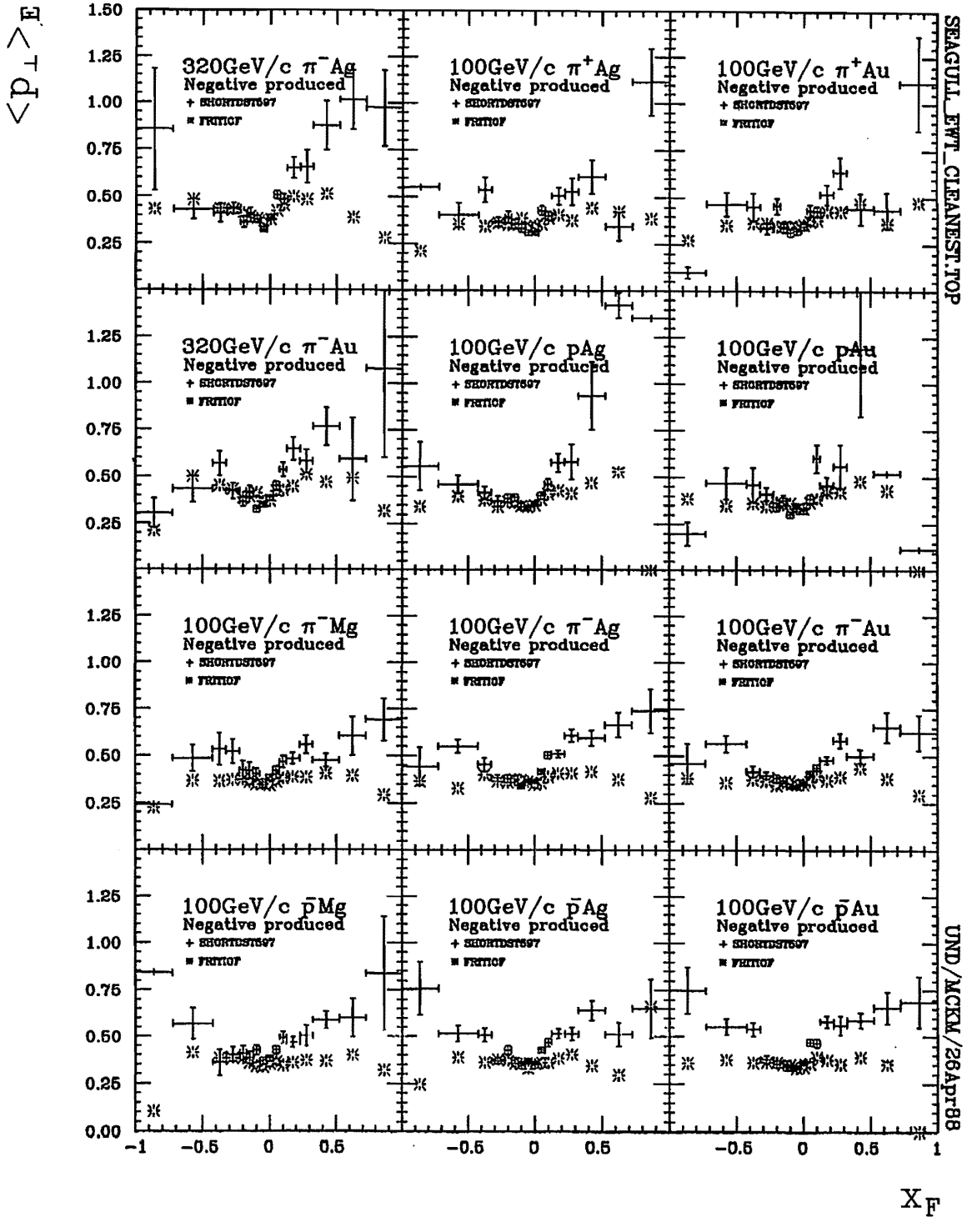

Figure 4.5.3 Energy-weighted average transverse momentum as a function of Feynman x to show the seagull effect in hA interactions for negative produced particles.

emitted from sources separated by small distances compared to their Compton wavelength will yield an estimate of the emission volume. Pions, as bosons, display BE enhancements or positive correlations while protons, as fermions, display Fermi-Dirac depletions or anti-correlations. Fermi-Dirac correlations for proton pairs have been used to study hA [Siemiarczuk 67; Azimov 74; Angelov 80; Bayukov 81; Azimov 83] and AA interactions [Koonin 77; Zarbakhsh 81]. Bose-Einstein correlations have been used to study hh [Biswas 76, Meijers 87], hA [De Marzo 84], and AA [Chacon 88] as well as e^+e^- [Aihara 85] interactions. Identically charged kaon as well as pion pairs have been employed [Lednicky 82; Grishin 87] as well as $\pi^+\pi^o$ pairs (which are explicitly exempted from BE correlations [Bowler 87b]). Experimental limitations (proton energy loss in target thicknesses) have precluded the use of FD correlation analysis with the present data, but BE enhancements have been readily observable.

These enhancements are determined by simple interference principles. Given two(2) simultaneously emitting sources, the total amplitude of the superposed outgoing waves is the sum of the partial amplitudes with the coincidence rate proportional to the square of the amplitudes. This reduces to an expression in terms of the source separation R and the detector angular separation θ. This expression displays modulating characteristics or 2nd order interference effects with maxima at $kR(\theta)/2\pi$ so the source separation in the plane of the two(2) detectors can be determined by the interference of coincidences. The symmetry of the waves determines the observed interference patterns as a consequence of the uncertainty principle and the path ambiguities introduced by separation R.

In this way *interference* indicates general effects arising from the superposition of fields rather than limited interference patterns. This is reasonable since single atoms emit photons one at a time. When a coincidence is observed, 2 quanta are surely involved from 2 different sources. A conventional fringe pattern cannot be expected since the atoms radiate with random phase. Even so, the intensity correlation function is not constant in space, but exhibits a characteristic modulation resulting from interference. This is so classically, but more so quantum mechanically, in which case coincidences cannot occur when the detectors are spaced at odd-half numbers of

fringe spacings of the fictitious interference pattern that would occur if the atoms were radiating with fixed phases. The corpuscular aspect of light actually enhances the structural order manifest in intensity correlations produced by two(2) independently emitted atoms and demonstrated by Hanbury Brown and Twiss. These intensity correlations are dependent on the level of coherence [Gyulassy 79] as well as the distances between sources. They are strongest when the sources are chaotic. While the pion wave functions are fixed, phases can be randomly and independently fluctuating. Average intensities can be assumed either constant in space or fluctuating, but spatial modulations are most most pronounced in the absence of fluctuations. Thus interferometry reveals not only space time structure but also the degree of coherence with which particles are produced.

4.6.1 Parameterization

Kopylov and Podgoretskii [Kopylov 73] proposed studying momentum differences of pion secondaries to measure the fireball region, the region from which produced secondaries are emitted rather than the interaction region. A correlation function $R(p_1, p_2)$ is defined so that it is equal to 1 when pions are uncorrelated in momentum space, regardless of whether the multiplicity distribution is Poissonian. At large relative momenta and for small energy differences, the reliability of R can be checked for supposed uncorrelated backgrounds. R should be flat, with its fluctuations centered about 1. When it is not and a rise seems inevitable due to other correlations present, a parameterization with a linear term is used to accommodate the rise.

In practice, the correlation function is determined by the ratio $R_{BE} = \rho_{1,2}/\rho_{1,2}^{background}$ of the measured 2-particle density $\rho_{1,2}$ and the background 2-particle density $\rho_{1,2}^{background}$. The correlation can be studied in terms of Lorentz invariant 4-momentum differences Q^2, 3-momentum differences q^2, energy differences q_0^2, and transverse 3-momentum differences $q_\perp^2$. While all of them have been employed and display BE effects, 4-momentum differences in the pair cms are Lorentz invariant and

give the clearest results. The ratios R_{BE} have been analyzed as functions of the form

$$R_{BE}(Q^2) = N(1 + \lambda e^{-\beta^2 Q^2})(1 + \delta Q)$$

which is a Goldhaber parameterization for which N is a normalization factor, λ designates the chaoticity (0 for none, 1 for maximum), $\hbar c\beta$ is the radius of the emission zone by Fourier transform, and δ accounts for other correlations at large Q by accommodating the residual slope.

4.6.2 Reference samples

When constructing suitable backgrounds with which to calculate R_{BE}, it must be remembered that pion correlations can emanate from considerations other than the quantum statistics of pions. Constraints from conservation laws and dynamical processes can produce pion correlations as well. Strong correlations can derive from translational and rotational symmetries (conserved energy and momentum) as well as internal symmetries (isospin and parity). Produced particles are related kinematically as well as by their multiplicity distributions. Correlations may also occur as a results of resonance production and some cluster models see pion production as a kind of fireball decay. Long range Coulomb interactions between final state pions also contribute to correlations – potentially dominating them at small relative momenta.

To isolate pion correlations resulting exclusively from quantum statistics, a background must be devised which includes conservation and dynamical effects but excludes BE effects. There is no unique prescription for building such a background. Various methods have been proposed, each with superior qualities as well as serious disadvantages. In the process of this analysis, many different reference samples have been constructed. These reference samples utilized

1. same event oppositely-charged pion pairs
2. same event identically-charged pion pairs with overall shuffled transverse momenta

3. same event oppositely-charged pion pairs with overall shuffled transverse momenta

4. same event, identically-charged pion pairs with shuffled transverse momenta

5. different event, like multiplicity, identically-charged pion pairs

6. different event, like multiplicity, oppositely-charged pion pairs

Analyses using all these backgrounds showed some degree of BE enhancement. Two of them, numbers 4 and 5, however, showed the clearest enhancement. They also have the greatest advantages and the least disadvantages. Because of the potential problems of the others, results are presented only for these.

Using oppositely-charged pion pairs certainly sidesteps the BE effect, but also introduces new dynamical correlations associated with ρ, η, and ω resonance production. Thus, simply using oppositely charged pion pairs is not enough to single out quantum effects. Neither is it wise to use any of the other oppositely-charged pion pair schemes to build a reliable background. Shuffling transverse momenta randomly among all particles and pairing the resultant fictitious tracks breaks the BE effect, retains momentum and energy conservation, and also destroys resonance correlations in oppositely-charged pairs, further reason to avoid using backgrounds built with oppositely-charged pion pairs.

Now longitudinal momentum distributions depend strongly on mass and charge and thus cannot be swapped without violating momentum conservation. But by restricting swaps to transverse momentum, the problem is largely avoided. But energy conservation is better safeguarded by swapping only like-particle pairs (same mass, same charge) [Azimov 83]. This approach has been one of the two preferred in this study.

Taking pions from different events to produce fictitious pairs certainly sidesteps BE effects but also endangers energy-momentum conservation. There are also hazards in mixing events of different proton and pion multiplicity such that internal symmetries are violated. To minimize these problems, the data were sorted by light

proton, proton, and pion multiplicities. Only events with common multiplicities have been mixed to produce backgrounds. Since this restriction in building backgrounds necessarily cuts out a number of multiplicity combinations represented in the sample, correlated pairs were restricted to multiplicity combinations occurring in the background only. Event mixing was also restricted to events involving the same thickness foil since tracks traversing the thicker foil will lose more momentum on the average than those traversing the thinner foil. Undoubtedly, these restrictions are tighter than necessary in view of the overall multiplicity errors, nevertheless, they have safeguarded against unforseen biases. The multiplicities used were corrected only for unmeasured tracks but tracks were accepted into pairs only if they passed the *cleanest* track quality criteria as described in Chapter 2. CRISIS identification of fast forward particles was included where available. The reference samples were normalized by requiring a vanishing BE effect at large relative distances (.6 $GeV^2/c^2 < Q^2 < 2GeV^2/c^2$).

4.6.3 Results

For the mass-restricted shuffled transverse momentum and the different event backgrounds, BE effects are large enough for estimates of the production region size to be made on the basis of Goldhaber parameterization 4-parameter fits. 100 GeV/c beams have been combined for the sake of statistics, but essentially the same effects are seen for each beam-target combination with larger errors. Cuts limited relative momentum errors dp/p to less than .8. Fits of data to background ratios in **Figure 4.6.1** imply estimates of chaoticity between .2 and .3. They also verify the normalization of the background within errors by the fact that N of the Goldhaber parameterization is fit to approximately 1. At large Q^2 the fits are consistent with R^{BE} oscillating about a slope described by $\delta \approx -.1$, and with β associated with emission radii $r = \hbar c\beta$ of .3 to 1.2 fm. These emission radii are in pion pair-average momentum rest frames. The radial size estimate is higher when utilizing the different events background than when utilizing the shuffled $p_\perp$ background, and shows possible A dependence when the fit is restricted to $Q^2 < 2$.

The chaoticity estimates, well below 1, may be indicating that some mul-

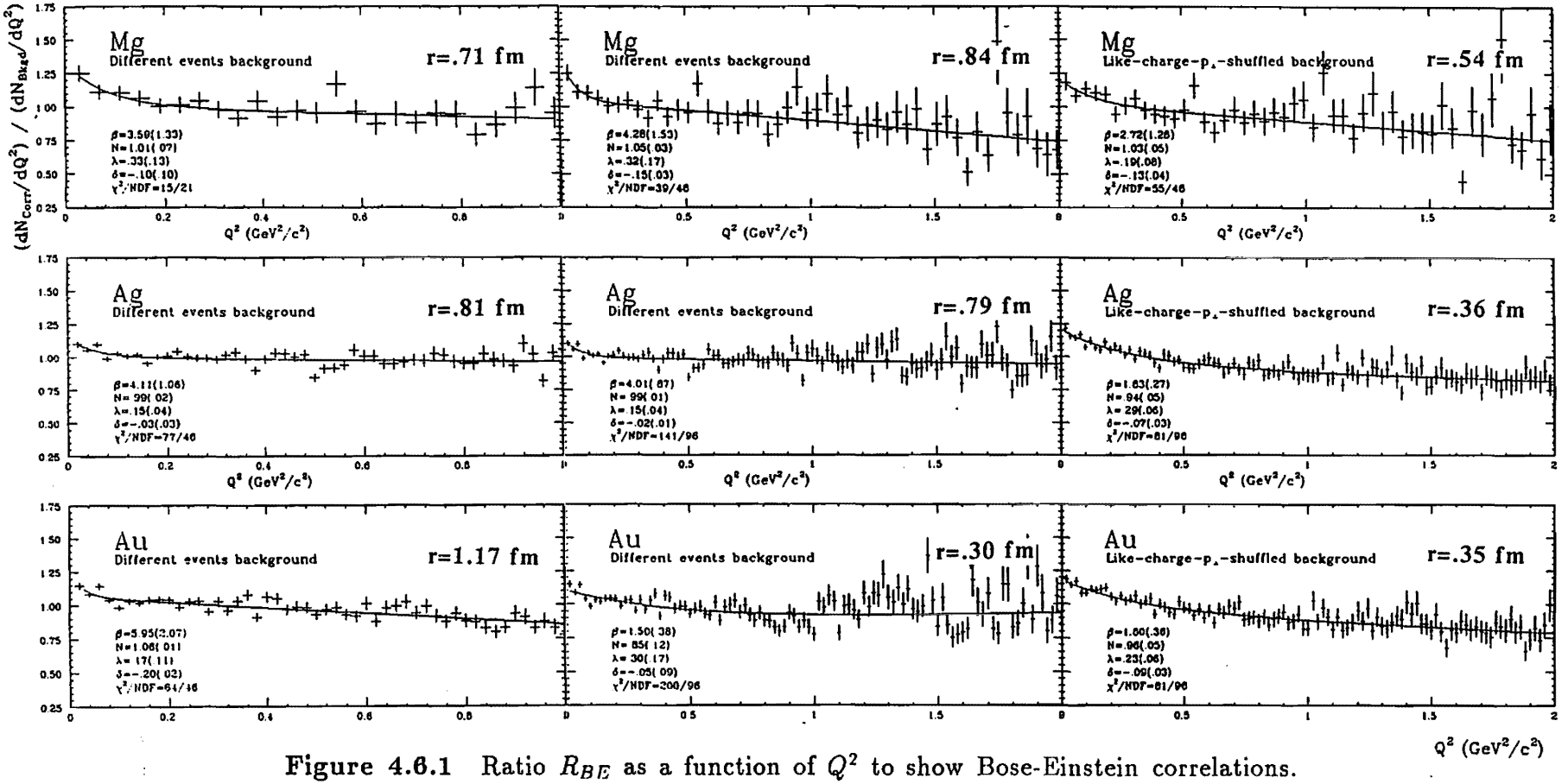

Figure 4.6.1 Ratio R_{BE} as a function of Q^2 to show Bose-Einstein correlations. Beams have been combined in order to reduce statistical errors and present smoother results, but individual interaction types show approximately the same features. R_{BE} is calculated using the two most reliable reference samples constructed from a) same event, identically-charged pion pairs with like-mass shuffled transverse momenta, and b) different event, like multiplicity, identically-charged pion pairs. Fits c), using the same reference sample as b), are rendered over a smaller region to avoid distortions from the fluctuations at higher Q^2.

tiparticle production is coherent. But until the sample of spike events is significant enough to analyze for BE correlations, coherent gluon radiation in spike events cannot be inferred.

The radial size estimates basically agree with original estimates based on average $p_\perp$ but are significantly smaller than the charge radii of participating nuclei (see **Table 1.4.2**). They are comparable to emission region radii reported for e^+e^- (r = .7 - .9 fm) [Aihara 85; Althoff 85a], for ℓh (r = .5 − .8 fm) and for hh (r_{π^+p,K^+p} = .77(.03) − .83(.02) fm) [Meijer 87]. Some caution must be exercised, however, in comparing radial values with any calculated or experimentally derived values. They are expected to be smaller in Lorentz invariant parameterizations (Q^2) than for Kopylov-Podgoretskii parameterizations (q_t and q_o). But one must also consider the rest frame for which the radius is given. Some values are given in secondary particle rest systems S^{sec}; others, in empirically determined systems S^o; others, in the lab; others, in the event cms system. DPM calculations for 200 GeV/c pAu [Ranft 88] describe emission regions both in secondary particle rest systems (r = 1 fm) and in empirically determined systems (r = 5 - 10 fm) related to the lab system by

$$r^{lab} = \tau^{lab}c = \gamma^{sec}\tau^{sec}c = \frac{E^{sec}}{m^{sec}}\tau^{sec}c = \frac{E^{sec}m^{sec}}{m^{sec^2} + p_\perp^{sec^2}}\tau^o c$$

Values found in this study, given in the rest frame of averaged pairs (ie. the frame for which the average momentum of a pair vanishes), are expected to be smaller than both lab values and secondary rest frame values. Single particle laboratory momentum distributions peak at lower values than pair average momentum distributions. That means secondary particle rest frames have on the average smaller γ than pair-average rest frames so that secondary particle rest frame values for radial dimensions are larger than pair-average rest frame values.

Whether heavier nuclei show smaller, larger, or comparable emission regions, however, has not been conclusively ascertained. A limited region fit on R_{BE} using the different events background shows the radius increasing with nuclear mass, but the fit on R using the shuffled $p_\perp$ background does not reproduce that dependence. Instead, the shuffled background result argues for comparable emission regions, and

the different events background result, within its errors, corroborates comparable emission regions. Thus, the results can only be used reliably to place upper limits on the size of the emission regions rather than specifically comparing emission regions for different nuclei. This upper limit ranges from .71 to 1.17 fm, is comparable to that of hh, and does not clearly exhibit a strong dependence on nuclear size. pp, $\bar{p}p$, pXe, and $\bar{p}Xe$ studies at 200 GeV/c [de Marzo 84] agree that hA emission volumes do not depend on nuclear size. (Note their larger emission radius of about 1.5 fm due to their use of a modified Kopylov-Podgoretskii $q \perp$ parameterization.) A comparison with pp results at $\sqrt{s} = 31$ GeV ($r \approx .8 - 1.0$ fm) [Breakstone 86] further confirms the comparable dimensions of hh and hA emission volumes, even at higher energies.

With radial dimensions around 1 fm, QGP is a possibility for large multiplicities. Using experimentally determined average transverse masses (transverse momenta measure temperature) to estimate minimum energy densities, the minimum produced particle multiplicity (particle densities measure entropy) required for QGP energy densities of 1 GeV/fm^3 can be as low as 2 for .5 fm emission zone radii, 11 for a 1 fm emission zone, or as high as 92 for 2 fm emission zone radii. High multiplicity spike events certainly pass under minimum QGP energy density criteria. But if QGP is being produced in hA interactions, some difference in emission volume might be expected. Thus, BE effects are not signalling QGP phase transitions.

4.7 Summary

- 131 events qualify as spike events. *Large fluctuations in rapidity density appear in hA often enough for quantitative studies of spike events.*

- Maximum local rapidity densities are as high as 136 particles/unit rapidity in hA interactions. *Spike events are candidates for QGP.*

- Density spikes of various heights occur in numbers larger than statistically expected. *Spike events are probably dynamically significant.*

- Density spike production is strongly correlated to produced particle multiplicity. Spike heights are directly proportional to produced particle multiplicity with a constant 1 particle per unit rapidity for each particle produced, essentially the same as for hh interactions. *This linear dependence of maximum rapidity density on total produced multiplicity seems to be universal, unaffected by energy, beam, or target considerations.*

- Spike events display *ring* features. *The random angular distribution of spike particles is consistent with expectations for coherent production analogous to Cerenkov radiation.*

- Seagull effects are observed in both 100 and 320 GeV/c events but are not consistent with FRITIOF. *The rise of the beam fragmentation wing cannot be accounted for without some large-momentum transfers and gluon radiation.*

- On the basis of Bose-Einstein correlations, the production size in hA interactions is estimated to be somewhat less than 1 fm. *The emission volume is small enough to make QGP possible at spike multiplicities.*

- The pion emission volumes inferred from Bose-Einstein correlations in hA are comparable to hh interactions and do not indicate a strong A dependence among themselves. *Therefore, QGP is nearly as likely (or unlikely) for light as heavy nuclei, given comparable multiplicities.*

CHAPTER 5

INTERMITTENCY

First introduced in the study of turbulence [Mandelbrot 74; Frisch 78; Shertzer 84], intermittency describes the pattern of fluctuations in stochastic distributions which occur at different scales and which incompletely populate available phase-space. In hydrodynamic frameworks, large fluctuations signal transitions between unstructured laminar flow and turbulent flow. Similarly, large rapidity fluctuations may be signaling transitions of some kind related to the substructure of hadronic media [Kittel 87]. By entertaining the possibility that these fluctuations reflect something unique about hadronization, current models of the process(es) transforming quarks, gluons, and QCD excitations into hadrons can be tested.

The term intermittency has been chosen to refer to all power-law relationships which simplify the complicated patterns of fluctuations over a number of scales. These patterns may be of dynamical and/or statistical origin, though some authors limit the term to dynamical origins. It has been proposed that fluctuations of ordinary dynamical origins can be separated from purely statistical ones by the power-law behavior of scaled moments, the higher orders increasingly affected by these fluctuations. But both quantum statistical [Carruthers 90] and deterministic cascading [Bialas 86] have been demonstrated to display intermittency. At present, models dealing with intermittency fall into one of three groups of models: random cascading, phase transition, or conventional. Random cascading models propose fluctuations in time-development mechanisms; phase transition models propose statistical mechanisms akin to spin-glass phase transitions; and conventional models propose quantum statistical or BE interference, resonance, and/or short-range correlation mechanisms

to account for intermittent behavior.

5.1 INTERMITTENCY SIGNAL

The signal for intermittency is found in log-log plots of factorial moments as functions of rapidity bin width. The reason factorial moments signal intermittency stems from the fact that cascading introduces new rapidity scales which can be detected by factorial moments. If factorial moments saturate with increasing resolution, ie. with decreasing interval size, then the fluctuations are behaving in an entirely statistical manner. If fluctuations follow a power law, they may be dynamical over a range of rapidity scales. Such power laws are characteristic of fractal and multi-fractal systems [Mandelbrot 87], discussed in Chapter 6. The recognized signal for intermittency is linearity down to the experimental resolution.

In principle this signal can be looked for in individual events, but an inclusive approach is usually preferable, using average factorial moments. Of course, events with extremely large multiplicities can be studied individually for intermittency using a normalized factorial moment of order q

$$G_q = \frac{1}{M_{bins}} \sum_{bin=1}^{M} \frac{k_{bin}(k_{bin}-1)...(k_{bin}-i+1)}{N_{prod}(N_{prod}-1)...(N_{prod}-q+1)}$$

where k_{bin} is an individual bin's population, M_{bins} is the total number of bins, and N_{prod} is the total produced particle multiplicity. But the dispersion of G_q is given by

$$D_q = [\langle F_q^2 \rangle - \langle F_q \rangle^2]^{1/2} = \frac{q}{\sqrt{N}} \sqrt{\langle F_{2q-1} \rangle}$$

where N is the produced particle multiplicity. Thus good resolution requires large multiplicities or large numbers of events. But multiplicities are more critical than numbers of events. The dispersion as given above is really the first term of an expansion whose error increases at small multiplicities. So larger multiplicities give better resolution than larger numbers of events. On the basis of multiplicity, hA studies may have an advantage over hh studies, but must still rely on an inclusive approach.

Various forms of scaled moments have been introduced to cope with the problems that low multiplicity events incur. It has been shown that factorial moments

F_q of order q

$$F_q = \frac{1}{M_{bins}} \sum_{bin=1}^{M_{bins}} k_{bin}^q (k_{bin}^q - 1)...(k_{bin}^q - q + 1)$$

where M is the number of bins partitioning the total rapidity width, significantly reduce the amount of statistical noise that finite multiplicities introduce. Current studies of intermittency have employed one or another form of factorial moment. Factorial moments are often normalized in some way by F_1^q. However, in calculating average factorial moments over a number of events, two(2) distinct methods have emerged—the *horizontal* and *vertical* averages [Bialas 86]. In the horizontal version, the factorial moments are first averaged over all bins for each event and the result then averaged over all events:

$$F_{q,horiz}^{evt} = \frac{1}{M_{bins}} \sum_{m=1}^{M_{bins}} k_{bin}^{evt} (k_{bin}^{evt} - 1)...(k_{bin}^{evt} - q + 1)$$

$$\phi_{q,horiz}^{evt} = \frac{F_{q,horiz}^{evt}}{(F_{1,horiz}^{evt})^q}$$

$$\langle \phi_{q,horiz} \rangle = \frac{1}{N_{evts}} \sum_{evt=1}^{N_{evts}} \phi_{q,horiz}^{evt}$$

In the vertical version, the factorial moments are first averaged over all events for each bin, and the result then averaged over all bins.

$$F_{q,vert}^{bin} = \frac{1}{N_{evts}} \sum_{evt=1}^{N_{evts}} k_{bin}^{evt} (k_{bin}^{evt} - 1)...(k_{bin}^{evt} - i + 1)$$

$$\phi_{q,vert}^{bin} = \frac{F_{q,vert}^{bin}}{(F_{1,vert}^{bin})^q}$$

$$\langle \phi_{q,vert} \rangle = \frac{1}{M_{bins}} \sum_{bin=1}^{M_{bins}} \phi_{q,vert}^{bin}$$

While these are not generally equivalent, both have been employed to determine intermittency in an inclusive approach. This study uses the horizontal average exclusively.

5.2 RESULTS

Figure 5.2.1 shows the average horizontal factorial moments for all events in the E597 samples as functions of rapidity bin width δy. Linearity, in most cases, extends

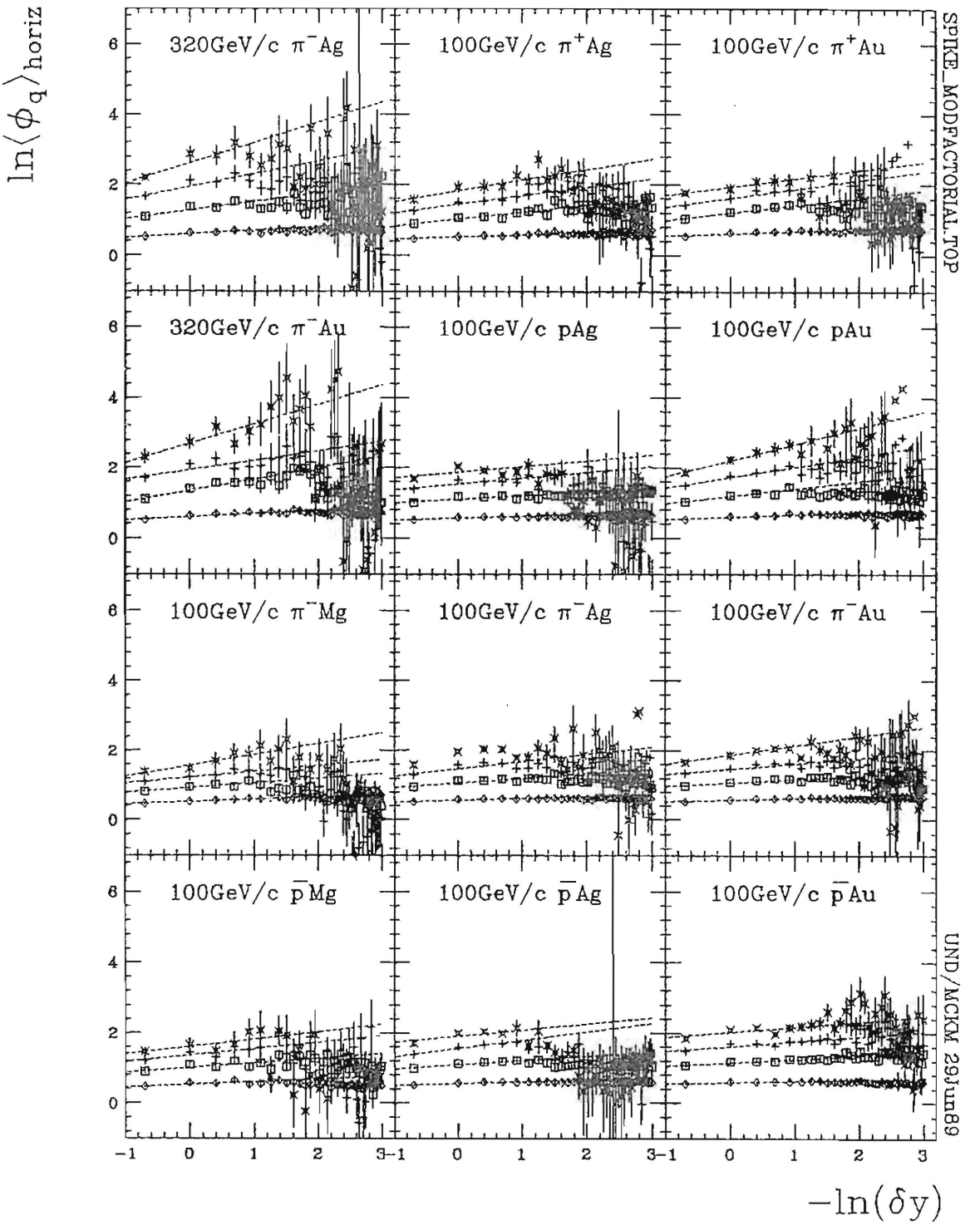

Figure 5.2.1 Normalized factorial moments of orders 2 through 5 function of rapidity resolution. Dashed lines are linear fits made in the rapidity resolution region extending from $\delta y = 2.0$ (-ln$\delta y = -.69$) to rapidity resolution $\delta y < .4$ (-ln$\delta y > .92$) at which the linear fit gives a correlation coefficient 90% or better. The slopes serve to guide the eye when looking for intermittent behavior and serve to measure the 'strengths' of the intermittencies, when present. Orders q=2 to 5 of $\langle\phi_q\rangle_{horiz}$ appear in ascending order bottom to top.

to $\delta y = .2$, though it extends further down to $\delta y = .1$ for pAu and $\bar{p}Au$ interactions. At smaller intervals, the factorial moments level out and drop off. This is pretty much the same behavior as for central 200 AGeV SAu interactions, which show a similar change in behavior for pseudorapidity intervals greater than .1. Thus non-statistical fluctuations are revealed only down to .1 unit rapidity for both hA and AA. [Adamovich 90]. The linear rise at small rapidity widths is due mostly to a few events, the spike events (those with 5 or more charged particles in .1 unit of rapidity). The rise significantly increases when the sample is limited to these high rapidity density events. Slopes f_q in **Figure 5.2.2** for spike events are larger than the slopes in **Figure 5.2.1** for all events by at least an order of magnitude. (Note the different scales used in each figure.) In the sense that intermittency means linearity down to the experimental resolution, hA data could be said to display intermittency. While the average rapidity resolution is around .03 units, the tails of most rapidity error distributions are significant enough at .1-.2 units to be responsible for the leveling off behavior.

The *strength* of intermittent effects is measured by the slope expressing the power relation between factorial moments and rapidity widths. Slopes have been determined using the greatest number of points which will still render a 90% correlation coefficient. These values are comparable to slopes fitted between rapidity resolution lengths $\delta y = 4$ and $\delta y = 2$. The slopes or strengths are larger than those reported for hh interactions [Ajinenko 89]. However, the larger slopes do not necessarily imply larger dynamical intermittency until it is clear that intermittency is a valid interpretation of the factorial moments. If it is a valid interpretation, then quantum statistical originals must also be ruled out in order to infer a new dynamics. If the E597 factorial moments are indeed signalling intermittency, the fact that the slopes are comparable or larger for hA interactions than for hh interactions is significant. Generally complex systems (e.g. hh as opposed to e^+e^-) have tended to display weaker intermittencies [Derado 90].

Intermittency has been shown to include a possible signal of QGP transitions [Bialas 90]. The anomalous fractal dimension of order q, d_q, related to the

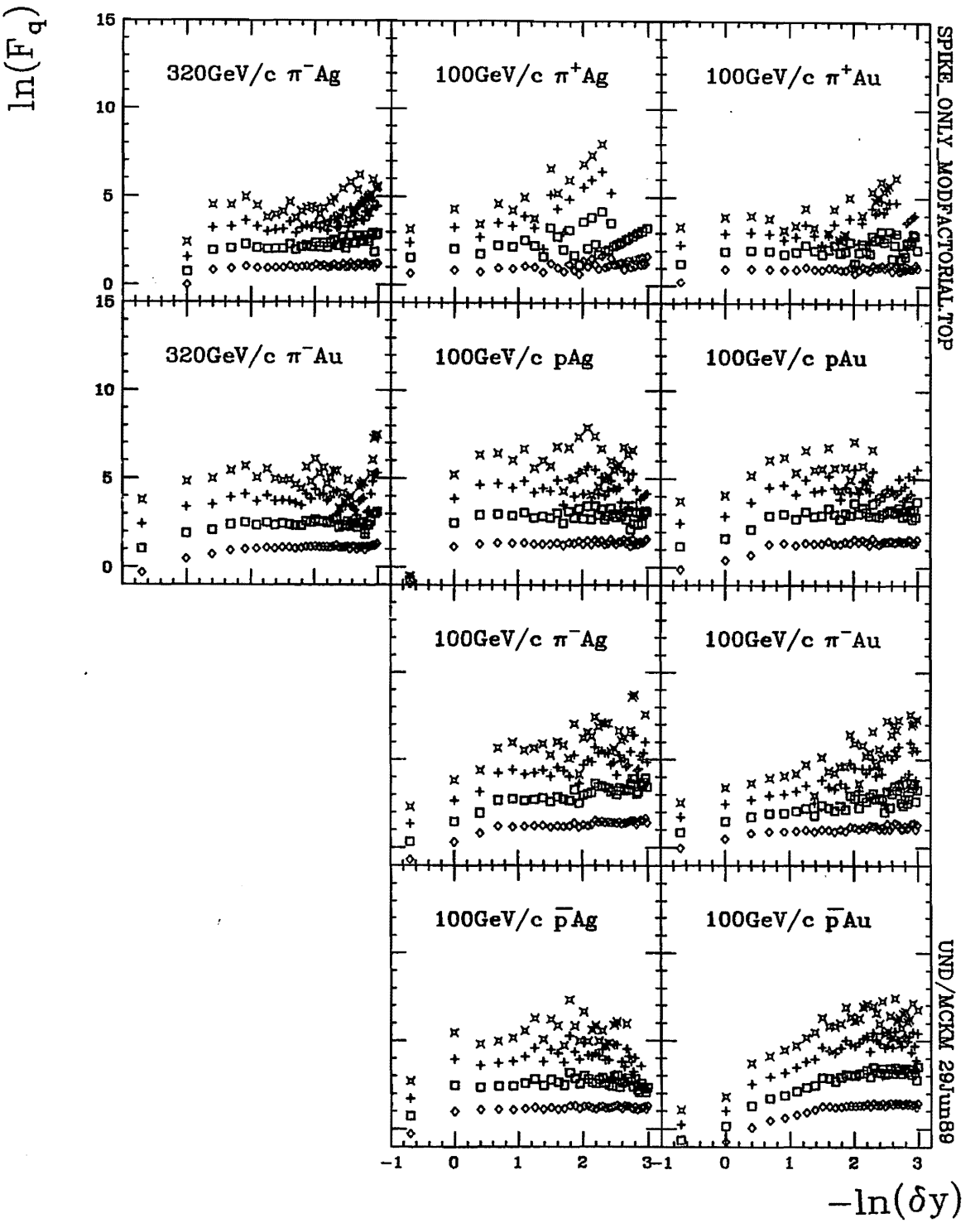

Figure 5.2.2 For spike events only, the normalized factorial moments of orders 2 through 5 as functions of rapidity resolution. Dashed lines are linear fits made in the rapidity resolution region extending from $\delta y = 2.0$ (-ln$\delta y = -.69$) to rapidity resolution $\delta y < .4$ (-ln$\delta y > .92$) at which the linear fit gives a correlation coefficient 90% or better. The slopes serve to guide the eye when looking for intermittent behavior and serve to measure the 'strengths' of the intermittencies, when present. Orders q=2 to 5 of $\langle \phi_q \rangle_{horiz}$ appear in ascending order bottom to top.

intermittency strengths or slopes f_q by

$$d_q = f_q/(q-1),$$

is expected to be approximately linear in q for cascading processes but approximately independent of q for second order QGP transitions. E597 results show that, though a strong correlation exists between slopes f_q and orders q (**Figure 5.2.3**), a similar plot of d_q as a function of q (**Figure 5.2.4**) is consistent with d_q being independent of q. Anomalous fractal dimensions for simple interaction systems, e.g. μp [Derado 90], e^+e^- [Buschbeck 88], have been shown to be very strongly correlated to q. Thus, on the basis of anomalous fractal dimension, hA interactions (particularly those known as spike events) are candidates for QGP transitions.

Possibly corroborating this conclusion is the fact that a Gaussian approximation in a random cascading model results in the recursive relation

$$f_{q+1} - f_q = q f_2$$

[Bialas 88] when the number of scales over which the cascades are occurring is large. This recursion relation, however, is not valid for the E597 samples as seen by comparing $3f_2^{prod}$ and f_3^{prod}; $6f_2^{prod}$ and f_4^{prod}; and $10f_2^{prod}$ and f_5^{prod} in **Table 5.2.1**. Either a random cascading model is inappropriate and/or the number of scales is small.

5.3 QUANTUM STATISTICAL DESCRIPTIONS

A question of great interest is whether the power law behavior of multiplicity fluctuations is dynamical or simply a quantum statistical effect. But even if QS is responsible for the power law behavior of most events, it may not account for spike event characteristics which may be signalling intermittency and/or QGP [Carruthers 90].

5.3.1 Bose-Einstein interference

There is evidence that quantum statistics alone cannot explain intermittency found in E597 interactions. It has been proposed that Bose-Einstein (BE) interference

Table 5.2.1 Intermittency strengths for charged and negative produced particles. These are defined as the slope of $\ln F_q$ as a function of -$\ln\delta y$ in the range $\delta y = 2$ to $\delta y = .4$ where F_q is the horizontally averaged factorial moment. The predicted values of the higher orders are also given (as multiples of f_2) as per the recursive relation expected between orders based on random cascade models. Correlation coefficients R designate the goodness of fit.

Projectile	320GeV/c		100GeV/c									
	π^-	π^-	π^+	π^+	p	p	π^-	π^-	π^-	$\bar{p}$	$\bar{p}$	$\bar{p}$
Target	Ag	Au	Ag	Au	Ag	Au	Mg	Ag	Au	Mg	Ag	Au
f_2^{prod}	.10	.14	.08	.11	.06	.11	.09	.08	.08	.09	.07	.05
Δf_2^{prod}	.02	.03	.02	.03	.02	.03	.02	.01	.01	.03	.01	.02
R	.96	.99	.95	.98	.91	.95	.99	.95	.99	.74	.95	.92
$f_2^{negprod}$	.10	.12	.07	.13	.07	.12	.10	.08	.07	.09	.08	.05
$\Delta f_2^{negprod}$	.03	.04	.04	.05	.03	.04	.04	.01	.02	.04	.02	.02
R	.97	.99	.82	.97	.83	.98	.94	.91	.99	.73	.99	.95
$3f_2^{prod}$	.30	.42	.24	.33	.18	.33	.27	.24	.24	.27	.21	.15
$\Delta 3f_2^{prod}$	.06	.09	.06	.09	.06	.09	.06	.03	.03	.09	.03	.06
f_3^{prod}	.23	.34	.19	.30	.13	.26	.17	.17	.17	.17	.18	.13
Δf_3^{prod}	.05	.07	.06	.06	.04	.06	.06	.03	.03	.06	.03	.03
R	.94	.98	.92	.99	.78	.96	.93	.90	.99	.79	.98	.96
$f_3^{negprod}$	.27	.22	.23	.15	.23	.17	.20	.14	.23	.16	.22	.15
$\Delta f_3^{negprod}$	.08	.09	.10	.10	.08	.10	.11	.05	.06	.11	.05	.06
R	.91	.95	.99	.92	.85	.66	.86	.89	.96	.78	.98	.92
$6f_2^{prod}$	.60	.84	.48	.66	.36	.66	.54	.48	.48	.54	.42	.30
$\Delta 6f_2^{prod}$	.12	.18	.12	.18	.12	.18	.12	.06	.06	.18	.06	.12
f_4^{prod}	.33	.27	.32	.40	.20	.46	.27	.27	.26	.24	.31	.20
Δf_4^{prod}	.09	.09	.09	.09	.06	.09	.11	.05	.05	.12	.05	.05
R	.91	.80	.97	.97	.81	.99	.98	.83	.99	.82	.98	.89
$f_4^{negprod}$	.18	.09	.36	.19	.23	.17	.49	.17	.34	.14	.26	.25
$\Delta f_4^{negprod}$	.13	.14	.16	.17	.08	.10	.22	.10	.12	.17	.10	.10
R	.87	.39	.98	.67	.85	.66	.99	.70	.98	.74	.97	.97
$10f_2^{prod}$	1.00	1.40	.80	1.10	.60	1.10	.90	.80	.80	.90	.70	.50
$\Delta 10f_2^{prod}$	.20	.30	.20	.30	.20	.30	.20	.10	.10	.30	.10	.02
f_5^{prod}	.51	.38	.47	.34	.23	.71	.45	-	.37	.27	.24	.11
Δf_5^{prod}	.13	.17	.18	.14	.07	.14	.18	-	.09	.21	.08	.06
R	.92	.80	.93	.97	.56	.99	.95	.62	.98	.73	.80	.36

FSLOPES.TEX UND/MCKM 4Sep90

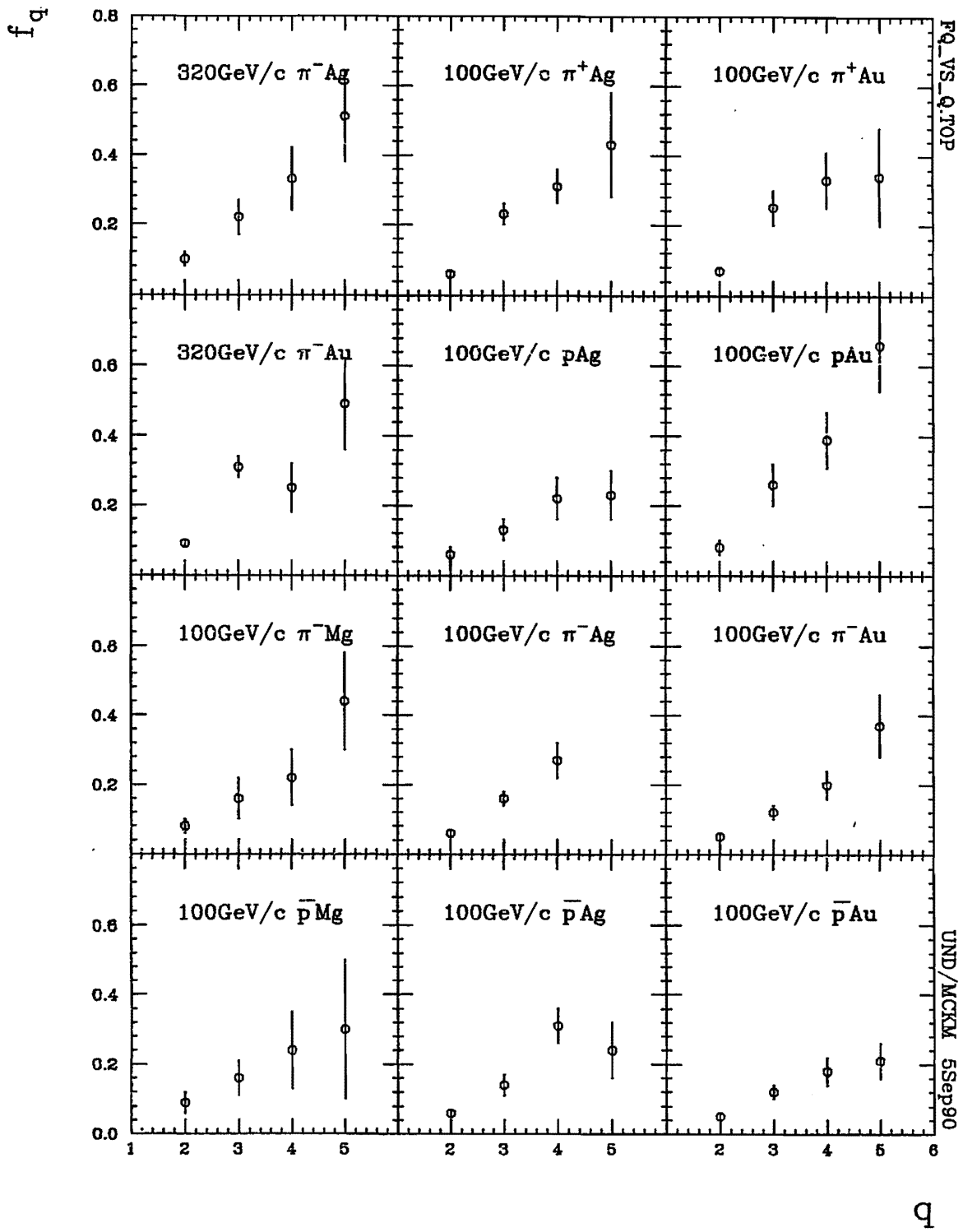

Figure 5.2.3 Slopes from the linear regression of normalized factorial moments as functions of order q. All charged produced particles are included.

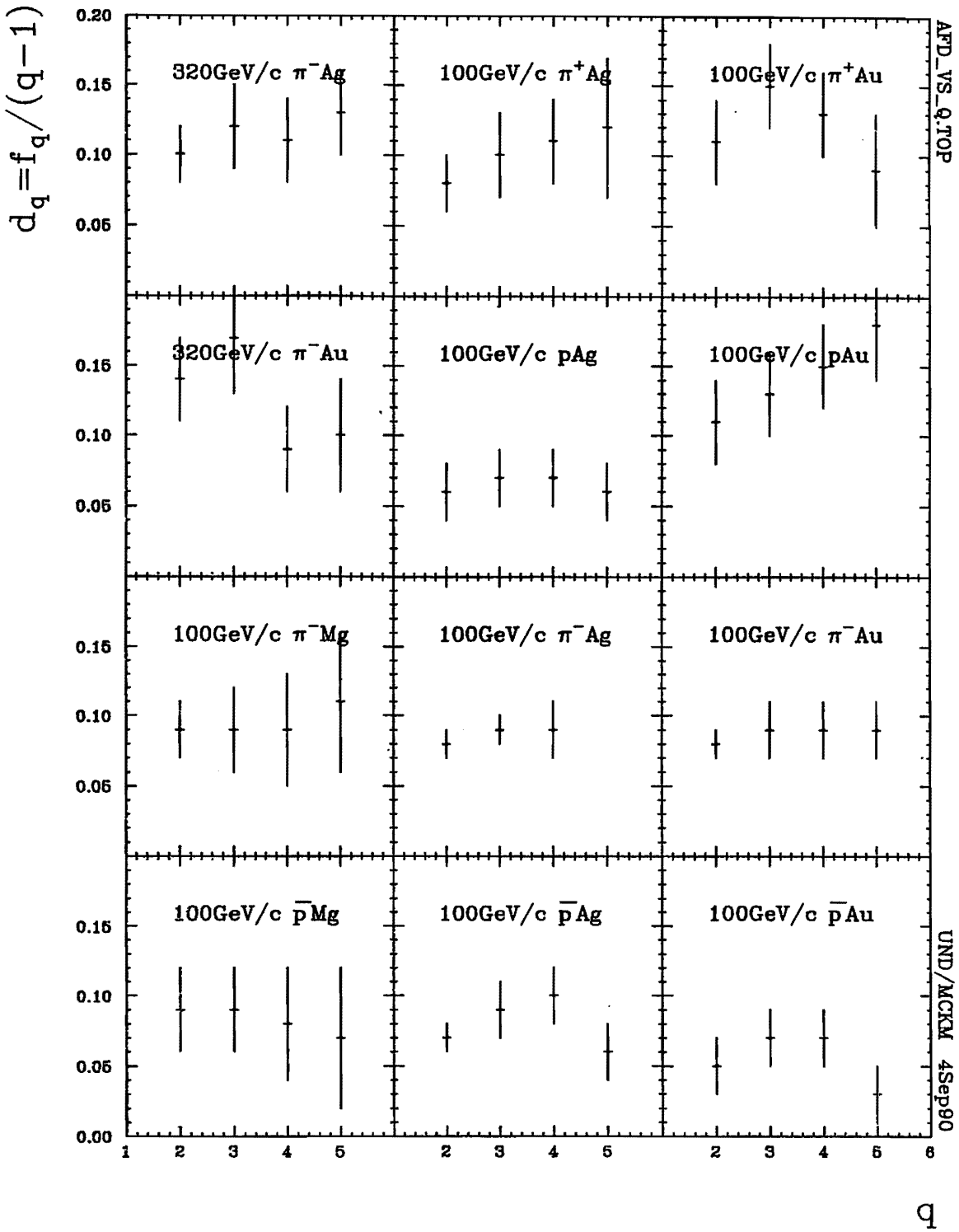

Figure 5.2.4 Anomalous fractal dimensions of orders 2 through 5 as functions of order q. All charged produced particles are included.

strengthens the signal for intermittency [Carruthers 89]. It is proposed that intermittency slopes should increase roughly by factor of 2 when the factorial moments are restricted to identically charged particles. But they do not. In fact, they closely parallel the slopes for all charged particles, as can be seen by comparing charged with negative produced particle results in **Table 5.3.1**. Similarly, e^+e^-, π^+p, and K^+p do not show a factor of 2 increase in the factorial moments when restricted to positive particle products [Kittel 90]. This provides a strong case against BE origins for intermittency [Gyulassy 90].

5.3.2 NBD interpretations

A natural theoretical relation exists between NBD parameters and factorial moments. This is not surprising from a phenomenological point of view since density spikes are strongly influenced by multiplicities which in turn are well described by NBD parameters. Since density spikes are responsible for most intermittency, NBD parameters must relate to intermittency.

Factorial moments of order q are calculated in terms of NBD parameter k:

$$\langle F_q \rangle_{NBD} = \frac{k(k+1)...(k+q-1)}{k^q}$$

In particular,

$$\langle F_2 \rangle_{NBD} = 1 + \frac{1}{k}$$

$$\langle F_3 \rangle_{NBD} = 1 + \frac{3}{k} + \frac{2}{k^2}$$

$$\langle F_4 \rangle_{NBD} = 1 + \frac{6}{k} + \frac{11}{k^2} + \frac{6}{k^3}$$

$$\langle F_5 \rangle_{NBD} = 1 + \frac{10}{k} + \frac{35}{k^2} + \frac{50}{k^3} + \frac{24}{k^4}$$

These are associated with factorial moments $\langle F_q^{cms} \rangle$ of the rapidity interval centered at the center-of-mass rapidity [Buschbeck 88]

$$\langle F_{cms}^i \rangle = \frac{\langle n^{cms}(n^{cms}-1)...(n^{cms}-q+1) \rangle}{\langle n^{cms} \rangle^q}$$

where n^{cms} is the population of the center-of-mass rapidity bin.

Experimentally, NBD parameters have been useful when rapidity information is not available. Factorial moments have been calculated for e^+e^- interactions [Derrick 86; Adamus 88] on the basis of NBD fits to the produced particle multiplicity distributions in limited intervals of rapidity, centered about the interaction cms. Data from hA interactions confirm the relation between $\langle F^i_{cms} \rangle$ and $\langle F_q \rangle_{NBD}$ and thus the feasibility of using NBD parameters. NBD fits are made for multiplicity distributions in a central rapidity bin of width δy to determine the parameter k needed to estimate $\langle F_q \rangle_{NBD}$. These are then compared in **Figure 5.3.1** with the factorial moments calculated directly for that central bin. The direct and NBD-based values essentially agree in the regions of δy for which both have been calculated considering the errors involved and the fact that $\langle F^i_{cms} \rangle$ is a direct bin average and $\langle F_q \rangle_{NBD}$ assumes a rapidity plateau not observed in hA interactions. But the link between NBD and intermittency parameters is of limited value, particularly for complex targets. The best agreement occurs for E597's simplest interactions, hMg.

5.3.3 Normalized factorial cumulants

If the power law dependence of $\langle \phi_q \rangle$ on the bin width δy is due to partially coherent systems, then two parameters describe the relative mix of fields in a quantum statistical treatment: chaoticity and coherence length. Chaoticity p is the fraction of the secondary multiplicity which originates from the chaotic component of the field. The coherence length ξ (assumed to be finite) is $\delta y/\beta$ where β is the available number of rapidity space cells available for coherent multiple production. β-scaling refers to the proposal that power-law dependencies are attributable to this number of cells changing.

Both hh and AA intermittency strengths have been successfully fit with curves obtained assuming exclusively quantum statistical origins. These fits are consistent with reported approximate chaoticity p=.32 and coherence length $\xi = 1$ for $\sqrt{s} = 22GeV$ pp data (NA22); with p=.44 and $\xi = 4.0$ for $\sqrt{s} = 540GeV$ (UA5). In obtaining these results, rapidity windows were centered about $y_{cms} = 0$ and k=1 was assumed. However, results are similar when they are obtained individually for

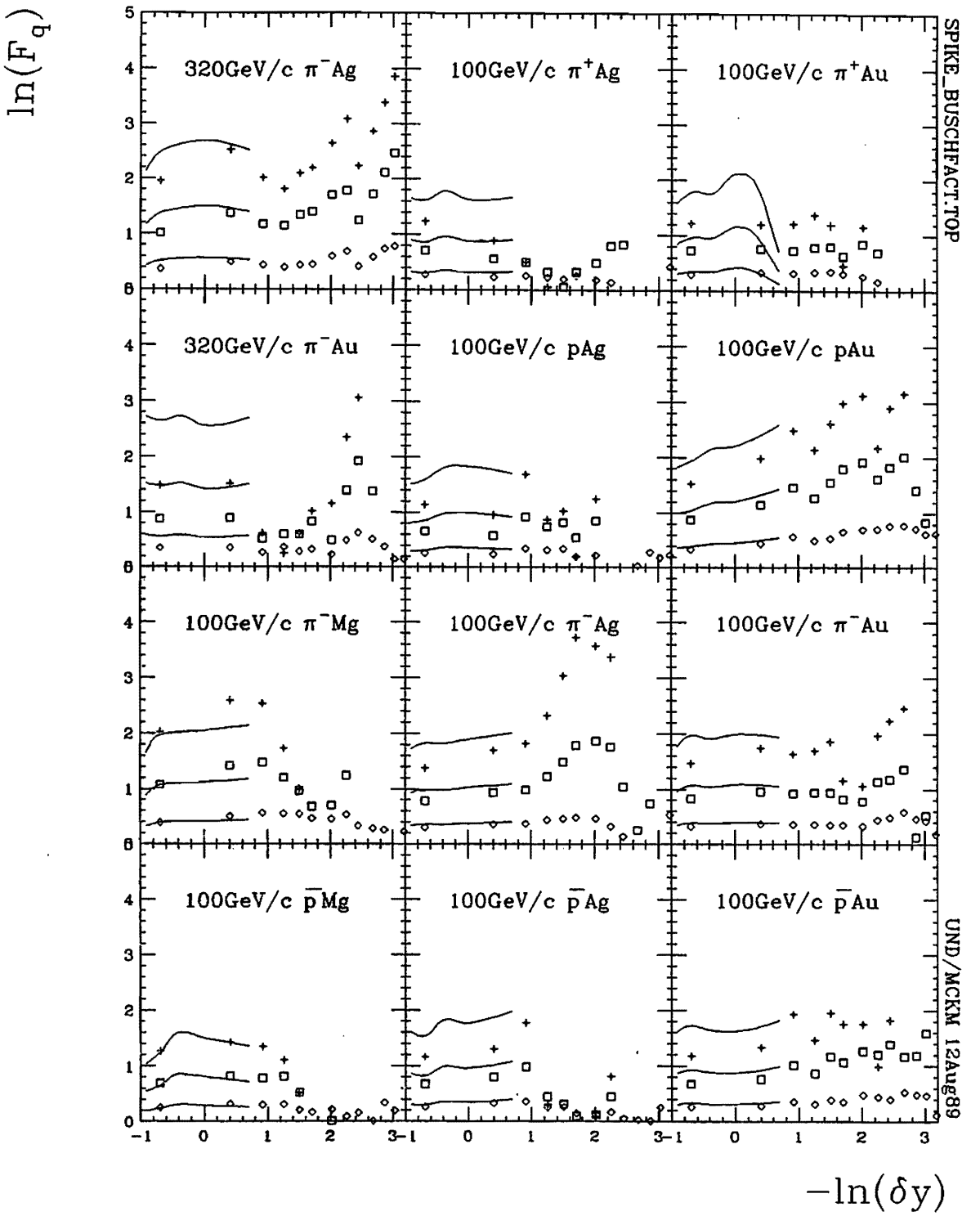

Figure 5.3.1 Factorial moments of orders 2 through 4 (bottom to top, respectively) calculated directly and using NBD parameters as a function of rapidity resolution. Lines are the NBD estimates, points are direct calculations.

rapidity windows of given rapidity width spanning the entire range and averaged over the windows. The chaoticity and coherence length for pp at 22 GeV (NA22) [Adamus 88c] and SAu at 200 AGeV (EMU01) [Stenlund 88] have been reported to be $p = .2$, $\xi = .9$ and $p = .015$ and $\xi = .2$, respectively [Carruthers 90]. So it might be expected that hA data falls somewhere between these values. Chaoticities for E597 hA samples have been found to be near those for hh.

The theoretical base for these fits has been developed in terms of cumulant factorial moments μ_i, which are sensitive to dynamical details than normalized factorial moments. These cumulant factorial moments are very simply related to standard normalized factorial moments ϕ_i [Fowler 88]:

$$\mu_1 = 1$$
$$\mu_2 = \phi_2 - 1$$
$$\mu_3 = \phi_3 - 3\phi_2 + 2$$
$$\mu_4 = \phi_4 - 4\phi_3 + 12\phi_2 - 3\phi_2^2 - 6$$
$$\mu_5 = \phi_5 - 5\phi_4 + 20\phi_3 - 60\phi_2 + 30\phi_2^2 - 10\phi_3\phi_2 + 24$$

In a QS treatment, cumulant factorial moments are related to chaoticity p and the effective number of participating cells k, where k plays the same role as it does when introduced in the context of NBD as the number of cells or groupings of indistinguishable, same-state bosons and 1/k is the fraction of identical bosons already present which participate in stimulated emission (see **Appendix 3A**). The parameter k can be expressed as the product k=cs, where c is the number of independent charge states and s, the number of independent sources. The cumulant factorial moments in a QS model are given as follows:

$$\mu_2 = \tfrac{1}{k}[p^2 B_2 + 2p(1-p)\tilde{B}_2]$$
$$\mu_3 = \tfrac{1}{k_2}[2p^3 B_3 + 6p^2(1-p)\tilde{B}_3]$$
$$\mu_4 = \tfrac{1}{k_3}[6p^4 B_4 + 24p^3(1-p)\tilde{B}_4]$$
$$\mu_5 = \tfrac{1}{k_4}[24p^5 B_5 + 120p^4(1-p)\tilde{B}_5]$$

where B and $\tilde{B}$ are functions of the available number of rapidity cells $\beta = \delta y/\xi$

[Jaiswal and Mehta 70]:

$$B_2 = \frac{e^{-2\beta}+2\beta-1}{2\beta^2}$$

$$B_3 = \frac{3[e^{-2\beta}(\beta+1)+\beta-1}{2\beta^3}$$

$$B_4 = \frac{e^{-4\beta}+4e^{-2\beta}(4\beta^2+10\beta+7)+20\beta-29}{8\beta^4}$$

$$\tilde{B}_2 = \frac{2(e^{-\beta}+\beta-1)}{\beta^2}$$

$$\tilde{B}_3 = \frac{-e^{-2\beta}+2e^{-\beta}(\beta+4)+4\beta-7}{\beta^3}$$

$$\tilde{B}_4 = \frac{e_{-3\beta}-e^{-2\beta}(4\beta+10)+e^{-\beta}(2\beta^2+18\beta+47)+16\beta-38}{2\beta^{-4}}$$

B_5 and $\tilde{B}_5$ have been tabulated from a Monte Carlo calculation [Fowler 88]:

β	B_5	$\tilde{B}_5$
.5	.45110	.52840
1.0	.22000	.29630
1.5	.11480	.17530
2.0	.06320	.10800
2.5	.03652	.06878
3.0	.02234	.04536
3.5	.01428	.03140
4.0	.00912	.02156
4.5	.00620	.01542
5.0	.00441	.01158

There are several ways to estimate the chaoticity and and coherence length. The first uses a small β approximation to determine p from the small rapidity interval data, and then fits the large intervals with an appropriate ξ. Having calculated horizontal average normalized factorial moments for decreasing bin size, one compares

the very small rapidity width moments with the Glauber-Lachs expression [Glauber 63, Lachs 65]

$$\langle \phi_q \rangle = q!(\frac{p}{k})^q L_q^{k-1}(x)$$

which should be valid when δy is small or $\beta << 1$. In the expression, L_q^{k-1} is a generalized Laguerre polynomial and $x = k(p-1)/p$. For E597 samples, the fit for coherence has been made at small δy, using the Glauber-Lachs expression for k=1, and q=2. The QS reason for choosing k=1 (the one-cell Bose Einstein condition) is emphasized when noting that at each k, p=0 (total coherence) and p=1 (total incoherence) form upper and lower bounds, respectively. When fields are totally coherent, P(n) is Poissonian and factorial moments have a lower bound $\phi_q \geq 0$. But when the field is totally chaotic, P(n) is negative binomial with normalized factorial moments related to order q and the NBD parameter k by

$$\phi_q = \frac{(q+k-1)!}{k^q(k-1)!}$$

with an upper bound when k=1

$$\ln \phi_q \leq \ln(q!)$$

which can be checked at small δy. Thus the following limits are expected:

$$\ln \phi_2 \leq .693$$
$$\ln \phi_3 \leq 1.782$$
$$\ln \phi_4 \leq 3.1781$$
$$\ln \phi_5 \leq 4.7875$$

Within errors, E597 factorial moments stay within these limits. In fact, the higher moments are considerably below their limits. This is in agreement with all other experimental data to date, which have been entirely consistent with these limits. But while the limits are respected, a very wide range of p is admissable. Thus only rough conclusions can be proffered with respect to chaoticity p on the basis of a fit of ϕ_2 to the Glauber-Lachs expression. The Glauber-Lachs expression for ϕ_2 is evaluated for k=1 and tabulated for convenience in **Table 5.3.1.** Observed values of

Table 5.3.1 Representative values of log normalized factorial moments of order 2 $\ln \phi_2$ calculated as a function of chaoticity p by the Glauber-Lachs expression valid for $\beta << 1$ which is in turn valid at small rapidity intervals. k=1 is assumed, so $\phi_2 = 2!p^2 L_2^0 \frac{(p-1)}{p}$.

p	$\ln \phi_2$	p	$\ln \phi_2$	p	$\ln \phi_2$
.01	.020	.34	.448	.67	.637
.02	.039	.35	.456	.68	.641
.03	.057	.36	.464	.69	.644
.04	.075	.37	.472	.70	.647
.05	.093	.38	.480	.71	.650
.06	.110	.39	.487	.72	.653
.07	.127	.40	.495	.73	.656
.08	.143	.41	.502	.74	.659
.09	.159	.42	.509	.75	.661
.10	.174	.43	.516	.76	.664
.11	.189	.44	.523	.77	.666
.12	.203	.45	.529	.78	.669
.13	.218	.46	.536	.79	.671
.14	.231	.47	.542	.80	.673
.15	.245	.48	.548	.81	.675
.16	.258	.49	.554	.82	.677
.17	.271	.50	.560	.83	.679
.18	.283	.51	.565	.84	.680
.19	.296	.52	.571	.85	.682
.20	.307	.53	.576	.86	.683
.21	.319	.54	.581	.87	.685
.22	.330	.55	.586	.88	.686
.23	.342	.56	.591	.89	.687
.24	.352	.57	.596	.90	.688
.25	.363	.58	.601	.91	.689
.26	.373	.59	.605	.92	.690
.27	.383	.60	.610	.93	.691
.28	.393	.61	.614	.94	.691
.29	.403	.62	.618	.95	.692
.30	.412	.63	.622	.96	.692
.31	.421	.64	.626	.97	.693
.32	.430	.65	.630	.98	.693
.33	.439	.66	.634	.99	.693

GLAUB.TAB UND/MCKM 8Sep90

Table 5.3.2 Estimated chaoticities p based on average cumulant factorial moments. Errors are considered to produce an upper and lower limit. Where the upper limit exceeds the theoretical maximum, 'TM' designates the assumption of the limiting value $\ln \phi_2 = .693$.

Projectile	320GeV/c		100GeV/c									
Target	π^- Ag	π^- Au	π^+ Ag	π^+ Au	p Ag	p Au	π^- Mg	π^- Ag	π^- Au	$\bar{p}$ Mg	$\bar{p}$ Ag	$\bar{p}$ Au
$\ln \phi_2^{upperlimit}$	TM	TM	.686	TM	.678	TM	TM	.641	.675	.562	.627	.597
$\langle \ln \phi_2 \rangle$	.725	.687	.594	TM	.605	.631	.615	.584	.618	.458	.571	.545
$\ln \phi_2^{lowerlimit}$	.626	.588	.502	.591	.532	.523	.498	.526	.560	.354	.515	.493
$p^{upperlimit}$	1	1	.88	1	.82	1	1	.68	.81	.50	.64	.57
$\langle p \rangle$	1	.89	.57	1	.59	.65	.61	.55	.62	.35	.52	.47
$p^{lowerlimit}$	.50	.55	.41	.56	.45	.44	.40	.44	.50	.24	.43	.40

CHAOT.TAB UND/MCKM 30Aug90

ϕ_2 are then compared with the calculated values of **Table 5.3.1** from which associated values of p are assigned. The observed values of ϕ_2 were averaged over $\delta y = .05 - .1$ and are listed with their corresponding values of chaoticity p in **Table 5.3.2**. Its values ranged generally greater than .40, which is larger than expected from hh and AA results ($p = .2$ for 22GeV pp [Adamus 88] and $p = .015$ for 200 AGeV SAu [Stenlund 88]). AA interaction chaoticities have been much smaller than hh, but the present hA factorial moments are fitted with chaoticities not much different from hh values at the lower limit.

Having estimated interaction chaoticity, one then can in principle estimate a coherence length by 1) finding β corresponding to a specific $\mu_2(\delta y)$ along the curve associated with the chaoticity p in **Figure 5.3.2** and 2) calculating the coherence length by the relation $\xi = \delta y/\beta$. This approach was used for two samples, $\pi^- Ag$ and $\pi^- Au$ at 100 GeV/c. The second order cumulant factorial moments for these samples appear as horizontal lines in **Figure 5.3.3**. The dashed lines represent the cumulant factorial moments calculated as as functions of β for chaoticities consistent with the minimum and maximum chaoticity p determined according to the Glauber-Lachs expression. The horizontal distance between the points where the dashed and solid lines intersect represents the range of β associated with given δy. When only the maximum chaoticity μ_q intersects, $\beta = 0$ is assigned at the lower end. These lengths are then plotted as a function of δy in **Figure 5.3.4**. If the β's were known precisely, the inverse slope of the line connecting them is the coherence length ξ. Given a range of β, an estimate of the coherence length is made by connecting the origin with the midpoint of the range at $\delta y = 2$ (the most reliable point, regardless of the fact that β has its largest range there), making sure that all the other ranges are intersected, and finding the inverse slope. Thus the coherence length is estimated to be 5.2 and 4.7 units for $\pi^- Ag$ and $\pi^- Au$ interactions, respectively.

However, as a function of these estimates of p and ξ, the higher order cumulant factorial moments do not agree with the observed values. The calculated values overshoot the observed values considerably. Presumably the k=1 assumption may be invalid. If so, chaoticities would be greater than or equal to those in hh interactions,

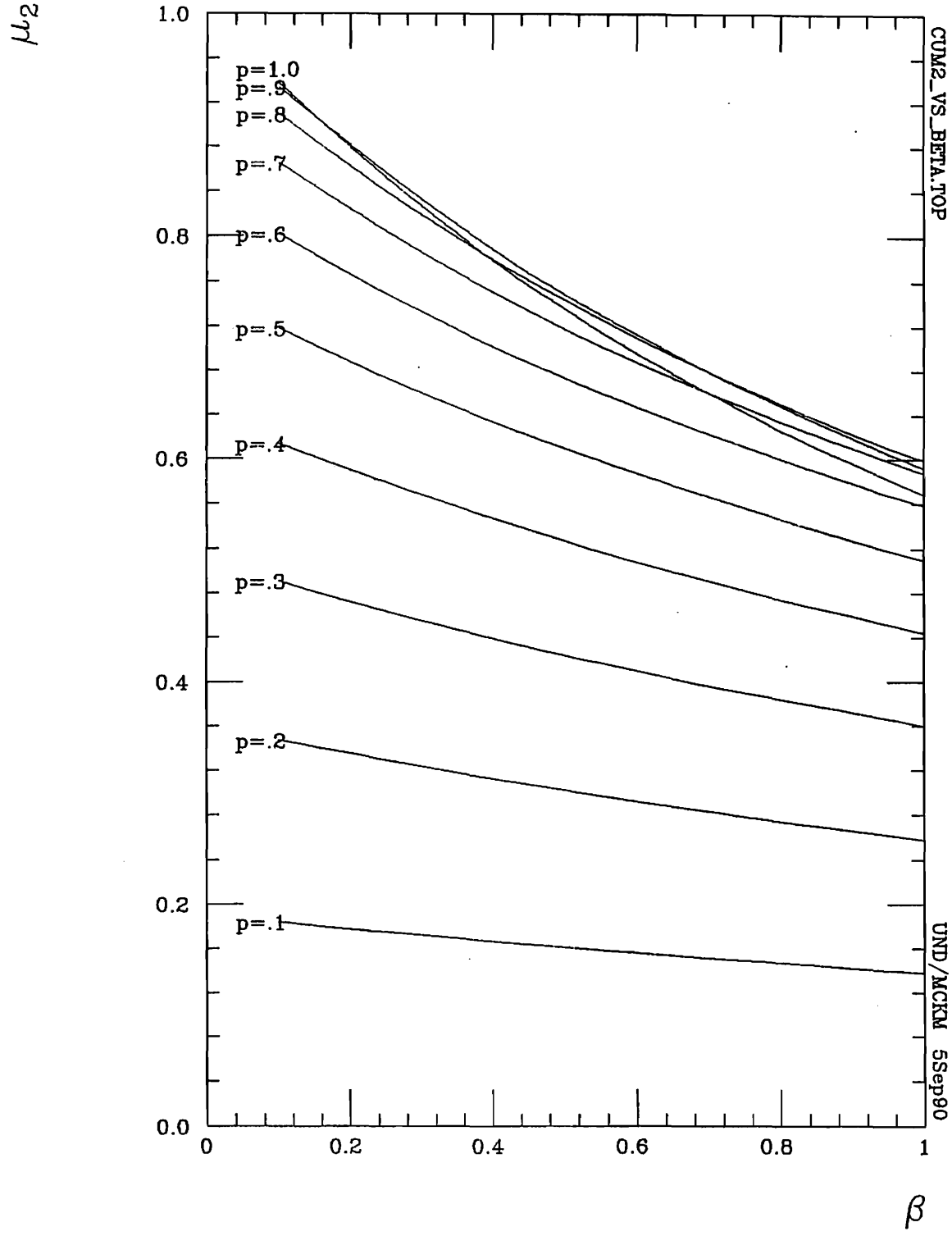

Figure 5.3.2 Normalized cumulant factorial moments as a function of β in a partial coherent quantum statistical model for varying chaoticity p.

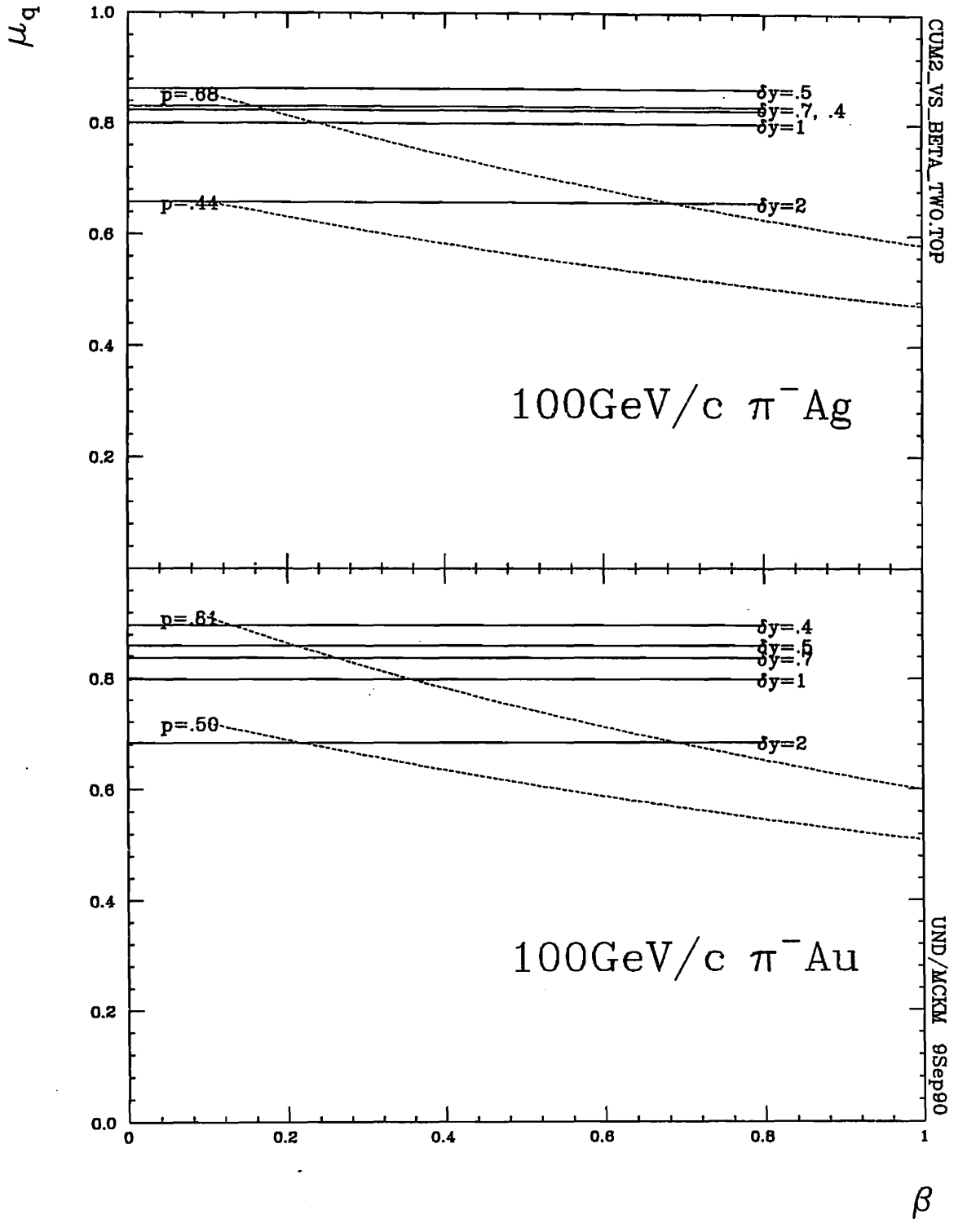

Figure 5.3.3 Normalized cumulant factorial moments as functions of β for estimated upper and lower limits of chaoticity p of two E597 data samples are given by the dotted lines. The horizontal lines are the experimentally observed moments at various rapidity resolutions δy. The horizontal range between intersections of the solid and dotted lines represents the β-range expected to be associated with δy.

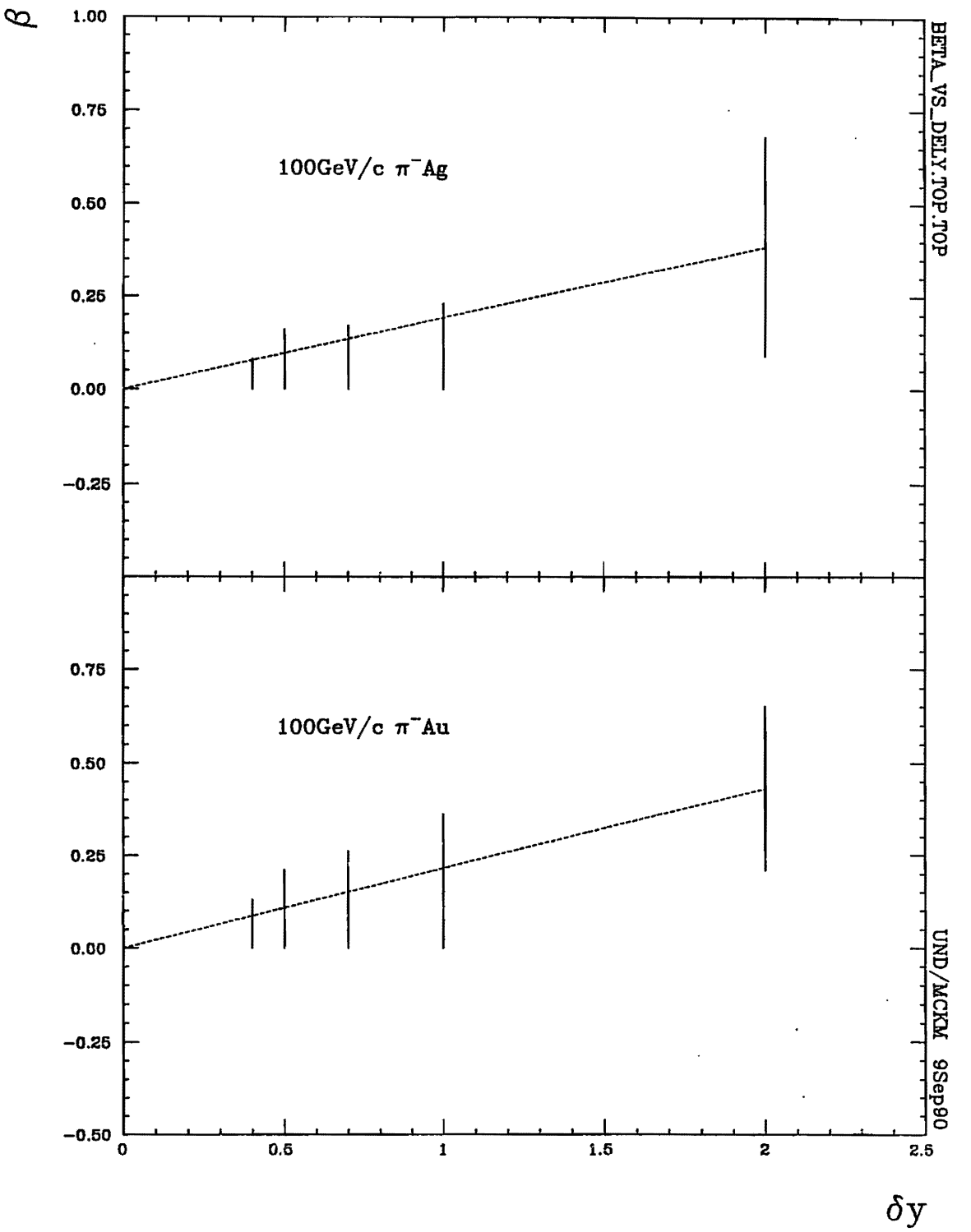

Figure 5.3.4 β as a function of δy for two E597 data samples based on the horizontal distances in **Figure 5.3.3**.

which they seem to be. But the large values of observed ϕ_2 rule out k=2. Both NA22 and UA5 studies reached a similar conclusion. So, introducing a greater number k of participating cells (*i.e.* k>1) does not improve agreement. However, fractional k are not automatically excluded and should be studied further.

In a further attempt to achieve agreement between observed and QS-calculated high order cumulants while preserving the agreement at low orders, direct fits were made to the full expression of $\mu_2(\beta)$ using two free parameters. But no single set of values could be found to describe all orders. However, at each order, the factorial moments could be fitted reasonably well. Throughout, the component coherent and incoherent fields have been assumed to have the same frequency, an assumption that is also used in quantum optics. The fact that high order μ_q are poorly described on the basis of μ_2 may be indicating that this assumption is inappropriate.

Individual fits for each order have been made for two samples, 100 GeV/c $\pi^- Ag$ and $\pi^- Au$, and appear in **Figure 5.3.5.** It is interesting to note that the two interactions share many of the same parameter values at given q: p ranging from .34 to .70, and ξ ranging from 1.9 to 3.4. Thus chaoticity seems to be larger than expected from comparisons of hh and AA data. But it compares favorably with E597 Bose-Einstein correlation estimates of chaoticity between .2 and .3. Also, chaoticity in hh interactions changes by about .1 when $\sqrt{s}$ increases from 22 to 540 GeV. Thus 100 GeV/c hA interactions ($\sqrt{s}$ = 13.6 when viewed in terms of hp collisions) are in general agreement with chaoticities between .2 and .3. So hA interactions are behaving with much the same mix of coherent and incoherent fields as hp interactions and may show an enhancement in the incoherent component.

5.4 SUMMARY

- A power-law relation exists between horizontal factorial moments and rapidity bin widths down to .1-.2 units rapidity in E597 data. *Linearity down to the experimental resolution could be signaling intermittency.*

- Intermittency strengths, the slopes describing the correlation between normalized

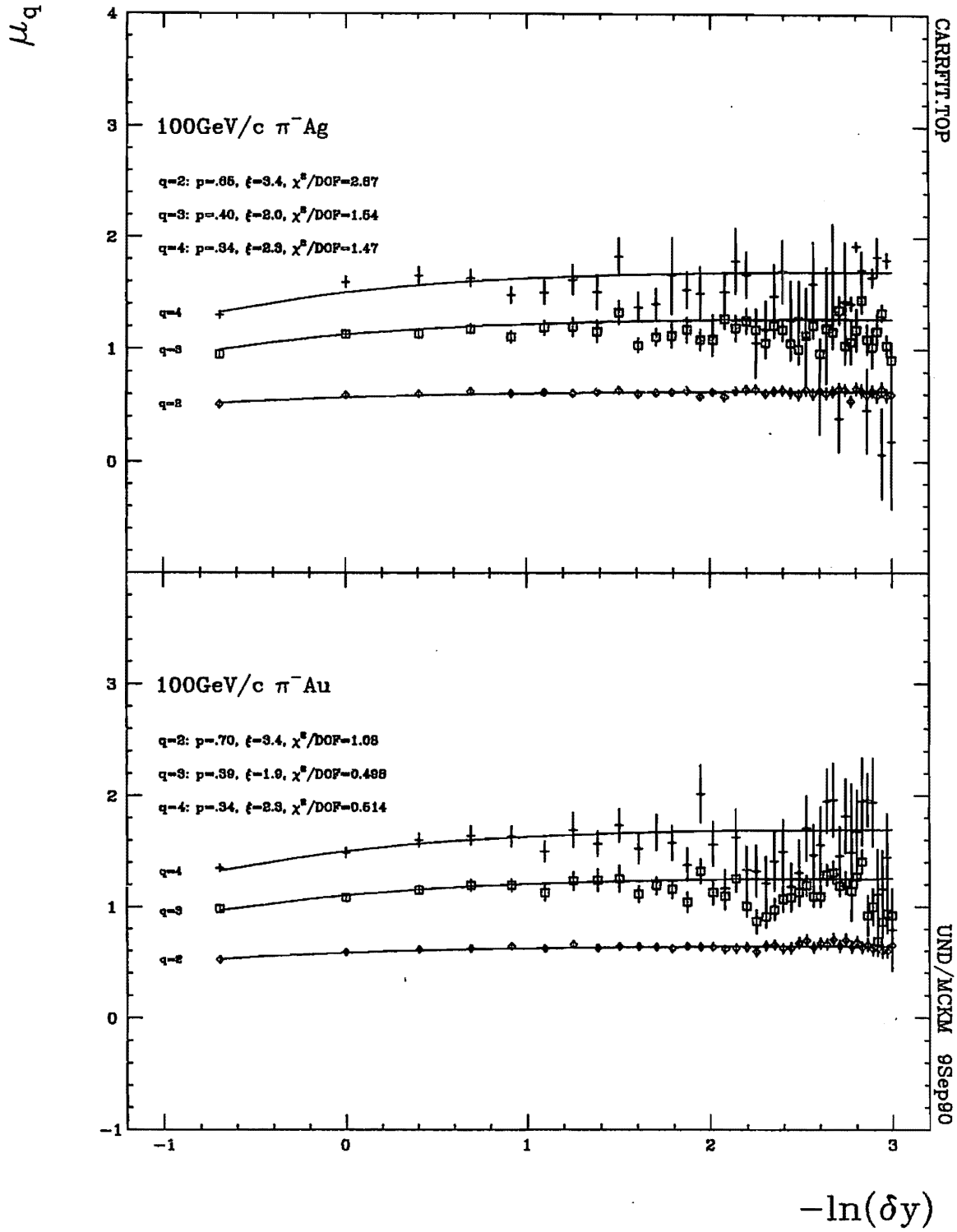

Figure 5.3.5 Normalized cumulant factorial moments as functions of rapidity resolution fitted according to a quantum statistical model. Each order is fitted independently since the parameters from the q=2 fit do not fit the higher orders.

factorial moments and the rapidity resolution length, are comparable in hA interactions to those associated with hh interactions, rather than significantly weaker. *QGP transitions are not ruled out as an origin of intermittency.*

- A strong correlation exists between the intermittency strengths and order q of the factorial moments, but not between the anomalous fractal dimension and q. *The anomalous fractal dimension is independent of q and thus is consistent with QGP second order transition behavior.*

- The intermittency strengths are not recursively related to one another as expected in random cascading models assuming a large number of scales. *Either the random cascading model is inappropriate and/or the number of scales over which the fluctuations occur is not very large.*

- Intermittency is stronger by at least an order of magnitude in spike events as compared all average events. *Increased intermittency strength is compatible with QGP transitions in spike events.*

- Factorial moments are approximated by NBD parameters. *Intermittency can be studied in the absence of rapidity data.*

- The factorial moments for small δy fall within limits set by QS for total coherence and total incoherence. *A partial stimulated emission view of multiparticle production is consistent with the data.*

- Chaoticity is estimated to be larger than .40. This is consistent with estimates based on Bose-Einstein correlations (k=1) and with NA22 pp data fits in a partial coherence approach.

CHAPTER 6

FRACTAL DIMENSION

The proposal to study intermittent fluctuations [Bialas 86] was originally made with cosmic ray data in mind. Even though cosmic ray data have characteristically high multiplicities, their scarcity makes event-by-event studies especially attractive. The present hA data are limited to multiplicities under 100. In this range, the validity of intermittency results may be statistically marginal. Errors of order 10, 20, 30,40, and 50% on the 1st, 2nd, 3rd, 4th, and 5th factorial moments, respectively, seriously limit the extent to which conclusions may be drawn. A single-event analysis technique which probes fluctuations is needed to substantiate and extend intermittency findings.

Dimension analysis in a fractal framework has been suggested as a possibility for single-event analysis [Dremin 87]. Natural phenomena are often characterized by their scaling behavior and it is precisely the scaling structure of hadronic interactions that has resisted conventional analysis to date. Like intermittency, fractals have fundamental ties with scaling behavior. Fractal objects, whose track record in the analysis of irregular forms is becoming impressive (simulations of clouds, smoke, trees, ferns as well as exotic abstract patterns generated by Julia sets popularized by Mandelbrot [Mandelbrot 74]), are particularly suited to the description of scaling behavior with chaotic outcomes. However, unlike intermittency, fractals emerge from an abstract, sophisticated, and elegant formalism — fractal geometry — which as yet has gone largely unimplemented in multiple production studies.

An entire discipline revolves about the topological behavior of fractal objects. As geometrical objects, fractals involve nondifferentiable curves and or surfaces and thus cannot be described by ordinary differential geometry. They exhibit singularities

and are said to contain fractional dimensions. Since these objects manifest infinite complexity under magnification, their study probes non-linearities and complexities associated with higher order cascading. If interactions are behaving fractally, simplicity can be extracted out of chaos and its evolution laws can be extracted from the jumble associated with hadron-nuclear interactions,

Hadron interaction chaos is presumed to involve basically simple evolution laws governing competing processes. Deterministic evolution laws are known to lead to chaotic behavior. Notwithstanding whatever simplicity they may display, cascading over just a few scales confuses patterns which would otherwise emerge independently at each scale. This confused pattern is *deterministic chaos* [Eckman 85].

Therefore, some chaotic behavior might be expected to be traceable to deterministic evolution laws in the context of suitably chosen fractal objects. As a first step, inelastic interactions (hh, hA, or AA) are treated as fractal objects. The interaction dynamics are directly associated with the geometry of the interaction products so the objects are chosen to be 3-momentum point sets corresponding to the end-points of all produced particle momentum vectors [Dremin 89b].

Scale is crucial in many models. An example of the role of scale in models is that of one of several interpretations for the EMC effect [Arnold 84; Aubert 83] which links it to changes in scale for a nucleon inside a nucleus [Jaffe 84]. This change in scale is thought to result from the swelling of nucleons for which the valence quarks are only partially deconfined [Ericson 86]. Total deconfinement characterizes quark-gluon plasma. Thus changes in scale may be signalling a new physics possiblity in tandem with the EMC effect.

In cases of deterministic chaos, definite fractal characteristics are displayed. These can be used to classify events, geometrically separating out folded processes. This classification of events is helpful in itself 1) to register rare processes, and 2) to provide an analytically manageable formalism [Hwa 89b]. But classification schemes have often been plagued with theoretical bias and fuzzy borders and no one scheme has clearly outperformed all others analytically. To build an unbiased, clear classification scheme with an automatic bonus, the primary characteristic of fractals—*dimension*—

is used. Dimension expresses the number of scales over which self-similarities occur. So in determining dimension, the extent to which different underlying dynamical mechanisms might be involved is being probed. Since cascading dynamics involve self-similar branching processes, separating out the cascades quite naturally fits into fractal avenues of investigation such as dimension analyses.

6.1 DETERMINING THE FRACTAL DIMENSION

Dimension, a seemingly familiar notion, is actually a subtle mathematical measure of sets. In the case of self-similar objects, dimension expresses the number of scales over which self-similarities occur, *e.g.* a sponge structure embedded within another sponge embedded within another sponge, and so forth. In the case of multiple production, an event's rapidity set describes a geometric object associated with an interaction and may derive from a self-similar object valid for all such interactions. Subdividing an event's rapidity distribution into intervals of width δ, dimensions d_q of that event satisfy the relation

$$< n_i^{q-1} >= \sum_{i=1}^{M} n_i^q \sim \delta y^{(q-1)d_q}$$

where M is $\Delta y/\delta y$ =number of intervals spanning rapidity space with Δy representing the full rapidity range and δy, the rapidity interval size, q is the dimension order, and n_i is the population of the ith interval. Thus d_q is the slope when plotting $\ln(\sum_{i=1}^{M} n_i^q)$ vs. $(q-1)\ln(\delta y)$ and is called the Renyii dimension of order q.

The fractal dimension D_F, otherwise known as the Hausdorff dimension, is d_0. With $q = 0$, it is calculated by determining the slope relating $\ln(N')$ and $-\ln(\delta y)$, where N' =the number of non-empty rapidity intervals. Whereas the ordinary notion of dimension, *topological dimension*, counts the number of independent directions one can move around a geometric object [Eckman 85], the notion of *fractal dimension* incorporates capacity as well. It measures porosity in a kind of 'box-counting algorithm' proposed by Hausdorff [Hausdorff 19] so that it can be described as the power to which the inverse length $1/\epsilon$ of a hypercube is taken in order to cover an object with an integral number $N'(\epsilon)$ of hypercubes of length ϵ and volume ϵ^{d_0}. In that

sense, it is the inverse ruler spacing power needed to construct a snug covering for a geometrical object. Sometimes this object is analogous to a self-similar dust of points; 'a sponge within a sponge within a sponge'; or, as Hagedorn [Hagedorn 65] envisioned hadronic collisions twenty-five(25) years ago, a *fireball* of fireballs, which in turn consist of fireballs. When an object is *sparse* in this sense, it will have non-integer fractal dimension and will be called a *fractal* in that sense. The Cantor set is a familiar example of such an object. Its fractal dimension is 2/3.

Applied to a dynamical system evolving deterministically but behaving chaotically, D_F estimates the number of independent relevant variables. Thus the number of degrees of freedom for the system n_f is given by

$$n_f = [D_F] + 1$$

where [ ] denotes the integer portion of D_F.

6.1.1 Rapidity distributions

Inclusive rapidity distributions like those shown in **Figure 6.1.1** vary smoothly for large statistics. They make inappropriate objects for fractal analysis when partitioned by varying resolution lengths δy. However, rapidity distributions like those shown in **Figure 6.1.2** for *individual* events are anything but smooth and could thus lend themselves to fractal analysis techniques which by their very nature capitalize on fluctuation. Rather than being studied in terms of average features in an effort to circumvent dissimilarities between events, events are individually studied with special attention to their fluctuations. Irregularities can be expressed in terms of the fractal nature of interactions. Individual events are classified in terms of fractal dimension and relate otherwise dissimilar topologies without forfeiting the search for unusual event features.

6.1.2 Limiting factors

Fractal dimension, however, is not considered to be a very good event measure unless the multiplicity is large. There are so few particles in a typical hh event at 100 and

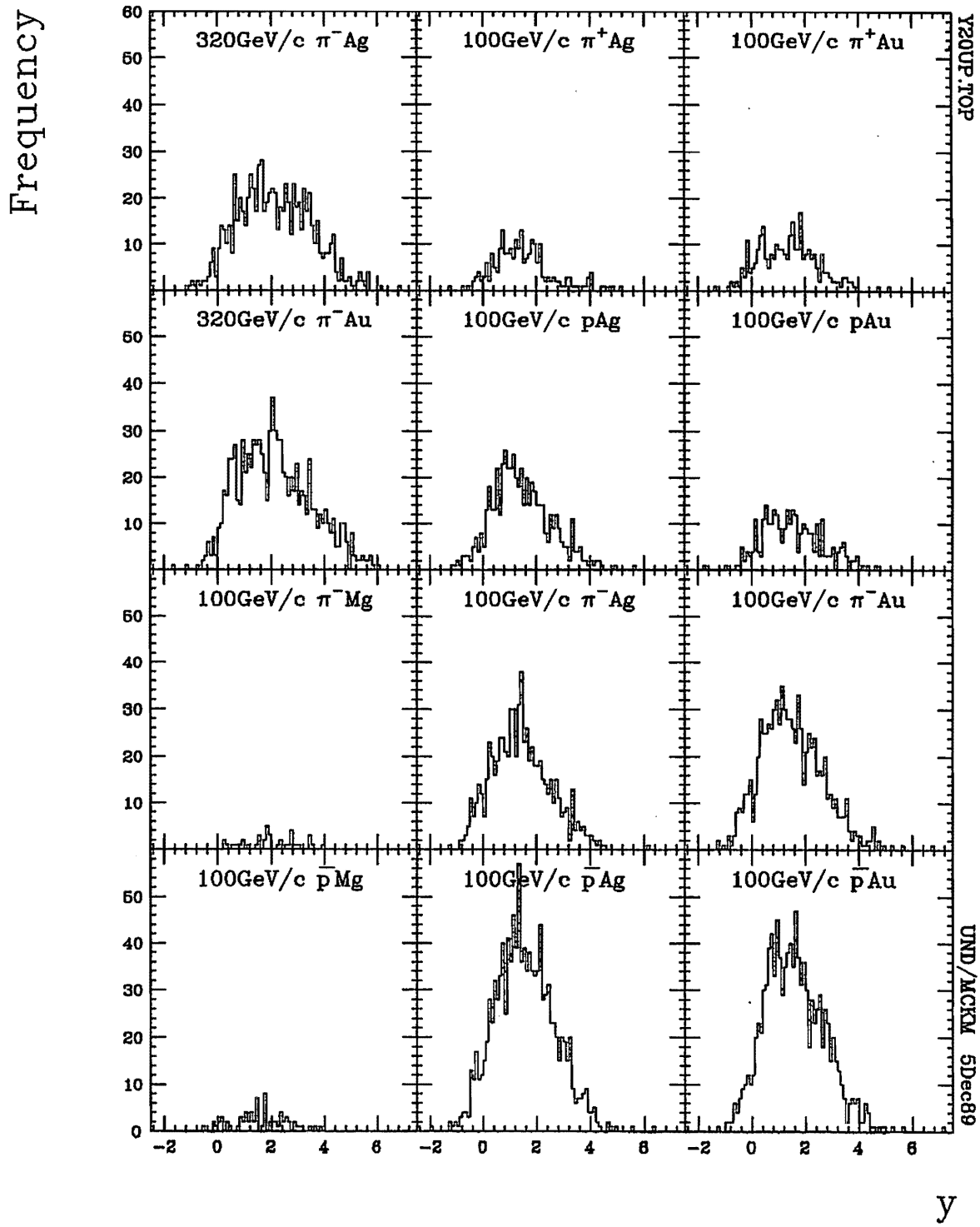

Figure 6.1.1 Inclusive rapidity distributions for hA events with produced particle multiplicities of 20 or more.

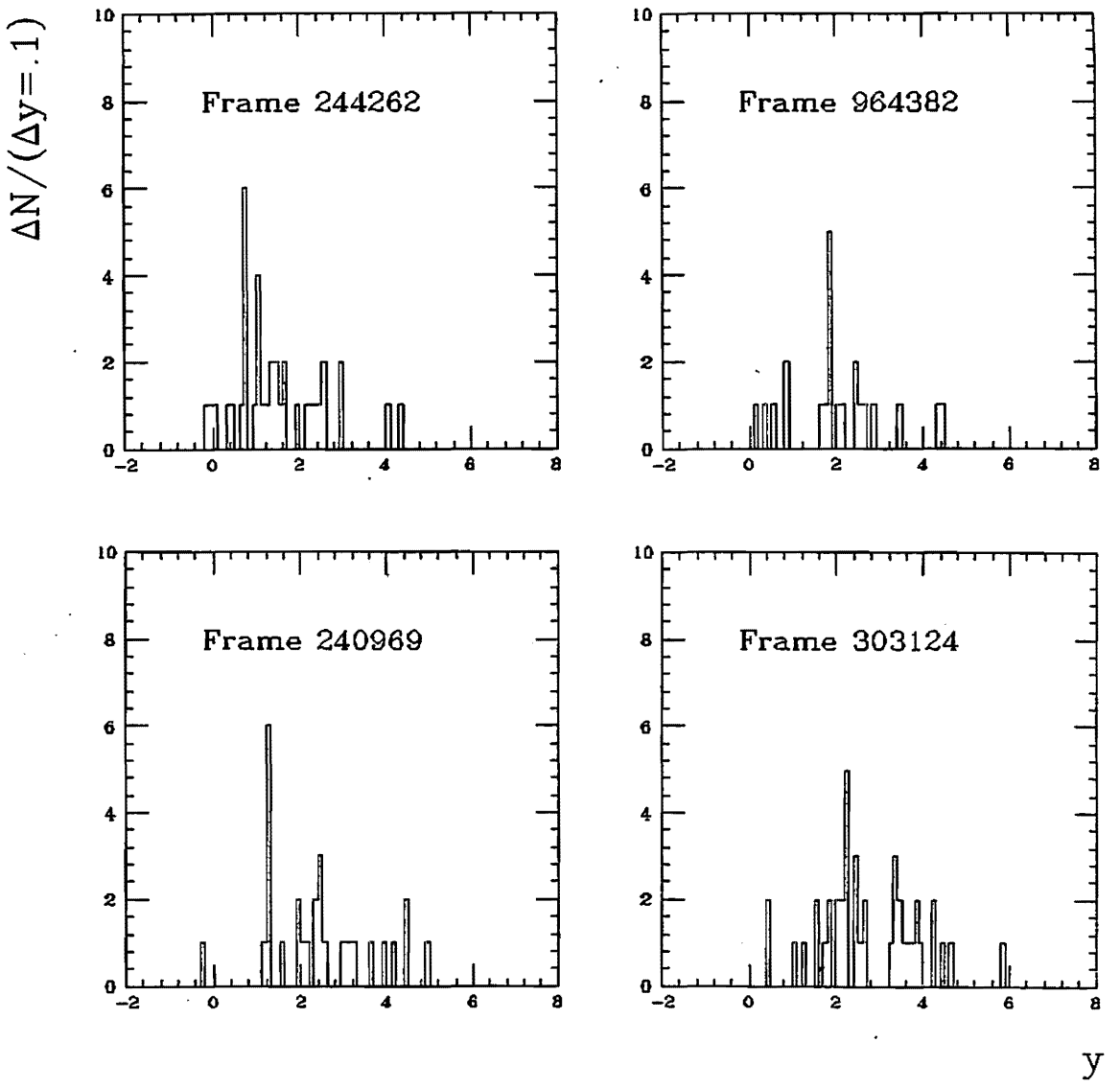

Figure 6.1.2 Sample rapidity distributions for single hA events with produced particle multiplicities of 20 or more.

320 GeV/c, that calculating a fractal dimension has little chance of success. But with larger multiplicities, as in hA and AA events, computing the fractal dimension makes more sense. With reasonably large multiplicities, hA events are better suited for fractal dimensional analysis. Nevertheless, there are a number of potential problems which must be seriously considered. Before attempting to calculate a fractal dimension, the limitations which could sabotage the fractal signature of the interactions should be addressed. These limitations dictate how the search for a valid fractal signature must be conducted.

Finite multiplicity Numerical experiments involving large number of points of order 10^4 have been plagued at times by noise that smears a fractal fingerprint [Carruthers 89]. An initial set of points will undergo a number of transformations. Attractors are the points to which initial points transform after an infinite number of transformations. Dynamical systems often have attractors. When attractors are interesting, they are called *strange attractors.*

Noise may be introduced at the level of the initial points used, shifting the sequences randomly, or as a consequence of sampling different parts of the attractor when the initial points are unknown. The latter has particular pertinence in the study of multiparticle production where related events presumably sample different portions of a common attractor. Since single events have finite numbers of elements, they undoubtedly sample different portions of an associated attractor (with its infinite number of elements). This precludes adding up event distributions before computing some dimension estimator D_e since event-specific distinctions, eg. impact parameter, leading particle effects, and charge/neutral fluctuations, will shift the rapidity distribution and blur the common fractal dimension among events. Hence, the fractal dimension is more appropriately defined as an average of event-by-event fractal dimension estimators $D_{F_{evt}}$

$$D_F = \langle D_{F_{evt}} \rangle$$

where

$$D_{F_{evt}} = \lim_{n \to N_e} \frac{\ln N'_n(\epsilon_n)}{\ln (1/\epsilon_n)}$$

with N'_n as the number of non-empty bins at resolution ϵ_n, and N_e as the total produced particle multiplicity which limits useful resolutions. As $N_e \rightarrow \infty$, estimators become reliable measures of fractal dimension. How good the estimators are is tested by how stable they are, *i.e.* whether they fluctuate a lot from event to event and from one resolution scale to another.

Fractional base A convenient way to proceed is to restrict ϵ to integral powers of some fraction λ. Ideally, any fraction would do – revealing the constant fractal dimension. In practice, however, one's choice of λ when partitioning the rapidity range can impact how good the estimator is and whether one can *see* a fractal [Carruthers 89]. Not being able to *see* a fractal does not preclude its existence but it runs contrary to the whole point of this investigation. The convergence problems illustrated in Cantor-set-generated events studied with λ of 1/2 and 1/3 could easily carry over to this study and degrade the quality of the results. Preliminary calculations showed that both 1/2 and 1/3 were not suited to the event structures. The location and width of the rapidity ranges were better served by larger fractions. Results were difficult to test for stability since the bin intervals decreased so quickly as shown in **Table 6.1.1**. In the process of choosing the more slowly varying fractions, a number of other factors were taken in consideration: 1) rapidity errors; 2) gap thresholds; and 3) saturation thresholds. Obviously λ must be greater than the average rapidity error and must take a significant number of values between the gap and saturation thresholds.

Rapidity errors Average rapidity errors in E597 samples are well below .1 unit rapidity. The distributions of these errors appear in **Figure 6.1.3**. To use n powers of $\lambda > 1$. before running into the rapidity error cutoff, it must be chosen greater than $10^{-1/n}$. For example, for 15 powers, λ must be greater than .86. On this basis, $\lambda = 9/10$ is tentatively chosen to explore the small scale features. It is of interest, however, to inspect the transition between small and large scale features. Thus $\lambda > 1$. is employed, in particular, $\lambda = 10/9$. Subsequently, limitations imposed by the gap

Table 6.1.1 Rapidity bin intervals or rapidity resolution lengths ϵ as integral powers of base fractions λ.

	$\epsilon_n = \lambda^n$						
n	$\lambda = \frac{1}{3}$	$\lambda = \frac{1}{2}$	$\lambda = \frac{3}{5}$	$\lambda = \frac{3}{4}$	$\lambda = \frac{9}{10}$	$\lambda = \frac{10}{9}$	$\lambda = \frac{4}{3}$
1	.333	.500	.600	.750	.900	1.11	1.33
2	.111	.250	.360	.563	.810	1.24	1.78
3	.037	.125	.216	.422	.729	1.37	2.37
4		.063	.130	.316	.656	1.52	3.16
5		.031	.078	.237	.590	1.69	4.21
6			.047	.178	.531	1.88	5.62
7			.028	.133	.478	2.09	7.49
8				.100	.430	2.32	9.99
9				.075	.387	2.58	
10				.056	.349	2.87	
11				.042	.314	3.19	
12				.032	.282	3.54	
13					.254	3.93	
14					.229	4.37	
15					.206	4.86	
16					.189	5.40	
17					.170	6.00	
18					.153	6.66	
19					.138	7.40	
20					.122	8.23	
21					.109	9.14	
22					.098		
23					.089		
24					.080		
25					.072		
26					.062		
27					.058		
28					.052		
29					.047		
30					.042		
31					.038		
32					.034		
33					.031		
34					.028		

RESOLVE.TAB UND/MCKM 10Jan90

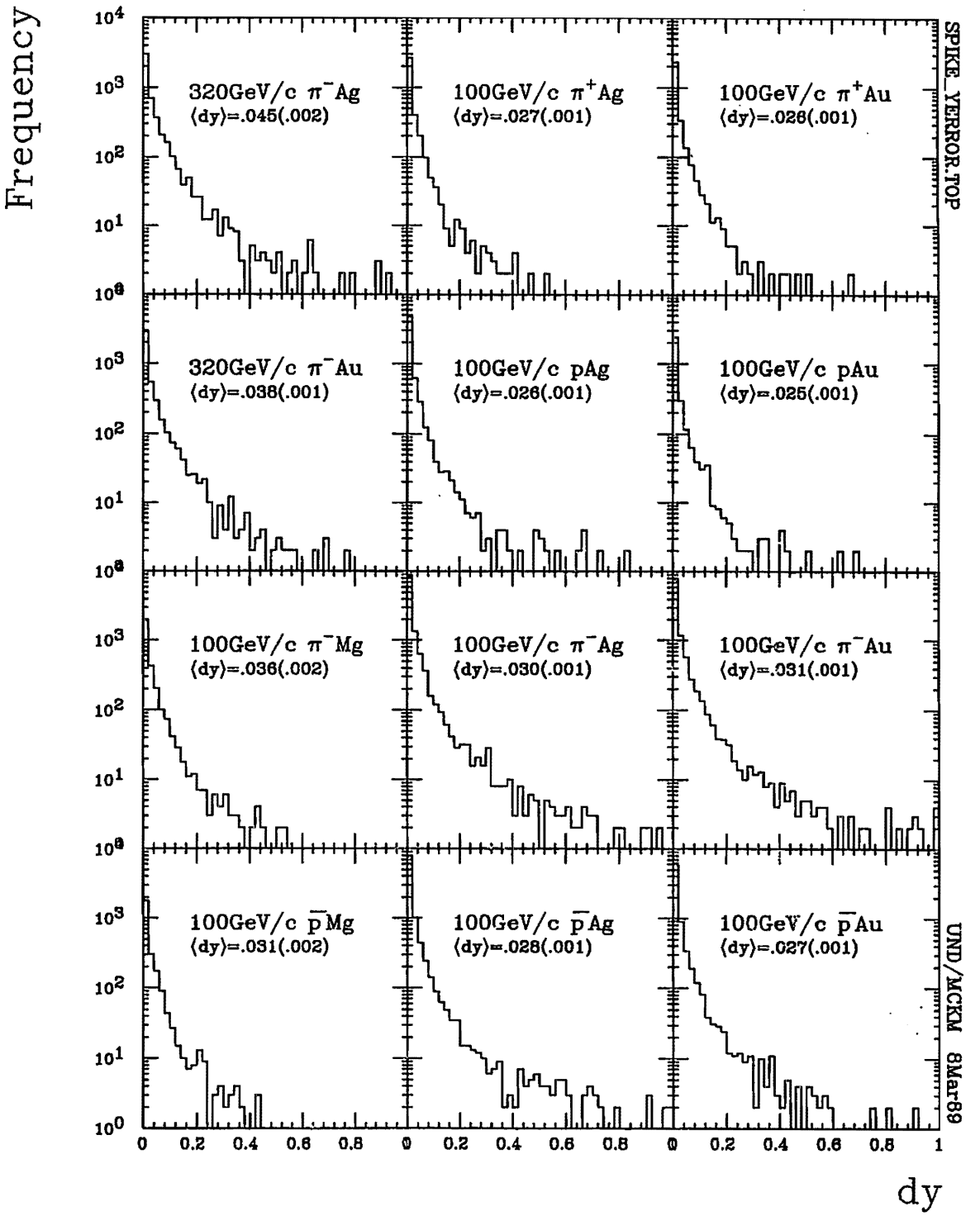

Figure 6.1.3 Distribution of produced particle rapidity errors.

threshold must be considered.

Gap thresholds The gap threshold is the bin width at which gaps begin to appear. Obviously, there is not much point in studying rapidity distributions at resolutions greater than this threshold since this study depends entirely on the existence of gaps. Using $\lambda = 10/9$ to partition the distributions, gaps between consecutive rapidity bins did not appear on the average above $(10/9)^7 = 2.09075$ (see **Figure 6.1.4.** But since $(10/9)^8 = 2.32306$, the threshold could be somewhere in between. This represents a fewer number of scales with which to study the larger scale features, but the purpose is to bridge the two scales, and that can be done with 7 orders. The full rapidity range per event (*i.e.* the maximum rapidity distance between charged produced particles in one event) averages approximately 4.5 units rapidity for events with more than 20 charged particles as seen in **Figure 6.1.5** in contrast to an inclusive rapidity range of approximately 9.5 units. That means gaps begin to appear first for events with larger-than-average spans in rapidity.

Saturation threshold Another threshold of interest is the saturation threshold which represents the value of ϵ at which all particles are resolved. Below this threshold, dimensions are expected to vary with the resolution rather than remaining essentially constant. Technically, the saturation point, where the number of nonempty bins equals the produced particle multiplicity, averages under .01 units rapidity (refer to **Figure 6.1.6**). However, the effects of saturation seem to show up at larger resolutions.

6.1.3 Calculation techniques

In principle, calculating the fractal dimensions is very straightforward. Having chosen some fraction λ (*e.g.* $\lambda = \frac{3}{4}$, $\frac{9}{10}$, or $\frac{10}{9}$), one partitions a given event's rapidity distribution with bins of width $\epsilon_n = \lambda^n$ for each $n = 1, 2, 3, ...n$. This is illustrated in **Figure 6.1.7** for an inclusive distribution using $\epsilon = 9/10^n$. One then counts the number N' of populated bins for each resolution width ϵ_n. Obviously, this is much

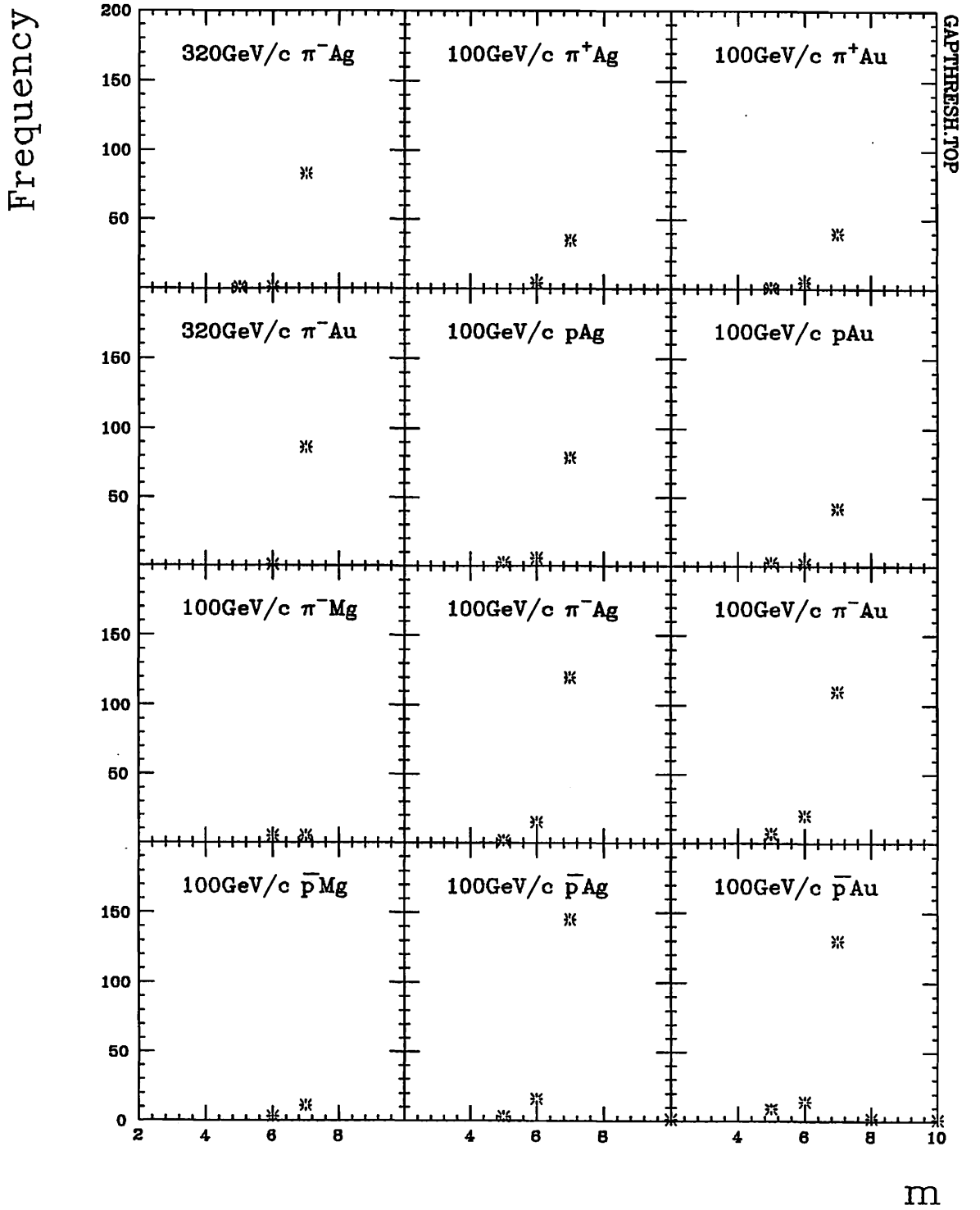

Figure 6.1.4 Distribution of minimum power to which 9/10 is taken for the resolution ϵ first to produce gaps between adjacent bins.

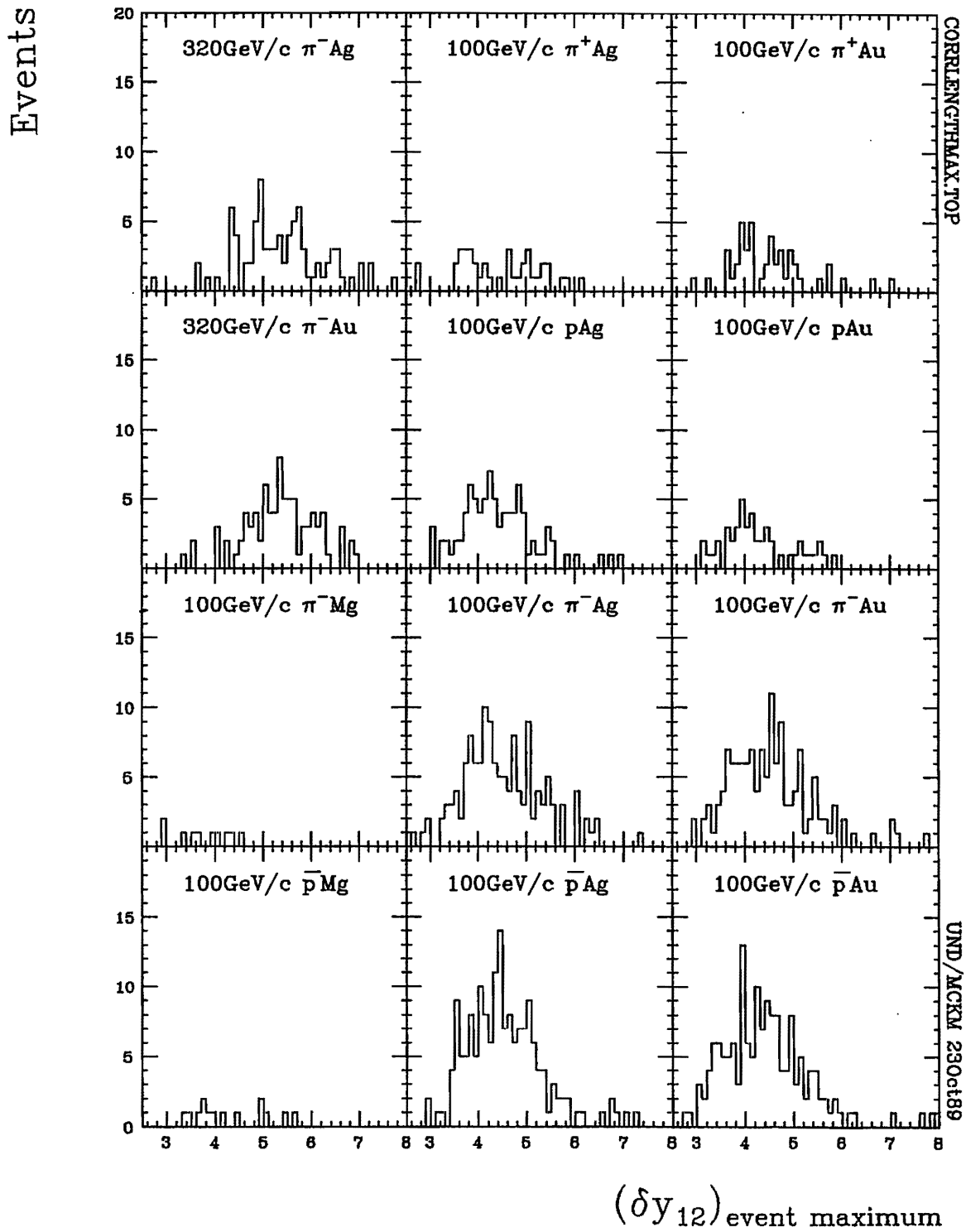

Figure 6.1.5 Distribution of rapidity range for events with produced particle multiplicities of 20 or more.

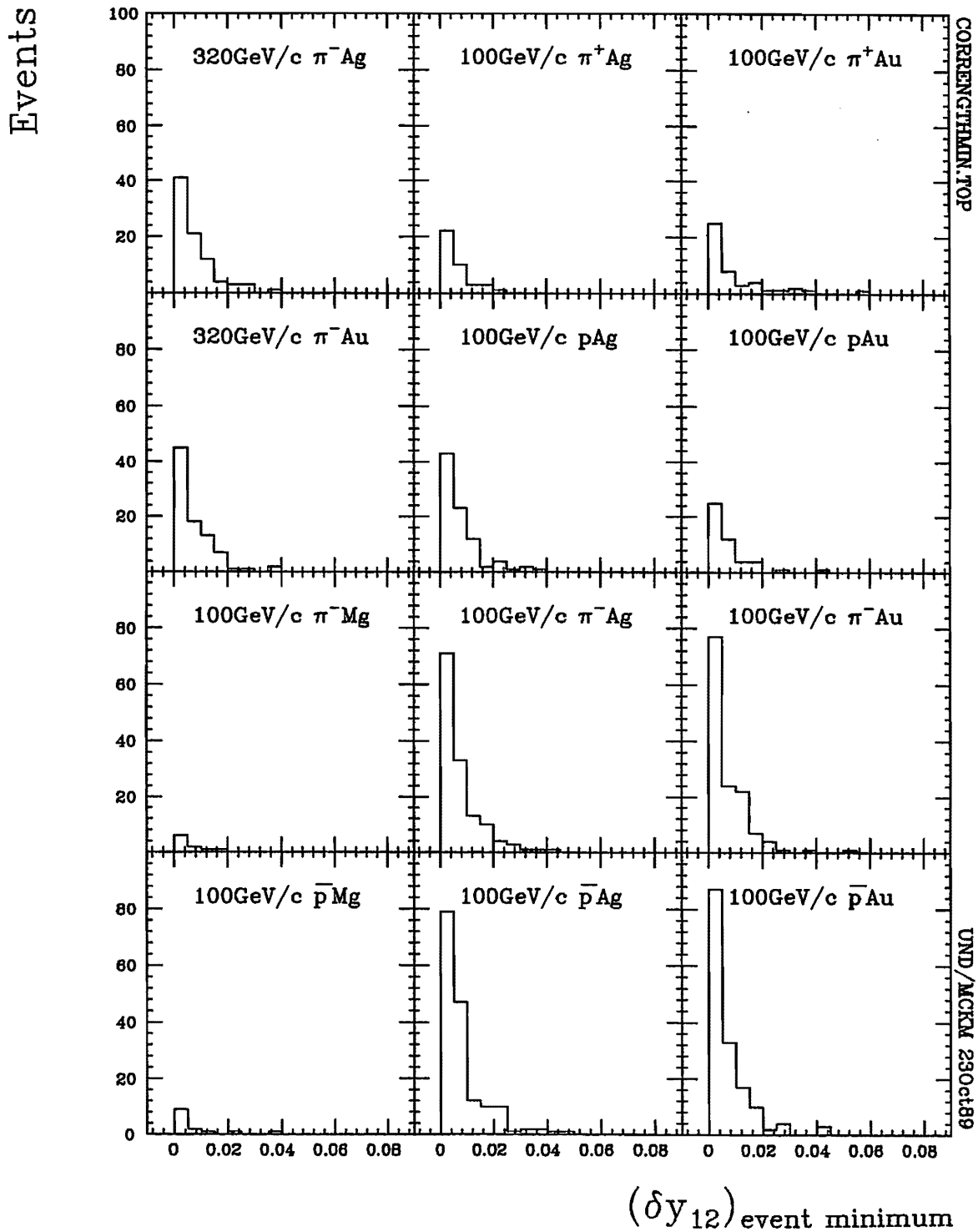

Figure 6.1.6 Distribution of minimum rapidity differences in events with produced particle multiplicities of 20 or more. These determine the saturation threshold when partitioning rapidity distributions.

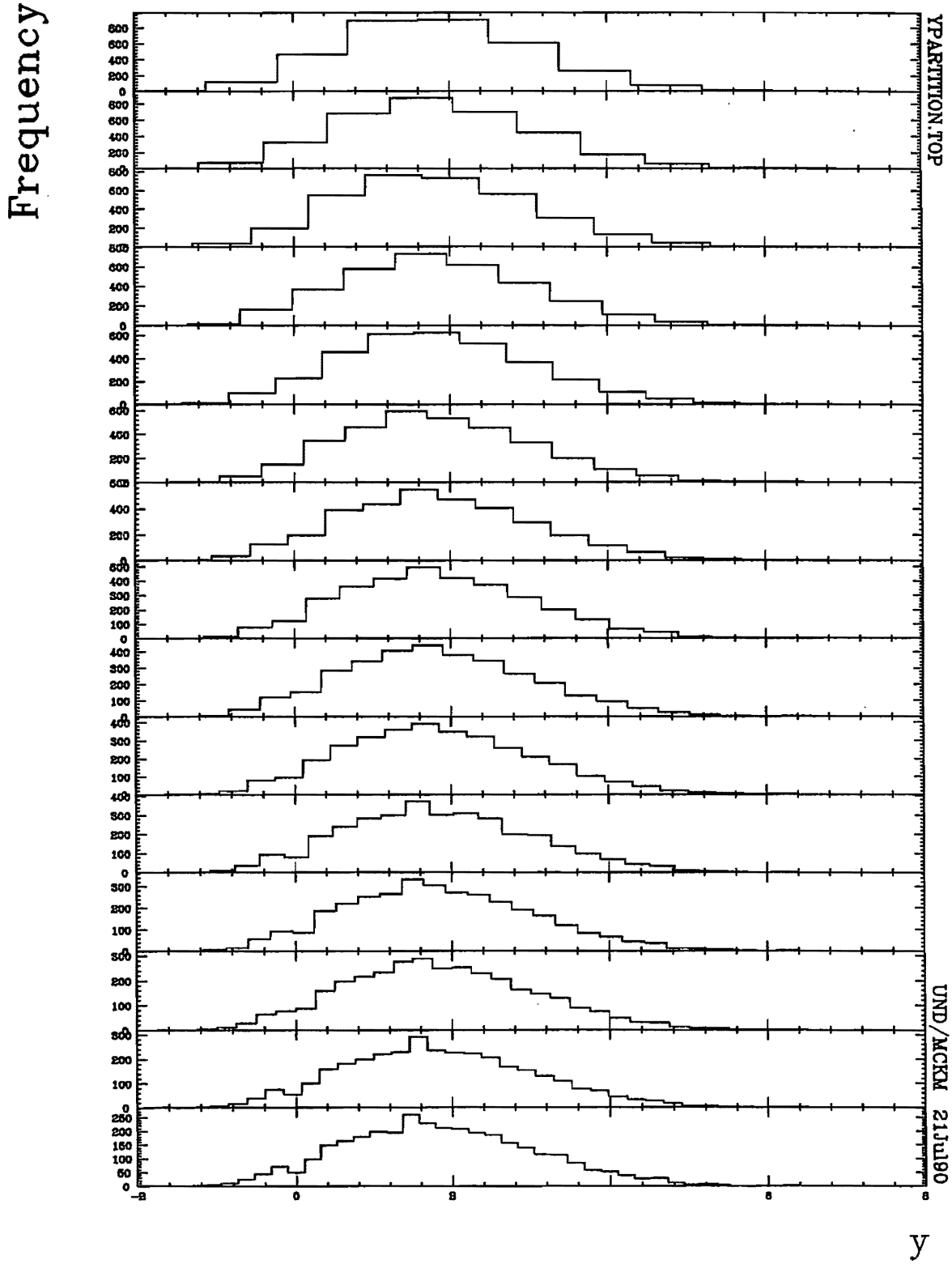

Figure 6.1.7 Inclusive rapidity distribution of high multiplicity 100 GeV/c $\pi^- Ag$ events partitioned by resolution lengths increasing as powers of 9/10.

more interesting and instructive for individual event distributions rather than for inclusive distributions since so few if any empty bins characterize the latter. Another way to handle the resolution ϵ' is to use the number of bins $M_n = \Delta Y/\epsilon'_n$ and count the number N' of populated bins as a function of n. But, since this paper compares results with others employing varying λ and varying rapidity range, N' is expressed exclusively in terms of $\epsilon = \delta y$ = rapidity bin width rather than in terms of the number of bins partitioning the rapidity range employed or in terms of a relative resolution $\epsilon' = \frac{\delta y}{\Delta y}$, where δy is the rapidity bin width and Δy the maximum width of the inclusive rapidity distribution.

The endpoints of the partition range are not critical unless the multiplicity is very small. Recall that this study has been limited to measured produced particle multiplicities of 20 or more. In any case fixing the endpoint has been verified not to impact results significantly as long as the partition range spans the inclusive rapidity range. In the present calculations the lower limit of the rapidity range has been fixed at -2. units rapidity (in accordance with the event minima shown in **Figure 6.1.8**, partitioning the distribution with a convenient 100 bins of width ϵ. With a minimum ϵ of $(9/10)^{15}$, that means the partition reached up to rapidities exceeding the largest event rapidity maxima shown in **Figure 6.1.9**.

In the limit of infinite multiplicity, the slope when plotting $\ln N'$ vs. $\ln \epsilon$ is the fractal dimension. This slope can be determined in a number of ways. Several of these have been employed to test the consistency of the results and to connect with recent theoretical work.

Linear regression The most direct approach is to employ linear regression. However, the context of finite multiplicities makes the fit region critical. Most events are characterized by a nearly linear rise in $\ln N'$ vs. $-\ln \delta y$ followed by a flatter trend as most of the particles become resolved and the maximum bin population (equal to the multiplicity) is approached. **Figure 6.1.10** is a random example of this characterization. All events were inspected in this regard. Since the flatter trend reflects a finite boundary effect which is exacerbated by low multiplicities, the analysis has

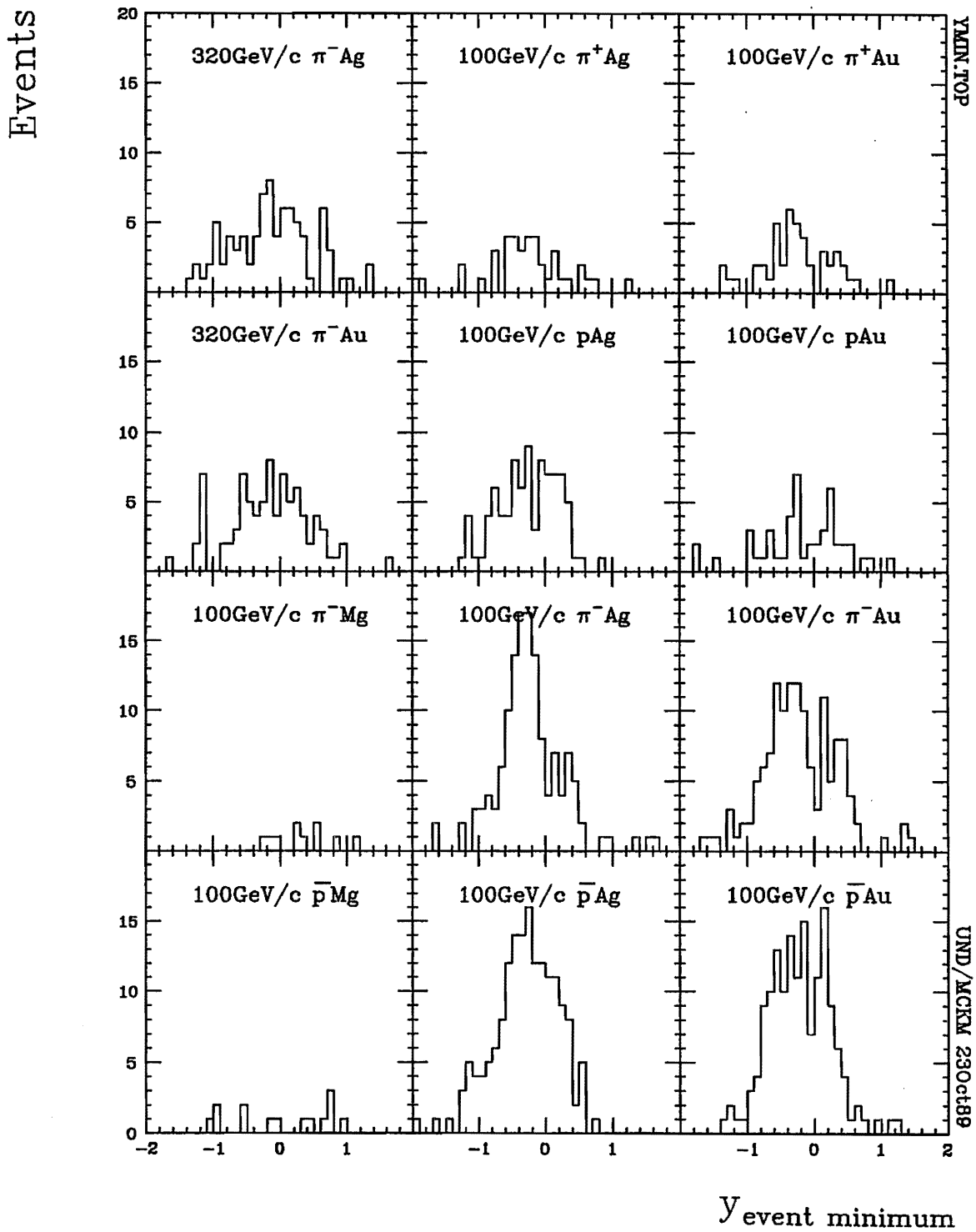

Figure 6.1.8 Distribution of rapidity minima for events with produced particle multiplicities of 20 or more.

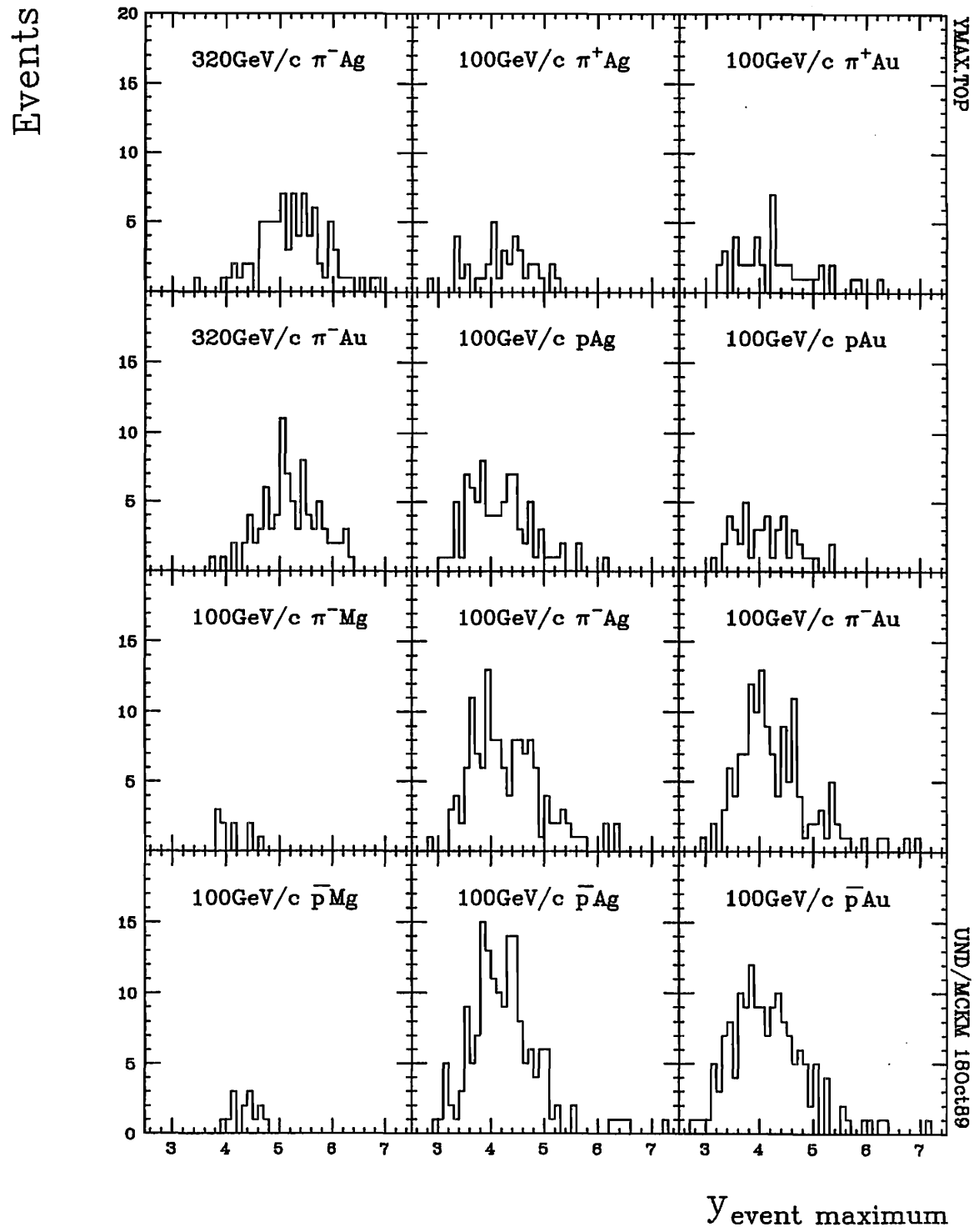

Figure 6.1.9 Distribution of event rapidity maxima for events with produced particle multiplicities of 20 or more.

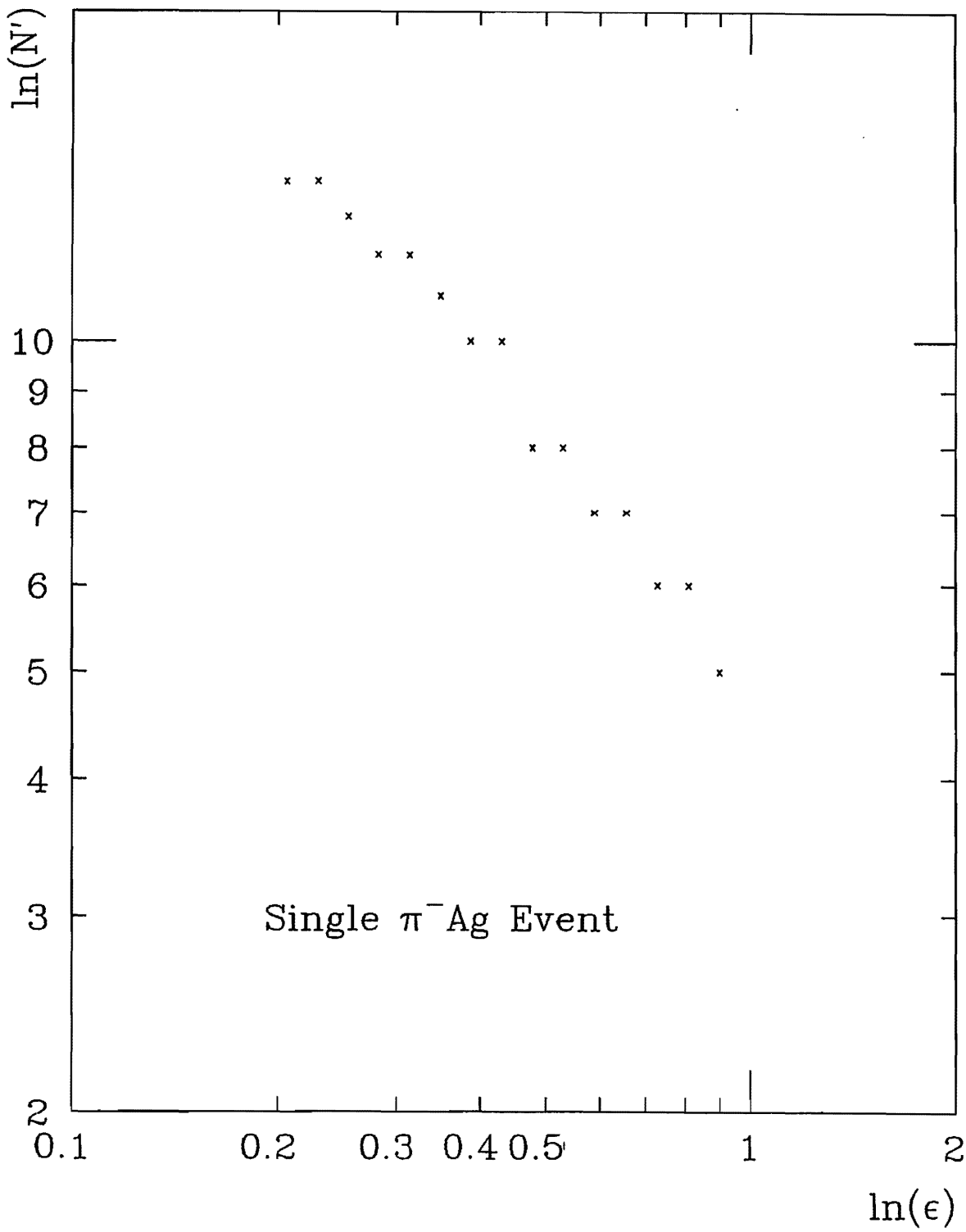

Figure 6.1.10 A random example of the dependence of the number of nonempty bins on the resolution ϵ equal to powers of the fraction $\lambda = 9/10$. All events show the same basic features.

been limited to events with multiplicities of 20 or more measured produced particles. In addition, linear fits have been made in a limited region $\epsilon = 0.1 - 1.0$ where slope distortions seem to be minimal. Averaging the slopes over each interaction type, the averaged slopes are interpreted to be the fractal dimensions associated with each interaction.

Four-bin averaging A less direct approach finds slopes over smaller intervals and looks for stability averages of these slopes [Carruthers 89]. Caution must be exercised to avoid problems stemming from the finiteness of the multiplicities. In calculating fractal dimensions for Cantor-type numerical events to show how optimized a search for fractality must be to be valid, Carruthers effectively takes averages of rise $\Delta(\ln N')$ over consecutive ϵ intervals. As a compromise between including too few intervals (which would introduce statistical distortions) and including too many intervals (which would obscure the boundary distortions which must be avoided), each set of four(4) consecutive intervals within the range $\epsilon = \lambda^1$ through $\epsilon = \lambda^{15}$ was averaged and the ensuing fractal dimension $D_{F_4}(\epsilon)$ was assigned to the central value of each set of intervals, *i.e.* to $\epsilon = \lambda^3$ through $\epsilon = \lambda^{13}$. These four-interval averages were calculated event by event. Subsequently these were averaged over the analysis sample and the averages plotted against ϵ. The plateau region between the gap threshold and the saturation point is expected to signal a valid fractal dimension.

Hand-picked stabilities A slight variation of this method is to hand pick the most stable four-interval average from each event and average these over the sample. 'Stable' means that the 4-interval average either does not decrease significantly or even increases slightly as ϵ decreases.

6.2 RESULTS

Fractal dimensions obtained from direct linear fits of N' vs. ϵ are distributed between .5 and .8 as shown in **Figure 6.2.1**. Averages range between .62 and .65 as shown in **Table 6.2.1** But though the distributions clearly peak near their averages, the dimen-

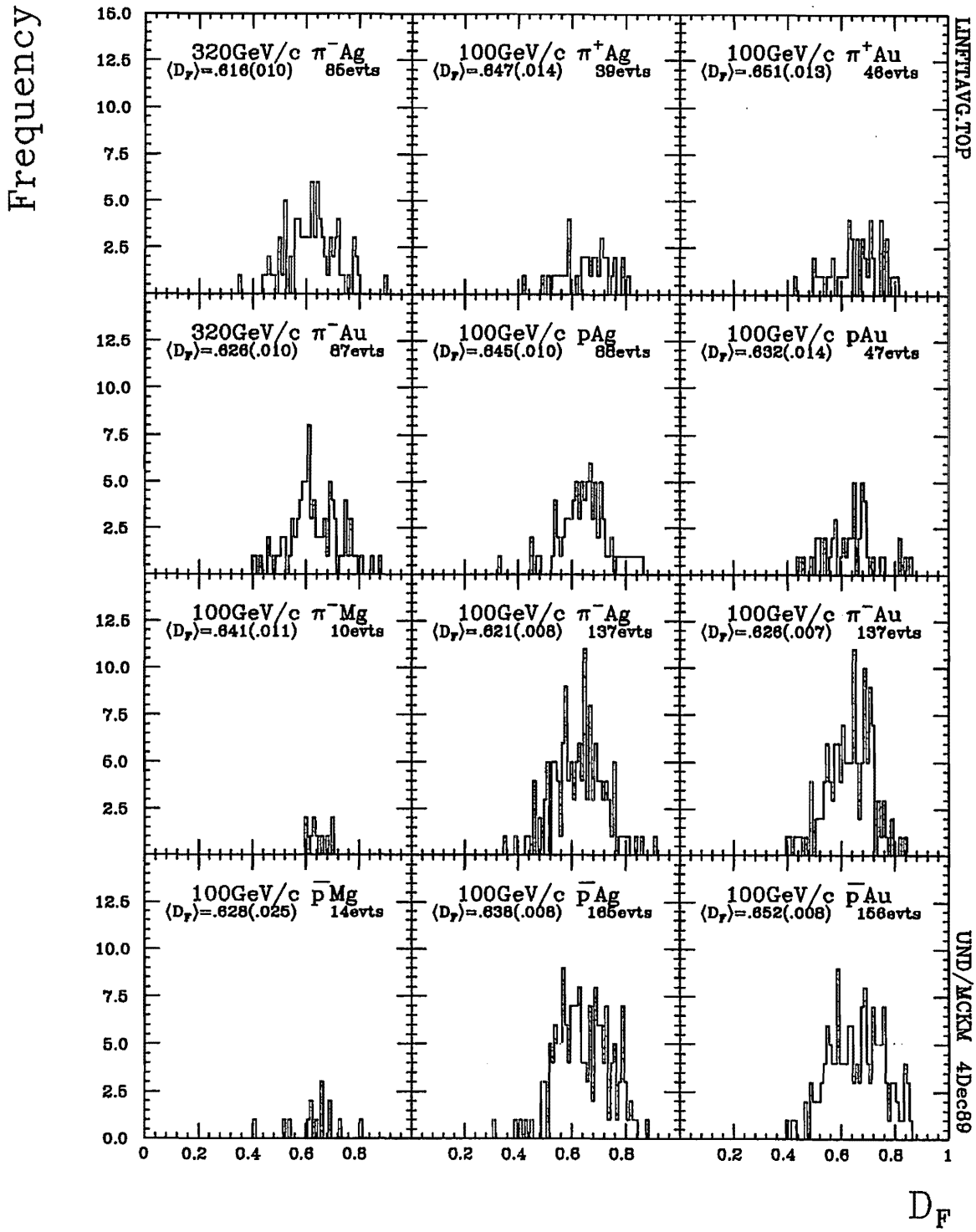

Figure 6.2.1 Distribution of fractal dimension estimators for events with produced particle multiplicities of 20 or more. Averages range from .62 to .65.

Table 6.2.1 Comparing average fractal dimension estimators determined by linear regression with various types of simulated data.

Projectile	320GeV/c		100GeV/c									
	π^-	π^-	π^+	π^+	p	p	π^-	π^-	π^-	$\bar{p}$	$\bar{p}$	$\bar{p}$
Target	Ag	Au	Ag	Au	Ag	Au	Mg	Ag	Au	Mg	Ag	Au
E597 data with $N_{prod} \geq 20$												
Nevts	85	87	39	46	88	47	10	137	137	14	165	156
D_F	.62	.63	.65	.65	.65	.63	.64	.62	.63	.63	.64	.65
ΔD_F	.04	.04	.04	.04	.04	.04	.04	.04	.04	.04	.04	.04
1000 FRITIOF events each with $N_{prod} \geq 20$												
D_F	.60	.61	.62	.62	.62	.64	.63	.63	.63	.60	.64	.63
ΔD_F												
1000 Data-like random events each												
D_F	.62	.61	.61	.61	.61	.66	.61	.66	.64	.66	.66	.66
ΔD_F	.01	.01	.01	.01	.01	.01	.01	.01	.01	.01	.01	.01

400 Scrambled π^- Ag events

N_{prod}	20	21	22	23	24	25	26	27	
D_F	.53	.56	.60	.59	.63	.64	.63	.60	
ΔD_F	.04	.04	.04	.04	.04	.04	.04	.04	

1000 Completely random events

D_F	.44	
ΔD_F	.04	

FITFRACT.TAB UND/MCKM 14Feb90

the dimensions may be fluctuating too much between individual events to be valid. Repeating the calculation using $\lambda = 10/9$, the calculated fractal dimension are corroborated. They are continuous with those calculated using $\lambda = 9/10$. The results of three sets of calculations in the four-bin-averaging method do indeed overlap, as seen in **Figure 6.2.2**. But one must optimize the analysis by using $\lambda = 9/10$ since $\lambda = 3/4$ results do not plateau and $\lambda = 10/9$ results jump around too much.

6.2.1 Plateau signal

The plateau region value is taken to be the valid fractal dimension. This relatively stable region begins at about $\epsilon \approx .4$ as seen in **Figure 6.2.3**. Significantly, the values of the fractal dimension signalled by these plateaus corroborate results from the linear fit method. The closely related method which crudely handpicks the fractal dimension estimator by looking for stability and averages them out also gives comparable results.

6.2.2 Dependencies

The measurables which modify the values of the fractal dimension should be investigated. Initially dependencies relative to spikes and local rapidity density maxima were studied, but as **Figure 6.2.4** shows, fractal dimension does not seem to depend on event maximum local rapidity densities and thus is not directly dependent on spikes.

Next dependencies relative to the number of light protons associated with an event were studied, since there is reason to believe that it is related to the impact parameter of the interaction. But fractal dimension does not seem to depend on light proton multiplicity, as seen in **Figure 6.2.5**. Either the fractal dimension is not being measured well enough to see the dependence, or indeed the fractal dimension is independent of impact parameter, a possibility which is not entirely foreign to sparse populations like fractals. It could be that the fractal dimension is determined by the basic quark-parton interaction rather than by the number of collisions. However, when a scatter plot of fractal dimension as a function of produced particle multiplicity

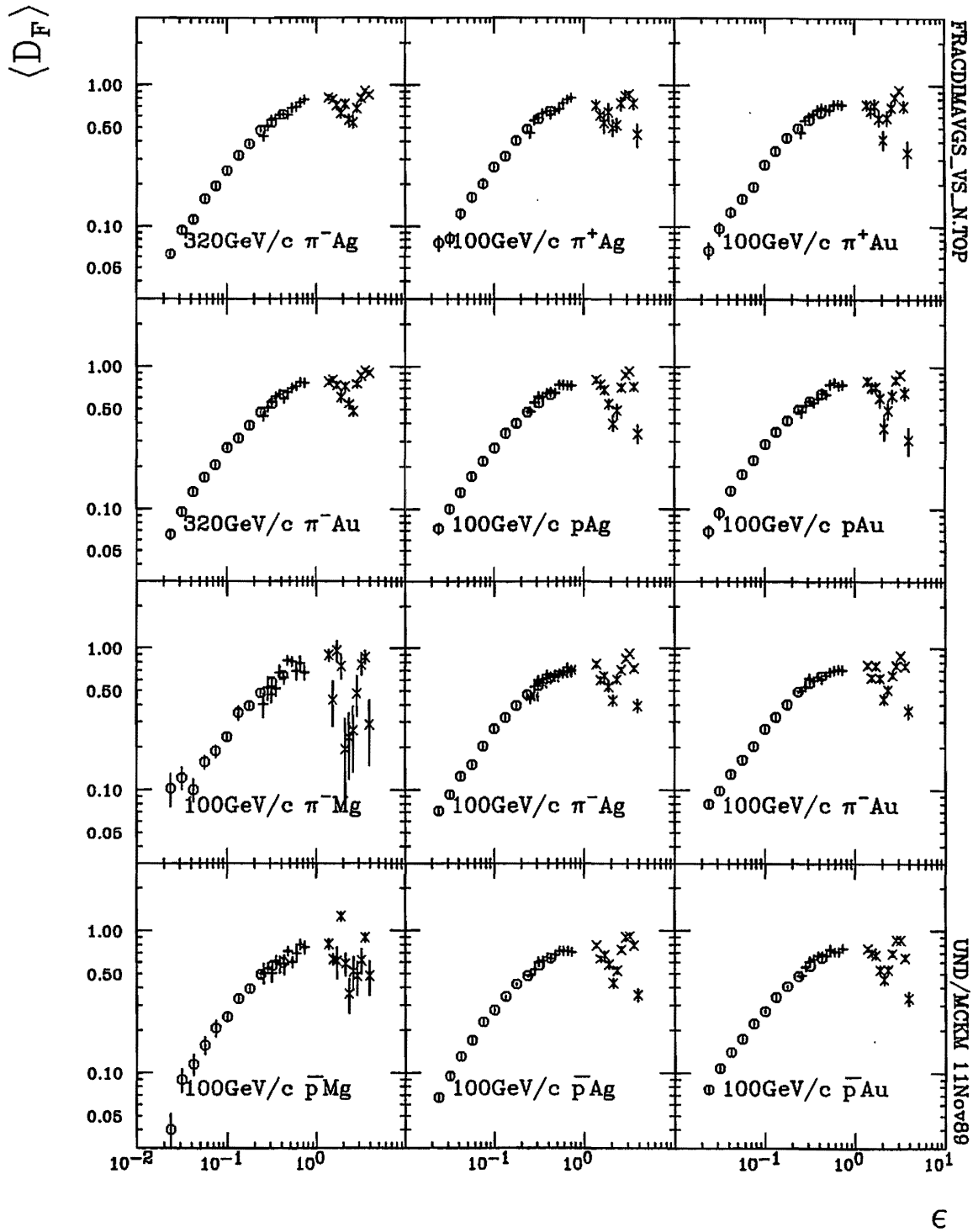

Figure 6.2.2 Four-bin-average estimators of the fractal dimension as a function of the resolution ϵ. These results are based on calculations using three(3) different values of λ: 3/4(o), 9/10(+), and 10/9(x). Note that the log scale deemphasizes the plateau regions but points out the role of each λ in the analysis.

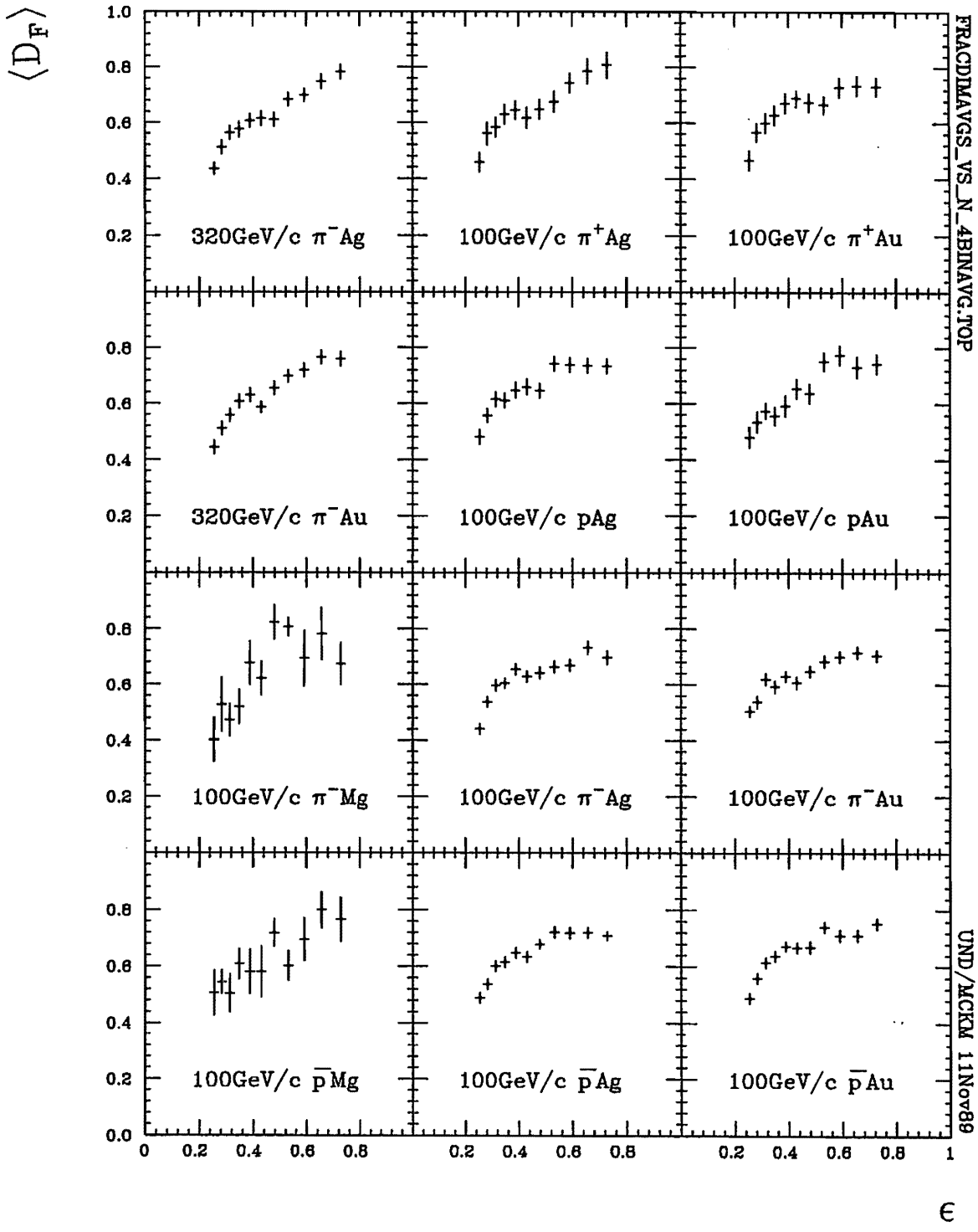

Figure 6.2.3 Four-bin-average estimators of the fractal dimension as a function of the resolution ϵ. These results are based on calculations using $\lambda = 9/10$ in order to emphasize the plateau region which emerges at $\epsilon \approx .4$.

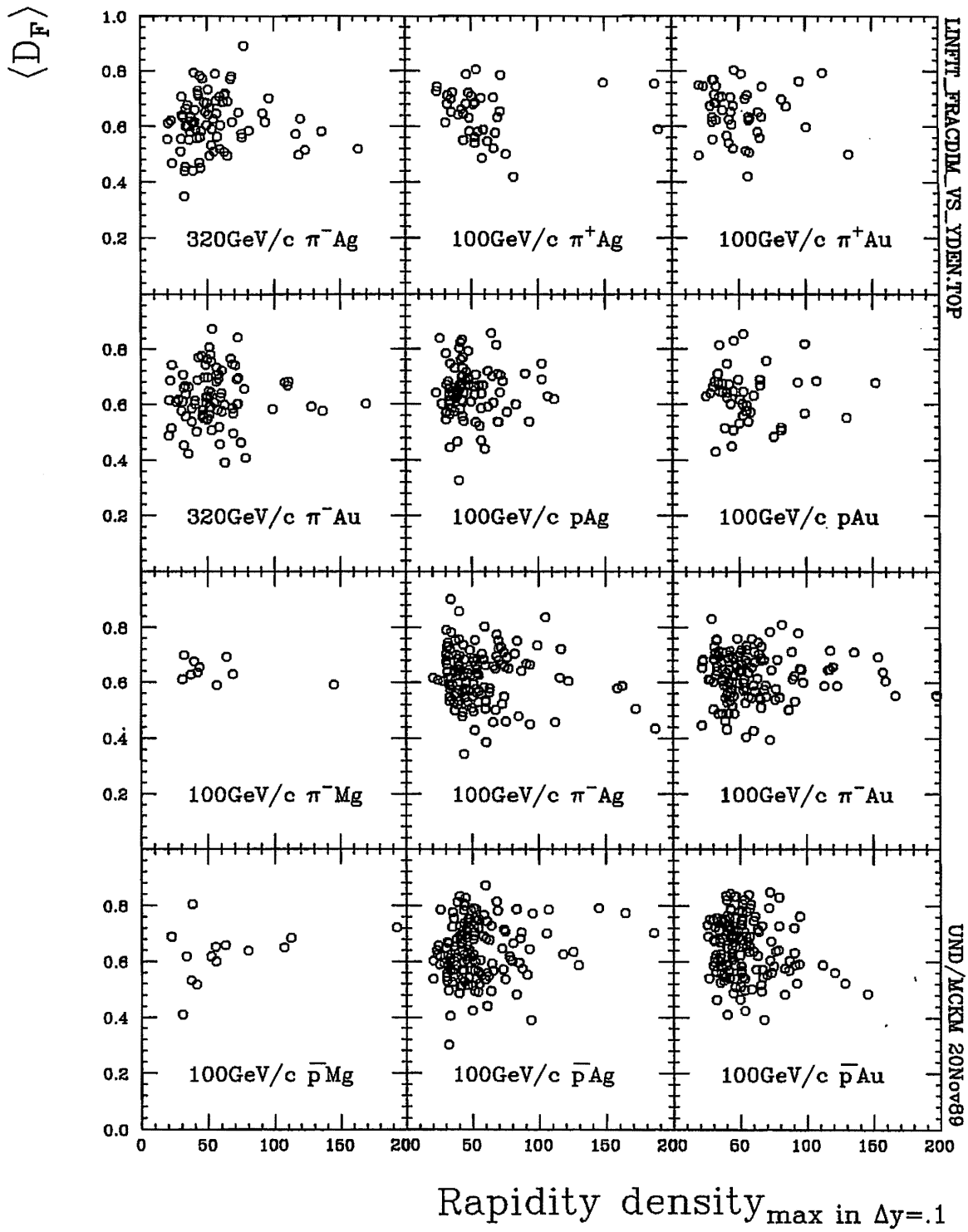

Figure 6.2.4 Scatter plot of fractal dimension estimators by linear regression as a function of local rapidity density for events with produced particle multiplicities of 20 or more.

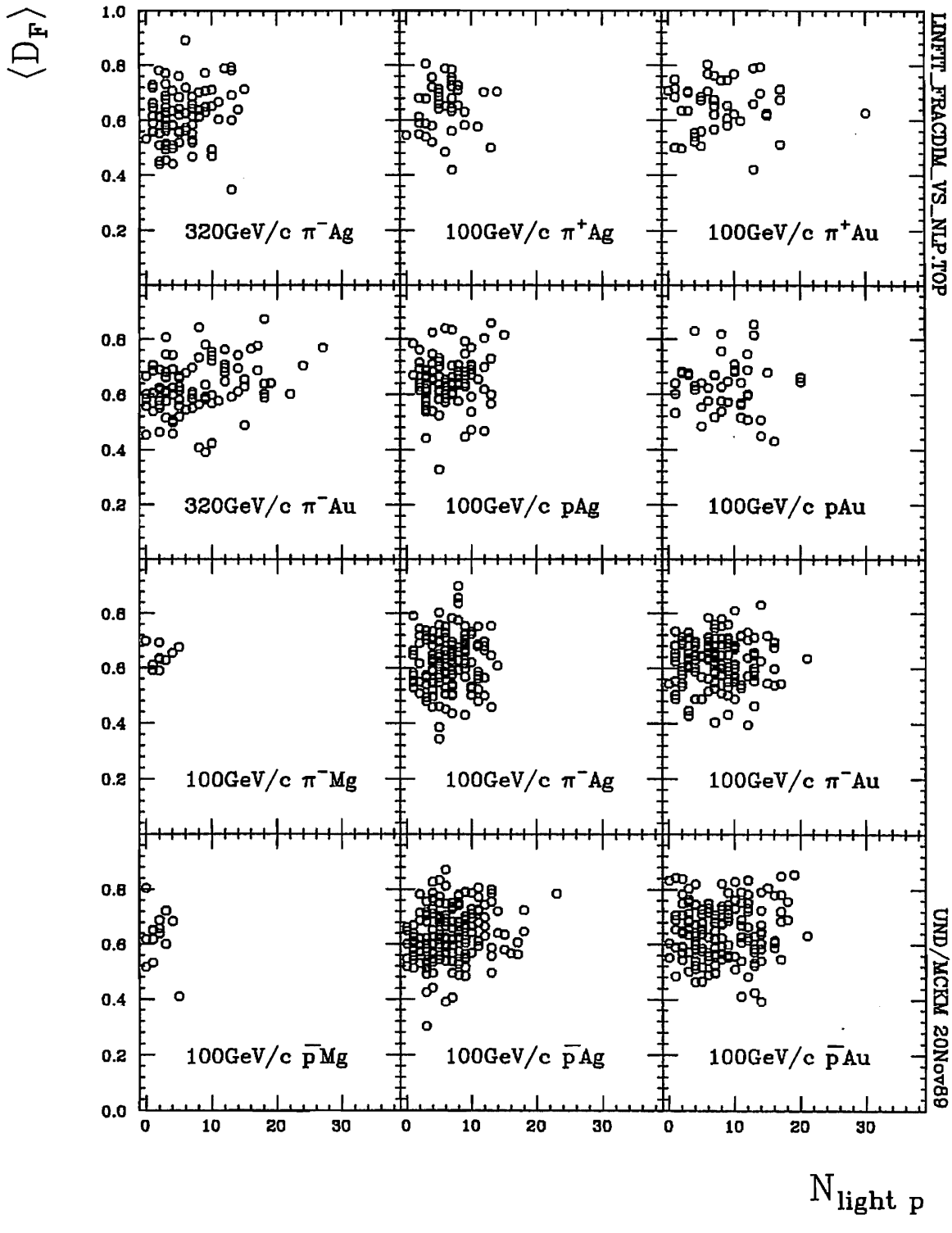

Figure 6.2.5 Scatter plot of fractal dimension estimators by linear regression as a function of *light* proton multiplicity for events with produced particle multiplicities of 20 or more.

was made, **Figure 6.2.6**, a clear dependence appears for the lower limit of the fractal dimension. Since the upper bound is independent of multiplicity, the average fractal dimension increases nearly linearly with produced particle multiplicity. **Figure 6.2.7** shows this linear rise and also contrasts it with the rise expected from random simulated events.

6.2.3 Simulations

To determine whether the fractal dimension has anything to do with dynamical rather than stochastic mechanisms, comparisons have been made with results from simulated data. First, an attempt was made to reproduce results from data in order to set a starting point for interpretation. This forms a basis for determining what kinds of mechanisms are consistent with experimentally determined fractal dimensions. An attempt was subsequently made to produce results which deviate from the observed results in order to see what it is that breaks particular fractal behavior and thus determines fractal behavior dependence.

FRITIOF For simulated data, FRITIOF Monte Carlo events were used. The fractal dimensions of 1000 FRITIOF events comparable to the E597 samples and restricted to produced particle multiplicities greater or equal to 20 were calculated event by event. They essentially reproduced the values given in **Table 6.2.1**. They also reproduce the leveling off seen in **Figure 6.2.3**. A direct comparison between the data and the FRITIOF simulation can be made from **Figure 6.2.8**.

The fractional value of the dimension and the fact that FRITIOF is a quark cascade model makes the interpretation of the fractal dimension as a signal for cascade behavior more credible. Cascades are intrinsically self-similar and fractal.

Broken events It is of obvious interest to investigate the fractal dimension of randomized events. If real data tracks are scrambled among events of equal multiplicity, internal relations between tracks as well as event-specific characteristics are expected to break. Two(2) of the larger samples ($\pi^- Ag$ and $\bar{p}Ag$) were sorted

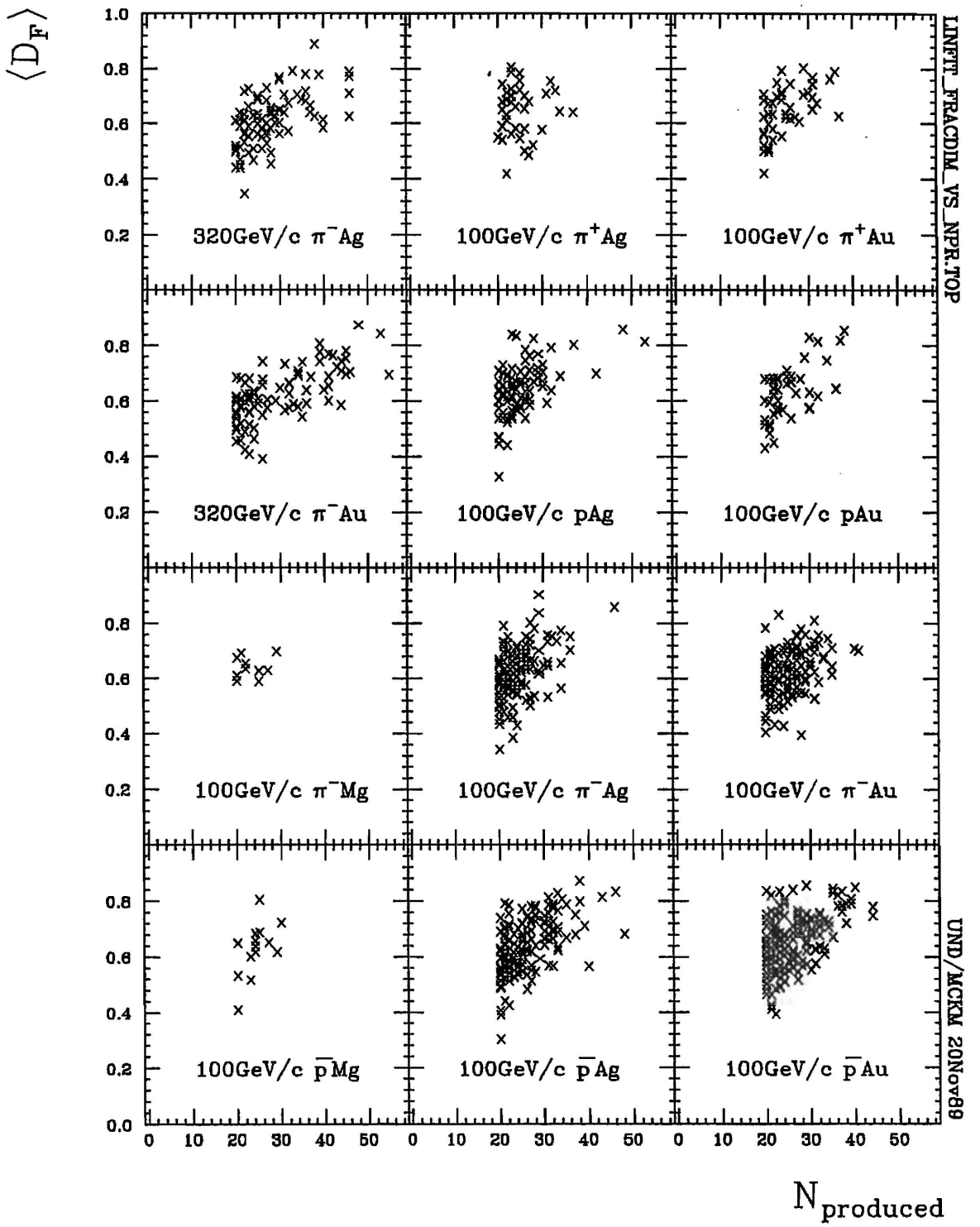

Figure 6.2.6 Scatter plot of fractal dimension estimators by linear regression as a function of produced particle multiplicity.

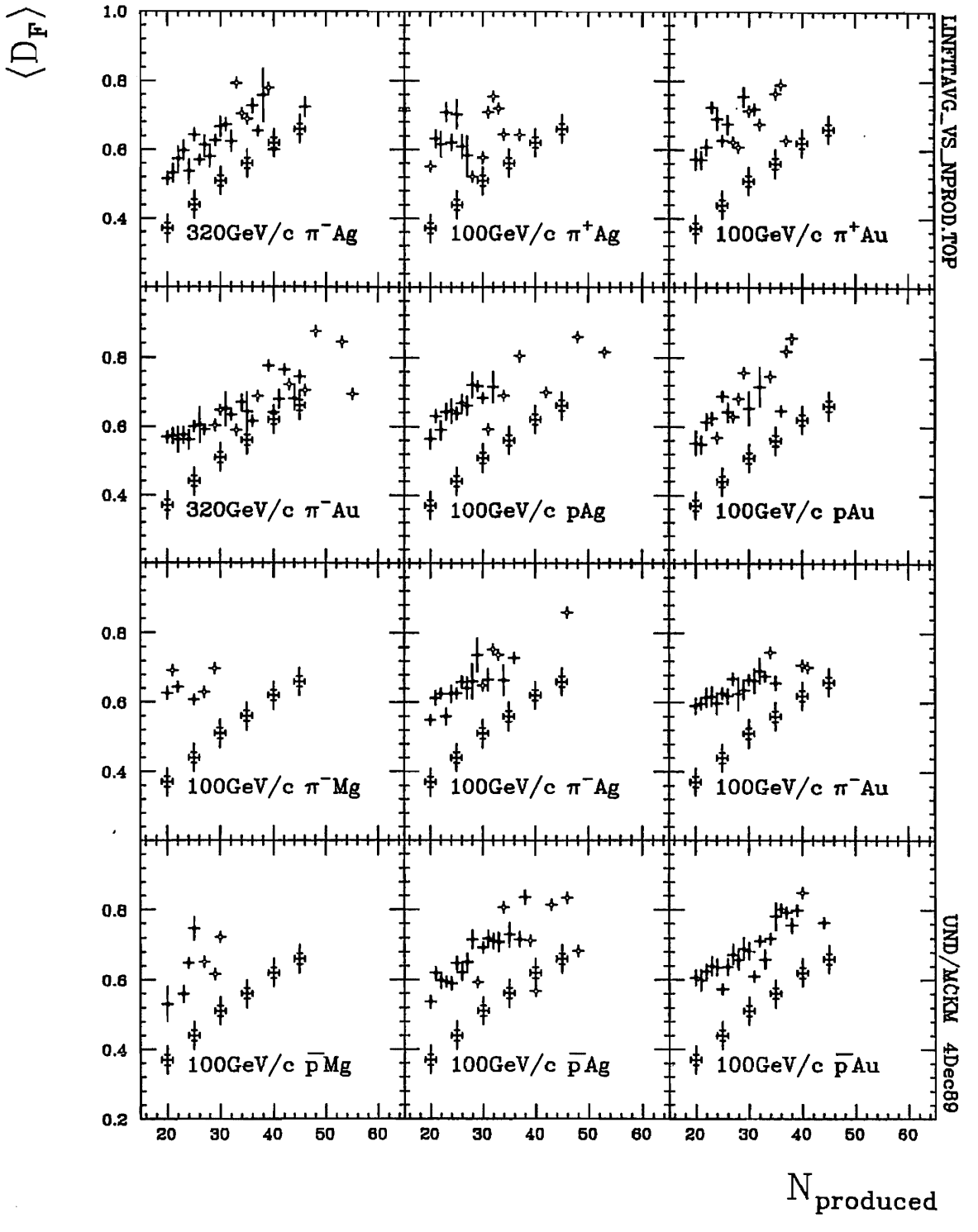

Figure 6.2.7 Average fractal dimension as a function of produced particle multiplicity for E597 events (upper values) and totally random simulated events (lower values).

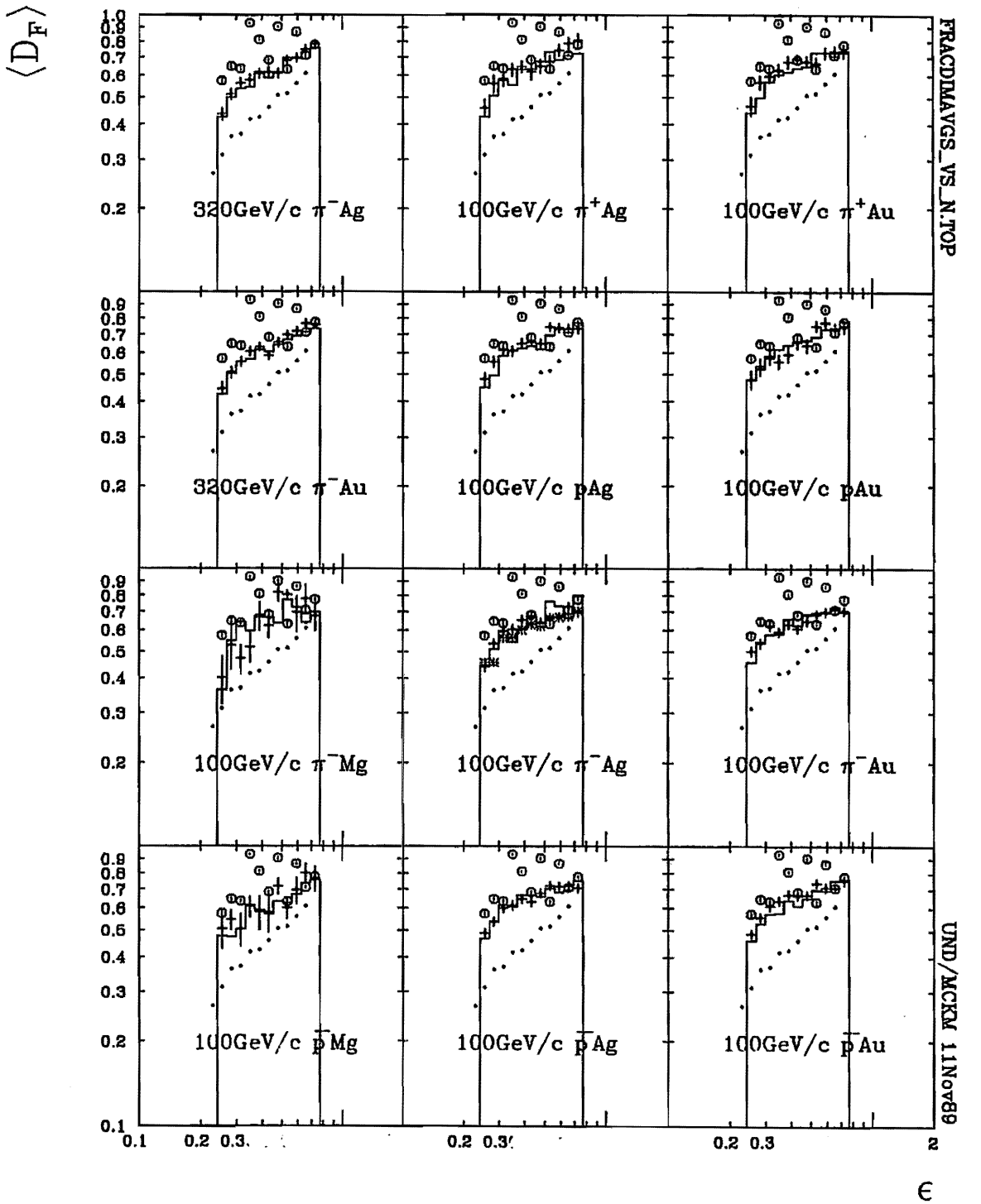

Figure 6.2.8 Four-bin-average estimators of the fractal dimension as a function of the resolution ϵ. These results are based on calculations using $\lambda = 9/10$ over a number of simulations as well as the E597(+) data: FRITIOF(solid histogram); random/equal-probabilities(...); random/data-probabilities(o).

by multiplicity and used to build pseudo-events by randomly selecting tracks from common pools of tracks at fixed multiplicities. The ensuing results did not differ significantly from the data. The $\ln N'$ vs. $\ln \epsilon$ plots were essentially the same and the linear fit values for the fractal dimension were nearly the same as for the real data (see **Table 6.2.1**). So the fractal dimension is evidently not subject to excessive event-to-event differences.

Random pseudo-events with data-like inclusive rapidity distributions It is also of obvious interest to study pseudo-event rapidity sets governed by real data rapidity probabilities. Thus simulated data were generated randomly whose inclusive rapidity distribution reproduces the experimental data. Results were nearly the same as for the experimental data in terms of the average fractal dimension values. However, it must be noted that the four-bin-average vs. ϵ behavior seen in **Figure 6.2.8** is not at all smooth and does not level off.

Totally random pseudo-events In a final attempt to break all dynamics, the fractal dimensions for totally random pseudo-events were calculated. These pseudo-events have tracks distributed across the whole rapidity range with uniform probability, clearly violating energy conservation constraints. Results from calculating fractal dimension were significantly below those for real data (**Table 6.2.1**) and **Figure 6.2.3**). Thus the fractal dimension must be sensitive to the shapes of the beam and target regions of rapidity, since that is the only difference between the totally random and the data-like rapidity distributions. This is born out by noting that in **Figure 6.2.9** low produced particle multiplicities exhibit a larger range of rapidity widths while the largest multiplicities exhibit a significantly limited range of widths. The fractal dimension average increases with increasing produced particle multiplicity because the lower limit increases (see **Figure 6.2.7**). So large rapidity widths are associated with low produced particle multiplicities which in turn are associated with small fractal dimensions. Since constant probability random distributions can be considered *broad*, the smaller fractal dimension is expected. In any case, random

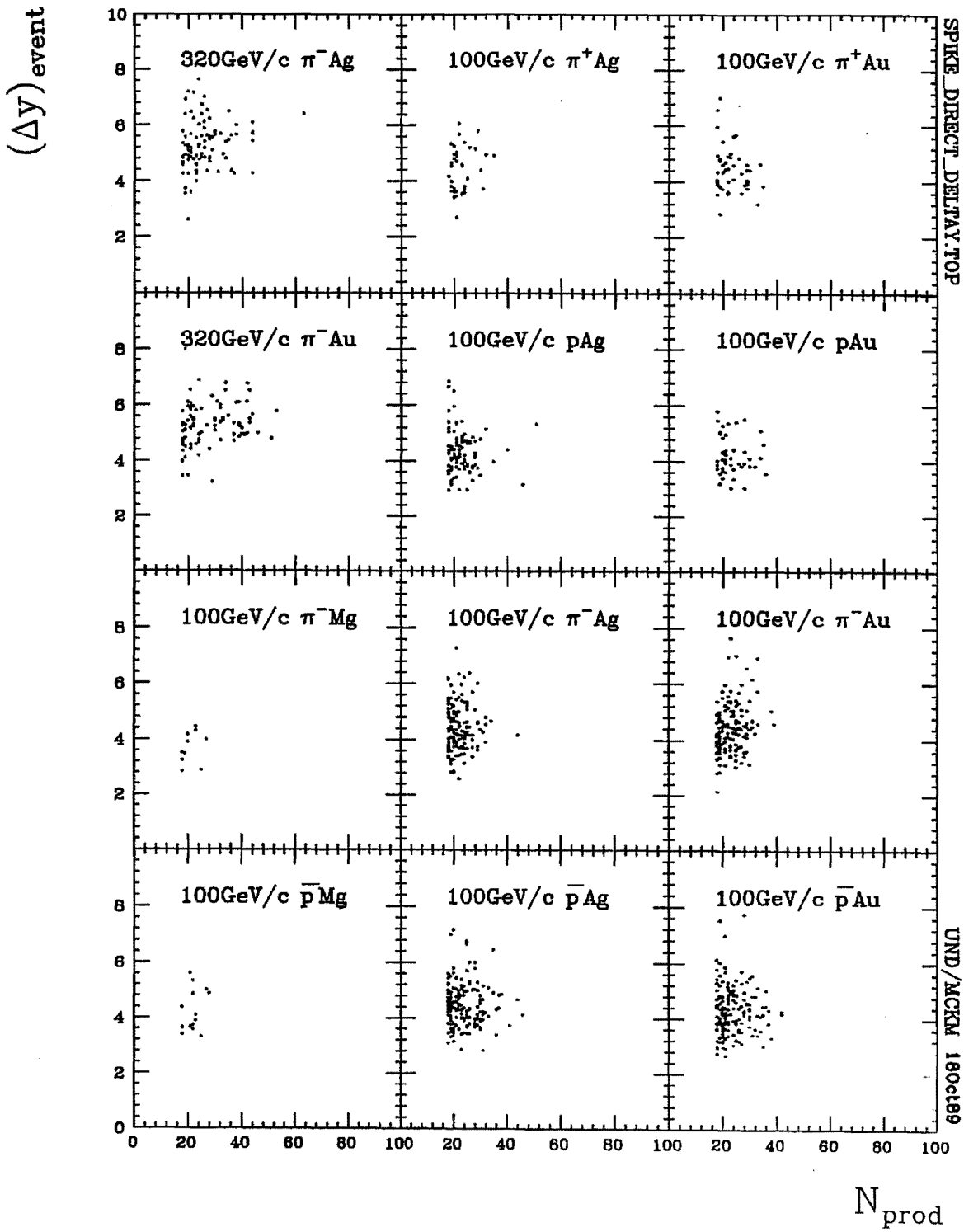

Figure 6.2.9 Scatter plot of event rapidity widths as a function of produced particle multiplicity.

processes certainly are not consistent with fractal dimension results.

6.3 CORRELATION DIMENSION

The correlation dimension is relatively immune to event-to-event noise from using bin probabilities directly. This is one of the distinct advantages the correlation dimension has over the information dimension, whose order is between that of the fractal dimension and the correlation dimension. The correlation dimension d_2 has been employed in studying π^+p interactions at 250 Gev/c and can be used as a lower limit on the fractal dimension [Dremin 88]. More importantly, it is dependent on event-internal relations only, further indicating that it is not subject to the vicissitudes of overall event-by- event momentum fluctuations. The correlation dimensions as calculated for E597 hA events are comparable to the fractal dimensions. Were the correlation dimensions to be significantly different from the fractal dimension, they would signal the multifractal nature of hadronic interactions.

As the third Renyii dimension d_2, the correlation dimension ν_n is defined in terms of the correlation function $C_n(l)$ which is determined by the fraction of produced particle pairs with rapidity differences less than resolution length l:

$$C_n(l) = \frac{1}{n(n-1)} \sum_{i=1}^{n} \sum_{j \neq i} \theta(l - |y_i - y_j|) \sim l^{\nu_n}$$

where θ is the Heaviside function and y_i, the rapidity of the i-th particle produced in an interaction. As a Renyii dimension of the second order, the correlation dimension is less than or equal to the information dimension, which in turn is less than or equal to the fractal dimension. The correlation dimensions shown in **Table 6.3.1** indicate that indeed they are comparable, not significantly different from the fractal dimensions, and certainly not significantly smaller than the fractal dimensions. Obviously, the fractal dimensions may be a bit low, but they are at least consistent with the correlation dimensions to within errors. Thus the fractality of most events seems to be homogeneous.

It has been suggested that events with large rapidity fluctuations have correlation functions with characteristically different forms from events more homogeneous

Table 6.3.1 A comparison of four-bin-averaged fractal and correlation dimensions calculated at $\epsilon = .4$ units rapidity.

Projectile	320GeV/c		100GeV/c									
	π^-	π^-	π^+	π^+	p	p	π^-	π^-	π^-	$\bar{p}$	$\bar{p}$	$\bar{p}$
Target	Ag	Au	Ag	Au	Ag	Au	Mg	Ag	Au	Mg	Ag	Au
Dimensions taken at .4 units rapidity; $N_{prod} \geq 20$												
Nevts	85	87	39	46	88	47	10	137	137	14	165	156
$D_F(4bin)$	.61	.61	.63	.68	.65	.62	.65	.64	.62	.58	.64	.67
Δ	.02	.02	.02	.02	.02	.02	.02	.02	.02	.02	.02	.02
d_2	.71	.72	.72	.71	.73	.73	.76	.74	.73	.75	.75	.75
Δ	.05	.05	.05	.05	.05	.05	.05	.05	.05	.05	.05	.05

COMPAREDIM.TAB UND/MCKM 14Feb90

in rapidity [Dremin 87] and that this distinctive form could serve as a means to classify events. In this scenario, spike events would exhibit something of a plateau in the plot of the correlation function $C_1(l)$ vs. the resolution length l compared to a steadier rise for non-spike events. In **Figure 6.3.1** and **Figure 6.3.2** this was demonstrated with handmade events [Dremin 88] and with 400 GeV/c pp events [Dremin 89b]. However, in the hadron-nuclear reactions of E597, spike events do not show this kind of clear difference. **Figure 6.3.3** shows the correlation dimension as a function of normalized resolution width ℓ, tagged for the maximum number of particles within any region of width .1 rapidity unit, for all 100 GeV/c $\bar{p}Ag$ interactions with $N_{prod} \geq 20$. Clearly the spike events (selected on the basis of 5 or more tracks populating any one rapidity bin of width .1) sometimes, but not always, manifest correlation functions with plateau features. Even when they do, the plateaus are not very marked. Furthermore, some events with 3 or 4 tracks populating a .1 rapidity region *do* show a marked plateau. Thus looking for plateaus is not a reliable way to characterize spike events.

What we do see, however, is the tendency for events with greater numbers of tracks in a .1 units rapidity width to have smaller correlation dimensions, *i.e.* smaller slopes, on the average at some fixed resolution length. This is clearly seen in **Figure 6.3.4** which plots the correlation dimension evaluated at .4 units relative rapidity resolution length as a function of the maximum number of tracks found in a .1 unit rapidity width. The correlation dimension definitely decreases with increasing maximum track density. Now it has been suggested that low correlation dimensions relate to very inhomogeneous quark-gluon plasmas exhibiting high internal dimensions of parton motion [Dremin 88]. Hwa [Hwa 89] agrees that this is not too far-fetched considering the enhanced probability of turbulent motion when latent energy transforms to kinetic energy. But, even so, only some of the collisions may be involving phase transitions so that averaging over events must be done with extreme caution in order to preserve the integrity of the signal. If the averaging is not distorting the signal excessively, the dependence of the correlation dimension on the maximum track density of individual events could be interpreted to be a signal for quark-gluon plasma.

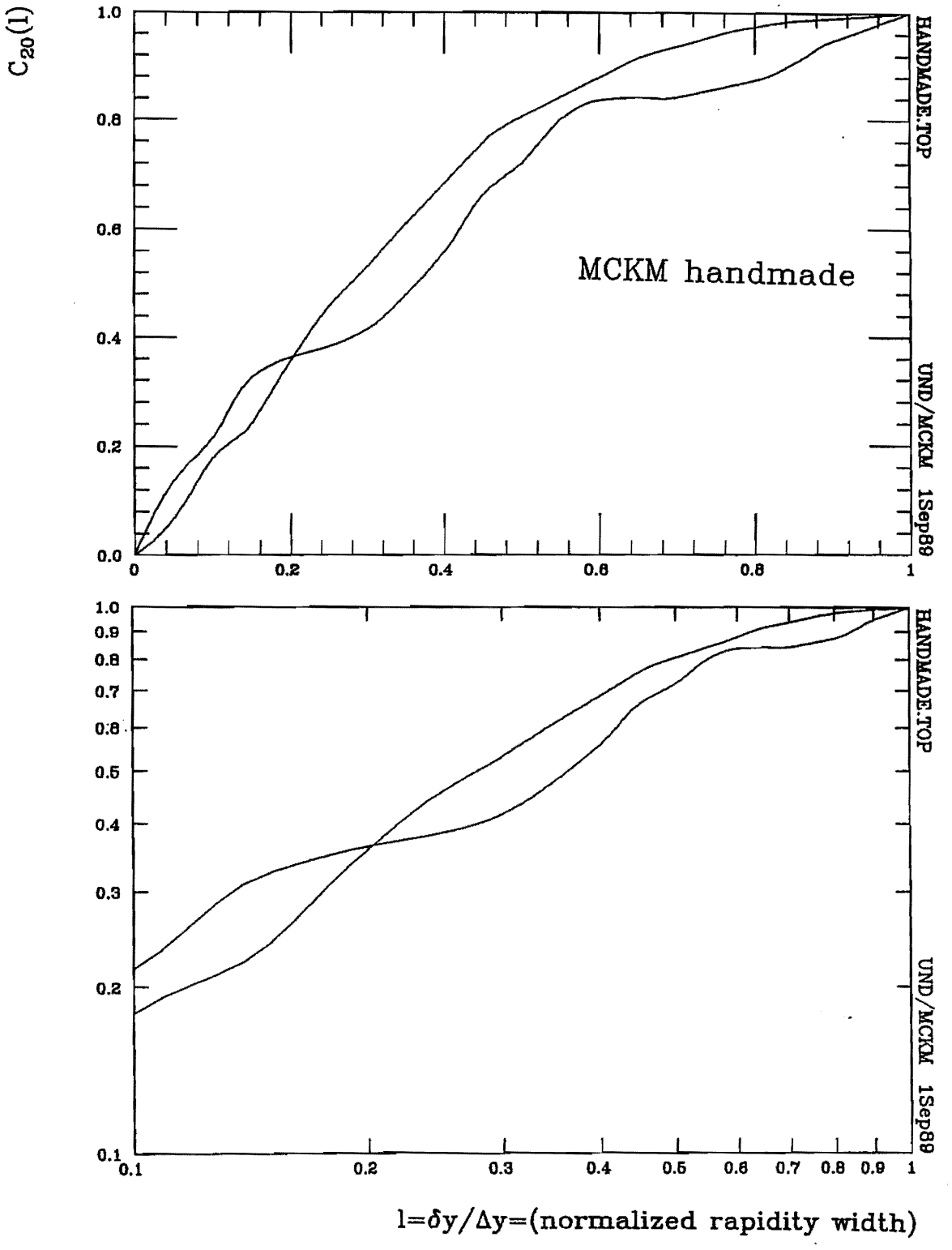

Figure 6.3.1 Correlation function dependence on relative rapidity resolution for a handmade spike event similar to that in [Dremin 88]. The upper plot is linear in C_{20} while the lower plot is logarithmic.

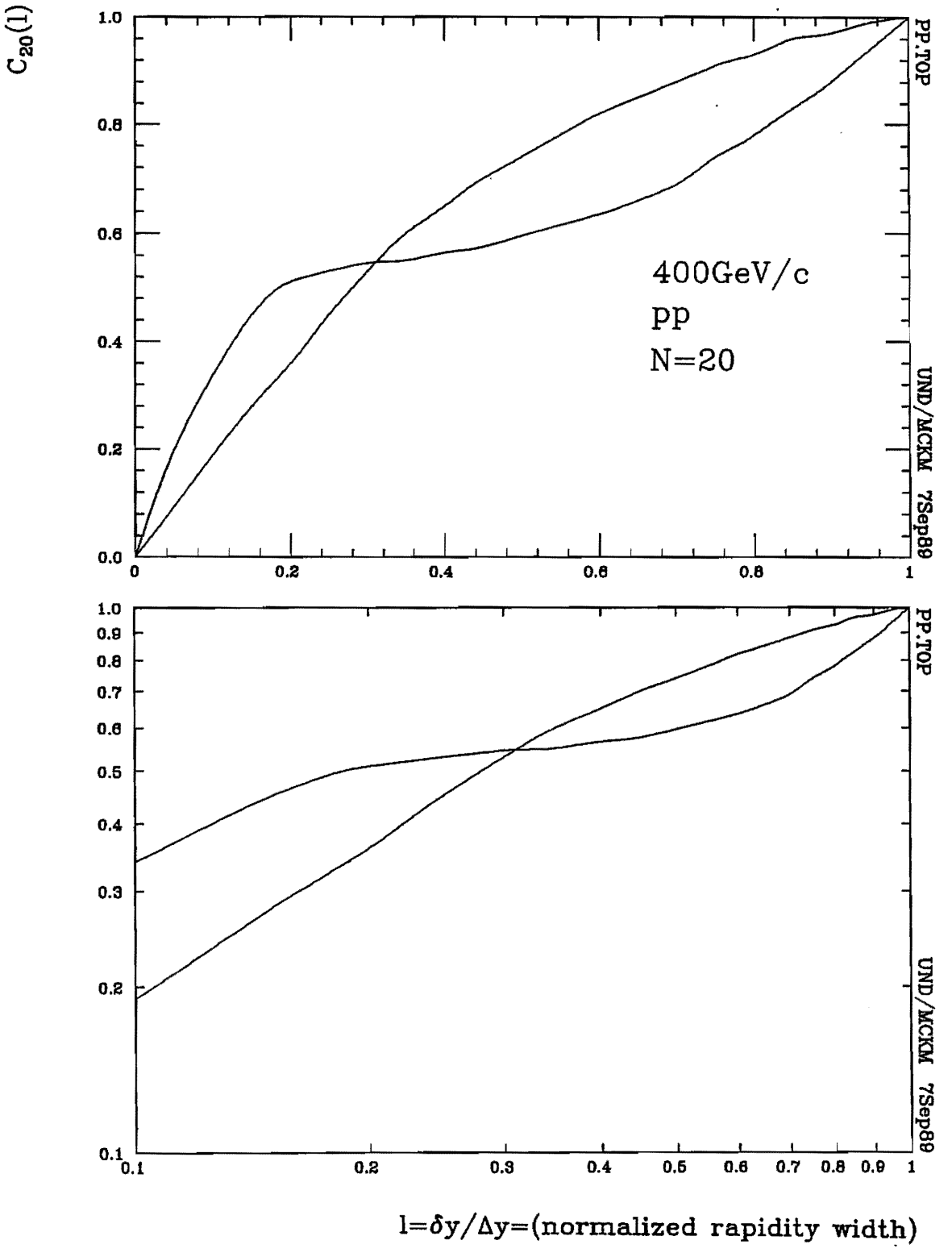

Figure 6.3.2 Correlation function dependence on relative rapidity resolution for two 400 GeV/c pp events (NA27) [Dremin 89b]. The upper plot is linear in C_{20} while the lower plot is logarithmic.

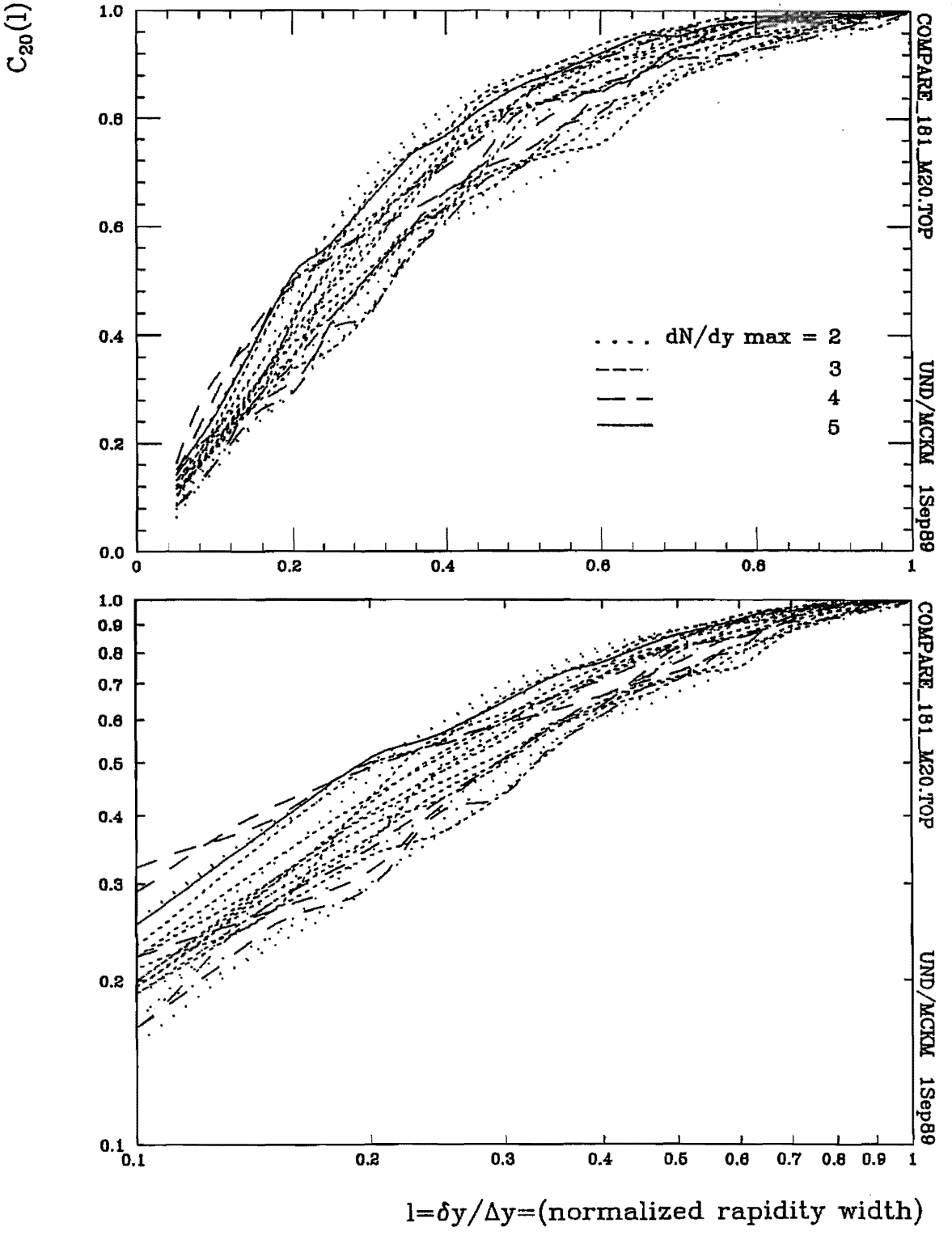

Figure 6.3.3 Representative examples of correlation dimension as a function of rapidity resolution from the spike event sample. The upper plot is linear in C_{20} while the lower plot is logarithmic.

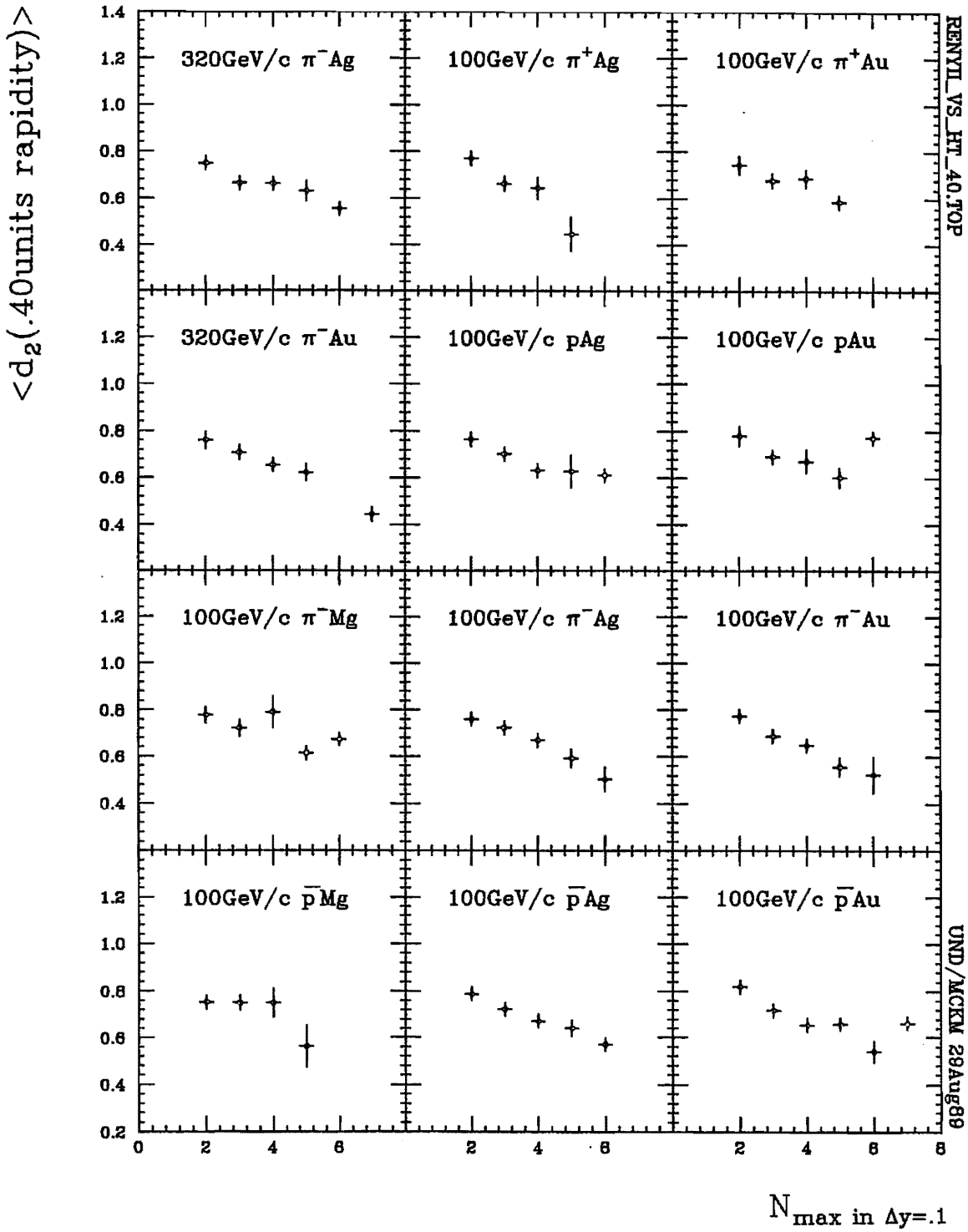

Figure 6.3.4 Correlation dimension evaluated at rapidity resolution length .4 units as a function of event maximum number of produced secondaries within any single rapidity window of .1 units.

6.4 SUMMARY

- The average fractal dimension of hA events is nearly constant, with values between .62(.04) and .65(.04) as calculated by direct linear fits of $N' vs. \epsilon$. *hA events have a fractal dimension comparable to that of Cantor sets.*

- Analysis for the fractal dimension is optimized with the base fraction $\lambda = 9/10$ for the resolution length. *The fractal dimension reaches a relatively stable region at* $\epsilon \approx .4$.

- Fractal dimension does not seem to depend on event maximum local rapidity densities. *Fractal dimension does not directly depend on* spike-*ness.*

- The lower limit of the fractal dimensions depends on produced particle multiplicity N_{prod}. *Average fractal dimensions increase nearly linearly with* N_{prod}.

- FRITIOF essentially reproduces E597 fractal dimensions. *Fractal dimensions could be a signal for cascading.*

- Broken events yield fractal dimensions comparable to those from the original pool of events. *Fractal dimension is not subject to excessive event-to- event differences.*

- Pseudo-events randomly generated from experimental inclusive rapidity distributions yield fractal dimensions comparable to those from the original pool at $\epsilon = .4$ but without a characteristic plateau feature. *Pseudo-events randomly generated from experimental inclusive rapidity distributions do not yield a stable fractal dimension.*

- Totally random simulations produce much lower values of the fractal dimension and no characteristic plateau feature. *The fractal dimension must be sensitive to the shapes of the beam and target regions of rapidity.*

- The correlation dimension as a function of rapidity resolution ϵ can be classified into three(3) different modes: straight, humped, and stair-step or plateau. *The*

stair-step is not a reliable signal for spike events. Stair-step behavior occurs in both spike and non-spike events.

- Quark-gluon plasma (QGP) phase transitions would be expected to manifest low correlation dimensions. The data shows decreasing correlation dimensions for increasing rapidity density fluctuations. QGP is more likely with increasing rapidity density. *The low correlation dimensions of E597 hA interactions with high rapidity densities are consistent with an interpretation which includes QGP phase transitions.*

CHAPTER 7

CONCLUDING SUMMARY

The various analyses show that the occurrence of anomalously high rapidity density events (*spikes*), the scaling of factorial moments down to very small rapidity resolutions (*intermittency*), and the fractional dimension of hA interactions (*fractals*) present enough evidence to justify entertaining new physics when supported by more conventional lines of analysis. New dynamics have been shown to be plausible in density spike events. These events feature large rapidity density maxima which

- occur in numbers larger than statistically expected [22],
- are linearly dependent on total produced multiplicities [23],
- are independent of energy, beam, or target composition [23], and
- are not necessarily signalled by a stair-step correlation dimension mode [44].

New dynamics may also be plausible by virtue of intermittency which

- is inferred from the linearity of horizontal factorial moments down to the experimental resolution [28], and
- may signal phase transitions [29].

Fractality in hadron-nucleus interactions could also be associated with new physics. Hadron-nucleus interactions, treated as fractal objects, are

- comparable in dimension to Cantor sets [36],
- sensitive to beam and target regions of rapidity [43],
- incompatible with random simulations [42; 43],

- relatively stable [**37; 41**],
- independent of an event's maximum rapidity density [**38**], and
- linearly increasing with charged produced multiplicity [**39**].

7.1 IN THE BIG PICTURE

The importance of this study's conclusions can be measured in terms of its addressing the big picture of multiple production in hA interactions. This big picture includes multiple collisions, partial stimulated emission, clustering, cascading, short and long range correlations, and quark-gluon plasma. While each of these elements has been addressed in this study and its results summarized as shown below, no single, consistent picture emerges.

Multiple collisions are indicated by

- produced particle multiplicity dependence on $\bar{\nu}$ [**1**],
- light proton multiplicity [**2**],
- cuts on leading particle rapidity and total charged produced particle multiplicity consistent with single collision Andersson model predictions [**3**],
- the success of an NBD parameterization of slow proton emission [**5**],
- extrapolation of 1/k to one collision consistent with hp [**8,**]
- evidence of FBC slopes sharply decreasing and going negative when gaps are introduced and when energy is partitioned unequally among collisions [**16**],
- FBC slope increases with $\bar{\nu}$ coupled with some A-dependent mechanism [**18**], and
- FBC slopes particularly dependent on the number of proton collisions [**19**].

Partial stimulated emission is consistent with

- energy dependence of the NBD parameter 1/k [**8**],

- factorial moments at small δy [34],
- chaoticity larger than .40 [35],
- Bose-Einstein correlations [26; 35], and
- ring features [24].

Clustering can be inferred from the NBD of multiplicities. The data are consistent with clusters characterized by

- rapidity widths of 4 units, comparable to hp results [9],
- cluster overlaps [12],
- occurrence frequencies averaging between 1 and 7 [12] independent of the numbers of collisions [11] but dependent on beam quark composition [13],
- cluster populations averaging between 1 and 4 depending on the number of collisions [11] as well as the energy [10].

Cascading is

- implied by a cascade cluster interpretation of NBD applied to intermittency [33],
- limited due to lack of a recursion relation between intermittency strengths [31] either because of an inappropriate random cascading model, or because the number of scales is not large, and
- signalled by fractal dimensions consistent with those for FRITIOF simulated data [40].

Short range correlations are

- largest for particles of opposite charge except for the very short range BE correlations [13] and
- maximized at rapidity distances less than 2.5 units [15]

while **long range correlations** are

- largest for particles of opposite charge [13] and
- characterized by anticorrelations [17].

Quark-gluon plasma projections are consistent with the

- frequencies of occurrence of spike events [21] which are dynamically significant [22] and are numerous enough for quantitative studies [20],
- ring features of spike events interpreted in terms of gluon coherent production [24],
- rise of the beam fragmentation wing in seagull effects [25],
- pion emission volume at spike multiplicities [26],
- A-independent processes [27],
- large maximum rapidity densities (up to 136 particles/unit rapidity) [21],
- increased intermittencies for spike events [32],
- an anomalous fractal dimension independent of order q [30],
- intermittency strengths comparable with those for hh interactions [29], and
- low correlation dimensions associated with high rapidity densities [45].

7.2 PROPOSED FOLLOW-UP

Having studied multiple collision, spike, intermittency, and fractal dimension phenomena individually in this study, an appropriate follow-up study would emphasize the interrelations between each of these. Spikes, intermittency, and fractal dimensions already share a closely common ground — rapidity fluctuations. As such they have been shown to be consistent with one another:

1) **SPIKE** *vs.* **INTERMITTENCY** Since spike events are conjectured to include some QGP, it is entirely expected that intermittency would be more pronounced in that sample. The data are consistent with this expectation. Intermittency is stronger for spike events than for non-spike events.

2) **SPIKE** *vs.* **DIMENSION** The correlation dimension has been shown to decrease with increasing local rapidity density or more pronounced spike characteristics.

3) **INTERMITTENCY** *vs.* **DIMENSION** The value of the fractal dimension at about .6 is consistent with expectations for the intermittency which is evident in hA interactions. Intermittency is believed to occur only at fractal dimensions less than or equal to 3 [Paladin 87]. It is conjectured that Renyii dimensions decrease as intermittencies increase [Dremin 89]. Since spike events, which have smaller dimensions, show stronger intermittencies, then stronger intermittencies are associated with smaller dimensions.

Having experimentally verified some consistencies between spike phenomena, intermittency, and fractal dimension, the question remains how the number of collisions ν can be interpreted in terms of these conceptually related measures of rapidity fluctuation and self-similar processes. Thus a study of spikes, factorial moments, and fractal dimension as functions of ν is an obvious sequel to this study. Since ν is a measure of the impact parameter, then a corroborating study should also be made in terms of the role of $p_\perp$ and $E_\perp$ in spike, intermittency, and dimension results.

7.3 COMPILATION OF CONCLUSIONS

MULTIPLE COLLISIONS (Chapter 3)

1 Produced particle multiplicities are linearly correlated to $\bar{\nu}(hA)$. *Multiple production involves multiple collisions.*

2 $\Pi_{hA}(\nu)$ distributions can be calculated geometrically by Monte Carlo. Andersson and Verbeure model predictions of light proton multiplicity probability distributions, based on such $\Pi_{hA}(\nu)$ distributions, are generally consistent with E597 data. *Light proton multiplicity is an indicator of the number of multiple collisions undergone in an interaction.*

3 Events with customized cuts on leading particle rapidity and total charged multiplicity are consistent with the Andersson model predictions for single collisions. *Data samples of hA events may be enriched for single collision events by applying leading particle rapidity and total charged multiplicity cuts.*

4 Andersson model estimates of ν on the basis of N_{lightp} have a smaller dispersion than $\bar{\nu}(hA)$. *$\nu_{Andersson}(N_{lightp})$ is a better measure of the number of multiple collisions than $\bar{\nu}(hA)$.*

5 Proton multiplicity distributions can be described adequately by NBD in phase space regions associated with *black*, *grey*, and *light* velocity designations. *Multiple collision models can use NBD parameters to prescribe the way multiple collisions affect slow proton emission.*

6 Andersson model estimates of ν on the basis of N_{lightp} are not significantly improved by Verbeure modifications which include the shape of the N_{lightp} distribution (described by NBD parameter k) as well as its average value as parameters. However, a simple approach used by Ledoux et al. estimates ν on the basis of $\sqrt{N_{lightp}}$ and produces a more linear correlation than either Andersson and Verbeure models can between produced particle multiplicity and the number of collisions inferred from N_{lightp}. *$\nu_{Ledoux}(N_{lightp}) = \sqrt{N_{lightp}}$ may be a closer estimate of ν than Andersson and Verbeure estimates.*

7 Produced particle multiplicities are not correlated to Andersson and Verbeure estimates of $\bar{\nu}(N_{lightp})$ in the same way that FRITIOF's produced particle multiplicities are correlated to its simulated numbers of collisions. Deviations mainly occur at large ν. Produced particle multiplicities are correlated, however, to Ledoux estimates of $\bar{\nu}(N_{lightp})$ very much like FRITIOF's produced particle multiplicities are correlated to its simulated numbers of collisions. *FRITIOF's simulated events are more consistent with Ledoux's simple model than the Andersson and Verbeure models.*

8 The inverse of NBD parameter k is energy dependent and strongly correlated to the number of collisions sustained. *When extrapolated to one collision, 1/k for hA is the same as for hp. The energy dependence of 1/k is in agreement with partial stimulated emission interpretations of NBD.*

9 In the cluster model interpretation of NBD parameters, clusters in E597 hA interactions extend about 4 units in rapidity. *In the cluster model interpretation, hA clusters extend about the same in rapidity as clusters in pp interactions.*

10 The number of particles in an NBD-based cluster increases with energy. *In the cluster model interpretation, cluster populations are energy dependent.*

11 In the cluster model interpretation, the particle content of NBD clusters increases with additional numbers of collisions, while the number of clusters does not.

12 NBD clusters in E597 hA interactions contain an average number of particles between 1 and 4 particles in 1 to 7 different clusters. *In the cluster model interpretation, considerable overlap exists between clusters.*

13 The number of NBD clusters is not energy dependent in E597 interactions. However, the number of clusters tends to be is smaller for meson beam interactions than for baryon beam interactions. *In the cluster model interpretation, the number of clusters seems to be beam dependent.*

14 The short and long range correlations observed for charged particles are due primarily to correlations between particles of different charge.

15 For central rapidity intervals of varying width, FBC slopes b_B reach maximum at about 1.25 units half-width except for $\bar{p}$ interactions ($\bar{p}Mg$ and $\bar{p}Ag$) for which they steadily increase into a kind of plateau. *Short range correlations have a range of about 2.5 units.*

16 FBC slopes b_B sharply decrease and become negative when a gap is introduced between forward and backward sectors. *The sharpness of the decrease cannot be accounted for by multiple collision models that partition energy equally among collisions.*

17 The differences between FBC results for total charged and negative charged produced particle multiplicities as a function of increasing gap size between forward

and backward sectors which are seen in hp interactions are not seen in hA interactions. In hp interactions a positive correlation peak appears in the charged mode but not in the negative charged mode. In hA interactions, no positive correlations appear beyond the gap size at which the minimum occurs. FBC slopes reach minimum values at about 1.25 units and come back up to zero, but never becomes positive again as they do for hp interactions. *Anticorrelations dominate long range hA interaction phenomena up to the kinematic limit.*

18 FBC slopes b_B tend to increase with the number of collisions $\bar{\nu}$ in target-dependent sequences. With an A-dependent shift of $\bar{\nu}$, FBC slopes can be unified to show a single ν dependence for all targets in agreement with pp results. *Multiple collisions must be coupled with some other A-dependent mechanism to produce FBC effects.*

19 The tendency for b_B to increase with the number of collisions $\bar{\nu}$ is strongest and most pronounced for positive/forward-negative/backward charge modes, suggesting a proton collision mechanism. FBC slopes are dependent on the number of proton collisions in approximately the same way for all target nuclei. *FBC effects show more correlation with the number of proton collisions than with total number of collisions.*

SPIKES (Chapter 4)

20 131 events qualify as spike events. *Large fluctuations in rapidity density appear in hA often enough for quantitative studies of spike events.*

21 Maximum local rapidity densities as high as 136 particles/unit rapidity are observed in hA interactions. *Spike events are candidates for QGP.*

22 Density spikes of various heights occur in numbers larger than statistically expected. *Spike events are probably dynamically significant.*

23 Density spike production is strongly correlated to produced particle multiplicity. Spike heights are directly proportional to produced particle multiplicity with a

constant 1 particle per unit rapidity for each particle produced, essentially the same as for hh interactions. *This linear dependence of maximum rapidity density on total produced multiplicity seems to be universal, unaffected by energy, beam, or target considerations.*

24 Spike events display *ring* features. *The random angular distribution of spike particles is consistent with expectations for coherent production analogous to Cerenkov radiation.*

25 Seagull effects are observed in both 100 and 320 GeV/c events but are not consistent with FRITIOF predictions. *The rise of the beam fragmentation wing cannot be accounted for without some large-momentum transfers and gluon radiation.*

26 On the basis of Bose-Einstein correlations, the production size in hA interactions is estimated to be somewhat less than 1 fm. *The emission volume is small enough to make QGP possible at spike multiplicities.*

27 The pion emission volumes inferred from Bose-Einstein correlations in hA are comparable to those in hh interactions and do not indicate a strong A dependence among themselves. *Therefore, QGP, if it occurs, is nearly as likely (or unlikely) for light as heavy nuclei, given comparable multiplicities.*

INTERMITTENCY (Chapter 5)

28 A power-law relation exists between horizontal factorial moments and rapidity bin widths down to .1-.2 units rapidity in E597 data. *Linearity down to the experimental resolution could be signaling intermittency.*

29 Intermittency strengths, the slopes describing the correlation between normalized factorial moments and the rapidity resolution length, are comparable in hA interactions to those associated with hh interactions, rather than significantly weaker. *QGP transitions are not ruled out as an origin of intermittency.*

30 A strong correlation exists between the intermittency strengths and order q of the factorial moments, but not between the anomalous fractal dimension and q. *The anomalous fractal dimension is independent of q and thus is consistent with QGP second order transition behavior.*

31 The intermittency strengths are not recursively related to one another as expected in random cascading models assuming a large number of scales. *Either the random cascading model is inappropriate and/or the number of scales over which the fluctuations occur is not very large.*

32 Intermittency is stronger by at least an order of magnitude in spike events as compared all average events. *Increased intermittency strength is compatible with QGP transitions in spike events.*

33 Factorial moments are approximated by NBD parameters. *Intermittency can be studied in the absence of rapidity data.*

34 The factorial moments for small δy fall within limits set by quantum statistics for total coherence and total incoherence. *A partial stimulated emission view of multiparticle production is consistent with the data.*

35 Chaoticity is estimated to be larger than .40. This is consistent with estimates based on Bose-Einstein correlations (k=1) and with NA22 pp data fits in a partial coherence approach.

FRACTAL PROPERTIES (Chapter 6)

36 The average fractal dimension of hA events is nearly constant, with values between .62(.04) and .65(.04) as calculated by direct linear fits of the number of non-empty bins as a function of rapidity resolution length ($N' vs. \epsilon$). *hA events have a fractal dimension comparable to that of Cantor sets.*

37 Analysis for the fractal dimension is optimized with the base fraction $\lambda = 9/10$ for the resolution length. *The fractal dimension reaches a relatively stable region at* $\epsilon \approx .4$.

38 Fractal dimension does not seem to depend on event maximum local rapidity densities. *Fractal dimension does not directly depend on* spike-*ness.*

39 The lower limit of fractal dimensions depends on produced particle multiplicity N_{prod}. *Average fractal dimensions increase nearly linearly with* N_{prod}.

40 FRITIOF, which includes QCD cascading, essentially reproduces E597 fractal dimensions. *Fractal dimensions could be a signal for cascading.*

41 Broken events yield fractal dimensions comparable to those from the original pool of events. *Fractal dimension is not subject to excessive event-to- event differences.*

42 Randomized pseudo-events with data-like inclusive rapidity distributions yield fractal dimensions comparable to those from the original pool at $\epsilon = .4$ but without the characteristic plateau feature. *Pseudo-events with data-like inclusive rapidity distributions do not yield a stable fractal dimension.*

43 Totally random simulations produce much lower values of the fractal dimension and no characteristic plateau feature. *The fractal dimension must be sensitive to the shapes of the beam and target regions of rapidity.*

44 The correlation dimension as a function of rapidity resolution ϵ can be classified into three(3) different modes: straight, humped, and stair-step or plateau. *The stair-step is not a reliable signal for spike events. Stair-step behavior occurs in both spike and non-spike events.*

45 Quark-gluon plasma (QGP) phase transitions would be expected to manifest low correlation dimensions. The data show decreasing correlation dimensions for increasing rapidity density fluctuations. QGP is more likely with increasing rapidity density. *The low correlation dimensions of E597 hA interactions with high rapidity densities are consistent with an interpretation which includes QGP phase transitions.*

APPENDIX 1A

NDBC AND NDBASIC COORDINATES

The origin of NDBC resides at the center of the inside face of the camera side bubble chamber glass window, i.e. at *Fiducial 1.* Its x-axis points approximately in the beam direction (NORTH). The NDBC y-axis points up; and its z-axis points into the chamber away from the cameras (EAST). It is defined specifically by the FNAL survey positions of the bubble chamber fiducials in **Table 1A.2.1.**

The NDBasic origin lies on the NDBC y-z plane. Its x-axis is defined with reference to the centers of four(4) upstream proportional wire chamber (PWC) planes: PWC2 and PWC3 far upstream, and PWC8 and PWC9 close to the bubble chamber. The y- and z-axes make a right-handed system with y pointing *up*, parallel to PWC3s wires; and with z pointing EAST .

To relate bubble chamber measurements with spectrometer data, spectrometer data in a local device coordinate system are transformed to NDBasic and then to NDBC. **Figure 1A.2.1** visually relates local PWC coordinates with NDBasic. The same applies to drift chamber (DC) coordinates and NDBasic. PWC/DC positions and orientations (in NDBasic) are specified in terms of x (distance of the plane center from the origin along the beam direction); β (the angle that the sense wires make with the y-axis in the direction of increasing wire number), pitch (the wire spacing), and ρ_o (the distance from the x-axis to the fictitious *wire number 0* located one wire spacing before wire number 1.

A rotation to NDBC is then applied as illustrated in **Figure 1A.2.2.** The transformation $(x^{NDBasic}, y^{NDBasic}, z^{NDBasic}) \rightarrow (x^{NDBC}, y^{NDBC}, z^{NDBC})$ is effected in

Table 1A.2.1 FNAL 30-inch bubble chamber fiducial coordinates measured in the January 1982 survey.

Fiducial No.	x (cm)	y (cm)	z (cm)
1	0.0000	0.0000	0.0000
2	20.3055	20.2687	0.0000
3	10.1261	20.2731	0.0000
4	-.0095	20.3409	0.0000
5	-20.3290	20.2599	0.0000
6	20.3175	.0520	0.0000
7	-20.2775	.0127	0.0000
8	20.3182	-20.2306	0.0000
9	10.1629	-20.2472	0.0000
10	.0260	-20.2573	0.0000
11	-20.3074	-20.2522	0.0000
12	-.0232	0.1086	37.7093
13	20.2675	20.3825	37.7180
14	-.0287	20.3895	37.7152
15	-10.1691	20.4008	37.7138
16	-20.3294	20.3882	37.7124
17	20.2763	.0981	37.7121
18	-20.3344	.0998	37.7065
19	20.2627	-20.1917	37.7062
20	-.0224	20.2071	37.7033
21	-10.1788	-20.2096	37.7019
22	-20.3255	-20.1980	37.7005

BCSURVEY.TAB UND/MCKM 30Apr87

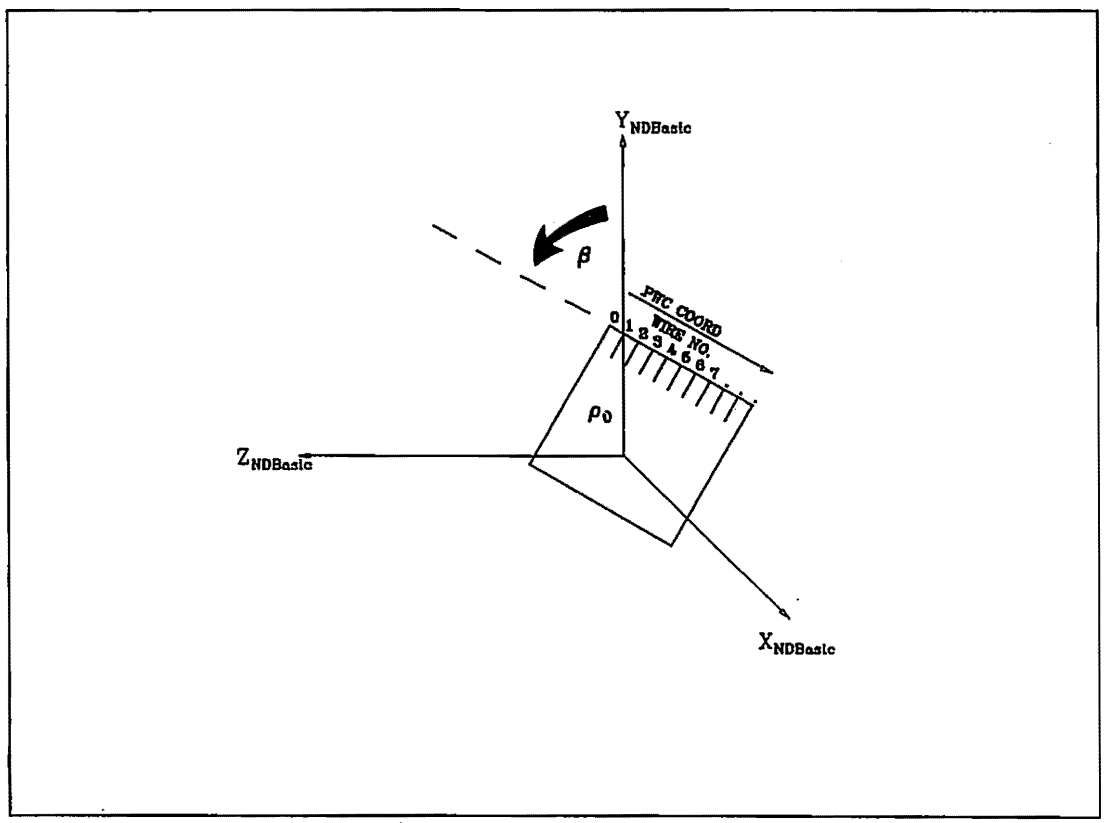

Figure 1A.2.1 Orientation convention of NDBasic with respect to PWC and DC devices.

four(4) steps:

- rotation by β about $y^{NDBasic}$-axis to (x',y',z')
- rotation by α about x'-axis to (x'',y'',z'')
- rotation by γ about z''-axis to (x''',y''',z''')
- translation by y_T and z_T along y'''- and z'''-axes, respectively

Specific values of transformation parameters β, α, and γ are tabulated in **Table 1A.2.2.**

The rotation matrix R relating the two systems in the general expression

$$\begin{pmatrix} x \\ y \\ z \end{pmatrix}^{NDBC} = R \begin{pmatrix} x \\ y \\ z \end{pmatrix}^{NDBasic} + \begin{pmatrix} 0 \\ y_T \\ z_T \end{pmatrix}$$

is calculated with the matrix product R

$$R = \begin{pmatrix} cos\gamma & sin\gamma & 0 \\ -sin\gamma & cos\gamma & 0 \\ 0 & 0 & 1 \end{pmatrix} \begin{pmatrix} 1 & 0 & 0 \\ 0 & cos\alpha & sin\alpha \\ 0 & -sin\alpha & cos\alpha \end{pmatrix} \begin{pmatrix} cos\beta & 0 & -sin\beta \\ 0 & 1 & 0 \\ sin\beta & 0 & cos\beta \end{pmatrix}$$

Example values for the matrix elements are given by [Elcombe 82]:

$$R_{Roll2133} = \begin{pmatrix} .999998331 & .001690022 & .000810936 \\ -.001690255 & .999998569 & .000286138 \\ -.000810451 & -.000287509 & .999999702 \end{pmatrix}$$

$$R_{Roll2158} = \begin{pmatrix} .999997079 & .001664774 & .001690921 \\ -.001666307 & .999998033 & .000905419 \\ -.001689411 & -.000908236 & .999998152 \end{pmatrix}$$

When cross-handling code from different institutions in the collaboration or comparing with Monte Carlo results, however, it may be important to note discrepancies between different coordinate systems. They differ as shown in **Figure 1A.2.3.**

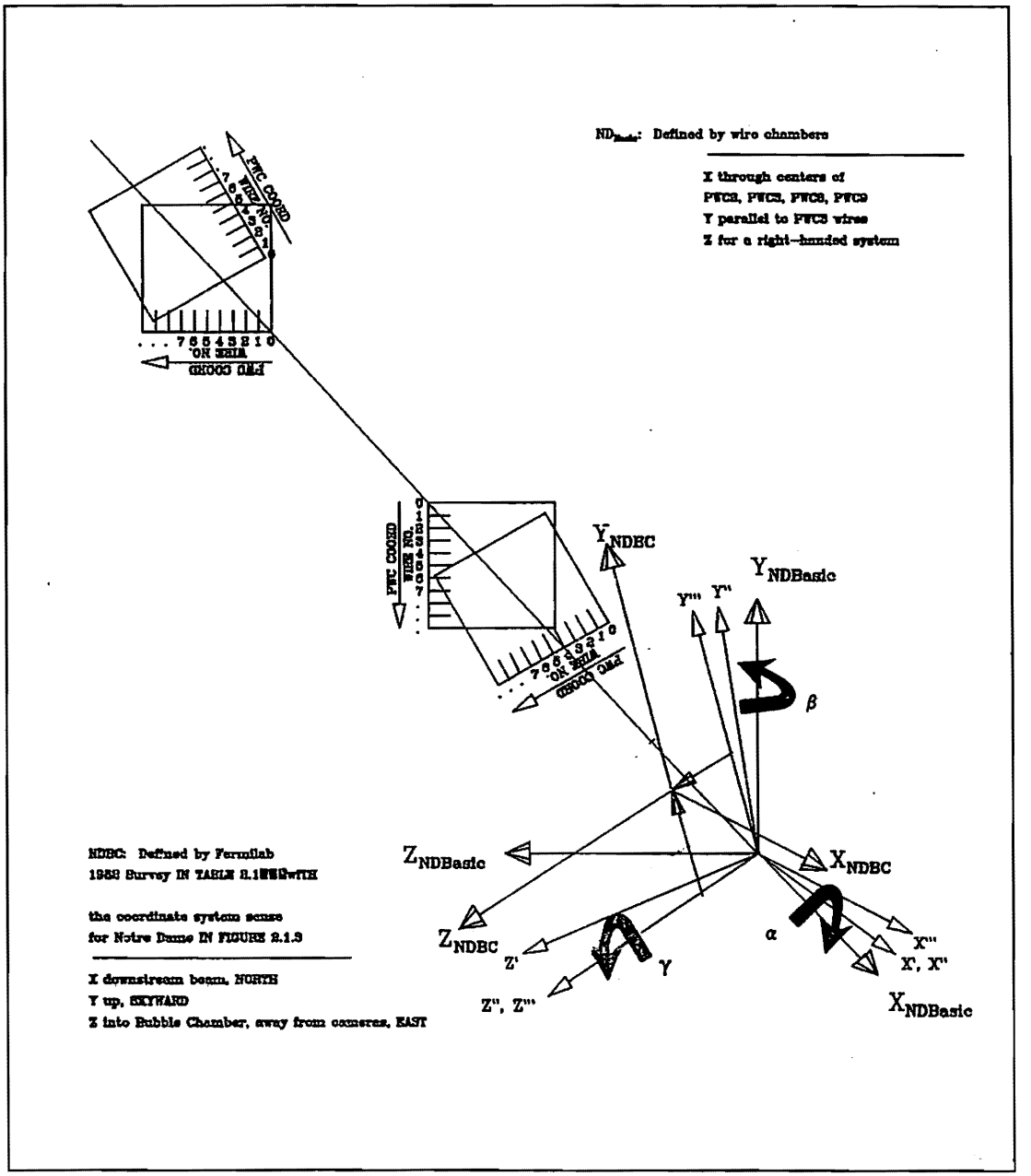

Figure 1A.2.2 Rotations and translations relating NDBC and NDBasic coordinate systems.

Table 1A.2.2 Rotation and translation parameter values required when transforming between NDBC and NDBasic coordinate systems.

Parameter		Roll 2133			Roll 2158		
β	(rad)	.00081	±	.00007	.00169	±	.00005
α	(rad)	.00029	±	.00002	.00091	±	.00001
γ	(rad)	-.00169	±	.00002	-.00166	±	.00001
y_T	(cm)	-6.248	±	.002	-6.270	±	.001
z_T	(cm)	19.404	±	.002	19.419	±	.001

TRANSFORMPAR.TAB UND/MCKM 14Mar89

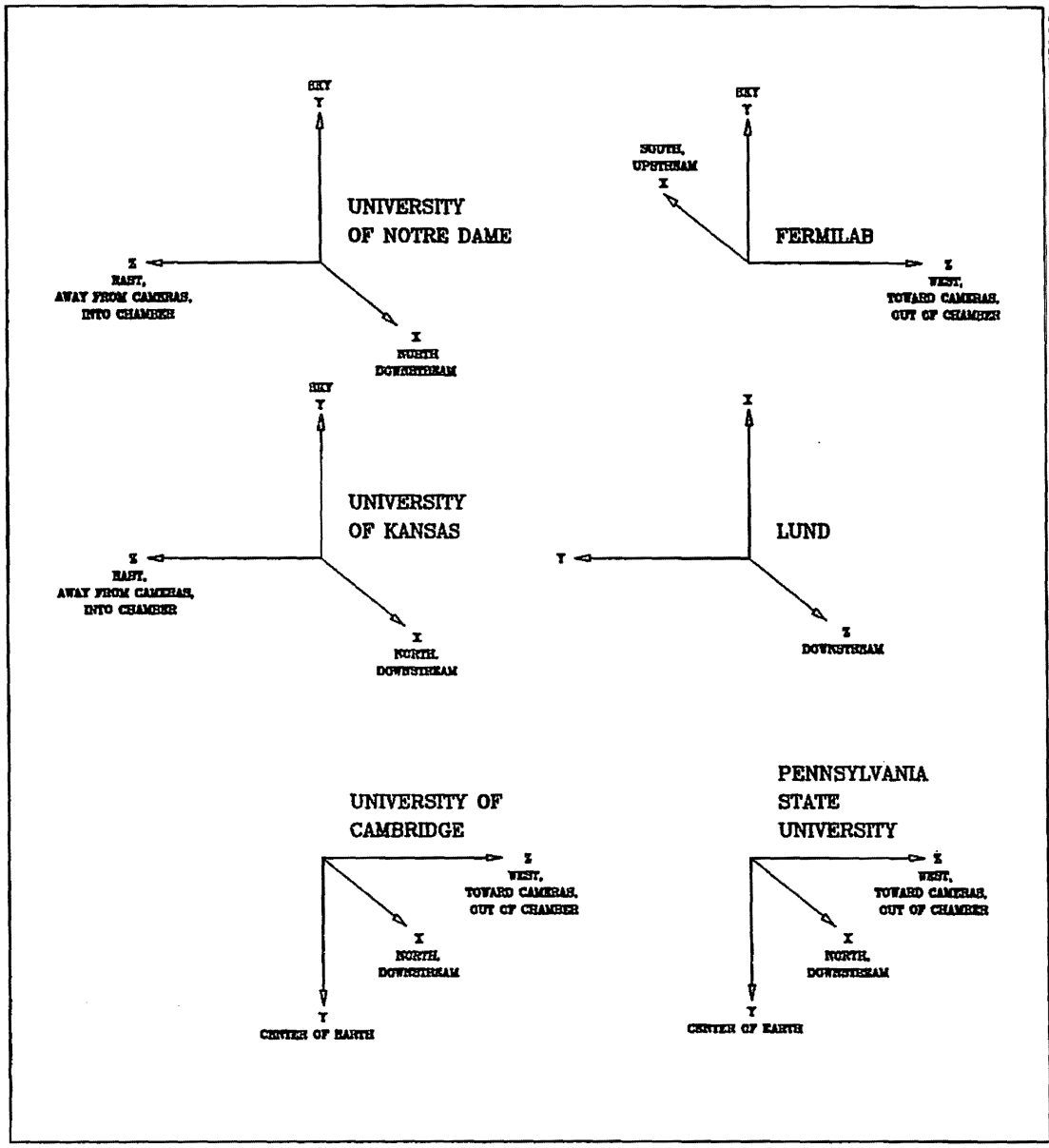

Figure 1A.2.3 Coordinate conventions adopted by participating groups in the E597 collaboration and FRITIOF, the Lund Monte Carlo.

APPENDIX 1B

FNAL E597 SPECTROMETER

1B.1 BEAM SYSTEM

The beam system provided mixed hadron beams in five(5) modes with relative compositions as given in **Table 1.4.1.** These beams were selected from projectiles emerging from collisions between 400 GeV/c protons from Fermilab's main ring (**Figure 1B.4.1**) and copper targets in the N3 beam line. The fraction of K^+ was enhanced by filtering beams through polyethylene and $\bar{p}$'s were produced at $\bar{p} : \pi^-$ ratios up to 40% using a halo technique on $\bar{\Lambda}$ decays [Neale 74].

Beam particles were bunched into 4-6 groups (*pings*) of 5-8 particles each. Each ping spanned 3 ms, but necessary time delays in the data acquisition systems restricted beam utilization to the latter portion of each ping. Since the bubble chamber was inherently non-triggerable, it underwent expansion at every ping and tracks in the bubble chamber volume were recorded photographically. The gross number of pings, or bubble chamber exposures, are given for each mode in **Table 1.4.1.**

1B.2 TAGGING SYSTEM

The upstream tagging system used in conjunction with the 30 inch BC hybrid spectrometer is shown in **Figure 1B.4.2.** A telescope of three(3) scintillator paddles (S1, S2, and S3); three(3) Cerenkov counters, two(2) with inner and outer rings, (C116I, C116O, C118I, C118O, and CDoghouse); and three(3) proportional wire chamber (PWC) triplets (A, B, and C) composed the beam tagging system. It provided data

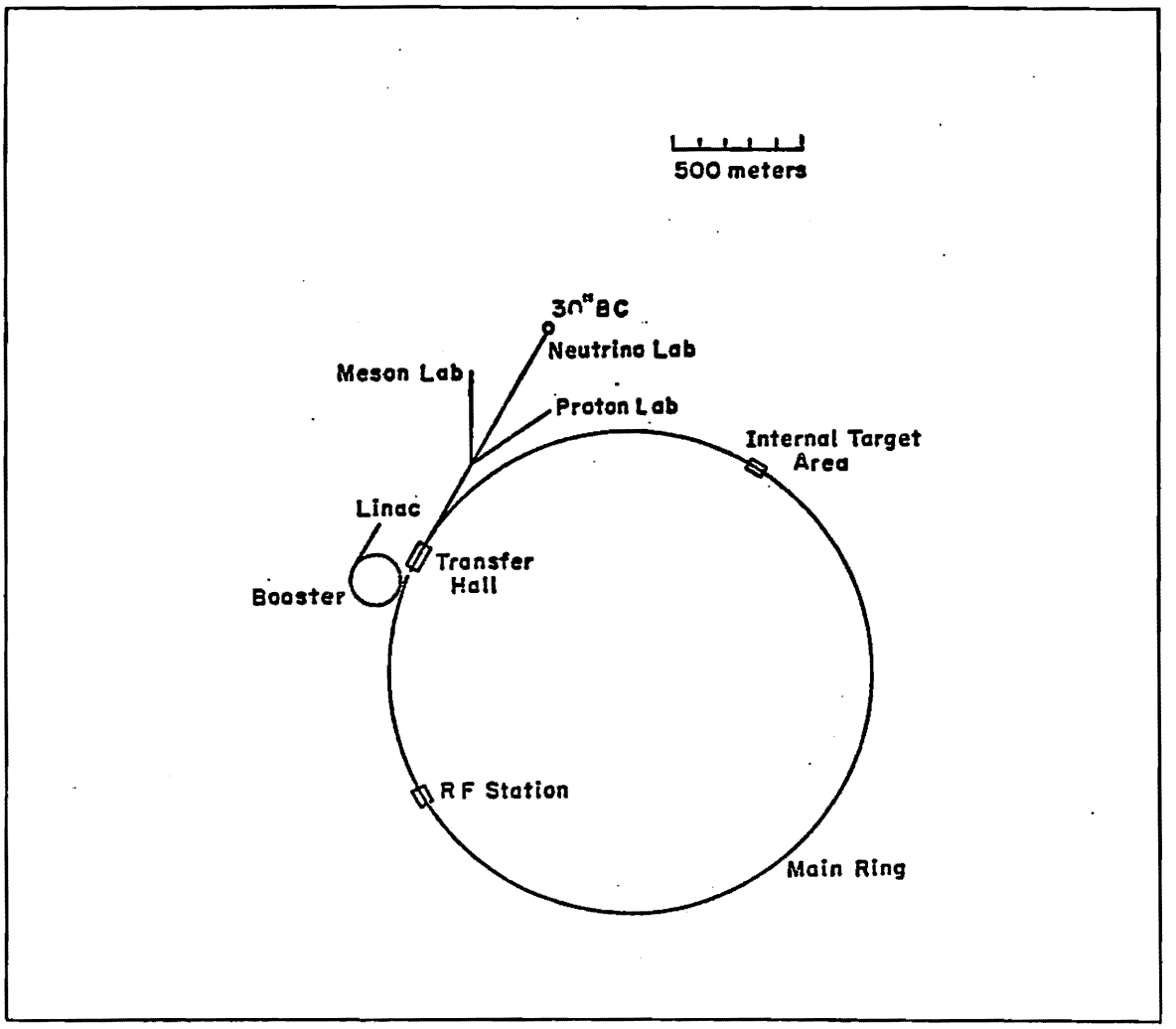

Figure 1B.4.1 Plan view of Fermilab.

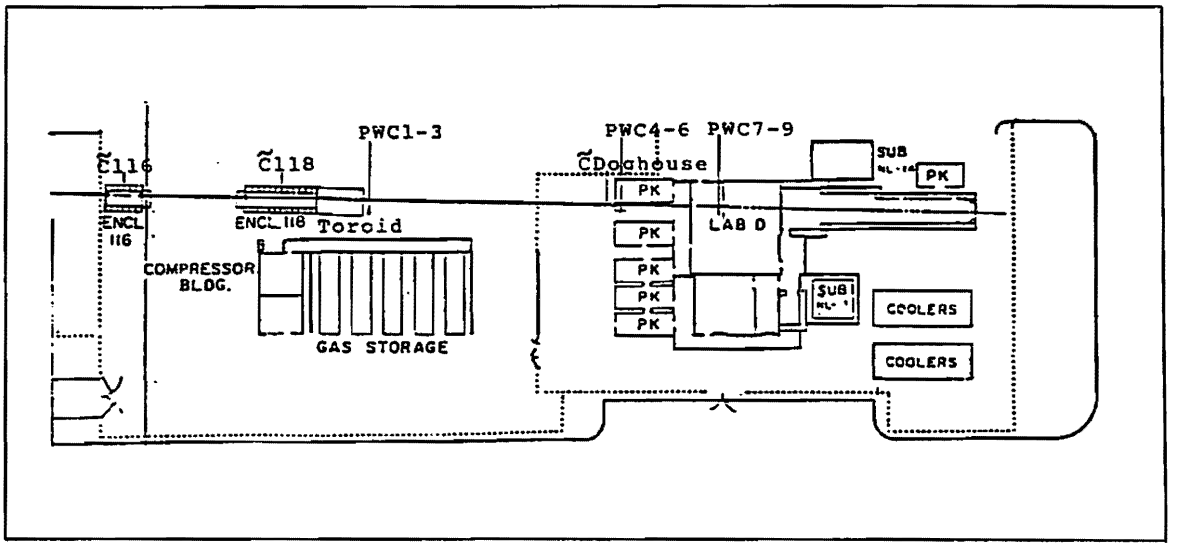

Figure 1B.4.2 Plan view of the E597 upstream beam tagging system.

by which to distinguish and identify individual projectiles in the mixed hadron beam. Mass separation schemes were based on PWC track reconstruction and five(5)-digit IOIOD codes reporting the presence or absence of light in the Cerenkov counters.

Matching a beam track in the BC with IOIOD information was made by determining the master gates associated with beam track reconstruction in the upstream PWCs. 3 ms master gate signals were formed by the coincidence of signals S1, S2, and S3. The master gate controlled the function of both the bubble chamber and all the electronic data devices. Upon receiving the master gate signal, the upstream proportional wire chamber (PWC) electronics strobed their data into memory and the rest of the devices began gathering data.

Signals from 48 sense wires spaced 2 mm apart and flanked by field wires maintained at a potential difference of -3.2 kV in a 70.8%:25%:4%:.2% gas mix of argon/isobutane/methylal/freon constituted the data for each of the nine(9) upstream PWCs. **Figure 1B.4.3** displays the details of PWC placement and relative orientation as verified in post-run alignments of reconstructed tracks. Each plane is rotated approximately 120° with respect to other planes in its respective triplet so Dalitz conditions could be employed.

Upstream PWC data were used to reconstruct beam paths correlated by time to the various mastergates occurring during each BC frame exposure. These were each compared with beam paths determined in BC stereographs but extrapolated back to the upstream PWCs. When the BC- and the PWC-determined paths overlapped sufficiently, the master gate number with all of its associated electronic data was assigned to the BC event frame.

Signals from upstream helium- and/or nitrogen-filled Cerenkov counters made it possible to separate particle velocities on the basis of the presence or absence of Cerenkov light in the inner and/or outer rings of the counters as a function of varying gas fills and pressures. At known momenta, the separation distinguishes between beam masses. The specific separation scheme is summarized in **Table 1B.4.1** with five(5)-digit IOIOD codes. In high to low order, the digits reported, respectively, the detection (1) or non-detection (0) of light in the counters C116(Inner ring),

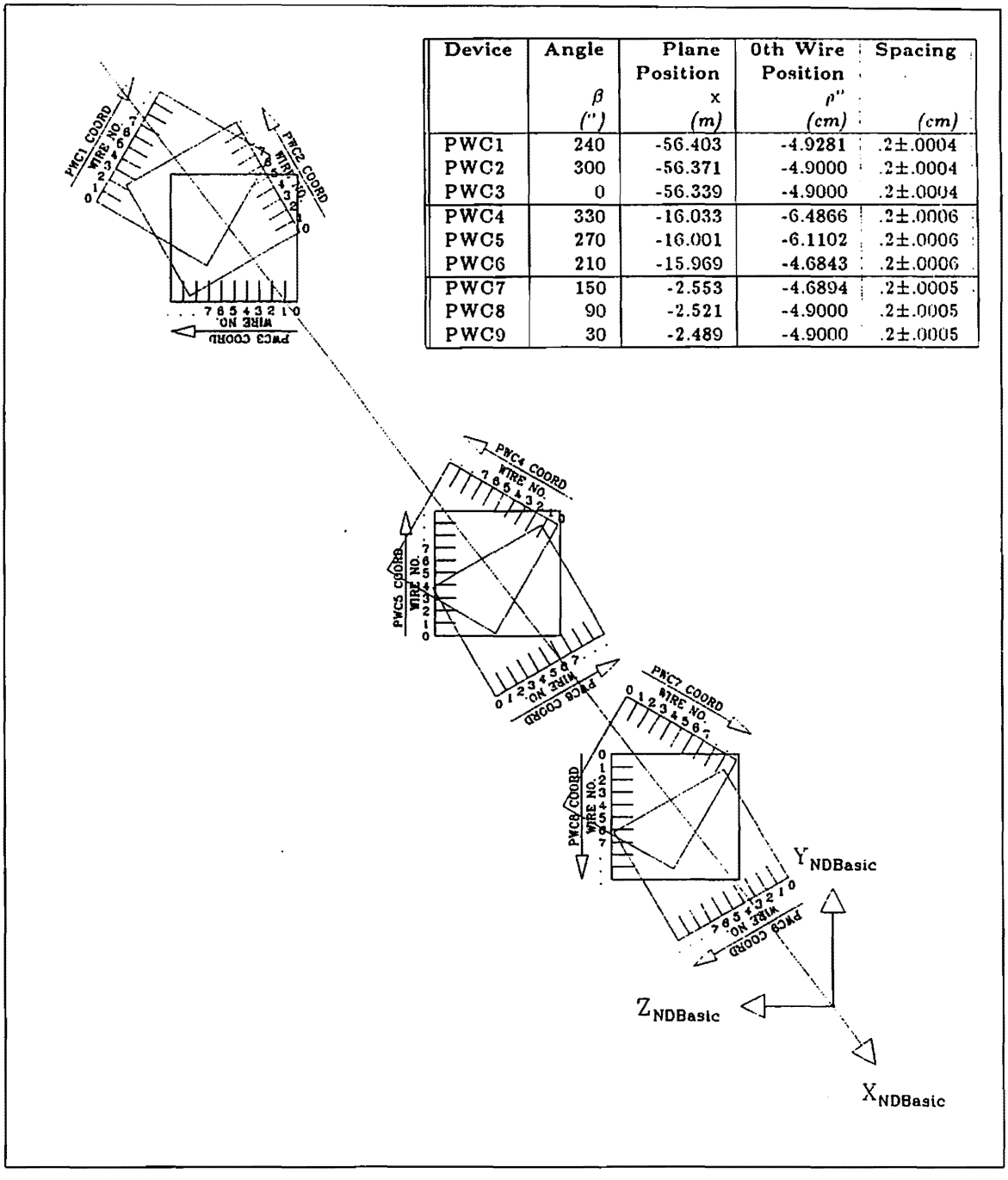

Device	Angle β (°)	Plane Position x (m)	0th Wire Position ρ'' (cm)	Spacing (cm)
PWC1	240	-56.403	-4.9281	.2±.0004
PWC2	300	-56.371	-4.9000	.2±.0004
PWC3	0	-56.339	-4.9000	.2±.0004
PWC4	330	-16.033	-6.4866	.2±.0006
PWC5	270	-16.001	-6.1102	.2±.0006
PWC6	210	-15.969	-4.6843	.2±.0006
PWC7	150	-2.553	-4.6894	.2±.0005
PWC8	90	-2.521	-4.9000	.2±.0005
PWC9	30	-2.489	-4.9000	.2±.0005

Figure 1B.4.3 Placement and orientation of upstream proportional wire chambers (PWC s 1-9).

Table 1B.4.1 Upstream Cerenkov counter running conditions and tagging criteria. IOIOD (116 Inner, 116 Outer, 118 Inner, 118 Outer, and Doghouse) code digits are read *vertically*. 0's and 1's signify the absence and presence, respectively, of light.

Beam	Rolls	Cerenkov Enclosure	Cerenkov Ring	Gas Fill	Pressure (psi)	Certain π IOIOD*	Probable π IOIOD*	Certain p IOIOD*	Probable p IOIOD*	Certain K IOIOD*
p/π^- 100GeV/c	2042-2076	116	Inner	He	2.78-	011	0011011	0	00011	
		116	Outer		2.88	101	0101101	0	00101	
		118	Inner	N_2	2.23-	000	0000000	1	11111	
		118	Outer		2.53	111	1000111	0	01000	
		Doghouse		He	4.44-	111	1111000	0	10000	
					4.80					
	2077-2098	116	Inner	He	3.99-					
		116	Outer		4.83	SAME	AS	ABOVE		
		118	Inner	N_2	2.30-					
		118	Outer		2.75					
		Doghouse		He	4.50-					
					5.00					
	2148-2200	116	Inner	He	3.74-					
		116	Outer		3.87	SAME	AS	ABOVE		
		118	Inner	N_2	2.30-					
		118	Outer		2.34					
		Doghouse	Doghouse	He	3.05-					
					3.46					
p 100GeV/c	2099-2121	116	Inner	He	4.02-			0	00011	
		116	Outer		4.11			0	00101	
		118	Inner	N_2	2.30-			1	11111	
		118	Outer		2.35			0	01000	
		Doghouse		He	4.30-			0	10000	
					4.70					
π^+/K^+ 100GeV/c	2122-2126	116	Inner	He	4.11	011	0001111			
		116	Outer			101	0110011			
		118	Inner	N_2	2.32	000	0000000			
		118	Outer			111	1010101			
		Doghouse		He	3.02-	111	1101010			
					3.20					
	2127-2147	116	Inner	He	5.88-	011	0011011			011
		116	Outer		7.06	101	0101101			101
		118	Inner	He	9.35-	000	0000000			111
		118	Outer		9.85	111	100011			000
		Doghouse		He	3.10-	111	1111000			000
					3.30					
π^- 320GeV/c	2201-2233	116	Inner	He	.16-	011	0			
		116	Outer		.19	101	0			
		118	Inner	He	1.6-	111	1			
		118	Outer		1.7	000	0			
		Doghouse		He	.4-	111	1			
					.5					

CERTAG.TAB UND/MCKM 9Apr87

C116(Outer ring), C118(Inner ring), C118(Outer ring), and CDoghouse(or CLabD).

1B.3 TARGET SYSTEM

General features of the bubble chamber and magnet are displayed in **Figure 1B.4.4.** The placement of the target bracket in the chamber is displayed in **Figure 1B.4.5.**

The bubble chamber underwent 4-6 consecutive expansion/compression cycles concurrent with as many pings in each accelerator cycle. Each *ping* coincided with a flux of five(5) to eight(8) beam particles whose identity was established in the beam tagging system upstream of the chamber. Four(4) cameras stereoscopically photographed bubbles forming along individual particle paths. This visual record of track and vertex information subsequently formed the basis for reconstructing particle trajectories from digitized film images. All BC data were referenced to fiducial markings on the front and back chamber windows as illustrated in **Figure 1B.4.6** and placed according to the survey positions given previously in **Table 1A.2.1.** The production run in the spring of 1982 produced 192 4-roll sets of film (each with about 3000 pictures per roll per camera) for a total of 582,439 bubble chamber exposures in 4 views, each exposure identified by a *frame number* in binary code displayed by a data box and appearing adjacent to the fiducial volume on film.

An analyzing magnet with a magnet current of 11.39772 kA (shunt voltage of 28.5 mV) produced a central field of 19.956 kG in the fiducial volume of the bubble chamber. The effective bend plane of the fringe field was 59.89 cm downstream from the bubble chamber center. The magnetic field was essentially the same as that reported in an early but reliable parameterization of both the fringe and central fields [Shephard 73]. At the bend plane the azimuthal angle effectively changed by $.32^{o}$/(track momentum in GeV/c). The curvature of outgoing tracks, seen directly in the bubble chamber or inferred from downstream detector information determined their momenta. One and a half rolls of film correspond to data taken with the magnet off. This zero field data makes it possible to determine beam momenta, to align the tagging and the DPI systems, and otherwise to facilitate reconstruction.

As a particle identifier, the bubble chamber served to distinguish particle

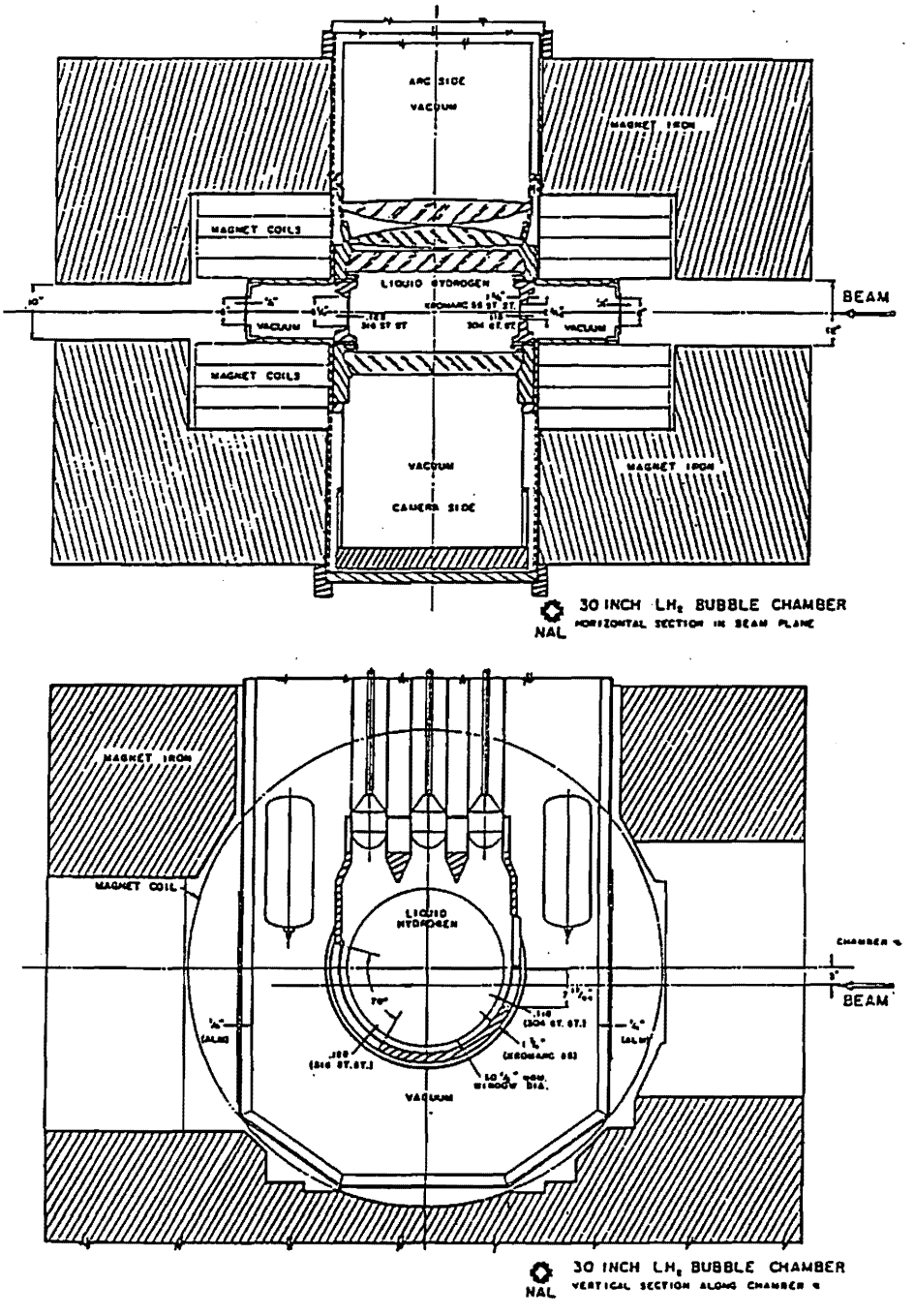

Figure 1B.4.4 Horizontal and vertical sections of the FNAL 30-inch bubble chamber.

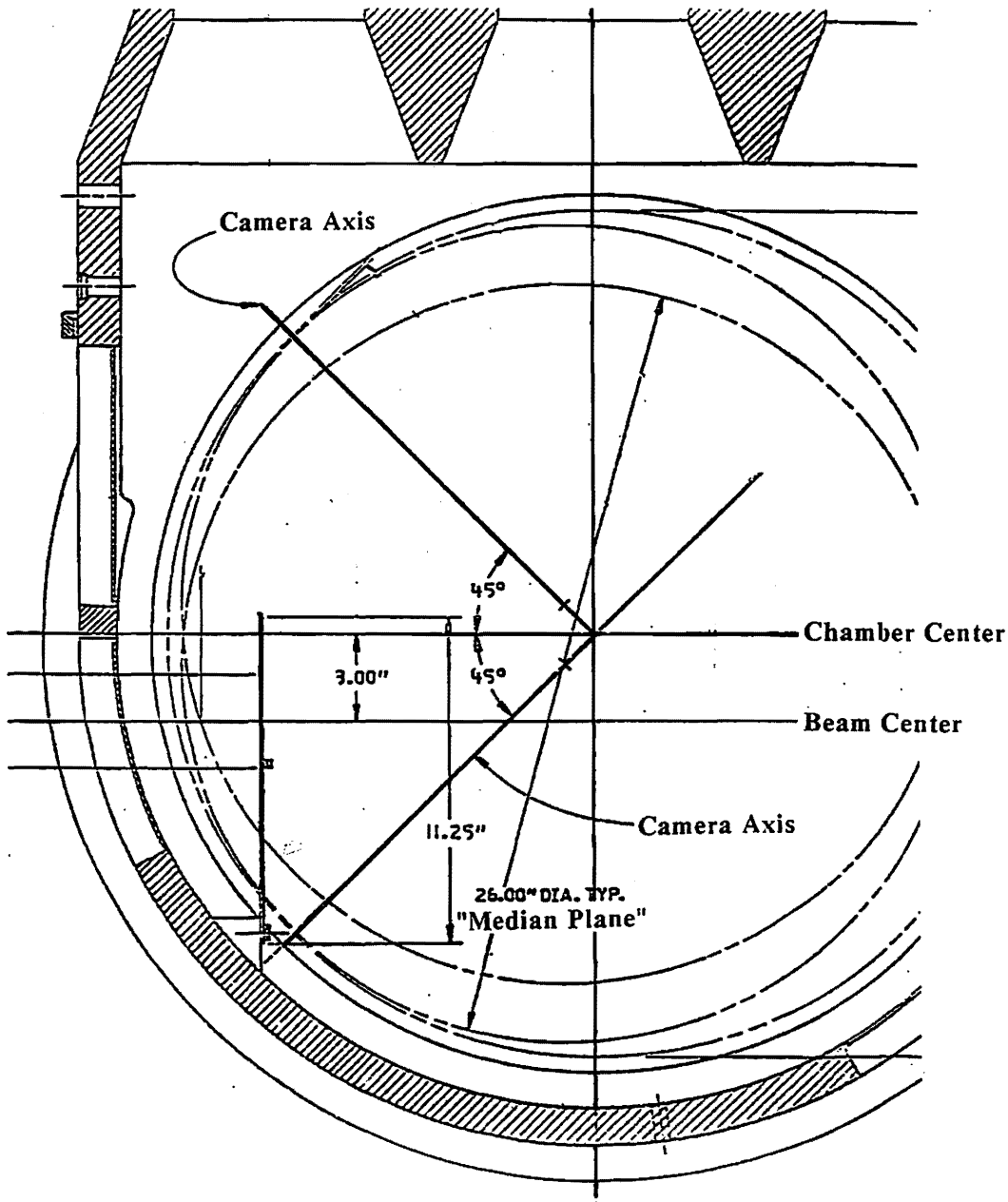

Figure 1B.4.5 Target bracket placement in the FNAL 30-inch bubble chamber.

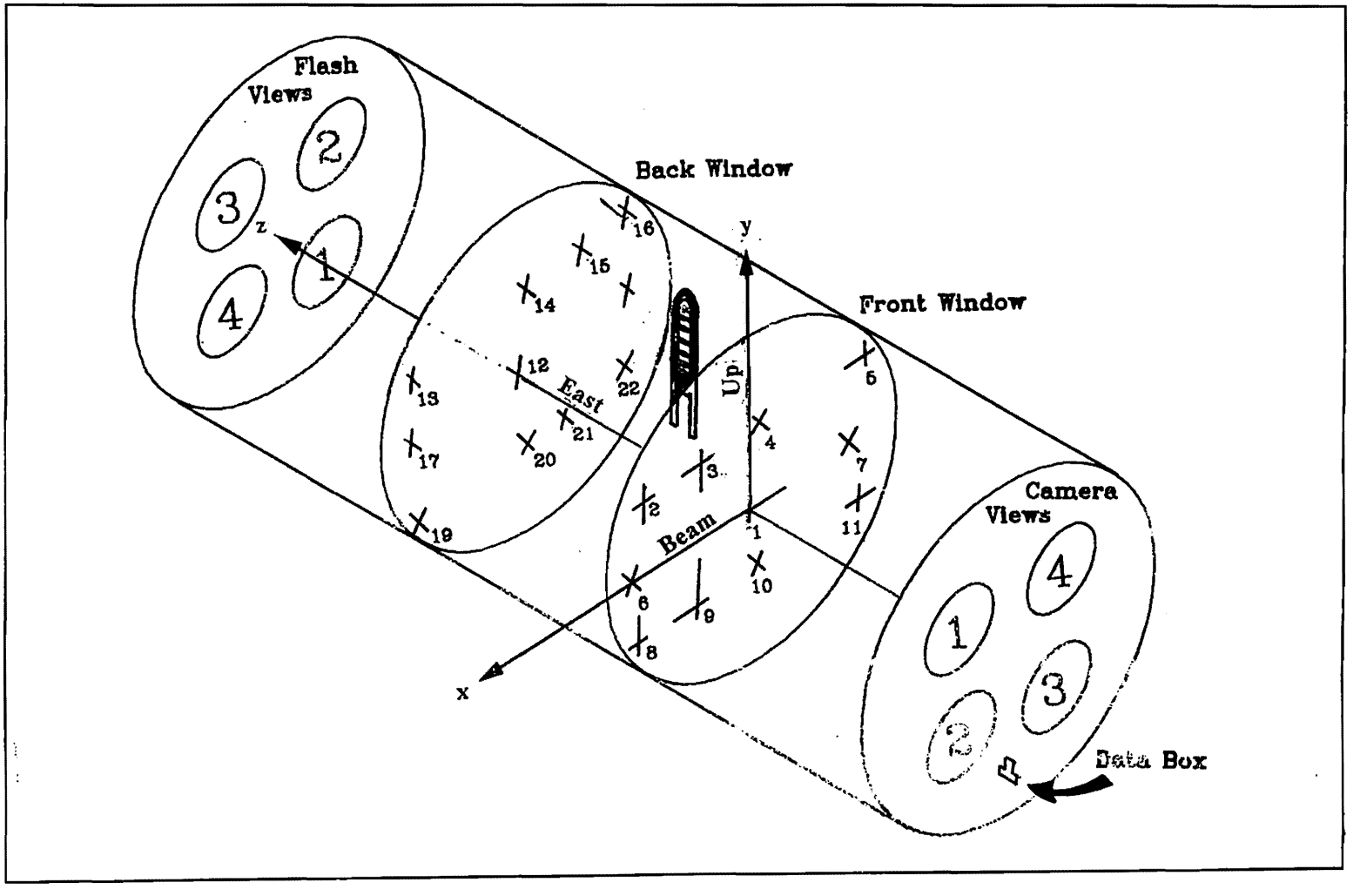

Figure 1B.4.6 FNAL 30-inch bubble chamber camera views, fiducial positions, and reference conventions.

masses, particularly π from p. For tracks of known momentum less than 1.3 GeV/c, their masses could be determined by visually inspecting bubble densities proportional to $1/\beta^2 cos\lambda$ as a particle traverses the liquid hydrogen. Particle identities are distinguished on the basis of how *dark* tracks appear compared to minimum ionizing tracks and the consistency of this comparison with expected relative bubble densities for various mass hypotheses at given momentum. Running conditions of the chamber and camera systems produced bubble densities between 10-15 bubbles/cm for minimum ionizing tracks, and bubble size to gap ratios between 60:40 and 75:25. Chamber conditions varied within the limits below:

pressure	P=67-70 psi
stroke	ΔP=41-44 psi
temperature	T=50-51 psi vapor pressure
flash delay	δt=2 ms

As a target device, the bubble chamber's liquid hydrogen (essentially protons) was complemented by thin metal foils configured as shown in **Figure 1B.4.7.** This combination of parallel target options uniquely suits the experimental data for direct comparative studies in A, unbiased by differing operating conditions and analysis streams. The atomic numbers were chosen to span a wide range in A and their thicknesses were chosen to produce for comparable numbers of events for the various A. The *thick* gold and silver targets have inelastic interaction lengths of the order 1% and radiation lengths of the order 20%. The *thin* targets have inelastic interaction lengths of the the order .5% and radiation lengths of the order 10%. The difference in thickness between foils of the same A was intended to make it possible to extrapolate to zero thickness. Specific values for interaction and radiation lengths as well and physical thickness are tabulated in **Table 1.4.1** for each nuclear target. Values for the nuclear radius from electron scattering data are also included for comparison with subsequent results in our analysis.

1B.4 DOWNSTREAM PARTICLE IDENTIFIER

Figure 1B.4.8 shows the plan view of the the data recording, target, and downstream

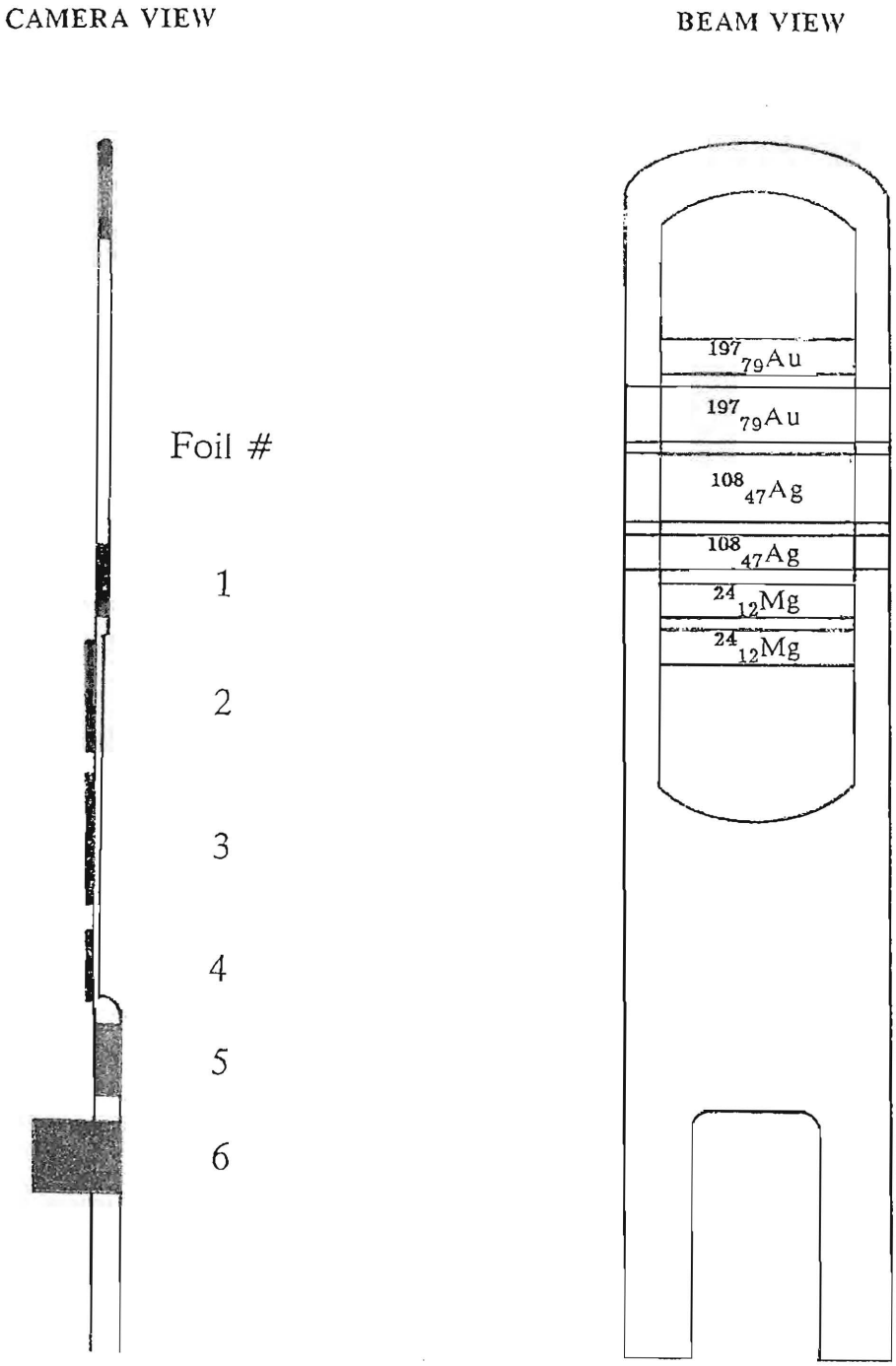

Figure 1B.4.7 Target schematic.

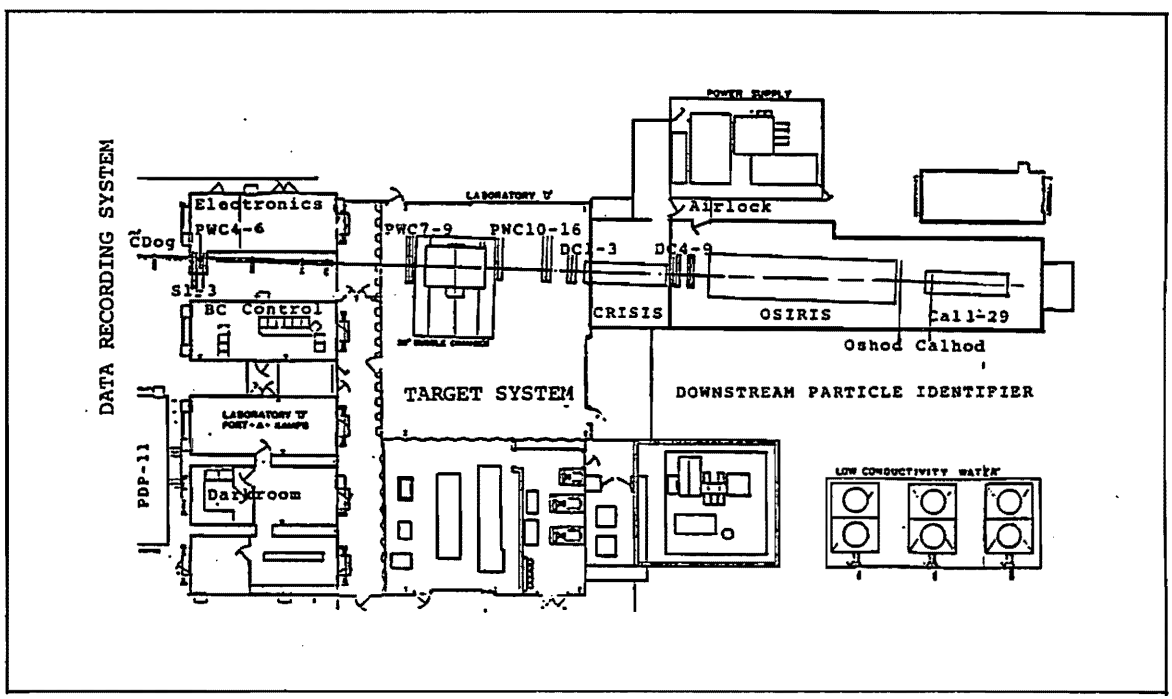

Figure 1B.4.8 Detailed plan view of the E597 data recording, target, and downsteam particle identifier (DPI) systems.

particle identifier (DPI) systems. Particles entered the downstream particle identifier system after passing through the target system proper and the analyzing magnet's fringe field. The clearance through the analyzing magnet itself is shown in **Figure 1B.4.9** with a 16^o horizonal span symmetric about the beam axis and a 37^o vertical span asymmetric to the beam axis.

1B.4.1 Proportional wire chambers

The downstream PWCs had 2 mm wire spacing (the same as the upstream PWCs), but each plane, with its 512 sense wires, subtended a larger solid angle than the upstream chambers. The gas mix with which they operated was the same as the upstream PWCs in content and proportion. The applied voltage was kept at approximately -3 kV. Device positions and orientations, verified in post-run analyses, are summarized in **Figure 1B.4.10.**

1B.4.2 Drift chambers

The downstream drift chambers had 5.08 cm (2 inch) spacing with a total of 24 sense wires each. With a time least count of 2 ns, accuracies of .1mm could be achieved. The gas mix in the DCs was argon/carbon dioxide/methane mixed in an 86.9%:12.0%:1.1% ratio. Anode voltages were kept at about -4 kV; cathode voltages, at about 1.6 kV. Device positions and orientations, verified in post-run analyses, are summarized in **Figure 1B.4.11.**

1B.4.3 CRISIS

The logarithmic rise in the ionization loss (dE/dx) as a function of momentum at relativistic momenta for given media may be used to determine particle mass. Once ionization loss and momentum are determined, the mass is determined for specific gas running conditions. **Figure 1B.4.12** shows the calculated rise in the momentum range .1 to 400 GeV/c superposed on ISIS data. Indeed the distributions of ionization charge data for particles at 200 GeV/c, clearly distinguish between p's and π's.

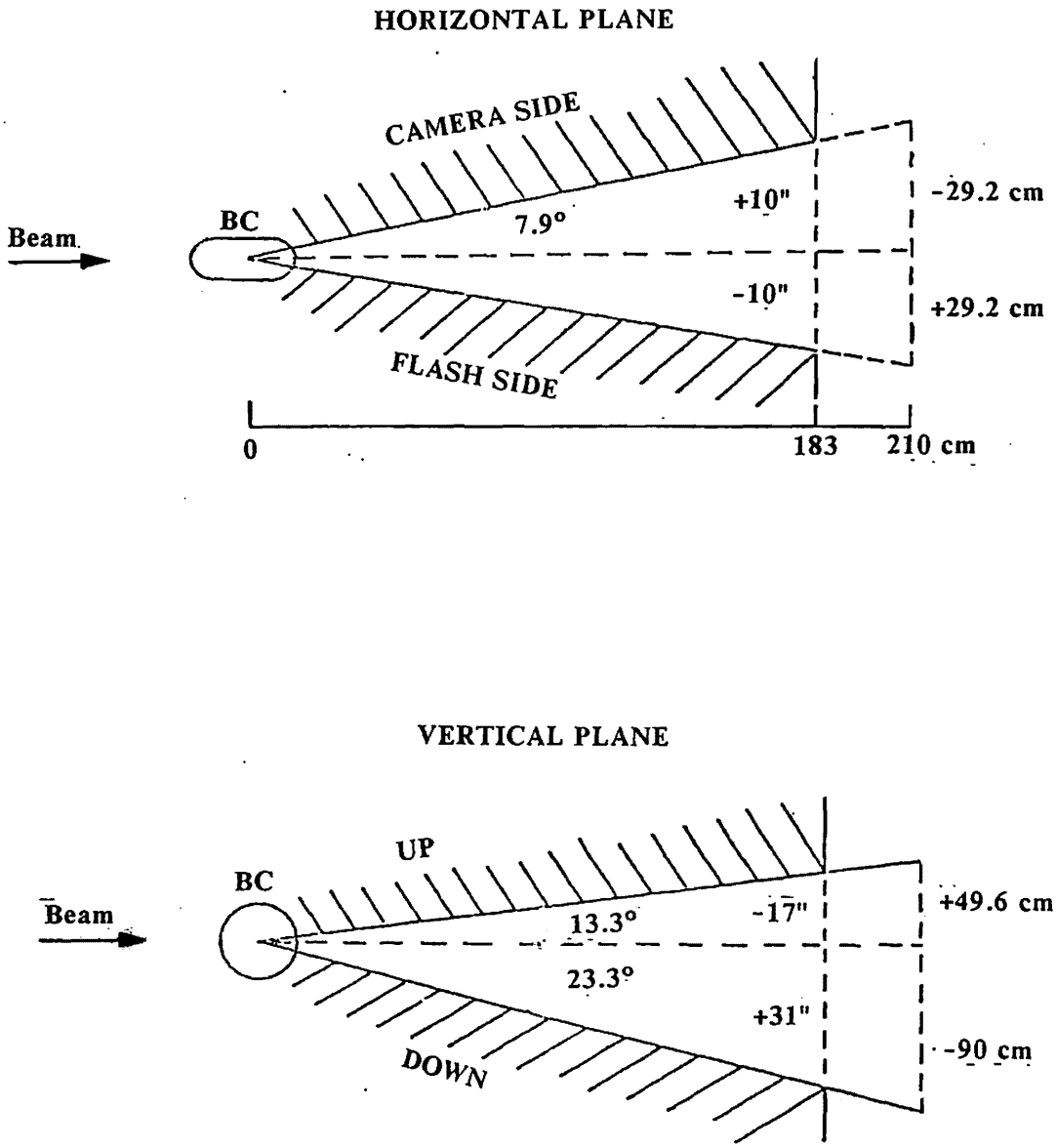

Figure 1B.4.9 Track clearance through the analyzing magnet into the downstream particle identifier (DPI).

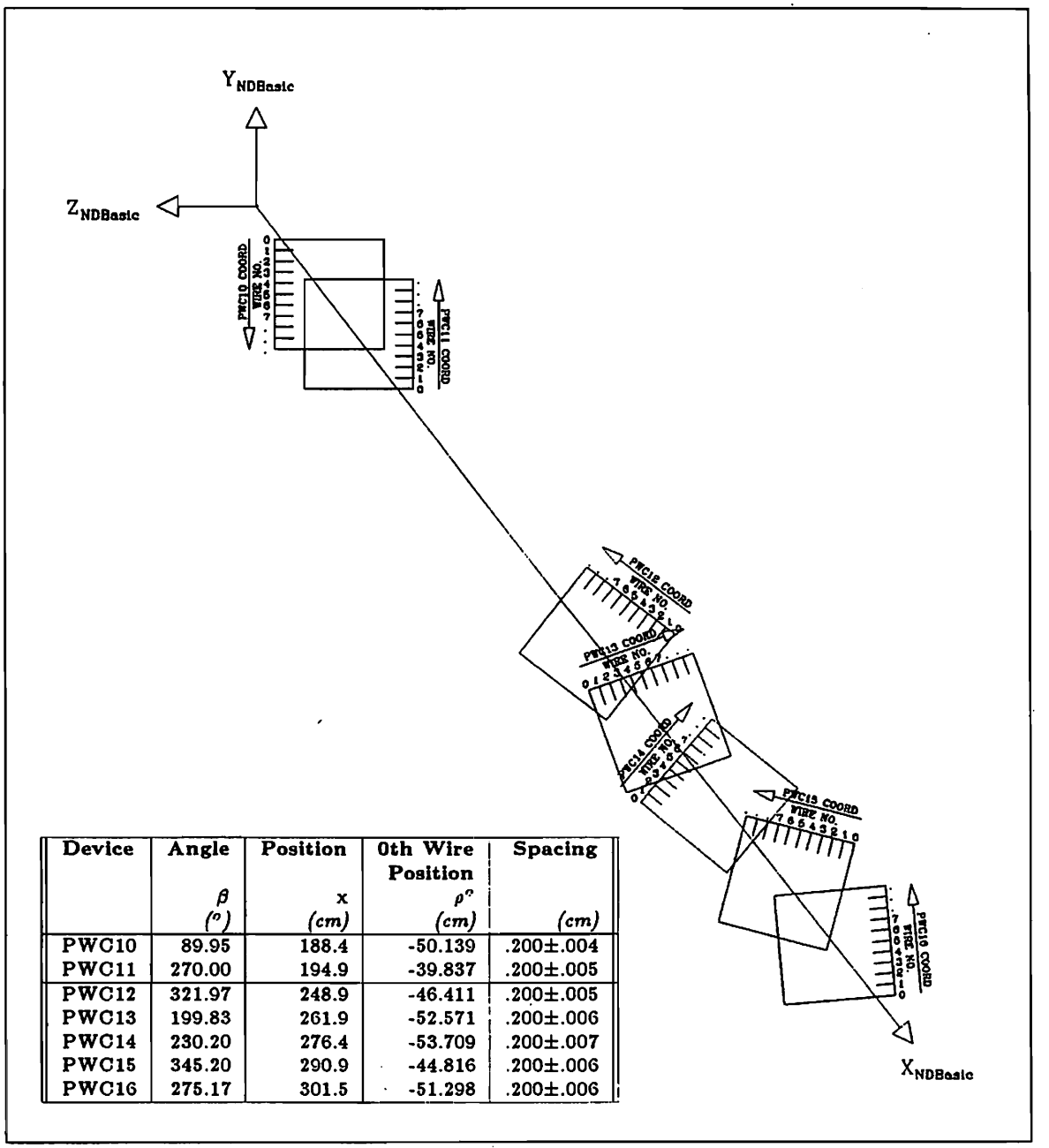

Device	Angle β (°)	Position x (cm)	0th Wire Position ρ^o (cm)	Spacing (cm)
PWC10	89.95	188.4	-50.139	.200±.004
PWC11	270.00	194.9	-39.837	.200±.005
PWC12	321.97	248.9	-46.411	.200±.005
PWC13	199.83	261.9	-52.571	.200±.006
PWC14	230.20	276.4	-53.709	.200±.007
PWC15	345.20	290.9	-44.816	.200±.006
PWC16	275.17	301.5	-51.298	.200±.006

Figure 1B.4.10 Placement and orientation of downstream proportional wire chambers (PWC's 10-16).

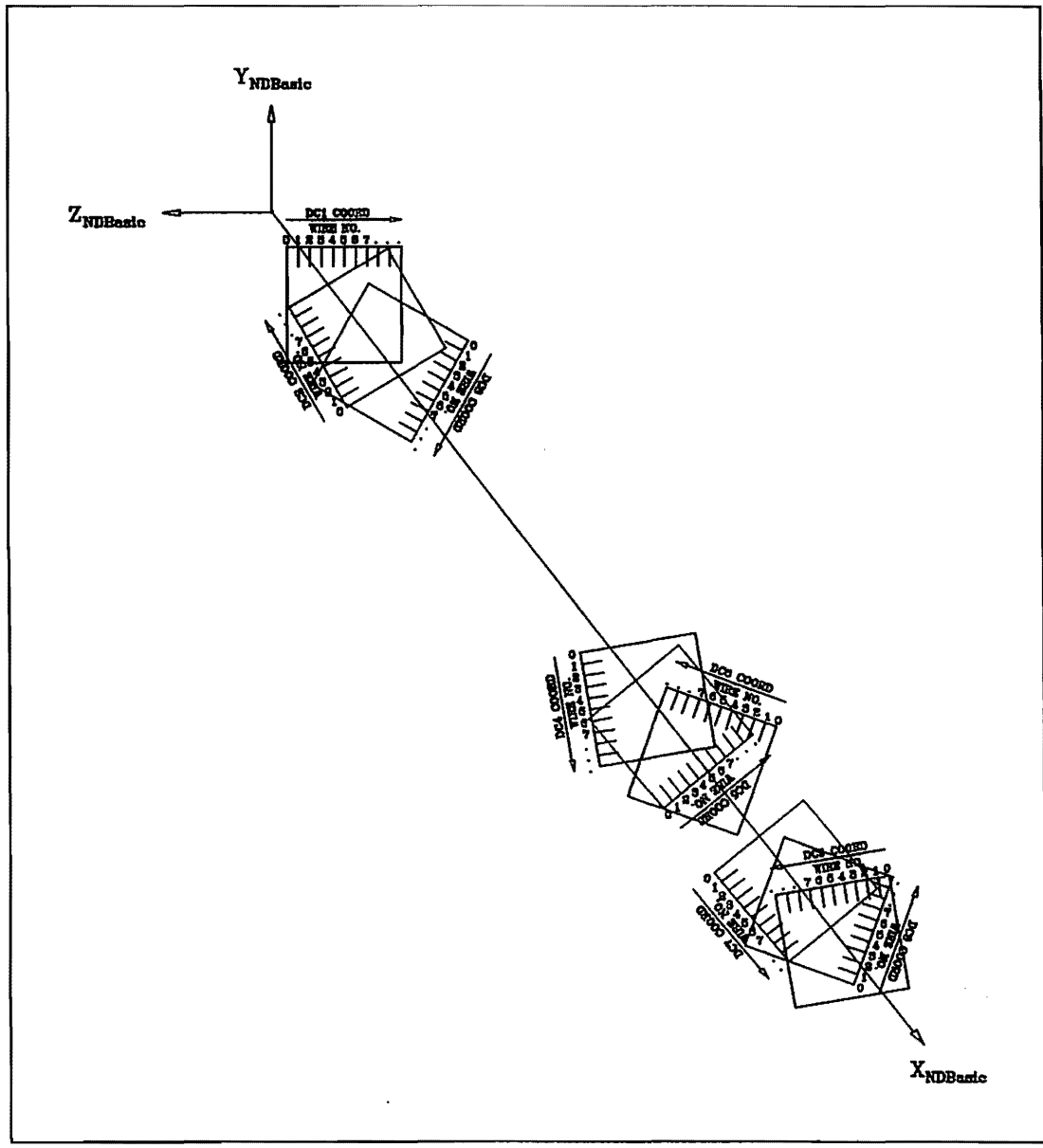

Figure 1B.4.11 Placement and orientation of downstream drift chambers (DC s 1-9).

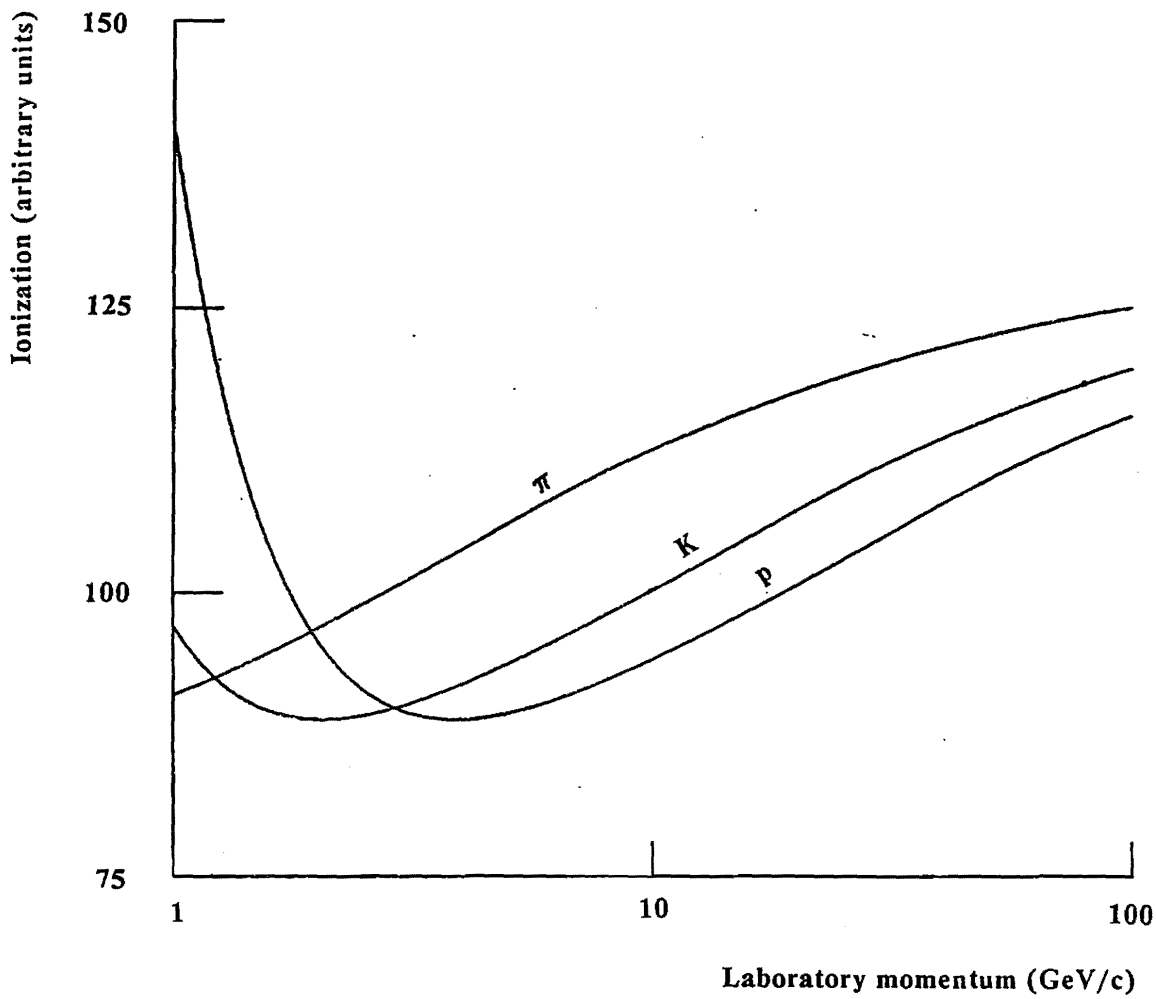

Figure 1B.4.12 Ionization loss as a function of momentum.

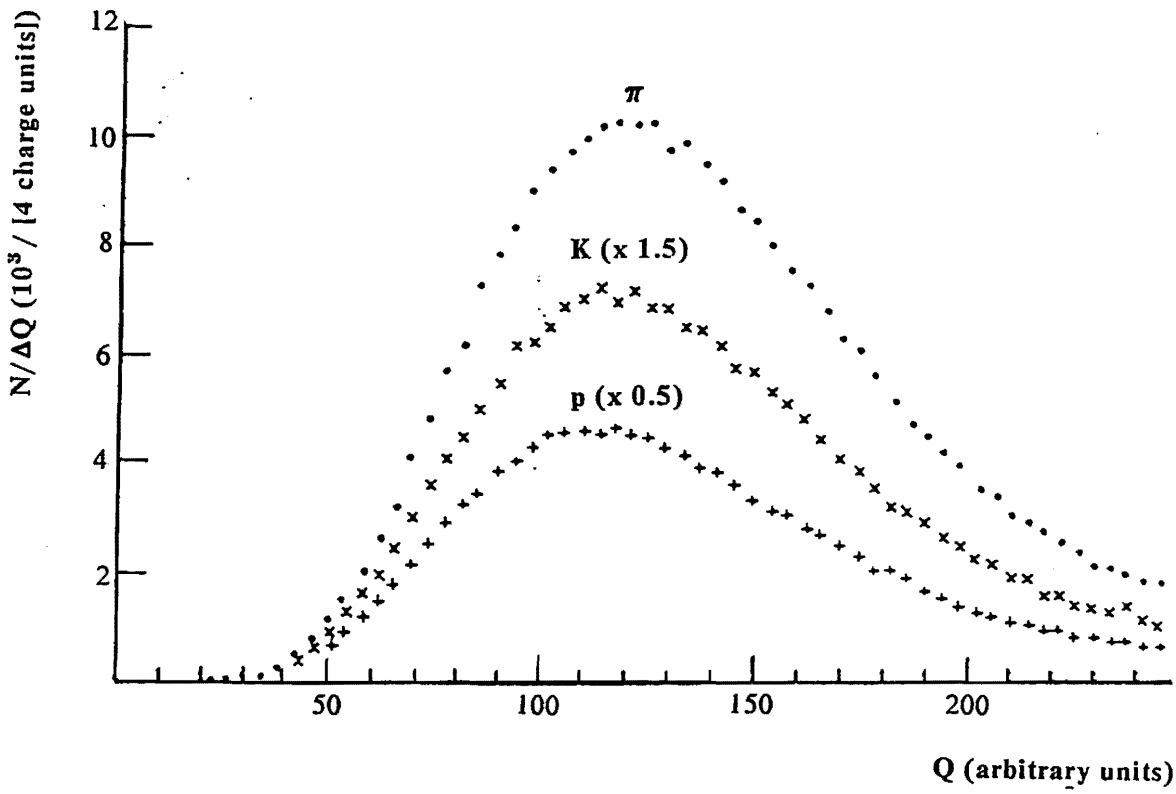

Figure 1B.4.13 Distribution of ionization charge produced by π's, K's, and p's at 200 GeV/c.

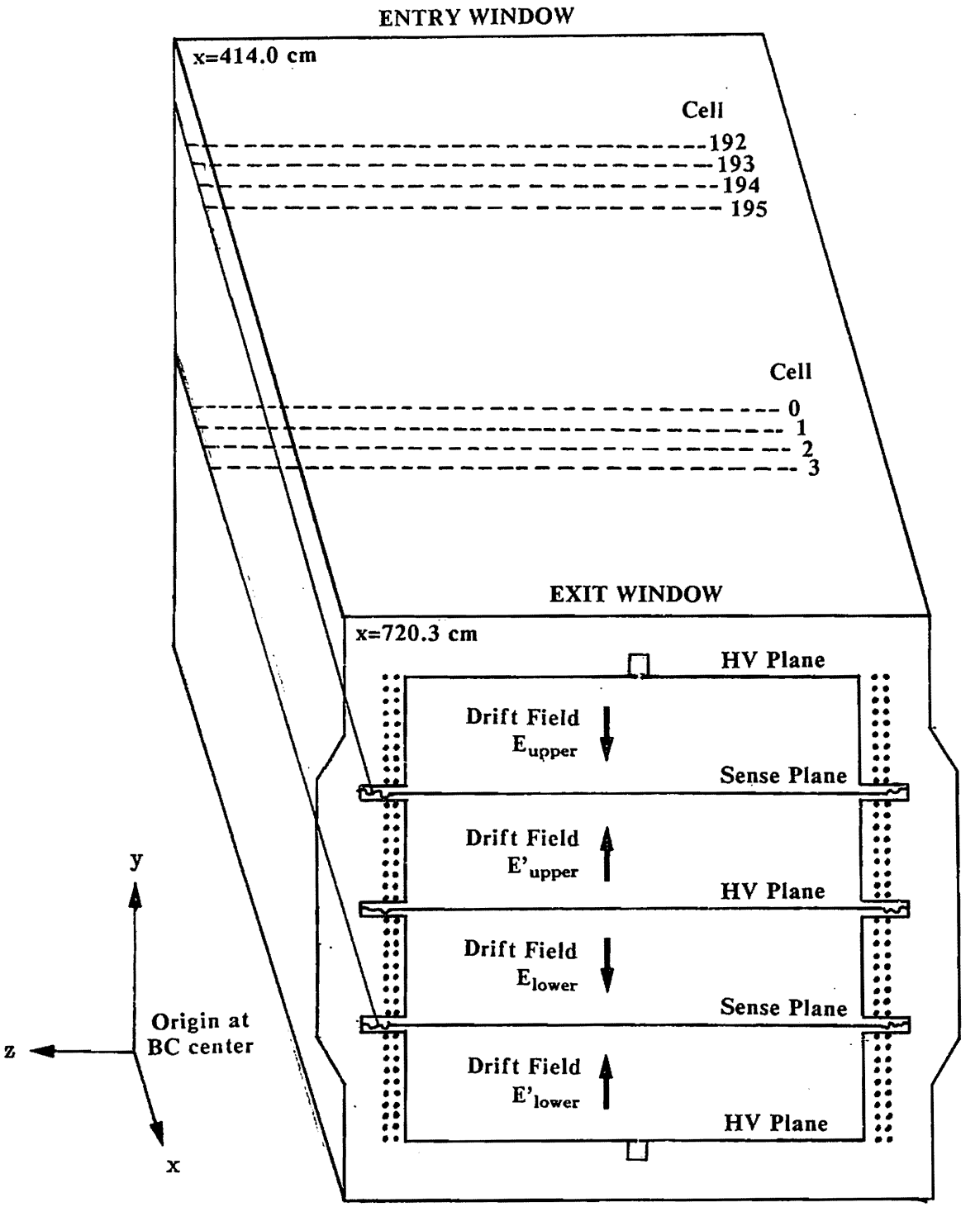

Figure 1B.4.14 Schematic representation of CRISIS.

However, with large fluctuations in ionization loss (see **Figure 1B.4.13**), a large number of ionization measurements are needed. So the Considerably Reduced Identification System by Ionization Sampling (CRISIS), patterned after the detector ISIS operating at CERN, was fitted with 384 cells of width 1.6 cm. These were divided between upper and lower sections with total dimensions of 1 m x 1 m x 3 m as shown in **Figure 1B.4.14**. In a nearly atmospheric pressure gas mix of argon/carbon dioxide in an 80%:20% ratio, CRISIS is capable of taking 192 samples of ionization loss for any given track traversing its volume.

The first of four(4) contiguous DPI components, CRISIS resided within the bubble chamber area separated from the rest of the DPI by a wall and accessed through an airlock. Placement of CRISIS and three(3) succeeding DPI components is tabulated in **Table 1B.4.2** in NDBasic coordinates.

In many respects, CRISIS is simply a compendium of drift chambers with drift velocity 4 cm/μs (or 80 microns per clock tick of 2 ns) and two sense planes for a maximum drift distance of 25.4 cm. Raw data included drift times as well as total deposited charge. The average charge was expected to be accurate to 8.13$\pm$.18% fwhm (7.8% for a full length traverse, 11.7% for a partial length traverse). Early estimates of the accuracy were 8.4% fwhm. With such accuracy, π's, K's, and p's could be separated in the range 5 to 40 GeV/c.

As a drift chamber device by default, CRISIS data supplemented track reconstruction data. Pseudo-visual tracking, with ambiguity with respect to top and bottom sections, could be directly produced for tracks traversing CRISIS's volume, as shown in **Figure 1B.4.15**.

1B.4.4 OSIRIS

Further particle identification can be achieved with data from OSIRIS, the second component of the contiguous DPI. A 2m x 2m x 5m helium-nitrogen atmospheric pressure Cerenkov counter with eight(8) cells, OSIRIS' function was to identify fast protons up to 100 GeV/c. Its eight(8) mirrors and associated photomultipliers are shown in **Figure 1B.4.16** and its threshhold momenta and response characteristics

Table 1B.4.2 CRISIS, OSIRIS, OSIRIS hodoscope, and neutral hadron calorimeter placement.

Device	Component	Position x *(cm)*
CRISIS	front	389.2
	1st wire	403.9
	last wire	716.9
	back	749.1
Wall		756.1
OSIRIS	front	885.8
	mirrors	1335.4
	back	1373.5
OSHOD		1392.5
Calorimeter	Cal 1	1446.5
	Cal 2	1451.5
	Pb 1	1462.0
	Pb 2	1465.4
	U Hod	1467.7
	Z Hod	1468.4
	Y Hod	1469.0

DPIPLACE.TAB UND/MCKM 10Apr87

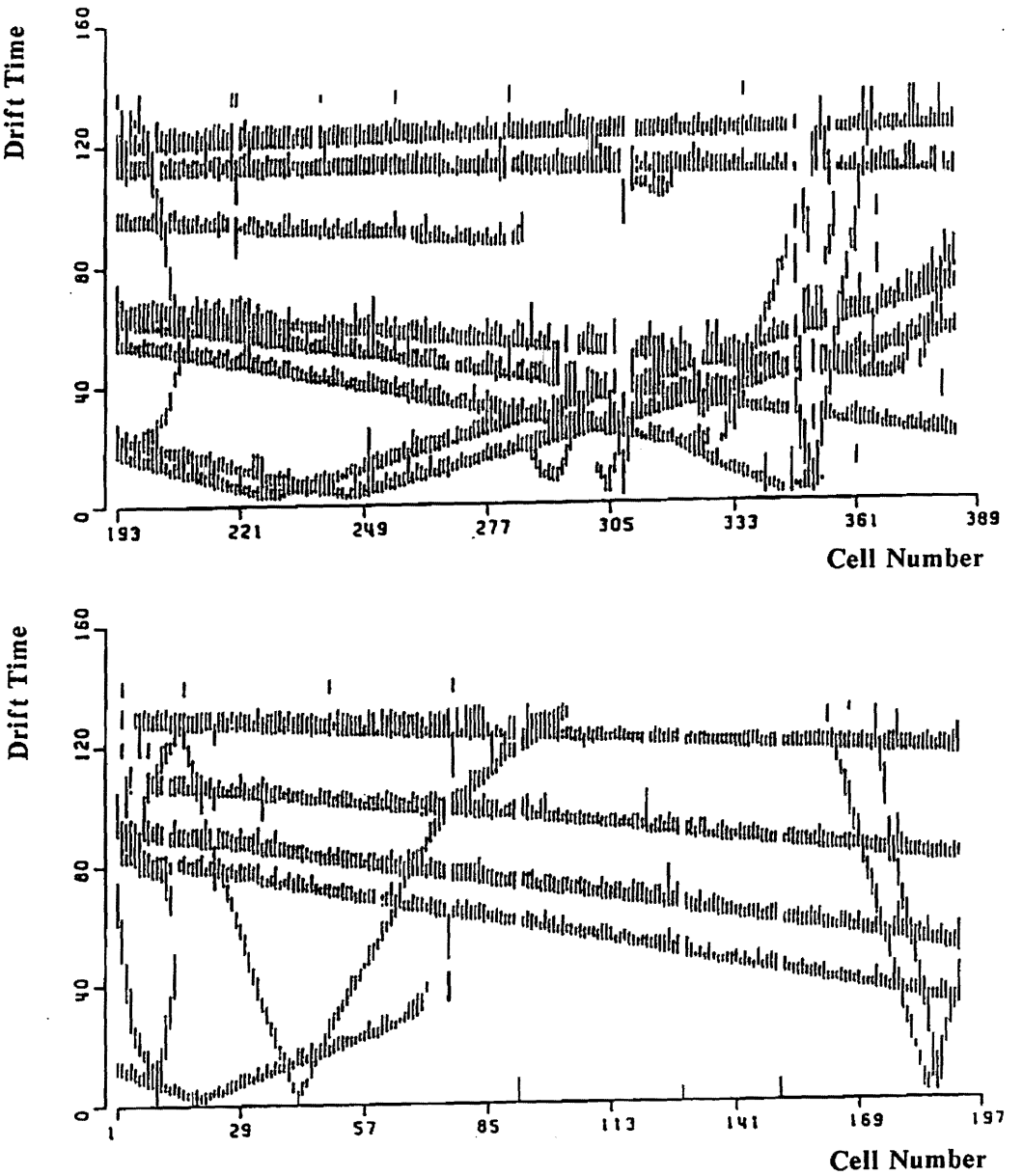

Figure 1B.4.15 Early example of CRISIS data showing pseudo-visual tracking.

HORIZONAL PLANE

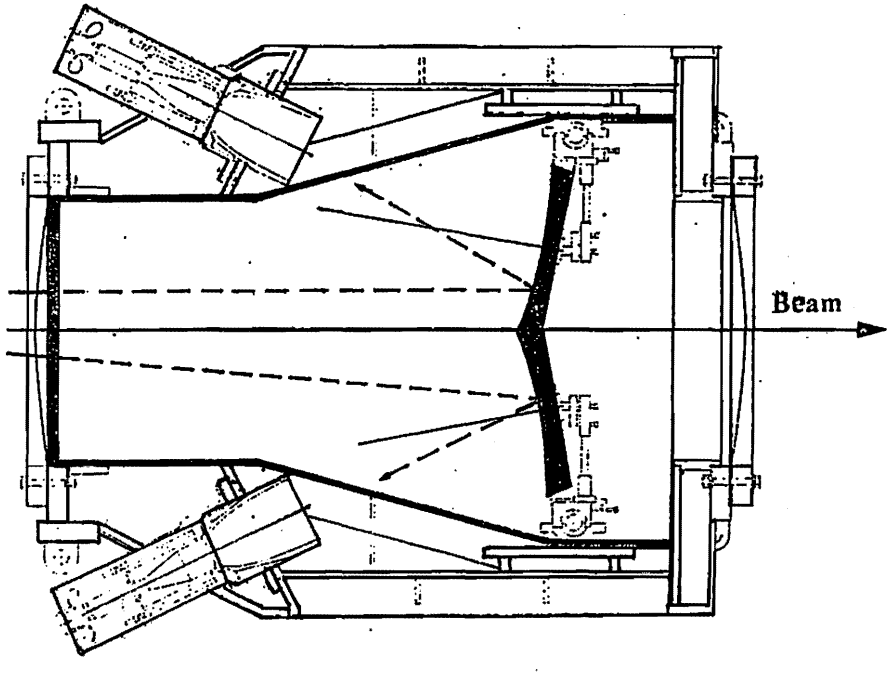

VERTICAL PLANE

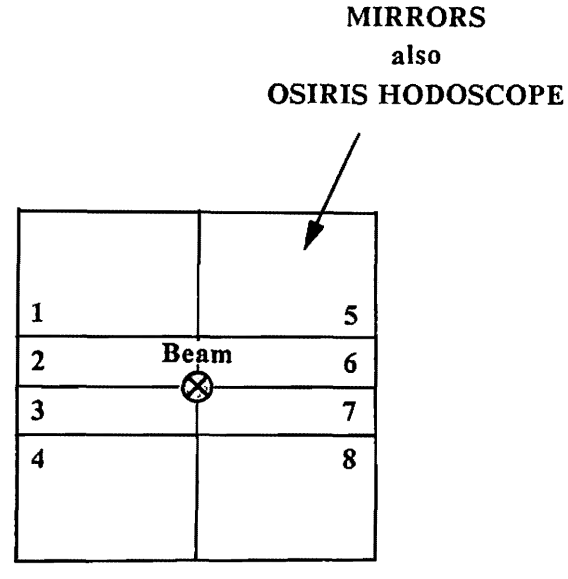

Figure 1B.4.16 Schematic representation of OSIRIS and its associated hodoscope OSHOD.

Table 1B.4.3 OSIRIS threshhold momenta and response characteristics.

R_{gas} Gas mix (% :%)	$(n-1)x10^6$ Index of refraction	r_{max} Max light cone radius (cm)	P Momentum (GeV/c)	P_{thresh} Threshold momentum (GeV/c)			$N(p)$ Number of photoelectrons $2.4(n-1)[1-(P_{thresh}/P)^2]L$		
				π	K	p	π	K	p
100.0: 0.0	32.70	4.0	100	17.3	61.0	116.0	3.2	2.1	0.0
			50				2.9		
			20				.8		
95.5: 4.5	44.02	4.7	100	14.9	52.6	100.0	4.4	3.2	0.0
			50				4.0		
			25				2.8		
			20				2.0		
77.5: 22.5	89.83	6.7	100	10.4	36.8	70.0	8.9	7.8	4.6
			50				8.6	4.1	
			25				7.4		
			15				4.7		
55.3: 44.7	145.5	8.5	100	8.3	29.0	55.0	14.5	13.4	10.2
			50				14.2	9.7	
			35				13.8	4.6	
			20				12.1		
			10				4.5		
0.0:100.0	285.00	11.9	100	5.9	20.7	39.3	26.4	27.3	24.1
			50				26.1	23.6	10.9
			25				27.0	9.0	
			15				24.2		
			10				18.8		
			7				8.6		

OSIRISRESP.TAB UND/MCKM 12Mar89

are tabulated in **Table 1B.4.3.** Protons can be identified in the 39-116 GeV/c range; kaons in the 21-61 GeV/c range, and pions in the 6-17 GeV range. Thus, OSIRIS complements CRISIS, extending proton identification to 100 GeV/c.

1B.4.5 Neutral particle calorimeter

The neutral particle calorimeter, furnished data with which to identify neutrons, anti-neutrons, and gammas from π^o decay. The basic configuration of this 31 inch x 31 inch x 88 inch device, **Figure 1B.4.17**, contains 4 radiation lengths of Pb;, a 3-plane hodoscope, **Figure 1B.4.18**; 26 sections of steel-scintillator sandwich; and a 3-paddle muon counter. The first 11 sections (Cal1-Cal11) contained 1 inch steel plate and .5 inch scintillator plastic slabs; the last 15 sections (Cal15-Cal29) contained 1.375 inch steel plate and .5 inch scintillator plastic slabs. With S114 upstream, two(2) additional scintillation paddles (Muon1 and Muon2) functioned as muon counters behind the calorimeter. The hodoscope carried 21 diagonal channels, 15 horizontal and 15 vertical channels. Light produced in the sandwiched paddles and the hodoscope elements and converted into analog signals by their attendant phototubes was subsequently converted into digital signals and recorded for each master gate.

Particles of given energy travel characteristic distances in the sandwich assembly before they interact and produce a shower of charged particles. Those distances are marked by the dramatic increase of scintillation light in the paddle ensemble. Photons and electrons deposit the majority of their energy in the first five(5) or six(6) plates while hadrons generally produce showers further downstream in the ensemble. Photons, electrons, and hadrons can be distinguished with a 90% efficiency. Studies on test calibration data verified clean separations between hadrons, muons, and electrons, on the basis of ratios of energy deposition in the front and back portions of the calorimeter. A comparison of the forward-backward distribution of summed pulse heights (Cal1-Cal9 vs. Cal10-Cal28) for 25 GeV/c electrons and pions in **Figure 1B.4.19** illustrates how clearly one may distinguish between electromagnetically and hadronically induced showers in the calorimeter.

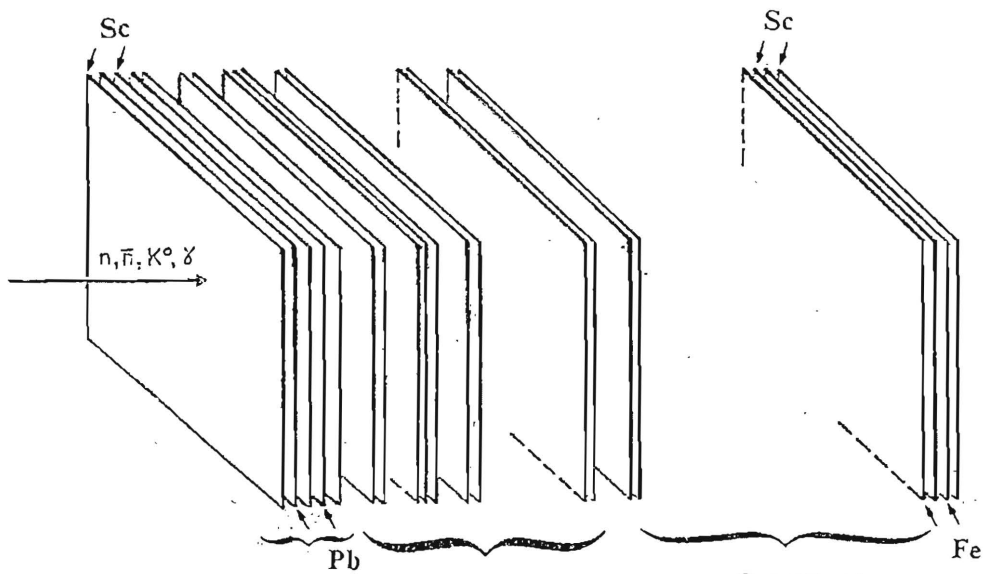

Figure 1B.4.17 Schematic view of the neutral hadron calorimeter.

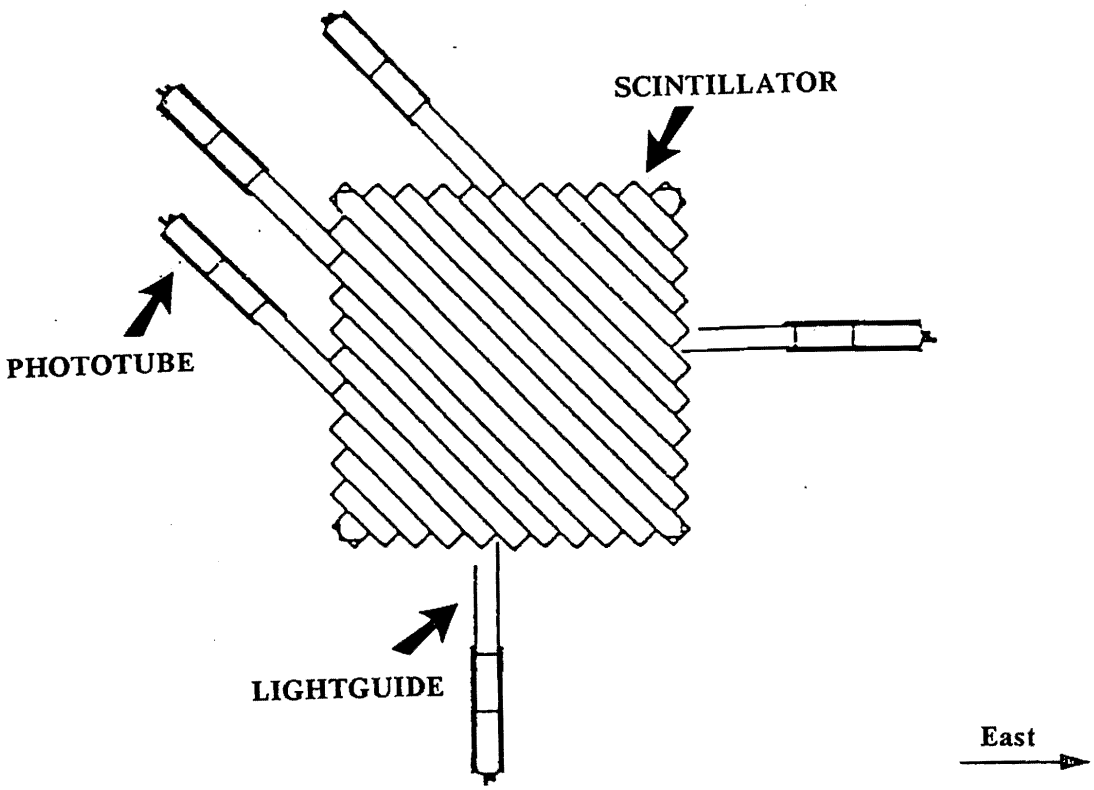

Figure 1B.4.18 Schematic representation of the neutral hadron calorimeter hodoscopes Y, Z, and U.

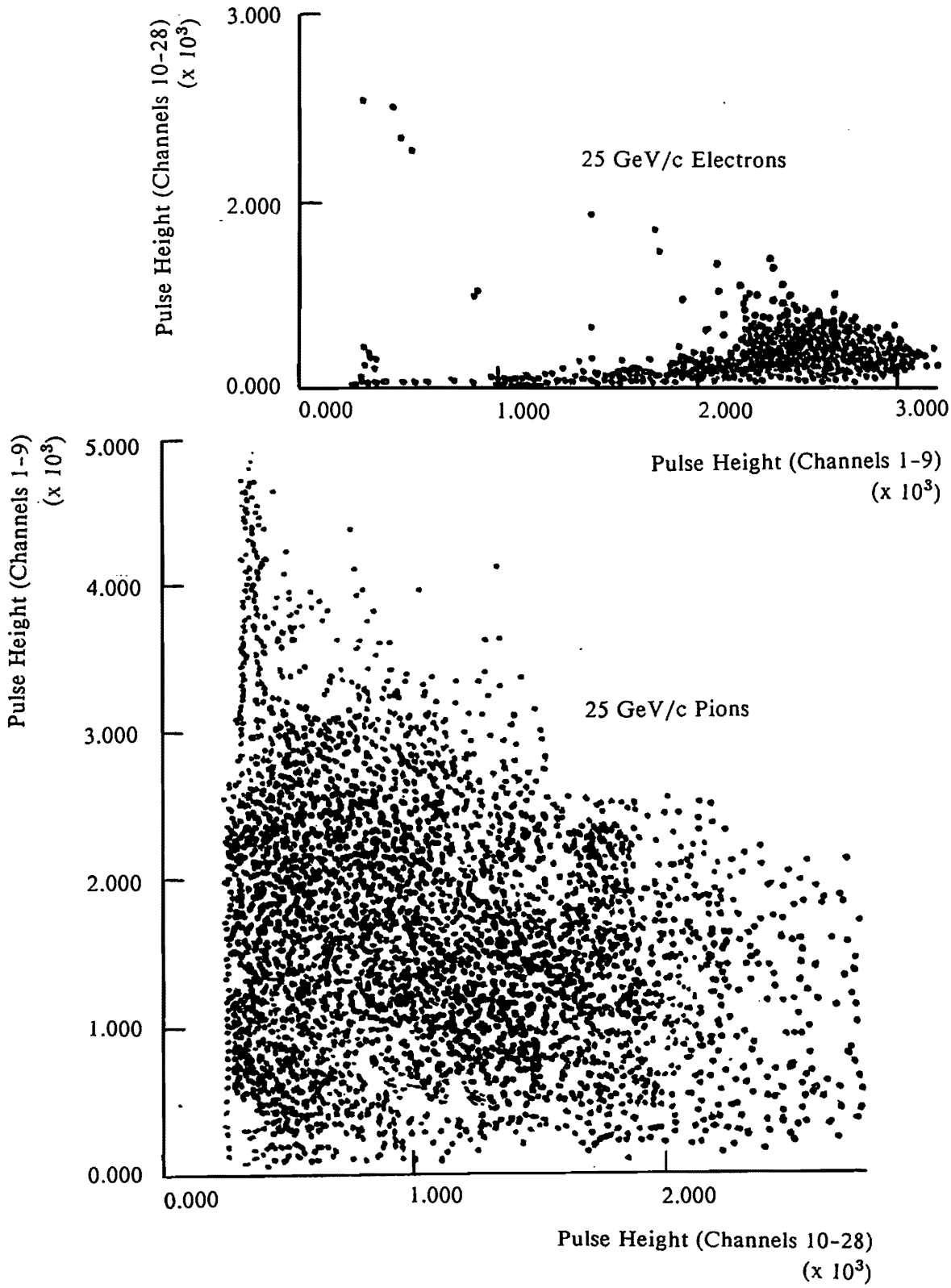

Figure 1B.4.19 Distinguishing between electromagnetic and hadronic showers by comparing energy deposition in the forward and backward portions of the neutral hadron calorimeter.

APPENDIX 2A

MULTIPLICITY CORRECTIONS

A number of inherent experimental limitations distort proton and produced particle multiplicities in E597 data. These limitations can be categorized in terms of 1) tracks which are unobservable, 2) tracks which are unmeasureable, 3) tracks whose identity cannot be determined by ionization techniques, and 4) tracks produced in secondary interactions. Estimates have been made of corrections for the attendent distortions incurred to average multiplicities. Corrected multiplicities have been compared with FRITIOF simulated results.

2A.1 UNOBSERVABLE TRACKS

All secondaries lose momentum as they traverse a portion of the foil target after they are produced in a single beam-nucleus interaction. **Figure 2A.1.1** shows the momentum loss expected as a function of momentum for pions and protons traversing thicknesses of the six E597 foil targets. At some point low-momentum tracks stop within the foil thickness and are unobservable. For the tracks that survive their traverse through the foil, the measured momentum is not the true momentum at which the track is produced in the primary interaction, but rather a 'leftover' momentum. The thickness of the foil introduces a significant momentum uncertainty dependent on track momenta. Faster particles will sustain smaller degradations than slower ones.

2A.1.1 Stopped tracks

To estimate the average stopping momentum for secondaries, interaction points were

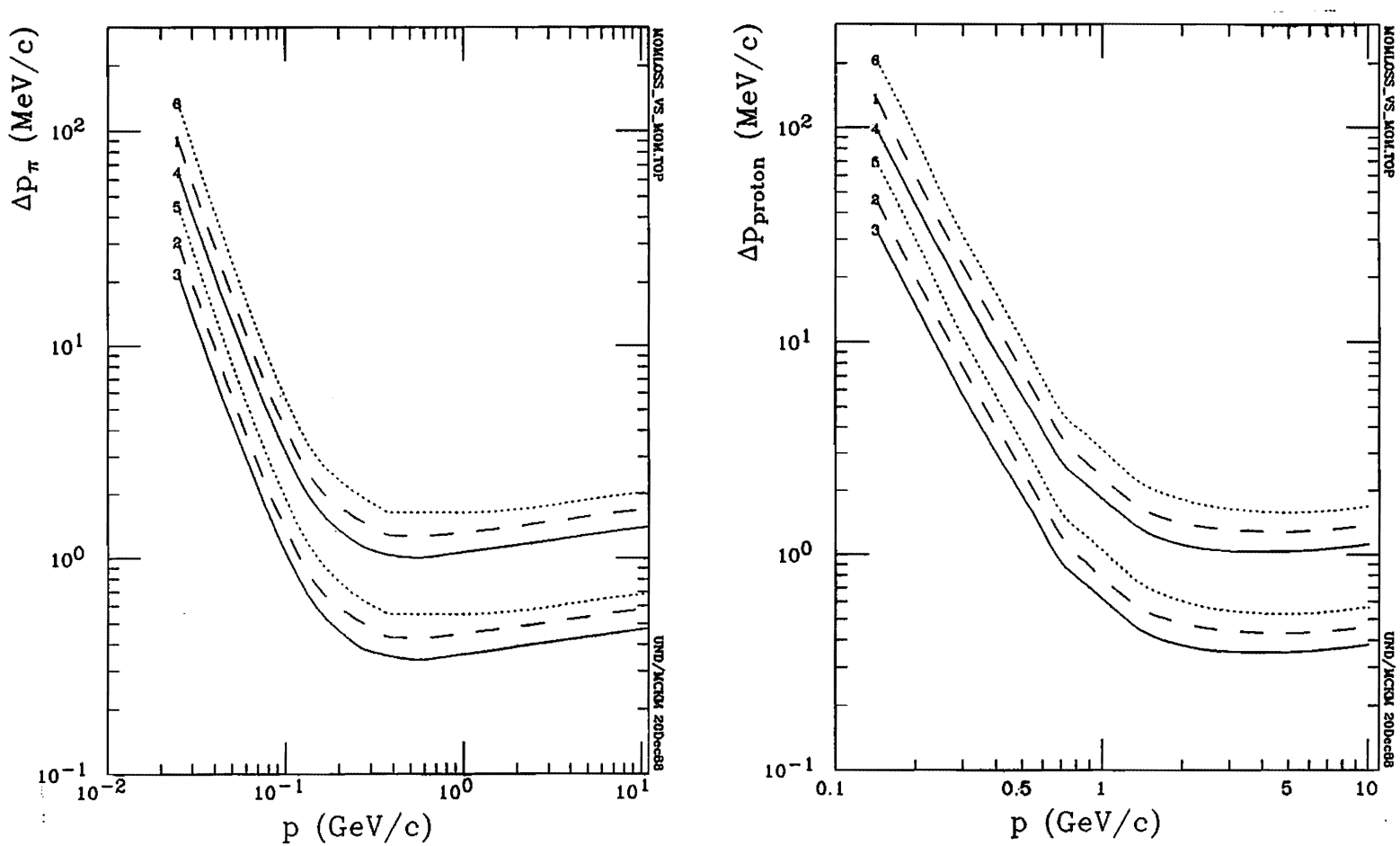

Figure 2A.1.1 Approximate momentum loss in E597 targets as a function of particle momenta for a) protons and b) pions. Adapted from [Trower 66]. Each curve corresponds to one of the six(6) targets designated by the foil number on the left edge.

assumed to occur halfway through the foil target thicknesses since the foils were too thin to make experimental determinations feasible. It was also assumed that secondaries traversed the foil at an exit polar angle θ with respect to the beam direction equal to $cos^{-1}(\frac{1}{\langle 1/cos\theta \rangle})$ where $\langle 1/cos\theta \rangle$ is experimentally determined. The average intrafoil pathlength $(.5t)/cos\theta$ and associated angle are tabulated in **Table 2A.1.1** Then, though momentum is not linear with pathlength, an average stopping momentum is estimated for secondaries using momentum-range plots [Trower 66] and assuming the average intrafoil pathlength to be the average stopping range. The average stopping momenta are tabulated in **Table 2A.1.2** as well as the momentum losses for 2 GeV/c p and π secondaries traversing a half thickness of each target. Particles with momentum less than the average stopping momenta (.1-.2 GeV/c for protons and .04-.06 GeV/c for pions) could be expected on the average to stop within the foil and thus escape detection in this experiment. However, event-by-event, momentum corrections cannot be made without knowing the exact pathlength through the foil from the interaction point. Low momentum particles will suffer the highest losses, but the scale by which most observed momenta are smeared is estimated by the momentum loss of 2 GeV/c pions through half target thicknesses.

2A.1.2 Angular depletion of protons

Since each secondary's pathlength L is equal to the distance along the beam direction from the interaction point to the surface of the foil times $1/cos\theta$, L explodes as $\theta \rightarrow 90^o$. Thus depletions at angles nearly parallel to the foil surface are expected beyond those stemming from reconstruction difficulties when $\lambda \rightarrow 90^o$. The depletion as $\theta \rightarrow 90^o$ is particularly noticeable when production is isotropic. Production angles for secondaries other than protons are very forward peaked and thus little affected by the 90^o depletion. But proton production angles significantly span the 90^o region with obvious particle density depletions near $cos\theta = p_x/p = 0$ in **Figure 2A.1.2**. This dip in the distribution is almost entirely attributable to *black* protons. The 90^o region for *black* protons is noticeably vacant in **Figure 2A.1.3** but less significantly so for the *grey* and *shower* protons of **Figures 2A.1.4** and **2A.1.5**, respectively.

Table 2A.1.1 Average pathlengths in target foils assuming secondaries are produced at one-half the target thickness with momenta directed along the exit angle.

THICK FOILS

Projectile	320GeV/c		100GeV/c									
	π^-	π^-	π^+	π^+	p	p	π^-	π^-	π^-	$\bar{p}$	$\bar{p}$	$\bar{p}$
$^{A}_{Z}Target$	$^{108}_{47}Ag$	$^{197}_{79}Au$	$^{108}_{47}Ag$	$^{197}_{79}Au$	$^{108}_{47}Ag$	$^{197}_{79}Au$	$^{24}_{12}Mg$	$^{108}_{47}Ag$	$^{197}_{79}Au$	$^{24}_{12}Mg$	$^{108}_{47}Ag$	$^{197}_{79}Au$
BTC	61	64	131	134	141	144	176	171	174	186	181	184
N_{events}	184	127	178	128	308	110	120	604	457	75	439	277
$t\ (g/cm^2)$	1.894	1.716	1.894	1.716	1.894	1.716	1.931	1.894	1.716	1.931	1.894	1.716
$(\frac{1}{cos\theta})p$	2.55	2.28	3.03	2.28	2.40	2.28	3.76	2.63	2.47	2.29	2.49	2.45
Δ	.21	.14	.30	.14	.11	.12	.87	.11	.09	.23	.11	.12
$(\frac{1}{cos\theta})prod$	1.41	1.38	1.44	1.38	1.51	1.43	1.22	1.43	1.34	1.34	1.53	1.35
Δ	.06	.06	.06	.04	.05	.06	.05	.03	.03	.10	.05	.02
$cos^{-1}(\frac{1}{\langle cos\theta \rangle})p$	67^o	64^o	71^o	64^o	63^o	64^o	75^o	68^o	66^o	64^o	66^o	66^o
$cos^{-1}(\frac{1}{\langle cos\theta \rangle})prod$	48^o	41^o	46^o	44^o	49^o	46^o	35^o	46^o	42^o	42^o	49^o	42^o
$.5t(\frac{1}{cos\theta})p$	2.42	1.96	2.87	1.96	2.27	1.96	3.63	2.49	2.12	2.21	2.36	2.10
Δ												
$.5t(\frac{1}{cos\theta})prod$	1.34	1.14	1.36	1.18	1.43	1.23	1.18	1.35	1.15	1.29	1.45	1.16
Δ												

THIN FOILS

Projectile	320GeV/c		100GeV/c									
	π^-	π^-	π^+	π^+	p	p	π^-	π^-	π^-	$\bar{p}$	$\bar{p}$	$\bar{p}$
$^{A}_{Z}Target$	$^{108}_{47}Ag$	$^{197}_{79}Au$	$^{108}_{47}Ag$	$^{197}_{79}Au$	$^{108}_{47}Ag$	$^{197}_{79}Au$	$^{24}_{12}Mg$	$^{108}_{47}Ag$	$^{197}_{79}Au$	$^{24}_{12}Mg$	$^{108}_{47}Ag$	$^{197}_{79}Au$
BTC	62	65	132	133	142	143	175	172	173	185	182	183
N_{events}	137	135	124	112	169	129	224	406	403	181	276	280
$t\ (g/cm^2)$	.6401	.5784	.6401	.5784	.6401	.5784	.6453	.6401	.5784	.6453	.6401	.5784
$(\frac{1}{cos\theta})p$	2.59	2.48	2.34	2.92	2.69	2.28	2.58	2.36	2.44	2.42	2.38	2.29
Δ	.19	.13	.15	.29	.19	.13	.37	.08	.10	.21	.11	.09
$(\frac{1}{cos\theta})prod$	1.26	1.36	1.43	1.52	1.42	1.32	1.25	1.46	1.42	1.37	1.49	1.45
Δ	.04	.06	.06	.10	.05	.03	.03	.05	.03	.07	.05	.04
$cos^{-1}(\frac{1}{\langle cos\theta \rangle})p$	67^o	66^o	65^o	70^o	68^o	64^o	67^o	65^o	66^o	66^o	65^o	64^o
$cos^{-1}(\frac{1}{\langle cos\theta \rangle})prod$	37^o	43^o	46^o	49^o	45^o	41^o	37^o	47^o	46^o	43^o	48^o	46^o
$.5t(\frac{1}{cos\theta})p$	.83	.72	.75	.84	.86	.66	.83	.76	.71	.78	.76	.66
Δ												
$.5t(\frac{1}{cos\theta})prod$	.40	.39	.46	.44	.45	.38	.40	.47	.41	.44	.48	.42
Δ												

FOILPATH.TEX UND/MCKM 5Sep88

Table 2A.1.2 Approximate minimum momenta (stopping momenta) at production assuming tracks emerging from target foils originate at one-half the target thickness. Also the momentum loss for 2 GeV/c secondaries traversing one-half the target thickness.

Target		Mg		Ag		Au	
X_o	(g/cm^2)	25.473		8.720		5.945	
Target #		6	5	1	2	4	3
t	(g/cm^2)	1.931	.645	1.894	.640	1.716	.578
.5t	(g/cm^2)	.966	.323	.947	.320	.858	.289
$p_p$min	(MeV/c)	225	165	205	145	180	130
$p_K$min	(MeV/c)	142	108	130	92	115	79
$p_\pi$min	(MeV/c)	59	42	53	38	48	34
$p_e$min	(MeV/c)	.600	.400	.530	.360	.480	.330
$\Delta p_{p(2GeV/c)}$	(MeV/c)	1.80	.55	1.40	.45	1.00	.35
$\Delta p_{\pi(2GeV/c)}$	(MeV/c)	2.00	.70	1.70	.50	1.40	.40

RANGETRAP.TEX UND/MCKM 30Aug88

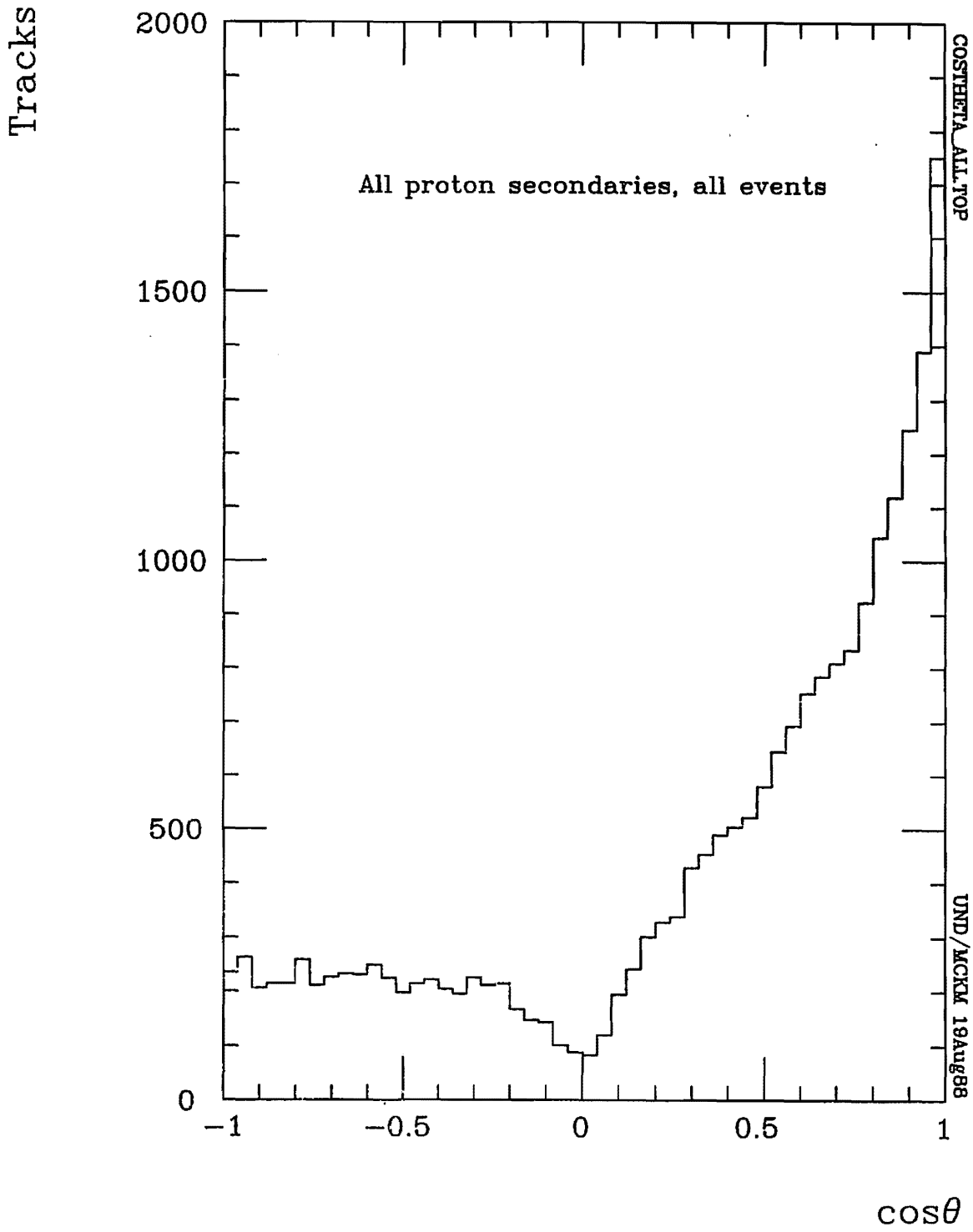

Figure 2A.1.2 Distribution of $\cos\theta$ for all proton secondaries emanating from any interaction. θ is the track angle with respect to the beam.

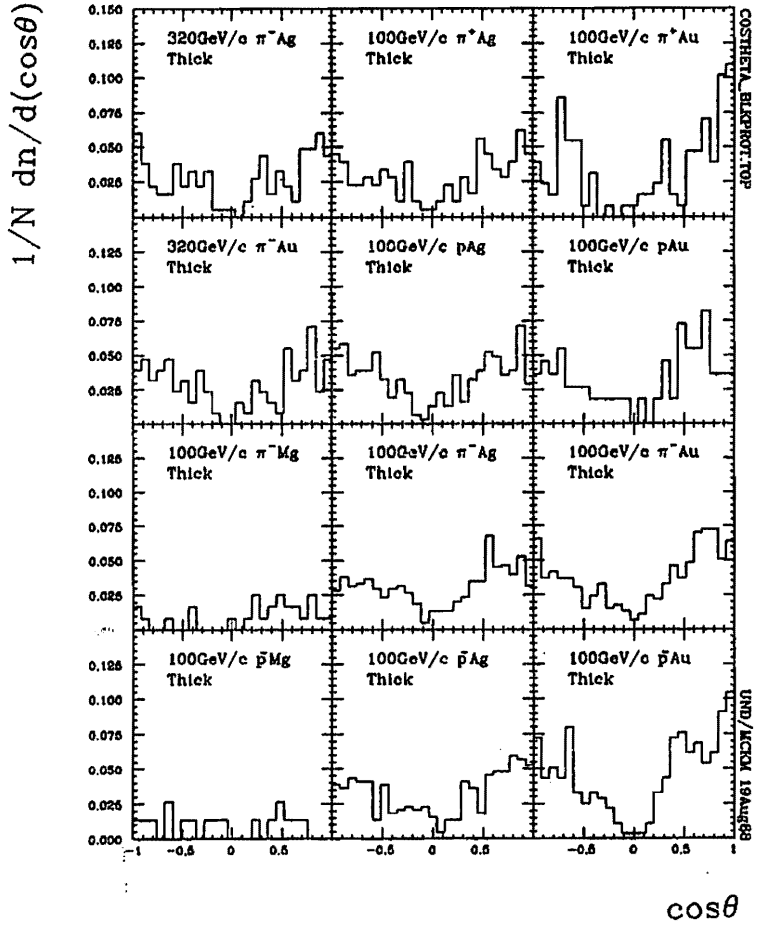

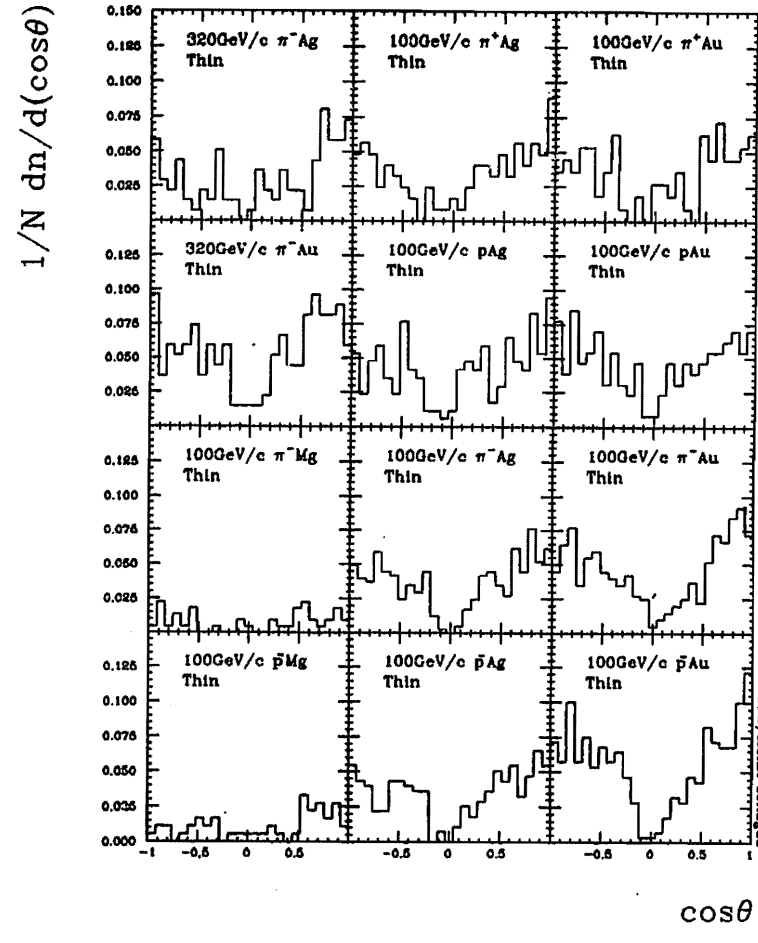

Figure 2A.1.3 Distributions of *cosθ* for *black* proton secondaries. θ is the track angle with respect to the beam.

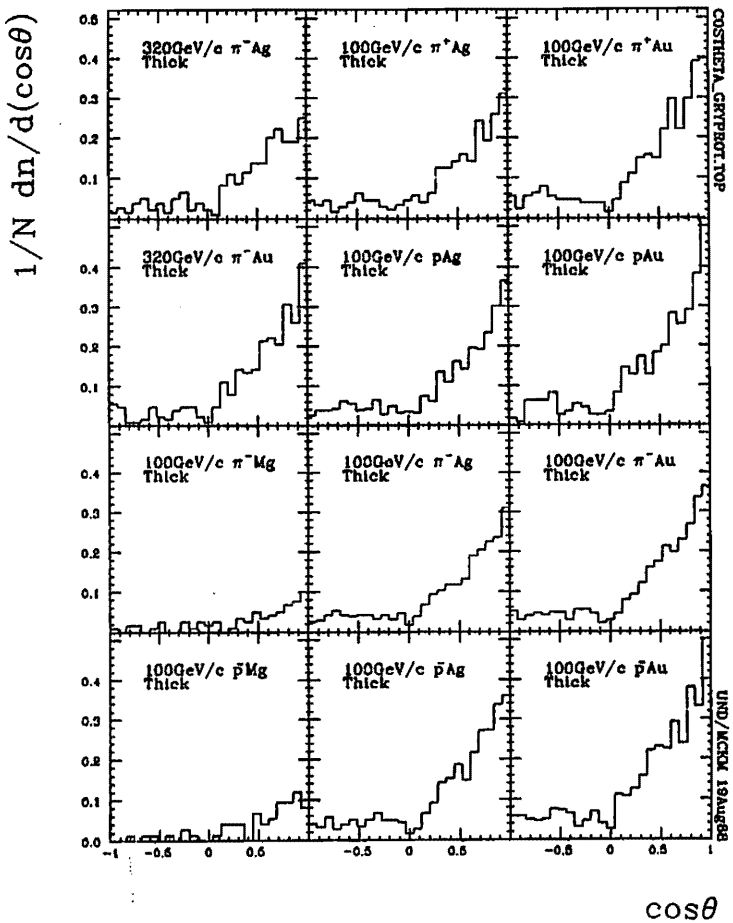

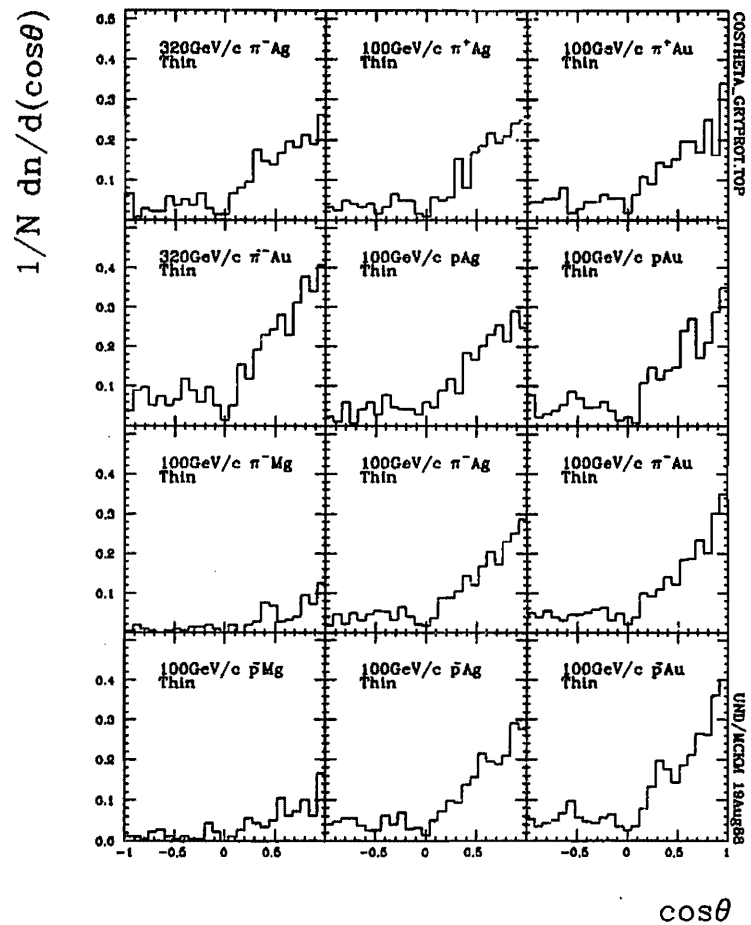

Figure 2A.1.4 Distributions of $cos\theta$ for *grey* proton secondaries. θ is the track angle with respect to the beam.

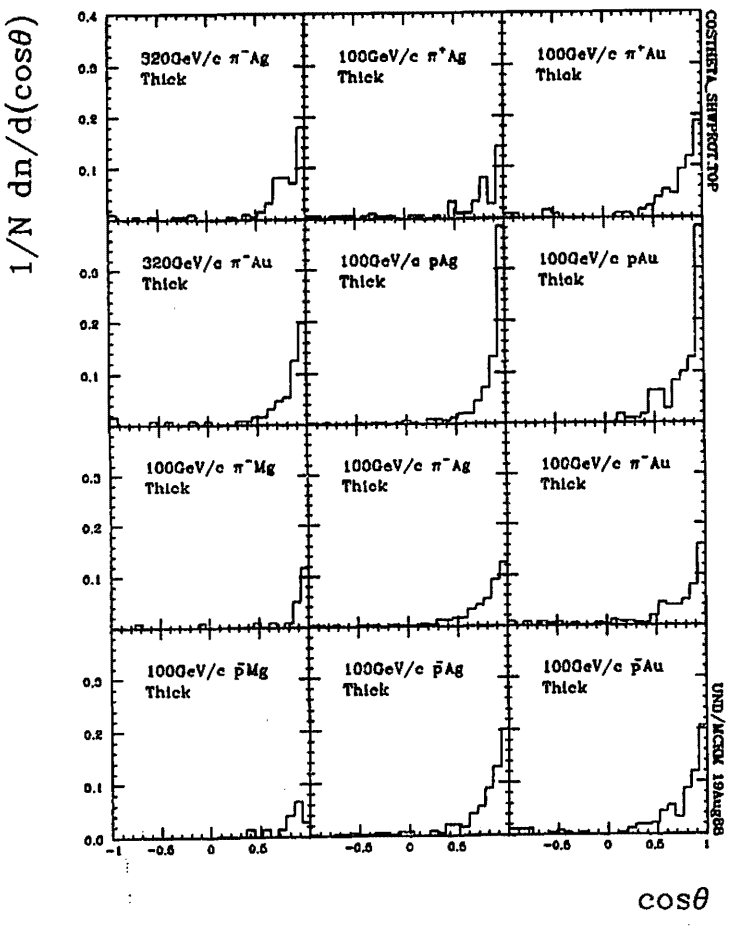

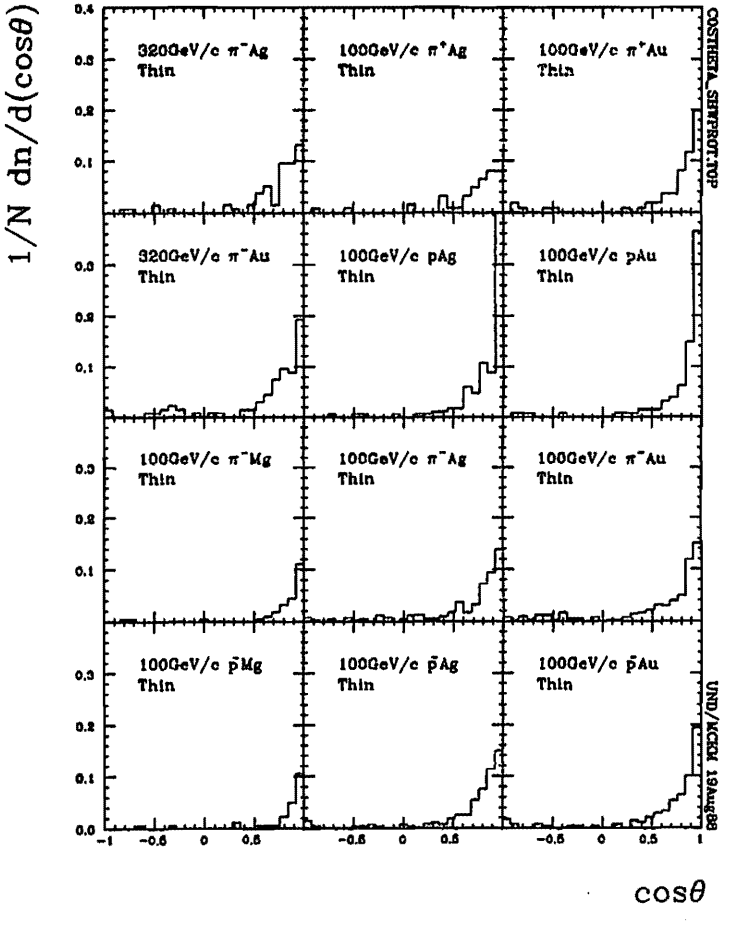

Figure 2A.1.5 Distributions of *cosθ* for *shower* proton secondaries. θ is the track angle with respect to the beam.

Since nuclear breakup or *evaporation* is modeled to be a truly isotropic process with low momentum products, and *black* protons show the angular depletion characteristic of isotropically produced particles as well as an only slightly anisotropic distribution, *black* protons are most likely produced in a predominantly evaporative process.

Based on the isotropy of such a process, *evaporation* protons observed in the backward hemisphere should have a corresponding distribution in the forward hemisphere (*forward* and *backward* refer to the lab reference frame). Thus the number of observed *evaporation* protons is estimated to be twice the number of *backward* protons. Similarly, the number of observed *recoil* protons (those produced in non-evaporative processes) is estimated by the difference between the total number of protons and the number of evaporation protons. While many grey protons appear in the backward hemisphere, only a few shower protons do. Although this study does not investigate these shower protons, they could be of considerable interest.

To begin calculating corrections for angular depletion in proton multiplicities, average proton densities in the range $-1. < cos\theta < -.3$ (backward protons per unit $cos\theta$) were calculated, shown by the dashed horizontal lines in **Figure 2A.1.6**). Each average density was then assigned to the rest of the backward range $-.3 < cos\theta < 0$ in order to estimate the total number of backward protons. (This amounts to filling in the 'dips' due to angular depletion near 90°.) The difference between this estimate of total number of backward protons and the experimentally measured number of backward protons produces an estimate of the angular depletion in the backward lab hemisphere. Because most of the depletion is assumed to occur among the isotropically produced *black* protons, the angular depletion in the forward lab hemisphere is expected to be comparable. $N_{cos\theta}$, the total number of unobserved protons emerging at nearly 90° to the beam direction, is estimated to be twice the number of protons depleted from the backward lab hemisphere. Values of this estimate, $N_{cos\theta}$, appear in **Table 2A.1.3**.

Of course, some of these missing protons could very well have been included in the number of *unmeasured* protons, discussed in a later subsection. This number

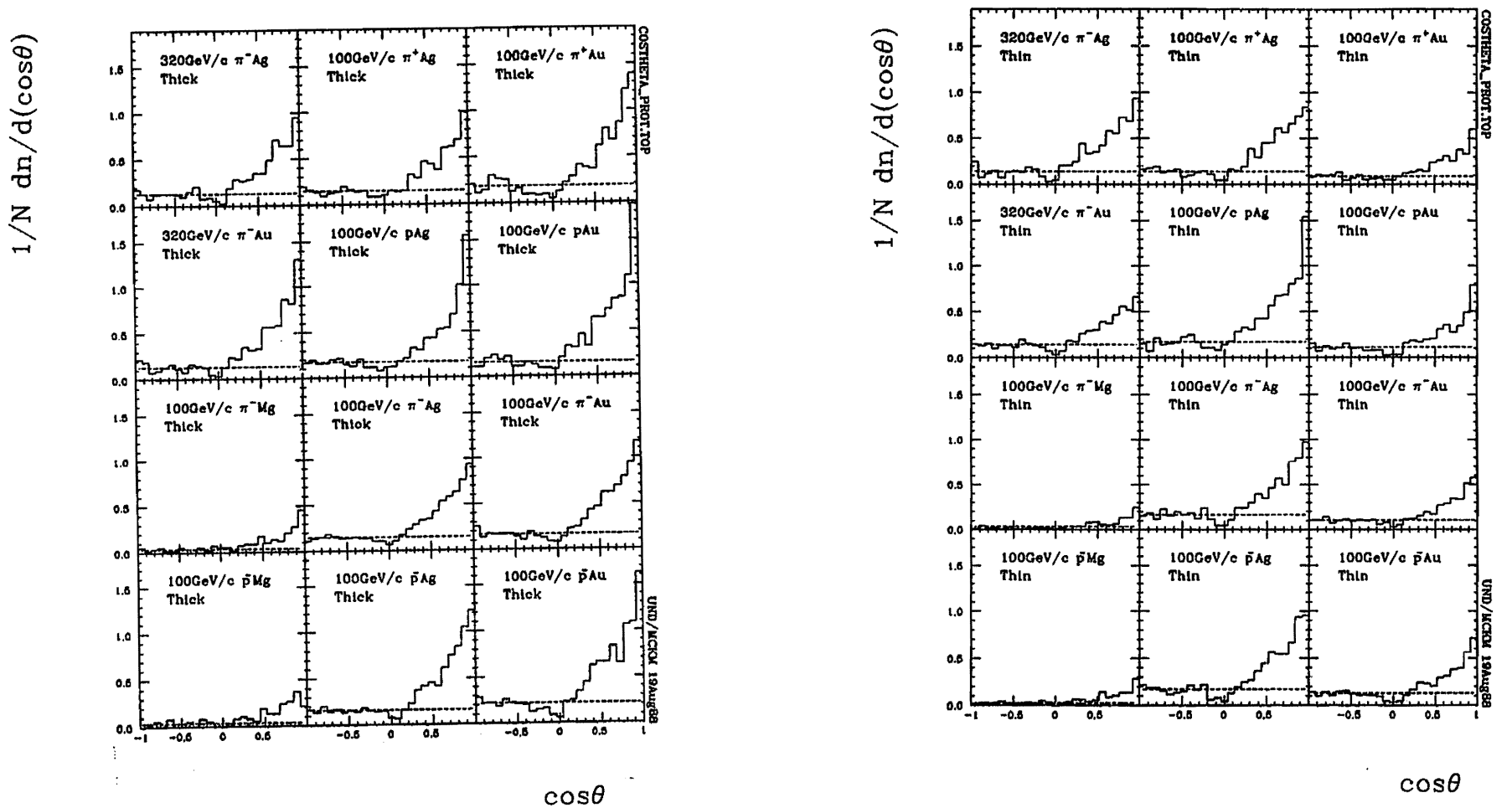

Figure 2A.1.6 Distributions of $cos\theta$ for proton secondaries. θ is the track angle with respect to the beam. Average proton densities in the range $-1. < cos\theta < -.3$ are given by the dashed lines .

Table 2A.1.3 Estimates of corrected proton multiplicity values for tracks obstructed by the target surface, *i.e.* track angles at or around 90 degrees to the beam direction.

THICK FOILS

Projectile	320GeV/c		100GeV/c									
	π^-	π^-	π^+	π^+	p	p	π^-	π^-	π^-	$\bar{p}$	$\bar{p}$	$\bar{p}$
$^{A}_{Z}Target$	$^{108}_{47}Ag$	$^{197}_{79}Au$	$^{108}_{47}Ag$	$^{197}_{79}Au$	$^{108}_{47}Ag$	$^{197}_{79}Au$	$^{24}_{12}Mg$	$^{108}_{47}Ag$	$^{197}_{79}Au$	$^{24}_{12}Mg$	$^{108}_{47}Ag$	$^{197}_{79}Au$
BTC	61	64	131	134	141	144	176	171	174	186	181	184
N_{events}	184	127	178	128	308	110	120	604	457	75	439	277
$\langle N_p \rangle$est isotrop	1.587	1.669	1.809	2.281	2.162	1.945	.383	1.775	2.044	.427	1.954	2.715
$\langle N_p \rangle$um	.223	.425	.247	.438	.299	.509	.092	.339	.602	.173	.355	.740
Δ	.038	.084	.048	.078	.042	.087	.029	.031	.057	.066	.036	.077
$\langle N_{evap} \rangle$	1.755	1.953	1.921	2.375	2.227	2.273	.508	1.988	2.453	.627	2.260	3.072
Δ	.175	.272	.218	.372	.168	.283	.086	.116	.164	.142	.141	.234
$\langle N_{cos\theta} \rangle$	.054	.142	.135	.172	.234	.182	-	.126	.193	-	.050	.383
Δ	.017	.033	.019	.052	.028	.041	.017	.014	.021	.019	.011	.037
$\langle N_{evap} \rangle$corr	1.809	2.095	2.056	2.547	2.461	2.455	.508	2.114	2.646	.627	2.310	3.455

THIN FOILS

Projectile	320GeV/c		100GeV/c									
	π^-	π^-	π^+	π^+	p	p	π^-	π^-	π^-	$\bar{p}$	$\bar{p}$	$\bar{p}$
$^{A}_{Z}Target$	$^{108}_{47}Ag$	$^{197}_{79}Au$	$^{108}_{47}Ag$	$^{197}_{79}Au$	$^{108}_{47}Ag$	$^{197}_{79}Au$	$^{24}_{12}Mg$	$^{108}_{47}Ag$	$^{197}_{79}Au$	$^{24}_{12}Mg$	$^{108}_{47}Ag$	$^{197}_{79}Au$
BTC	62	63	132	133	142	143	175	172	173	185	182	183
N_{events}	137	135	124	112	169	129	224	406	403	181	276	280
$\langle N_p \rangle$est isotrop	1.752	3.541	1.774	2.250	2.130	2.791	.411	2.034	2.566	.564	2.130	3.186
$\langle N_p \rangle$um	.467	.726	.282	.571	.497	.705	.83	.542	.824	.171	.598	.882
Δ	.081	.101	.058	.093	.068	.141	.039	.049	.068	.036	.063	.083
$\langle N_{evap} \rangle$	2.015	3.911	1.879	2.607	2.391	3.109	.594	2.443	3.221	.768	2.496	3.668
Δ	.259	.181	.250	.317	.236	.398	.087	.169	.227	.111	.203	.287
$\langle N_{cos\theta} \rangle$	.204	.356	.177	.214	.237	.388	-	.133	.169	.033	.232	.400
Δ	.039	.051	.038	.044	.037	.055	-	.018	.020	.014	.029	.036
$\langle N_{evap} \rangle$corr	2.219	4.267	2.056	2.821	2.628	3.497	.594	2.576	3.390	.801	2.728	4.068

COSTHETA_THICKTHIN.TEX UND/MCKM 19Aug88

predominantly represents *black*, extremely short proton tracks, just the variety eligible for angle-dependent depletion. In this study, however, unmeasured protons have been assumed to be isotropic themselves. Consequently, some double-counting could be taking place.

To calculate the average number of isotropically produced protons, $\langle N_{p_{evapcorr}} \rangle$, the correction $N_{cos\theta}$ is added to the average number $\langle N_{p_{evap}} \rangle$ of measured *evaporation* protons estimated by the sum of twice the measured backward proton multiplicity and the unmeasured proton multiplicity, ie. $2\langle N_{p_{back}} \rangle + \langle N_p \rangle$um. But since the sum $2\langle N_{p_{back}} \rangle + N_{cos\theta}$ can be construed to be the measured isotropic proton multiplicity $\langle N_{p_{isotrop}} \rangle$ with its depletion dip filled in, and since the unmeasured proton multiplicity $\langle N_p \rangle$um is presumed to be isotropic, the average number of isotropically produced protons can be expressed by the sum $\langle N_{p_{isotrop}} \rangle + \langle N_p \rangle$um. **Table 2A.1.3** shows the corrected number of isotropically produced protons $\langle N_{evap} \rangle corr$ broken down in terms of these two(2) equivalent sums. In most cases, targets with heavier nuclei have larger evaporation multiplicities, as expected. But these results also show a greater number of evaporation products from thin foils than for thick foils. While data were treated separately for the various thicknesses, corrections were made on the basis of angular considerations alone, not thickness. They did not consider the fact that low momentum evaporation products are less likely to emerge from thick targets than from thin ones. Thus the fact that evaporation multiplicity is lower for the thick targets is reasonable.

2A.1.3 Slow protons

Slow, beam-directed secondaries, unobservable when they stop within the target thickness, also contribute to the number of evaporation products. Although corrections have been made for depletions arising from an angle-dependent thickness, there remains an overall depletion associated with the beam-direction distance from the interaction point to the foil surface. This overall depletion becomes particularly important for isotropic *evaporation* which predominantly produces low momentum particles. *Black* proton multiplicities can be expected to be significantly lower than

those reported in emulsion experiments since they detect secondaries much closer to the interaction points and thus detect secondaries at much lower momenta. A comparison of E597 data in **Figure 2A.1.7** shows that blacks are suppressed to a larger extent in the thicker targets. A comparison of **Figure 2A.1.7** with **Figure 2A.1.8** for 67 GeV/c pEm and 200 GeV/cπEm data [Stenlund 82b] confirms the fact that thickness effects have severely inhibited our observation of black tracks. The emulsion is comparable to the Ag foil targets since it included AgBr as well as CNO. Including protons close to the vertex, emulsion data exhibit an average of 12 or 13 *black* tracks for events with 10 *grey* tracks while E597 data, inhibited by the thickness of its foils, shows only 2 or 3 *black* tracks for events with 10 *grey* tracks. Many of the *black* are being lost. This loss of *black* protons distorts the expected relation between average *grey* proton multiplicity and *black* proton multiplicity. **Figure 2A.1.9** displays this relation for emulsion events. But because of the severe depletion of *black* protons, it is quite different from its counterpart for E597 samples in **Figure 2A.1.10.**

Corrections for individual track momenta and overall depletions in *black* protons multiplicity are not made. Only corrections for foil-pathlength-dependent depletions of a global nature are made similar to those for the angular depletion of protons.

2A.1.4 Small radii of curvature

Even if particles survive their intrafoil traverse, low-momentum tracks will be unobservable if their initial radii of curvature R in the bubble chamber proper approach the radius of the bubbles marking their passage. The radius of curvature can be calculated by the well-known relation

$$R = \frac{pcos\lambda}{(300)(B)}$$

where the radius R is expressed in cm; the magnetic field B is expressed in gauss; and $pcos\lambda$, the momentum perpendicular to B, is expressed in eV/c. With bubble radii of under .5 mm, track momenta must be greater than 1 MeV/c in order for that track to be distinguishable from the bubbles that mark its path. This becomes a problem

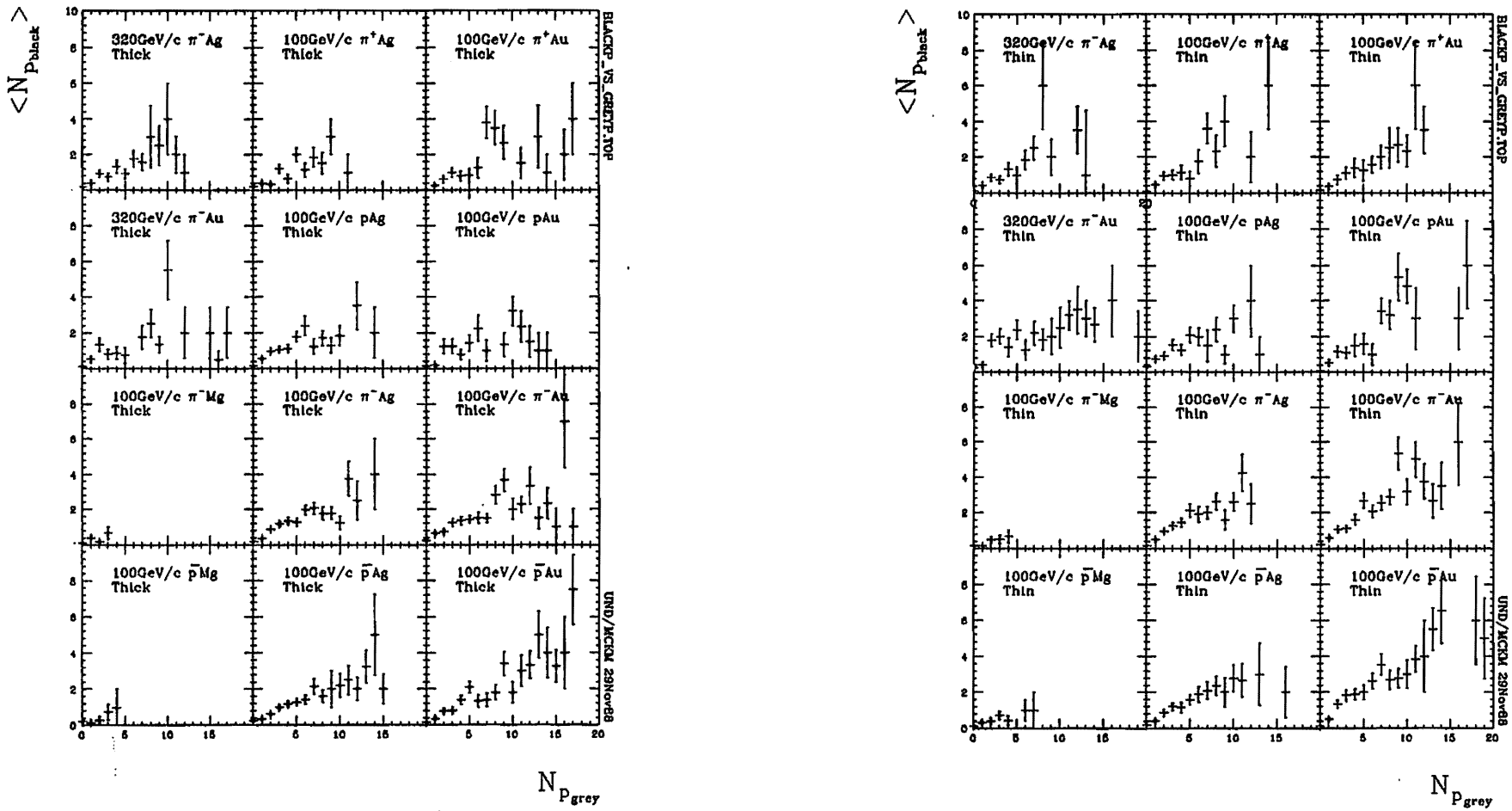

Figure 2A.1.7 Average *black* proton multiplicity as a function of *grey* proton multiplicity.

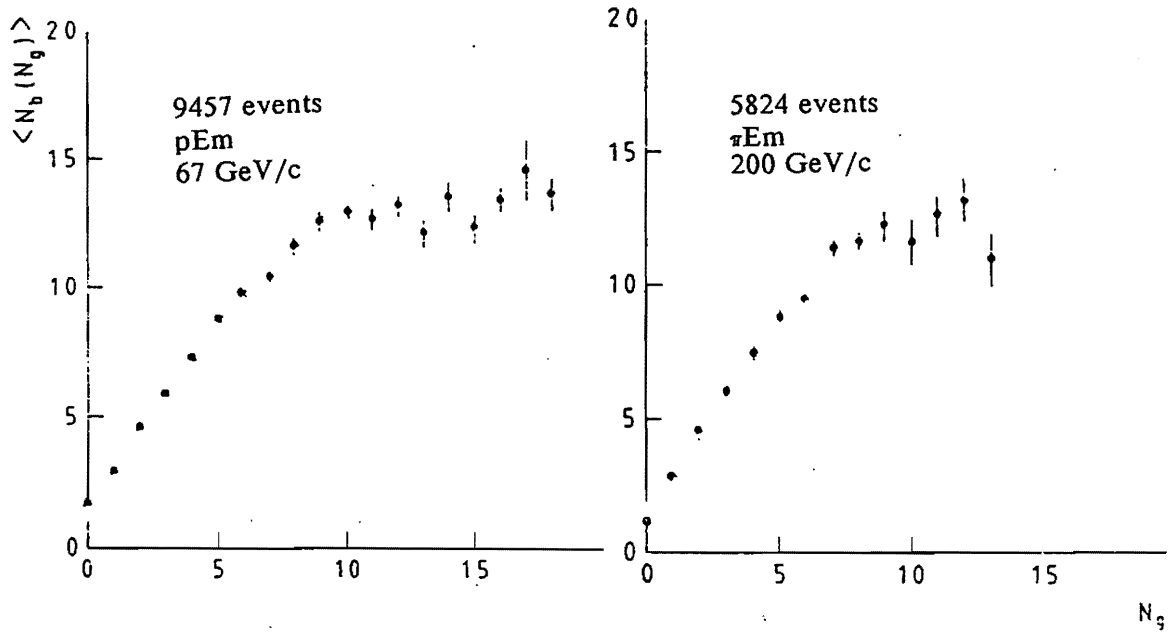

Figure 2A.1.8 Average *black* proton multiplicity as a function of *grey* proton multiplicity from emulsion data [Stenlund 82b].

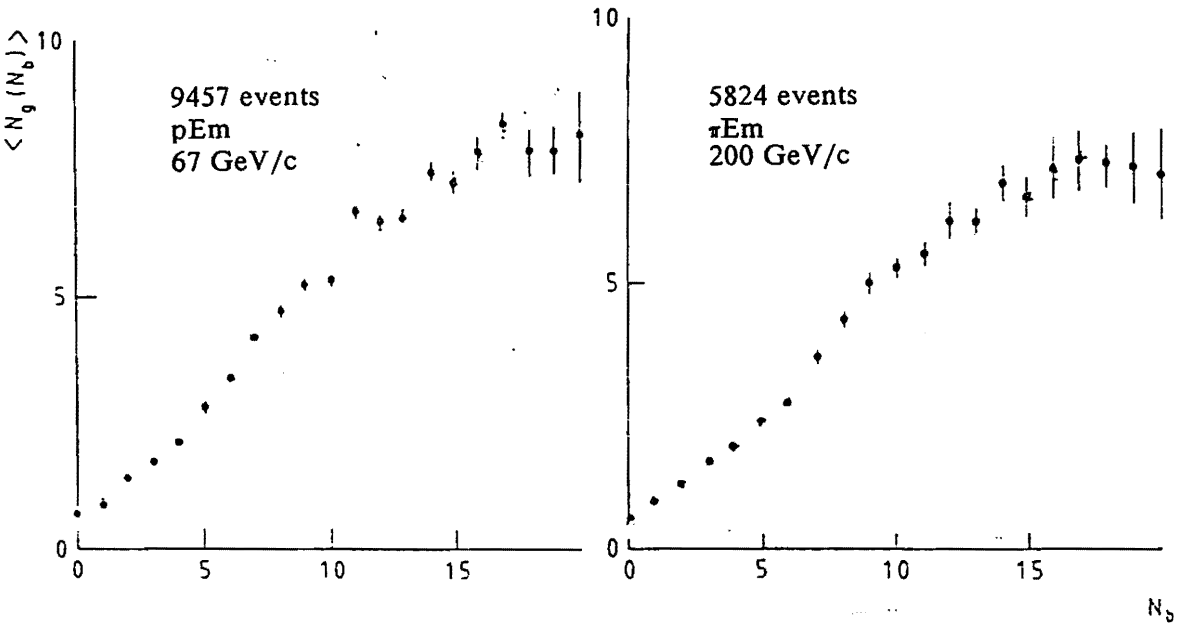

Figure 2A.1.9 Average *grey* proton multiplicity as a function of *black* proton multiplicity from emulsion data [Stenlund 82b].

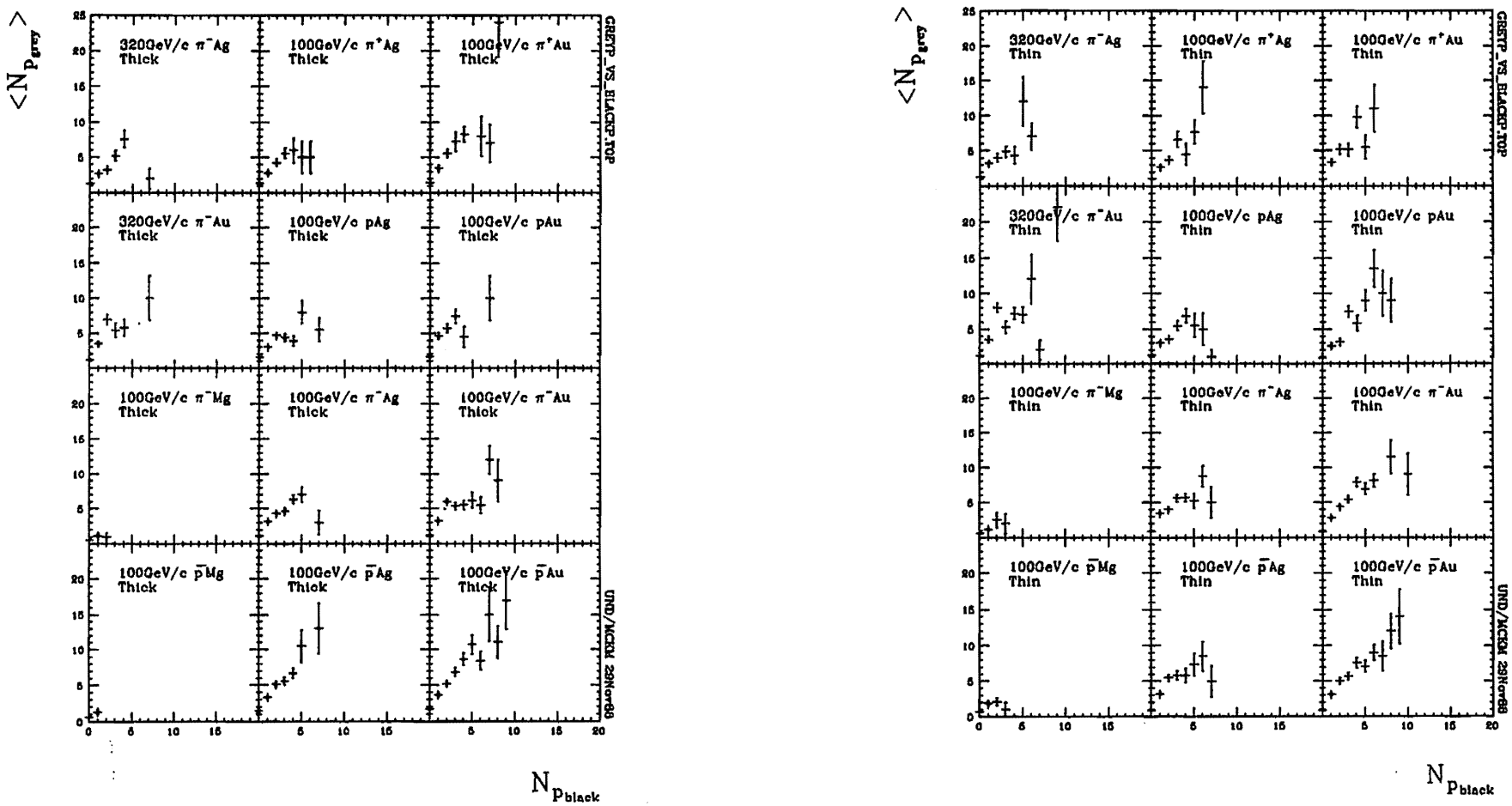

Figure 2A.1.10 Average *grey* proton multiplicity as a function of *black* proton multiplicity.

only in treating delta rays, or knock-on electrons. In a subsequent correction for misidentified fast electrons, delta rays are counted and must be adjusted to include unobservable ones.

2A.2 UNMEASURED TRACKS

Correcting for tracks visible but unmeasureable is much easier than correcting for unobservable ones. The measuring technicians annotated the measurement record with code specifying what type and how many tracks they were unable to measure when any of the following were encountered:

1. Tracks which could not be measured because they could not be adequately traced through the clutter of a high multiplicity event. Another track or the foil target itself might obscure the track.

2. Tracks too short or with too small a radius of curvature for the measurer to digitize enough points for reconstruction. Slow protons and particles undergoing secondary interactions accounted for most of the short tracks while slow electrons accounted for the tracks with small radii of curvature.

3. Tracks with such large radius of curvature that determining the momentum associated with the reconstructed nearly-straight track becomes a problem.

4. Tracks invalidated by random measurement errors. This was uncommon since remeasurements were routinely made at the time of the initial measurement.

5. Tracks which did not not pass the on-line reconstruction routine after repeated measurement attempts. This only occurred a small fraction of the time. When it did, the measurer treated that track as unmeasureable and made the proper annotation.

6. Tracks failing reconstruction failed in the off-line processing of the digitized data. At this point the track was manually flagged with a *kill* code in the measurement record and the unmeasurable count augmented. Only a few dozen events contained tracks that did not reconstruct off-line.

Separate counts were kept for unmeasureable protons, π^+, π^-, e^+, and e^-. Unmeasured protons were identified based on the occurrence of smooth, dark tracks (i.e. *black* tracks with $\beta < .3$). So visible, very slow protons were accounted for despite their unmeasurably short lengths.

Slow electrons, identified by by small, decreasing track curvatures (spirals) in the momentum range .005 GeV/c $< p <$.2 GeV/c can also be accounted for. Here .2 GeV/c is the limit at which an electron can be distinguished from a pion by ionization. A .2 GeV/c electron also has a radius of curvature 33.33 cm, just under the chamber radius of 38.10 cm, so that the spiral could be easily detected unless it heads well toward the side to which it bends.

All other unmeasured tracks were designated as pions by default and are included in the ambiguous multiplicities $N_{a^+}^{um}$ and $N_{a^-}^{um}$. These so-called *unmeasured* pions actually include an admixture of fast protons ($p > 1.3$ GeV/c), pions, and fast electrons ($p > .2$ GeV/c). They could also include short proton tracks with momenta below 1.3 GeV but whose ionization might have been hard to estimate over such a short length. **Tables 2A.2.1** summarizes the average unmeasured multiplicities for *black* protons, positive ambiguously identified particles, negative ambiguously identified particles, electrons, and positrons. These are respectively labeled $\langle N_{p_{black}} \rangle$um, $\langle N_{a^+} \rangle$um, $\langle N_{a^-} \rangle$um, $\langle N_{e^+} \rangle$um, and $\langle N_{e^-} \rangle$um.

2A.3 LIMITED IDENTIFICATION

Consideration is also given to the limits within which particles can be reliably identified by ionization. The major limitation is one's inability to distinguish ionization or bubble densities which differ from minimum ionizing densities by a factor less than 1.5 or greater than 4. This ratio for particles of the same momentum is a function of their relative velocities β_1 and β_2:

$$R = \frac{\beta_2^2}{\beta_1^2}$$

Figure 2.4.1 shows how protons are distinguishable from pions only for $p \leq 1.3$ GeV/c; pions, from electrons only for $p \leq .2$ GeV/c; kaons, from protons only for $p \leq 1$ GeV/c; and kaons, from pions only for $p \leq .7$ GeV/c. Fast protons ($p > 1.3$

Table 2A.2.1 Unmeasured particle multiplicities.

THICK FOILS

Projectile	320GeV/c		100GeV/c									
	π^-		π^+		p		π^-			p		
$\frac{A}{Z}$ Target	$^{108}_{47}Ag$	$^{197}_{79}Au$	$^{108}_{47}Ag$	$^{197}_{79}Au$	$^{108}_{47}Ag$	$^{197}_{79}Au$	$^{24}_{12}Mg$	$^{108}_{47}Ag$	$^{197}_{79}Au$	$^{24}_{12}Mg$	$^{108}_{47}Ag$	$^{197}_{79}Au$
BTC	61	64	131	134	141	144	176	171	174	186	181	184
N_{events}	184	127	178	128	308	110	120	604	457	75	439	277
$\langle N_{pblack}\rangle$um	.223	.425	.247	.458	.290	.509	.092	.359	.602	.175	.355	.740
Δ	.038	.084	.048	.078	.042	.087	.029	.031	.057	.066	.036	.077
$\langle N_{a+}\rangle$um	.125	.268	.062	.125	.104	.127	.058	.108	.142	.027	.144	.185
Δ	.030	.096	.024	.041	.021	.034	.024	.016	.020	.019	.023	.028
$\langle N_{a-}\rangle$um	.092	.181	.096	.094	.078	.118	.083	.089	.153	.053	.103	.191
Δ	.025	.070	.027	.028	.013	.044	.035	.015	.029	.032	.018	.036
$\langle N_{e+}\rangle$um	.049	.087	.045	.055	.062	.073	.008	.060	.092	.040	.112	.162
Δ	.018	.025	.016	.025	.016	.028	.008	.010	.018	.023	.020	.027
$\langle N_{e-}\rangle$um	.076	.118	.079	.070	.101	.118	.008	.123	.133	-	.150	.162
Δ	.021	.048	.020	.023	.020	.038	.008	.015	.019	-	.021	.026

UNMEASURED.TEX UND/MCKM 11Oct88

THIN FOILS

Projectile	320GeV/c		100GeV/c									
	π^-		π^+		p		π^-			p		
$\frac{A}{Z}$ Target	$^{108}_{47}Ag$	$^{197}_{79}Au$	$^{108}_{47}Ag$	$^{197}_{79}Au$	$^{108}_{47}Ag$	$^{197}_{79}Au$	$^{24}_{12}Mg$	$^{108}_{47}Ag$	$^{197}_{79}Au$	$^{24}_{12}Mg$	$^{108}_{47}Ag$	$^{197}_{79}Au$
BTC	62	63	132	133	142	143	175	172	173	185	182	183
N_{events}	137	135	124	112	169	129	224	406	403	181	276	280
$\langle N_{pblack}\rangle$um	.467	.726	.282	.571	.497	.705	.183	.542	.824	.171	.598	.882
Δ	.081	.101	.058	.093	.068	.141	.039	.049	.068	.036	.063	.083
$\langle N_{a+}\rangle$um	.088	.141	.073	.089	.047	.132	.049	.074	.127	.066	.098	.154
Δ	.028	.055	.026	.030	.018	.042	.016	.017	.023	.023	.024	.029
$\langle N_{a-}\rangle$um	.058	.119	.032	.089	.089	.124	.076	.113	.139	.061	.116	.121
Δ	.020	.033	.016	.032	.031	.035	.021	.030	.026	.019	.024	.121
$\langle N_{e+}\rangle$um	.036	.037	.010	.036	.021	.023	.004	.057	.065	.006	.058	.061
Δ	.019	.016	.021	.022	.012	.013	.004	.012	.013	.005	.014	.017
$\langle N_{e-}\rangle$um	.022	.050	.073	.027	.050	.031	.013	.071	.079	.033	.051	.082
Δ	.012	.023	.028	.015	.018	.010	.008	.016	.016	.013	.014	.016

UNMEASURED.TEX UND/MCKM 11Oct88

GeV/c), fast kaons ($p > .7$ GeV/c), and fast electrons ($p > .2$ GeV/c thus contaminate secondaries said to be pions. Because produced particle multiplicities include default classified pions as well as unambiguously identified pions, it is important to estimate the degree to which this contamination drives up the positive and negative produced particle multiplicities and depresses the proton multiplicities.

2A.3.1 Fast electrons

The number of fast, misidentified electrons(positrons) emerging from target foils can be estimated in two series of calculations–one for an estimate based on e^+e^- production, the other for an estimate based δ-ray production. e^+e^- production is anticipated from π^o's decaying into γ's and Dalitz pairs, with some of the γ's subsequently converting into additional e^+e^- pairs near the interaction point. δ-rays from simple knock-on collisions between produced secondaries and atomic electrons in the foils are also anticipated. Most δ-rays, identifiable by their characteristically tight spirals in a direction consistent with that of negative particles, were generally not measured. However, hard single δ-rays might have been mistaken for produced tracks. This over-representation among the negative produced particles must be corrected.

In what follows is a detailed development of estimated e^+e^-- and δ-ray-based corrections. Each step is discussed and the correction calculated in tables paralleling each step.

e^+e^- Contamination Produced particle multiplicities are expected to include some degree of contamination from fast, misidentified e^+e^- products. An outline of steps is given in detail below for estimating e^+e^- contamination in produced particle multiplicities. This outline is followed by short discussions of each step and references to values calculated and tabulated at each step.

1. Estimate π^o multiplicity N_{π^o}, assuming π^o production is comparable to π^+ and π^- production:

$$\langle N_{\pi^o} \rangle \approx \frac{1}{2}(\langle N^m_{\pi^+} \rangle + \langle N^m_{a^+} \rangle + \langle N^{um}_{a^+} \rangle + \langle N^m_{\pi^-} \rangle + \langle N^m_{a^-} \rangle + \langle N^{um}_{a^-} \rangle)$$

To estimate e^+e^- production, the π^o multiplicity must first be estimated. The average between π^+ and π^- multiplicities is probably a good estimate even if the multiplicities are corrected only for unmeasured tracks:.

$$\langle N_{\pi^o} \rangle \approx \frac{1}{2}\langle N_{\pi^+} + N_{\pi^-} \rangle$$

2. Estimate e^+e^- multiplicity $N_{e^+e^-\leftarrow\pi^o}$ from π^o decay:

$$\langle N_{e^+e^-\leftarrow\pi^o} \rangle = 2\Phi_{\gamma\gamma}\Phi^{.5t,X_o}_{\gamma\rightarrow e^+e^-} + \Phi_{\gamma e^+e^-}\Phi^{.5t,X_o}_{\gamma\rightarrow e^+e^-} + \Phi_{\gamma e^+e^-}$$

   (a) considering only the two(2) most probable decay channels with probabilities

$$\begin{aligned} \Phi_{\gamma\gamma} &= 98.802\% \\ \Phi_{\gamma e^+e^-} &= 1.198\% \end{aligned}$$

   (b) calculating the gamma conversion probability for a particle traversing one-half target thicknesses at angle θ so $x = .5t/cos\theta$

$$\Phi^{.5t,X_o}_{\gamma\rightarrow e^+e^-} = 1 - e^{-7x/(9cos\theta X_o)} = 1 - e^{-.35t/9X_o}$$

   where X_o is the radiation length.

   π^o's will predominantly decay in the two-gamma and Dalitz decay channels. Gammas subsequently convert to e^+e^- pairs as they traverse thickness x of the target. . Assuming the gammas traverse one-half the thickness of the foil, on the average, the number of observable e^+e^- pairs from π^o decay is expected to be

$$\begin{aligned} N_{e^+e^-} &= \Phi_{\gamma e^+e^-} + 2\Phi_{\gamma\gamma}\Phi_{\gamma conversion(t,2X_o)} + 1\Phi_{\gamma e^+e^-}\Phi_{\gamma conversion(t,2X_o)} \\ &= 2.00000 - 1.98802e^{-.77778\frac{t}{2X_o}} \end{aligned}$$

3. Estimate the fraction $F_{e\pm}$ of $e^\pm$'s that emerges, after traversing one-quarter target thicknesses, with sufficient momentum to be mistaken for pions:

   (a) estimating π^o momentum distribution $P_{\pi^o}(p) \approx \frac{1}{2}(P_{\pi^+} + P_{a^+} + P_{\pi^-} + P_{a^-})$.

(b) approximating the $e^{\pm}$ momentum distribution by

$$P_{e^{\pm}}(\frac{p}{4}) \approx P_{\pi^o}(p)$$

(c) assuming the average π^o is produced at one-half thickness, and the average $e^{\pm}$ is produced at 3/4 thickness, and determining the momentum $p^{stopping}(.25t)$) at which $e^{\pm}$'s stop in the one-quarter thickness remaining, and the minimum momentum $p_{min}^{mislabeled}(.25t) = p^{stopping}(.25t) + .2$ GeV/c at which e's will emerge and be mistaken for π's.

(d) determining the fraction

$$F_{e^{\pm}} = \frac{\int_{p_{min}^{mislabeled}(.25t)}^{\infty} P_{e^{\pm}} dp}{\int_0^{\infty} P_{e^{\pm}} dp}$$

of the momentum distribution $P_{e^{\pm}}(p)$ that falls above $p^{mislabeled}(.25t)$.

Not all of these e^+e^- pairs can be expected to be observable. Some will stop within the foil, depending on their range and momentum. The e^+e^- momentum distribution can be crudely estimated by one-fourth the π^o momentum distribution (adding the π^+ and π^- momentum distributions, normalizing, and dividing by four(4)). This is an underestimate since low momentum e^+e^- can occur even when the π^o distribution divided by four(4) is not small. From momentum-range tables [Trower 66], the minimum momentum at which an electron is expected to emerge in association with interaction points at the center of the foil target can be estimated for each foil as summarized previously in **Table 2A.1.2.** Since it was assumed that the π^o's were produced on the average at one-half the foil thickness, then the conversion electrons will, on the average, traverse a little more than one-fourth the foil thickness. So the minimum electron momentum at which an electron is expected to emerge is assumed to be the momentum at which an electron is stopped in one-fourth the foil thickness.

4. Calculate expected e^+e^- multiplicity $N_{e^+e^-\leftarrow\pi^o}^{fast\ emerging}$ from π^o decay which should be visibly emerging from the foil targets at momenta of .2 GeV/c

$$N_{e^+e^-\leftarrow\pi^o}^{fast\ emerging} \approx \langle N_{\pi^o}\rangle \langle N_{e^+e^-\leftarrow\pi^o}\rangle F_{e^{\pm}}$$

5. Verify the plausibility of $\langle N_{e^+e^-\leftarrow\pi^o}^{fastemerging}\rangle$ by comparing with the observed sum of 'pseudopaired' e^+e^- and 'unpaired' $e^\pm$ multiplicities:

$$N_{e^+e^-\leftarrow\pi^o}^{fast\ emerging} \approx \langle N_{\pi^o}\rangle\langle N_{e^+e^-\leftarrow\pi^o}\rangle F_{e^\pm} \overset{?}{\approx} \langle N_{e^+e^-}^{m\ pseudopr}\rangle + \langle N_{e^+}^{m\ unpr}\rangle + \langle N_{e^-}^{m\ unpr}\rangle$$

where 'pseudopaired' e^+e^- multiplicity is the e^+ multiplicity which has comparable e^- multiplicity, and vice versa; and where 'unpaired' $e^\pm$ multiplicity is the e^+ or the e^- multipicity in excess of the 'pseudopaired' multiplicity, namely

$$N_{e^+e^-}^{m\ pseudopr} = \begin{cases} N_{e^+}^{m+um} & when\ N_{e^-}^{m+um} > N_{e^+}^{m+um} \\ N_{e^-}^{m+um} & when\ N_{e^+}^{m+um} > N_{e^-}^{m+um} \end{cases}$$

$$N_{e^\pm}^{m\ unpr} = \mid N_{e^+}^{m+um} - N_{e^-}^{m+um} \mid$$

(Note that δ-rays could also be involved, probably but not necessarily when $N_{e^-} > N_{e^+}$.)

The calculated number of identifiable electrons is consistent with the observed e^+e^- pseudopair multiplicity added to twice the observed unpaired e^+ multiplicity. It is also consistent with the observed e^+ multiplicity.

6. Estimate the number of mislabeled $\pi^\pm$:

$$\langle N_{\pi^\pm}^{mislabeled}\rangle = \langle N_{e^+e^-}^{fast\ emerging}\rangle - \langle N_{e^+e^-}^{pseudopr}\rangle$$

This number of mislabeled $\pi^\pm$'s is the correction term subtracted from pion multiplicities for final adjusted values.

Of course, these corrections are all foil thickness dependent. Ideally one should extrapolate to zero target thickness, especially for heavy targets where the thickness plays a larger part. However, this is not feasible with the magnitude of our statistics. Only overall corrections on multiplicities for each of the foils are made and displayed in **Table 2A.3.1.**

Table 2A.3.1 Estimates of the number of observable e^+e^- pairs associated with π^o decays. The π^o multiplicity is approximated by $N_{\pi^o}est = \frac{1}{2}(\langle N_{\pi^+}\rangle + \langle N_{\pi^+}\rangle)$.

THICK FOILS

Projectile	320GeV/c		100GeV/c									
	π^-	π^-	π^+	π^+	p	p	π^-	π^-	π^-	p	p	p
$^{A}_{Z}Target$	$^{108}_{47}Ag$	$^{197}_{79}Au$	$^{108}_{47}Ag$	$^{197}_{79}Au$	$^{108}_{47}Ag$	$^{197}_{79}Au$	$^{24}_{12}Mg$	$^{108}_{47}Ag$	$^{197}_{79}Au$	$^{24}_{12}Mg$	$^{108}_{47}Ag$	$^{197}_{79}Au$
X_o	8.720	5.945	8.720	5.945	8.720	5.945	25.473	8.720	5.945	25.473	8.720	5.945
t	1.894	1.716	1.894	1.716	1.894	1.716	1.931	1.894	1.716	1.931	1.894	1.716
$C_{cos\theta,prod}$	1.41	1.33	1.44	1.38	1.51	1.43	1.22	1.43	1.34	1.34	1.53	1.35
Δ	.06	.06	.06	.04	.05	.06	.05	.03	.03	.10	.05	.02
$1-e^{-\frac{7(.51C)}{9X_o}}$	.112	.139	.115	.144	.120	.148	.035	.114	.140	.039	.121	.141
Δ	.004	.006	.005	.004	.004	.006	.001	.002	.003	.003	.004	.002
BTC	61	64	131	134	141	144	176	171	174	186	181	184
N_{events}	184	127	178	128	308	110	120	604	457	75	439	277
$N_{\pi^o}est$	7.829	8.229	5.959	6.699	6.589	6.818	4.425	6.051	6.458	5.353	7.388	6.048
Δ	.236	.252	.215	.231	.193	.219	.138	.117	.120	.163	.153	.155
N_{π^o}est ide	2.046	2.063	1.907	2.238	2.205	2.455	.904	1.890	2.056	1.280	2.522	2.742
Δ	.075	.090	.073	.094	.060	.106	.061	.040	.047	.092	.054	.070
$\frac{N_{\pi^o}estide}{N_{\pi^o}est}$	.265	.258	.324	.340	.339	.367	.208	.318	.326	.241	.347	.348
Δ	.011	.013	.014	.016	.011	.018	.015	.008	.009	.019	.009	.010
$P_{e^+e^-}$	.23464	.28831	.24060	.29825	.25054	.30621	.08156	.23861	.29030	.08951	.25253	.29229
Δ	.00089	.00166	.00114	.00115	.00095	.00177	.00007	.00045	.00083	.00023	.00096	.00056
$N_{e^+e^-}calc$	1.837	2.373	1.434	1.998	1.651	2.088	.361	1.444	1.875	.479	1.866	2.352
Δ	.049	.075	.045	.069	.037	.077	.016	.024	.035	.024	.034	.050
$N_{e^+e^-}$calc ide	.480	.595	.459	.667	.552	.752	.074	.451	.597	.115	.637	.801
Δ	.018	.026	.018	.028	.015	.033	.005	.010	.014	.008	.014	.021
$\langle N_{e^+e^-}\rangle$	.152	.307	.180	.211	.162	.273	.008	.200	.256	-	.257	.375
Δ	.029	.049	.032	.041	.023	.050	.008	.018	.024	-	.024	.037
$\langle N_{e^+}\rangle$unpr	.158	.102	.146	.180	.195	.145	.042	.141	.190	.067	.180	.217
Δ	.029	.028	.029	.038	.025	.036	.019	.015	.020	.030	.020	.028
$\langle N_{e^-}\rangle$unpr	.364	.402	.202	.203	.253	.300	.117	.300	.337	.093	.355	.354
Δ	.044	.056	.034	.040	.029	.052	.031	.022	.027	.035	.028	.036
$\langle N_{e^+e^-}\rangle$ +2$\langle N_{e^+}\rangle$unpr	.468	.511	.472	.571	.552	.563	.092	.482	.636	.134	.617	.809
Δ	.050	.063	.052	.068	.042	.071	.028	.028	.037	.042	.061	.090
$\langle N_{e^+}\rangle$m+um	.571	.591	.500	.602	.533	.764	.066	.565	.724	.107	.704	.906
Δ	.056	.068	.053	.069	.042	.083	.023	.031	.040	.038	.040	.057

Table 2A.3.1 Continued.

THIN FOILS

Projectile	320GeV/c		100GeV/c									
	π^-	π^-	π^+	π^+	p	p	π^-	π^-	π^-	p	p	p
$^{A}_{Z}Target$	$^{108}_{47}Ag$	$^{197}_{79}Au$	$^{108}_{47}Ag$	$^{197}_{79}Au$	$^{108}_{47}Ag$	$^{197}_{79}Au$	$^{24}_{12}Mg$	$^{108}_{47}Ag$	$^{197}_{79}Au$	$^{24}_{12}Mg$	$^{108}_{47}Ag$	$^{197}_{79}Au$
X_o	8.720	5.945	8.720	5.945	8.720	5.945	25.473	8.720	5.945	25.473	8.720	5.945
t	.6401	.5784	.6401	.5784	.6401	.5784	.6453	.6401	.5784	.6453	.6401	.5784
$C_{cos\theta,prod}$	1.26	1.36	1.43	1.52	1.42	1.32	1.25	1.46	1.42	1.37	1.49	1.45
Δ	.04	.06	.06	.10	.05	.03	.03	.05	.03	.07	.05	.04
$1-e^{-\frac{7(.51C)}{9X_o}}$	.035	.050	.040	.056	.040	.049	.012	.041	.052	.013	.042	.053
Δ	.001	.002	.002	.004	.001	.001	.0003	.001	.001	.001	.001	.001
BTC	62	63	132	133	142	143	175	172	173	185	182	183
N_{events}	137	135	124	112	169	129	224	406	403	181	276	280
$N_{\pi^o est}$	7.635	8.563	5.722	5.995	6.272	6.206	4.248	5.579	5.834	4.832	6.421	6.716
Δ	.236	.252	.215	.231	.193	.219	.138	.117	.120	.163	.153	.155
$N_{\pi^o est\ ide}$	1.807	2.296	1.766	1.911	1.973	1.950	.953	1.667	1.720	1.163	2.115	2.220
Δ	.081	.092	.084	.092	.076	.087	.046	.045	.046	.057	.062	.063
$\frac{N_{\pi^o estide}}{N_{\pi^o est}}$	.239	.272	.312	.324	.318	.321	.228	.304	.302	.244	.340	.337
Δ	.012	.012	.017	.018	.014	.016	.012	.009	.009	.013	.011	.011
$P_{e^+e^-}$	.08156	.11138	.09150	.12331	.09150	.10939	.03584	.09349	.11536	.03782	.09548	.11735
Δ	.00007	.00020	.00016	.00045	.00008	.00010	.00001	.00008	.00010	.00003	.00008	.00011
$N_{e^+e^-calc}$	.623	.954	.524	.739	.574	.679	.152	.522	.673	.183	.613	.788
Δ	.019	.028	.020	.029	.018	.024	.005	.011	.014	.006	.015	.018
$N_{e^+e^-calc\ ide}$	.147	.256	.162	.236	.181	.213	.034	.156	.198	.044	.205	.261
Δ	.007	.010	.008	.011	.007	.010	.002	.004	.005	.002	.006	.007
$\langle N_{e^+e^-}\rangle$	.073	.052	.081	.116	.059	.054	.004	.076	.112	.006	.065	.129
Δ	.023	.020	.026	.032	.019	.020	.004	.014	.017	.006	.015	.021
$\langle N_{e^+}\rangle_{unpr}$	.080	.141	.073	.098	.089	.124	.027	.099	.099	.050	.112	.146
Δ	.024	.032	.024	.034	.023	.031	.011	.016	.016	.017	.020	.023
$\langle N_{e^-}\rangle_{unpr}$	.168	.156	.145	.196	.154	.155	.076	.190	.226	.099	.159	.200
Δ	.035	.034	.034	.042	.030	.035	.018	.022	.024	.023	.024	.027
$\langle N_{e^+e^-}\rangle + 2N_{e^+})_{unpr}$	.233	.334	.227	.312	.148	.302	.058	.274	.310	.106	.289	.421
Δ	.041	.049	.043	.058	.038	.048	.016	.027	.028	.025	.032	.039
$\langle N_{e^+}\rangle_{m+um}$	.255	.341	.298	.420	.472	.302	.058	.301	.358	.111	.294	.386
Δ	.043	.050	.049	.061	.053	.048	.016	.027	.030	.025	.033	.037

EPEM_THIN.TEX UND/MICKM 11Oct88

δ-ray Contamination δ-rays were not generally measured. However, should they occur (however unlikely) at high momenta, they cannot be distinguished from pions in the bubble chamber and are erroneously measured and identified as pions. Since δ-rays are electromagnetically produced when a charged particle passes in the neighborhood of an atom, all primaries and secondaries passing through a foil target can produce electrons which, if they are produced inside the target and emerge at momenta greater than .2 GeV/c, are construed to be produced particles. An outline of steps is given in detail below for estimating δ-ray contamination of produced particle multiplicities. This outline is followed by short discussions of each step and references to values calculated and tabulated at each step.

1. Determine minimum kinetic energies for δ-ray electrons emerging from the target with enough momentum to be mistaken for pions, assuming

   (a) they were produced at one-quarter target thickness by a beam particle

   (b) they were produced at three-quarter target thickness by produced secondaries

   For this estimate of fast, emerging δ-ray production, it is assumed that the average event occurs at one-half the foil thickness, that δ-rays associated with a primary will on the average travel three-fourths of a foil thickness, and that the δ-rays associated with a secondary will on the average traverse over one-fourth of a foil thickness. The latter is adjusted by a factor of $1/cos\theta$ to take into account the greater path in the foil when the emergent angle is greater than zero.

   Using standard range-momentum distributions, minimum momenta $p_{min}^{emerging}$ are determined for δ-rays associated with primaries and δ-rays associated with secondaries emerging from the foils. Of course, most δ-rays are ignored in the measurement process. They generally have small radii of curvature. Measurers only measured spiralling tracks with radii of curvature substantially greater than those normally associated with δ-rays. Tracks were not to be measured

with radii of curvature less than one or two centimeters. The average minimum momentum $\langle p_{min} \rangle \approx .005$ GeV/c is consistent with a radius of curvature of .833 cm.

2. Determine maximum δ-ray kinetic energies which can be produced

   (a) by a beam particle

   (b) by produced secondaries

   Maximum δ-ray momenta are calculated according to

$$T_{max} = \frac{2m_e c^2 p_{sec}^2 c^2}{m_e^2 c^4 + m_{sec}^2 c^4 + 2m_e c^2 E_{sec}}$$

   which expresses the maximum kinetic energy as a function of the secondary momentum and energy p_{sec} and E_{sec} [Rossi].

3. Calculate the numbers of δ-rays $N_\delta^{fast\ emerging}$ with kinetic energy between the minimum and maximum observable in E597 data for

   (a) beam velocities β_{bm}

   (b) produced secondary velocities β_{sec}

   (Repeating this calculation using .2 GeV/c for a maximum, makes essentially no difference since δ-ray production is abundant only at subrelativistic velocities.)

   The number of δ-rays with kinetic energy between T_1' and T_2' produced as a result of the passage of a secondary with kinetic energy T through a thickness t (in our case, t is the 1/4 or 3/4 foil thickness divided by $cos\theta$) is

$$\begin{aligned} t\int_{T_1'}^{T_2'} \Phi_{col}(T,T')dT' &= t\int_{T_1'}^{T_2'} \frac{2Cm_e c^2}{\beta^2}\frac{dT'}{T_1'^2}(1-\beta^2\frac{T'}{T_{max}'}+\frac{1}{2}\frac{T'^2}{E^2}) \\ &= t2Cm_e c^2(\int_{T_1'}^{T_2'}\frac{1}{\beta^2 T'^2}dT' - \int_{T_1'}^{T_2'}\frac{1}{T_{max}'T'} \\ &\quad +\frac{1}{2}\int_{T_1'}^{T_2'}\frac{1}{\beta^2 E^2 dT'}) \\ &= t2Cm_e c^2(-\frac{1}{\beta^2}(\frac{1}{T_2'}-\frac{1}{T_1'})-\frac{1}{T_{max}'}\ln\frac{T_2'}{T_1'} \end{aligned}$$

$$+\frac{1}{2\beta^2 E^2}(T_2' - T_1'))$$

(7.4)

where C represents the total 'area' covered by one gram of electrons, each with the classical electron radius r_e, and is calculated according to

$$C = \pi N_o \frac{Z}{A} r_e = .150 \frac{Z}{A} cm^2/g$$

Pion calculations do not include the $1/E^2$ term.

To calculate the total number of δ-rays, the contributions of all primaries and secondaries in each event are simply summed, calculating each track's contribution over an energy range consistent with the minimum and maximum momenta. The values for the calculated delta-ray contribution, consistent with both modes of calculation, are tabulated as $N_\delta$calc in **Table 2A.3.2**

4. Verify the plausibility of the previous result by

   (a) finding $\langle N_{e^+}^{m+um} - N_{e^-}^{m+um} \rangle$

   (b) inspecting the momentum distribution of $N_{e^+}^{m} - N_{e^-}^{m}$

   Observable δ-ray production can also be estimated by the difference in e^+ and e^- production below .2 GeV/c ($N_\delta$exp) and the difference between unpaired multiplicities ($\langle N_{e^-} \rangle - \langle N_{e^+} \rangle$). A comparison of these estimates in Table **2A.3.2** reveals reasonable agreement in most cases between the calculated δ-ray multiplicity and these two other estimates.

   Futhermore, the difference momentum distributions **Figure 2A.3.1** are consistent with what is expected for δ-rays. The difference distribution shows only significant contributions at very low momenta and a tapering off from the maximum towards the radius-of-curvature cutoff.

5. Calculate the multiplicity of fast δ-rays mislabeled π^-:

$$N_\delta^{mislabeled} \approx N_{e^+e^- \leftarrow \pi^o}^{fast\ emerging} + N_\delta^{fast\ emerging} - N_{e^-}^{m+um}$$

Table 2A.3.2 Calculated and experimental estimates of the number of observable delta rays in the momentum range .005 GeV/c < p < .2 GeV/c. The calculated estimates $N_\delta$calc are determined as described in the text. The experimental estimates $N_\delta$exp are simply the multiplicity differences $\langle N_{e^-,p<.2}\rangle - \langle N_{e^+,p<.2}\rangle$.

THICK FOILS

Projectile	320GeV/c		100GeV/c									
	π^-	π^-	π^+	π^+	p	p	π^-	π^-	π^-	$\bar{p}$	$\bar{p}$	$\bar{p}$
$^{A}_{Z}Target$	$^{108}_{47}Ag$	$^{197}_{79}Au$	$^{108}_{47}Ag$	$^{197}_{79}Au$	$^{108}_{47}Ag$	$^{197}_{79}Au$	$^{24}_{12}Mg$	$^{108}_{47}Ag$	$^{197}_{79}Au$	$^{24}_{12}Mg$	$^{108}_{47}Ag$	$^{197}_{79}Au$
X_0	8.720	5.945	8.720	5.945	8.720	5.945	25.473	8.720	5.945	25.473	8.720	5.945
t	1.894	1.716	1.894	1.716	1.894	1.716	1.931	1.894	1.716	1.931	1.894	1.716
BTC	61	64	131	134	141	144	176	171	174	186	181	184
N_{events}	184	127	178	128	308	110	120	604	457	75	439	277
$N_\delta$calc	.213	.193	.194	.160	.184	.143	.141	.174	.142	.166	.213	.188
Δ	.010	.014	.019	.014	.015	.008	.008	.006	.004	.009	.011	.013
$N_\delta$exp	.190	.306	.051	-.024	.059	.127	.100	.132	.107	.013	.170	.130
dN_δexp	.106	.136	.087	.122	.071	.141	.046	.054	.074	.054	.069	.105
$N_{unpr\ diff}$	.206	.300	.056	.023	.058	.155	.075	.159	.147	.026	.175	.137
Δ	.053	.063	.045	.055	.038	.063	.036	.027	.034	.046	.034	.046

THIN FOILS

Projectile	320GeV/c		100GeV/c									
	π^-	π^-	π^+	π^+	p	p	π^-	π^-	π^-	$\bar{p}$	$\bar{p}$	$\bar{p}$
$^{A}_{Z}Target$	$^{108}_{47}Ag$	$^{197}_{79}Au$	$^{108}_{47}Ag$	$^{197}_{79}Au$	$^{108}_{47}Ag$	$^{197}_{79}Au$	$^{24}_{12}Mg$	$^{108}_{47}Ag$	$^{197}_{79}Au$	$^{24}_{12}Mg$	$^{108}_{47}Ag$	$^{197}_{79}Au$
X_0	8.720	5.945	8.720	5.945	8.720	5.945	25.473	8.720	5.945	25.473	8.720	5.945
t	.6401	.5784	.6401	.5784	.6401	.5784	.6453	.6401	.5784	.6453	.6401	.5784
BTC	62	63	132	133	142	143	175	172	173	185	182	183
N_{events}	137	135	124	112	169	129	224	406	403	181	276	280
$N_\delta$calc	.071	.061	.063	.047	.062	.050	.044	.054	.046	.064	.063	.070
Δ	.004	.004	.009	.003	.008	.008	.002	.002	.002	.012	.010	.017
$N_\delta$exp	.103	.022	.033	.116	-.147	.046	.045	.068	.066	.027	.036	.050
dN_δexp	.074	.076	.085	.108	.061	.075	.027	.048	.053	.039	.050	.063
$N_{unpr\ diff}$	.088	.015	.072	.098	.065	.031	.049	.091	.127	.049	.047	.054
Δ	.042	.047	.042	.054	.038	.047	.021	.027	.029	.029	.031	.035

Figure 2A.3.1 Momentum distributions for positron and electron secondaries in all 100 GeV/c hA interactions. Also the momentum difference distribution, the positron distribution subtracted from the electron distribution, which is consistent with the expected δ-ray momentum distribution.

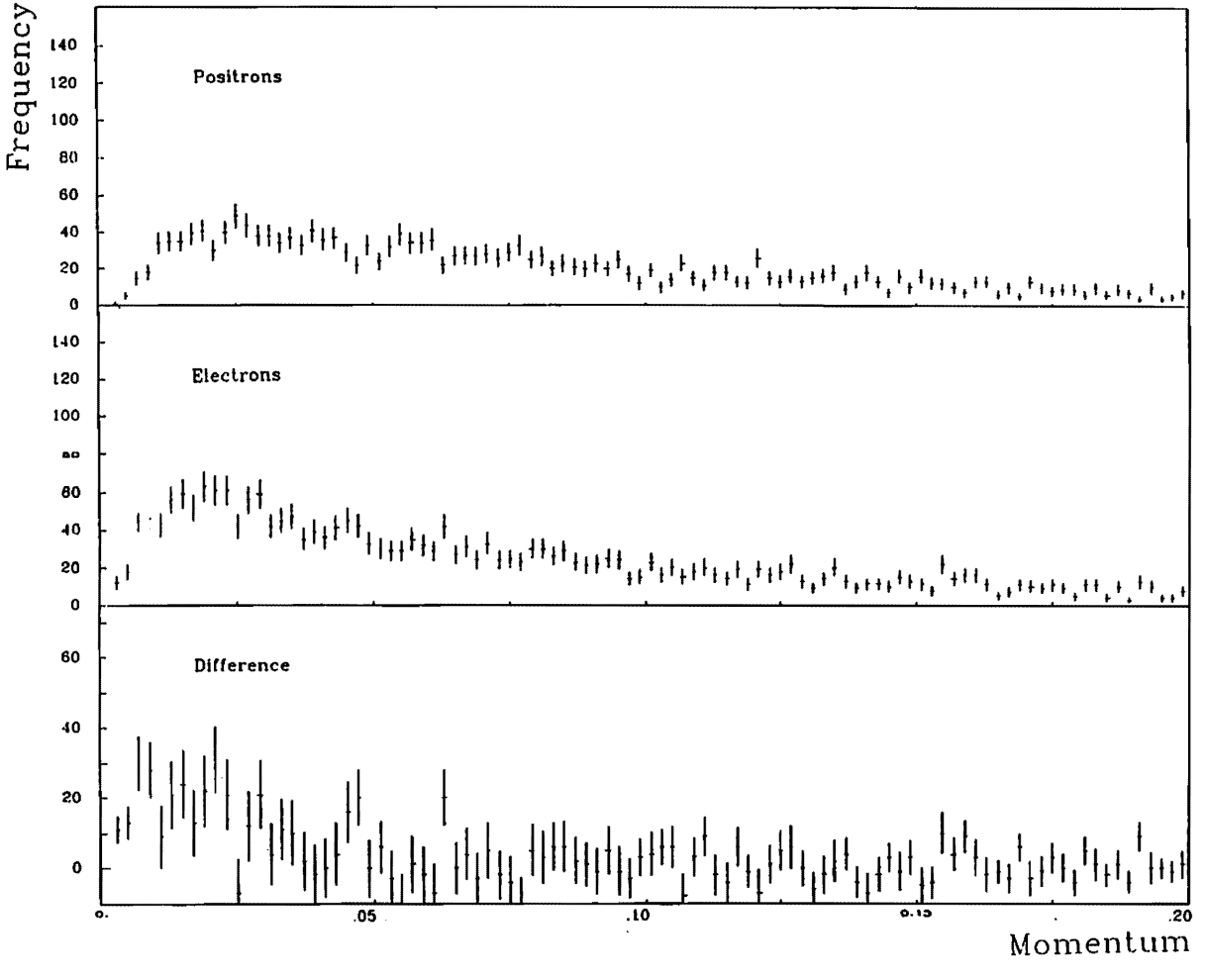

Total fast electron correction The total corrections due to misidentified fast electrons are simply the sums of e^+e^-- and δ-ray-based corrections

$$N_{e^-}^{correction} = -N_{\pi^-}^{correction} = N_{e^+e^-}^{mislabeled} + N_{\delta_{mislabeled}}$$

while the total correction due to misidentified fast positrons is just the e^+e^--based correction

$$N_{e^+}^{correction} = -N_{\pi^+}^{correction} = N_{e^+e^-}^{mislabeled}$$

The corrections increase electron(positron) multiplicities and reduce $\pi^-(\pi^+)$ and thus produced particle multiplicities. In **Table 2A.3.3**, the contributions to these corrections are tabulated and summed.

2A.3.2 Fast protons

A significant number of protons are produced with momenta too large for identificaton by ionization in the bubble chamber. Thus protons with momenta greater than 1.3 GeV/c were classified as default pions, contributing to the ambiguous particle multiplicities N_{a+} and N_{a-} and thus to the produced particle multiplicities N_{prod+} and N_{prod-}. Because the production and hadronization mechanisms for these protons are of so much more interest than slow evaporation protons, a correction for these fast protons should be found. This correction is based on CRISIS identification of fast protons in a momentum region of 4-100 GeV/c and on smoothly connecting the momentum distribution for protons identified in CRISIS with those identified in the BC.

CRISIS region CRISIS corrections are applied to the momentum region above 4 GeV/c up to the beam momentum. Collaborators at PSU have distinguished fast protons(pbars) from pions with momenta greater than 4 GeV/c using CRISIS of the DPI for all beams with efficiencies between 40 and 50%. At the time this correction was made, fast proton identification included only three(3) beams: p, π^-, and $\bar{p}$. Thus estimated corrections for only these beams are included.

Table 2A.3.3 Total fast electron corrections made on the basis of average measured positron and electron multiplicities $\langle N_{e+}\rangle$m and $\langle N_{e-}\rangle$m; average unmeasured positron and electron multiplicities $\langle N_{e+}\rangle$um and $\langle N_{e-}\rangle$um; and the calculated estimates $\langle N_{e+e-}\rangle$calc and $\langle N_{\delta}\rangle$calc of e^+e^- and δ-ray contamination, respectively.

THICK FOILS

Projectile	320GeV/c		100GeV/c									
	π^-		π^+		p		π^-			p		
$^{A}_{Z}Target$	$^{108}_{47}Ag$	$^{197}_{79}Au$	$^{108}_{47}Ag$	$^{197}_{79}Au$	$^{108}_{47}Ag$	$^{197}_{79}Au$	$^{24}_{12}Mg$	$^{108}_{47}Ag$	$^{197}_{79}Au$	$^{24}_{12}Mg$	$^{108}_{47}Ag$	$^{197}_{79}Au$
BTC	61	64	131	134	141	144	176	171	174	186	181	184
N_{events}	184	127	178	128	308	110	120	604	457	75	439	277
$\langle N_{e+}\rangle$m	.522	.504	.455	.547	.471	.691	.058	.505	.632	.067	.592	.744
Δ	.061	.078	.059	.085	.046	.096	.024	.034	.045	.029	.044	.065
$\langle N_{e+}\rangle$um	.049	.087	.045	.055	.062	.073	.008	.060	.092	.040	.112	.162
Δ	.018	.025	.016	.025	.016	.028	.008	.010	.015	.023	.020	.027
$\langle N_{e+e-}\rangle$calc	1.837	2.373	1.434	1.998	1.651	2.088	.361	1.444	1.875	.479	1.866	2.352
Δ	.049	.075	.045	.069	.037	.077	.016	.024	.035	.024	.034	.050
$\langle N_{e+}\rangle$corr	-1.266	-1.782	-.934	-1.396	-1.118	-1.324	-.295	-.879	-1.151	-.372	-1.162	-1.446
Δ	.080	.111	.076	.112	.061	.126	.030	.043	.059	.044	.059	.086
$\langle N_{e-}\rangle$m	.701	.772	.478	.555	.490	.800	.133	.601	.737	.133	.729	.881
Δ	.082	.097	.059	.081	.048	.092	.037	.038	.053	.039	.045	.073
$\langle N_{e-}\rangle$um	.076	.118	.079	.070	.101	.118	.008	.123	.133	-	.150	.162
Δ	.021	.048	.020	.023	.020	.038	.008	.015	.019	-	.021	.026
$\langle N_{e+e-}\rangle$calc	1.837	2.373	1.434	1.998	1.651	2.088	.361	1.444	1.875	.479	1.866	2.352
Δ	.049	.075	.045	.069	.037	.077	.016	.024	.035	.024	.034	.050
$\langle N_{\delta}\rangle$calc	.213	.193	.194	.160	.184	.143	.141	.174	.142	.166	.213	.188
Δ	.010	.014	.019	.014	.015	.008	.008	.006	.004	.009	.011	.013
$\langle N_{e-}\rangle$corr	-1.273	-1.676	-1.071	-1.533	-1.244	-1.313	-.361	-.894	-1.147	-.512	-1.200	-1.497
Δ	.098	.132	.079	.110	.066	.126	.042	.048	.066	.047	.061	.093

FASTECORR_THICK.TEX UND/MCKM 11Oct88

Table 2A.3.3 Continued.

THIN FOILS

Projectile	320GeV/c		100GeV/c									
	π^-		π^+		p		π^-			$\bar{p}$		
$^{A}_{Z}Target$	$^{108}_{47}Ag$	$^{197}_{79}Au$	$^{108}_{47}Ag$	$^{197}_{79}Au$	$^{108}_{47}Ag$	$^{197}_{79}Au$	$^{24}_{12}Mg$	$^{108}_{47}Ag$	$^{197}_{79}Au$	$^{24}_{12}Mg$	$^{108}_{47}Ag$	$^{197}_{79}Au$
BTC	62	63	132	133	142	143	175	172	173	185	182	183
N_{events}	137	135	124	112	169	129	224	406	403	181	276	280
$\langle N_{e+}\rangle$m	.219	.304	.258	.384	.231	.279	.054	.244	.293	.105	.236	.325
Δ	.043	.052	.052	.066	.037	.045	.015	.028	.029	.024	.033	.038
$\langle N_{e+}\rangle$um	.036	.037	.040	.036	.024	.023	.004	.057	.065	.006	.058	.061
Δ	.019	.016	.021	.022	.012	.013	.004	.012	.013	.005	.014	.017
$\langle N_{e+e-}\rangle$calc	.623	.954	.524	.739	.574	.679	.152	.522	.673	.183	.613	.788
Δ	.019	.028	.020	.029	.018	.024	.005	.011	.014	.006	.015	.018
$\langle N_{e+}\rangle$corr	-.368	-.613	-.226	-.319	-.319	-.377	-.094	-.221	-.315	-.072	-.319	-.402
Δ	.051	.061	.060	.075	.043	.053	.016	.032	.035	.025	.039	.045
$\langle N_{e-}\rangle$m	.321	.296	.298	.491	.260	.302	.094	.333	.404	.127	.290	.357
Δ	.056	.048	.058	.081	.043	.055	.021	.033	.039	.027	.032	.044
$\langle N_{e-}\rangle$um	.022	.059	.073	.027	.059	.031	.013	.071	.079	.033	.051	.082
Δ	.012	.023	.028	.015	.018	.019	.008	.016	.016	.013	.014	.016
$\langle N_{e+e-}\rangle$calc	.623	.954	.524	.739	.574	.679	.152	.522	.673	.183	.613	.788
Δ	.019	.028	.020	.029	.018	.024	.005	.011	.014	.006	.015	.018
$\langle N_{\delta}\rangle$calc	.071	.061	.063	.047	.062	.050	.044	.054	.046	.064	.063	.070
Δ	.004	.004	.009	.003	.008	.008	.002	.002	.002	.012	.010	.017
$\langle N_{e-}\rangle$corr	-.351	-.660	-.216	-.268	-.317	-.396	-.089	-.172	.236	-.087	-.335	-.419
Δ	.060	.060	.068	.087	.051	.063	.023	.038	.044	.033	.039	.053

FASTECORR_THIN.TEX UND/MCKM 11Oct88

1. Estimate the number of fast protons that would have been identified at 100% CRISIS efficiencies from 4 GeV/c up to the beam momentum using CRISIS efficiencies cited elsewhere [Whitmore 89]:
   $N_p^{fast} = \frac{N_p^{CRISIS\ id}}{eff_{CRISIS}^{p>4\ GeV/c}}$.

2. Check for charge bias in CRISIS by comparing $N_p^{CRISIS\ id} - N_{\bar{p}}^{CRISIS\ id}$ with $N_{a^+}^{no\ CRISIS\ id} - N_{a^-}^{no\ CRISIS\ id}$.

   For each of the interactions with CRISIS identification the total number $N_{p_{crisis}^{est}}$ of *fast* protons(pbars) is estimated at 100% efficiency in **Table 2A.3.4**. It is calculated by the number of *fast* protons(pbars) identified by CRISIS, $N_{p_{identified}^{CRISIS}}$, divided by its efficiency of about $60 \pm 5\%$.

   The additional net charge contributed to the $p+\bar{p}$ multiplicity beyond that which was actually CRISIS-identified, can be compared with the charge excess for all ambiguous particles CRISIS was unable to identify. In the p and $\bar{p}$ samples, the use of the efficiency to estimate the total proton and pbar contributions is consistent with the assumption that the charge excess in the ambiguous particles is attributable to unidentified protons and pbars. In the π^- beam samples, using the efficiency underestimates the charge excess in the ambiguous particles.

Intermediate-region Corrections CRISIS identification was feasible only for momenta greater than 4 GeV/c. That means an identification gap exists between 1.3 GeV/c where bubble chamber identification leaves off and 4 GeV/c where CRISIS identification picks up. Protons with momenta between 1.3 and 4 GeV/c are as a rule mislabeled π^+. But CRISIS efficiency did not plateau until 10 GeV, and the BC identification is most efficient below 1 GeV/c, so a correction should cover an even larger intermediate region extending from 1 GeV/c to 10 GeV/c. An estimate of this correction is outlined below in steps. **Table 2A.3.5** summarizes the resultant values.

1. Estimate number $N_p^{connecting\ p<1.3\ GeV/c\ to\ p>10\ GeV/c}$ of protons in the momentum gap between 1 and 10 GeV/c by

Table 2A.3.4 Estimates of the number of fast protons(pbars) among the ambiguous particles in the CRISIS momentum region: p > 4 GeV/c.

THICK FOILS

Projectile	320GeV/c		100GeV/c									
	π^-		π^+		p		π^-			$\bar{p}$		
$^{A}_{Z}$ Target	$^{108}_{47}Ag$	$^{197}_{79}Au$	$^{108}_{47}Ag$	$^{197}_{79}Au$	$^{108}_{47}Ag$	$^{197}_{79}Au$	$^{24}_{12}Mg$	$^{108}_{47}Ag$	$^{197}_{79}Au$	$^{24}_{12}Mg$	$^{108}_{47}Ag$	$^{197}_{79}Au$
BTC	61	64	131	134	141	144	176	171	174	186	181	184
N_{events}	184	127	178	128	308	110	120	604	457	75	439	277
$N_{p^{CRISIS}_{identified}}$					.237	.209		.060	.072		.034	.018
Δ					.026	.041		.010	.012		.009	.009
$N_{p^{CRISIS}_{estimate}}$					.395	.348		.100	.120		.057	.030
Δ					.043	.068		.017	.020		.015	.015
$N_{p^{CRISIS}_{identified}}$					.016	.018		.045	.039		.134	.181
Δ					.007	.013		.009	.010		.017	.024
$N_{p^{CRISIS}_{estimate}}$					.027	.030		.075	.065		.223	.302
Δ					.012	.022		.015	.017		.028	.040

CRISISID_THICK.TEX UND/MCKM 22Nov88

THIN FOILS

Projectile	320GeV/c		100GeV/c									
	π^-		π^+		p		π^-			$\bar{p}$		
$^{A}_{Z}$ Target	$^{108}_{47}Ag$	$^{197}_{79}Au$	$^{108}_{47}Ag$	$^{197}_{79}Au$	$^{108}_{47}Ag$	$^{197}_{79}Au$	$^{24}_{12}Mg$	$^{108}_{47}Ag$	$^{197}_{79}Au$	$^{24}_{12}Mg$	$^{108}_{47}Ag$	$^{197}_{79}Au$
BTC	62	63	132	133	142	143	175	172	173	185	182	183
N_{events}	137	135	124	112	169	129	224	406	403	181	276	280
$N_{p^{CRISIS}_{identified}}$					.278	.240		.101	.079		.033	.025
Δ					.037	.041		.015	.014		.012	.009
$N_{p^{CRISIS}_{estimate}}$					.463	.400		.168	.132		.055	.042
Δ					.062	.068		.025	.118		.122	.015
$N_{p^{CRISIS}_{identified}}$					.024	.023		.054	.035		.145	.189
Δ					.012	.013		.011	.009		.022	.024
$N_{p^{CRISIS}_{estimate}}$					.040	.038		.090	.058		.242	.315
Δ					.020	.022		.018	.015		.037	.040

CRISISID_THIN.TEX UND/MCKM 22Nov88

Table 2A.3.5 Estimates of the average number of fast protons(pbars) $\langle N_{p_{int}}\rangle$corr($\langle N_{p_{int}}\rangle$corr) among ambiguous particles essentially outside the BC and CRISIS momentum regions, *i.e* the *intermediate* momentum region: 1 GeV/c < p < 10 GeV/c. Corrections are made in terms of $\langle N_{p_{int}}\rangle$est($\langle N_{\bar{p}_{int}}\rangle$est), the number of protons(antiprotons) expected in the region, and $\langle N_{p_{crid;int}}\rangle$($\langle N_{\bar{p}_{crid;int}}\rangle$), the number detected in CRISIS. The charge excess $\langle I_{a_{crid:int}}\rangle$ of particles remaining ambiguous after CRISIS identification attempts is compared to the charge excess estimated by $\langle N_{p_{int}}\rangle$corr and $\langle N_{p_{int}}\rangle$corr, and pion beam charge $\pi bmch$, and the charge excess $\langle I_{surp}\rangle$ of identified protons(pbars).

THICK FOILS

Projectile	320GeV/c				100GeV/c							
	π^-		π^+		p		π^-			$\bar{p}$		
$^{A}_{Z}$ Target	$^{108}_{47}Ag$	$^{197}_{79}Au$	$^{108}_{47}Ag$	$^{197}_{79}Au$	$^{108}_{47}Ag$	$^{197}_{79}Au$	$^{24}_{12}Mg$	$^{108}_{47}Ag$	$^{197}_{79}Au$	$^{24}_{12}Mg$	$^{108}_{47}Ag$	$^{197}_{79}Au$
BTC	61	64	131	134	141	144	176	171	174	180	181	184
N_{events}	184	127	178	128	308	110	120	604	457	75	139	277
$\langle N_{p_{int}}\rangle^{est}$					1.506	1.681		1.305	1.420		.866	1.096
$\langle N_{p_{crid:int}}\rangle$					.399	.482		.346	.387		.497	.527
$\langle N_{p_{int}}\rangle^{corr}$					1.107	1.199		.959	1.033		.369	.571
$\langle N_{p_{int}}\rangle^{est}$					.018	.018		.014	.022		.037	.056
$\langle N_{p_{crid:int}}\rangle$					.003	.009		.008	-		-	.029
$\langle N_{p_{int}}\rangle^{corr}_{\Delta}$					.015	.009		.006	.022		.037	.029
$\langle N_{p_{int}}\rangle^{corr}$ $\cdot\langle N_{p_{int}}\rangle^{corr}$ $\cdot\pi bmch + I_{surp}$					1.135	1.126		.154	.415		.250	.317
$\langle I_{a_{crid:int}}\rangle$					.071	1.100		.242	.444		.206	.317

Table 2A.3.5 Continued.

THIN FOILS

Projectile	320GeV/c		100GeV/c									
	π^-		π^+		p		π^-			p		
$^{A}_{Z}Target$	$^{108}_{47}Ag$	$^{197}_{79}Au$	$^{108}_{47}Ag$	$^{197}_{79}Au$	$^{108}_{47}Ag$	$^{197}_{79}Au$	$^{24}_{12}Mg$	$^{108}_{47}Ag$	$^{197}_{79}Au$	$^{24}_{12}Mg$	$^{108}_{47}Ag$	$^{197}_{79}Au$
BTC	62	63	132	133	142	143	175	172	173	185	182	183
N_{events}	137	135	124	112	169	129	224	406	403	181	276	280
$\langle N_{p_{int}} \rangle_{est}$					1.506	1.081		1.305	1.420		.866	1.098
$\langle N_{p_{cerid:int}} \rangle$					.420	.305		.406	.429		.420	.431
$\langle N_{p_{int}} \rangle_{corr}$					1.080	1.286		.899	.991		.446	.667
$\langle N_{p_{int}} \rangle_{est}$					.018	.032		.031	.015		.026	.040
$\langle N_{p_{cerid:int}} \rangle$						.023		.007	-		-	.004
$\langle N_{p_{int}} \rangle_{corr}$					.018	.009		.024	.015		.026	.045
$\langle N_{p_{int}} \rangle_{corr}$ $-\langle N_{p_{int}} \rangle_{corr}$ $-\pi_{bmch}+I_{surp}$					.992	1.226		.344	.400		.407	.431
$\langle I_{a_{cerid:int}} \rangle$					1.030	1.178		.268	.462		.388	.468

(a) adjusting the CRISIS distributions for efficiencies $P_p^{adj\ CRISIS} = \frac{p_p^{CRISIS}}{eff_{CRISIS}}$

(b) smoothly connecting the .1-1.3 GeV/c region (BC identification) and the 10-100 GeV/c region (CRISIS identification) in an 'eyeball' approximation favoring regions of greatest efficiency (10-100 GeV/c and .1-1.0 GeV/c) in **Figure 2A.3.2**

(c) estimating the average number of fast protons in the 1-10 GeV/c region by determining the area under the curve connecting the BC and CRISIS regions

2. Calculate the correction term $N_p^{no\ BC/CRISIS}$ due to protons missed by BC and CRISIS identification in the intermediate region:
$N_p^{no\ BC/CRISIS} = N_p^{connecting\ p<1.3\ GeV/c\ to\ p>10\ GeV/c} - N_p^{CRISIS 4\ GeV/c<p<10\ GeV/c}$

3. Verify that this correction accounts for net charge excesses $I = N_{\pi^+}^m - N_{\pi^-}^m + N_p^m - N_{\bar{p}}^m + N_p^{CRISIS\ id} - N_{\bar{p}}^{CRISIS\ id}$ by comparing with the ambiguous net charge excess $I^{ambiguous} = N_{a^+}^{no\ CRISIS\ id} - N_{a^-}^{no\ CRISIS\ id}$

Table 2A.3.5 compares the measured net charge (including the known pion beam charge where necessary as well as the leftover charge excess from the CRISIS estimate) with the net charge of the ambiguous particles which could not be identified by CRISIS in the 1-10 GeV/c momentum region. Essentially all the excess charge among the ambiguous particles has been accounted for. Assuming that positive net charge is primarily attributable to misidentified protons and pbars , a hand drawn momentum-based estimate and a net charge-calculated estimate are consistent with one another.

(Note that particles are initially designated *ambiguous* when their track momenta are greater than 1.3 GeV/c. When, the momentum is less than 4 GeV/c, there is no chance of losing this ambiguity by using CRISIS information. Thus the intermediate region particles contribute to the net charge of ambiguous particles which remain ambiguous after an attempt has been made to identify them with CRISIS information.)

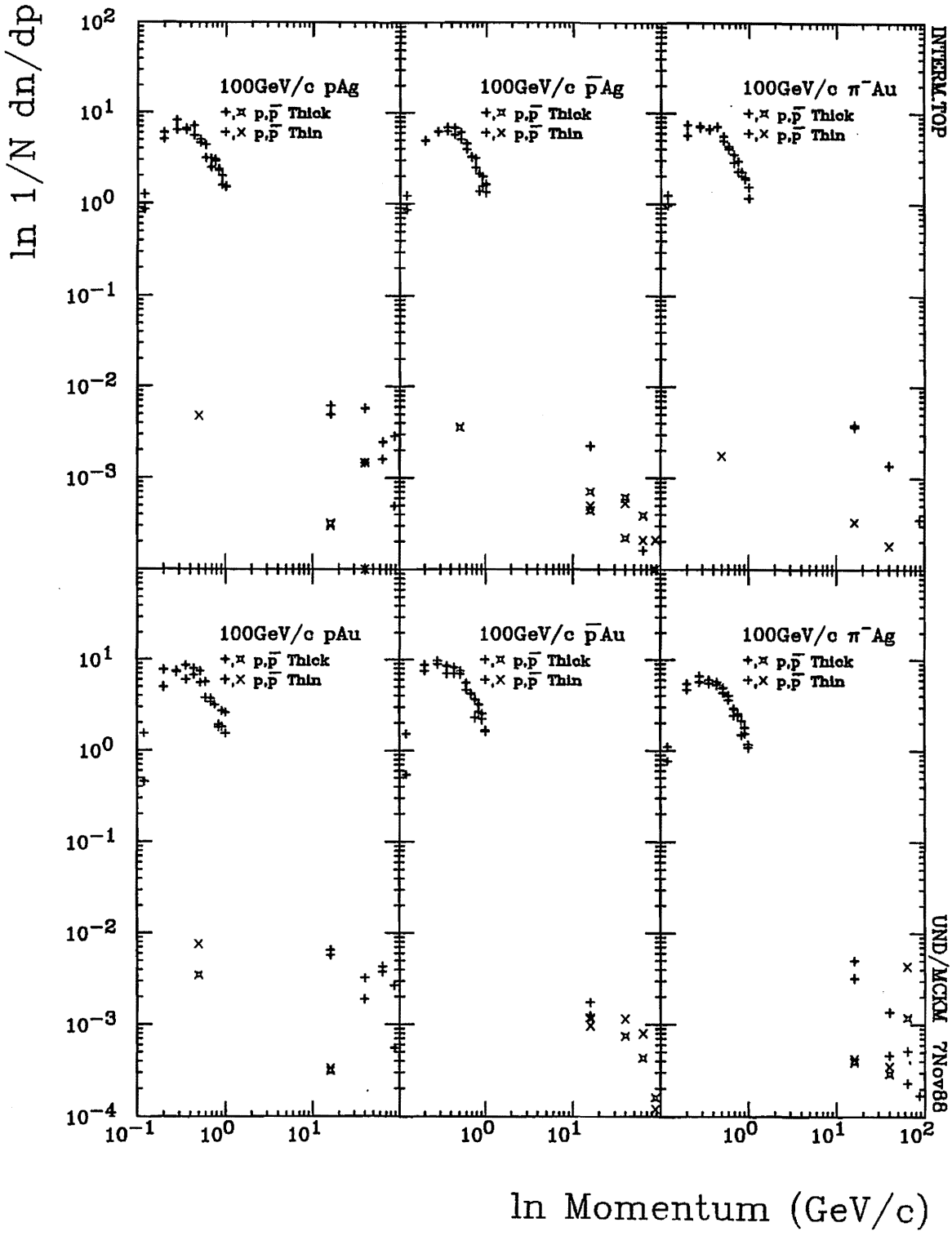

Figure 2A.3.2 Momentum distribution of protons(pbars) for the purpose of connecting the CRISIS region with the BC region to estimate the corrections for the *intermediate* region which is not observable with the DPI.

Total fast proton corrections

1. Find the total number of fast protons(antiprotons) in the CRISIS and intermediate momentum regions:

$$N_p^{fast} = N_p^{connecting\ p<1\ to\ p>10GeV/c} + N_p^{adj\ CRISIS\ p>10GeV/c}$$
$$N_{\bar{p}}^{fast} = N_{\bar{p}}^{connecting\ p<1\ to\ p>10GeV/c} + N_{\bar{p}}^{adj\ CRISIS\ p>10GeV/c}$$

2. Determine the fast proton correction by subtracting out CRISIS identified proton multiplicity: $N_p^{correction} = N_p^{fast} - N_p^{m\ p>1GeV/c} - N_p^{id\ CRISIS}$

3. Compare the previous correction with total fast proton correction estimated from maximum net charge:

   (a) Defining β_p as the minimum velocity for which protons are identified in CRISIS

   (b) Plotting the net produced particle charge

$$\langle N_{prod^+} - N_{prod^-} + N_p^{\beta<\beta_p} - N_{\bar{p}}^{\beta<\beta_p}$$

   as a function of β_p

   (c) Determining the charge excess smoothly approached as faster and faster protons are excluded. This minimum excess charge probably accounts for unidentified proton and pion beam charge. $N_p^{unidentified} \approx I_{min}$

Table 2A.3.6 summarizes the corrections for all the interactions under study. These corrections are consistent with estimates of the total fast proton and pbar corrections based on net charge of produced particles with $\beta < \beta_p$. Overall net excess positive charge increases with A, suggesting that it is primarily due to nuclear breakup or multiple collisions, in any case target-dependent processes. That excess smoothly approaches a minimum as faster and faster identified protons are taken out, ie. as the maximum identified proton momentum increases. This is well illustrated in **Figure 2A.3.3** which displays $\langle N_+ + N_- + N_{p_{\beta<\beta_p}} - N_{\bar{p}_{\beta<\beta_p}} \rangle$ or the net produced particle charge as a function of β_p, the relative velocity limit up to which protons are

Table 2A.3.6 Average total fast proton(pbar) corrections $\langle N_p \rangle$ and $\langle N_{\bar{p}} \rangle$ based on the overlap of BC and DPI identified particles $\langle N_{p_{bcid:cr}} \rangle$, CRISIS efficiency eff_{cr}^{+}, and the intermediate region corrections $\langle N_{p_{int}} \rangle$ and $\langle N_{\bar{p}_{int}} \rangle$.

THICK FOILS

Projectile	320GeV/c		100GeV/c									
	π^-		π^+		p		π^-			$\bar{p}$		
$\frac{A}{Z}$ Target	$^{108}_{47}Ag$	$^{197}_{79}Au$	$^{108}_{47}Ag$	$^{197}_{79}Au$	$^{108}_{47}Ag$	$^{197}_{79}Au$	$^{24}_{12}Mg$	$^{108}_{47}Ag$	$^{197}_{79}Au$	$^{24}_{12}Mg$	$^{108}_{47}Ag$	$^{197}_{79}Au$
BTC	61	64	131	134	141	144	176	171	174	186	181	184
N_{events}	184	127	178	128	308	110	120	604	457	75	439	277
$\langle N_{p_{crest}} \rangle$					.395	.348		.100	.120		.057	.030
Δ					.043	.068		.017	.020		.015	.015
$-\frac{\langle N_{p_{bcid:cr}} \rangle m}{eff_{cr}^{+}}$					-.017	-.060		-.013	-.022		-.012	-.007
Δ					.007	.037		.007	.022		.007	.007
$\langle N_{p_{int}} \rangle$corr					1.107	1.199		.959	1.033		.369	.571
Δ												
$\langle N_p \rangle$corr					1.485	1.487		1.046	1.131		.414	.594
Δ												
$\langle N_{\bar{p}_{crest}} \rangle$					.027	.030		.075	.065		.223	.302
Δ					.012	.022		.015	.017		.028	.040
$-\frac{\langle N_{\bar{p}_{bcid:cr}} \rangle m}{eff_{cr}^{-}}$					-	-		-	-		-	.004
Δ					-	-		-	-		-	.004
$\langle N_{\bar{p}_{int}} \rangle$corr					.015	.009		.006	.022		.037	.029
Δ												
$\langle N_{\bar{p}} \rangle$corr					.042	.039		.081	.087		.260	.330
Δ												

FASTPCORR_THICK.TEX UND/MICKM 22Nov88

Table 2A.3.6 Continued.

THIN FOILS

Projectile	320GeV/c		100GeV/c									
	π^-		π^+		p		π^-			p		
$\frac{A}{Z}$ Target	$^{108}_{47}Ag$	$^{197}_{79}Au$	$^{108}_{47}Ag$	$^{197}_{79}Au$	$^{108}_{47}Ag$	$^{197}_{79}Au$	$^{24}_{12}Mg$	$^{108}_{47}Ag$	$^{197}_{79}Au$	$^{24}_{12}Mg$	$^{108}_{47}Ag$	$^{197}_{79}Au$
BTC	62	63	132	133	142	143	175	172	173	185	182	183
N_{events}	137	135	124	112	169	129	224	406	403	181	276	280
$\langle N_{p_{crest}} \rangle$					.463	.400		.168	.132		.055	.042
Δ					.062	.068		.025	.118		.122	.015
$-\frac{\langle N_{p_{bkid:cr}} \rangle^m}{eff^+_{cr}}$					-.020	-.027		-.025	-.042		-.018	-.018
Δ					.013	.018		.010	.015		.010	.010
$\langle N_{p_{int}} \rangle_{corr}$					1.080	1.286		.899	.991		.446	.667
Δ												
$\langle N_p \rangle_{corr}$					1.523	1.659		1.042	1.081		.483	.691
Δ												
$\langle N_{\bar{p}_{crest}} \rangle$					.040	.038		.090	.058		.242	.315
Δ					.020	.022		.018	.015		.037	.040
$-\frac{\langle N_{\bar{p}_{bkid:cr}} \rangle^m}{eff^-_{cr}}$					-	-		-	-		-	-
Δ					-	-		-	-		-	-
$\langle N_{\bar{p}_{int}} \rangle_{corr}$					.018	.009		.024	.015		.026	.045
Δ												
$\langle N_{\bar{p}} \rangle_{corr}$					.058	.047		.114	.073		.268	.360
Δ												

FASTPCORR_THIN.TEX UND/MCKM 22Nov88

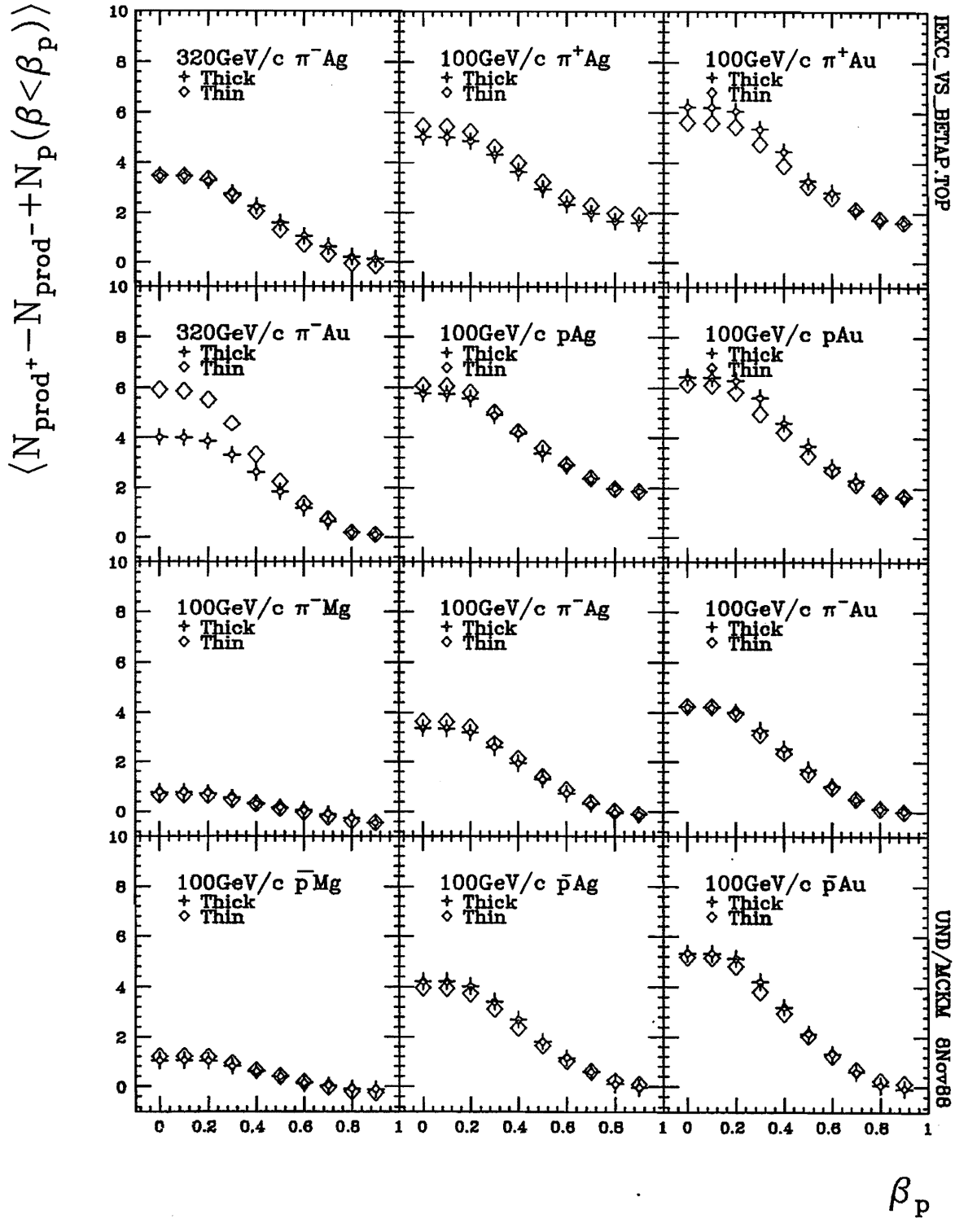

Figure 2A.3.3 Produced particle excess charge plus the multiplicity of protons at relative velocities less than β_p as a function of β_p. The minima are reasonable estimates of the unidentified proton multiplicity.

identified and beyond which protons are counted into the produced particle multiplicity. The minimum net or excess charge is reasonably associated with protons that were not identified. Since the pion beam charge is not taken into account, the pion beam charge must be subtracted off before this minimum net charge can be compared with the net charge of the fast proton and pbar corrections. When these adjustments are made, excellent agreement is found.

2A.4 SECONDARY STRONG INTERACTIONS

In the finite thickness of foil targets, primary interaction products undergo subsequent strong interactions with small but non-negligible probability. The produced particles from these secondary interactions become confused with those from the primary interaction. In the measurement process, all measured tracks, other than those with visible secondary interaction points, are presumed to emanate from a primary interaction. A certain fraction F_j^{sec} of the produced j-type tracks observed, however, is associated with secondary strong interactions. Only the remaining fraction F_j^{bm} is associated with the primary-induced strong interactions of interest. This fraction is the ratio

$$F_j^{bm} = \frac{\langle N_j^{bm} \rangle}{\langle N_j^{m+um} \rangle}$$

where $\langle N_j^{bm} \rangle$ is the primary-induced, j-type multiplicity and $\langle N_j^{m+um} \rangle$ is the experimentally observed, average j-type multiplicity including both measured and unmeasured tracks. An estimate of this fraction is outlined in the following steps.

With the probability σ_i that an i-type primary interaction product undergoes an interaction as it traverses one-half the target thickness, $\sigma_i \langle N_i^{bm} \rangle$ is the average number of secondary interactions attributable to i-type primary interaction products, and $\sum_i \sigma_i \langle N_i^{bm} \rangle$ is the average number of secondary interactions attributable to all types primary products. However, since both σ_i and $\langle N_i^{bm} \rangle$ are angle and momentum dependent, either an averaging or a Monte Carlo approach must be introduced to implement the final form of this estimate. An averaging approach uses an average σ_i taken over all i-type, primary-induced tracks, while a Monte Carlo method sums track by track contributions to the ratio. For simplicity, it is assumed that the

averages taken over observed tracks will not differ significantly from averages over only primary-induced tracks. Both approaches have been taken using the *cleanest* track criteria to avoid momentum error distortions.

A final form for the estimate is reached by noting that
$\langle N_j^{sec} \rangle$ = (# secondary interactions) (secondary interaction j-type multiplicity).
But to first order, each secondary interaction is assumed to produce multiplicity distributions comparable to those for primary interactions at the same energy. Thus the multiplicity of j-type particles emanating from secondary interactions is

$$\langle N_j^{sec} \rangle = (\underbrace{\sum_i \sigma_i \langle N_i^{bm} \rangle}_{\#sec\ interactions})\langle N_j^{bm} \rangle$$

Since any experimentally determined j-type multiplicity $\langle N_j^{m+um} \rangle$ can be expressed as the sum of primary and secondary interaction products with an adjustment for the number of secondary interactions which reduce the number of primary interaction products observed,

$$\langle N_j^{m+um} \rangle = \langle N_j^{bm} \rangle - \sigma_j \langle N_j^{bm} \rangle + \langle N_j^{sec} \rangle = \langle N_j^{bm} \rangle - \sigma_j \langle N_j^{bm} \rangle + \sum_i \sigma_i \langle N_i^{bm} \rangle \langle N_j^{bm} \rangle$$

This makes it possible to estimate the primary portion of any average multiplicity with the relatively simple relation

$$F_j^{bm} = \frac{\langle N_j^{bm} \rangle}{\langle N_j^{m+um} \rangle} = \frac{1}{1 - \sigma_j + \sum_i \sigma_i \langle N_i^{bm} \rangle}$$

The probability σ_j that a j-type product of a primary interaction will sustain a secondary interaction at given angle and momentum is calculated by

$$\sigma_j = \frac{\lambda}{L_{interaction}} = \frac{\lambda}{\frac{A}{N_A \sigma_o A^\alpha}} = \lambda N_A \sigma_o A^{\alpha-1} = (\frac{\rho(.5t)}{cos\theta}) N_A \sigma_o A^{\alpha-1}$$

where λ is the surface density, L is the interaction length, σ_o and α are cross-section parameters interpolated from [Carroll 79], and t is the target thickness. The average σ_j is about 1%.

The factor $\langle N_i^{bm} \rangle$ is also momentum dependent. Thus E597 event averages cannot be used. Instead, an indirect estimate must be made employing hA:hp multiplicity ratios with empirical momentum relations for hp multiplicities as a function of

momentum [Meijers 87]. For hp multiplicities, only two relations are used, dividing secondary interactions into only meson and baryon categories:

$$\langle N_{ch}\rangle_{\pi^- p} = \langle N_{ch}\rangle_{\pi^+ p} = 2.53 + .71 \ln \sqrt{s} + .485 \ln^2 \sqrt{s}$$

$$\langle N_{ch}\rangle_{\bar{p}p} = \langle N_{ch}\rangle_{pp} = 2.44 + .35 \ln \sqrt{s} + .612 \ln^2 \sqrt{s}$$

Having determined average hp multiplicities for the j particle type distributions of track momenta, the ratios $R_{\pi^\pm} = \frac{\langle N_{ch}\rangle_{\pi^\pm A}}{\langle N_{ch}\rangle_{\pi p}}$, $R_p = \frac{\langle N_{ch}\rangle_{pA}}{\langle N_{ch}\rangle_{pp}}$, and $R_{\bar{p}} = \frac{\langle N_{ch}\rangle_{\bar{p}A}}{\langle N_{ch}\rangle_{\bar{p}p}}$ are calculated for A = 24, 108, and 197 at 100 and 360 GeV/c. These ratios in principle vary with momentum but probably do not vary much more than .3 [Fredriksson 84]. For purposes of this estimate, R is assumed constant:

$$\langle N_j^{bm}\rangle_{hA} = R_{hA} \langle N_j^{bm}\rangle_{hp}$$

Values for average $\sigma_j \langle N_j^{bm}\rangle$ are shown in **Table 2A.4.1.** ranging between .02 and .10 secondary products per primary product. Since the average track's probability of sustaining a secondary interaction is about 1%, an average primary product produces between 2 and 10 secondary interaction products if and when it sustains a secondary interaction.

Between 91 and 98% of the observed produced tracks are estimated to emanate from primary interactions.

2A.5 CORRECTED MULTIPLICITIES

In **Table 2A.5.1** corrected multiplicities for protons are presented. Corrections include unmeasured protons multiplicities $\langle N_p\rangle$um, angular depeletion corrections $\langle N_{cos\theta}\rangle$, CRISIS momentum range corrections $\langle N_{crisp}\rangle$, and intermediate momentum range corrections $\langle N_{int}\rangle$. The designations *black*, *grey*, and *shower* correspond to β in the ranges .15-.30 (.15 is a de facto experimental minimum, not an imposed cutoff), .30-.70, and .70-.83, respectively. Unmeasured but identified protons are assumed to be *black*. The designation *heavy* corresponds to the union of *black* and *grey*; *light*, to the union of *grey* and *shower* . The designations *forward* and *backward* are with respect to the lab reference frame. The number of *evaporation* protons is estimated

Table 2A.4.1 Estimates of secondary interaction contributions to multiplicity based on Monte Carlo estimates of primary and secondary charged particle frequencies $n_{ch;MC}prim$ and $n_{ch;MC}sec$, the resultant Monte Carlo fractions $F_{prim;MC}$ and $F_{sec;MC}$ of multiplicities which are primary and secondary interaction induced, corresponding estimates in an analytical approach F_{prim} and F_{sec}, and the average number of secondary interactions attributable to primary interactions $\sigma_j\langle N_j^{bm}\rangle$ producing j-type products.

THICK FOILS

Projectile	320GeV/c		100GeV/c									
	π^-		π^+		p		π^-			p		
$^A_Z Target$	$^{108}_{47}Ag$	$^{197}_{79}Au$	$^{108}_{47}Ag$	$^{197}_{79}Au$	$^{108}_{47}Ag$	$^{197}_{79}Au$	$^{24}_{12}Mg$	$^{108}_{47}Ag$	$^{197}_{79}Au$	$^{24}_{12}Mg$	$^{108}_{47}Ag$	$^{197}_{79}Au$
BTC	61	64	131	134	141	144	176	171	174	186	181	184
N_{events}	184	127	178	128	308	110	120	604	457	75	439	277
$n_{ch;MCsec}$	1280	849	975	781	2025	679	503	3439	2521	397	3132	1878
$n_{ch;MCprim}$	30776	23001	23941	20413	45705	17700	10951	82491	68278	8089	73150	52307
$F_{prim;MC}$	.960	.964	.961	.963	.958	.963	.956	.960	.964	.953	.959	.965
$F_{sec;MC}$	.040	.036	.039	.037	.042	.037	.044	.040	.036	.047	.041	.035
$\sigma_i\langle N_i^{bm}\rangle$	.0426	.0364	.0420	.0366	.0411	.0372	.0377	.0416	.0361	.0378	.0407	.0363
F_{prim}	.961	.966	.961	.966	.962	.965	.965	.961	.966	.965	.962	.966
F_{sec}	.039	.034	.039	.034	.038	.035	.035	.039	.034	.035	.038	.034

SECINT_THICK.TEX UND/MCKM 1Feb89

THIN FOILS

Projectile	320GeV/c		100GeV/c									
	π^-		π^+		p		π^-			p		
$^A_Z Target$	$^{108}_{47}Ag$	$^{197}_{79}Au$	$^{108}_{47}Ag$	$^{197}_{79}Au$	$^{108}_{47}Ag$	$^{197}_{79}Au$	$^{24}_{12}Mg$	$^{108}_{47}Ag$	$^{197}_{79}Au$	$^{24}_{12}Mg$	$^{108}_{47}Ag$	$^{197}_{79}Au$
BTC	62	63	132	133	142	143	175	172	173	185	182	183
N_{events}	137	135	124	112	169	129	224	406	403	181	276	280
$n_{ch;MCsec}$	302	369	277	208	404	198	238	819	702	274	527	593
$n_{ch;MCprim}$	23089	26470	42868	15554	24999	18981	19977	52615	54722	18509	39889	44318
$F_{prim;MC}$	.987	.986	.983	.987	.984	.990	.988	.985	.987	.985	.987	.987
$F_{sec;MC}$	.013	.014	.017	.013	.016	.010	.012	.015	.013	.015	.013	.013
$\sigma_i\langle N_i^{bm}\rangle$	.0160	.0133	.0155	.0131	.0161	.0130	.0130	.0160	.0127	.0131	.0155	.0127
F_{prim}	.985	.987	.985	.987	.984	.987	.987	.985	.988	.987	.985	.988
F_{sec}	.015	.013	.015	.013	.016	.013	.013	.015	.012	.013	.015	.012

SECINT_THIN.TEX UND/MCKM 1Feb89

Table 2A.5.1 Summary of corrected proton multiplicities. These include corrections made on measured (m) and unmeasured (um) multiplicities of *black*, *grey*, and *shower* protons as well as *light* and *heavy* multiplicities. Corrections are based on estimated angular depletions $\langle N_p \rangle cos\theta$, fast proton multiplicities $\langle N_p \rangle$corr, and estimates of primary ($\langle N_p \rangle$prim) and secondary ($\langle N_p \rangle$sec) contributions.

THICK FOILS

Projectile	320GeV/c		100GeV/c									
	π^-		π^+		p		π^-			p		
$^{A}_{Z}$Target	$^{108}_{47}Ag$	$^{197}_{79}Au$	$^{108}_{47}Ag$	$^{197}_{79}Au$	$^{108}_{47}Ag$	$^{197}_{79}Au$	$^{24}_{12}Mg$	$^{108}_{47}Ag$	$^{197}_{79}Au$	$^{24}_{12}Mg$	$^{108}_{47}Ag$	$^{197}_{79}Au$
BTC	61	64	131	134	141	144	176	171	174	186	181	184
N_{events}	184	127	178	128	308	110	120	604	457	75	439	277
$\langle N_{p_{black}} \rangle$m	.679	.717	.713	.883	.844	.818	.225	.767	.923	.227	.811	1.126
Δ	.083	.103	.081	.131	.071	.113	.045	.047	.064	.052	.054	.100
$\langle N_{p_{black}} \rangle$um	.223	.425	.247	.438	.299	.509	.092	.339	.602	.173	.355	.740
Δ	.038	.084	.048	.078	.042	.087	.029	.031	.057	.066	.036	.077
$\langle N_p \rangle cos\theta$	.054	.142	.135	.172	.234	.182	.033	.126	.193	.027	.050	.383
Δ												
$\langle N_{p_{black}} \rangle$final	.956	1.284	1.095	1.493	1.377	1.509	.350	1.232	1.718	.427	1.216	2.249
$\langle N_{p_{grey}} \rangle$m	2.147	2.654	2.332	3.117	2.565	3.318	.658	2.303	2.805	.773	2.822	3.614
Δ	.189	.336	.186	.341	.158	.376	.082	.112	.164	.122	.148	.237
$\langle N_{p_{shower}} \rangle$m	.495	.520	.365	.586	.474	.664	.208	.404	.460	.147	.579	.614
Δ	.062	.096	.049	.086	.046	.090	.047	.030	.037	.041	.044	.060
$\langle N_p \rangle$corr					1.485	1.487		1.046	1.131		.414	.594
$\langle N_{p_{shower}} \rangle$final					1.959	2.151		1.450	1.591		.993	1.208
$\langle N_{p_{heavy}} \rangle$final	3.103	3.938	3.427	4.610	3.942	4.827	1.008	3.535	4.523	1.200	4.038	5.863
$\langle N_{p_{light}} \rangle$final	2.642	3.174	2.697	3.703	5.141	5.975	.866	3.931	4.585	.920	3.917	4.883
$\langle N_p \rangle$m	3.353	3.929	3.472	4.633	3.935	4.882	1.092	3.507	4.245	1.173	4.276	5.426
Δ	.276	.467	.261	.505	.230	.501	.117	.160	.230	.148	.209	.356
$\langle N_{p_{black}} \rangle$um	.223	.425	.247	.438	.299	.509	.092	.339	.602	.173	.355	.740
Δ	.038	.084	.048	.078	.042	.087	.029	.031	.057	.066	.036	.077
$\langle N_p \rangle cos\theta$	.054	.142	.135	.172	.234	.182	.033	.126	.193	.027	.050	.383
$\langle N_p \rangle$subfinal	3.630	4.496	3.854	5.243	4.468	5.573	1.217	3.972	5.040	1.373	4.681	6.549
Δ												
$\langle N_p \rangle$corr					1.485	1.487		1.046	1.131		.414	.594
$\langle N_p \rangle$final					5.953	7.060		5.018	6.171		5.095	7.143
$\langle N_p \rangle$prim					5.727	6.813		4.822	5.961		4.901	6.900
$\langle N_p \rangle$sec					.226	.247		.196	.210		.194	.243

P_MULTI.TEX UND/MCKM 2Feb89

Table 2A.5.1 Continued.

THIN FOILS

Projectile	320GeV/c		100GeV/c									
	π^-		π^+		p		π^-			p		
$\frac{1}{Z}$ Target	$^{108}_{47}Ag$	$^{197}_{79}Au$	$^{108}_{47}Ag$	$^{197}_{79}Au$	$^{108}_{47}Ag$	$^{197}_{79}Au$	$^{24}_{12}Mg$	$^{108}_{47}Ag$	$^{197}_{79}Au$	$^{24}_{12}Mg$	$^{108}_{47}Ag$	$^{197}_{79}Au$
BTC	62	63	132	133	142	143	175	172	173	185	182	183
N_{events}	137	138	124	112	169	129	224	406	403	181	276	280
$\langle N_{p_{black}}\rangle$m	.774	1.356	.863	.866	1.059	1.171	.192	.909	1.122	.276	.855	1.371
Δ	.105	.152	.114	.125	.104	.150	.030	.065	.083	.041	.074	.112
$\langle N_{p_{black}}\rangle$um	.467	.726	.282	.571	.497	.705	.183	.542	.824	.171	.598	.882
Δ	.081	.101	.058	.093	.068	.141	.039	.049	.068	.036	.063	.083
$\langle N_p\rangle$cosθ	.204	.356	.177	.214	.237	.388	-	.133	.169	.033	.232	.400
Δ												
$\langle N_{p_{black}}\rangle$final	1.445	2.438	1.322	1.651	1.793	2.264	.375	1.584	2.115	.480	1.685	2.653
$\langle N_{p_{grey}}\rangle$m	2.365	3.837	2.315	2.598	2.651	2.806	.701	2.382	2.615	.967	2.511	3.118
Δ	.235	.423	.240	.302	.224	.317	.069	.141	.169	.101	.189	.224
$\langle N_{p_{shower}}\rangle$m	.460	.622	.339	.491	.515	.481	.228	.458	.506	.204	.486	.525
Δ	.066	.079	.062	.086	.059	.078	.031	.040	.046	.038	.050	.054
$\langle N_p\rangle$corr					1.523	1.659		1.042	1.081		.483	.691
$\langle N_{p_{shower}}\rangle$final					2.038	2.140		1.500	1.587		.969	1.216
$\langle N_{p_{heavy}}\rangle$final	3.810	6.275	3.637	4.249	4.444	5.070	1.076	3.966	4.730	1.447	4.196	5.771
$\langle N_{p_{light}}\rangle$final	2.825	4.459	2.654	3.089	5.314	5.510	.929	4.153	4.387	1.171	3.576	4.382
$\langle N_p\rangle$m	3.642	5.867	3.573	4.027	4.278	4.504	1.129	3.808	4.315	1.459	3.906	5.082
Δ	.349	.571	.366	.462	.318	.494	.095	.215	.265	.136	.270	.347
$\langle N_{p_{black}}\rangle$um	.467	.726	.282	.571	.497	.705	.183	.542	.824	.171	.598	.882
Δ	.081	.101	.058	.093	.068	.141	.039	.049	.068	.036	.063	.083
$\langle N_p\rangle$cosθ	.204	.356	.177	.214	.237	.388	-	.133	.169	.033	.232	.400
$\langle N_p\rangle$subfinal	4.313	6.949	4.032	4.812	5.012	5.597	1.312	4.483	5.308	1.663	4.736	6.364
$\langle N_p\rangle$corr					1.523	1.659		1.042	1.081		.483	.691
$\langle N_p\rangle$final					6.535	7.256		5.525	6.389		5.219	7.055
$\langle N_p\rangle$prim					6.430	7.162		5.442	6.312		5.141	6.970
$\langle N_p\rangle$sec					.105	.094		.083	.077		.078	.085

by twice the backward, and the number of *recoil* protons by the difference between the total number of protons and the number of evaporation protons.

In **Tables 2A.5.2** and **2A.5.3** corrected multiplicities for positive and negative produced particles are presented. *Produced* means all particles NOT identified (by measurement or by default) to be protons or electrons. Corrections are made for unmeasured ambiguous and electron multiplicities $\langle N_{a\pm}\rangle$um and $\langle N_{e\pm}\rangle$um, unidentified fast electrons $\langle N_{e+}\rangle$corr and $\langle N_{e-}\rangle$corr, unidentified fast protons and anti-protons $\langle N_p\rangle$corr and $\langle N_{\bar{p}}\rangle$corr, and secondary interaction products $\langle N_{prod+}\rangle$sec and $\langle N_{prod-}\rangle$sec.

Table 2A.5.2 Summary of corrected positive produced particle multiplicities $\langle N_{prod+}\rangle$final with estimated primary ($\langle N_{prod+}\rangle$prim) and secondary ($\langle N_{prod+}\rangle$sec) contributions. The corrections consider measured (m) and unmeasured (um) contributions of π's, K's, σ's, and ambiguously identified (a) particles. They include the fast positron correction $\langle N_{e+}\rangle$corr and the fast proton correction $\langle N_p\rangle$corr.

THICK FOILS

Projectile	320GeV/c		100GeV/c									
	π^-		π^+		p		π^-			p		
$^{A}_{Z}$Target	$^{108}_{47}Ag$	$^{197}_{79}Au$	$^{108}_{47}Ag$	$^{197}_{79}Au$	$^{108}_{47}Ag$	$^{197}_{79}Au$	$^{24}_{12}Mg$	$^{108}_{47}Ag$	$^{197}_{79}Au$	$^{24}_{12}Mg$	$^{108}_{47}Ag$	$^{197}_{79}Au$
BTC	61	64	131	134	141	144	176	171	174	186	181	184
N_{events}	184	127	178	128	308	110	120	604	457	75	439	277
$\langle N_{\pi+}\rangle$m	2.641	2.756	2.596	2.968	2.977	3.164	1.533	2.490	2.757	1.920	3.319	3.653
Δ	.207	.281	.189	.245	.163	.277	.149	.102	.130	.176	.144	.194
$\langle N_{K+}\rangle$m	.060	.079	.045	.086	.026	.036	.008	.028	.035	.013	.052	.065
Δ	.021	.024	.016	.025	.009	.018	.008	.007	.009	.013	.012	.017
$\langle N_{\Sigma+}\rangle$m	-	.016	-	-	.006	.018	-	.005	.011	.013	.005	.001
Δ	-	.016	-	-	.005	.013	-	.003	.005	.013	.003	.001
$\langle N_{a+}\rangle$m	5.087	5.260	4.000	4.313	4.357	4.309	2.642	3.369	3.545	3.253	3.861	4.148
Δ	.247	.348	.160	.205	.129	.236	.156	.085	.107	.244	.119	.145
$\langle N_{prod+}\rangle$m	7.788	8.110	6.640	7.367	7.367	7.527	4.183	5.892	6.348	5.200	7.237	7.870
Δ	.400	.576	.278	.389	.246	.443	.227	.166	.201	.331	.229	.294
$\langle N_{a+}\rangle$um	.125	.268	.062	.125	.104	.127	.058	.103	.142	.027	.144	.155
Δ	.030	.096	.024	.041	.021	.034	.024	.016	.020	.019	.023	.028
$\langle N_{prod+}\rangle$m+um	7.913	8.378	6.702	7.492	7.471	7.655	4.242	5.995	6.490	5.227	7.380	8.025
Δ	.411	.610	.280	.398	.251	.453	.229	.165	.207	.337	.235	.304
$-\langle N_{e+}\rangle$corr	-1.266	-1.782	-.934	-1.396	-1.118	-1.324	-.295	-.879	-1.151	-.372	-1.162	-1.446
Δ	.080	.111	.076	.112	.061	.126	.030	.043	.059	.044	.059	.086
$\langle N_{prod+}\rangle$subfinal	6.647	6.596	5.768	6.096	6.353	6.331	3.947	5.116	5.339	4.855	6.218	6.579
Δ	.419	.620	.290	.413	.258	.470	.231	.171	.215	.340	.242	.316
$-\langle N_p\rangle$corr					-1.485	-1.487		-1.046	-1.131		-.414	-.591
$\langle N_{prod+}\rangle$final					4.868	4.844		4.070	4.208		5.804	5.985
$\langle N_{prod+}\rangle$prim					4.683	4.674		3.911	4.065		5.583	5.782
$\langle N_{prod+}\rangle$sec					.185	.170		.159	.143		.221	.203

Table 2A.5.2 Continued.

THIN FOILS

Projectile	320GeV/c		100GeV/c									
	π^-		π^+		p		π^-			p		
$^{A}_{Z}Target$	$^{108}_{47}Ag$	$^{197}_{79}Au$	$^{108}_{47}Ag$	$^{197}_{79}Au$	$^{108}_{47}Ag$	$^{197}_{79}Au$	$^{24}_{12}Mg$	$^{108}_{47}Ag$	$^{197}_{79}Au$	$^{24}_{12}Mg$	$^{108}_{47}Ag$	$^{197}_{79}Au$
BTC	62	63	132	133	142	143	175	172	173	185	182	183
N_{events}	137	135	124	112	169	129	224	406	403	181	276	280
$\langle N_{\pi^+}\rangle$m	2.365	2.844	2.565	2.696	2.769	2.465	1.339	2.221	2.266	1.625	2.833	2.982
Δ	.226	.265	.247	.238	.205	.207	.108	.106	.119	.122	.161	.168
$\langle N_{K^+}\rangle$m	.015	.037	.032	-	.047	.008	.013	.047	.037	.039	.040	.016
Δ	.010	.019	.016	-	.018	.008	.008	.012	.010	.016	.012	.013
$\langle N_{\Sigma^+}\rangle$m	-	.007	-	.009	.006	.016	.004	.002	.002	-	.004	.004
Δ	-	.007	-	.009	.106	.011	.004	.003	.002	-	.004	.004
$\langle N_{a^+}\rangle$m	5.109	5.578	4.040	4.027	4.355	4.419	2.634	3.227	3.434	2.994	3.500	3.611
Δ	.264	.337	.185	.186	.174	.225	.112	.104	.111	.140	.132	.146
$\langle N_{prod^+}\rangle$m	7.489	8.467	6.637	6.732	7.178	6.907	3.991	5.498	5.739	4.657	6.377	6.643
Δ	.432	.527	.365	.374	.326	.362	.175	.178	.203	.219	.262	.279
$\langle N_{a^+}\rangle$um	.088	.141	.073	.089	.047	.132	.049	.074	.127	.066	.098	.151
Δ	.028	.055	.026	.030	.018	.042	.016	.017	.023	.023	.024	.029
$\langle N_{prod^+}\rangle$m+um	7.577	8.607	6.710	6.821	7.225	7.039	4.040	5.571	5.866	4.724	6.475	6.796
Δ	.440	.547	.370	.384	.330	.372	.178	.182	.209	.223	.268	.287
$-\langle N_{e^+}\rangle$corr	-.368	-.613	-.226	-.319	-.319	-.377	-.094	-.221	-.315	-.072	-.319	-.402
Δ	.051	.061	.060	.075	.043	.053	.016	.032	.035	.025	.039	.045
$\langle N_{prod^+}\rangle$subfinal	7.209	7.994	6.484	6.502	6.906	6.662	3.946	5.350	5.551	4.652	6.156	6.394
Δ	.443	.550	.375	.391	.333	.376	.179	.185	.212	.224	.271	.291
$-\langle N_p\rangle$corr					-1.523	-1.659		-1.042	-1.081		-.183	-.691
$\langle N_{prod^+}\rangle$final					5.383	5.003		4.308	4.470		5.673	5.703
$\langle N_{prod^+}\rangle$prim					5.297	4.938		4.243	4.416		5.588	5.635
$\langle N_{prod^+}\rangle$sec					.086	.065		.065	.054		.085	.068

Table 2A.5.3 Summary of corrected negative produced particle multiplicities $\langle N_{prod-}\rangle$final with estimated primary ($\langle N_{prod-}\rangle$prim) and secondary ($\langle N_{prod-}\rangle$sec) contributions. The corrections consider measured (m) and unmeasured (um) contributions of π's, K's, σ's, and ambiguously identified (a) particles. They include the fast electron correction $\langle N_{e-}\rangle$corr.

THICK FOILS

Projectile	320GeV/c		100GeV/c									
	π^-		π^+		p		π^-			p		
A Z Target	$^{108}_{47}Ag$	$^{197}_{79}Au$	$^{108}_{47}Ag$	$^{197}_{79}Au$	$^{108}_{47}Ag$	$^{197}_{79}Au$	$^{24}_{12}Mg$	$^{108}_{47}Ag$	$^{197}_{79}Au$	$^{24}_{12}Mg$	$^{108}_{47}Ag$	$^{197}_{79}Au$
BTC	61	64	131	134	141	144	176	171	174	186	181	184
N_{events}	184	127	178	128	308	110	120	604	457	75	439	277
$\langle N_{\pi-}\rangle$m	2.750	3.031	2.388	3.023	2.918	3.263	1.275	2.632	2.849	1.893	3.177	3.765
Δ	.203	.285	.166	.266	.151	.280	.122	.104	.124	.203	.149	.197
$\langle N_{K-}\rangle$m	.005	.008	.006	.031	.003	-	.008	.010	.004	-	.009	.011
Δ	.005	.008	.006	.019	.003	-	.008	.005	.003	-	.005	.006
$\langle N_{\Sigma-}\rangle$m	-	-	.006	-	.003	-	-	.002	.007	-	.002	-
Δ	-	-	.006	-	.003	-	-	.002	.004	-	.002	-
$\langle N_{\pi-}\rangle$m	4.962	4.961	2.775	2.875	2.744	2.655	3.258	3.409	3.470	3.560	3.872	4.184
Δ	.191	.262	.120	.154	.101	.156	.165	.068	.079	.180	.091	.117
$\langle N_{prod-}\rangle$m	7.717	8.000	5.174	5.930	5.669	5.918	4.542	6.053	6.330	5.453	7.360	7.960
Δ	.347	.499	.227	.350	.205	.361	.217	.134	.168	.291	.195	.259
$\langle N_{a-}\rangle$um	.092	.181	.096	.094	.078	.118	.083	.089	.153	.053	.103	.191
Δ	.025	.070	.027	.028	.015	.044	.035	.015	.029	.032	.018	.036
$\langle N_{prod-}\rangle$m+um	7.810	8.181	5.270	6.023	5.747	6.036	4.625	6.142	6.484	5.507	7.162	8.152
Δ	.353	.526	.235	.358	.206	.372	.220	.137	.175	.295	.200	.268
$-\langle N_{e-}\rangle$corr	-1.273	-1.676	-1.071	-1.533	-1.244	-1.313	-.361	-.894	-1.147	-.512	-1.200	-1.497
Δ	.098	.132	.079	.110	.066	.126	.042	.048	.066	.047	.061	.093
$\langle N_{prod-}\rangle$subfinal	6.537	6.505	4.199	4.490	4.503	4.723	4.264	5.248	5.337	4.995	6.262	6.655
Δ	.366	.542	.248	.375	.216	.393	.224	.145	.187	.299	.209	.284
$-\langle N_{\bar{p}}\rangle$corr					-.042	-.039		-.081	-.087		-.260	-.330
$\langle N_{prod-}\rangle$final					4.461	4.684		5.167	5.250		6.002	6.325
$\langle N_{prod-}\rangle$prim					4.291	4.520		4.965	5.072		5.774	6.118
$\langle N_{prod-}\rangle$sec					.170	.164		.202	.179		.228	.215

PROD_MULTIB.TEX UND/MCKM 2Feb89

Table 2A.5.3 Continued.

THIN FOILS

Projectile	320GeV/c		100GeV/c									
	π^-		π^+		p		π^-			p		
$^{A}_{Z}$Target	$^{108}_{47}Ag$	$^{197}_{79}Au$	$^{108}_{47}Ag$	$^{197}_{79}Au$	$^{108}_{47}Ag$	$^{197}_{79}Au$	$^{24}_{12}Mg$	$^{108}_{47}Ag$	$^{197}_{79}Au$	$^{24}_{12}Mg$	$^{108}_{47}Ag$	$^{197}_{79}Au$
BTC	62	63	132	133	142	143	175	172	173	185	182	183
N_{events}	137	135	124	112	169	129	224	406	403	181	276	280
$\langle N_{\pi^-}\rangle$m	2.723	3.415	2.411	2.357	2.710	2.713	1.352	2.256	2.417	1.724	2.783	3.039
Δ	.218	.290	.220	.235	.194	.232	.103	.106	.124	.120	.168	.176
$\langle N_{K^-}\rangle$m	.015	.015	.024	-	.018	-	.004	.012	.005	.006	.007	.011
Δ	.010	.010	.014	-	.010	-	.004	.005	.003	.005	.005	.007
$\langle N_{\Sigma^-}\rangle$m	.007	-	.008	-	-	-	.009	.005	-	-	-	-
Δ	.007	-	.008	-	-	-	.006	.003	-	-	-	-
$\langle N_{a^-}\rangle$m	4.927	5.030	2.323	2.732	2.574	2.558	3.045	3.266	3.285	3.193	3.518	3.525
Δ	.230	.240	.137	.160	.135	.176	.100	.084	.084	.117	.106	.109
$\langle N_{prod^-}\rangle$m	7.672	8.459	4.766	5.089	5.302	5.271	4.411	5.539	5.707	4.923	6.308	6.579
Δ	.387	.446	.284	.318	.267	.327	.156	.151	.161	.187	.216	.230
$\langle N_{a^-}\rangle$um	.058	.119	.032	.089	.089	.124	.076	.113	.139	.061	.116	.121
Δ	.020	.033	.016	.032	.031	.035	.021	.030	.026	.019	.024	.121
$\langle N_{prod^-}\rangle$m+um	7.730	8.578	4.798	5.179	5.391	5.395	4.487	5.653	5.846	4.983	6.424	6.700
Δ	.389	.455	.287	.326	.275	.331	.158	.157	.165	.191	.222	.238
$-\langle N_{e^-}\rangle$corr	-.351	-.660	-.216	-.268	-.317	-.396	-.089	-.172	.236	-.087	-.335	-.419
Δ	.060	.060	.068	.087	.051	.063	.023	.038	.044	.033	.039	.053
$\langle N_{prod^-}\rangle$subfinal	7.379	7.918	4.582	4.911	5.074	4.999	4.398	5.481	5.610	4.896	6.089	6.281
Δ	.394	.459	.295	.337	.280	.337	.160	.162	.171	.194	.225	.244
$-\langle N_{\bar{p}}\rangle$corr					-.058	-.047		-.114	-.073		-.268	-.360
$\langle N_{prod^-}\rangle$final					5.016	4.952		5.367	5.537		5.821	5.921
$\langle N_{prod^-}\rangle$prim					4.936	4.888		5.286	5.471		5.734	5.850
$\langle N_{prod^-}\rangle$sec					.080	.064		.081	.066		.087	.071

APPENDIX 3A

NEGATIVE BINOMIAL DISTRIBUTIONS

3A.1 BASICS

The negative binomial distribution (NBD)

$$P(n,m,k) = \frac{k(k+1)\cdots(k+n-1)}{n!}\left(\frac{k}{m+k}\right)^k\left(\frac{m}{m+k}\right)^n$$

$$= \begin{pmatrix} k+n-1 \\ k-1 \end{pmatrix}\left(\frac{k}{m+k}\right)^k\left(\frac{m}{m+k}\right)^n$$

is so named because the probabilities $P(n,m,k)$ can be extracted from successive terms from an expansion of the negative binomial

$$\left[\frac{m+k}{k} - \frac{m}{k}\right]^{-k} = \sum_{n=k}^{\infty}\begin{pmatrix} k+n-1 \\ k-1 \end{pmatrix}\left(\frac{k}{m+k}\right)^k\left(\frac{m}{m+k}\right)^n = 1$$

NBDs are 'built' mathematically to give the probability of having to wait $n+k$ trials until outcome A occurs k times and outcome B occurs n times, assuming that only the two(2) outcomes, A and B, are possible and that the probability for each at any one trial is constant. So, the NBD can be said also to give the probability of obtaining outcome A k times while waiting for outcome B to occur n times. However, NBD can be better understood if they are obtained in terms of the probability of obtaining outcome A in a single trial. If the probability of obtaining outcome A in one trial is constant and equal to p, then the probability q of obtaining the outcome B in a single trial is 1 - p if events are dichotomous and p is assumed constant. To determine the

total probability $P(u,N)$ of obtaining outcome A u times in N trials, a number of factors must be included: 1)the probability of obtaining outcome A $u-1$ times in $N-1$ trials

$$p^{u-1}$$

and 2)the probability of obtaining outcome B $(N-1)-(u-1)=N-u$ times (*i.e.* the rest of the times) in $N-1$ trials

$$(1-p)^{N-u}$$

and 3)a permutation factor

$$\frac{(N-1)!}{(u-1)!(N-u)!}$$

to include all possible orderings since it doesn't matter how the outcomes A and B are ordered in the $(N-1)$ trials as long as there are $(u-1)$ outcomes A and $(N-u)$ outcomes B, and 4) the probability p of obtaining outcome A on the N^{th} trial. Thus the probability takes the final form

$$P(u,N)=\frac{(N-1)!}{(u-1)!(N-u)!}p^u(1-p)^{N-u}=\left(\begin{array}{c}N-1\\u-1\end{array}\right)p^u(1-p)^{N-u}$$

Parameters k, $\frac{k}{m+k}$, n, $\frac{m}{m+k}$, and $n+k$ correspond to u, p, $N-u$, q, and N as follows:

k	u	the number of occurrences of outcome A
$k/(m+k)$	p	probability of outcome A in a single trial
n	$N-u$	the number of occurrences of outcome B
$m/(m+k)$	q	the probability of outcome B in a single trial
$n+k$	N	total number of trials

Since n is the produced particle multiplicity, outcome B is associated with multiparticle production, and $n+k$ is associated to the total number of trials necessary to obtain multiplicity n.

To clarify the roles of NBD parameters in multiplicity distributions, a number of potentially significant measurables such as expectation values and variances of the

n and N should be considered. The expectation value of n

$$\begin{aligned}
\langle n \rangle &= \textstyle\sum_{n=0}^{\infty} nP(n,m,k) \\
&= \textstyle\sum n \frac{(k+n-1)!}{(k-1)!n!} p^k q^n \\
n \rightarrow n+1 & \\
&= \textstyle\sum (n+1) \frac{(k+(n+1)-1)!}{(k-1)!(n+1)!} p^k q^{n+1} \\
\textit{pulling } k \textit{ out}, & \\
&= k \textstyle\sum \frac{(k+n)!}{k!n!} p^k q^{n+1} \\
\textit{under summation } k \rightarrow k-1 & \\
&= k \textstyle\sum \frac{(k+n-1)!}{(k-1)!n!} p^{k-1} q^{n+1} \\
\textit{pull } q \textit{ and } p \textit{ out} & \\
&= \tfrac{kq}{p} \textstyle\sum \frac{(k+n-1)!}{(k-1)!n!} p^k q^n \\
\textit{summation} = 1 & \\
&= \tfrac{kq}{p}
\end{aligned}$$

where $p = \frac{k}{m+k}$ and $q = \frac{m}{m+k}$ in this study so that $\langle n \rangle = k(\frac{m}{m+k})(\frac{m+k}{k}) = m$

The expectation value for the number of trials which give k outcomes A, and consequently n outcomes B, can be determined by noting that

$$N = k + n$$

so

$$\langle N \rangle = \langle k + n \rangle = \langle k \rangle + \langle n \rangle$$

since k is a constant as a fit parameter,

$$\langle N \rangle = k + \frac{kq}{p} = k + m$$

To get the variance of n, $\langle n^2\rangle - \langle n\rangle^2$, the expectation value of n^2 is needed:

$$\begin{aligned}
\langle n^2\rangle &= \sum n^2 \tfrac{(k+n-1)!}{(k-1)!n!} p^k q^n \\
\textit{factorial manipulation} & \\
&= \sum n \tfrac{(k+n-1)(k+n-2)!}{(k-1)!(n-1)!} p^k q^n \\
n \to n+1 & \\
&= \sum (n+1) \tfrac{(k+n)(k+n-1)!}{(k-1)!n!} p^k q^{n+1} \\
\textit{pulling } q \textit{ out} & \\
&= q \sum (n+1) \tfrac{(k+n)(k+n-1)!}{(k-1)!n!} p^k q^n \\
\textit{expanding } (n+1)(k+n) & \\
&= qk \sum n \tfrac{(k+n-1)!}{(k-1)!n!} p^k q^n + qk \sum \tfrac{(k+n-1)!}{(k-1)!n!} p^k q^n \\
&\quad + q \sum n^2 \tfrac{(k+n-1)!}{(k-1)!n!} p^k q^n + \sum n \tfrac{(k+n-1)!}{(k-1)!n!} p^k q^n \\
&= qk \sum \tfrac{(k+n-1)!}{(k-1)!(n-1)!} p^k q^n + qk + q\langle n^2\rangle + q\langle n\rangle \\
n \to n+1 & \\
&= q^2 k \sum \tfrac{(k+n)!}{(k-1)!n!} p^k q^n + qk + q\langle n^2\rangle + q\langle n\rangle \\
&= q^2 k \sum \tfrac{(k+n)(k+n-1)!}{(k-1)!n!} p^k q^n + qk + q\langle n^2\rangle + q\langle n\rangle \\
&= q^2 k \langle N\rangle + qk + q\langle n^2\rangle + q\langle n\rangle \\
\textit{collecting } \langle n^2\rangle \textit{ terms} & \\
&= \tfrac{1}{1-q}(q^2 k(k + \langle n\rangle) + q(k + \langle n\rangle)) \\
&= (k + \langle n\rangle)^{\frac{q^2 k + q}{p}} \\
&= (k + \langle n\rangle)^{\frac{q^2 k^2 + qk}{kp}} \\
&= \tfrac{q^2 k^2 + qk}{p^2}
\end{aligned}$$

so the variance is

$$\langle n^2\rangle - \langle n\rangle^2 = \frac{q^2 k^2 + qk}{p^2} - \frac{q^2 k^2}{p^2} = \frac{qk}{p^2} = \frac{m}{p}$$

In finding another expression for the variance $\langle N^2\rangle - \langle N\rangle^2$ of N

$$\begin{aligned}\langle N^2\rangle - \langle N\rangle^2 &= \langle (n+k)^2\rangle - \langle n+k\rangle^2 \\ &= \langle n^2 + 2nk + k^2\rangle - (\langle n\rangle + \langle k\rangle)^2 \\ &= \langle n^2\rangle + 2k\langle n\rangle + k^2 - \langle n\rangle^2 - 2k\langle n\rangle - k^2 \\ &= \langle n^2\rangle - \langle n\rangle^2 \\ &= \langle n\rangle \\ &= m\end{aligned}$$

When $k = 1$,

$$P(n,m,k) = \frac{(1+n-1)!}{(1-1)!n!}p^1q^n = pq^n = \frac{1}{m+1}\frac{m}{m+1})^n = \frac{m^n}{(m+1)^{n+1}}$$

and the distribution is Bose-Einstein for a single state. That implies a simple recurrence relation:

$$\frac{(n+1)P(n+1)}{P(n)} = (n+1)\frac{(1+n+1-1)!}{(1-1)!(n+1)!}p^1q^{n+1}\frac{(1-1)!n!}{(1+n-1)!1n} = (n+1)q$$

When $k \to \infty$,

$$P(n,m) \to P(n) = \frac{e^{-m}m^n}{n!} \qquad (Poisson\ distribution)$$

The probability p will be small as well as constant while the probability $(1-p)$ will be infinitely close to 1. The mean value of n as well as its variance is simply N_p , thus

$$\langle n\rangle = m \pm \sqrt{m}$$

3A.2 INTERPRETATIONS

3A.2.1 Recurrence

A general recurrence relation between P(n) and P(n+1) is simply

$$\frac{(n+1)P(n+1)}{P(n)} = (k+n)\frac{m}{m+k} = N(1-p)$$

This recurrence relation can first of all give us a means to characterize NBDs. The function

$$g(n) = \frac{(n+1)P(n+1)}{P(n)}$$

is introduced [Giovannini 86a] assuming linearity in n:

$$g(n) = a + bn$$

This function provides the relative probability for the addition of an $(n+1)th$ particle to the already n existing ones. The idea is to explore the specific dependence of this relative probability on n in order to unfold possible properties of the production mechanisms. Now when $k \to \infty$, as it does for independent emission of particles, *i.e.* Poissonian distributions with $p \to 0$,

$$g(n) \to m = \langle n \rangle$$

a result notably independent of n. This result makes sense since the production of an additional particle was assumed not to depend on n particles already present – *i.e.* independent emission of particles. When $k = 1$, as it does for identical bosons emitted in the same quantum state, the production of an additional particle is enhanced by a factor of $n + 1$ when n particles are already present,

$$g(n) = (n + 1)\frac{m}{m + 1}$$

This is consistent with Bose-Einstein statistics. It can then be assumed that each of the two terms, a and bn, stem from processes distinct from one another (one n-independent, the other n-dependent).

3A.2.2 Partial stimulated emission

The interpretation of NBD in terms of stimulated emission begins with Bose-Einstein statistics for identical bosons emitted in a common quantum state. The probability for emission of an $(n + 1)th$ boson is enhanced by a factor of $n + 1$, *i.e.*

$$g(n) = a(n + 1)$$

but, in general,

$$g(n) = a + bn = \frac{m}{m + k}(k + n)$$

with $a = \frac{m}{m+1}$ and $b = \frac{m}{m+k}$ so obviously $k = \frac{a}{b} = 1$ And of course, when $k = 1$, the NBD is the Bose-Einstein distribution of identical bosons in a single state. Now in hh or hA interactions, all bosons are not generally expected to be identical and in the same state, so groupings of bosons identical to one another and in the same state might be expected but with the type and state of the bosons varying from group to group. Thus a Bose-Einstein enhancement in the group growth is expected, *i.e.* production of new members in a given group, but n-independence in the growth of the number of groups, *i.e.*production of new groups. Since Bose-Einstein enhancement would only occur on the level of the individual groups and not on a global level, the enhancement is attributed to *partial* stimulated emission. The groupings will occur at a number of levels in a cascade. Involving parameters (such as time, effective mass of a fragmenting parton, or an energy variable) which describes depths of cascade makes the model *stochastic.* This is the view of the stochastic cell model of k identical cells which convolutes k Bose-Einstein distributions, each with mean multiplicity $\frac{\langle n \rangle}{k}$ [ ]. The basic difference is that the stochastic cell model assumes identical cells (and thus integer k) while non-identical cells (and thus continuous k as found experimentally) are of interest. But consider the characteristic function

$$g(n) = a + bn$$

in terms of the Bose-Einstein enhancement that comes only from the second term since it is the only term that depends on the number of particles. Using the cell model idea of k as the number of cells or groupings of indistinguishable same-state bosons, n particles can be said to be already present, so the average number of particles per cell is $\frac{n}{k}$. That means that the $(n+1)th$ particle will be the $(\frac{n}{k}+1)th$ particle of an average cell, which means the probability for that particle's production will be enhanced by the factor $\frac{n}{k}+1$ over that of independent emission. It is already known that for the case of independent emission, $g(n) = a$, so in this case of stimulated emission within cells which are independently produced,

$$g(n) = a(\frac{n}{k}+1)$$

Since it can be seen that $\frac{n}{k}$ is the average number of particles per cell, and thus the

average number of particles per cell that contribute to the Bose-Einstein enhancement, $\frac{1}{k}$ can be interpreted to be the fraction of all n particles already present which will participate in stimulated emission. Practically speaking then, assuming only partial stimulated emission for all particle production, specific trends with varying energy and phase space intervals can be expected. Were energy to be kept constant with widening phase space intervals, the Bose-Einstein enhancement can be expected to to weaken. The enhancement range in phase space was presumed to be finite so that, on the average, particles will not be as close in the wider interval. So $\frac{1}{k}$ is expected to decrease, or k to increase. However, if the phase space interval is fixed and the energy increased, more and more particles will be crowded into the same interval and thus will encounter more and more Bose-Einstein interference. That means $\frac{1}{k}$ will increase, or k will decrease. Even if phase space is not limited, more and more particles will be crowded into unit phase space as the energy is increased, so k will generally decrease as energy increases in any case.

3A.2.3 Cascading

Another way to interpret the NBD of produced particles is to assume no stimulated emission, only cascading as the production mechanism. By *cascading* is meant particles emitting additional particles, changing their original momentum and quantum numbers as they do so. The idea is that *ancestor* particles produce *clusters* of particles. Presumably, *ancestors* are produced independently in collisions while *cluster* development depends on the number of particles resident in the cluster. Looking again at the function

$$g(n) = a + bn$$

it is reasonable to associate a with the production of an additional particle as an additional one-particle cluster, and bn with the production of an additional particle in an existing cluster assuming that its production is proportional to the total number of particles n which have already been produced. The idea is similar to partial stimulated emission where grouping or cell production is n-independent, while production

of cell members is n-dependent. The difference lies in no specific Bose-Einstein effect. If the phase space interval is widened keeping energy constant, the n-dependence is expected to weaken since the density of particles in phase space decreases, *i.e.* the number of particles per cell, $\frac{n}{k}$, decreases and k will increase. There is no straightforward prediction for increases in energy while phase space intervals are held constant. Properties for clusters have been extracted iteratively assuming the Poissonian distribution or independent emission for the number N of clusters and n-dependent emission for the population of existing clusters [Giovannini 86]. One is the average size of the clusters, *i.e.* the number of particles which populate the average cluster

$$n_c' = -\frac{b}{(1-b)\ln(1-b)}$$

Once the average size of a cluster is known, then the average number of clusters is

$$N' = \frac{m}{n_c'}$$

and the variance is

$$\langle n_c'^2 \rangle - \langle n_c' \rangle^2 = n_c'/(1-b) - n_c'^2$$

Iif phase space is limited to domain D of rapidity or pseudorapidity, the domain boundaries could exclude members of a cluster. Since it is the number of members in a cluster that determines the strength of the n-dependence, a decrease of the number of members of clusters is associated with a decrease in b. So when domains are small, $\langle n \rangle \ll k$ and $b \ll 1$. And since $n_c'^2$ would then approach n_c' which would approach 1, then the number of clusters approaches the number of particles in a clear case of predominantly single-particle clusters. On the other hand, when domains are large, there exists a higher probability of clusters attaining within the limited domain the size they normally have in the full domain. The parameter $\langle n \rangle \ll k$ and $b \to 1$. So the clusters should be large with large dispersion:

$$n_c' \approx \frac{m}{k \ln \frac{m}{k}}$$

$$\langle n_c'^2 \rangle - \langle n_c' \rangle^2 \approx n_c'^2 (\ln \frac{m}{k} - 1)$$

LIST OF REFERENCES

Adamus 88c M. Adamus et al. (EHS/NA22) *Phase space dependence of the multiplicity distribution in π^+p and pp collisions at 250 GeV/c.* ZEITSCHRIFT FUR PHYSIK – PARTICLES AND FIELDS **C37** (1988) 215.

Adamus 88b M. Adamus et al. (EHS/NA22) *Multiplicity distributions in separated phase space intervals of π^+p collisions at 250 GeV/c.* PHYSICS LETTERS **B205** (1988) 401.

Adamus 88a M. Adamus et al. (EHS/NA22) *Multiplicity distributions in K^+Al and K^+Au collisions at 250 GeV/c and a test of the multiple collision model.* Nijmegen preprint.

Adamus 87 M. Adamus et al. (EHS/NA22) *Maximum particle densities in rapidity space of π^+p, K^+p and pp collisions at 250 GeV/c.* PHYSICS LETTERS **185** (1987) 200.

Adamus 86 M. Adamus et al. (EHS/NA22) *Cross sections and charged multiplicity distributions for π^+p, K^+p and pp interactions at 250 GeV/c.* ZEITSCHRIFT FUR PHYSIK – PARTICLES AND FIELDS **C32** (1986) 475.

Aihara 85 H. Aihara et al. (TPC) *Study of Bose-Einstein correlations in e^+e^- annihiliation at 29 GeV.* PHYSICAL REVIEW **D31** (1985) 996.

Aivazyan 88 V.V. Aivazyan et al. (EHS/NA22) *Forward-backward multiplicity correlations in π^+p, K^+p and pp collisions at 250 GeV/c.* ZEITSCHRIFT FUR PHYSIK – PARTICLES AND FIELDS **C42** (1989) 533.

Ajinenko 89 I.V. Ajinenko et al. (EHS/NA22) *Intermittency patterns in π^+p and K^+p collisions at 250 GeV/c.* PHYSICS LETTERS **B222** (1989) 306.

Ajinenko 87 I.V. Ajinenko et al. (EHS/NA22) *Indication of an onset of hard- like effects in K^+p, π^+p and pp collisions at 250 GeV/c.* Nijmegen preprint HEN-287.

Aleksejeva 62 K.I. Aleksejeva et al. IZV. AKAD. NAUK. SSR **26** (1962) 128; JOURNAL OF THE PHYSICAL SOCIETY OF JAPAN **17 A-III** (1962) 409.

Alner 87 G.J. Alner et al. (UA5) *The UA5 high energy $\bar{p}p$ simulation program.* NUCLEAR PHYSICS **B291** (1987) 445.

Alner 85 G.J. Alner et al. (UA5) *A new empirical regularity for multiplicity distributions in place of KNO scaling* PHYSICS LETTERS **B160** (1985) 199. *Multiplicity distributions in differnt pseudorapidity intervals at a cms energy of 540 GeV* PHYSICS LETTERS **B160** (1985) 193.

Alpgard 83 K. Alpgard et al. (UA5) *Forward-backward multiplicity correlations in $\bar{p}p$-collisions at $\sqrt{s}$=540 GeV.* PHYSICS LETTERS **123B** (1983) 365.

Althoff 85a M. Althoff et al. *Particle correlation observed in e^+e^- annihilations into hadrons at c.m. energies between 29 and 37 GeV.* ZEITSCHRIFT FUR PHYSIK – PARTICLES AND FIELDS **C29** (1985) 29.

Andersson 87b B. Andersson. *The FRITIOF dynamics.* Invited talk, Shandong Workshop, Jinan, China, July, 1987. Lund preprint LU TP 87-21.

Andersson 80 B. Andersson, G. Gustafson, T. Sjostrand. *How to find the gluon jets in e^+e^- annihilation.* PHYSICS LETTERS **B94** (1980) 211.

Andersson 78 B. Andersson, I. Otterlund, and E. Stenlund. *On the correlations between fast target protons and the number of hadron-nucleon collisions in high-energy hadron- nucleus reactions.* PHYSICS LETTERS **73B** (1978) 343.

Andersson 75 B. Andersson and I. Otterlund. *On the correlations between the number of heavy prongs and the number of shower particles in proton-nucleus collisions.* NUCLEAR PHYSICS **B99** (1975) 425.

Angelov 80 *Two-particle correlations of secondary protons in π^- ^{12}C interactions at 40 GeV/c.* SOVIET JOURNAL OF NUCLEAR PHYSICS **32** (1980) 700.

Ansorge 88 R.E. Ansorge et al. (UA5) *Charged particle correlations in $p\bar{p}$ collisions at c.m. energies of 200, 546 and 900 GeV.* ZEITSCHRIFT FUR PHYSIK – PARTICLES AND FIELDS **C37** (1988) 191.

Apanasenko 79 G.V. Apanasenko et al. *New interpretation of some 'anomalous' events in cosmic rays.* JETP LETTERS **30** (1979) 145.

Arata 78 N. Arata. *A cosmic-ray nuclear event of abnormally high multiplicity and large transverse momentum.* NUOVO CIMENTO **A43** (1978) 455.

Arneodo 85 M. Arneodo et al. (EMC) *Bose Einstein correlations in deep inelastic μp interactions at 280 GeV.* ZEITSCHRIFT FUR PHYSIK – PARTICLES AND FIELDS **C32** (1986) 1.

Arnold 84 R.G. Arnold et al. *Measurement of the A dependence of deep-inelastic electron scattering from nuclei.* PHYSICS REVIEW LETTERS **52** (1084) 727.

Aubert 83 J.J. Aubert et al. *The ratio of the nucleon structure functions F_2^N for iron and deuterium.* PHYSICS LETTERS **123B** (1983) 275.

Azimov 83 *A study of correlations between secondary protons produced in proton-neon interactions at 300 GeV/c.* Preprint.

Azimov 81 S.A. Azimov et al. *Forward and backward multiplicities in high-energy proton-nucleus and proton-nucleon collisions.* ZEITSCHRIFT FUR PHYSIK – PARTICLES AND FIELDS **C10** (1981) 1.

Azimov 74 *Study of pairing correlations of protons in pion-carbon interactions at 4.0 and 7.5 GeV/c.* SOVIET JOURNAL OF PHYSICS **19** (1974) 157.

Balatoni 56 J. Balatoni and A. Renyi. PUB MATH INST HUNGARIAN ACAD SC 1 (1956) 9.

Bardadin 63 M. Bardadin et al. PROCEEDINGS OF THE SIENNA CONFERENCE ON ELEMENTARY PARTICLES, 1963, p. 628.

Bayukov 81 Y. Bayukov et al. *Correlation of cumulative baryons at small relative momenta.* SOVIET JOURNAL OF NUCLEAR PHYSICS **34** (1981) 54.

Bialas 90 A. Bialas. *Intermittency parameters as a possible signal for quark-gluon plasma formation.* CERN preprint CERN-TH-5754/90.

Bialas 88 A. Bialas and R. Peschanski. *Intermittency in multiparticle production at high energy.* NUCLEAR PHYSICS **B308** (1988) 857-867.

Bialas 86b A. Bialas and R. Peschanski. *Moments of rapidity distributions as a measure of short-range fluctuations in high-energy collisions.* NUCLEAR PHYSICS **B273** (1986) 703.

Bialas 86a A. Bialas and A. Szczerba. *Decay angular distribution of clusters and forward-backward correlations in the Giovannini-Van Hove model.* Paper presented at THE XVII INTERNATIONAL SYMPOSIUM ON MULTIPARTICLE DYNAMICS, SEEWINKEL, AUSTRIA, JUNE 1986. Jagellonian preprint TPJU 18/86 (September 1986).

Biswas 76 N.N. Biswas et al. *Direct evidence for the Bose-Einstein effect in inclusive two-particle reaction correlations.* PHYSICAL REVIEW LETTERS **35** (1976) 175.

Bowler 87b M.G. Bowler. *Bose-Einstein correlations and isospin.* PHYSICS LETTERS **B197** (1987) 443.

Breakstone 86 A. Breakstone et al. *Multiplicity dependence of the average transverse momentum and of the particle source size in p-p interactions at $\sqrt{s}$=62, 44 and 31 GeV.* CERN preprint CERN/EP 86-132 (12 September 1986).

Buschbeck 88 B. Buschbeck, P. Lipa, and R. Peschanski. *Signal for intermittency in e^+e^- reactions obtained from negative binomial fits.* PHYSICS LETTERS **B215** (1988) 788.

Burnett 83 T.H. Burnett et al. (JACEE) *Extremely high multiplicities in high-energy nucleus-nucleus collisions.* PHYSICAL REVIEW LETTERS **50** (1983) 2062.

Capella 83b A. Cappela and J. Tranh Van. *Forward-backward correlations at SPS energies and the nature of multiple scattering.* ZEITSCHRIFT FUR PHYSIK – PARTICLES AND FIELDS **C18** (1983) 85.

Capella 82e A. Capella and J. Tran Thanh Van *Forward-backward correlations at SPS energies and the nature of multiple- scattering.* ZEITSCHRIFT FUR PHYSIK – PARTICLES AND FIELDS **C18** (1983) 85.

Carlson 84 P. Carlson. Proceedings of the 4th Workshop on $\bar{p}p$ Collider Physics, Bern, 1984. CERN Yellow Report 84-09 (1984).

Carruthers 90 P. Carruthers et al. *Multiplicity fluctuations in finite rapidity windows: intermittency or quantum statistical correlation?* PHYSICS LETTERS **B222** (1989) 487.

Carruthers 89 P. Carruthers. *Fractal structures and correlations in hadronic multiparticle distributions.* INTERNATIONAL JOURNAL OF MODERN PHYSICS **A4** (1989) 5587.

Carruthers 85 P. Carruthers and C. Shih. *Statistical interpretation of the correlations between forward and backward hadrons at collider energies.* PHYSICS LETTERS **B165** (1985) 209.

Chacon 88 A.D. Chacon et al. *Observation of a nonspherical pion source in relativistic heavy-ion collisions.* PHYSICAL REVIEW LETTERS **60** (1988) 780.

Cocconi 74 G. Cocconi. *Second-order interference as a tool for the determination of hadron fireball dimensions.* PHYSICS LETTERS **49B** (1974) 459.

Dahlqvist 89 P. Dahlqvist, B. Andersson, and G. Gustafson. *Intermittency and multifractal structures in QCD cascades.* NUCLEAR PHYSICS – PARTICLES AND FIELDS **B328** (1989) 76.

De Marzo 84 C. De Marzo et al. *Measurement of the average transverse momentum and of the pion-emission volume in proton-nucleus and antiproton-nucleus reactions at 200 GeV.* PHYSICAL REVIEW **D29** (1984) 363.

De Marzo 82 C. De Marzo et al. *Multiparticle production on hydrogen, argon, and xenon targets in a streamer chamber by 200-Gev/c proton and antiproton beams.* PHYSICAL REVIEW **D26** (1982) 1019.

Derado 90 I. Derado et al. (EMC) *Investigation of intermittency in muon-proton scattering at 280 GeV.* ZEITSCHRIFT FUR PHYSIK – PARTICLES AND FIELDS **C47** (1990) 23.

Derrick 86 M. Derrick et al. (HRS) *Rapidity dependence of the charged particle multiplicity distributions in e^+e^- annihilations at 29 GeV.* PHYSICS LETTERS **B168** (1986) 299.

Derrick 86 M. Derrick et al. (HRS) *Charged particle multiplicity distributions in e^+e^- annihilation at 29 GeV: A comparison with hadronic data.* ZEITSCHRIFT FUR PHYSIK – PARTICLES AND FIELDS **C35** (1987) 323.

Dias de Deus 87 J. Dias de Deus. *Intermittency model for rapidity particle density fluctuations.* PHYSICS LETTERS **B194** (1987) 297.

Dremin 89b I.M. Dremin. *Multifractality of inelastic events.* Fermilab preprint FERMILAB-PUB-89/71-T (10 March 1989).

Dremin 89a I.M. Dremin. *Multifractality and intermittency in multiparticle production.* Notre Dame seminars (2 March 1989).

Dremin 88 I.M. Dremin. *The fractal correlation measure for multiple production.* MODERN PHYSICS LETTERS **A3** (1988) 1333.

Dremin 87 I.M. Dremin. *Fluctuations, intermittency and fractal dimensions in multiple production.* PROCEEDINGS OF THE XVIII INTERNATIONAL SYMPOSIUM ON MULTIPARTICLE DYNAMICS, TASHKENT, USSR, SEPTEMBER 8-12, 1987, p.161.

Eckmann 85 J.-P. Eckmann and D. Ruelle. *Ergodic theory of chaos and strange attractors.* REVIEWS OF MODERN PHYSICS **57** (1985) 617.

Elcombe 82 P. Elcombe. Minutes of the E597 Collaboration Meeting, Fermilab, 22 Dec 82, Camb-E597 Note 9.

Elias 80 J.E. Elias et al. *Experimental study of multiparticle production in hadron-nucleus interactions at high energy.* PHYSICAL REVIEW **D22** (1980) 13.

Ericson 86 M. Ericson. *The EMC effect and the swelling of nucleons in nuclei.* CERN preprint CERN-TH.4485/86 (July 1986).

Fialkowski 86c K. Fialkowski. *Forward-backward correlations in hadron-nucleus collisions.* Preprint.

Fialkowski 86b K. Fialkowski *A note on multiplicity distributions in rapidity intervals in the hadron-nucleus collisions.* PHYSICS LETTERS **B191** (1987) 191.

Fialkowski 86a K. Fialkowski. *Multiplicity distribution in rapidity intervals and the minimal model.* Lund preprint LU TP 86-4 (March 1986).

Fialkowski 82 K. Fialkowski and W. Kittel. *Parton models of low momentum transfer processes.* Review article on request from REPORTS ON PROGRESS IN PHYSICS. Nijmegen preprint HEN-82-226.

Fowler 88 G.N. Fowler et al. *Rapidity scaling of multiplicity distributions in a quantum-statistical approach.* PHYSICAL REVIEW **D37** (1988) 3127.

Fung 78 S.Y. Fung et al. *Observation of pion interferometry in relativistic nuclear collisions.* PHYSICS REVIEW LETTERS **41** (1978) 1592.

Geich-Gimbel 85 Ch. Geich-Gimbel. *The quark structure of matter.* Bonn preprint Bonn-HE-85-36 (1985).

Giovannini 86a A. Giovannini and L. Van Hove *Negative binomial multiplicity distributions in high energy hadron collisions.* ZEITSCHRIFT FUR PHYSIK – PARTICLES AND FIELDS **C30** (1986) 391.

Glauber 63 R.J. Glauber. *Coherent and incoherent states of the radiation field.* PHYSICAL REVIEW **131** (1963) 2766.

Goldhaber 60 G. Goldhaber, S. Goldhaber, W. Lee, and A. Pais. *Influence of Bose-Einstein statistics on the antiproton-proton annihilation process.* PHYSICAL REVIEW **120** (1960) 300.

Grässler 87 M. Grassler. (NA22) *Forward-backward multiplicity correlations in π^+ and K^+p collisions at 250 GeV/c.* PROCEEDINGS OF THE XVIII INTERNATIONAL SYMPOSIUM ON MULTIPARTICLE DYNMAICS, TASHKENT, SEPTEMBER 1987.

Grässler 83 M. Grassler. *Multiplicities of secondary hadrons produced in νp and $\bar{\nu} p$ charged current interactions.* NUCLEAR PHYSICS **B223** (1983) 269.

Grishin 87 V.G. Grishin et al. *Observation of $\pi^o\pi^o$- interference effect and size of neutral pion emission volume in $\pi^- Xe$- interactions at 3.5 GeV/c.* SOVIET JOURNAL OF NUCLEAR PHYSICS **47** (1988) 278.

Grishin 71 V.G. Grishin, G.I. Kopylov, and M.I. Podgoretskii. *Interference of identical particles in processes involving excited nuclei and resonances.* SOVIET JOURNAL OF NUCLEAR PHYSICS **13** (1971) 638.

Gurtu 74 A. Gurtu et al. Multiplicity in proton nucleus interactions at 200 GeV/c PHYSICS LETTERS **50B** (1974) 391.

Gyulassy 90 M. Gyulassy. *Is intermittency casued by Bose-Einstein interference?* FESTSCHRIFT LEON VAN HOVE. eds. A. Giovannini and W. Kittel. (World Scientific, 1990), p. 479.

Gyulassy 84 M. Gyulassy et al. *Deflagrations and detonations as a mechanism of hadron bubble growth in supercooled quark-gluon plasmas.* NUCLEAR PHYSICS **B237** (1984) 477.

Gyulassy 79 M. Gyulassy, S.K. Kauffmann, and L. Wilson. *Pion interferometry of nuclear collisions. I. Theory.* PHYSICAL REVIEW **C20** (1979) 2267.

Hagedorn 65 R. Hagedorn. *Statistical thermodynamics of strong interactions at high energies.* NUOVO CIMENTO SUPPL. **3** (1965) 147.

Hanbury Brown 56 R. Hanbury Brown and R.Q. Twiss. NATURE **177** (1956) 27 and **178** (1956) 1046.

Hausdorff 19 MATHEMATICA ANNALES **79** (1919) 157.

Hwa 89c R.C. Hwa. *Self-similarity in multiplicity fluctuations.* Oregon preprint OITS 430 (November 1989).

Hwa 89b R.C. Hwa. *Fractal measures in multiparticle production.* PHYSICS REVIEW **D41** (1990) 1456.

Jaffe 84 R. Jaffe, F. Close, R. Roberts, and G. Ross. *On the nuclear dependence of electroproduction.* PHYSICS LETTERS **134B** (1984) 449.

Jain 81 P.L. Jain and G. Das. *Correlations in multiparticle production.* PHYSICAL REVIEW **D23** (1981) 2506.

Jaiswal 70 A.K. Jaiswal and C.L. Mehta. *Photon counting statistics of harmonic signal mixed with thermal light. I. Single photoelectron counting.* PHYSICAL REVIEW **A2** (1970) 168.

Khinchin 57 A. Ya. Khinchin. *Mathematical foundations of information theory.* Dover (NY: 1957).

Kittel 90 W. Kittel. (EHS/NA22) *Low p_T intermittency in π^+p and K^+p collisions at 250 GeV/c.* Paper presented at THE SANTA FE WORKSHOP ON INTERMITTENCY IN HIGH-ENERGY COLLISIONS, MARCH 18-21, 1990.

Kittel 87b W. Kittel et al. (EHS/NA22) *Soft and semi-hard hadronic compared to e^+e^- and lh collisions.* Invited review talk at THE XVIII INTERNATIONAL SYMPOSIUM ON MULTIPARTICLE DYNAMICS, TASHKENT, SEPTEMBER 1987. Nijmegen preprint HEN-292.

Kittel 87a W. Kittel et al. (EHS/NA22) *Results from NA22 (π^+p, K^+p and pp collisions at 250GeV/c).* Invited summary talks at THE SHANDONG WORKSHOP ON MULTIPARTICLE PRODUCTION, JINAN, CHINA, 7 JULY TO 28 JUNE 1987. Nijmegen preprint, HEN-293.

Koonin 77 S.E. Koonin. *Proton pictures of high-energy nuclear collisions.* PHYSICS LETTERS **70B** (1977) 43.

Kopylov 73 G.I. Kopylov and M.I. Podgoretskii. *Multiple production and interference of particles emitted by moving sources.* SOVIET JOURNAL OF NUCLEAR PHYSICS **18** (1974) 336.

Lachs 65 G. Lachs. *Theoretical aspects of mixtures of thermal and coherent radiation.* PHYSICAL REVIEW **138** (1965) 1012.

Lednicky 82 R. Lednicky and V.L. Lyuboshits. *Effect of the final- state interaction on pairing correlations of particles with small relative momenta.* SOVIET JOURNAL OF NUCLEAR PHYSICS **35** (1982) 770.

Ledoux 86 R.J. Ledoux et al. (E565) *Leading particle distributions in 200AGeV/c p+A interactions.* Preprint.

Lu 81 J.J. Lu et al. *Exploratory studies on relativistic heavy-ion central collisions.* PHYSICS REVIEW LETTERS **46** (1981) 898.

Mandelbrot 77 B. Mandelbrot. *Physical objects with fractional dimension: seacoasts, galaxy clusters, turbulence and soap.* Fluid dynamics. R. Bialian, J.-L. Peube, Eds. Gordon and Breach (London: 1977), p. 555.

Mandelbrot 74 B. Mandelbrot. *Intermittent turbulence in self- similar cascades: divergence of high moments and dimension of the carrier.* JOURNAL OF FLUID MECHANICS **62** (1974) 331.

Marutyan 79 N.A. Marutyan et al. *Separation of jets by the relative-density method.* SOVIET JOURNAL OF NUCLEAR PHYSICS **29** (1979) 804.

Meijers 87 F. Meijers. *Multiplicities in phase space intervals and Bose-Einstein correlations in hadronic interactions at 250 GeV/c.* Ph.D. Dissertation, University of Nijmegen, May 1987.

Navelet 85 H. Navelet and R. Peschanski. Saclay preprint SPhT/85/102.

Neale 74 W. W. Neale. *Enriched particle beams for the bubble chambers at FNAL.* Fermilab Report FN-259 (June 1974).

Nikolaev 81 N.N. Nikolaev. *Quarks in high-energy interactions of hadrons, photons, and leptons with nuclei.* SOVIET PHYSICS USPEKHI **24** (1981) 531.

Nilsson 80 G. Nilsson and E. Stenlund *A Calculation of ν-distributions in hadron-nucleus interactions.* Lund preprint LU-TP 80-9, LUIP 8001 (October 1980).

Nilsson-Almqvist 86a B. Nilsson-Almqvist. *The Lund model for low-pt hadronic reactions.* PROCEEDINGS OF THE XVII INTERNATIONAL SYMPOSIUM ON MULTIPARTICLE DYNAMICS 1986, SEEWINKEL, AUSTRIA, JUNE 1620, 1986.

Nilsson-Almqvist 86b B. Nilsson-Almqvist and E. Stenlund. *Interactions between hadrons and nuclei. The Lund Monte Carlo. FRITIOF Version 1.6* Lund preprint LU-TP 86-14, August 1986.

Paladin 87 G. Paladin and A. Vulpiani. *Anomalous scaling laws in multifractal objects.* PHYSICS REPORTS **4** (1987) 147.

Pernegr 60 J. Pernegr, V. Simak, and M. Votruba. *On the momentum spectra of particles in cosmic ray jets.* NUOVO CIMENTO **17** (1960) 129.

Peschanski 87 . R. Peschanski. *Intermittency patterns in hadron multiproduction.* PROCEEDINGS OF THE XVIII INTERNATIONAL SYMPOSIUM ON MULTIPARTICLE DYNAMICS, TASHKENT, USSR, SEPTEMBER 8-12, 1987, p.149.

Ranft 88 J. Ranft. *Hadron production in hadron-nucleus and nucleus -nucleus collisions in a dual parton model modified by a formation zone intranuclear cascade.* ZEITSCHRIFT FUR PHYSIK – PARTICLES AND FIELDS **C43** (1989) 439.

Ranft 85 J. Ranft and S. Ritter. *Rapidity ratios, Feynman-x distributions and forward-backward correlations in hadron-nucleus collisions in a dual Monte-Carlo multi-chain fragmentation model.* ZEITSCHRIFT FUR PHYSIK – PARTICLES AND FIELDS **C27** (1985) 569.

Rushbrooke 83 J.G. Rushbrooke. 6th High Energy Heavy Ion Study, Berkeley, 1983.

Shephard 73 W. D. Shephard, J. M. Bishop, E. Fokitis. *Magnetic field of the 30-inch hydrogen bubble chamber at NAL: Report on results of fringe-field measurements and central-field measurements.* Notre Dame preprint NDHEP 73-9 Revised (May 1973).

Siemiarczuk 67 T. Siemiarczuk and P. Zielinski. *Correlated proton pairs in a high energy nuclear reaction.* PHYSICS LETTERS **24B** (1967) 675.

Sjostrand 85 T. Sjostrand. *The Lund Monte Carlo for jet fragmentation and e^+e^- physics – JETSET version 6.2.* Lund preprint LU TP 85-10 (October 1985).

Solmitz 66 F.T. Solmitz, A.D. Johnson, and T.B. Day. *Three view geometry program.* 2nd Edition. Lawrence Radiation Laboratory, Alvarez Group Programming Note P-117 (20 June 1966).

Stenlund 88 E. Stenlund et al. (EMU01) PROCEEDINGS OF THE CONFERENCE ON QUARK MATTER '88, LENNOX, SEPTEMBER 1988.

Uhlig 78 S. Uhlig et al. *Observation of charged particle correlations between the forward and backward hemispheres in pp collisions at ISR energies.* NUCLEAR PHYSICS **B132** (1978) 15.

Van Hal 87 P. Van Hal. *Particle production in hadron-proton interactions at 250 GeV/c incident beam momentum.* Ph.D. Dissertation, University of Nijmegen, 1987.

Van Hove 84 L. Van Hove. *Two problems concerning hot hadronic matter and high energy collisions (Equilibrium formation, plasma deflagration)* ZEITSCHRIFT FUR PHYSIK – PARTICLES AND FIELDS **C21** (1984) 93.

Verbeure 83 F. Verbeure et al. (NA22) *Multiple collisions inside nuclei in π^+ and K^+ interactions with Al and Au nuclei at 250GeV/c.* PROCEEDINGS OF THE XIVTH INTERNATIONAL SYMPOSIUM ON MULTIPARTICLE DYNAMICS, GRANLIBAKKEN, LAKE TAHOE, CALIFORNIA, JUNE 22-27, 1983.

Ward 88 D.R. Ward. *Properties of soft proton antiproton collisions.* CERN preprint CERN/EP/87-178 (29 September 1987).

Ward 86 D.R. Ward. WORKSHOP ON PHYSICS SIMULATION AT HIGH ENERGIES, MADISON, 1986. Preprint CERN/EP 86-80 (1986).

Wosiek 77 B. Wosiek. *Correlations in hadron-nucleus collisions.* ACTA PHYSICA POLONICA **B8** (1977) 493.

Zarbakhsh 81 F. Zarbakhsh et al. *Correlations at small relative momenta among protons produced in collisions of 1.8 GeV/nucleon ^{40}Ar with a KCl target.* PHYSICAL REVIEW LETTERS **46** (1981) 1268.